JOURNAL OF THE
MYANMAR ACADEMY OF
ARTS AND SCIENCE

Physics

Vol. XVIII, No.2B, July, 2020

Myanmar Academy of Arts and Science

Journal of the Myanmar Academy of Arts and Science

Vol. XVIII, No.2B

Contents

Physics

Edition

2020, July, 1000 Copies

Published by

Dr Aung Min (00322) Chairman, Journal Publication Committee,
Myanmar Academy of Arts and Science

ISSN 2520-0186
LCCN 2003-323143

Printed by

U Win Aung (00171), Manager,
Universities Press, Yangon, Myanmar

J. Myanmar Acad. Arts Sci. 2020 **Vol. XVIII.No.2**B

COMPARISON OF CHARACTERIZATION OF $BaSnO_3$ POWDER AND $BaSnO_3$ FILM

Mi Aye Aye Mon Hlaing[1], Myo Myat Kyaw, San San Wai

Abstract

Barium stannate was prepared from Barium Carbonate and Tin (IV) Oxide by using solid state reaction method had been grown on glass substrate by using spin coating method. Barium Stannate powder and Barium Stannate film were characterized by Scanning Electron Microscopy (SEM) and X-ray diffraction (XRD). The crystallite size was investigated from XRD result and the grain size was investigated from SEM result. From calculation, compare the value of crystallite size and grain size of powder sample and film of Barium Stannate.

Keywords: Stannate, X-ray diffraction (XRD) and Scanning Electron Microscope (SEM)

Introduction

Barium Stannate is normally referred to as $BaSnO_3$. $BaSnO_3$ is the best known, the most thoroughly investigated and the most useful compound. Barium Stannate belong to the perovskite group of compounds. These compounds pose a similar structure as that of the mineral perovskite $CaTiO_3$. Such compound has a structure formula which can be generalized as A^{2+} B^{4+} O_3 where A is an alkaline earth (group IIA) metal element or a transition metal element in +2 oxidation state and B is a transition metal element [Doan Tuan Anh, (2017)]. $BaSnO_3$ has an ideal cubic structure with space group Pm3M and is an n-type semiconductor with a band gap. $BaSnO_3$ of unit cells are composed of cubes [Cerda, J.,(2002)]. $BaSnO_3$ is a nearly colorless compound with a weak tings of yellow. $BaSnO_3$ with cubic perovskite structure exhibits good dielectric properties. Because of these characteristic properties of $BaSnO_3$ is becoming more and more important on material technology, It can be used to prepare thermally stable capacitor. In recent years $BaSnO_3$ has been found to be a very promising sensor material and has therefore received most attention. A suitable synthesis route for preparing $BaSnO_3$ powder has high specific surface area. $BaSnO_3$ will be attempted so that the fabricated gas sensor can exhibit sensitivity and selectivity$BaSnO_3$ can be used to fabricate multilayer capacitors and boundary layer capacitors [Deepa, A.S., (2011)]. The application of Barium Stannate is a sensor material.

Experimental Details

Sample preparation of $BaSnO_3$ powder and film

Firstly, the required powders (which will be selected to use in this research) were collected. To prepare the Barium Stannate, Barium Carbonate and Tin (IV) oxide powders were selected as the starting material. XRD was used to determine the phase purity of the powders. In the second stage, dry Barium Carbonate powders and Tin (IV) oxide powders were mixed by stoichiometric amounts, weighed with digital balance. Each of the powders stoichiometric amount of (1:1) was used, 28.3492g of $BaCO_3$ powders were mixed 21.6508 of SnO_2 powders. And then, the mixed powder was ground by an agate mortar and pastel for three days to be homogeneous and fine powder. The fine powder was heated 1150 ºC for two hours to remove carbon dioxide. The sample $BaSnO_3$ powders were prepared by this procedure. The last stage,

---

[1] Dr, Lecturer, Department of Physics, Loikaw Unversity

[2] Lecturer, Department of Physics, Loikaw University

[3] Professor, Department of Physics, Loikaw Unversity

Barium Stannate powder was deposited at room temperature by spin coating method using glass substrate. Glass substrates were cleaned with acetone an washed with distilled water for ten minutes and dried in air. And then $BaSnO_3$ powder added with 2methoxyethanol at 100 ºC for six hours. The $BaSnO_3$ films were deposited from the precursor solution. These films were annealed at 350 ºC for one hour. Fig (1) shows the flow chart of the preparation of $BaSnO_3$ sample.

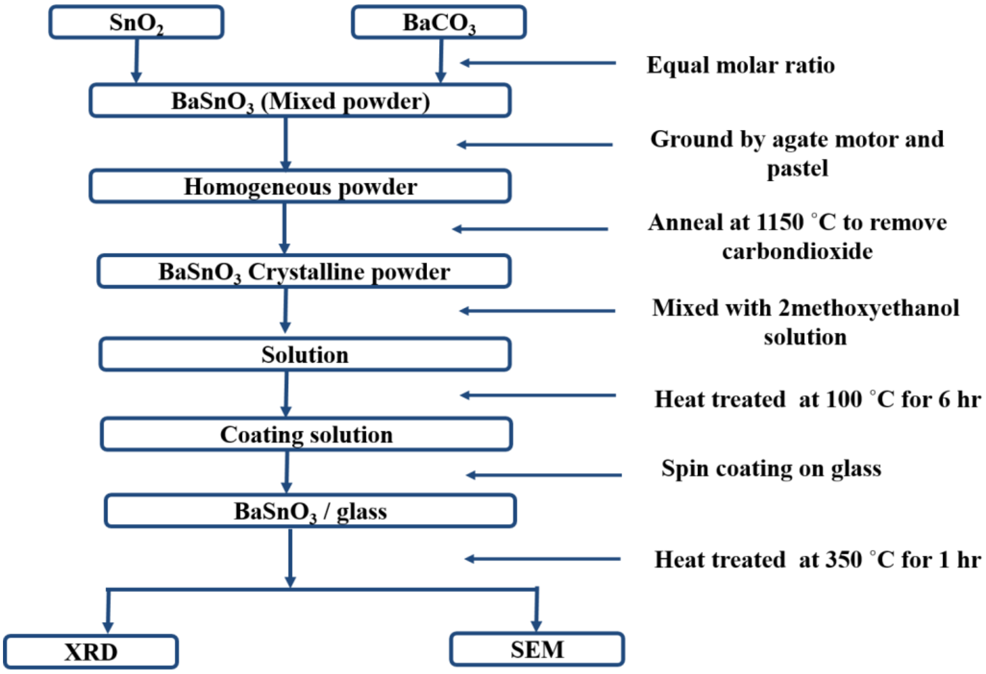

Figure 1 Flow chart of the preparation of $BaSnO_3$ sample

XRD Characterization of the Sample

These $BaSnO_3$ powder and film were analyzed by X-ray diffraction at room temperature is used to investigate structural properties of crystalline materials. XRD patterns of $BaSnO_3$ samples were observed by RIGAKU MULTIFLEX X-ray Diffractometer.

SEM Characterization of the Sample

$BaSnO_3$ powder and film samples were investigated by SEM image. They were required to get the information of the interconnectivity between grains, porosity and surface morphology. SEM micrographs of $BaSnO_3$ powder and film were observed by JEOL JSM_5610LV Scanning Electron Microscope.

Results and Discussions

XRD Analysis of $BaSnO_3$ Powder and Film Sample

Fig (2) shows the powder XRD pattern of $BaSnO_3$. It was found that the many sharp peaks appeared in which the most sharp peaks (dominant) is (110) plane at diffraction angle 30.91 º. They were complete agreement with standard XRD pattern of $BaSnO_3$ (JCPDS card no. 00-015-0780) indicating the formation of crystalline phase pure $BaSnO_3$. $BaSnO_3$ powder sample was cubic structure.

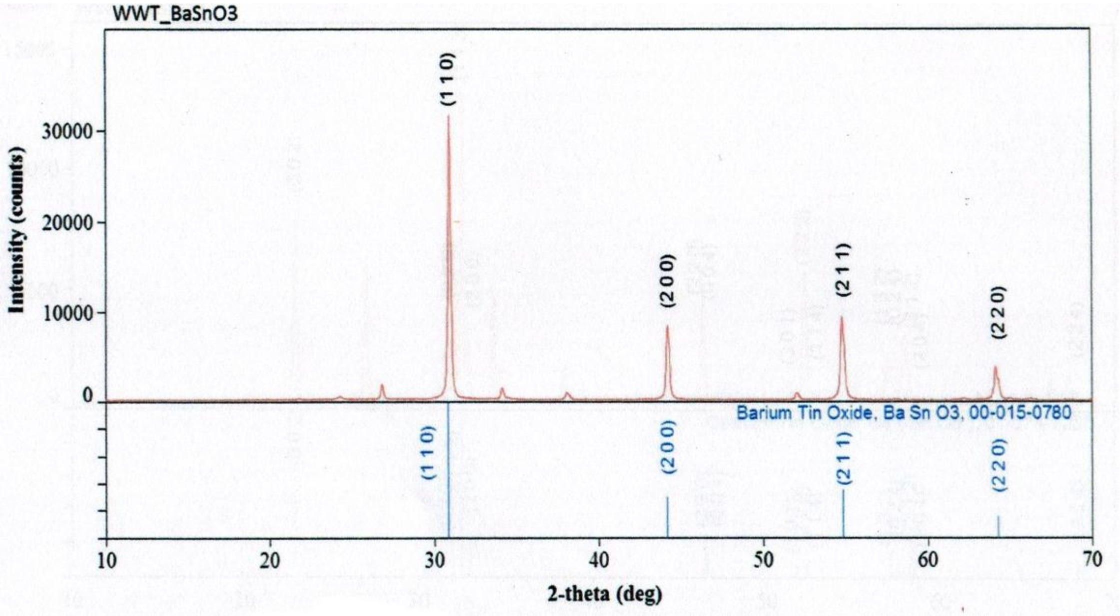

Figure 2 XRD pattern of $BaSnO_3$ powder sample

Fig (3) shows the XRD pattern of $BaSnO_3$ film. It was found that (110), (111), (200), (211) and (220) planes were appeared in which the dominant peak is (110) plane at the value of diffraction angle is 31.048 ° and $BaSnO_3$ film was also cubic structure.

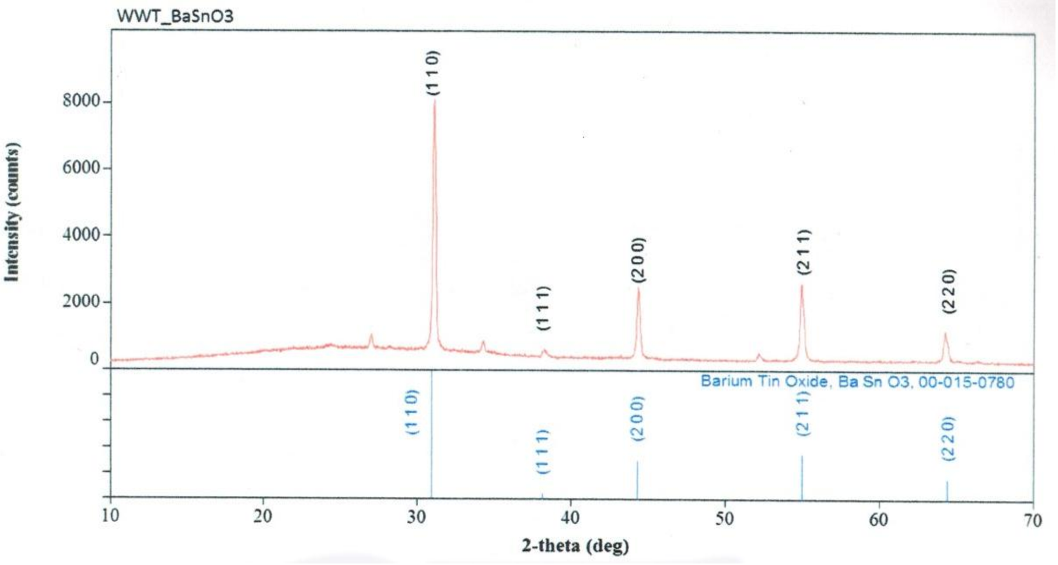

Figure 3 XRD pattern of $BaSnO_3$ film sample

From XRD analysis, the lattice constant “a”, “b” and “c” and unit cell volume of these samples were calculated by using the following relationship for cubic structure,

$$\frac{1}{d^2} = \frac{h^2+k^2+l^2}{a^2} \quad \text{-------} \quad (1)$$

$$V = a^3 \quad \text{--------} \quad (2)$$

And then the crystallite size of $BaSnO_3$ samples were calculated by Debye Scherer’s formula

$$D = \frac{0\ .9\ \lambda}{\beta cos\theta} \qquad \text{--------} \qquad (3)$$

Where, λ is the X-ray wavelength (1.54056Å),θ is a Bragg's angle and β is full width at half maximum (FWHM). These values were shown in Table (1) and (2).

Table 1 Unit Cell Volume and Crystallite Size of $BaSnO_3$Powder and Film Sample

No	Sample	Maximum peak (hkl)	Unit cell volume V $(nm)^3$	Crystallite size D (nm)
1	$BaSnO_3$ (powder)	(110)	0.0683	50.6239
2	$BaSnO_3$ (film)	(110)	0.0674	46.5238

Table 2 Lattice Parameters of BaSnO3 Powder and Film Sample

No	Sample	a (nm)	b (nm)	c (nm)
1	$BaSnO_3$ (powder)	0.4089	0.4089	0.4089
2	$BaSnO_3$ (film)	0.4070	0.4070	0.4070

SEM Analysis of $BaSnO_3$ Powder and Film Sample

Fig (4) shows the SEM micrograph of $BaSnO_3$ powder sample. It was observed that the particles were in spherical shape and well crystallized there were non- uniformity in the shape and existence of porosity. The grain size of $BaSnO_3$ powder sample was (0.5829) µm.

Fig (5) shows the SEM micrograph of $BaSnO_3$ film sample. It was observed that these particles were also spherical shape and non- uniformity. The grain size of $BaSnO_3$ film was (0.6158) µm.

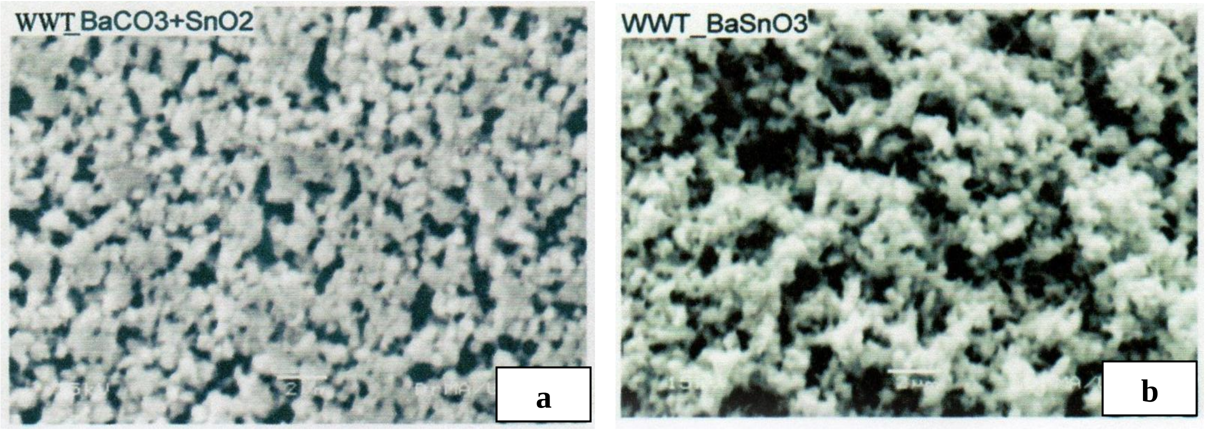

Figure 4 SEM micrograph of (a) $BaSnO_3$ powder sample (b) $BaSnO_3$ film sample

These samples were estimated using the line intercept method. Table (3) shows the value of grain size of $BaSnO_3$ powder and film sample.

Table 3 Grain Size of $BaSnO_3$ Powder and Film Sample

No	Sample	Grain size (µm)
1	$BaSnO_3$ (powder)	0.5829
2	$BaSnO_3$ (film)	0.6158

Conclusion

Perovskite type $BaSnO_3$ powder and film were successfully prepared by the solid state reaction method at temperature 1150 ºC. From XRD results, it was observed that the dominant peak appeared from the samples were equal. The crystallite sizes of these samples were nearly equal. The structure of the powder sample was cubic. When $BaSnO_3$ was deposited on the glass substrate by spin coating method, the structure didn't change. The intensities (counts) were high in powder sample but low in film sample. From SEM image the particles in the powder and film sample were spherical shape. The grain sizes were nearly equal. In $BaSnO_3$ film revealed that agglomerations of well connected. Small crystallite size, well-formed intergranular connectivity there were desired features of gas-sensing devices. This was also important to remark that if an electrical device such as capacitor is to be fabricated from these materials.

Acknowledgements

The authors would like to thank Dr Htay Aung Pro-rector and Dr Soe Myint Thein, Pro-rector of Loikaw University, for their kind permission to carry out this research work. We also grateful to thank Professor Dr San San Wai, Head of Department of Physics, Loikaw University, for her encouragement to do this work. We wish to express my thanks to all our colleagues in the Department of Physics, Loikaw University, for providing suggestions in this research.

References

Abdul-Majeed Azad et al (1997) "Characterization of $BaSnO_3$ Based Ceramics Part 1. Synthesis Processing and Micro Structural Development" Department of Physics, University of Putra Malaysia, Malaysia.

Cerda, J., J. Arbiol, (2002) "Synthesis of perovskite-type BaSnO3 particles obtained by a new simple wet chemical route based on a sol–gel process" Departament d'Electro `nica, Facultat de Fı ´sica, Universitat de Barcelona, *Materials Letters* 56 (2002) 131–136.

Deepa, A.S. et al (2011) "Structural and Optical Characterization of $BaSnO_3$ Nano powder synthesized through a Novel Combustion Technique".

Doan Tuan Anh, Nguyen Trong Thanh (2017), "Investigation of Optical Properties on BaSnO3 Materials", Institute of Materials Science, Vietnam Academy of Science & Technology, Vietnam, *Universal Journal of Physics and Application,* 11(6): 235-238.

Lucas, A.Haf and Jana AbouZiki (2017) "Micro Hole Drilling on Glass Substrates", Department of Mechanical & Industrial Engineering, Concordia University, Canada.

J. Myanmar Acad. Arts Sci. 2020 **Vol. XVIII.No.2**B

CHARACTERIZATION OF COPPER-COBALT FERRITES FOR HUMIDITY SENSOR APPLICATION

Aye Aye Lwin[1] & Win Kyaw[2]

Abstract

Nanosized Copper-Cobalt ferrites with the general formula $Cu_xCo_{1-x}Fe_2O_4$ (where $x = 0.00 – 1.00$ with the step of 0.25) were prepared by auto-combustion method using Analytical Reagent (AR) grade Copper Nitrate, $Cu(NO_3)_2$, Cobalt Nitrate Hexahydrate, $Co(NO_3)_2.6H_2O$ and Ferric Nitrate Nonahydrate, $Fe(NO_3)_3.9H_2O$. The samples were firstly characterized by X-ray diffraction to examine the crystal structure. The average crystallite sizes were estimated from line broadening of the collected XRD patterns to determine the nanosized ferrites. Microstructural characteristics of grain shape, grain size and homogeneity of the samples were examined by Scanning Electron Microscopy (SEM). It was found that the grain shapes of the samples varied from block shape to stone-like shape with the contents x of Cu. The grain size, generally, of $x = 0.50$ was the largest one among the investigated samples. For the applications of humidity sensors, the samples were made into circular shape pellets and the variations of the electrical resistance with the corresponding humidity range were studied in this work.

Keywords: $Cu_xCo_{1-x}Fe_2O_4$, auto-combustion method, XRD, SEM, humidity sensors.

Introduction

The hunt for new applications of nanostructured systems is now a major area of research in materials science and technology. To exploit the full potential that nano-systems offer, it is important that novel methods of manipulation and fabrication be developed, in addition to extending current techniques of sample characterization to smaller sizes. Success in devising and assembling systems on the scale of nanometers will require a deeper understanding of the basic processes and phenomena involved. Hence, one of the current key objectives is to adapt and develop a range of techniques that can characterize the structural, electronic, magnetic and optical properties of nanostructured systems.

Humidity measurement is one of the most significant issues in various areas of applications such as instrumentation, automated systems, agriculture and climatology. In recent years improvements in sensor manufacturing technologies have occurred driven by post-process high-speed, low-power and low-cost microelectronic hybrid circuits, modern signal conditioning methods and advances in miniaturization technologies.

This work deals with the preparation of Copper-Cobalt ferrites, $Cu_xCo_{1-x}Fe_2O_4$ (where $x = 0.00 – 1.00$ with the step of 0.25) using auto-combustion method and their structural and microstructural characteristics were reported by XRD and SEM. For the applications of humidity sensing materials, the samples were made into pellets and their electrical resistances were investigated in the humidity range of 50 RH% – 99 RH%.

---

[1] Dr, Associate Professor, Department of Physics, Loikaw University

[2] Dr, Associate Professor, Department of Physics, Pyay University

Experimental Details

Preparation of the Samples

For the preparation of desired materials of Copper-Cobalt ferrites, $Cu_xCo_{1-x}Fe_2O_4$ (where x = 0.00 – 1.00 with the step of 0.25), Analytical Reagent (AR) grade Copper Nitrate, $Cu(NO_3)_2$, Cobalt Nitrate Hexahydrate, $Co(NO_3)_2.6H_2O$ and Ferric Nitrate Nonahydrate, $Fe(NO_3)_2.9H_2O$ were used as the starting materials. Citric Acid, $C_6H_8O_7.H_2O$ was used as the fuel. Desired stoichiometric compositions of these Nitrates and Citric Acid were mixed with (1:1) ratio and prepared the aqueous solutions. The pH of the solution was adjusted to 7 using liquor Ammonia.

The obtained solution was allowed to evaporate in a beaker by keeping the solution temperature at 80°C – 90°C and it was a viscous gel. The resultant gel was heated at 450°C for 2 h. Photographs of the weighed starting materials, as-burnt and as-prepared samples of $Cu_xCo_{1-x}Fe_2O_4$ for x = 1.00 sample are shown in Figures 1(a – c). Flow diagram of the sample preparation process is shown in Figure 2.

Figure 1 Photographs of (a) the weighed starting materials and (b) as-burnt $Cu_xCo_{1-x}Fe_2O_4$ for x = 1.00

Figure 1 (c) Photograph of as-burnt $Cu_xCo_{1-x}Fe_2O_4$ for x = 1.00

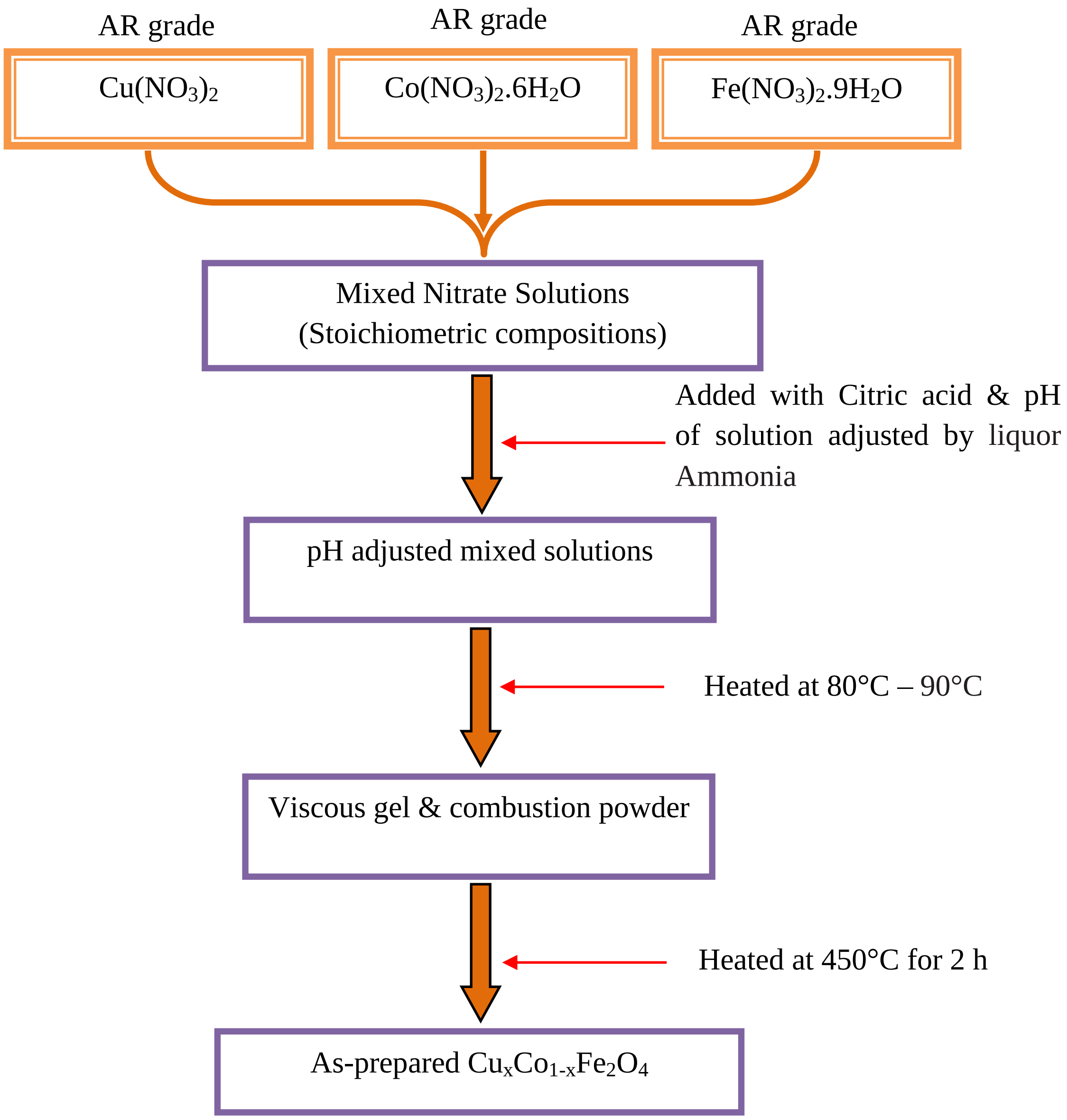

Figure 2 Flow-diagram of the $Cu_xCo_{1-x}Fe_2O_4$sample preparation process

XRD and SEM Measurements

To investigate the phase formation, structure analysis, variation of lattice parameters and estimation of crystallite sizes, the samples were characterized by XRD. Powder XRD patterns of the samples were observed by using PC-controlled RIGAKU, MULTIFLEX X-ray Diffractometer [Universities′ Research Centre (URC), University of Yangon]. To examine the grain shape, grain sizes and pore formation, the samples were characterized by using JEOL JSM-5610LV SEM [Universities′ Research Centre (URC), University of Yangon] with the accelerating voltage of 15 kV and 5500 times of photo magnification.

Humidity Sensitive Electrical Resistance Measurement

For the applications of humidity sensors, the as-prepared ferrites were firstly made into circular shape pellets by using SPECAC hydraulic pellet-maker with the pressure 5 ton (~70 MPa). Thickness and area of the each of the sample were as 2.95 mm and 1.14×10^{-4} m^2

respectively. Silver paste was used for ensure good electrical contact. Copper ring electrodes were used to observe the resistance of the sample. In this measurement, XSW TDK 0302 Humidity Meter was used as the humidity sensing element. Humidity sensitive electrical resistances were observed in the relative humidity range of 50 RH% - 99 RH% by two probe method using FLUKE 189 digital multimeter. The refrigerator (Haier) was used as the humidity generator. Photographs of the experimental setup of humidity sensitive electrical resistance measurement are shown in Figures 3(a) and (b). Figure 4 shows the schematic diagram of the humidity sensitive electrical resistance measurement.

Figure 3 Experimental setup of humidity sensitive electrical resistance measurements, (a) the sample and sensor placed in the same condition (altitude) and (b) wiring connection of sample and resistance meter

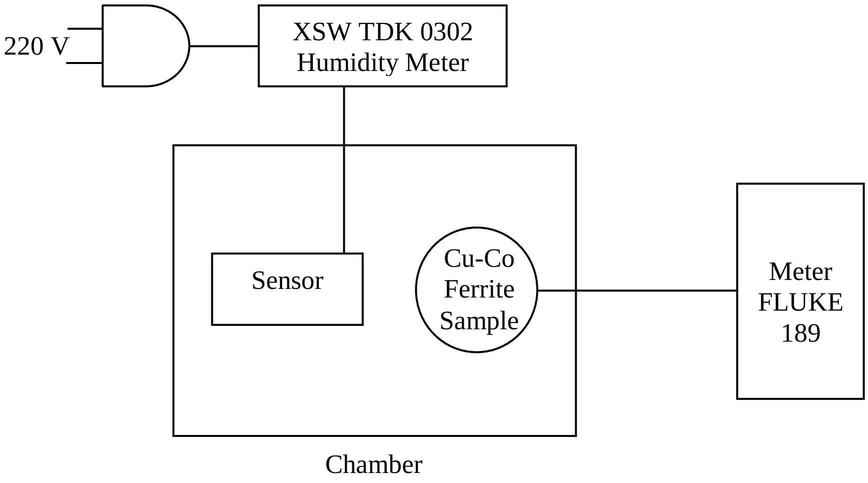

Figure 4 Schematic diagram of the humidity sensitive electrical resistance measurement

Results and Discussion

XRD Study

The indexed powder X-ray diffraction patterns are shown in Figures 5(a – e). The collected XRD lines were identified by using the following JCPDS data files:

(i) Cat. No. 22-1086>$CoFe_2O_4$ – Cobalt Iron Oxide for x = 0.00 sample

(ii) Cat. No. 22-1086>$CoFe_2O_4$ – Cobalt Iron Oxide and Cat. No. 77-0010>$CuFe_2O_4$ – Copper Iron Oxide for x = 0.25, 0.50 and 0.75 samples and

(iii) Cat. No. 77-0010>$CuFe_2O_4$ – Copper Iron Oxide for x = 1.0 sample.

XRD patterns showed the formation of cubic structure with dominant peak corresponding to (311) reflection indicating that the crystallites were preferentially oriented along (311) plane. The lattice parameters were evaluated by using crystal utility of the equation of $\frac{\sin^2\theta}{(h^2+k^2+l^2)}=\frac{\lambda^2}{4a^2}$ where θ is the diffraction angle (°), (hkl) is the miller indices, λ is the wavelength of incident X-ray (Å) and *a* is the lattice parameter of the samples (Å). The observed lattice parameters and evaluated lattice parameters are tabulated in Table 1. Figure 6 shows the variation of the lattice parameters of the $Cu_xCo_{1-x}Fe_2O_4$ ferrites with increase in Cu concentration. The lattice parameters were found to be varied with increase in Cu concentration. Muthurani, S. et. al. (2010) has reported that the lattice parameters of the Co-ferrite, Cu-Co ferrite and Cu ferrite are 8.381 Å, 8.372 Å and 8.370 Å respectively [Muthurani, et.al. (2010)]. In this work, the obtained lattice parameters are found to be agreed with the data of Muthurani, S. et. al. (2010).

The crystallite sizes of the samples were estimated by using the Scherrer formula,

$D=\frac{0.9\lambda}{B\cos\theta}$, where D is the crystallite size (nm), λ is the wavelength of incident X-ray (Å), θ is the diffraction angle of the peak under consideration at FWHM (°) and B is the observed FWHM (radians). The breadth of the Bragg peak is a combination of both instrument and sample dependent effects. To decouple these contributions, it is necessary to collect a diffraction pattern from the line broadening of a standard material such as silicon to determine the instrumental broadening. In this work, the instrumental effects on the breadth of the Bragg peak neglected.

In the present work, the FWHM of the strongest peak (I = 100%) of (311) planes of the XRD patterns were used to calculate the crystallite size and the estimated crystallite sizes of $Cu_xCo_{1-x}Fe_2O_4$ samples. The obtained crystallite sizes are also presented in Table 1. It indicates the nanosized Cu-Co ferrites materials. Variation of the crystallite sizes with increase in Cu concentration is shown in Figure 6.

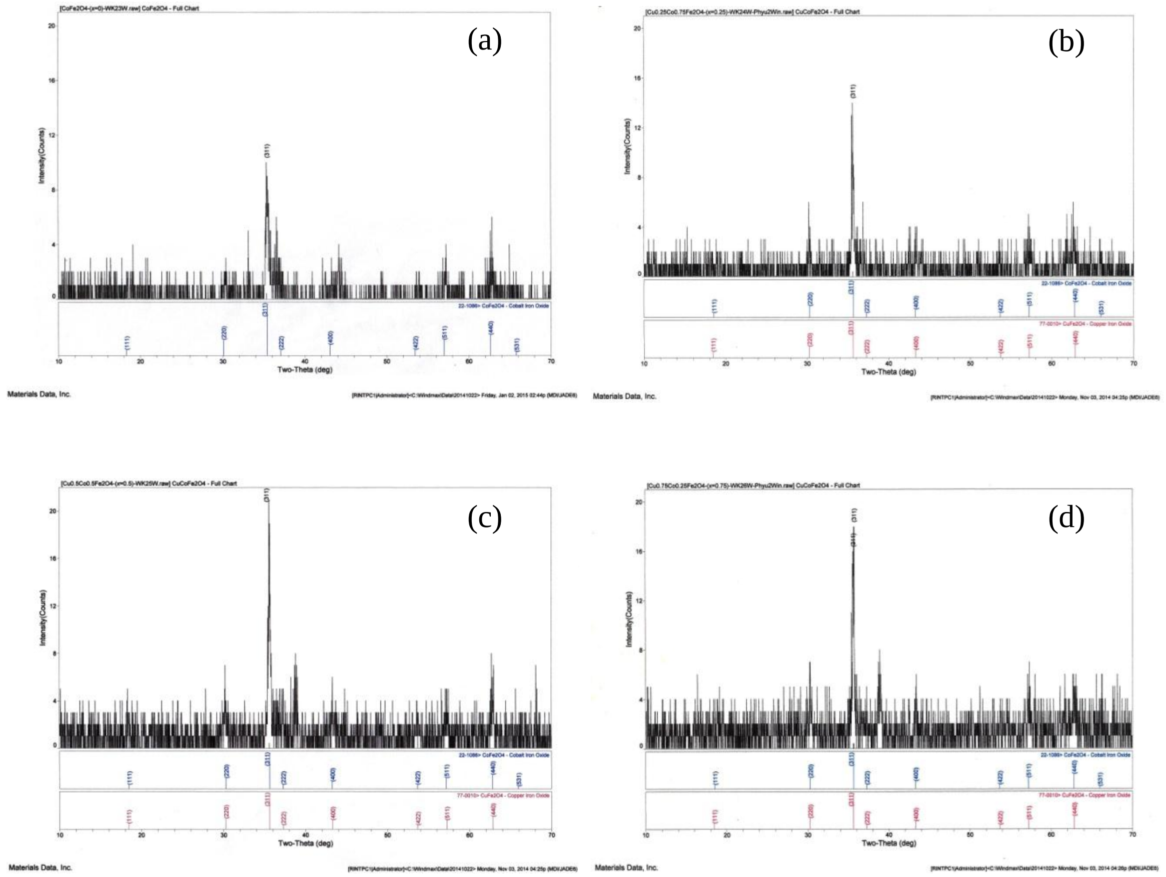

Figure 5 XRD patterns of $Cu_xCo_{1-x}Fe_2O_4$ where (a) x = 0.00, (b) x = 0.25, (c) x = 0.50, and (d) x = 0.75

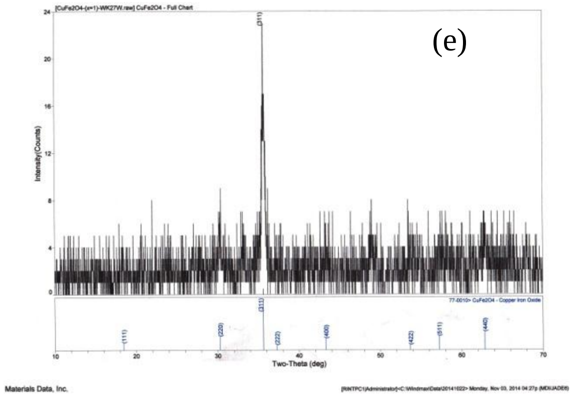

Figure 5 (e) XRD pattern of $Cu_xCo_{1-x}Fe_2O_4$ where x = 1.00

Table 1 The observed and calculated lattice parameters and crystallite sizes of $Cu_xCo_{1-x}Fe_2O_4$ samples

Sample (Contents x of Cu)	**Obs. *a=b=c* (Å)**	**Cal. *a=b=c* (Å)**	***D* (nm)**
0.00	8.4063	8.4063	38.42
0.25	8.3596	8.3596	70.08
0.50	8.3601	8.3601	43.44
0.75	8.3463	8.3464	46.61
1.00	8.3472	8.3574	31.36

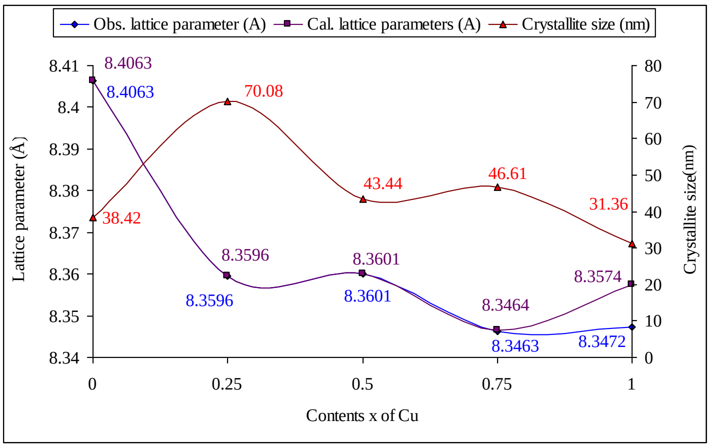

Figure 6 Variations of the observed and calculated lattice parameters with increase in concentration of Cu and the crystallite sizes with the increase in concentration of Cu of $Cu_xCo_{1-x}Fe_2O_4$

SEM Analysis

Due to the microstructure has a major role in the performance of a ceramic sensor, in this work, the microstructures of the end products by SEM to investigate the external morphology of grain shape, size and pore formation of the as-prepared ferrite samples. SEM micrographs of the $Cu_xCo_{1-x}Fe_2O_4$ samples are shown in Figures 7(a – e). As shown in Figure 7(a), the grain shape of the x = 0.00 sample is block shape in which large intergranular porosities are found. The grain sizes are obtained as in the range of 0.20 μm – 1.20 μm. In Figure 7(b), the grain shape of x = 0.25 sample is block shape. A few and small intergranular porosities are found and the obtained samples composed of agglomerated particles with poor grain boundary. The grain sizes are obtained as in the range of 0.10 μm – 0.80 μm. In Figure 7(c) of x = 0.50 sample, the stone like block shape grains are found and they can be clearly seen as non-homogeneous with some holes. The grains sizes are obtained as 2.50 μm – 20.00 μm. A few intergranular porosities are found with clear grain boundary. As depicted in Figures 7(d) and (e) of x = 0.75 and x = 1.00 samples, the stone like block shape grains are also found with clear grain boundary. A few and small intergranular porosities are also found in the micrographs. The grain sizes are obtained as in the range of 2.20 μm – 18.50 μm for x = 0.75 and 1.80 μm – 22.50 μm for x = 1.00. The obtained grain sizes are listed in Table 2.

In the observed SEM micrographs, there are intergranular porosities due to the decomposition of starting materials (nitrates). According to literature, grain size and pore structure have a major effect on the properties in polycrystalline materials.

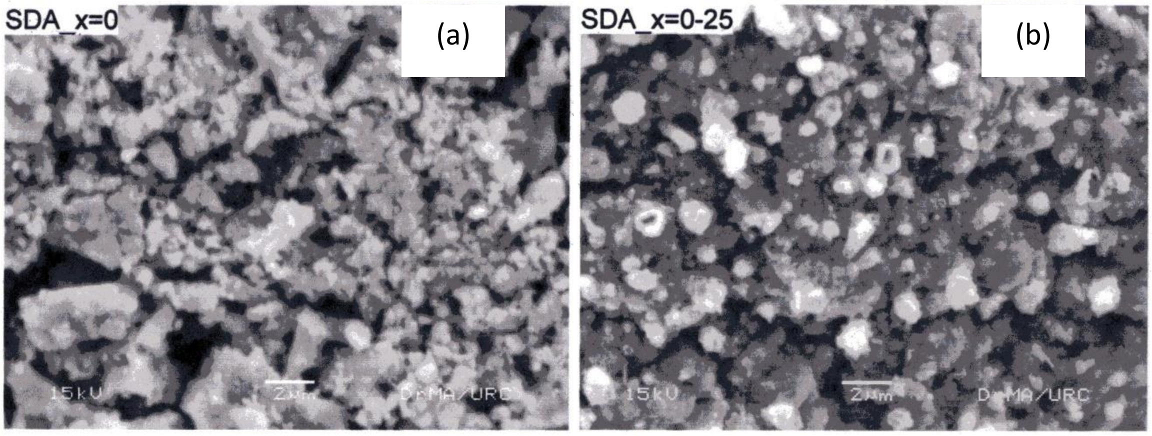

Figure 7 SEM micrographs of $Cu_xCo_{1-x}Fe_2O_4$ where (a) x = 0.00 and (b) x = 0.25

Humidity Sensitive Electrical Resistance Study

The spinel ferrites are chemically stable, have porous structure and resistive type. This type of property of the materials can be used as humidity sensors applications. In the present work, humidity sensitive electrical resistances R of the samples in the relative humidity range of 50 RH% – 99 RH% with the step of 1 RH% were observed to examine the change in electrical resistance with increased in humidity. Variations of the electrical resistances R vs. relative humidity RH% of the samples in the whole relative humidity ranges of 50 – 99 RH% are shown in Figures 8(a – e).

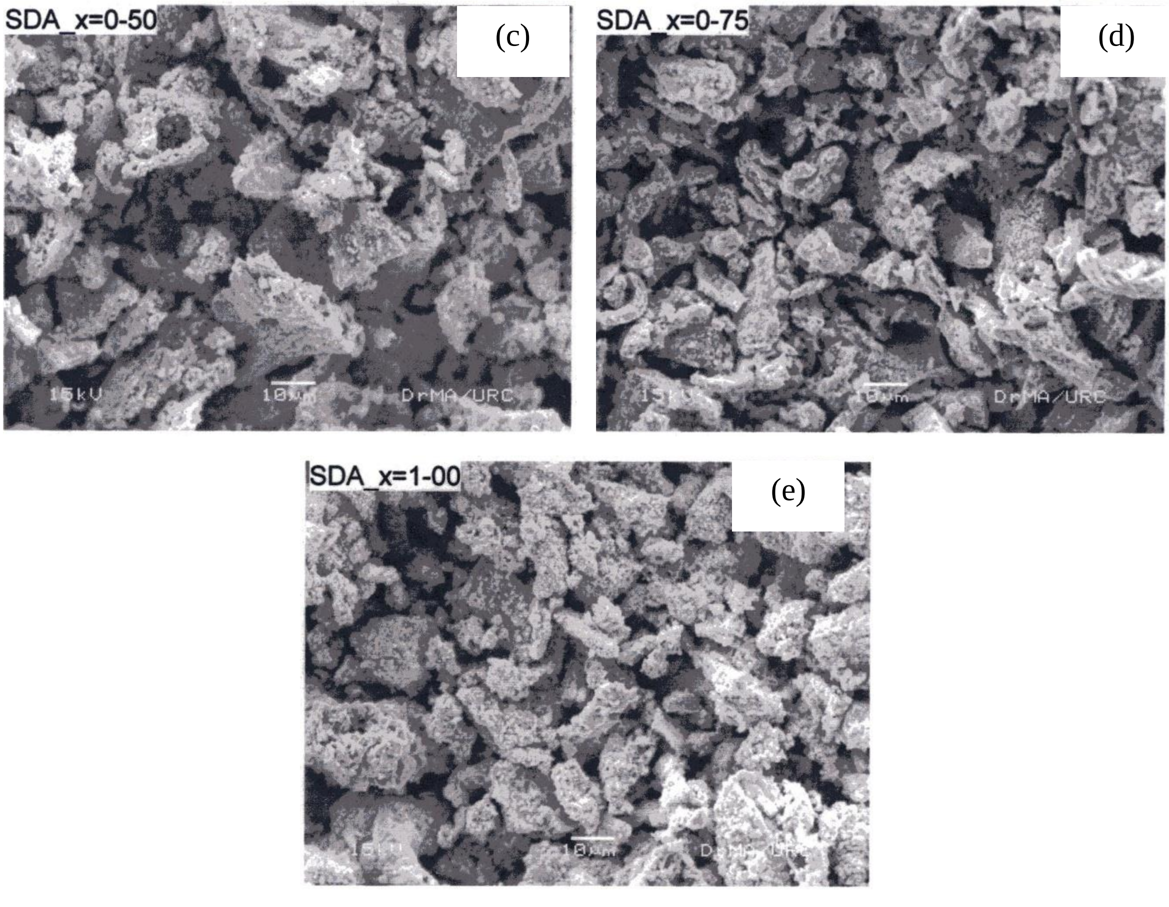

Figure 7 SEM micrographs of $Cu_xCo_{1-x}Fe_2O_4$ where (c) x = 0.50, (d) x = 0.075 and (e) x = 1.00

Table 2 The grain sizes of $Cu_xCo_{1-x}Fe_2O_4$ samples

Sample (Contents x of Cu)	Grain size (µm)
0.00	0.20 – 1.20
0.25	0.10 – 0.80
0.50	2.50 – 20.00
0.75	2.20 – 18.50
1.00	1.80 – 22.50

The electrical resistance of the samples decreased with increase in relative humidity. In each of the R vs. RH% graph, it was clearly seen that the change in electrical resistances

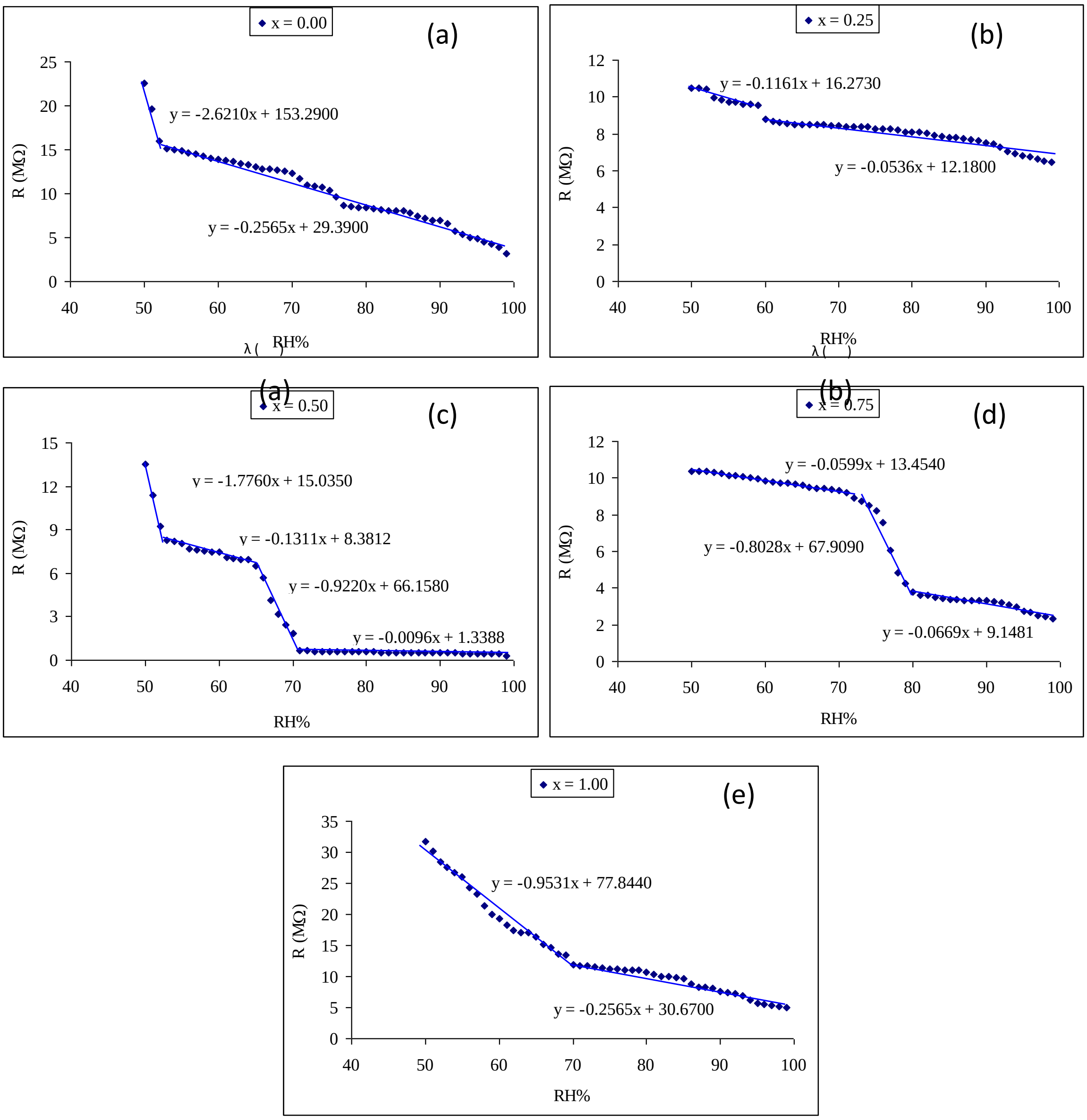

Figure 8 Humidity sensitive electrical resistance graphs of $Cu_xCo_{1-x}Fe_2O_4$ where (a) x = 0.00, (b) x = 0.25, (c) x = 0.50, (d) x = 0.75 and (e) x = 1.00

with relative humidity or slopes of the curves in the R vs. RH% graphs are generally two portions, three portions and four portions with the corresponding humidity ranges. It can be explained as the resistance of the sensing materials slightly decreased because the water molecule is not only physically absorbed in the active group of the ferrites but also can be polarized. The effect can generate space charge and dipoles, and then accumulate and degenerate between electrodes.

In this work, detail variations of the decreased changes in electrical resistances with the corresponding relative humidity ranges or slopes of the R vs. RH% graphs are also presented in Figures 8(a – e). The obtained changes in electrical resistances with the corresponding humidity ranges are tabulated in Table 3.

It was obviously that the changes in electrical resistances with relative humidity or slopes of the R vs. RH% graphs of x = 0.00 (pure $CoFe_2O_4$), x = 0.25 ($Cu_{0.20}Co_{0.75}Fe_2O_4$) and x =1.00 (pure $CuFe_2O_4$) are found to be in two regions. The four step slopes are found in the R vs. RH% graph of x = 0.50 ($Cu_{0.50}Co_{0.50}Fe_2O_4$). The three step slopes are found in the R vs. RH% graph of x = 0.75 ($Cu_{0.75}Co_{0.25}Fe_2O_4$). The decreased changes in electrical resistances with relative humidity or slopes of the R vs. RH% graphs of the samples varied with increased in concentration of Cu on the $Cu_xCo_{1-x}Fe_2O_4$.

Table 3 Change in electrical resistances with the corresponding relative humidity ranges of the $Cu_xCo_{1-x}Fe_2O_4$ samples

Sample (Contents x of Cu)	Slope (MΩ/RH%)	Humidity range (RH%)
x = 0.00	2.6210	50 – 53
	0.2565	54 – 99
x = 0.25	0.1161	50 – 59
	0.0536	60 – 99
x = 0.50	1.7760	50 – 53
	0.1311	54 – 64
	0.9220	65 – 71
	0.0096	72 – 99
x = 0.75	0.0599	50 – 72
	0.8028	73 – 80
	0.0669	81 – 99
x = 1.00	0.9531	50 – 70
	0.2565	71 – 99

The sensitivity factor of a humidity sensor can be generally evaluated as follow:

$$S = R_{\text{initial RH\%}} / R_{\text{final RH\%}} = R_{50RH\%} / R_{99RH\%}$$

where S is the sensitivity factor, $R_{\text{initial RH\%}}$ is the resistance at initial relative humidity and $R_{\text{final RH\%}}$ is the resistance at final relative humidity. In this work, the sensitivity factors of $Cu_xCo_{1-x}Fe_2O_4$ humidity sensors are obtained as the followings:

$$S_{x=0.00} = (R_{50RH\%})_{x=0.00} / (R_{99RH\%})_{x=0.00} = 22.61\ M\Omega / 3.18\ M\Omega = 7.11$$

$$S_{x=0.25} = (R_{50RH\%})_{x=0.25} / (R_{99RH\%})_{x=0.25} = 10.49\ M\Omega / 6.46\ M\Omega = 1.62$$

$$S_{x=0.50} = (R_{50RH\%})_{x=0.50} / (R_{99RH\%})_{x=0.50} = 13.51\ M\Omega / 0.32\ M\Omega = 42.10$$

$$S_{x=0.75} = (R_{50RH\%})_{x=0.75} / (R_{99RH\%})_{x=0.75} = 10.38\ M\Omega / 2.34\ M\Omega = 4.44$$

$$S_{x=1.00} = (R_{50RH\%})_{x=1.00} / (R_{99RH\%})_{x=1.00} = 31.68\ M\Omega / 5.05\ M\Omega = 6.28$$

The sensitivity factor of the $x = 0.50$ ($Cu_{0.50}Co_{0.50}Fe_2O_4$) is the largest one among the investigated samples. It shows that the $x = 0.50$ sample is the most suitable for the application of humidity sensing material.

Conclusion

Copper-Cobalt ferrites, $Cu_xCo_{1-x}Fe_2O_4$ (where $x = 0.00, 0.25, 0.50, 0.75$ and 1.00) were successfully prepared by auto-combustion method. Structural, microstructural and humidity sensitive electrical resistance of the samples were studied in this work. XRD patterns reveal that the samples analogous to cubic structure. The lattice parameters and crystallite sizes varied alternatively with increase in concentration of Cu. SEM micrographs showed that the grain shape and grain sizes varied with the concentration of Cu. The intergranular porosities appeared in each of the SEM micrograph and the samples composed of agglomerated particles. Experimental results from the humidity sensitive electrical resistances measurements showed that the electrical resistances decreased with increase in relative humidity. The changes in electrical resistances of the samples were examined from R vs. RH% graphs. Furthermore, the sensitivity factor of the $x = 0.50$ ($Cu_{0.50}Co_{0.50}Fe_2O_4$) was the largest one among the investigated samples. It showed that the $x = 0.50$ sample was the most suitable for the application of humidity sensor.

Acknowledgements

We express our gratitude and appreciation to Professor Dr Pho Kaung, Rector, University of Yangon (UY), for his providing necessary research facilities in UY and keen interest for this work. The authors would like to acknowledge Professor Dr Tun Khin, Acting-Rector (Rtd.), University of Yangon (UY) and Professor Dr Myint Kyi, Principal, Hinthada Degree College, for their stimulated suggestions to prepare this paper.

The authors would like to acknowledge Professor Dr Khin Khin Win, Head of Department of Physics, University of Yangon, for her valuable suggestion and comments for this work. The authors would like to thank Professor Dr San San Wai, Head of Department of Physics, Loikaw University, for her kind permission to carry out this work.

References

Ahmad, I. & Farid, M.T. (2012). Characterization of Cobalt Based Spinel Ferrites with Small Substitution of Gadolinium. *World Applied Sciences Journal*, 19, 464–469.

Fawzi, A.Z., Sheikh, A.D. & Mathe, V.L. (2010). Structural, Dielectric Properties and AC Conductivity of $Ni_{(1-x)}Zn_xFe_2O_4$ Spinel Ferrite. *Journal of Alloys and Compounds*, 502, 231–237.

Maria1, K.H., Choudhury, S. & Hakim, M.A. (2013). Structural phase transformation and hysteresis behavior of Cu-Zn ferrites. *International Nano Letters*, 3, 1–10.

Praveena, K., Sadhana, K. & Murthy, S. R. (2013). Elastic behaviour of Sn doped Ni-Zn ferrites, *International Journal of Scientific and Research Publications*, 3, 1–4.

Rezlescu, N., Rezlescu, E., Popa, P. & Tudorache, F. (2002). ON THE HUMIDITY SENSITIVITY OF A CERAMIC ELEMENT. STRUCTURE AND CHARACTERISTICS. *Journal of Institute of Technical Physics*, 8, 89–97.

Sharma, R.K., Suwalka, O., Lakshmi, N., Venugopala, K., Banerjee, A. & Joy, P.A. (2005). Synthesis of Chromium Substituted Nano Particles of Cobalt Zinc Ferrites by Co-precipitation. *Materials Letters*, 59, 3402–3405

(2011). *The Humidity/Moisture Handbook*, Machine Applications Corporation.

J. Myanmar Acad. Arts Sci. 2020 **Vol. XVIII.No.2**B

SCATTERING PARAMETERS FOR PROTON-NEUTRON SCATTERING WITH YUKAWA POTENTIAL

Khin Mar Win[1] and Htun Htun Oo[2]

Abstract

The purpose of the research work is to calculate the scattering parameters for two-nucleon system with Yukawa potential. We have calculated the scattering phase shift, effective range and scattering length. To calculate the phase shift, the transition matrix (T-matrix) is formulated from Lippmann-Schwinger equation for two-body scattering state. The Lippmann-Schwinger equation is the Schrödinger equation with boundary condition. The numerical values of T-matrix are obtained by using Gauss elimination Method with FORTRAN code. And then, the effective range and scattering length are calculated by using the phase shift.

Keywords: Scattering phase shift, effective range, scattering length

Introduction

Nucleon-nucleon interactions are studied based on scattering experiments. The interaction between two nucleons is basis for all of nuclear physics. The scattering is related to the behavior of the interaction. The simplest bound system in nature is the deuteron which consists of a neutron and a proton. A phenomenological nucleon-nucleon interaction based on the meson exchanges. The meson exchange idea introduced by Yukawa in 1934 is a good starting point to examine nucleon-nucleon interaction. In the Yukawa picture, the interaction between two nucleons is mediated by the exchange of mesons.

Protons and neutrons are lowest energy bound states of quarks and gluons. When we put two or more of these particles together, they interact, scatter and sometimes form bound states due to the strong interaction. On first tries to extract the nucleon-nucleon interaction from the nucleon-nucleon scattering data. For neutron scattering, there are two major sources for incident beam. At low energies, neutrons from nuclear reactors may be used. At higher energies, one can make use of neutrons produced a beam of protons. However, both the intensity and the energy resolution of neutron beam obtained in these ways are much more limited than those for proton beams. As a result neutron scattering is a more difficult experiment than those with protons. The information obtained from proton-neutron (np) and proton-proton(pp) scattering may not be any different from that in np- and pp-scattering is whether the neutron or the proton is the target. If nuclear force is charge independent, the results of pp- and nn-scattering can only be different by the contribution made by coulomb interaction. A comparison of pp- and nn-scattering results is the charge independence of nuclear interaction.

Phase shift, Scattering length and effective range are scattering parameters. These parameters provide a useful way to parameterize information on low-energy nucleon-nucleon scattering. These parameters may be related to observations other than NN-scattering, such as deuteron binding energy. In addition, very accurate results can be obtained for the np- system by scattering slow neutrons off protons in hydrogen atoms. For these reasons, a great deal of attention is devoted to the measurement and understanding of these parameters. Any potential

---

[1] Dr, Lecturer, Department of Physics, Sagaing University of Education

[2] Associate Professor, Department of Physics, Lashio University,

shape can be used to obtain these parameters by a proper choice of the range and depth of the well. We can relate these parameters to the properties of ground state of the deuteron.

In our calculation, the Yukawa type Malfliet-Tjon potential is used. The Malfliet-Tjon potential is the Yukawa type potential including also ‘soft core’ repulsion. This potential is a central potential independent of spin and isospin.

The nucleon-nucleon interaction in the ${}^{1}S_{0}$ channel is a superposition of two Yukawa potential one of which is repulsive, i.e.

$$V(r)=V_A\frac{e^{-\mu_A r}}{r}+V_R\frac{e^{-\mu_R r}}{r}\, with \quad \mu_R=2\mu_A$$

The potential constants were determined from a fit to the low energy parameters and the phase shifts up to 300MeV lab energy.

Using proton-proton scattering data and bound state of the neutron system, potential representing the interaction between two nucleons can be constructed. Although they ignore the important spin degree of freedom, the Malfliet-Tjon potentials are very useful in determining qualitative feature of nucleon system and providing test case.

Table 1 The various parameters sets of the Malfliet-Tjon potentials

Potential no.	**v$_A$** $\hbar c$	**u$_A$ fm**	**v$_R$** $\hbar c$	**u$_R$ fm**
I (${}^{1}S_{0}$)	2.6	1.55	7 .39	3.11
II (${}^{1}S_{0}$)	0.266	0.809	0	0
III (${}^{3}S_{1}$)	3.22	1.55	7.39	3.11
IV (${}^{3}S_{1}$)	0.330	0.633	0	0

The Lippmann-Schwinger Equation

The Lippmann-Schwinger equation is actually Schrödinger equation plus boundary condition independent of particular representation. The Lippmann-Schwinger equation is an exact equation for the scattering problem that can be expressed in momentum space as well as in configuration space. The Lippmann-Schwinger equation is the following equation:

$$\left|\Psi^{(+)}_{p_0}\right\rangle=\left|p_0\right\rangle+\frac{1}{E-\hat{H}_0+i\varepsilon}\hat{V}\left|\Psi^{(+)}_{p_0}\right\rangle \qquad (1)$$

Now by operating with V from the left hand side of equation (1)

$$\hat{V}\left|\Psi^{(+)}\right\rangle=\hat{V}\left|\Phi\right\rangle+\hat{V}\frac{1}{E-\hat{H}_0+i\varepsilon}\hat{V}\left|\Psi^{+}\right\rangle \qquad (2)$$

We define the transition operator $\hat{T}$ with respect to the plane wave state.

$$\hat{V}\left|\Psi^{(+)}\right\rangle=\hat{T}\left|\Phi\right\rangle \qquad (3)$$

Φ is the plane wave. The operator $\hat{T}$ is defined so that the effect of $\hat{V}$ on Ψ^{+} is the same as the effect of $\hat{T}$ on Φ.

And then equation (2) is become the following equation:

$$\hat{T}|\Phi\rangle = \hat{V}|\Phi\rangle + \hat{V}\frac{1}{E-\hat{H}_0+i\varepsilon}\hat{T}|\Phi\rangle \tag{4}$$

An operator equation for $\hat{T}$ is

$$\hat{T} = \hat{V} + \hat{V}\frac{1}{E-\hat{H}_0+i\varepsilon}\hat{T} \tag{5}$$

$$\hat{T} = \hat{V} + \hat{V}G_0\hat{T} \tag{6}$$

Where $$G_0 = \frac{1}{E-\hat{H}_0+i\varepsilon}$$

Then we project it onto the momentum space as follows:

$$\langle p|\hat{T}|p'\rangle = \langle p|\hat{V}|p'\rangle + \int p''^2 dp'' \langle p|\hat{V}G_0|p''\rangle\langle p''|\hat{T}|p'\rangle \tag{7}$$

By inserting the completeness relation in the second term of the above equation, the following equation is obtained.

$$\langle p|\hat{T}|p'\rangle = \langle p|\hat{V}|p'\rangle + \int p''^2 dp'' \frac{1}{E+i\varepsilon-\frac{p''^2}{2m}}\langle p|\hat{V}|p''\rangle\langle p''|\hat{T}|p'\rangle \tag{8}$$

Here E is the incident energy and it has $\frac{p_0^2}{2m}$, the Eq.(8) becomes

$$\langle p|\hat{T}|p\rangle = \langle p|\hat{T}|p'\rangle + 2m\int p''dp'' \frac{1}{p_0^2+i\varepsilon-p''^2}\langle p|\hat{V}|p''\rangle\langle p''|\hat{T}|p'\rangle \tag{9}$$

Then $2m\int p''^2 dp'' \frac{p_0^2}{p_0^2+i\varepsilon-p''^2}\langle p|\hat{V}|p_0\rangle\langle p_0|\hat{T}|p_0\rangle$ is added and subtracted into the second term of the above equation.

$$\begin{aligned}\langle p|\hat{T}|p'\rangle &= \langle p|\hat{V}|p'\rangle + 2m\int p''^2 dp'' \frac{1}{p_0^2+i\varepsilon-p''^2}\langle p|\hat{V}|p''\rangle\langle p''|\hat{T}|p'\rangle \\ &+ 2m\int p''^2 dp'' \frac{p_0^2}{p_0^2+i\varepsilon-p''^2}\langle p|\hat{V}|p_0\rangle\langle p_0|\hat{T}|p_0\rangle \\ &- 2m\int p''^2 dp'' \frac{p_0^2}{p_0^2+i\varepsilon-p''^2}\langle p|\hat{V}|p_0\rangle\langle p_0|\hat{T}|p_0\rangle\end{aligned} \tag{10}$$

Using the principal value theorem $\lim_{i\varepsilon\to 0}\frac{1}{x+i\varepsilon} = \frac{p}{x} - i\pi\delta(x)$, the Eq.(10) becomes

$$\langle p|\hat{T}|p'\rangle = \langle p|\hat{V}|p'\rangle + 2m\int dp''p''^2\,\frac{\langle p|\hat{V}|p''\rangle\langle p''|\hat{T}|p_0\rangle - p_0^2\langle p|\hat{V}|p_0\rangle\langle p_0|\hat{T}|p_0\rangle}{p_0^2 - p''^2} + mp_0\langle p|\hat{V}|p_0\rangle\langle p_0|\hat{T}|p_0\rangle\left[\ln\left|\frac{p_0+p_{\max}}{p_{\max}-p_0}\right| - i\pi\right] \qquad (11)$$

The integral limit is zero to infinity but we determine $p_{\max}$ is enough for that limit and the saturation for $p' = p_0$, the eq.(11) becomes

$$T(p,p_0) = V(p,p_0)2m\int dp''p''^2\,\frac{V(p,p'')T(p'',p_0) - p_0^2V(p,p_0)T(p_0,p_0)}{p_0^2 - p''^2} + mp_0\langle p|\hat{V}|p_0\rangle\langle p_0|\hat{T}|p_0\rangle\left[\ln\left|\frac{p_0+p_{\max}}{p_{\max}-p_0}\right| - i\pi\right] \qquad (12)$$

This equation can be solved numerically by using the FORTRAN code.

Numerical Calculation

To obtain the numerical value of the T-matrix, we transform the Eq.(12) into the discrete form. By using the Gauss numerical integration method, these equations can be written as

$$T(p,p_0) = V(p,p_0) + 2m\sum_j^N W_j p_j^2\,\frac{V(p_i,p_j)T(p_j,p_0)}{p_0^2 - p_j^2} - 2m\sum_j^N W_j\,\frac{p_0^2V(p,p_0)T(p_0,p_0)}{p_0^2 - p_j^2} + mp_0\langle p|\hat{V}|p_0\rangle\langle p_0|\hat{T}|p_0\rangle\left[\ln\left|\frac{p_0+p_{\max}}{p_{\max}-p_0}\right| - i\pi\right] \qquad (13)$$

Where W_j and p_j are the Gauss weight and Gauss point. The following notations are used to simplify the equation

$$\widetilde{W}_j = \frac{2mW_j}{p_0^2 - p_j^2}$$

$$C_i = mp_0V(p_i,p_0)\left[\ln\left|\frac{p_0+p_{\max}}{p_{\max}-p_0}\right| - i\pi\right]$$

$$\widetilde{C}_i = C_i - \sum_j^N \widetilde{W}_j p_0^2 V$$

For FORTRAN CODE, the final equation is

$$T_i = V_i + \sum_j^N \widetilde{W}_j p_j^2 V_{ij} T_j + \widetilde{C}_j T_0 \qquad (14)$$

Here the index i run from 0 to N and j runs from 1 to N. in general, the above equation can be written in the matrix form

$$\begin{bmatrix} \tilde{C}_0 - 1 & \tilde{W}_1 p_1^0 V_{01} & \ldots \tilde{W}_N P_N^2 V_{0N} \\ \tilde{C}_1 & \tilde{W}_1 p_1^0 V_{11} - 1 & \ldots \tilde{W}_N P_N^2 V_{1N} \\ \tilde{C}_2 & \tilde{W}_1 p_1^0 V_{21} & \ldots \tilde{W}_N P_N^2 V_{2N} - 1 \\ \vdots & \vdots & \ldots \\ \tilde{C}_N & \tilde{W}_1 p_1^0 V_{N1} & \ldots \tilde{W}_N P_N^2 V_{NN} - 1 \end{bmatrix} \begin{bmatrix} T_0 \\ T_1 \\ T_2 \\ \vdots \\ T_N \end{bmatrix} = \begin{bmatrix} -V_0 \\ -V_1 \\ -V_2 \\ \vdots \\ -V_N \end{bmatrix} \qquad (15)$$

The above matrix is denoted as

$$\sum_{j=1} A_{ij} T_j = B_i$$

The Eq(15) is a set of ‘N’ equations in ‘N’ unknowns. We can solve this equation by using Gauss Elimination Method. And then we obtain the T-matrix elements.

Using T-matrix, we calculated the phase shift. The relation between T-matrix and phase shift is given the following equation:

$$S = 1 - i\, m\, \pi\, p_0\, T(p_0, p_0)$$

The phase shift $\delta = \frac{1}{2}\, tan^{-1} \left(\frac{Img(S)}{Re(S)} \right)$

Then the effective range and scattering length are calculated. We have the equation

$$k \cot \delta = \frac{-1}{a} + \frac{1}{2} r\, k^2$$

where δ is the phase shift of a function of energy E.

$$k = \sqrt{2mE}$$

The effective range ‘r’ and the scattering length ’a’ do not depend on energy E.

For the two values of input energy, the following two equations is obtained

$$-\frac{1}{a} + \frac{1}{2} k^2(E_1) r_0 = k(E_1) \cot \delta(E_1)$$

$$-\frac{1}{a} + \frac{1}{2} k^2(E_2) r_0 = k(E_2) \cot \delta(E_2)$$

These equations can be written as the following matrix forms:

$$\begin{pmatrix} -1 & \frac{1}{2} k^2(E_1) \\ -1 & \frac{1}{2} k^2(E_2) \end{pmatrix} \begin{pmatrix} \frac{1}{a} \\ r_0 \end{pmatrix} = \begin{pmatrix} k(E_1) \cot \delta(E_1) \\ k(E_2) \cot \delta(E_2) \end{pmatrix}$$

This equation is two unknown two equations. Two unknowns ‘a’ and ‘r’ can be calculated by using Gauss elimination method.

Results and Discussions

T-matrix elements are obtained by solving the Lippmann Schwinger equation with Gauss elimination method. And then, the phase shifts for various incident energies are calculated by sing the T-matrix elements. We have calculated the phase shifts for the singlet ($^1S_0$) and the triplet ($^3S_1$) potentials of Yukawa type which are given in table (1). The potential I and II are the singlet ($^1S_0$) potentials and the potential III and IV are triplet ($^3S_1$) potentials. The results of the $^1S_0$ phase shift for potential I and potential II is given in table (2) and figure (1). The results of the $^3S_1$ phase shift for potential III and potential IV is given in table (3) and figure (2). We compare the calculated results and experimental results.

Our calculated values of scattering length for $^1S_0$ potential I and II are -23.78fm and-23.67fm. Therefore our calculated values are in good agreement with experiment value of -23.75. The negative scattering length implies that the system has no bound state. Our calculated results of scattering length for $^3S_1$ potential III and IV are 5.34fm and 5.50fm. Our calculated values are in good agreement with the experimental value of 5.423fm. The positive scattering length implies that a bound state exists. The results of effective range for $^1S_0$ potential I and II are 2.84fm and 2.88fm and these results are in good agreement with the experimental value of 2.73fm. Our calculated results of effective range for $^3S_1$potential III and IV are 1.87fm and 1.73fm and these results are in good agreement with the experimental value of 1.73fm.

Table 2 Neutron-proton scattering phase shift for singlet state ($^1S_0$)

Elab (MeV)	Phase shift(Deg)		
	Exp (Deg)	Potential I (Deg)	Potential II (Deg)
1	62.1	64.65	61.12
10	60.0	58.41	59.75
25	50.9	47.04	53.31
50	40.5	34.96	47.47
100	26.8	20.35	41.38
150	16.9	10.90	37.86
200	8.9	3.90	35.32

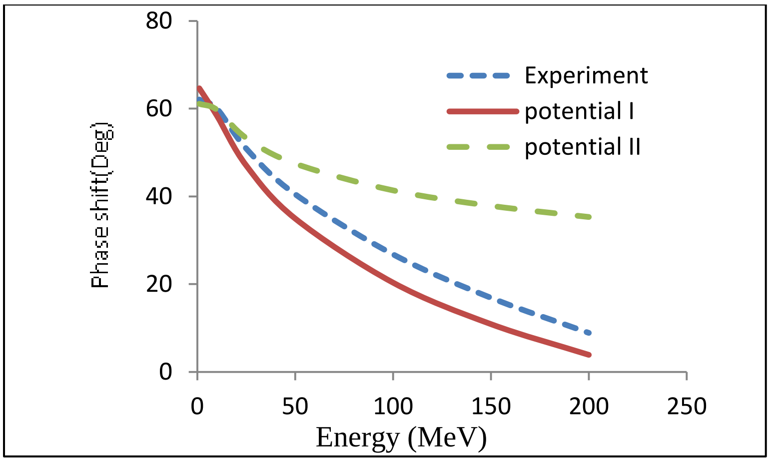

Figure 1 n-p phase shift for $^1S_0$ state

Table 3 Neutron-proton scattering phase shifts for triplet ($^3S_1$) state

Elab (MeV)	Phase shift(Deg)		
	Exp;	Potential III	Potential IV
24	81.7	79.83	86.03
48	63.3	61.77	73.25
96	42.9	43.17	61.74
144	29.8	32.10	55.57
208	17.1	21.99	50.35

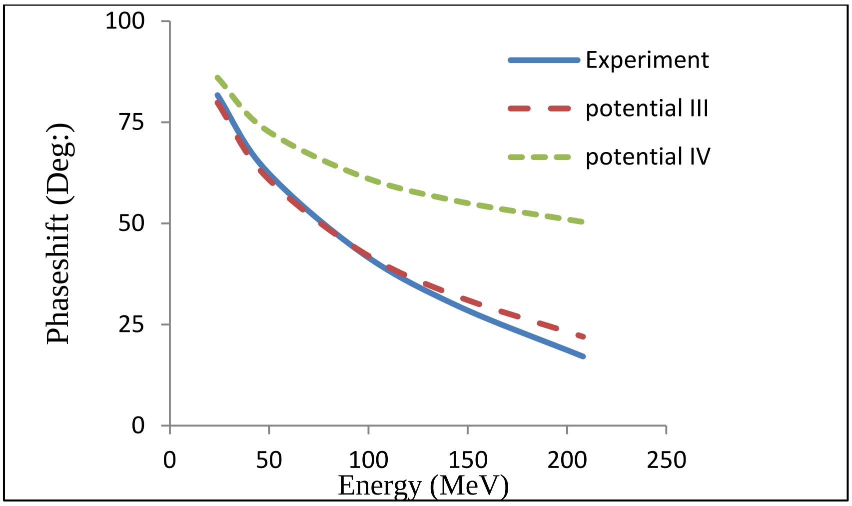

Figure 2 n-p phase shifts for triplet $^3S_1$ state

Table 4 The n-p scattering length and effective range for four parameter sets of Malfliet-Tjon potential

	$^1S_0$ state			$^3S_1$ state		
	I	II	Exp:[1]	III	IV	Exp:[1]
a (fm)	-23.78	-23.67	-23.715	5.34	5.50	5.423
r (fm)	2.84	2.88	2.73	1.87	1.73	1.73

Conclusion

The phase shifts for Yukawa type Malfliet-Tjon potential have been calculated. We obtained the T-matrix elements by solving the Lippmann-Schwinger equation with Gauss Elimination method. The phase shifts for various parameter sets of Malfliet-Tjon potential have been calculated. Potential II and IV are purely attractive potentials. The calculated phase shifts of Potential II and IV do not agree with the experimental results. Potential I and III are two-range potential including attractive and repulsive parts. Therefore, the results of phase shift for Potential I and Potential III are in good agreement with experimental results.

Acknowledgement

The author would like to thank Professor Dr Khin Swe Myint, Rector (Rtd), emeritous Professor, physics Department, Mandalay University for her encouragement.

References

E. Balagurusamy, “Numerical Methods”, Tata McGraw-Hill Publishing Company Limitec, New Delhi (2000).

L.Coraggio and A.Covello, “Nuclear Structure Calculations and Modern Nucleon-Nucleon Potentials”, (Feb 6, 2008).

R.A. Malfliet and J.A. Tjon, Nucl.Phys. **A127** (1969)161

R.V. Reid, “Local Phenomenological Nucleon-Nucleon Potentials”, Cornell University, Physics Department, Ithaca, New York (1968)14850.

S.M. Wong, ”Introductory Nuclear Physics”, University of Toronto (2004)

J. Myanmar Acad. Arts Sci. 2020 **Vol. XVIII.No.2**B

PHOTOVOLTAIC PERFORMANCE OF SOLID-STATE DYE-SENSITIZED SOLAR CELLS (SSDSSCS) USING NATURAL DYES EXTRACT

Nan Kyi Kyi Thein[1] and Than Zaw Oo[2]

Abstract

The natural dye solutions were extracted from henna leave, red Dragon fruit flesh and red Spinach leave as photosensitizer for solid-state dye-sensitized solar cells (ssDSSCs). In this work, the ssDSSCs were fabricated using these natural dye extracts and their photovoltaic performance was examined against dye extracting temperature and relative ratio of co-solvents (dimethylformamide (DMF) and ethanol (EtOH)). It is found that the device efficiencies are almost insensitive to the extracting temperature for all dye extracts being studied. The efficiency of red Spinach devices decreased with increasing DMF concentration in ethanol whiles those of Henna and red Dragon fruit devices were almost invariant. Thus co-solvent effect would differ system to system. Among all, the efficiency of red Spinach device (extracted at 45 °C in EtOH) is as high as 0.11 %.

Keywords: *natural dyes, efficiencies, solid-state dye-sensitized solar cells*

Introduction

Dye sensitized solar cell (DSSC) is a device for the conversion of light into electricity and its performance is based on the sensitization of wide band gap semiconductors [Gratzel M. et al., (2003) , *J. Photochem. Soc*. 6, 889]. It is a low-cost solar cell belonging to the group of thin film solar cells [O'Regan and Gratzel M. , (1991), *Nature*. 353, 737]. Solar cells are usually divided into three main generations. First generation is single crystal silicon solar cells. They are expensive to produce, and their efficiency hits more than 20%. Second generation is polycrystalline silicon solar cells, amorphous silicon solar cells and polycrystalline non-silicon based solar cells. They have lower efficiency, but are much cheaper to produce, such that the cost per watt is lower than in first generation cells. Third generation solar cells are organic polymer heterojunction solar cells, dye-sensitized solar cells and hybrid solar cells. Most technologies in this generation are not yet commercialized, but there is a lot of research going on in this area. One major advantage of third generation solar cells is the cost-effectiveness for their production [Deibel C. and Dyakonov V. , (2010), *Rep. Prog. Phys*. 73, 39].

DSSC is one of the most promising photovoltaic technologies. Liquid electrolyte-based DSSCs have reached efficiencies as high as 11.1% [Gao F. et al., (2008), *J. Am. Chem. Soc*. 130, 10720]. However, these liquid based DSSCs suffer from potential leakage and corrosion which have sparked research in solid state hole transport materials (HTMs) instead of liquid electrolytes [Snaith H. J. & Schmidt-Mende L. , (2007), *Adv. Mater* 19, 3187]. One of the most widely-used HTMs is spiro-OMeTAD (2,2’,7,7’ – tetrakis - (N,N-di-p-methoxyphenylamine) -9,9’-spirobifluorene) [Bach U. et al., (1998), *Nature* . 395, 583]. Solid-state dye-sensitized solar cells (ssDSSCs) with spiro-OMeTAD as HTM have attained efficiencies exceeding 5%, which is still far below the efficiency of liquid electrolyte DSSCs [Snaith H. J. et al., (2007), *Nano Lett*. 7, 3372]. The lower efficiency is primarily a consequence of incomplete light harvesting. The highest-performing ssDSSCs to date have a 2-3 μm thick active layer [Schmidt-Mende L. et al., (2005), *Appl. Phys. Lett*. 86,

---

[1] Dr, Assistant Lecturer, Materials Science Research Laboratory, Department of Physics, University of Mandalay
[2] Dr, Professor, Universities’ Research Centre, University of Yangon

013504], far thinner than the thickness needed to achieve good optical absorption. There are two factors that limit the ssDSSCs from being more efficient at thicknesses > 2 μm: electron-hole recombination and incomplete filling of the mesoporous TiO_2 films with spiro-OMeTAD. Studies on recombination show that recombination in ssDSSCs is two orders of magnitude faster than in liquid DSSCs [Fabregat-Santiago F. et al., (2009), *J. Am. Chem. Soc*. 131, 558] and the electron diffusion length (L_D) in mesoporous TiO_2 is 6-12 μm, much larger than the optimized 2 μm film thickness.

Since metal oxide nanoparticles [zinc oxide (ZnO) and titanium dioxide (TiO_2)] have been used in DSSC as the photoelectrode sensitized by organic dyes. They have several approaches to improve light-harvesting efficiencies and cell performance: developing photoelectrodes with larger surface areas that could adsorb large amount of dye and synthesizing dyes with broader absorption ranges [Anderson S. et al., (1979), *Nature* . 280, 571].

Experiment

This section details about the preparation of natural dye-sensitizers, fabrication of solid-state dye-sensitized solar cells (ssDSSCs) and device efficiency measurement.

Preparation of Natural Dye-sensitizers

The natural dye solutions were extracted from Henna leave, red Dragon fruit flesh and red Spinach leave. The fresh Henna leaves were dried at 100 °C for 45 min and crushed into fine powder using a mortar and pestle. The powder was immersed and stirred in 10 ml EtOH (95 % absolute ethanol) at room temperature for 45 min. The solid residues in solution were then filtrated out, and the filtrates were concentrated for the use as sensitizers. The Henna dye solutions with different concentrations (0.05-0.35 g/ml) were prepared. In addition, the dyes were extracted at different temperature (45-70 °C). Using the optimal dye concentration, the dye solutions were also prepared in the solvent mixture (various volume ratio of DMF to EtOH). Following the similar procedure of Henna dye synthesis, the red Dragon fruit flesh and red Spinach fresh leave were washed with distilled water, crushed and immersed in the solvent. Fig. 1 shows the preparation of natural dye-sensitizers (Henna leave, red Dragon fruit flesh and red Spinach leave).

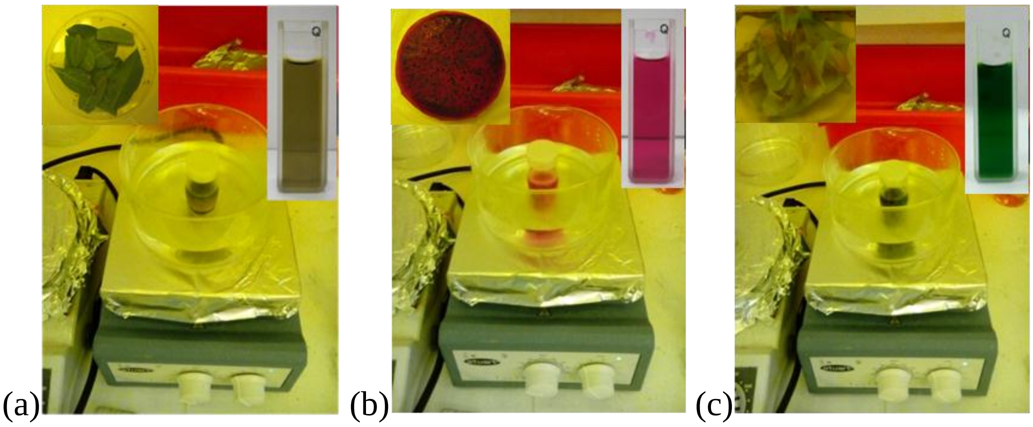

Figure 1 Preparation of natural dye solutions extracted from (a) Henna leaves, (b) Red Dragon fruit flesh and (c) Red Spinach leaves in ethanol

Fabrication of Solid-state Dye-sensitized Solar Cells

(i) Substrate Preparation

Fluorine-doped SnO_2 (FTO) coated glasses (2 cm x 10 cm) were etched with zinc powder and HCl (2M) to obtain the required electrode pattern. They were pre-treated with a 1M aqueous $TiCl_4$ at 70 °C for 30 min followed by washing with detergent (2% Hellmanex in water), distilled water, ethanol and acetone for 15 min each. Finally, they were blown with N_2 gas for drying purpose and treated under UV Ozone for 20 min for removing the last traces of organic residues. The FTO sheets were subsequently coated with a compact layer of TiO_2 by aerosol spray pyrolysis deposition at 450°C using a commercial titanium diisopropoxide bis(acetylacetonate) solution (75% in 2-propanol, Sigma-Aldrich) diluted in ethanol (volume ratio of 1:9) as precursor and oxygen as carrier gas. After cooling to room temperature they were treated in a 1M aqueous solution $TiCl_4$ for 30 min at 70°C, rinsed with distilled water and dried at 500°C for 30 min.

(ii) Formation of Mesoporous TiO_2 Photoanode

The mesoporous TiO_2 layer was developed to be used as working electrode in ssDSSC. A 3-μm-thick mesoporous TiO_2 layer composed of 30-nm-sized particles was deposited by screen printing using a commercial TiO_2 paste (Dyesol 18NRT, Dyesol). Mesoporous TiO_2 films were slowly heated to 500°C (ramped over 30 min) and baked at this temperature for 30 min using tap control hot plate. The last step is to allow the TiO_2 films to cool down naturally to room temperature.

(iii) Infiltration of Dye and Hole-transporting Materials (HTM)

In order to load the dye on the TiO_2 mesoporous electrode, the film electrodes were submerged in 3ml of a dye solution at room temperature for 12 hr in a dark place. The dye-adsorbed TiO_2 thin film was rinsed gently with distilled water to remove unwanted solids, and then with the ethanol which serves to remove water from the porous TiO_2. The dyed films were rinsed briefly in acetonitrile and dried in air for 1 min. The HTM was then deposited by spin coating at 4000 r.p.m. for 30 s in nitrogen atmosphere. The 2,2',7,7'-tetrakis(N,N-di-p-methoxyphenyamine)-9,9'-spirobifluorene (spiro-OMeTAD) was dissolved in 1 ml chlorobenzene. After fully dissolving the hole transporter, 4-tert-butylpyridine (TBP) was added with a volume-to-mass ratio of 1:26 μl mg^{-1} TBP: spiro-OMeTAD. Lithium bis (trifluoromethylsulfonyl) imide salt (Li-TFSI) was pre-dissolved in acetonitrile at 170 mg ml^{-1} and added to the hole transporter solution at 1:12 μl mg^{-1} of Li-TFSI solution : spiro-OMeTAD. The spin coating formulation was prepared by dissolving 180 mg (spiro-OMeTAD), 6.92 μl 4-tert-butylpyridine, 14.99 μl of a stock solution of 170 mg ml^{-1} lithium bis (trifluoromethylsulphonyl) imide in acetonitrile and 2.88 μl of a stock solution of 320 mg ml^{-1} tris (2-(1H-pyrazol-1-yl)-4-tert-butylpyridine)cobalt(III) bis (trifluoromethylsulphonyl) imide (FK102) in acetonitrile in 1 ml chlorobenzene.

The concentration of spiro-OMeTAD in the solution, so that the ratio of spiro-OMeTAD to TBP, Li-TFSI and FK102 was kept constant. For spin-coating, a small quantity of the hole transporter solution (50 μl) was dispensed onto each substrate and left to wet the films for 5s before spin-coating. After spiro-OMeTAD infiltration, a chlorobenzene-soaked cotton swab was used the substrate that was not on top of the mesoporous TiO_2 film to remove the excess spiro-OMeTAD.

(iv) Deposition of Gold Electrode

The films were left overnight in an air atmosphere before placing them in a thermal evaporator where 180-nm-thick gold electrodes were deposited through a shadow mask under high vacuum (10^{-6} mbar). Fig. 2 shows the active area of the device was defined by metal optical mask with 0.4 cm × 0.5 cm aperture.

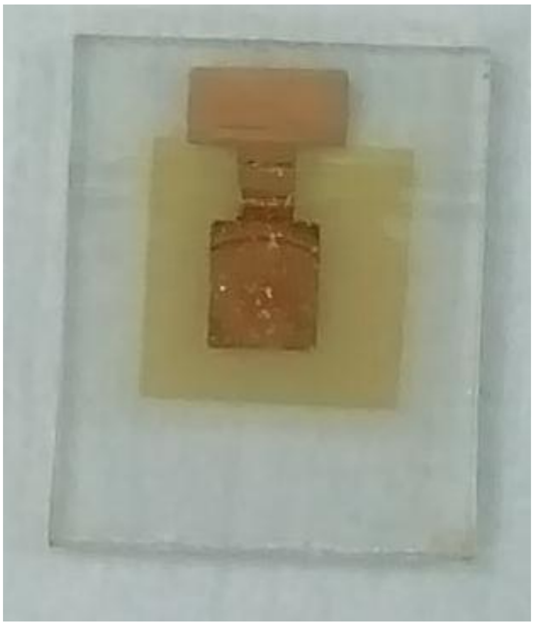

Figure 2 Photograph of complete ssDSSC device

Measurement of the Device Efficiency

The power conversion efficiencies (PCE) of DSSCs were evaluated by recording J-V characteristics of the device. It was measured using a computer-controlled digital source meter (Keithley 2400) under illumination with a Newport solar simulator (AM 1.5, 1000 W/m^2). A Keithley source meter was used to supply an input voltage and measure the output current of DSSCs. The light source was a 450 W xenon lamp (Oriel) equipped with a Schott K113 Tempax sunlight filter (Praezisions Glas & Optik GmbH) to match the emission spectrum of the lamp to the AM 1.5 G standards. Before each measurement, the exact light intensity was determined using a calibrated Si reference diode. Fig. 3 shows the experimental setup for PCE measurement.

Figure 3 Experimental setup for the measurement of power conversion efficiency (PCE)

Results and Discussion

The section mainly discusses the effect of extracting temperature and solvent on the photovoltaic performance of ssDSSCs using Henna, red Dragon fruit and red Spinach dye extracts is presented.

Photovoltaic Performance of ssDSSCs

We examined the photovoltaic performance of ssDSSCs using Henna, red Dragon fruit and red Spinach dye solutions extracted at different temperatures and dissolved in different solvents.

(i) Varying the Dye Extracting Temperature in Ethanol

Fig. 4 shows J-V characteristics of the ssDSSCs using Henna, and red Dragon fruit and red Spinach dye extracts prepared at RT, 45 °C, 60 °C and 70 °C under AM 1.5 illumination (1000 Wm^{-2}). Device parameters for ssDSSCs using Henna, red Dragon fruit and red Spinach dye solutions extracted in ethanol at different extracting temperatures are listed in Table 1. With Henna dye extracted at RT, 45 °C and 60 °C, the ssDSSC generated similar values of V_{OC}, J_{SC} and FF, and thus PCE. At higher extracting temperature of 70 °C, V_{OC} decreased from 0.46 V to 0.41 V and J_{SC} decreased from 0.15 mA/cm^2 to 0.07 mA/cm^2 while FF increased from 0.41 to 0.47. Overall the PCE decreased from 0.03 % to 0.01 %. In ssDSSC using red Dragon fruit dye and red Spinach dye, we can observe that all the device parameters of ssDSSC were not significantly changed upon varying the extracting temperatures.

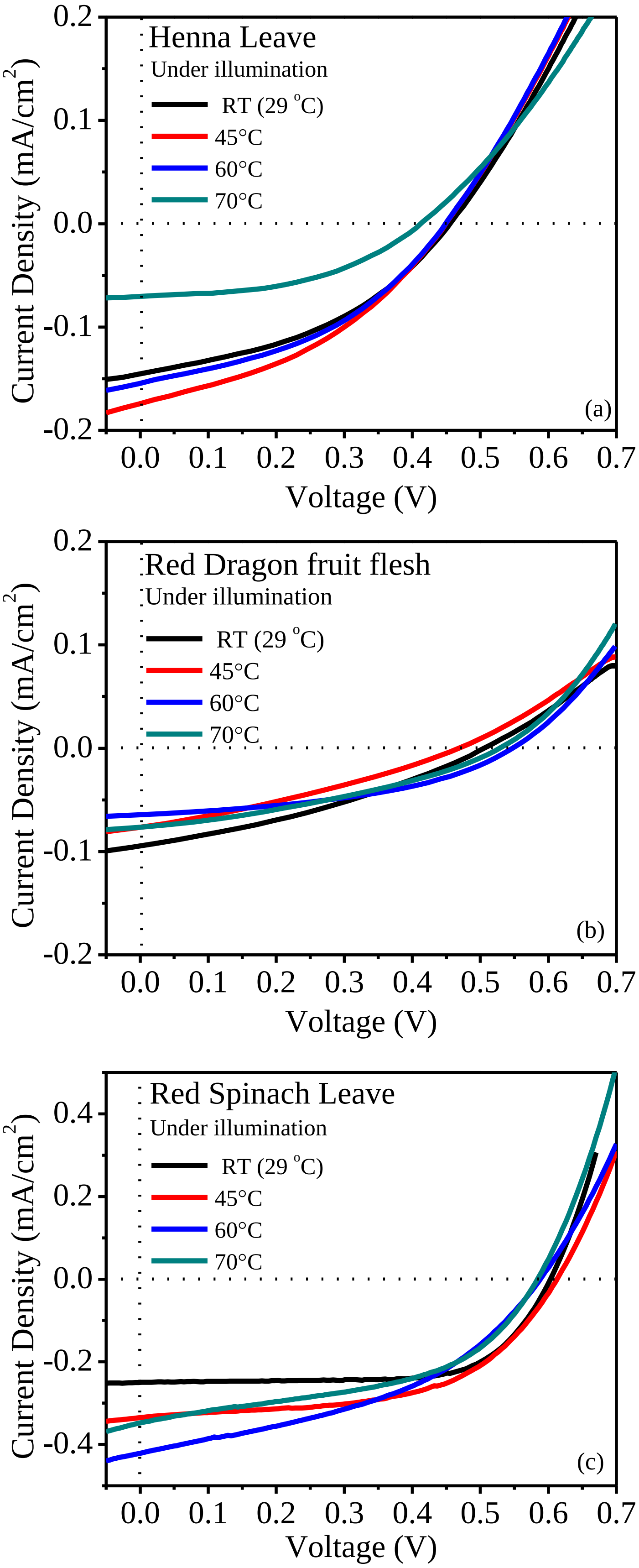

Figure 4 J-V characteristics of the ssDSSCs using (a) Henna, (b) red Dragon fruit and (c) red Spinach dye solutions extracted at RT, 45 °C, 60 °C and 70 °C

Table 1 Device parameters for ssDSSCs using Henna, red Dragon fruit and red Spinach dye solutions in ethanol extracted at different temperatures.

ssDSSC Devices	Extracting Temperature	V_{OC} (V)	J_{SC} (mA/cm^2)	FF	PCE (%)
Henna Dye	RT(29 °C)	0.46	0.15	0.41	0.03
	45 °C	0.45	0.17	0.39	0.03
	60 °C	0.45	0.16	0.41	0.03
	70 °C	0.41	0.07	0.47	0.01
Red Dragon Fruit Dye	RT(29 °C)	0.51	0.09	0.33	0.02
	45 °C	0.47	0.08	0.31	0.01
	60 °C	0.55	0.06	0.43	0.02
	70 °C	0.53	0.08	0.35	0.01
Red Spinach Dye	RT(29 °C)	0.60	0.25	0.69	0.10
	45 °C	0.61	0.34	0.55	0.11
	60 °C	0.59	0.42	0.42	0.10
	70 °C	0.58	0.34	0.48	0.10

In ssDSSCs with red Dragon fruit dye extract, V_{OC} and J_{SC} are not significantly changed upon varying extracting temperature. FF is higher at extracting temperature of 60 °C. The almost similar PCE values of 0.01-0.02% were obtained. In ssDSSC with red Spinach dye extract, V_{OC} are not significantly changed upon varying extracting temperature. Highest J_{SC} of 0.42 mA/cm^2 was produced at extracting temperature of 60 °C. FF of the device (extracting temperature RT) is 0.69 which is higher than those of the devices (higher extracting temperature 45-70 °C). The PCE values are the same at around 0.10- 0.11%. Among the ssDSSCs with three different extracts, the best performance was observed from the ssDSSCs with red Spinach dye extracted at 45 °C in ethanol, which showed a conversion efficiency (PCE) of 0.11 %, with open circuit voltage (V_{OC}) of 0.61 V, short circuit current density (J_{SC}) of 0.34 mA/cm^2, and fill factor (FF) of 0.55, under the irradiance of 1000 W/m^2.

(ii) Varying the Concentration of Co-solvents in Solvent-mixture

Fig. 5 shows J-V characteristics of the ssDSSCs using Henna, and red Dragon fruit and red Spinach dye extracts prepared in the solvents with different concentration of DMF in ethanol under AM 1.5 illumination (1000 W/m^2). Device parameters for ssDSSCs using Henna, red Dragon fruit and red Spinach dye solution extracted in different solvents (varying concentration of DMF in EtOH) at room temperature are listed in Table 2.

In ssDSSC using Henna dye in the solvent with varying concentration of DMF in ethanol, V_{OC} remained almost unchanged at around 0.45-0.48 V. However J_{SC} kept changed with maximum J_{SC} of 0.19 mA/cm^2 (DMF : EtOH - 4 : 6) and minimum J_{SC} of 0.08 mA/cm^2 (DMF: EtOH - 2 : 8). The maximum FF is 0.53 for (DMF : EtOH - 8 : 2). Thus PCE of the device (DMF : EtOH - 4 : 6) is 0.04% which is higher than those with other concentrations.

With red Dragon fruit dye extracted in solvent with varying concentration of DMF in ethanol, the ssDSSC generated V_{OC} value of 0.51-0.55 V. At concentration of DMF in ethanol (8 : 2), J_{SC} is maximum (0.16 mA/cm^2) and FF is minimum (0.37) among other concentrations of DMF in ethanol. Since PCE is determined from three device parameters

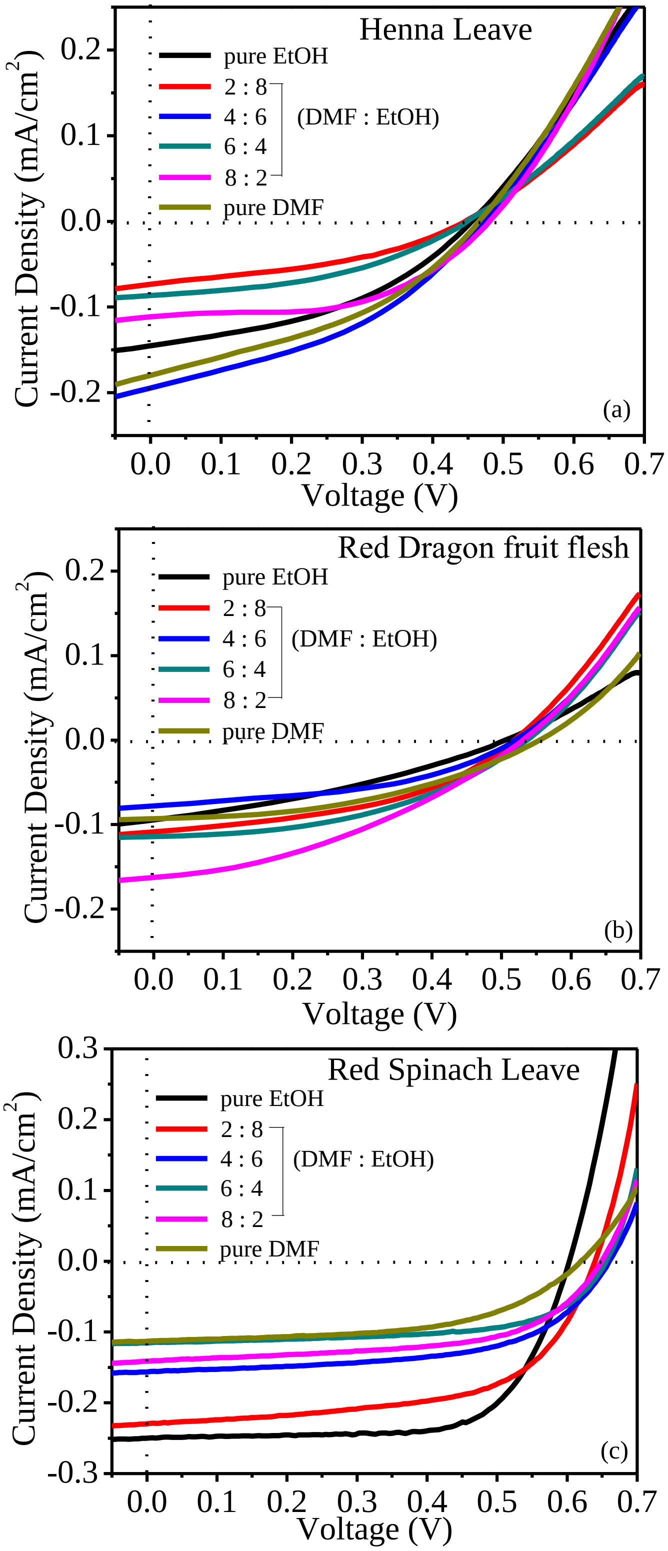

Figure 5 J-V characteristics of the ssDSSCs using (a) Henna, (b) red Dragon fruit and (c) red Spinach dye extracts in different solvents

Table 2 Device parameters for ssDSSCs using Henna, red Dragon fruit and red Spinach dye solution in solvent-mixtures (increasing concentration of DMF in ethanol) at room temperature.

ssDSSC Devices	Solvents	V_{OC} (V)	J_{SC} (mA/cm^2)	FF	PCE (%)
Henna Dye	Pure EtOH	0.46	0.15	0.41	0.03
	(DMF : EtOH - 2: 8)	0.45	0.08	0.38	0.01
	(DMF : EtOH - 4: 6)	0.47	0.19	0.39	0.04
	(DMF : EtOH - 6: 4)	0.45	0.09	0.42	0.02
	(DMF : EtOH - 8: 2)	0.48	0.11	0.53	0.03
	Pure DMF	0.47	0.18	0.38	0.03
Red Dragon Fruit Dye	Pure EtOH	0.51	0.09	0.33	0.02
	(DMF : EtOH - 2: 8)	0.52	0.11	0.43	0.02
	(DMF : EtOH - 4: 6)	0.52	0.08	0.44	0.02
	(DMF : EtOH - 6: 4)	0.54	0.11	0.44	0.03
	(DMF : EtOH - 8: 2)	0.53	0.16	0.37	0.03
	Pure DMF	0.55	0.09	0.42	0.02
Red Spinach Dye	Pure EtOH	0.60	0.25	0.69	0.10
	(DMF : EtOH - 2: 8)	0.64	0.23	0.59	0.09
	(DMF : EtOH - 4: 6)	0.66	0.16	0.58	0.06
	(DMF : EtOH - 6: 4)	0.65	0.12	0.62	0.05
	(DMF : EtOH - 8: 2)	0.65	0.14	0.58	0.05
	Pure DMF	0.62	0.11	0.55	0.04

V_{OC}, J_{SC} and FF, the PCE of red Dragon fruit device is around 0.02-0.03% regardless of varying solvent. Again V_{OC} is not significantly changed upon varying volume ratio in red Spinach device. J_{SC} and FF gradually decreased from 0.25 mA/cm^2 to 0.11 mA/cm^2 and from 0.69 to 0.55 respectively upon increasing DMF concentration. The efficiency of device using red Spinach in pure EtOH is as high as 0.10%.

Summary and Conclusion

In this work, the ssDSSC devices were fabricated using Henna, red Dragon fruit and red Spinach dye extracts. The photovoltaic performance was examined upon varying the dye extracting temperature in ethanol, and the concentration of DMF in ethanol. The highest extracting temperature of 70 °C degraded the device efficiency for Henna dye extracts while the device efficiency is almost insensitive to extracting temperature for red Dragon fruit and red Spinach dye extracts. Upon increasing concentration of DMF in ethanol, the device efficiencies keep fluctuating for Henna extracts, remain unchanged for red Dragon fruit extracts and offer highest efficiency of 0.10% for red Spinach extracts in pure ethanol. Among all, the efficiency of red Spinach device (extracted at 45 °C in ethanol) is as high as 0.11 %.

Acknowledgement

One of the authors (Nan Kyi Kyi Thein) gratefully acknowledges Associate Professor Nripan Mathews for the measurements including field-emission scanning electron microscopy (FESEM), electrochemical impedance spectroscopy (EIS) and device efficiencies during her internship at Energy Research Institute @ NTU (ERI@N), Nanyang Technological University, Singapore.

References

Anderson S. et al., (1979), *Nature*. 280, 571.

Bach U. et al., (1998), *Nature*. 395, 583.

Deibel C. and Dyakonov V. , (2010), *Rep. Prog. Phys*. 73, 39.

Fabregat-Santiago F. et al., (2009), *J. Am. Chem. Soc*. 131, 558.

Gratzel M. et al., (2003) , *J. Photochem. Soc*. 6, 889.

Gao F. et al., (2008), *J. Am. Chem. Soc*. 130, 10720.

O'Regan and Gratzel M. , (1991), *Nature*. 353, 737.

Snaith H. J. & Schmidt-Mende L. , (2007), *Adv. Mater* 19, 3187.

Snaith H. J. et al., (2007), *Nano Lett*. 7, 3372.

Schmidt-Mende L. et al., (2005), *Appl. Phys. Lett*. 86, 013504.

Snaith H. J. & Gratzel M. , (2007), *Adv. Mater*. 19, 3643.

J. Myanmar Acad. Arts Sci. 2020 **Vol. XVIII.No.2**B

CHARACTERIZATION OF GRAPHENIC MATERIAL COATED ON SAND FOR WATER PURIFICATION APPLICATION

Aung Thu Lin[1], Ye Chan[2], Myat Shwe Wah[3]

Abstract

In this research, a suitable methodology was introduced to synthesize of graphenic material on sand as graphenic material coated sand composite (GSC). Graphenic material was prepared from sugar and normal sand as a media of adhesion in order to produce graphenic material coated sand media which is well known as graphenic material coated sand composite (GSC). GSC was used to remove lead from lead solution. Physical and chemical tests were carried out for water purification applications. Structural properties of the obtained composites were analyzed by X-ray diffraction (XRD) and the morphology studied of GSC was characterized by scanning electron microscopy (SEM). And then residual lead concentration of the lead solution after filtration process were observed by using atomic absorption spectroscopy (AAS). The current study reveals the importance of water purification application using GSC.

Introduction

One of the most socially relevant aspects of nanotechnology is in the field of environmental remediation. Diverse applications of nanomaterials in decontamination of air, water and soil are intensely pursued in the recent past· The availability of large surface area and unusual electronic structure imparts new properties to nanomaterials. One of the early applications of such materials is the halocarbon decomposition and the use of this technology in pesticide removal· Numerous other applications of noble metal nanoparticles have been reported in the literature. Chemical interaction at noble metal nanoparticle surfaces often led to charge transfer and subsequent cleavage of chemical bonds, the most often encountered is reductive dehalogenation. Enhanced surface chemistry leading to faster kinetics is reported on noble metal nanoparticles. Carbon has been the most versatile material used for water purification in history. Very early account of the use of charcoal in water purification is found in the Vedic literature. It is believed that people of Indus valley civilization used carbon and porous materials, such as earthen vessels, for filtering and storing drinking water. The most widely used material for water purification today is activated carbon (AC) derived from plant sources. It has the best possible surface area and could be produced at low cost, making it the most affordable adsorption medium in diverse applications. A number of other forms of carbon have appeared with very large adsorption capacities. Advanced techniques such as membrane filtration, reverse osmosis and ion-exchange can be used in treatment and removal of contaminants from water. However, higher cost limits the large scale application of such treatment techniques in developing countries. One of the fascinating new additions into the carbon family is graphene' the one-atom thick sheets of carbon. Carbon materials, such as activated carbon, charcoal, carbon nano-tubes, have been used extensively in water purification and, hence, are indispensible components of all commercial water technologies. Materials derived from plant sources may even be more eco-friendly than those from fossil source such as petroleum. Among the simplest of natural sources of carbon are

---

[1] Dr, Lecturer, Department of Physics, Loikaw University

[2] Dr, Professor, Head of Universities' Research Centre, University of Yangon

[3] Dr, Associate Professor, Head of Department of Physics, University of Computer Studies (Kyaing Tong)

sugars, which upon dehydrogenation get converted completely to elemental carbon, leaving only water to escape. Similar reactions are applicable to decomposition of sugars of various kinds. This transformation is simple and effective. The carbon so obtained could be anchored on inorganic surfaces, and a subsequent chemical treatment could transform it to graphenic carbon (GC). Activation of newly formed surfaces may produce highly effective adsorbents. In this research, was observed in situ creation of graphenic material anchored onto the surfaces of river sand without the need of any additional binder. And also studied the application of this material in water purification

Materials and Methods

Materials

The raw materials used for the synthesis were common sugar, river sand, and sulfuric acid.

Methods of Characterization

X-ray diffraction patterns were recorded using X-ray diffractometer (Rigaku-Multiflex 2kW) which was operated at 30kV and 40mA with X-ray source of CuKα radiation having wavelength 1.5406° A. The XRD patterns in the 2θ range of (10°-70°) were recorded at room temperature. The surface morphology of GSC was imaged using a high resolution scanning electron microscopy JEOL JSM-5610LV model scanning electron microscope (SEM). And then residual lead concentration of the lead solution after removing process were observed by using atomic absorption spectroscopy (AAS).

Preparation of the Composite

Common sugar (sucrose crystals) was used as the carbon source. At first, the (160g) of sugar was dissolved in (100mL) distilled water and then, the solution was mixed with (40g) of sand (riversand). The mixture was dried at∼95°C on a magnetic stirrer for about 6 h with constant stirring. The sugar-coated sand was then placed in a ceramic crucible and heated in a furnace. The furnace temperature was programmed as follows: (a)from room temperature to 100°C in 30 min, (b) 100−200°C in 30 min(c), held at 200°C for 1 h (to melt sugar to form a uniform coating; melting point of sucrose is around 186°C), (d) ramped to 750°Cin1h,and (e) held for 3 h at 750°C (to ensure complete graphenic material of sugar). The furnace was switched off and the material was cooled to room temperature. The temperature of 750± 5°C was chosen as the final temperature after optimization through several experiments. No special care was taken in controlling the cooling rate. The black sample was named graphenic material coated sand composite (GSC). For activation, 5 g of the composite was treated with 10 mL of concentrated sulfuric acid and kept undisturbed at room temperature for 30 min. The mixture was then filtered and dried at 120°C. The activated GSC is labeled as GSC. The Figure (1) shows the preparation of graphenic material coated sand composite GSC.

Preparation of Pb^{2+}solution and Commercial Soft Drink with GSC Filtration

(1000 mg/L) stocks solution were prepared for $Pb^{2+}$by dissolving (1.5985g) of $Pb(NO_3)_2$ in one liter of distilled water then diluted to (50 mg/L) concentration to be used in subsequent experiments. Firstly, (3g) of GSC were packed in a tubular column of 20mL capacity with 8mm diameter and poured (15mL) of Pb^{2+}solution above the tubular column as shown in the following Figure(2). After that were made filtering process. The residual Pb^{2+} concentration of the Pb^{2+} solution after filtering process were observed by using atomic absorption spectroscopy (AAS). And then were calculated removal efficiency by using following equation.

$$\% \, Removal \, Efficiency = \frac{C_{0} - C_{e}}{C_{0}} \times 100$$

Where $C_0 \, and \, C_e$ is the initial and final concentration of solution (mg/L) respectively.

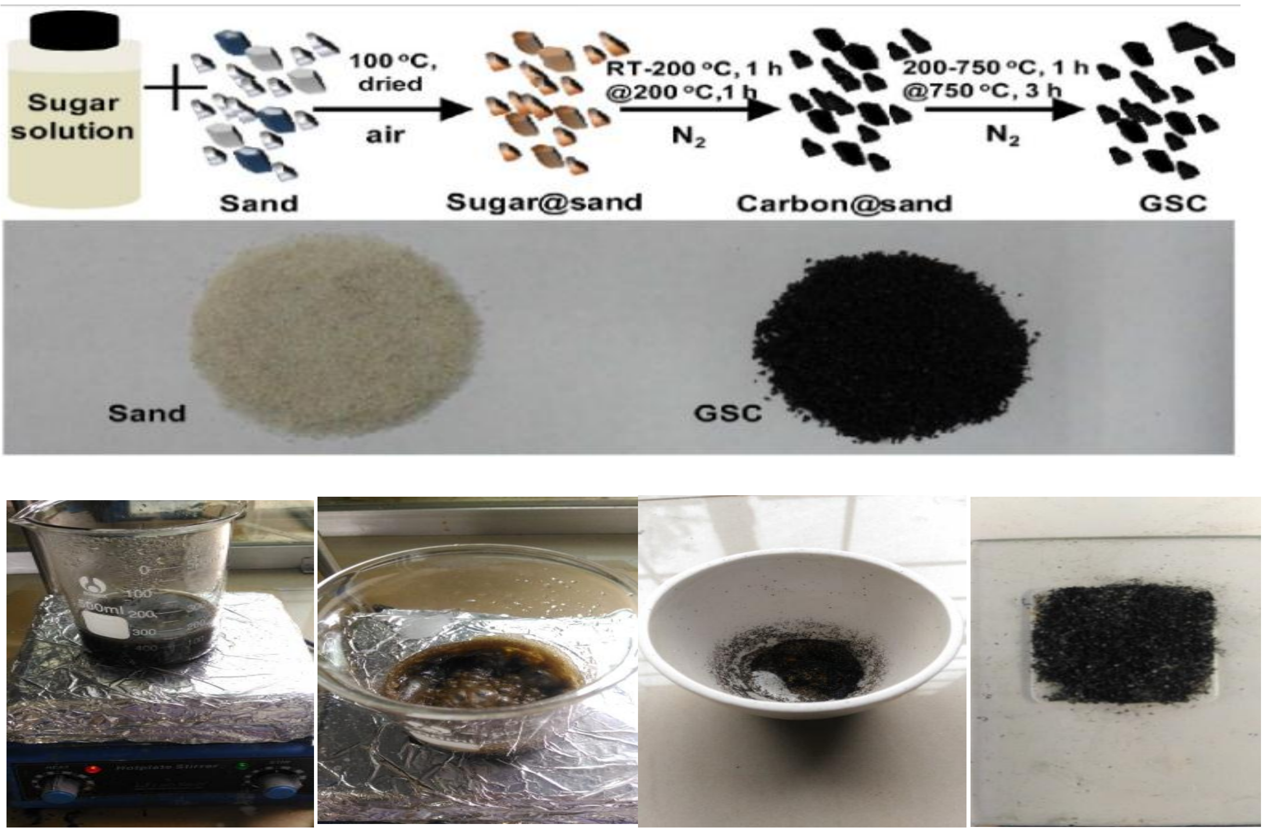

Figure 1 Photograph of preparation of graphenic material coated sand composite GSC

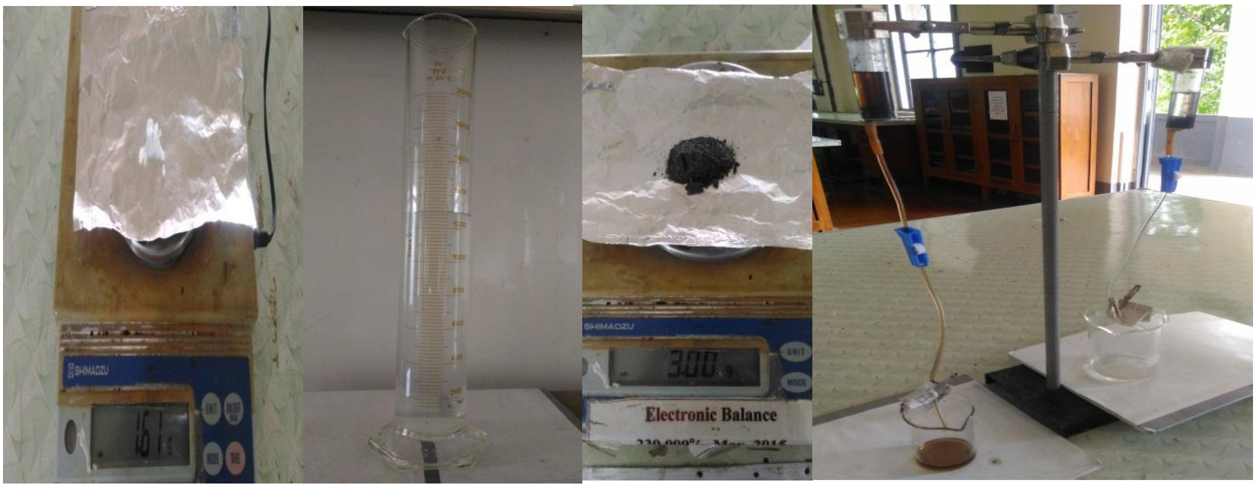

Figure 2 Photograph of preparation of Pb^{2+}solution and Filtration with GSC.

Results and Discussion

XRD Measurement

Structural studies of the GSC with heat-treated at 750°C for 3 hours were done with X-ray diffraction (XRD) technique. The crystalline sharp peaks in the diffraction pattern were identified by using the International Centre for Diffraction Data (ICDD). The crystalline size was calculated by using Scherer's equation; $D = (k\lambda)/(\beta \cos\theta)$ where, β is the peak width measured at half intensity (radian), λ is the wavelength measured in Å, k is the particle shape factor or Scherer constant (k= 0.9) and D is the crystallite size of the crystallites (Å).

The XRD spectra for GSC at750°C are depicted in Figure 3. XRD diffraction peaks belonging to (100), (101), (110), (102), (111), (200), (201), (112), (202), (103),(210) and (211) were observed in all these GSC which are well matched with the powder diffraction data of " *00-003-1161> Quartz, syn-SiO2* and *00-023-0064>Graphite* " were also well matched with diffraction peaks (002), (110), (101), (004). "*01-080-3905>syn-Carbon"* were also well matched with diffraction peaks (100). The diffraction peak at Quartz in (101) plane was pronounced sharper indicating that the crystallinity of GSC was improved at this processing condition. Agreement of lattice constant values ($a=b\neq c$) of GSC proved that quartz (SiO_2) has trigonal structure and carbon (C) has hexagonal structure.

Surface Morphology of GSC

Surface morphology of GSC sample was examined by scanning electron microscopy (SEM). SEM images of GSC layers heat-treated at750°C for 3 hr are shown in Figure 4. According to the images, it was observed that the graphenic materials coated on the sand in the form of flakes pattern. The graphenic materials were uniformly spread over the sand surface and it reveals the micro-grain structure with small crystallite sizes. The micron size grains are visualized on the surface of GSC.

AAS Measurement

The residual lead concentration of the lead solution after removing process were observed by using atomic absorption spectroscopy (AAS) is shown in Table 2. After filtering process with GSC sample, the initial (50mg/L) concentration of lead solution slightly decrease to (4.3 mg/L) concentration. Percentage of removing efficiency of GSC is (91.4%).The results prove that GSC has efficiently removed the lead concentration present in the initial (50mg/L) concentration of lead solution.

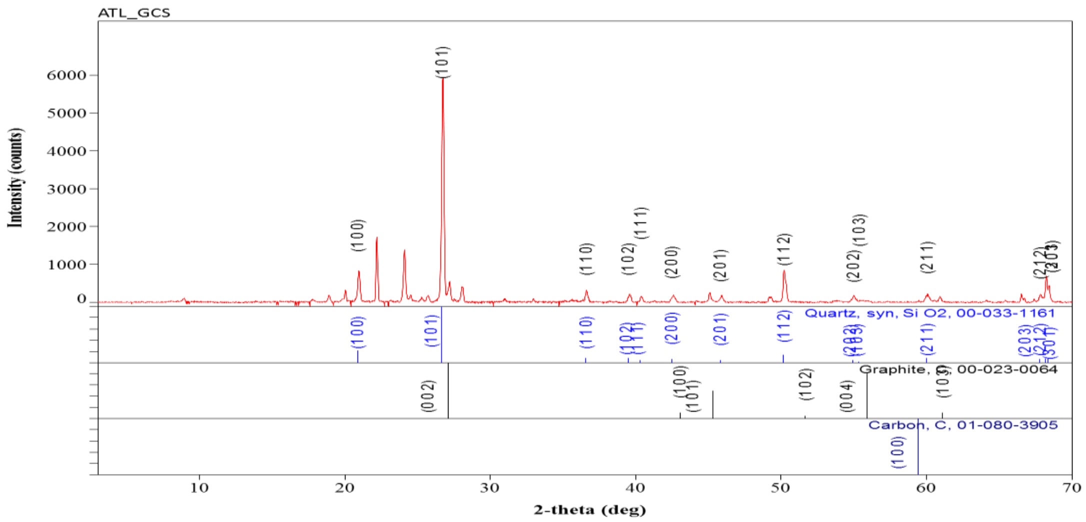

Figure 3 The XRD pattern of Graphenic material coated sand composite (GSC).

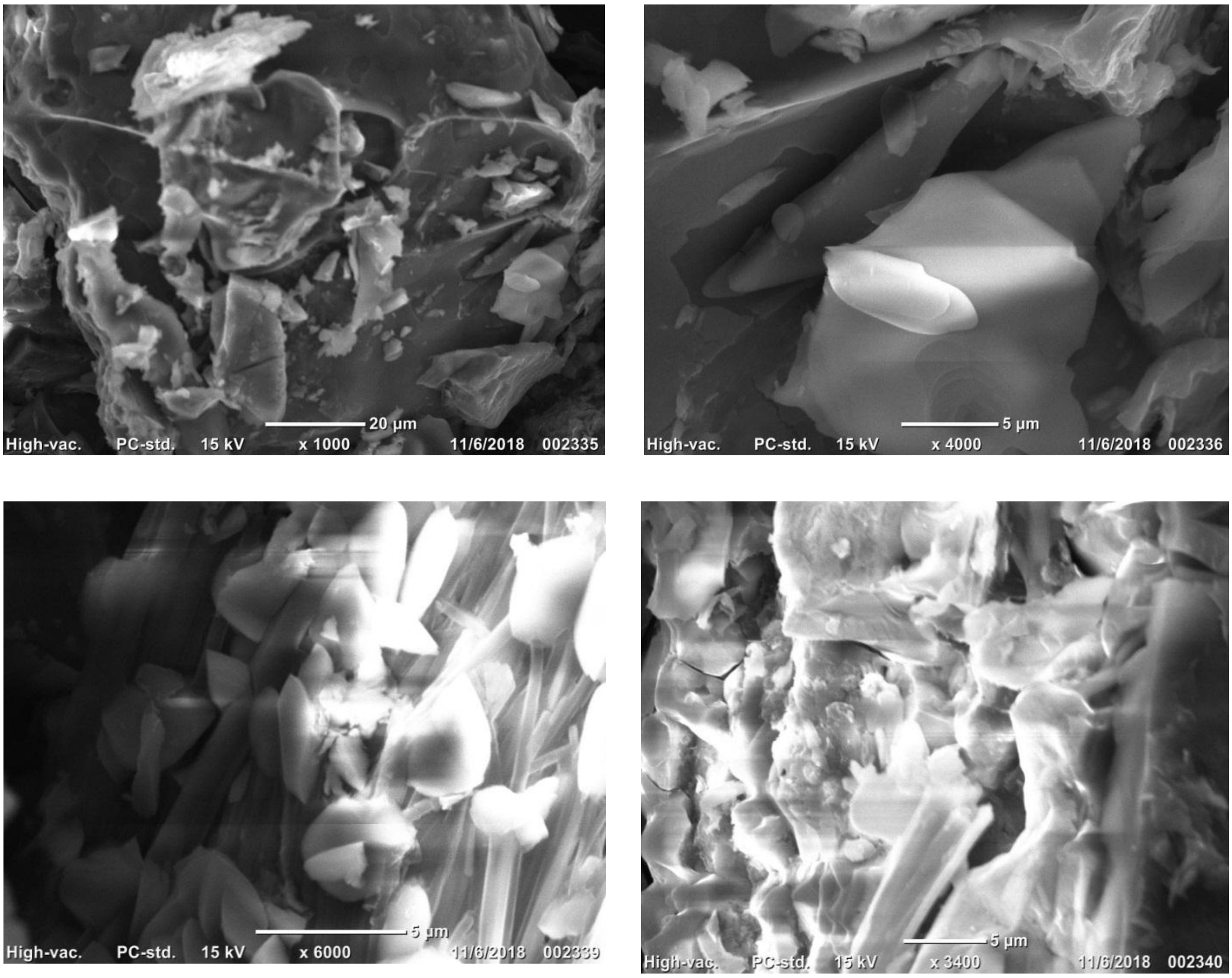

Figure 4 The SEM image of Graphenic material coated sand composite (GSC).

Table 1 The XRD result data of Graphenic material coated sand composite (GSC).

Sample	2-theta (deg)	d (Ȧ)	Phase name	FWHM (deg)
GSC	26.7229	3.3333	Quartz, syn(1,0,1)	0.1593
	27.176	3.2787	Graphite(0,0,2)	0.169
	59.476	1.5529	Carbon(1,0,0)	0.105

Table 2 The residual lead concentration of lead solution before and after filtration process with GSC.

The concentration of Lead Solution before filtering with GSC	The concentration of Lead Solution after filtering with GSC	% Removal Efficiency
50 mg/L	4.3 mg/L	91.4%

Conclusion

Graphenic material was prepared from sugar and normal sand as graphenic material coated sand composite (GSC) with slow carbonization at 200°C. In this research, the synthesized GSC was used to remove lead from lead solution. The XRD pattern of the sample GSC exhibited a stong peak for loading ratio of (160 g) sugar and (40g) sand (river sand) which corresponds to an interlayer spacing of about 0.333 nm, 0.327 nm and 1.552 nm, indicating the presence of SiO_2, graphenic material and carbon functionalities. The peak around 26.72˚, 27.17˚, and 59.47˚ are responsible for the presence of SiO_2, graphenic material and carbon and all other peaks corresponds for the elements present in the natural river sand and trace impurity of sand. The morphology of GSC was evident in the SEM images. Thin sheets of carbon are protruding outward and are visible as composites layers of graphenic material and sand mixture. It was observed that the synthesis of sugar-derived graphenic material supported on sand. The utilization of this material for water purification is evident from the data presented. The large percentage of removing efficiency, the availability of the raw materials and cost effective and environmental friendly synthesis method for preparing GSC are high potential to use in water purification and water treatment applications.

Acknowledgements

I do express my sincere thanks to Professor Dr Khin Khin Win, Head of Department of Physics, University of Yangon, for her kind permission and supporting this work.

I wish to show my sincere thanks to Dr Myo Lwin, Professor, Department of Physics, Dr Ye Chan, Professor and Head, Universities' Research Centre, Dr Aye Aye Thant , Professor, Department of Physics, Dr Yin Maung Maung, Professor, Department of Physics and Dr Thant Zaw Oo, Professor, Universities' Research Centre, University of Yangon for their helpful advice to carry out of this work.

References

Anonymous.Lancet(1912),180, 1025−1026.

Adams, B. A.Lancet(1932),219, 724−724.

Al-Rifai, J. H.; Khabbaz, H.; Scha□fer, A. I.Sep. Purif. Technol.(2011),77,60−67.

Bootharaju, M. S.; Pradeep, T.Langmuir (2012),28, 2671−2679.

Demirbas, A.J. Hazard. Mater.(2009),167,1−9.

Duran, A.; Tuzen, M.; Soylak, M.J. Hazard. Mater.(2009),169,466−471.

Gupta, R.; Kulkarni, G. U.ChemSusChem.(2011),4, 737−743.

Goyal, M.; Bhagat, M.; Dhawan, R.J. Hazard. Mater.(2009),171,1009−1015.

Ghosh, P. K.; Philip, L.J. Environ. Sci. Health., Part B(2005),40,425−441.

Geim, A. K.; Novoselov, K. S.Nat. Mater.(2007),6, 183−191.

Hager, D. G.Environ. Sci. Technol.(1967),1, 287−291.

Ka□mpf, H. J.Water Res. (1972),6, 493−494.

Litter, M. I.; Choi, W.; Dionysiou, D. D.; Falaras, P.; Hiskia, A.; LiPuma, G.; Pradeep, T.; Zhao, J.J. Hazard. Mater.(2012),211−212,1−2.

Matheson, L. J.; Tratnyek, P. G.Environ. Sci. Technol.(1994),28,2045−2053.

Matsui, Y.; Fukuda, Y.; Inoue, T.; Matsushita, T.Water Res.(2003),37, 4413−4424.

Novoselov, K. S.; Geim, A. K.; Morozov, S. V.; Jiang, D.; Zhang, Y.;Dubonos, S. V.; Grigorieva,I. V.; Firsov, A. A.Science (2004),306, 666−669.

Pradeep, T.; Anshup.Thin Solid Films (2009),517, 6441−6478.

Ruparelia, J. P.; Duttagupta, S. P.; Chatterjee, A. K.;Mukherji,S.Desalination (2008),232, 145−156.

Ruan, G.; Sun, Z.; Peng, Z.; Tour, J. M.ACS Nano(2011),5, 7601−7607.

Ruiz-Hitzky, E.; Darder, M.; Fernandes, F. M.; Zatile, E.;Palomares, F. J.; Aranda, P.Adv. Mater.(2011),23, 5250−5255.

Semiao, A. J. C.; Scha□fer, A. I.J. Membr. Sci.(2011),381, 132−141.

Yang, S.; Li, J.; Shao, D.; Hu, J.; Wang, X.J. Hazard. Mater.(2009),166, 109−116.

Zabihi, M.; Ahmadpour, A.; Asl, A. H.J. Hazard. Mater.(2009),167,230−236.

Zhang, S.; Li, X.-y.; Chen, J. P.Carbon(2010),48,60−67.

Zhang, H.; Zhu, G.; Jia, X.; Ding, Y.; Zhang, M.; Gao, Q.; Hu, C.;Xu, S.J. Environ. Sci.(2011),23,1983−1988.

J. Myanmar Acad. Arts Sci. 2020 **Vol. XVIII.No.2**B

DESIGN AND CONSTRUCTION OF SOLAR PANEL CHARGING CONTROLLER

San San Aye[1], Myat Myat Swe Win[2], Hla Ohn Mar[3]

Abstract

The solar panel charging controlled system is designed and constructed using the microcontroller and light sensor. The design of solar panel charging controlled system consists of a mid-range PIC microcontroller (PIC16F877A), an alphanumeric liquid crystal display, a crystal oscillator and a 5V relay. The controller circuit was operated by a 5V dc power supply. Microcontroller checks the specified minimum and maximum voltage or less than voltage of battery. If the battery voltage is lower than the predetermined minimum or maximum voltage, battery is charged. If the battery voltage is greater than the maximum voltage, the charging circuit is cut off via relay. This can be saved the battery life span and prevent from the setting fire.

Materials and Method

Materials

In this research, PIC microcontroller, solar cell panel, LCD display, relay and push buttons are used as hardware and Basic Pro language is used as software. The PIC16F877A is a high performance reduced instruction set computer CPU. It is necessary to learn 35 single word instructions to use the device. The device can be operated with 20MHz clock input and it contains 8K x 14 words of FLASH Program Memory, 368 x 8 bytes of Data Memory and 256 x 8 bytes of EEPROM Data Memory. The PIC16F877A comes in 40 pin packages as shown in Figure 1. There are 5 I/OPORTS, PORTA, PORTB, PORTC, PORTD and PORTE. Moreover, the device consists of 14 interrupts and both serial and parallel communication features. The serial communication uses MSSP (Master Slave Serial Programming) and USART (Universal Synchronous Asynchronous Receiver Transmitter). The parallel communication uses PSP (Parallel Slave Port).

Photovoltaic solar panels absorb sunlightas a source of energy to generate electricity. A photovoltaic (PV) module is a packaged; connect assembly of typically 6x10 photovoltaic solar cells. Photovoltaic modules constitute the photovoltaic array of a photovoltaic system that generates and supplies solar electricity in commercial and residential applications. Each module is rated by its DC output power under standard test conditions (STC), and typically ranges from 100 to 365 Watts (W). The efficiency of a module determines the area of a module given the same rated output an 8% efficient 230 W module will have twice the area of a 16% efficient 230 W module. There are a few commercially available solar modules that exceed efficiency of 22% and reportedly also exceeding 24%.

The HD44780 dot-matrix liquid crystal displays alphanumeric, Japanese katakana characters, and symbols. It can be configured to drive a dot-matrix liquid crystal display under the control of a 4- or 8-bit microprocessor. Since all the functions such as display RAM, character generator, and liquid crystal driver, required for driving a dot-matrix liquid crystal display are internally provided on one chip, a minimal system can be interfaced with this

---

[1] Dr, Lecturer, Department of Physics, Pyay University

[2] Dr, Lecturer, Department of Physics, Pyay University

[3] Dr, Lecturer, Department of Physics, Pyay University

controller/driver. The HD44780 character generator ROM is extended to generate 208 5 × 8 dot character fonts and 32 5 × 10 dot character fonts for a total of 240 different character fonts. The low power supply (2.7V to 5.5V) of the HD44780 is suitable for any portable battery-driven product requiring low power dissipation.

Method

The schematic diagram of solar panel charging control system is shown in Figure 1. The circuit design consists of PIC16F877A, a 4MHz crystal oscillator, voltage divider circuits, three control input switches, a reset switch, a 5V relay and an alphanumeric liquid crystal display.

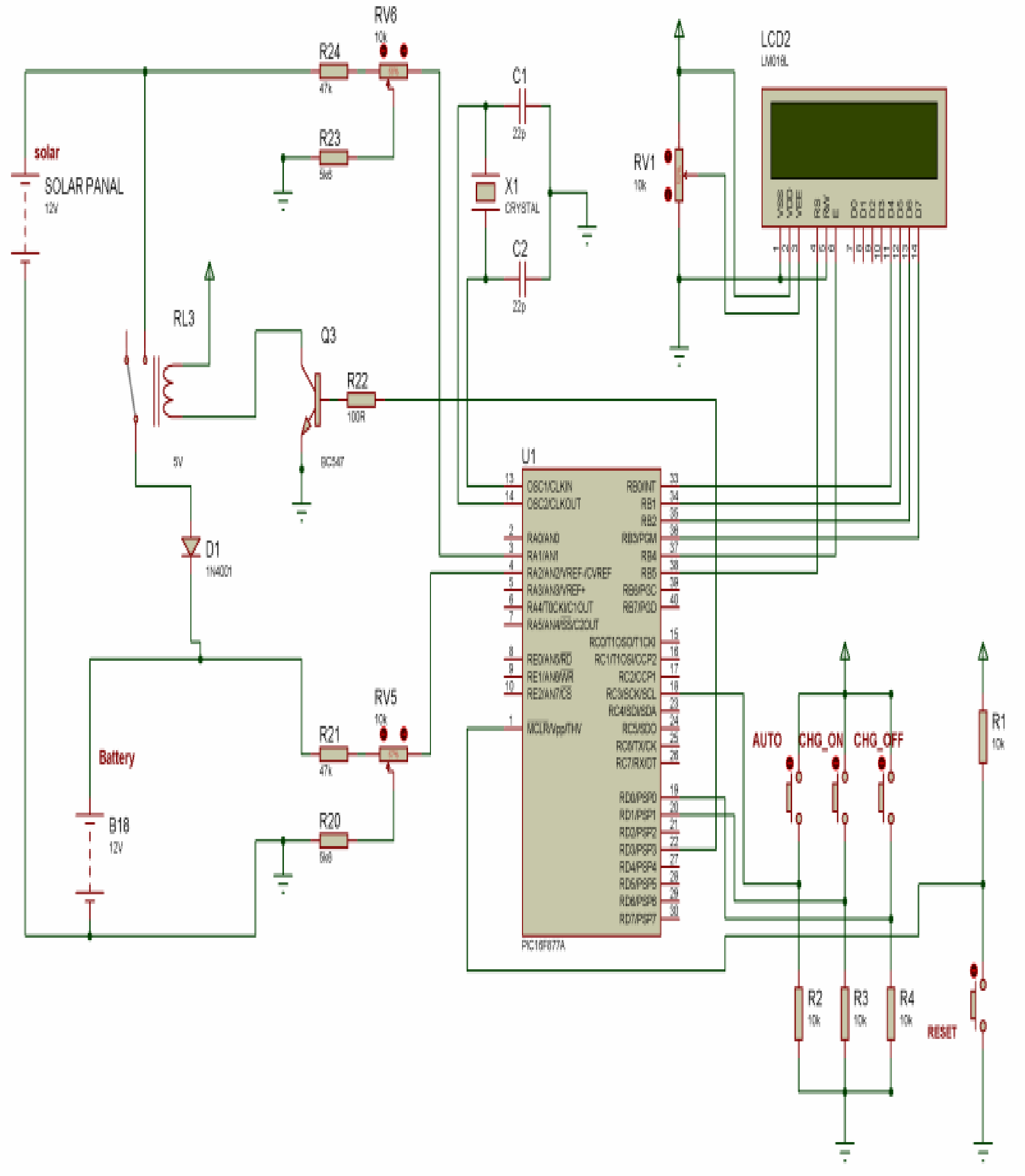

Figure 1 Schematic circuit diagram of Solar panel charging controlled system

The initial step to create the program sketch is drawing an outline flow diagram and it is usually known as flowchart diagram. The flowchart illustrate, programming flow with blocks and labels. In regular statements, it is illustrated with rectangular shape text boxes. In decision making process, it is illustrated with diamond shape text boxes. The flowchart is illustrated in Figure 2.

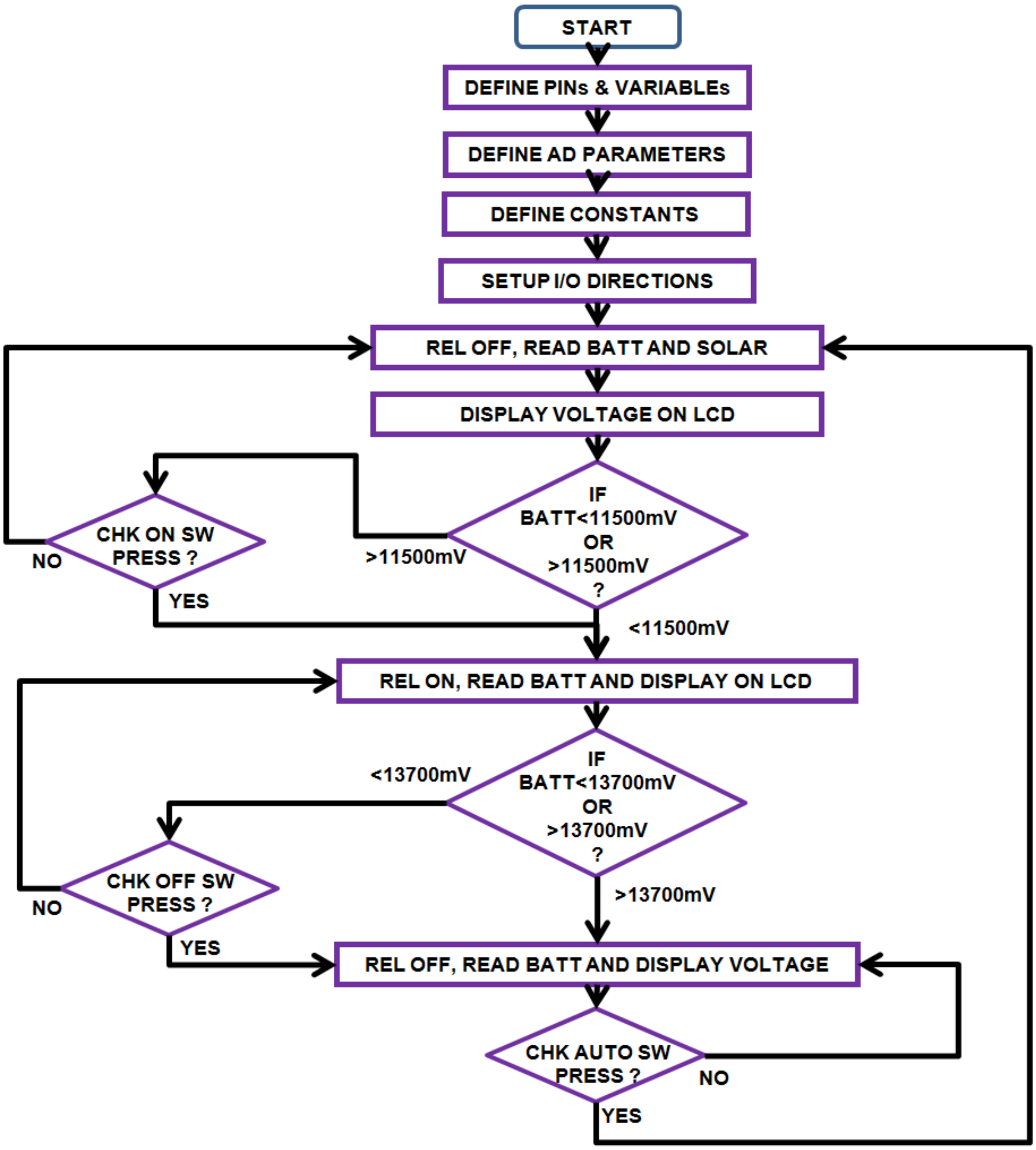

Figure 2 Flowchart

At the beginning of the program, I/O pins and variables are defined with suitable names. Then, analog to digital conversion parameters are defined to read battery and solar voltages. In this stage, the ADC resolution was taken for maximum 10 bit resolution. Therefore, minimum voltage the microcontroller can measure was 4.88mV. ADC conversion clock is operated with internal RC clock and data sampling time is about 50µs. Then, the input and output pin directions are setup for their operations. The program looping started by initially switch off the relay for original condition. Then, the battery and solar voltages are read and display on the LCD as mV.

Then, the conditional testing for battery voltage was checked whether it is above or below the 11500mV (11.5V, recharge level). If the battery voltage is above 11500mV, the program checks for charging on switch. If the switch is not pressed, the program loops back to initial state.

If the battery voltage is lower than 11500mV or charging on switch is pressed, the program jump to charging on routine. In this routine relay is switched on and read the battery voltage and display on LCD. Then, the program check the battery voltage condition, whether it is greater than maximum charging level (13700mV or 13.7V). If it is less than 13700mV, the program jumps to check the charging off switch. If the switch is not pressed, the program loops back to charging on routine.

If the battery voltage is greater than maximum voltage level or charging off switch is pressed, the relay is switched off to disconnect the solar panel and battery. Then, the program again checks for auto function switch. If it is not pressed, the system cannot initiate automatic charging function. If it is pressed, the program loops back to initial routine.

Operation of solar cell panel charging controlled system

The circuit of solar cell panel charging controlled system is constructed and connected to solar cell panel as shown in Figure 3.Before connecting the battery and solar panel, their voltages are checked with a digital voltmeter. The solar panel used in the circuit is TATA BP SOLAR and the voltage rating is 12V-5Watt solar panel. The voltage of solar panel in the room is about 5.5V, but in the bright sun light, it is about 14.5V.Therefore, the solar panel is required to locate under the bright sunlight for charging the battery. Then, measure the battery voltage. The battery is Leopard sealed lead acid 12V 4Ahr battery. The voltmeter indicates the new battery is about 12.7V and it is ready to use. Then, the battery and solar cell panel are installed on the control circuit terminals.

Then, the power supply is switched on for the control circuit. The LCD display cannot illuminate the characters clearly on the display; therefore, the yellow variable resistor on the left side of the LCD display is adjusted to achieve clear fine contrast characters on the display. Then, the reset switch is pressed again the LCD display initiated with the research title as shown in Figure 4.

Then, the battery and solar panel voltages are read with analog input of microcontroller and display on the LCD. The charging off condition is display on the right side of the LCD as shown in Figure 5. Since the battery voltage is 12930mV and solar voltage is 14490mV so that the battery voltage is above the charging level and charging condition is in the off state. It will not be automatically charge unless the battery voltage is below the minimum battery level. The minimum battery level is setup for about 11500mV in this control system. But the user can manually charge by pressing the charging on switch. There is a click sound from the relay when the switch is pressed and display illuminated as shown the Figure 6 for charging on state. While it is charging, the battery level gradually increases and after a few hours, the battery voltage becomes greater than the maximum voltage level (13700 mV). Then, the relay is automatically switched off the charging and back to initial state. Another method to stop the charging before the battery level become maximum voltage level is charging off switch. Pressing the charging stop button switched off the charging condition and display for battery and solar voltages, but did not loop back to automatic initial state. Therefore, to be back to automatic charging condition, the automatic function input switch is required to press, if conditional charging stop was made by using charging off switch. In this way, the battery can be automatically repeatedly charge within safe battery charging level and the battery is ever ready to use.

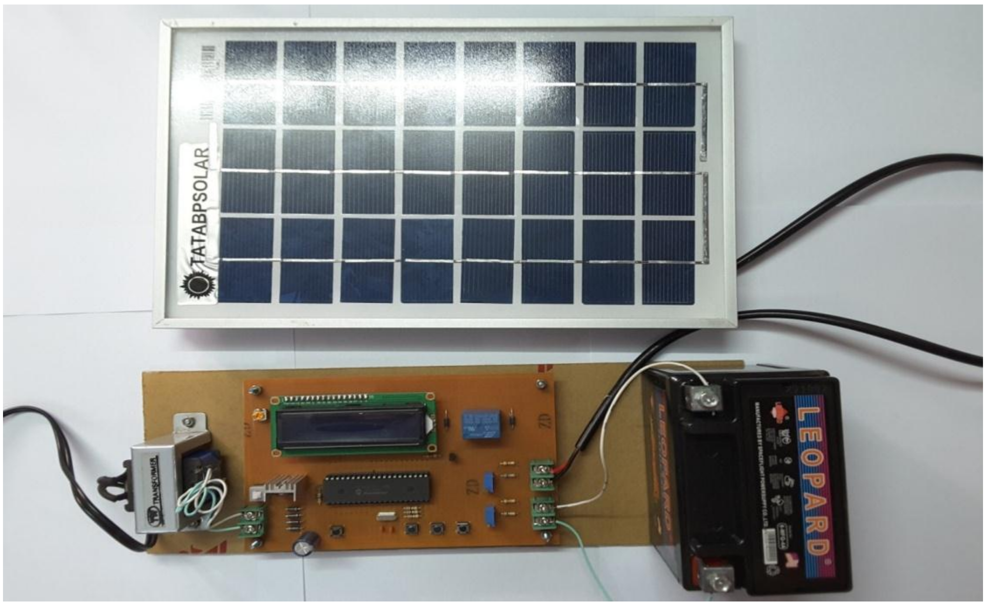

Figure 3 Complete connection of solar charging control system

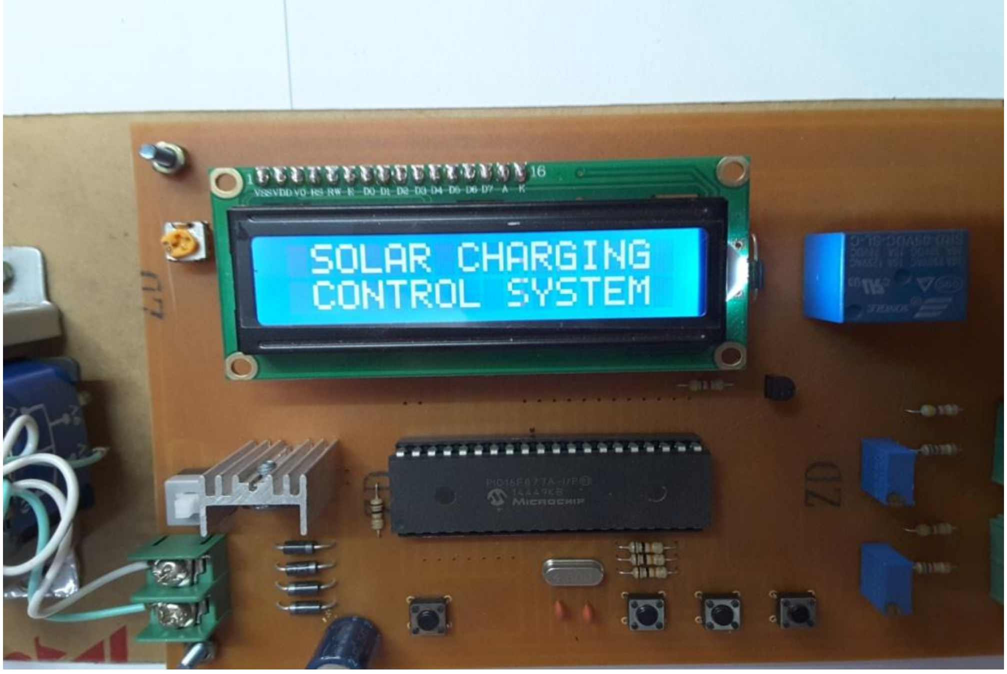

Figure 4 Initiating the program

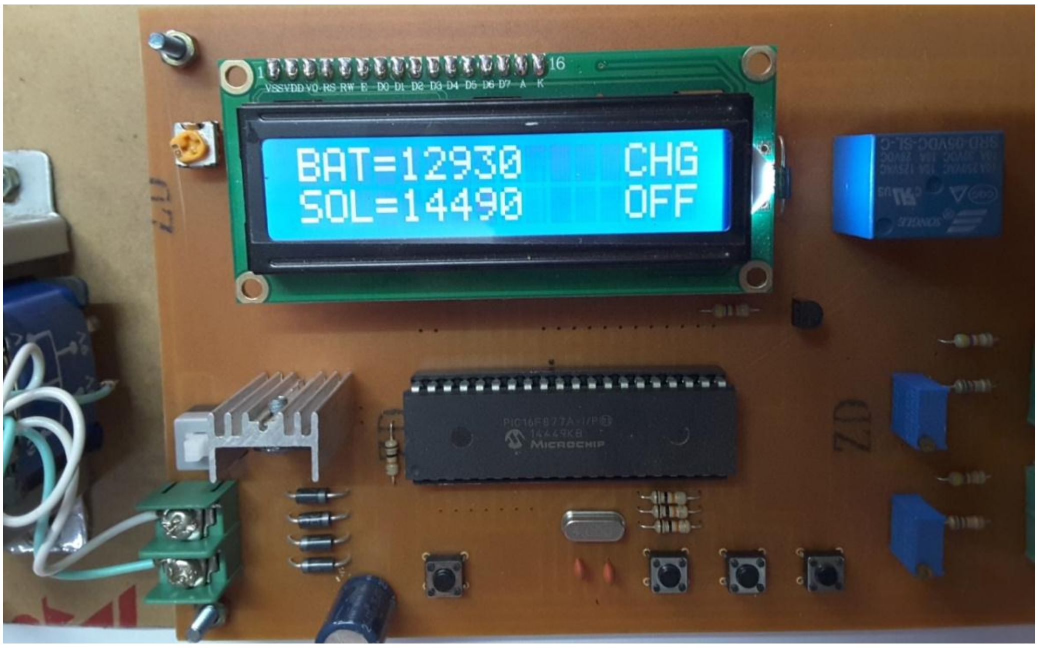

Figure 5 Charging off

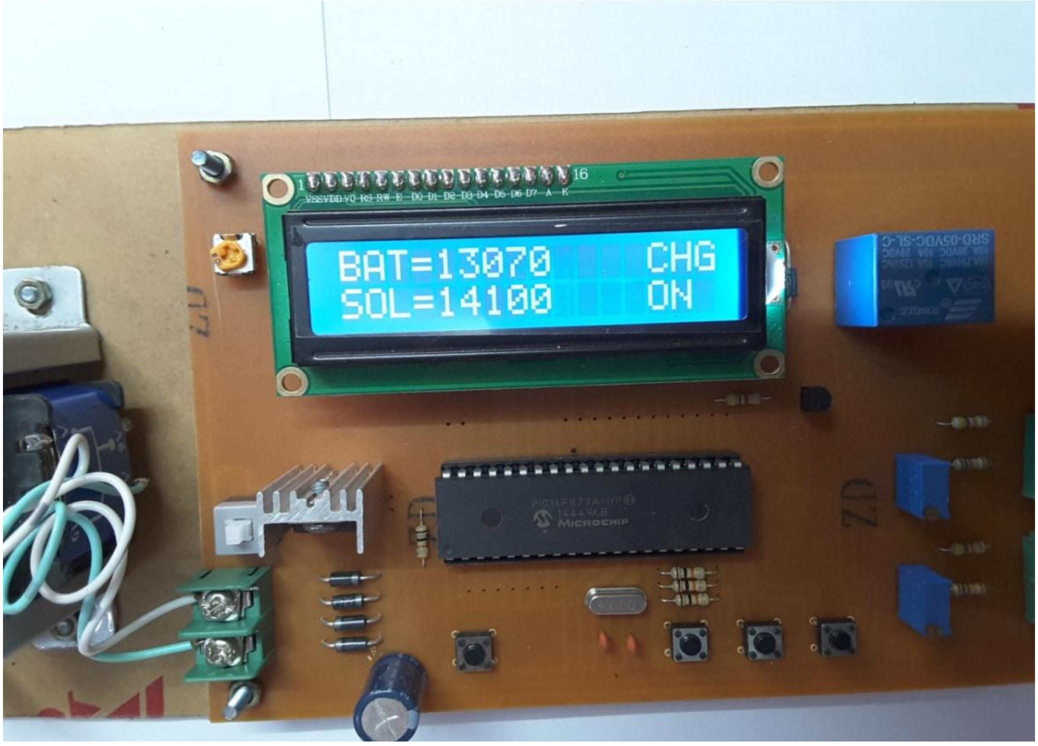

Figure 6 Charging on

Discussion

The solar charging controller is successfully constructed by PIC Microcontroller 16F877A. The four major portions consist in this circuit. There are PIC16F877A Microcontroller, inputs, outputs and display. The power supply unit is adding in this circuit for display of adjust input and output voltage to battery. This circuit is adjusted by manual and automatic operation. This circuit is control between solar panel and battery.

Conclusion

The solar panel charging control system is constructed and tested. As soon as the power switch is on, the battery level immediately display on the LCD in mV. The testing of the circuit results are illustrated with the photos. When the battery level falls to low level, charging started automatically. The manual input switch is supported to manual charging, before battery level falls to low level. When the charging complete, the charging automatically stop to prevent overcharging battery. The battery can be applied for any other 12 V devices for lighting, dc fan operating and so on. Normally, the charging period lasted for about 4 hours under test running for 4000 mAhr battery. But the charging time may vary according to the sunlight intensity. Discharging the battery by using a 3W LED lamp lasted for about 16 hours. It is reliable and able to use full life time of a battery.

Acknowledgement

I would like to express sincere gratitude to Dr Aung Aung Min, Rector of Pyay University, for his kind permission to submit this paper and profound gratitude to Dr Thwe Lin Ko, Pro-rector of Pyay University, for her encouragement. I acknowledge Professor and Head Dr Sue Sue Nwe, and Professor Dr Naw Htoo Lar Phaw, Department of Physics, Pyay University, who gave us the opportunity to do this research.

References

Microchip Technology Incorporated (1999) “PIC 16F877A Instruction Set” (New York: Microchip Technology)

Marston R.M. (1996) “Modern CMOS Circuit Manual” (London: B H Newnes)

Nick Dossis (3/2002) "Everyday Practical Electronics" (London: Wimborne Publishing)

Sid Katzen (2000) “The Quintessential PIC Microcontroller” (Berlin:Springer)

Sinclair I. R. (2001) “Practical Electronics Handbook” (London: B H Newnes)

Thomas l. Floyd (1996) “Electronic Devices” (New Jersey: Prentice-Hall)

J. Myanmar Acad. Arts Sci. 2020 **Vol. XVIII.No.2**B

SYNTHESIS AND CHARACTERIZATION OF TiO_2 THIN FILMS BY SPRAY PYROLYSIS METHOD

Ni Lar[1], Min Maung Maung[2], and Aung Min[3]

Abstract

In this research work, anatase TiO_2 sample was mixed with the methoxyethanol solution was used as the starting materials. The n type Silicon <100> plane was used as a substrate. The silicon substrate was annealed at 1000°C in furnace. The mixture solution was deposited on SiO_2/Si substrate using spray pyrolysis- like method at different temperatures at 100°C, 200°C and 300°C respectively. The structural properties of $TiO_2/SiO_2/Si$ films were analysed by XRD. The morphological properties of these films were determined by SEM. The optical properties of films were investigated by UV-Vis spectrophotometer.

Keywords: TiO_2 thin films, silicon substrate, XRD, illumination, spray pyrolysis.

Introduction

The development of new materials, blends, composites and advanced materials is a necessity for modification of mechanical, electrical, optical and thermal properties of thin films to fulfill the demand for improved materials in industries. The studies of semi-conducting thin film are being pursued with increasing interest on the account of their proven and potential applications in many semiconductor devices. [Chen, X. & Mao, S.S.(2007)]. Titanium dioxide (TiO_2) is a widely recognized candidate for photovoltaic (PV) applications because of its photoactive and electrical properties. It is a large band gap (3–3.2 eV) semiconductor with remarkable electrical and optical properties such as high refractive index, good transmission in the VIS and NIR regions, and high dielectric constant. TiO_2/Si structures constitute a primary component in the fabrication of photovoltaic and optoelectronic devices and recent research has paid special attention to the search for novel appropriate techniques to enhance their efficiency.[Mo,S.,& Ching,W.(1995)]. Titanium oxide thin film has been one of the most extremely studied oxides because of its role in various applications namely photo-induced water splitting, dye synthesized solar cells, environmental purifications gas sensors display devices, batteries etc. The present research work, on the spray-pyrolysis processing, structure, optical and electrical properties of TiO_2 thin films as a function of deposition and annealing temperatures was discussed. The energy band gap of TiO_2 thin film coated on silicon substrate was evaluated with the aid of UV spectrophotometer.[Mo,S.,& Ching,W.(1995)].

Materials and Method

Experimental Procedure

The precursor solution contained titanium dioxide and Methoxyethanol ($C_3H_8O_2$) was stirred with magnetic stirrer for 10 min to get homogeneous solution. The solution was atomized by a pneumatic spray system using compressed air as a carrier gas onto Si (100) wafers. The films were deposited at 100-300°C by a pulsed solution feed. The pulse consists of one minute of

---

[1] Daw, Lecturer, Department of Physics, Mawlamyine University.

[2] Dr, Associate Professor, Department of Physics, University of Yangon.

[3] U, Lecturer, Department of Physics, Mawlamyine University.

spray time and one minute of pause; up to three pulses were performed. The films were subsequently heat treated at 100°C, 200°C and 300°C for 30 min.

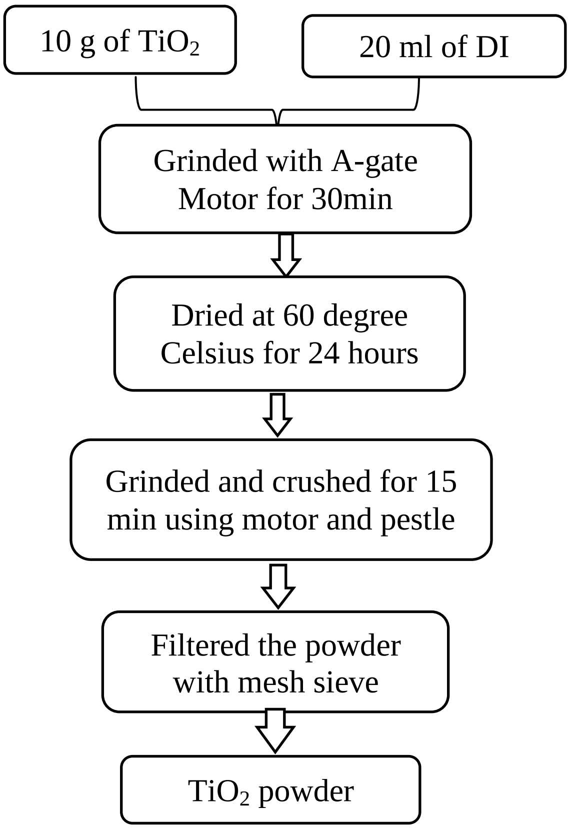

Figure1 Preparation of TiO_2 powder

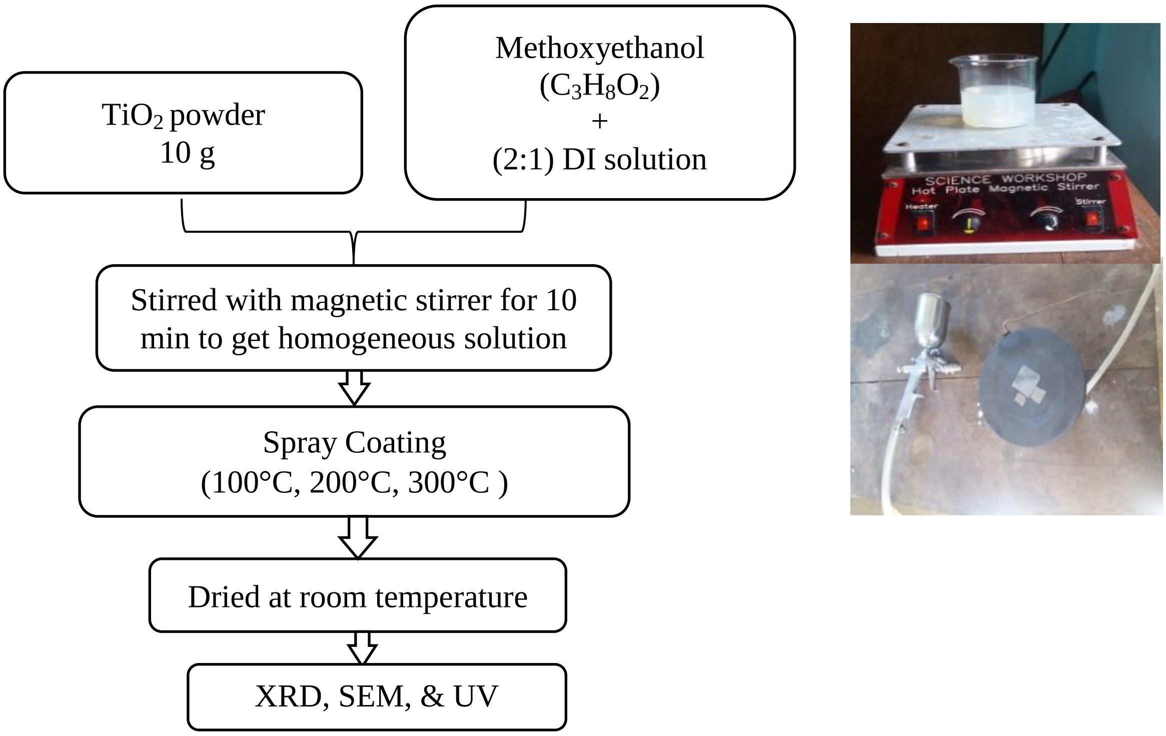

Figure 2 Flow chart of the deposition of $TiO_2/Si/SiO_2$ film

Results and Discussion

Structural Properties of $TiO_2/SiO_2/Si$ Thin Tilms

Structural studies of the $TiO_2/SiO_2/Si$ films with heat-treated at 100°C for 30 minutes were done with X-ray diffraction (XRD) technique. X-ray diffraction patterns were recorded using X-ray diffractometer (Rigaku-Multiflex 2kW) which was operated at 30kV and 40mA with X-ray source of CuKα radiation having wavelength 1.5406Å. The XRD patterns in the 2θ range of (10°-70°) were recorded at room temperature. The crystalline sharp peaks in the diffraction pattern were identified by using the International Centre for Diffraction Data (ICDD). The crystallite size was calculated by using Scherer's equation; $D = (k\lambda)/(\beta \cos\theta)$ where, β is the peak width measured at half intensity (radian), λ is the wavelength measured in Å, k is the particle shape factor or Scherer constant ($k= 0.9$) and D is the crystallite size of the crystallites (Å). The XRD spectra for $TiO_2/SiO_2/Si$ films at 100°C, 200°C and 300°C are depicted in Figure 3, 4 and 5. XRD diffraction peaks belonging to (101), (103), (004), (112), (200), (105), (211), (213), (204), and (116) were observed in all these $TiO_2/SiO_2/Si$ films which are well matched with the powder diffraction data of 03-065-5714>Anatase, syn-TiO_2 and 01-075-3162>Silicon Oxide, SiO_2 were also well matched with diffraction peaks (101), (110), (111), (102), (200), (112), (211), (202), (113), (212), (004) and (203). For the sample at 100°C, 200°C and 300°C, the diffraction peaks were pronounced sharper indicating that the crystallinity of $TiO_2/SiO_2/Si$ was improved at this processing condition. The crystallite sizes estimated by using Scherer's equation were found to be 59.8nm, 61.7nm and 66.4nm as shown in Table 1.The lattice constant was obtained from peak locations and miller indices yielded the parameters of $TiO_2/SiO_2/Si$. Agreement of lattice constant values ($a=b\neq c$) proved that $TiO_2/SiO_2/Si$ has tetragonal structure.

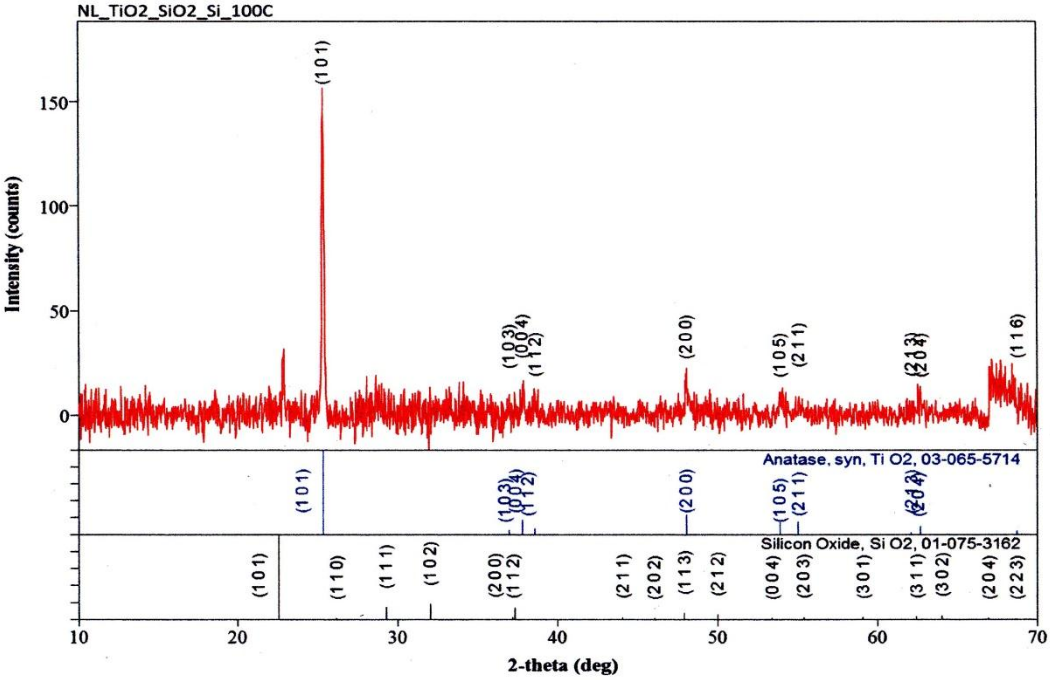

Figure 3 X-ray diffraction pattern of TiO_2 /SiO_2/Si film at 100 °C

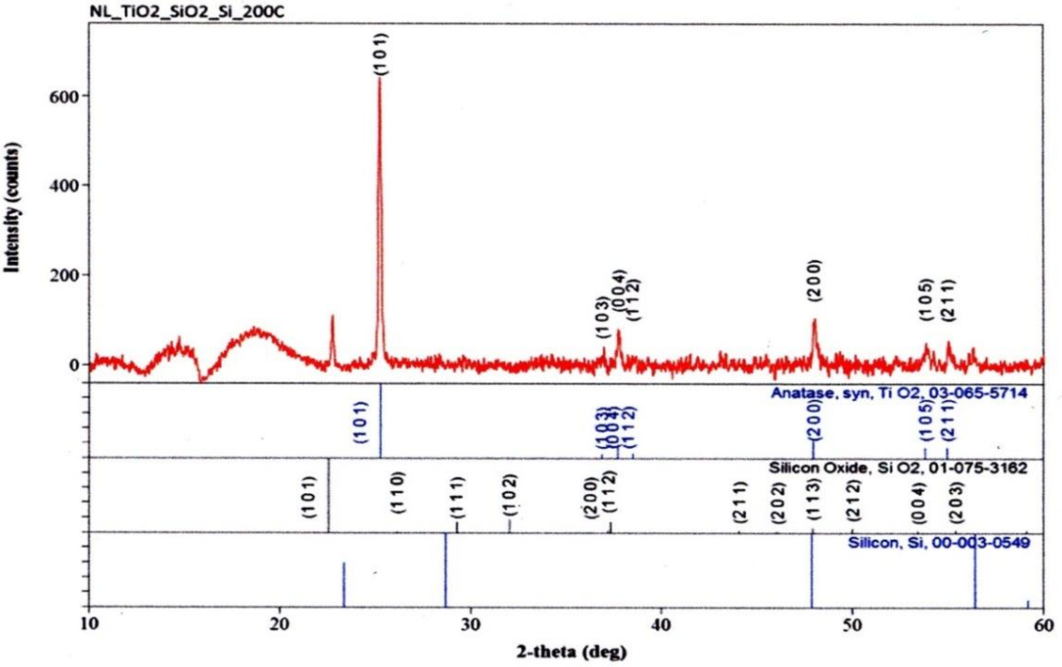

Figure 4 X-ray diffraction pattern of TiO_2 /SiO_2/Si film at 200 °C

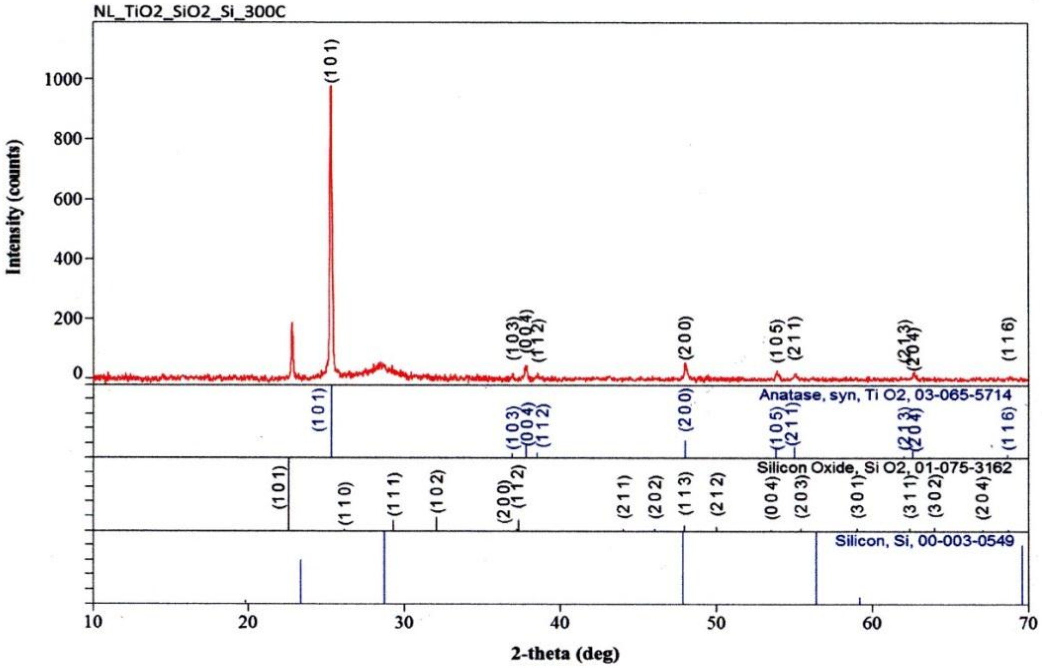

Figure 5 X-ray diffraction pattern of TiO_2 /SiO_2/Si film at 300 °C

Table 1 Structural properties of $TiO_2/SiO_2/Si$

Temperature (°C)	2-theta (deg)	d (Å)	Phase name	FWHM (deg)	Crystallite Size (nm)	a (Å)	c (Å)	c/a
100	25.285	3.5195	Anatase, syn (101)	0.142	59.8	3.7839	9.5843	~ 3
200	25.220	3.5284	Anatase, syn (101)	0.138	61.7	3.7932	9.5305	~ 3
300	25.246	3.5248	Anatase, syn (101)	0.128	66.4	3.7895	9.5202	~ 3

Surface Morphology of $TiO_2/SiO_2/Si$ Layer

The surface morphology of the anti-refractive layer was imaged using a high resolution scanning electron microscopy JEOL JSM-5610LV model scanning electron microscope (SEM). Surface morphology of $TiO_2/SiO_2/Si$ layer was examined by scanning electron microscopy (SEM). SEM images of TiO_2 /SiO_2/Si layers heat-treated at 100°C, 200°C and 300°C are shown in Figure 6(a-c). The $TiO_2/SiO_2/Si$ layers were uniformly spread over the substrate and it reveals the micro-grain structure with small crystallite sizes. The micron size tetragonal $TiO_2/SiO_2/Si$ grains were visualized on the surface of $TiO_2/SiO_2/Si$ film. The grain sizes of the $TiO_2/SiO_2/Si$ layers are 208nm, 303nm and 414nm as shown in Table 2. The thickness of the silicon substrate is about 0.173µm as shown in Figure 7(a). The thickness of the TiO_2 /SiO_2/Si film is about 2.03µm as shown in Figure 7(b) & (c).

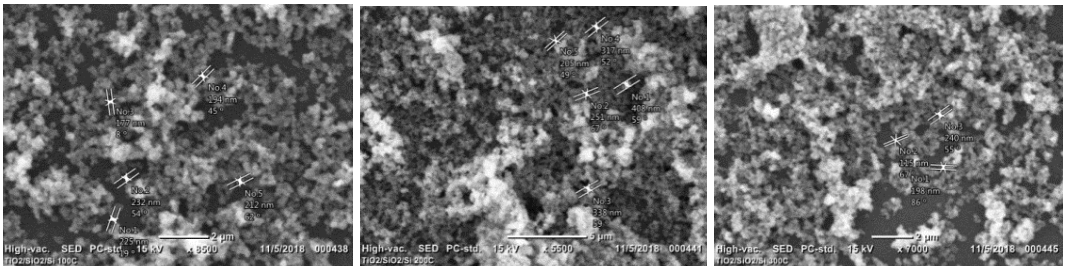

(a) (b) (c)

Figure 6 Scanning Micrograph of TiO_2 /SiO_2/Si at (a) 100 °C (b) 200 °C and (c) 300 °C

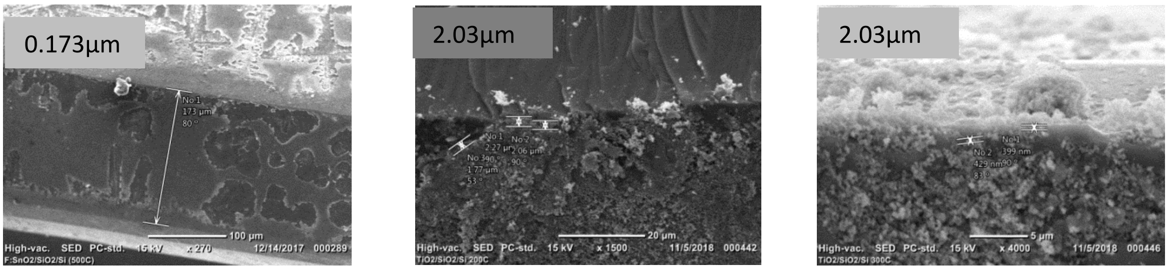

(a) (b) (c)

Figure 7 The thickness of (a) Silicon substrate (b) TiO_2 /SiO_2/Si at 200 °C and (c) TiO_2 /SiO_2/Si at 300°C

Table 2 The values of grain size of TiO_2 /SiO_2/Si samples

Temperature (^{o}C)	Grain size (nm)
100	208
200	303
300	414

Energy band gap Analysis

Ultraviolet–visible spectroscopy or ultraviolet-visible spectrophotometry (UV-Vis or UV/Vis) refers to absorption spectroscopy or reflectance spectroscopy in the ultraviolet-visible spectral region. The absorption spectra of TiO_2/SiO_2/Si layer at 500°C on quartz were recorded in the wavelength range of 300 to 800 nm using UV/VIS-1800 spectrophotometer in absorbance mode. To verify the photocatalytic behaviour, it was necessary to establish the optical absorption properties as an initial step. Shimadzu UV–Vis double beam spectrophotometer (Shimadzu UV-1800) was used to record the absorption spectra in the range of 300–800nm. The optical absorption spectrum of TiO_2 nanoparticles was obtained by using UV spectrophotometer at room temperature in the transmission mode. It was well known that the semiconductor nanoparticle energy gap increases with decreasing grain size.

The optical band gap of TiO_2/SiO_2/Si layers were estimated from the plot of $(\alpha h\nu)^2$ vs (hν). The $(\alpha h\nu)^2$-hν plot is shown in Figure (8). The optical band gap of TiO_2/SiO_2/Si layers were found to be (~ 2.85eV). High transmission and wide band gap of TiO_2/SiO_2/Si layers are the favorable properties of interfacial layer in photovoltaic (PV) devices.

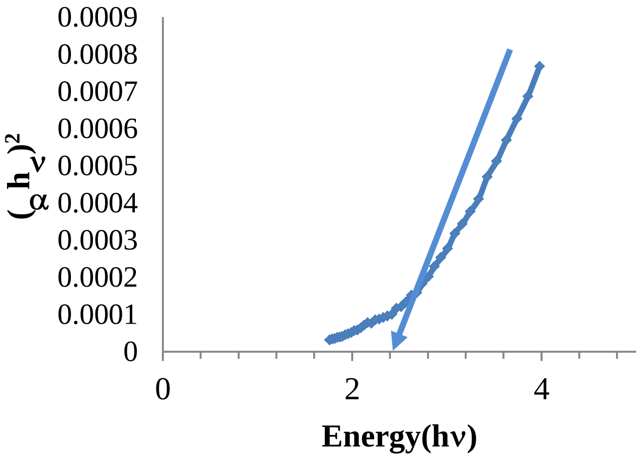

Figure 8 Energy band gap of TiO_2 with MEOH

Conclusion

$TiO_2/SiO_2/Si$ layer were prepared by spray pyrolysis- like method. From the XRD analysis, their lattice parameters were nearly the same in all samples. It could be improved that their lattice parameters were independent in the annealing temperature effect. The crystallite sizes are 59.8nm, 61.7nm and 66.4nm. The grain sizes are 208nm, 303nm and 414nm, respectively. $TiO_2/SiO_2/Si$ layer showed its wide optical band gap (~ 2.85eV) and the thicknesses of its active layer is 2.03 µm. The crystallize size and grain size increase with the temperature increase. It was nearly agreed that the energy band gap of the $TiO_2/SiO_2/Si$ sample with the literature values.

Acknowledgements

I would like to thank Professor Dr Khin Khin Win, Professor and Head, Department of Physics, University of Yangon, for her kind permission to carry out this work and her valuable supervision for this research.

I wish to show my sincere thanks to Professor Dr Aye Aye Thant, Department of Physics, University of Yangon, Professor Dr Yin Yin Myint, Head of Department of Physics, Mawlamyine University for their fruitful discussions to this work.

I deeply thank for my co-supervisor Dr Myat Shwe Wah, Associate Professor, Head of Department of Physics, University of Computer Studies Kyaing Tong, for her valuable guidance.

References

Chen, X. & Mao, S.S. (2007). "Titanium dioxide Nanomaterials: Synthesis, properties, modifications and applications" Chem. Rev.; 107: 2891.

Cromer, D .T. & Herrington, K. (1955). “The structures of anatase and rutile”. J. Am. Chem. Soc, 77: 4708.

Mo, S., & Ching, W. (1995). “Electronic and optical properties of three phases of titanium dioxide: Rutile, anatase and brookite’’ Phys. Rev B, 51: 13023.

Setiawati, E. & Kawano, K. (2008). “Stabilization of anatase phase in the rare earth; Eu and Sm ion doped nanoparticle TiO_2 ’’ J. Alloys Compd.; 451 (1-2): 293- 296.

Simons, P Y. & Dachille, F. (1967). "The structure of TiO_2II, a high- pressure phase of TiO_2" Acta Cryst, 23: 334.

Thamaphat, K., Limsuwan, P. & Ngotawornchai, B. (2008). “Phase Characterization of TiO_2 Powder by XRD and TEM”. J. (Nat. Sci.) ; 42: 357-361.

Wu, F., Li, X., Wang , Z., Guo, H., Wu, L., Xiong, X. & Wang, X. (2011). “A novel method to synthesize anatase TiO_2 nanowires as an anode material for lithium-ion batteries” J. Alloys Compd., 509 (8): 3711-3715.

J. Myanmar Acad. Arts Sci. 2020 **Vol. XVIII.No.2**B

PREPARATION AND STRUCTURAL PROPERTIES OF COPPER FERRITE BY SOL-GEL METHOD

Su Su Tha[1] & Hsan Htoo[2]

Abstract

Copper ferrite materials were synthesized by sol-gel method. The X-ray diffraction (XRD) confirmed the phase formation and the structural characterization of these samples. The lattice parameter "a" of cubic structure was slightly decreased with increasing sintering temperature. The crystallite size of these samples was also evaluated. The grain size and grain boundary of ferrite samples were also analyzed by scanning electron microscope (SEM).

Keywords: *Copper Ferrite*, XRD and SEM

Introduction

Magnetic materials are widely used as components in various applications of industrial and medical equipments. Ferrites have emerged as novel materials with vast technological and scientific interest considering their brilliant physical properties such as reliable magnetization, high coercive force, large magnetocrystalline anisotropy as well as remarkable chemical stability and low cost. Since their discovery in the 1950 the degree of interest in them has grown enormously, and is still growing today. The ferrite materials may be classified into three different classes; spinel ferrites, garnet ferrites and hexagonal ferrites. The ferrites used for magnetic recording, data storage materials, radar absorbing materials due to their strong magnetic losses at the range of GHz frequency, magnetoelectric applications. These materials have a potential application at high frequency range due to their very low electrical conductivity, fairly large magneto-crystalline anisotropy, relatively large saturation magnetization, mechanical hardness, excellent chemical stability and low production costs [Gholamreza Nabiyouni et al./ JNS 3(2013)].

Various methods are used to synthesize ferrite nanoparticles, such as: combustion, mechano-chemical method, redox process, forced hydrolysis, co-precipitation, sol–gel, hydrothermal, polymer combustion method (PC), solid state method (SS), micro-emulsion, sonochemical, electrochemical and thermal decomposition method. Among the various methods, the sol-gel method is probably opted for homogeneity and improved characteristics.

The structure properties and the confirmation of cubic inverse spinel phase of copper ferrite nanoparticles are studied in the present work using the X-ray diffraction (XRD). The investigation of surface morphology of ferrite samples were carried out by using scanning electron microscope (SEM).

Materials and Method

Experimental Procedure

The nanoparticles composition of $CuFe_2O_4$ chemical were synthesized by the sol-gel method. The chemical precursors used in reaction were iron (III) nitrate nonahydrate [$Fe(NO_3)_3.9H_2O$], copper nitrate [$Cu(NO_3)_2$], and de-ionized water. In first the metal nitrates

---

[1] PhD Candidate, Lecturer, Department of Physics, Mawlamyine University

[2] Dr, Lecturer, Universities Research Centre, University of Yangon

dissolved in de-ionized water in required molar ratios. The obtained solution was heated using a magnetic stirrer on 70°C with stirring until forming the gel. Then the temperature was remained at 75°C until preparation a dry gel. Afterwards, the copper ferrite powder was heated in different temperatures such as 500°C, 600°C, 700°C, 800°C and 900°C for 1hr. Flow diagram of the sample preparation procedure of copper ferrite is given in Figure 1.

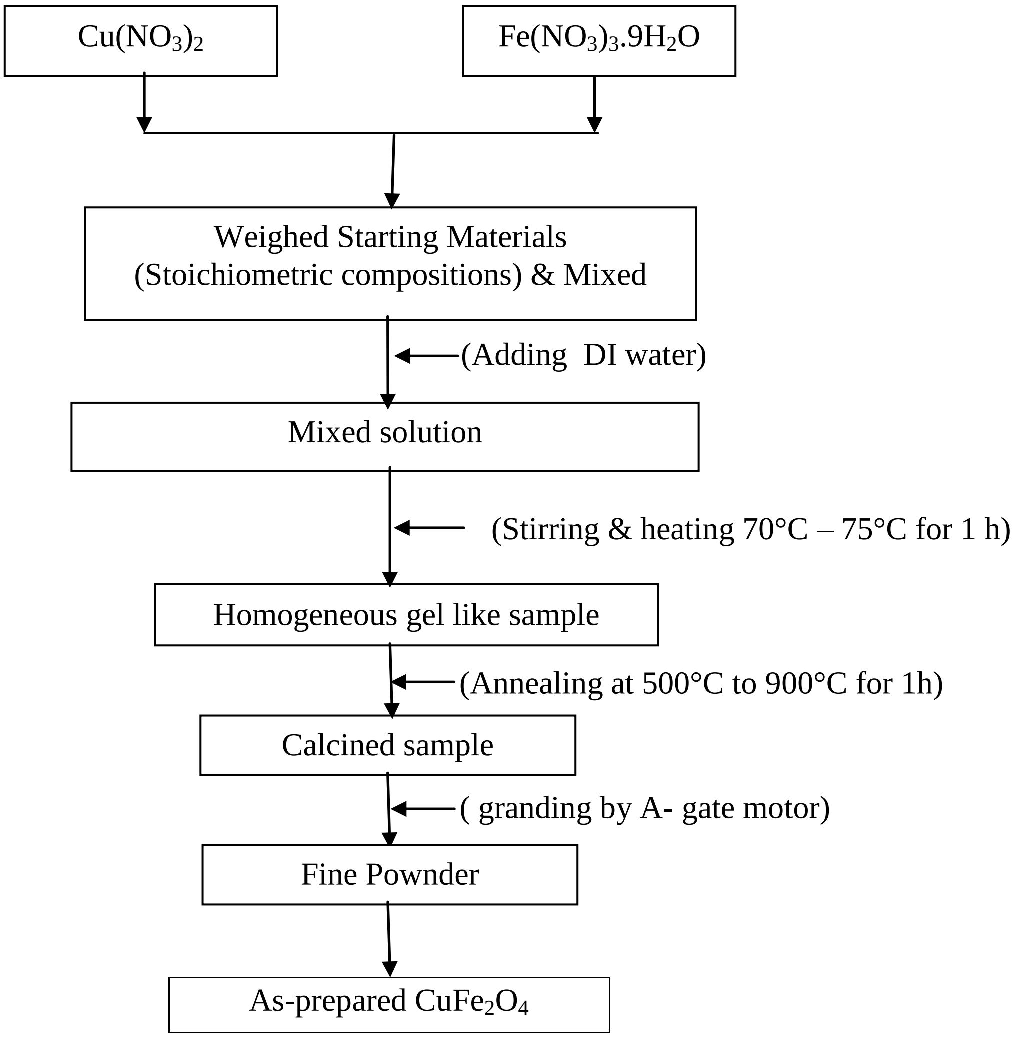

Figure 1 Flow diagram of the sample preparation procedure of $CuFe_2O_4$

Results and Discussion

Structure Analysis

XRD analysis was carried out to study the crystal structure and properties of $CuFe_2O_4$. It was performed using monochromatic Cu-K_α radiation ($\lambda = 1.54056$ Å) operated at 40 kV (tube voltage) and 40 mA (tube current). Specimen was scanned from 10° to 70° in diffraction angle, 2θ with step-size of 10° per minute. The observed XRD profiles of $CuFe_2O_4$ were shown in following figures. The reference profile was 25-0283 > $CuFe_2O_4$ of International Centre for Diffraction Data (ICDD) library file. The dominant peak are (111), (220), (311), (222), (400), (511) and (440) reflection. The crystal structure of $CuFe_2O_4$ is Cubic structure. Comparison of crystallite size of samples between various temperatures were investigated and presented in the following table. The crystallite size can be measured as following Debye-Scherrer formula.

$$D = \frac{k\lambda}{B \cos \theta}$$

Where, D = Crystallite size (nm). λ = The wavelength of X-ray use (1.5405 Å)

B = Full Width Half Maximum of dominant peak (radians)

θ = Angle of diffraction (radians), *k* = Scherrer constant

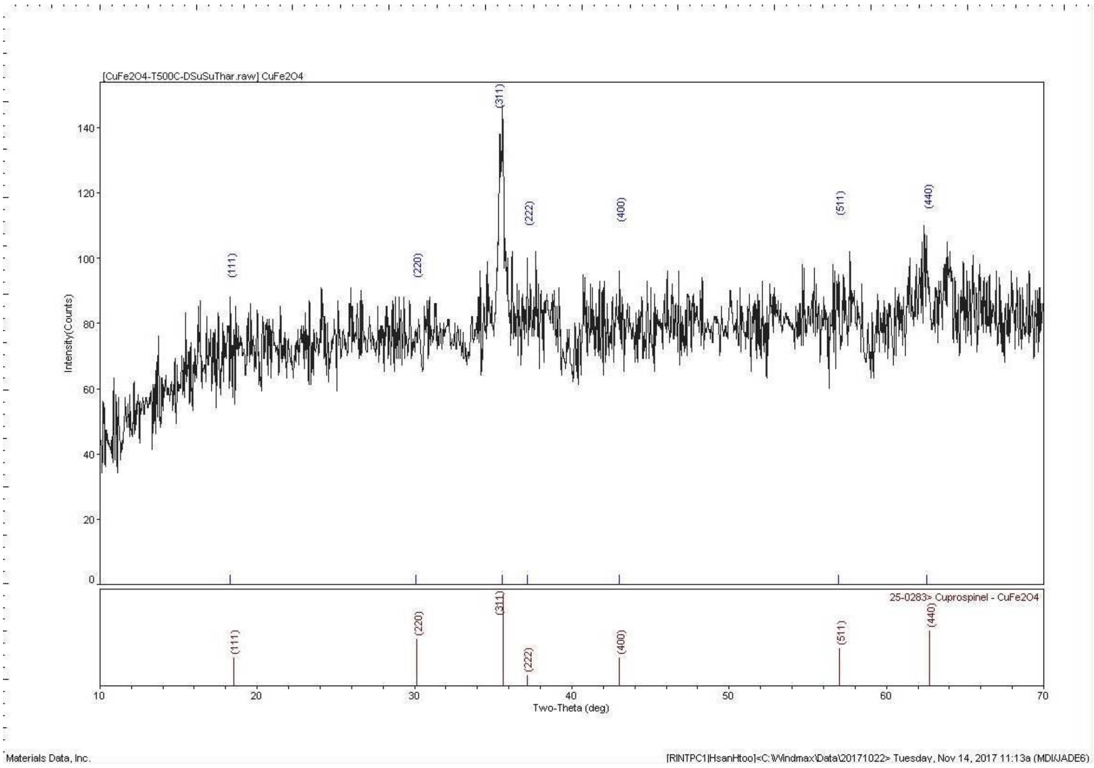

Figure 2 (a) XRD pattern for $CuFe_2O_4$ ferrite sample (500°C)

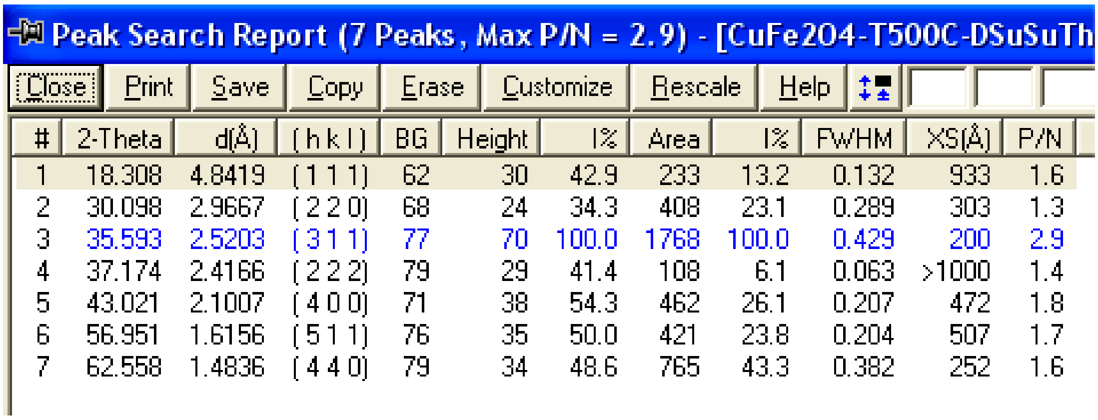
Peak Search Report (7 Peaks, Max P/N = 2.9) - [CuFe2O4-T500C-DSuSuTh

#	2-Theta	d(Å)	(h k l)	BG	Height	I%	Area	I%	FWHM	XS(Å)	P/N
1	18.308	4.8419	(1 1 1)	62	30	42.9	233	13.2	0.132	933	1.6
2	30.098	2.9667	(2 2 0)	68	24	34.3	408	23.1	0.289	303	1.3
3	35.593	2.5203	(3 1 1)	77	70	100.0	1768	100.0	0.429	200	2.9
4	37.174	2.4166	(2 2 2)	79	29	41.4	108	6.1	0.063	>1000	1.4
5	43.021	2.1007	(4 0 0)	71	38	54.3	462	26.1	0.207	472	1.8
6	56.951	1.6156	(5 1 1)	76	35	50.0	421	23.8	0.204	507	1.7
7	62.558	1.4836	(4 4 0)	79	34	48.6	765	43.3	0.382	252	1.6

Figure 2 (b) XRD result data of Peak Search Report for $CuFe_2O_4$ ferrite sample (500°C)

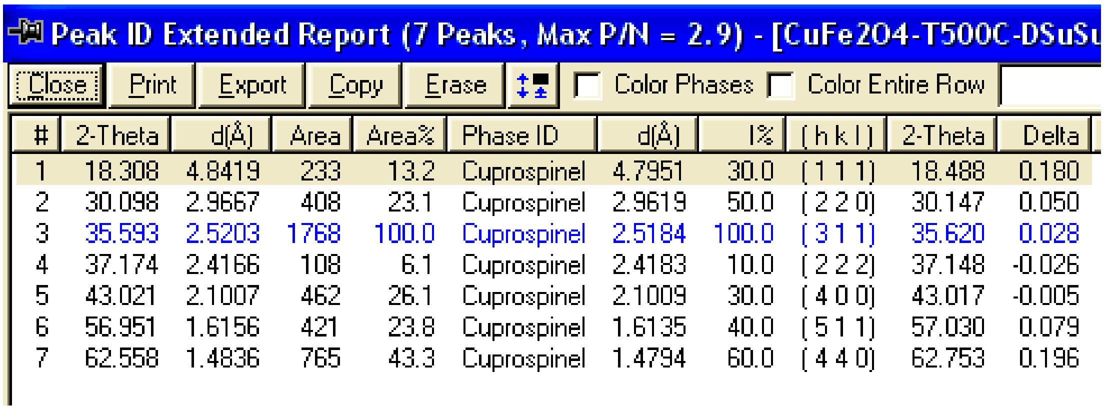

#	2-Theta	d(Å)	Area	Area%	Phase ID	d(Å)	I%	(h k l)	2-Theta	Delta
1	18.308	4.8419	233	13.2	Cuprospinel	4.7951	30.0	(1 1 1)	18.488	0.180
2	30.098	2.9667	408	23.1	Cuprospinel	2.9619	50.0	(2 2 0)	30.147	0.050
3	35.593	2.5203	1768	100.0	Cuprospinel	2.5184	100.0	(3 1 1)	35.620	0.028
4	37.174	2.4166	108	6.1	Cuprospinel	2.4183	10.0	(2 2 2)	37.148	-0.026
5	43.021	2.1007	462	26.1	Cuprospinel	2.1009	30.0	(4 0 0)	43.017	-0.005
6	56.951	1.6156	421	23.8	Cuprospinel	1.6135	40.0	(5 1 1)	57.030	0.079
7	62.558	1.4836	765	43.3	Cuprospinel	1.4794	60.0	(4 4 0)	62.753	0.196

Figure 2 (c) XRD result data of Peak ID Report for $CuFe_2O_4$ ferrite sample (500°C)

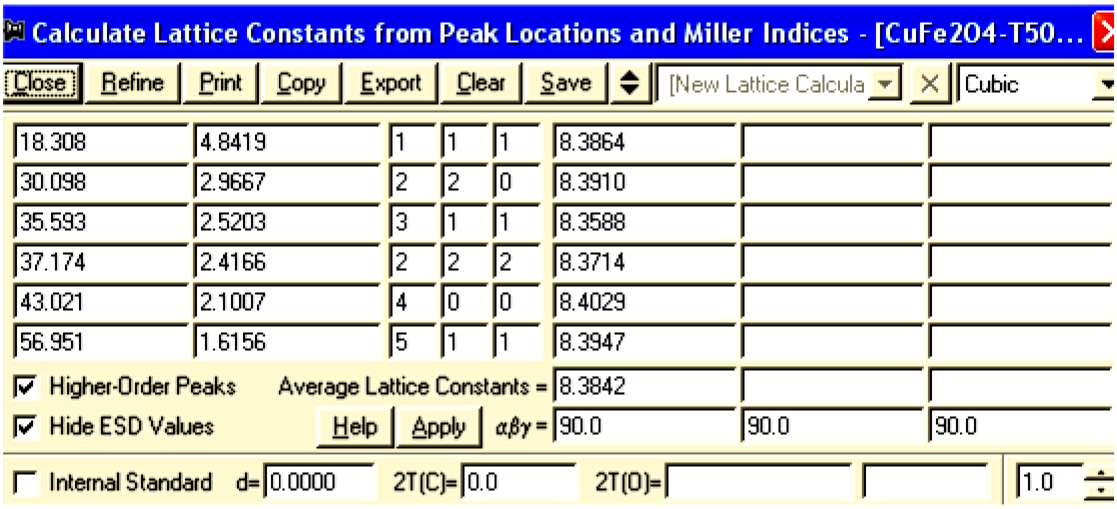

Cubic

18.308	4.8419	1	1	1	8.3864		
30.098	2.9667	2	2	0	8.3910		
35.593	2.5203	3	1	1	8.3588		
37.174	2.4166	2	2	2	8.3714		
43.021	2.1007	4	0	0	8.4029		
56.951	1.6156	5	1	1	8.3947		

☑ Higher-Order Peaks Average Lattice Constants = 8.3842

☑ Hide ESD Values αβγ = 90.0 90.0 90.0

☐ Internal Standard d= 0.0000 2T(C)= 0.0 2T(0)= 1.0

Figure 2 (d) XRD result data of Structure Report for $CuFe_2O_4$ ferrite sample (500°C)

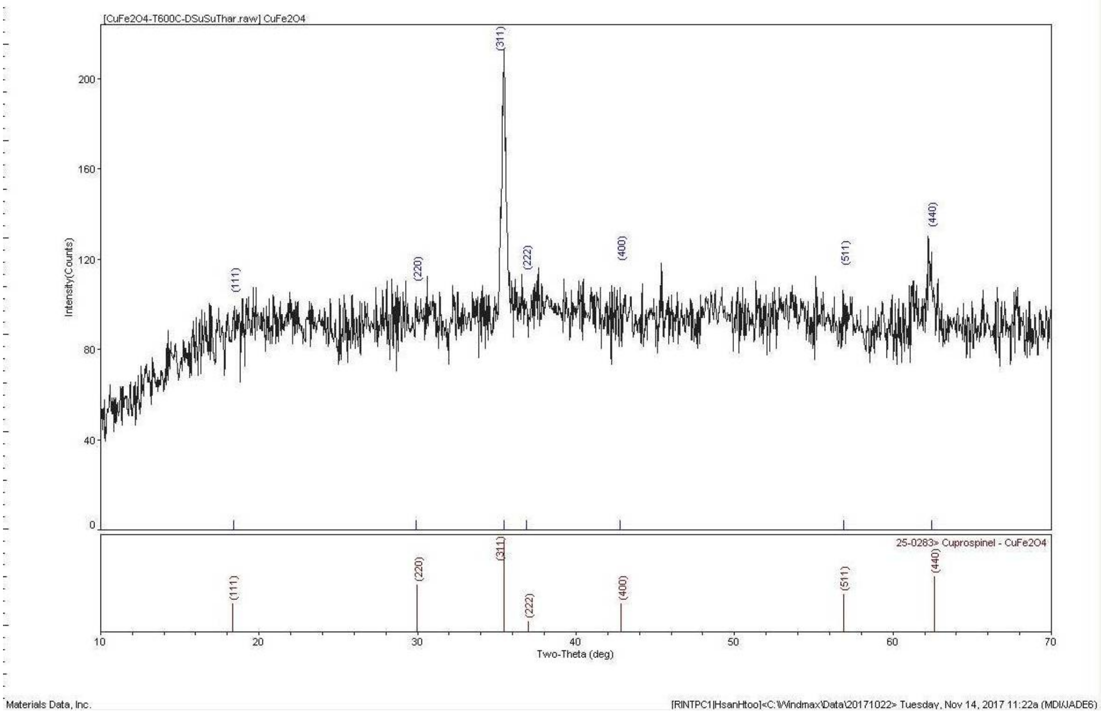

Figure 3 (a) XRD pattern for $CuFe_2O_4$ ferrite sample (600°C)

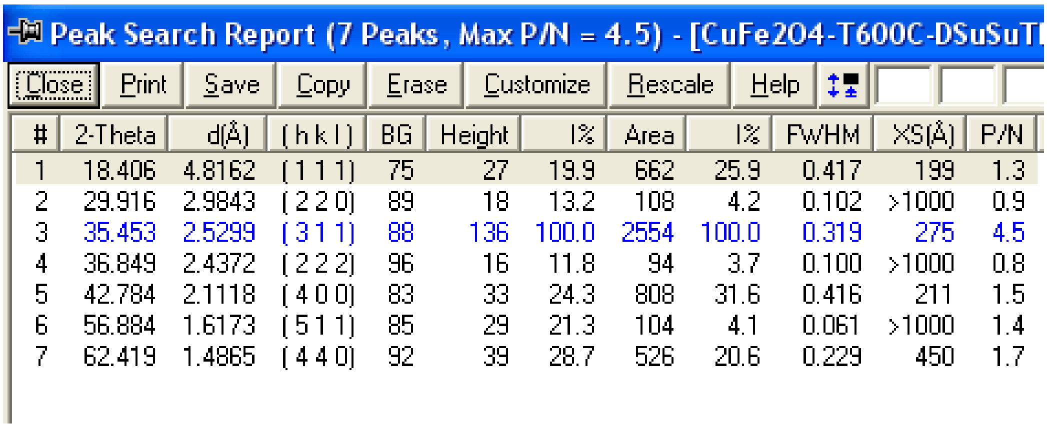

Peak Search Report (7 Peaks, Max P/N = 4.5) - [CuFe2O4-T600C-DSuSuT

#	2-Theta	d(Å)	(h k l)	BG	Height	I%	Area	I%	FWHM	XS(Å)	P/N
1	18.406	4.8162	(1 1 1)	75	27	19.9	662	25.9	0.417	199	1.3
2	29.916	2.9843	(2 2 0)	89	18	13.2	108	4.2	0.102	>1000	0.9
3	35.453	2.5299	(3 1 1)	88	136	100.0	2554	100.0	0.319	275	4.5
4	36.849	2.4372	(2 2 2)	96	16	11.8	94	3.7	0.100	>1000	0.8
5	42.784	2.1118	(4 0 0)	83	33	24.3	808	31.6	0.416	211	1.5
6	56.884	1.6173	(5 1 1)	85	29	21.3	104	4.1	0.061	>1000	1.4
7	62.419	1.4865	(4 4 0)	92	39	28.7	526	20.6	0.229	450	1.7

Figure 3 (b) XRD result data of Peak Search Report for $CuFe_2O_4$ ferrite sample (600°C)

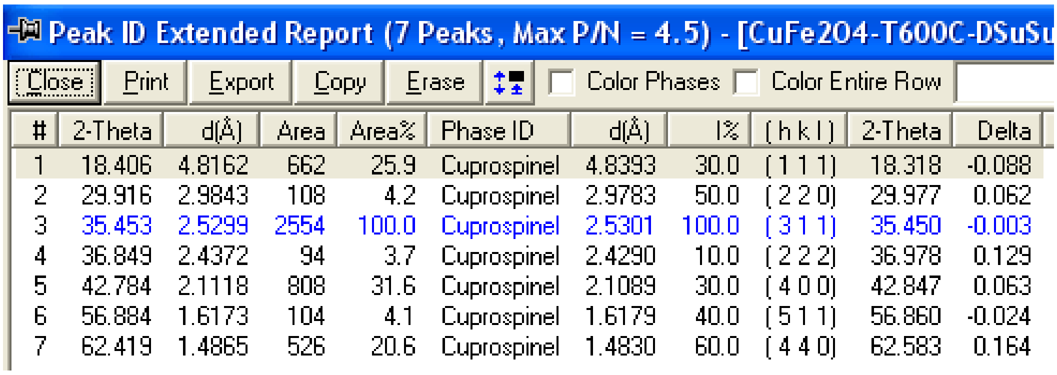

Peak ID Extended Report (7 Peaks, Max P/N = 4.5) - [CuFe2O4-T600C-DSuSu

☐ Color Phases ☐ Color Entire Row

#	2-Theta	d(Å)	Area	Area%	Phase ID	d(Å)	I%	(h k l)	2-Theta	Delta
1	18.406	4.8162	662	25.9	Cuprospinel	4.8393	30.0	(1 1 1)	18.318	-0.088
2	29.916	2.9843	108	4.2	Cuprospinel	2.9783	50.0	(2 2 0)	29.977	0.062
3	35.453	2.5299	2554	100.0	Cuprospinel	2.5301	100.0	(3 1 1)	35.450	-0.003
4	36.849	2.4372	94	3.7	Cuprospinel	2.4290	10.0	(2 2 2)	36.978	0.129
5	42.784	2.1118	808	31.6	Cuprospinel	2.1089	30.0	(4 0 0)	42.847	0.063
6	56.884	1.6173	104	4.1	Cuprospinel	1.6179	40.0	(5 1 1)	56.860	-0.024
7	62.419	1.4865	526	20.6	Cuprospinel	1.4830	60.0	(4 4 0)	62.583	0.164

Figure 3 (c) XRD result data of Peak ID Report for $CuFe_2O_4$ ferrite sample (600°C)

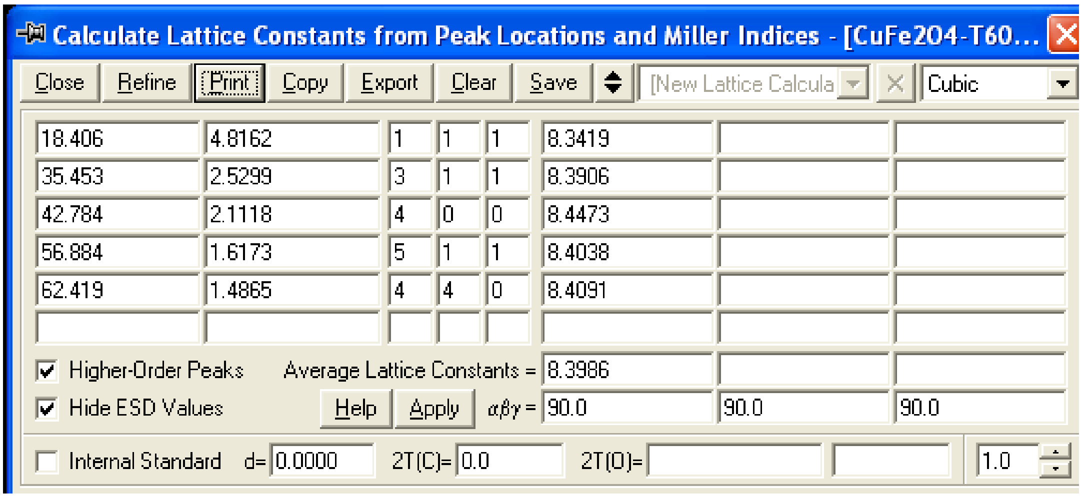

Calculate Lattice Constants from Peak Locations and Miller Indices - [CuFe2O4-T60...

Cubic

18.406	4.8162	1	1	1	8.3419		
35.453	2.5299	3	1	1	8.3906		
42.784	2.1118	4	0	0	8.4473		
56.884	1.6173	5	1	1	8.4038		
62.419	1.4865	4	4	0	8.4091		

☑ Higher-Order Peaks Average Lattice Constants = 8.3986

☑ Hide ESD Values αβγ = 90.0 90.0 90.0

☐ Internal Standard d= 0.0000 2T(C)= 0.0 2T(0)= 1.0

Figure 3 (d) XRD result data of Structure Report for $CuFe_2O_4$ ferrite sample (600°C)

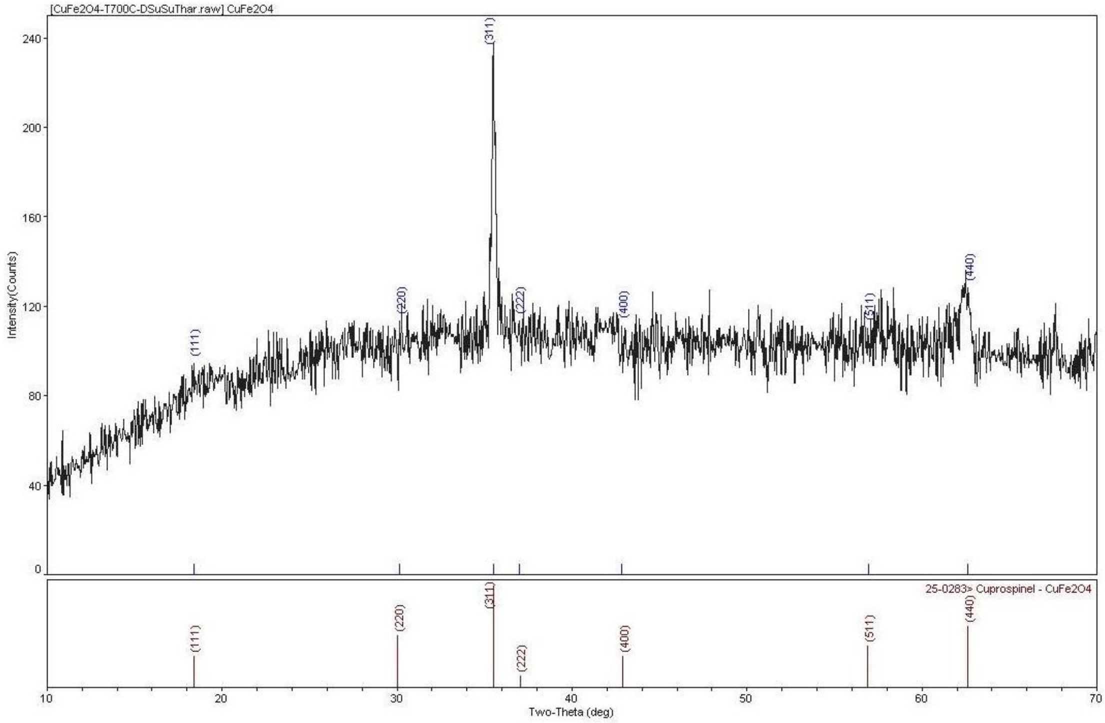

Figure 4 (a) XRD pattern for $CuFe_2O_4$ ferrite sample (700°C)

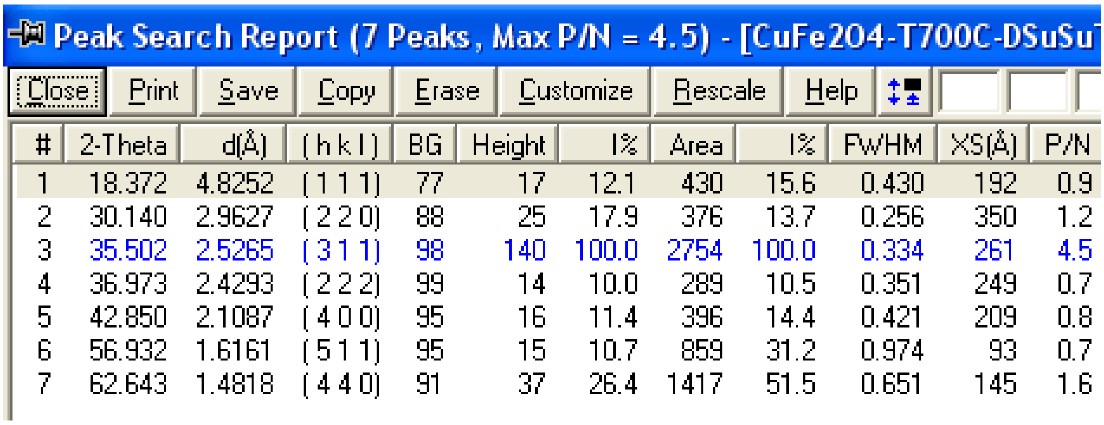

#	2-Theta	d(Å)	(h k l)	BG	Height	I%	Area	I%	FWHM	XS(Å)	P/N
1	18.372	4.8252	(1 1 1)	77	17	12.1	430	15.6	0.430	192	0.9
2	30.140	2.9627	(2 2 0)	88	25	17.9	376	13.7	0.256	350	1.2
3	35.502	2.5265	(3 1 1)	98	140	100.0	2754	100.0	0.334	261	4.5
4	36.973	2.4293	(2 2 2)	99	14	10.0	289	10.5	0.351	249	0.7
5	42.850	2.1087	(4 0 0)	95	16	11.4	396	14.4	0.421	209	0.8
6	56.932	1.6161	(5 1 1)	95	15	10.7	859	31.2	0.974	93	0.7
7	62.643	1.4818	(4 4 0)	91	37	26.4	1417	51.5	0.651	145	1.6

Figure 4 (b) XRD result data of Peak Search Report for $CuFe_2O_4$ ferrite sample (700°C)

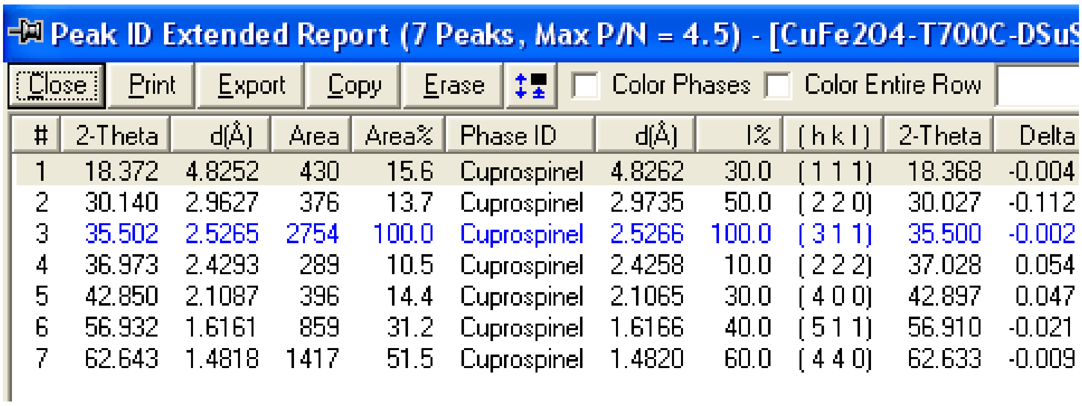

#	2-Theta	d(Å)	Area	Area%	Phase ID	d(Å)	I%	(h k l)	2-Theta	Delta
1	18.372	4.8252	430	15.6	Cuprospinel	4.8262	30.0	(1 1 1)	18.368	-0.004
2	30.140	2.9627	376	13.7	Cuprospinel	2.9735	50.0	(2 2 0)	30.027	-0.112
3	35.502	2.5265	2754	100.0	Cuprospinel	2.5266	100.0	(3 1 1)	35.500	-0.002
4	36.973	2.4293	289	10.5	Cuprospinel	2.4258	10.0	(2 2 2)	37.028	0.054
5	42.850	2.1087	396	14.4	Cuprospinel	2.1065	30.0	(4 0 0)	42.897	0.047
6	56.932	1.6161	859	31.2	Cuprospinel	1.6166	40.0	(5 1 1)	56.910	-0.021
7	62.643	1.4818	1417	51.5	Cuprospinel	1.4820	60.0	(4 4 0)	62.633	-0.009

Figure 4 (c) XRD result data of Peak ID Report for $CuFe_2O_4$ ferrite sample (700°C)

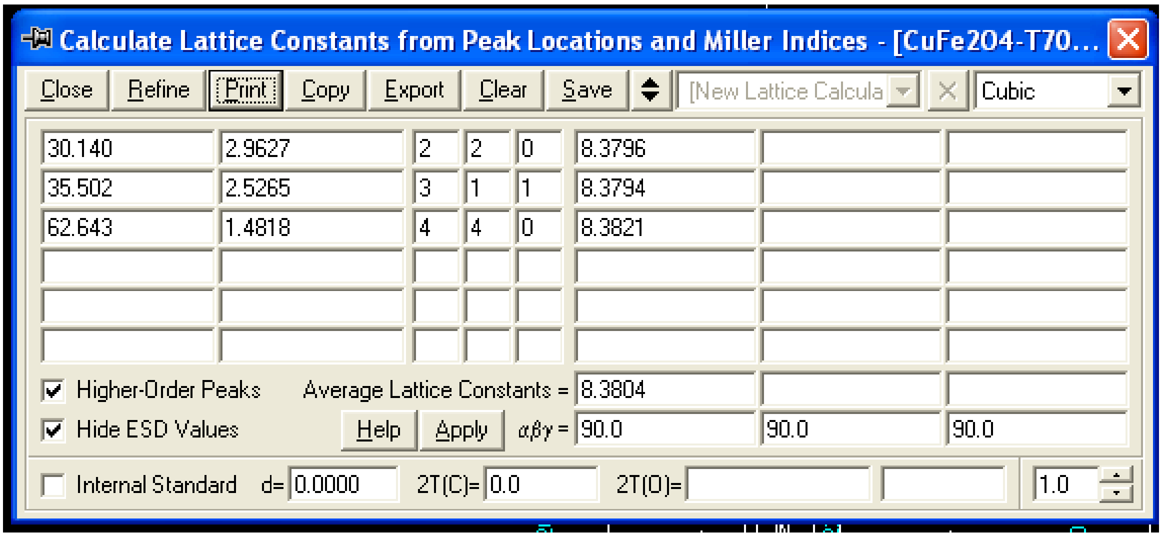

Cubic

30.140	2.9627	2	2	0	8.3796
35.502	2.5265	3	1	1	8.3794
62.643	1.4818	4	4	0	8.3821

☑ Higher-Order Peaks

Average Lattice Constants = 8.3804

☑ Hide ESD Values

αβγ = 90.0 90.0 90.0

☐ Internal Standard d= 0.0000 2T(C)= 0.0 2T(0)= 1.0

Figure 4 (d) XRD result data of Structure Report for $CuFe_2O_4$ ferrite sample (700°C)

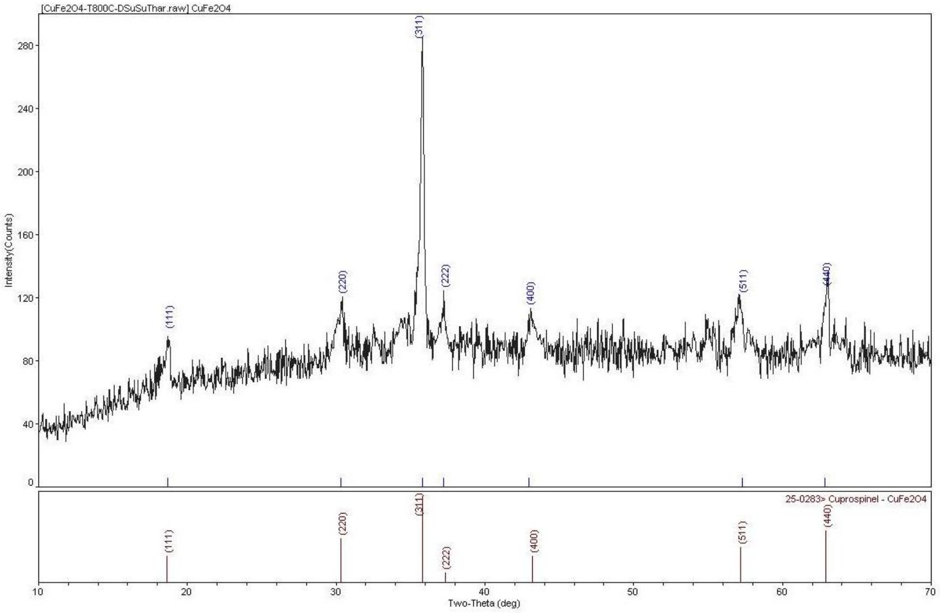

Figure 5 (a) XRD pattern for $CuFe_2O_4$ ferrite sample (800°C)

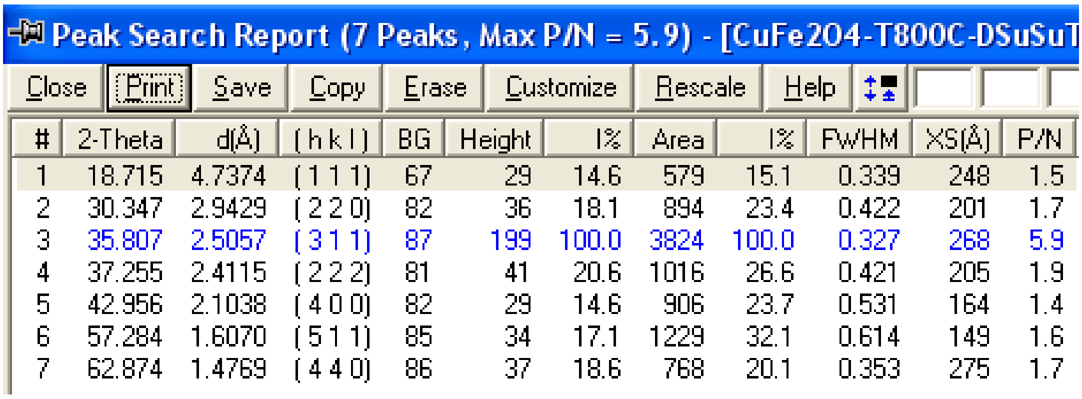

#	2-Theta	d(Å)	(h k l)	BG	Height	I%	Area	I%	FWHM	XS(Å)	P/N
1	18.715	4.7374	(1 1 1)	67	29	14.6	579	15.1	0.339	248	1.5
2	30.347	2.9429	(2 2 0)	82	36	18.1	894	23.4	0.422	201	1.7
3	35.807	2.5057	(3 1 1)	87	199	100.0	3824	100.0	0.327	268	5.9
4	37.255	2.4115	(2 2 2)	81	41	20.6	1016	26.6	0.421	205	1.9
5	42.956	2.1038	(4 0 0)	82	29	14.6	906	23.7	0.531	164	1.4
6	57.284	1.6070	(5 1 1)	85	34	17.1	1229	32.1	0.614	149	1.6
7	62.874	1.4769	(4 4 0)	86	37	18.6	768	20.1	0.353	275	1.7

Figure 5 (b) XRD result data of Peak Search Report for $CuFe_2O_4$ ferrite sample (800°C)

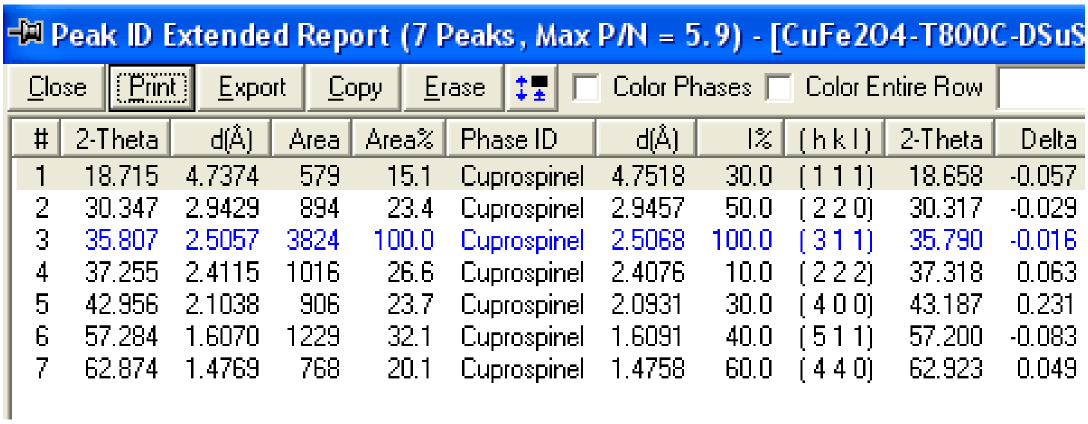

#	2-Theta	d(Å)	Area	Area%	Phase ID	d(Å)	I%	(h k l)	2-Theta	Delta
1	18.715	4.7374	579	15.1	Cuprospinel	4.7518	30.0	(1 1 1)	18.658	-0.057
2	30.347	2.9429	894	23.4	Cuprospinel	2.9457	50.0	(2 2 0)	30.317	-0.029
3	35.807	2.5057	3824	100.0	Cuprospinel	2.5068	100.0	(3 1 1)	35.790	-0.016
4	37.255	2.4115	1016	26.6	Cuprospinel	2.4076	10.0	(2 2 2)	37.318	0.063
5	42.956	2.1038	906	23.7	Cuprospinel	2.0931	30.0	(4 0 0)	43.187	0.231
6	57.284	1.6070	1229	32.1	Cuprospinel	1.6091	40.0	(5 1 1)	57.200	-0.083
7	62.874	1.4769	768	20.1	Cuprospinel	1.4758	60.0	(4 4 0)	62.923	0.049

Figure 5 (c) XRD result data of Peak ID Report for $CuFe_2O_4$ ferrite sample (800°C)

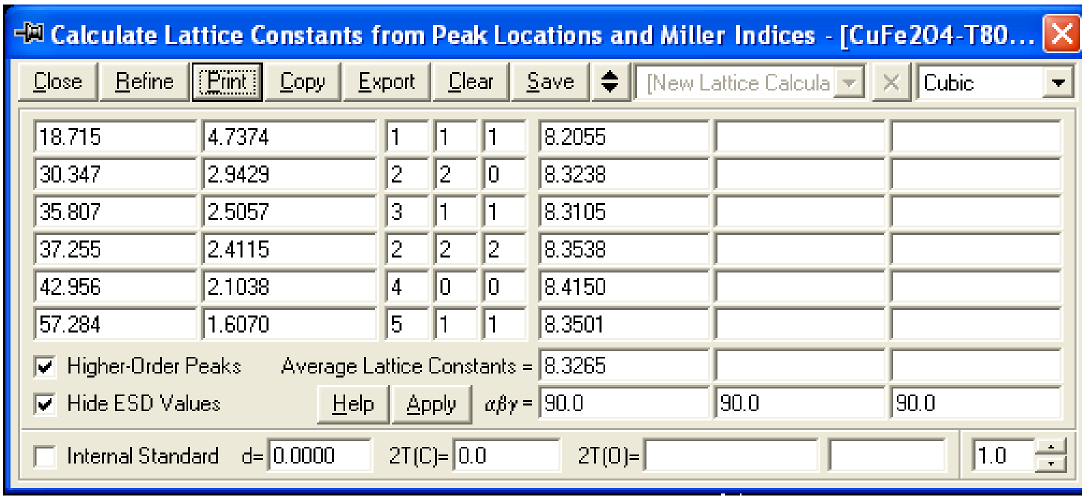

18.715	4.7374	1	1	1	8.2055		
30.347	2.9429	2	2	0	8.3238		
35.807	2.5057	3	1	1	8.3105		
37.255	2.4115	2	2	2	8.3538		
42.956	2.1038	4	0	0	8.4150		
57.284	1.6070	5	1	1	8.3501		

☑ Higher-Order Peaks Average Lattice Constants = 8.3265

☑ Hide ESD Values $\alpha\beta\gamma$ = 90.0 90.0 90.0

☐ Internal Standard d= 0.0000 2T(C)= 0.0 2T(0)= 1.0

Figure 5 (d) XRD result data of Structure Report for $CuFe_2O_4$ ferrite sample (800°C)

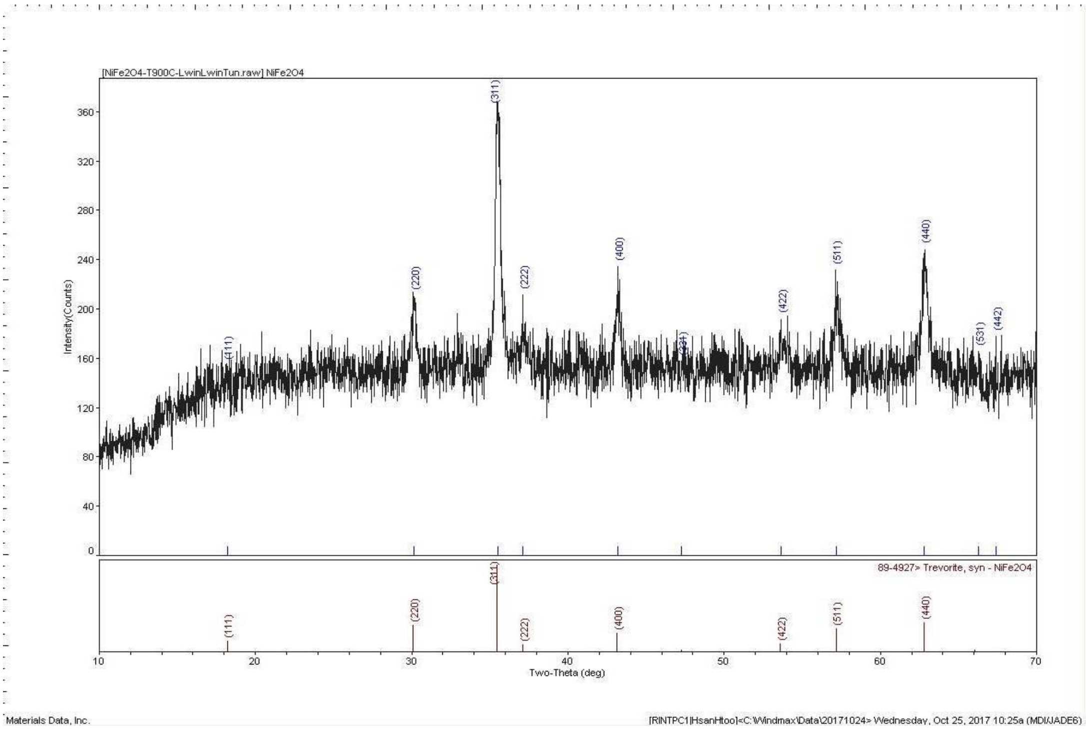

Figure 6 (a) XRD pattern for $CuFe_2O_4$ ferrite sample (900°C)

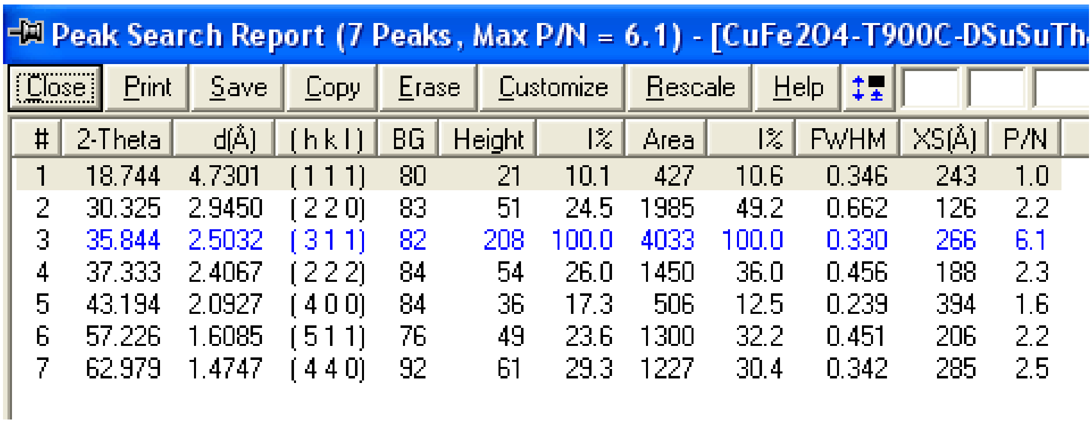

#	2-Theta	d(Å)	(h k l)	BG	Height	I%	Area	I%	FWHM	XS(Å)	P/N
1	18.744	4.7301	(1 1 1)	80	21	10.1	427	10.6	0.346	243	1.0
2	30.325	2.9450	(2 2 0)	83	51	24.5	1985	49.2	0.662	126	2.2
3	35.844	2.5032	(3 1 1)	82	208	100.0	4033	100.0	0.330	266	6.1
4	37.333	2.4067	(2 2 2)	84	54	26.0	1450	36.0	0.456	188	2.3
5	43.194	2.0927	(4 0 0)	84	36	17.3	506	12.5	0.239	394	1.6
6	57.226	1.6085	(5 1 1)	76	49	23.6	1300	32.2	0.451	206	2.2
7	62.979	1.4747	(4 4 0)	92	61	29.3	1227	30.4	0.342	285	2.5

Figure 6 (b) XRD result data of Peak Search Report for $CuFe_2O_4$ ferrite sample (900°C)

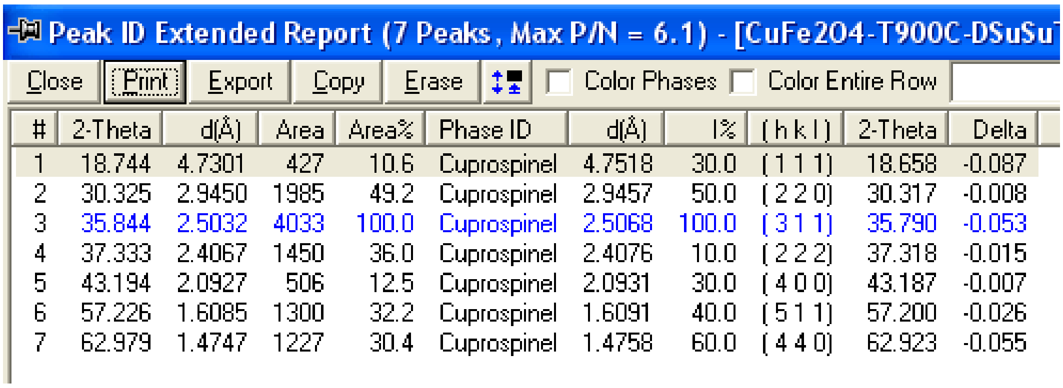

#	2-Theta	d(Å)	Area	Area%	Phase ID	d(Å)	I%	(h k l)	2-Theta	Delta
1	18.744	4.7301	427	10.6	Cuprospinel	4.7518	30.0	(1 1 1)	18.658	-0.087
2	30.325	2.9450	1985	49.2	Cuprospinel	2.9457	50.0	(2 2 0)	30.317	-0.008
3	35.844	2.5032	4033	100.0	Cuprospinel	2.5068	100.0	(3 1 1)	35.790	-0.053
4	37.333	2.4067	1450	36.0	Cuprospinel	2.4076	10.0	(2 2 2)	37.318	-0.015
5	43.194	2.0927	506	12.5	Cuprospinel	2.0931	30.0	(4 0 0)	43.187	-0.007
6	57.226	1.6085	1300	32.2	Cuprospinel	1.6091	40.0	(5 1 1)	57.200	-0.026
7	62.979	1.4747	1227	30.4	Cuprospinel	1.4758	60.0	(4 4 0)	62.923	-0.055

Figure 6 (c) XRD result data of Peak ID Report for $CuFe_2O_4$ ferrite sample (900°C)

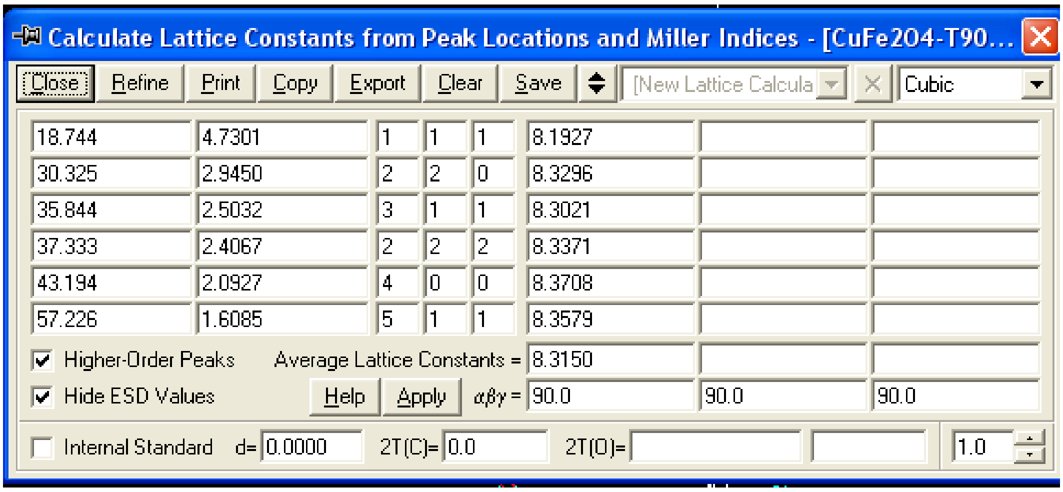

18.744	4.7301	1	1	1	8.1927		
30.325	2.9450	2	2	0	8.3296		
35.844	2.5032	3	1	1	8.3021		
37.333	2.4067	2	2	2	8.3371		
43.194	2.0927	4	0	0	8.3708		
57.226	1.6085	5	1	1	8.3579		

☑ Higher-Order Peaks Average Lattice Constants = 8.3150

☑ Hide ESD Values αβγ = 90.0 90.0 90.0

☐ Internal Standard d= 0.0000 2T(C)= 0.0 2T(0)= 1.0

Figure 6 (d) XRD result data of Structure Report for $CuFe_2O_4$ ferrite sample (900°C)

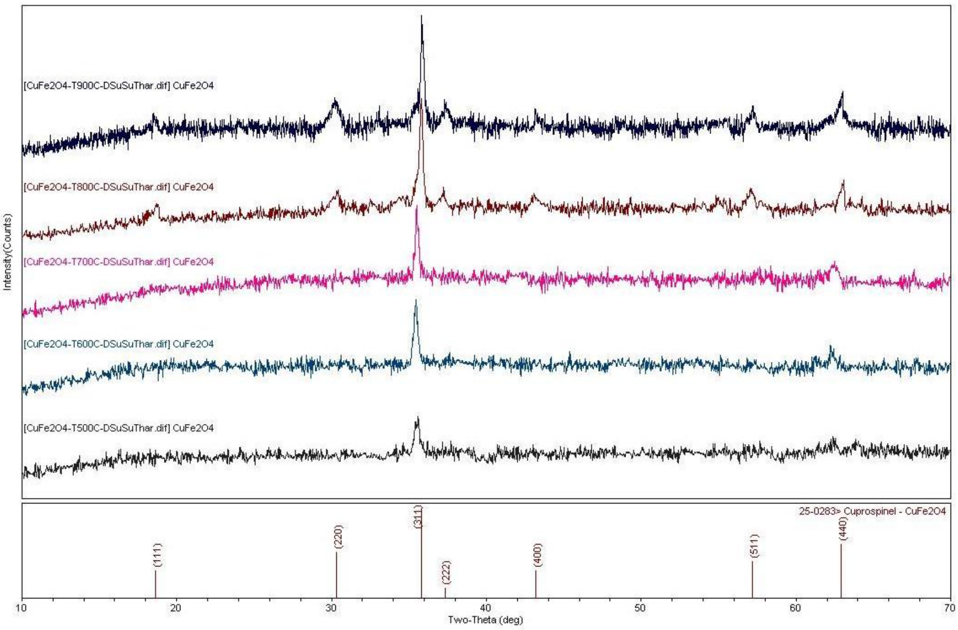

Figure 7 Peak comparison of XRD patterns for $CuFe_2O_4$ ferrite sample at various temperatures

Table 1 Comparison for Crystallite size of $CuFe_2O_4$ in various temperatures

Temperature	2θ (degree)	θ (radians)	FWHM (radians)	λ (Å)	cos θ	Crystallite size(nm)
500ºC	35.59	0.31	8.59×10^{-3}	1.5406	0.95	**16.9**
600ºC	35.45	0.31	5.57×10^{-3}	1.5406	0.95	26.1
700ºC	35.50	0.31	5.89×10^{-3}	1.5406	0.95	24.9
800ºC	35.81	0.31	5.71×10^{-3}	1.5406	0.95	25.5
900ºC	35.84	0.31	5.76×10^{-3}	1.5406	0.95	25.3

Table 2 Comparison for Lattice parameter of $CuFe_2O_4$ in various temperatures

Temperature	**d**	**h**	**k**	**l**	**Lattice Parameter(a)**
500ºC	2.5203	3	1	1	**8.3588**
600ºC	2.5299	3	1	1	8.3906
700ºC	2.5265	3	1	1	8.3794
800ºC	2.5057	3	1	1	8.3105
900ºC	2.5032	3	1	1	8.3021

Microstructure Observation

The microstructure and morphology play the important roles in the determining the magnetic and electric transport properties. These studied for the materials are essential in order to understand the relationship between their processing parameters as well as the behavior when used in practical applications. Microstructures of the sinter ferrite specimen were analyzed by a high resolution scanning electron microscope (SEM). The surface morphology and microstructural analysis of all the five samples of ferrites were carried out using scanning electron microscope (SEM) JEOL-JSM 5610LV operated at 15kV in the secondary electron image (SEI) mode. The average values of the grain size for each sample were carried out comparison with SEM ruler. This method is based on the line intercept method.

The microstructures of the sintered ferrites with different temperature are shown in figure from 8(a) to (e). The measured grain size values are tabulated in table (3). It was found that the surface morphology of the samples is rough and non-uniform microstructure because the average particle size for every sample was different. Each grain usually contained a large number of atoms.

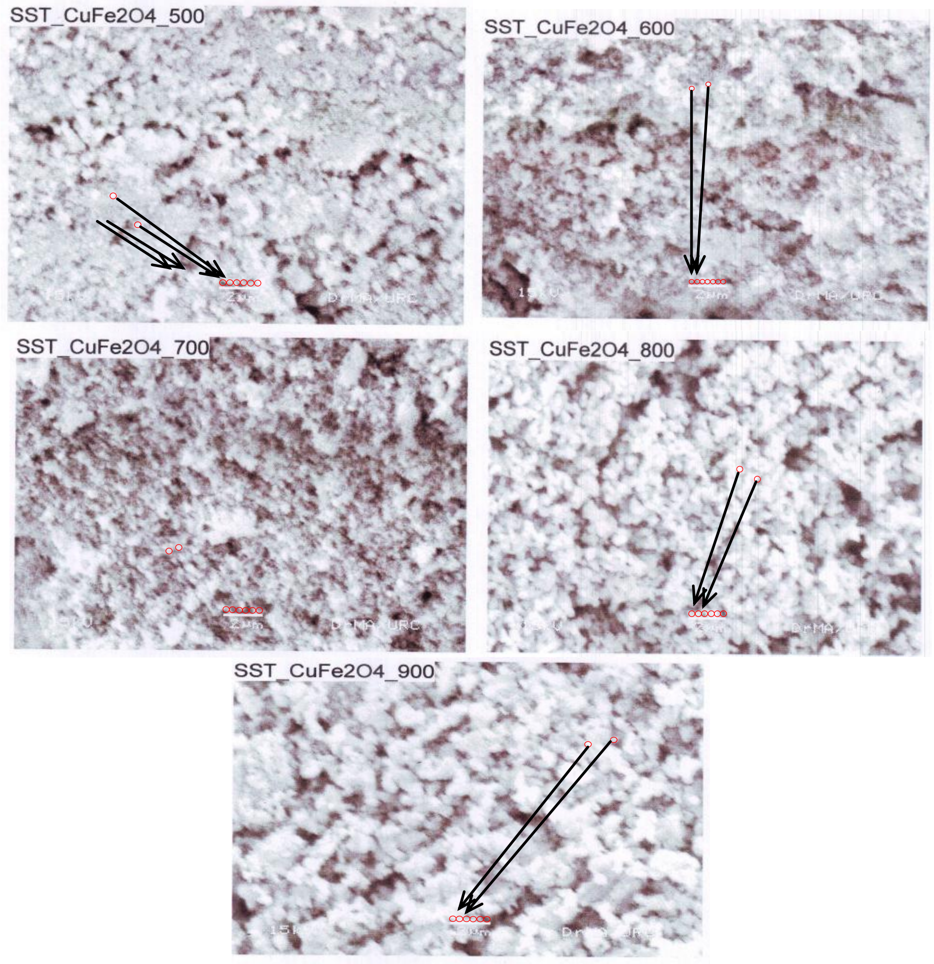

Figure 8 SEM image of copper ferrite (a) at 500˚C, (b) at 600˚C (c) at 700˚C, (d) at 800˚C and (e) at 900˚C

Table 3 Grain size for copper ferrite in various temperature

T(ºC)	QTY	SEM Ruler*(μm)*	Grain Size*(μm)*
500	5.5	2	0.3636
600	7	2	0.2857
700	6	2	0.3333
800	6	2	0.3333
900	6	2	0.3333

The scanning electron microscope (SEM) was used to analyze the microstructure and to determine the average grain size. The microstructure and morphology have an important role in determining the magnetic and electric transport properties and those were examined by a high resolution scanning electron microscope. These studied for the materials are essential in order to understand the relationship between their processing parameters as well as the behavior when used in practical applications. The microstructures of the prepared samples are shown in figures from 8(a) to (e). SEM images give information about the intergranular and intragranular pores as well as the sub-structural defects within the grains. Average grain size was determined by using SEM ruler.

Conclusion

Copper ferrites with the general formula, $CuFe_2O_4$ in various temperatures were successfully prepared by the sol-gel method. The broad peaks in the XRD patterns indicate a fine particle nature of the samples.

XRD results show that the as-prepared ferrite samples under investigation show the single phase (primitive) cubic structure. The lattice parameters were obtained in the range 8.3021 Å - 8.3906 Å. The lattice parameters agree with the literature value. The crystallite size of the samples also varies between 16.9 nm and 26.1 nm. According to experimental results, the sample at 500ºC is the smallest crystallize size of 16.9 nm. The surface morphology of the ferrite samples were determined by using the SEM photograph consists of grain varying from 0.2857 μm to 0.3636 μm. These grain sizes were approximately equal and mostly homogeneous.

Acknowledgement

I would like to thank Professor Dr Khin Khin Win, Professor and Head, Department of Physics, University of Yangon, for her kind permission to carry out this work.

I wish to show my sincere thanks to Professor Dr Aye Aye Thant, Department of Physics, University of Yangon, and Professor Dr Yin Yin Myint, Head of Department of Physics, Mawlamyine University, for their suggestion and comment for this work.

References

Bondyopadhyay A. K., (2010), "Nano Materials" (New Delhi: New Age)

Chattopadhyay K. K. & Banerjee A. N., (2009), "Introduction to Nanoscience and Nanotechnology" (New Delhi: PHI Learning)

Cullity B. D., (1978), "Elements of X-Ray Diffraction" (Reading: Wesley)

Echlin P (2009) “Handbook of Sample Preparation for Scanning Electron Microscopy and X-ray Microanalysis” (Cambridge: CUP)

Goldman A (2006) “Modern Ferrite Technology” (New York: Springer)

Gholamreza Nabiyouni et al./ JNS 3(2013) 155-160

Iyer R., et al (2009), Bulletins Materials Science 32 (2) 141

Justus S. M., et al (2005), Ceramics International 31 897

Kittle C (1996) “Introduction to Solid State Physics”, (New York : Wiley)

K. Hedayati et al. / JNS 5(2015)

Pillai S. O., (2006), "Solid State Physics" (New Delhi: New Age)

Suryanayana C & Grant Norton M (1956) “X-Ray Diffraction, Practical Approach” (New York: Plenum)

Wahab M. N., et al (2009), International Journal of Mechanical and Materials Engineering (IJMME) 4 (2) 115

J. Myanmar Acad. Arts Sci. 2020 **Vol. XVIII.No.2**B

ANALYSIS OF PROTON SCATTERING FROM CARBON ISOTOPES

Maung Maung Chit[1], Thida Wint[2], Khin Mar Win[3] & Khin Maung Maung[4]

Abstract

Reaction cross section of carbon isotopes for proton scattering is computed with the wide incident energy region. Calculations are based on eikonal approximation which is a high energy (small scattering angle) that depends on the nucleon nucleus (NA) optical potential. The proton-carbon optical potential is obtained by a folding integral of the nucleon nucleon (NN) transition amplitude and matter density of carbon. Analytical formulas of optical potential are used to present in position-space representation for carbon isotope by using harmonic well nuclear densities($A<20$). The eikonal phase function is presented in the momentum-space representation which is obtained from computing the fourier transform of the position-space optical potential in order to compare each other.

Keywords: Eikonal approximation, Optical potential, Reaction cross section

Introduction

In this present work, proton-carbon isotope scattering will be studied in order to predict the size of carbon isotope in the frame work of eikonal approximation. The scattering of particles from nuclei has provided invaluable information on charge, matter densities distribution and root-mean-square radius of stable nuclei near the stability line. Proton elastic scattering is expected to be the most suitable experiment besides electron scattering in order to obtain such information on the stable nuclei. For scattering problem of composite particle, the exact solution of Schrodinger is very difficult. So the appropriate approximation is indispensable. In this study, the eikonal approximation is used to calculate the differential cross section and reaction cross section of proton carbon scattering. It is well-suited for the prediction of cross sections for projectile with kinetic energies in the laboratory frame greater than 150 MeV/n. The differential cross section is computed from the absolute square of scattering amplitude that is obtained by integrating the eikonal phase function. The eikonal phase function is related to the optical potential which depends on NN transition amplitude and density profile of carbon. In this study, nuclei are composite particles whose fundamental constituents are nucleons (protons and neutrons). The quark structure of the nucleons is not considered. It is assumed that the inner structure of nucleon will be probed at higher energies, and these effects are considered to be included in the NN transition amplitude. The NN transition amplitude is a function of total cross section, slope parameter and real to imaginary ratio. Electron scattering experiments are used to estimate the charge density of nuclei. Harmonic well densities are used for light nuclei. Nuclear matter density is obtained from dividing the nuclear charge density by the Gausian charge distribution of the proton. In the position-space representation, the optical potential is a six dimensional nuclear matter densities and the NN transition amplitude. In momentum space representation, it is the product of the matter densities and NN transition amplitudes as a function of momentum transfer.

---

[1] Lecturer, Department of Physics, Loikaw University

[2] Dr, Associate Professor, Department of Physics, Mandalay University of Distance Education

[3] Dr, Lecturer, Department of Physics, Sagaing University of Education

[4] Dr, Professor, Physics and Astronomy, The University of Southern Mississippi, MS 39406

Theory

Eikonal Approximation

The time independent Schrodinger equation is given by

$$\hat{H}|\psi>=E|\psi> \qquad (1)$$

$$\hat{H}=\hat{H}_0+\hat{V}$$

$\hat{H}$ = Halmiltonian, $\hat{V}$ =potential energy operator and $\hat{H}_0$ = kinetic energy operator

$$(\hat{H}_0+\hat{V})|\psi>=E|\psi>$$

$$|\psi>=\frac{V}{E-\hat{H}_0}|\psi> \qquad (2)$$

To avoid the singular nature of the operator $\frac{1}{E-\hat{H}_0}$, $\pm i\varepsilon$ is added into equation (2)

$$|\psi^{\pm}>=\frac{V}{E-\hat{H}_0\pm i\varepsilon}|\psi^{\pm}> \qquad (3)$$

The solution of above equation is given by

$$|\psi^{\pm}>=|\phi>+\frac{V}{E-\hat{H}_0\pm i\varepsilon}|\psi^{\pm}> \qquad (4)$$

This is known as Lippmann-Schwinger equation

Where, $|\phi>$ is the solution of free particle Schrödinger equation, $\psi^{\pm}$ is

outgoing (incoming) wave function

By using the completeness relation, we obtained

$$<\vec{r}\,|\psi^{\pm}>=<\vec{r}\,|\varphi>+\int d\vec{r}'<\vec{r}\,|\frac{1}{E-\hat{H}_0\pm i\varepsilon}|\vec{r}'><\vec{r}'|V||\psi^{\pm}> \qquad (5)$$

Eikonal approximation is useful approximation techniques when the de Broglie wavelength λ = h/p of the incident particle is sufficiently short compared with the distance in which the potential varies appreciably. If the potential varies smoothly and has a range "a", this short wavelength condition is equivalent to the requirement that ka >>1.

Let's consider high energy, non-relativistic potential and assume that ka >> 1 (short wavelength) and V_0 /E<<1 (high energy)

We start the Lippmann Schwinger equation

$$\Psi^{(+)}_{\vec{k}i}(\vec{r}) = \frac{e^{(i\vec{k}_i \bullet \vec{r})}}{(2\pi)^{3/2}} + \int G_0^{(+)}(\vec{r},\vec{r}\,')\ \Psi^{(+)}_{\vec{k}i}(\vec{r}\,')\ U(\vec{r}\,')d\vec{r}\,' \qquad (6)$$

Where, $U(\vec{r}) = \frac{2mV(r)}{\hbar^2}$, strength of reduce potential

Where, the Green's function is given by

$$G_0^{(+)}(\vec{r},\vec{r}\,') = -\frac{1}{4\pi}\frac{e^{\{ik|\vec{r}-\vec{r}\,'|\}}}{|\vec{r}-\vec{r}\,'|}$$

$$G_0^{(+)}(\vec{r},\vec{r}\,') = -\frac{1}{(2\pi)^3}\int d\vec{\kappa}\,\frac{e^{\{i\vec{k}\bullet(\vec{r}-\vec{r}\,')\}}}{\kappa^2 - k_i^2 - i\varepsilon} \qquad (7)$$

When the potential varies slowly over the scale of the incident wavelength, the full wave function Ψ_k^+, is given by

$$\Psi^{(+)}_{ki}(\vec{r}) = \frac{e^{i\vec{k}_i \bullet \vec{r}}}{(2\pi)^{3/2}}\phi(\vec{r}) \qquad (8)$$

Where, $\phi(\vec{r})$ is slowly varying function when ka is large.

The eikonal scattering wave function is obtained by

$$\Psi_E^{(+)}(\vec{r}) = \frac{1}{(2\pi)^{3/2}}\exp(i\vec{k}_i \bullet \vec{r} - \frac{i}{2.k}\int_{-\infty}^{z} U(x,y,z')\,d\,z') \qquad (9)$$

Calculation of eikonal scattering amplitude

Eikonal scattering wave function is given by

$$\Psi_E^{+}(\vec{r}) = \frac{1}{(2\pi)^{3/2}}\exp\{i\vec{k}_i\vec{r} - \frac{i}{2k}\int_{-\infty}^{Z} U(x,y,z')\,dz'\}$$

The scattering amplitude and the scattered wave function is related by

$$f_E = -\frac{(2\pi)^{3/2}}{4\pi}\int e^{(-i\vec{k}_f\vec{r})}U(\vec{r})\psi_E^{+}(\vec{r})d\vec{r} \qquad (10)$$

Substituting $\psi_E^{+}(\vec{r})$ into (10)

$$f_E = -\frac{(2\pi)^{3/2}}{4\pi}\int e^{(-i\vec{k}_f\vec{r})}U(\vec{r})\frac{1}{(2\pi)^{3/2}}\exp\{i\vec{k}_i\vec{r} - \frac{i}{2k}\int_{-\infty}^{Z} U(x,y,z')\,dz'\}d\vec{r}$$

$$f_E = -\frac{1}{4\pi}\int d\vec{r}e^{i(\Delta.\vec{r})}U(\vec{r})\exp\{-\frac{i}{2k}\int_{-\infty}^{Z} U(x,y,z')\,dz'\}$$

Where, $\Delta = \vec{k}_i - \vec{k}_f$ is wave vector transfer

For cylindrical coordinate system, $d\vec{r} = d^2\vec{b}d\vec{z}$

$$f_E = -\frac{1}{4\pi}\int d^2\vec{b}\int_{-\infty}^{\infty} d\vec{z}e^{i(\Delta.\vec{b})}U(\vec{b},z)\exp\{-\frac{i}{2k}\int_{-\infty}^{z} U(\vec{b},z')dz'\} \tag{11}$$

z' integration in (11) along a $\hat{n}$ parallel to the bisector of the scattering angle .

$\vec{r} = \vec{b} + z\vec{k}_i$ and $\Delta.\vec{r} = \Delta(\vec{b} + z\vec{k}_i) = \Delta.\vec{b} + kz(1-\cos\theta) \approx \Delta.\vec{b}$

Now eikonal scattering amplitude becomes as below

$$f_E = \frac{k}{2\pi.i}\int d^2\vec{b}e^{i(\Delta\bullet\vec{b})}[\exp\{i\chi(k,b)\}-1] \tag{12}$$

Where, eikonal phase shift function is $\chi(k,\vec{b}) = -\frac{1}{2k}\int_{-\infty}^{+\infty} U(\vec{b},z)dz$ (13)

Where, $d^2\vec{b} = bdbd\phi$ for cylindrical coordinate system

So, $$f_E = \frac{k}{2\pi i}\int_0^{\infty}\int_0^{2\pi} bdbd\varphi e^{i(\Delta.\vec{b})}[\exp\{i\chi(k,b)\}-1]$$

$$f_E = \frac{k}{2\pi i}\int_0^{\infty} bdb\int_0^{2\pi} d\varphi e^{i(\Delta.b\cos(\varphi))}[\exp\{i\chi(k,b)\}-1]$$

The ordinary Bessel Function J_0 is given by

$$J_0(x) = \frac{1}{2\pi}\int_0^{2\pi} d\varphi e^{(ix\cos\varphi)} \tag{14}$$

$$f_E = \frac{k}{i}\int_0^{\infty} bdbJ_0(\Delta.b)[\exp\{i\chi(k,b)\}-1] \tag{15}$$

where, b is the impact parameter, k is the relative momentum of the projectile-target system in the center of mass (CM) frame.

$$k = \sqrt{\frac{2\mu m_{At}T_{lab}}{m_{A_p} + m_{A_T}}}$$

where, $\mu = \frac{m_{A_p}m_{A_T}}{m_{A_p} + m_{A_T}}$, T_{lab} is the kinetic energy of the projectile in laboratory frame.

The elastic differential cross section is computed from the absolute square of the scattering amplitude.

$$\frac{d\sigma}{d\Omega} = \left| f(\theta) \right|^2 \tag{16}$$

Total elastic cross section is obtained by integrating over the solid angle

$$\sigma_{\mathrm{el}}^{tot} = \frac{\mathrm{d}\sigma}{\mathrm{d}\Omega}\mathrm{d}\Omega$$

$$= 4\pi \int_0^\infty [1 - e^{-\operatorname{Im}\chi} \cos(\operatorname{Re}\chi)]bdb - 2\pi \int_0^\infty [1 - e^{-2\operatorname{Im}\chi}]bdb \tag{17}$$

The scattering amplitude is satisfies the optical theorem, so the total cross section is given by

$$\sigma_{tot} = \frac{4\pi}{k} \operatorname{Im} f(\theta = 0) = 4\pi \int_0^\infty [1 - e^{-\operatorname{Im}\chi} \cos(\operatorname{Re}\chi)]bdb \tag{18}$$

The reaction cross section is obtained by $\sigma_{\mathrm{re}} = \sigma_{tot} - \sigma_{el}$

$$\sigma_{\mathrm{re}} = 2\pi \int_0^\infty [1 - e^{-2\operatorname{Im}\chi}]bdb \tag{19}$$

Optical Potential

Differential cross sections are function of eikonal phase function which depends on the optical potential, as shown in equation (13). For Nucleus-Nucleus (AA) scattering, the optical potential can be expressed as [9]

$$U(r) = A_p A_T \int t_{NN}(|\vec{r}_{NN}|)\rho_p(|\vec{r}_P|)\rho_T(|\vec{r}_T|)d\vec{r}_T d\vec{r}_{NN} \tag{20}$$

Where, A is the number of nucleon, p is projectile, T represent the target, t_{NN} is NN transition amplitude and ρ is nuclear matter density. The vectors used for the AA optical potential are illustrated in figure (1). The distance from the center of the projectile nucleus to a nucleon in the projectile can be expressed as $\mathbf{r}_p = \mathbf{r} + \mathbf{R} = \mathbf{r} + \mathbf{r}_T + \mathbf{r}_{NN}$, which , when substituted into (20),

$$U(r) = A_p A_T \int t_{NN}(|\vec{r}_{NN}|)\rho_p(|\vec{r} + \vec{r}_T + \vec{r}_{NN}|)\rho_T(|\vec{r}_T|)d\vec{r}_T d\vec{r}_{NN} \tag{21}$$

Where, $|\vec{r}| = \sqrt{b^2 + z^2}$ in the cylindrical coordinate system.

The eikonal phase function can be obtained by integrating the optical potential in the position-space representation. In this section, it is expressed as a function of momentum transfer in order to reduce the number of integration dimensions.

Nucleon-Nucleon Transition Amplitude and Nuclear Matter Density

In present work, differential cross section is calculated with the eikonal approximation using the momentum-space representation of the optical potential, which depends on the nucleon-nucleon (NN) transition amplitude and nuclear matter density. The harmonic-well nuclear matters density is given by [9]

$$\rho_A(r) = \frac{\rho_0 a^3}{8s^3}[(1 + \frac{3\gamma}{2} - \frac{3\gamma a^2}{8s^2}) + \frac{\gamma a^2}{16s^4}\gamma^2]e^{(\frac{-r^2}{4s^2})} \tag{22}$$

$$\rho_0 = \frac{1}{\pi^{3/2}a^3[1+\frac{3}{2}\gamma]} \qquad s = \sqrt{(\frac{a^2}{4} - \frac{r_p{}^2}{6}}$$

The Fourier transform of the harmonic-well nuclear matters density is given by

$$\rho_A(q) = \rho_0 \pi^{3/2} a^3 [(1+\frac{3\gamma}{2} - \frac{3\gamma a^2}{4} q^2)] e^{(q^{-2}s^2)} \tag{23}$$

The simplest form of NN transition amplitude is expressed as follow

$$t_{NN}(r) = -\sqrt{\frac{e}{m_p}} \frac{\hbar}{[2\pi B(e)](3/2)} \sigma(e)[\kappa(e)+i] e^{-r^2/2B(e)} \tag{24}$$

where, e is the kinetic energy of two nucleon center of momentum system, B(e) is the slope parameter of pp(pn) elastic scattering cross section, σ(e) is the pp(pn) cross section and $\kappa(e)$ is the real to imaginary ratio of the pp(nn) cross section. The input parameters of NN transition amplitude are displayed in table (1). The Fourier transform of NN Transition amplitude is given by

$$t_{NN}(q) = \frac{-\hbar^2 k \sigma(e)}{16\pi^3 \mu} [\kappa(e)+i] e^{-\frac{B(e)q^2}{2}} \tag{25}$$

where $\hbar$ is Planck's constant, μ is the reduced mass of the NN system and k is the relative momentum in the CM frame.

For the case of Nucloen-Nucleus (N-A) collision, optical Potential in position space is computed by using harmonic nuclear matter density and NN transition amplitude.

$$U(r) = (C_0 + C_1 r^2) e(-C_2 r^2) \tag{26}$$

where

$$C_0 = \tau A_T (\frac{\pi}{\mu_1 + \mu_2})^{3/2} [\alpha_T + \frac{3\beta_T}{2(\mu_1+\mu_2)}] \qquad C_1 = \frac{\tau \alpha_T \beta_T \mu_1 \pi^{3/2}}{(\mu_1+\mu_2)^{7/2}} \qquad C2 = \mu_1 + \frac{\mu_1^2}{(\mu_1+\mu_2)}$$

$$\tau_{NN}(r) = -\sqrt{\frac{e}{m_p}} \frac{\hbar}{[2\pi B(e)](3/2)} \sigma(e)[\kappa(e)+i]$$

$$\mu_1 = \frac{1}{2B} \qquad \mu_2 = \frac{1}{4s_T^2} \qquad s = \sqrt{(\frac{a^3}{4} - \frac{r_p{}^2}{6})}$$

Optical Potential in momentum space is obtained with the help of fourier transforms of the NN transition amplitude and nuclear matter density.

$$U(q) = A_p A_T t_{NN}(\vec{q}) \rho_p(\vec{q}) \rho_T(\vec{q}) \tag{27}$$

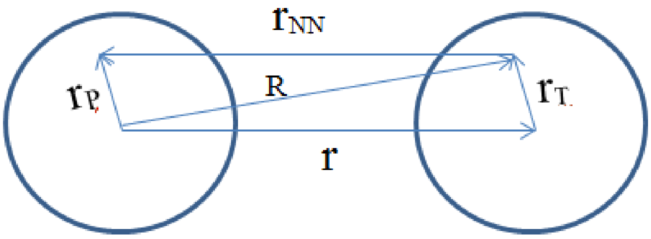

Figure 1. Illustration of vectors used for the AA optical potential. r_{NN} is the vector between a nucleon in the projectile and a nucleon in the target; $\mathbf{r}_p$ is the vector that extends from the center of projectile to a nucleon in the projectile; $\mathbf{r}_T$ is the vector between the center of the target nucleus to a nucleon in the target; **r** is the relative distance between the centers of the projectile and target nuclei; $\mathbf{R} = \mathbf{r} + \mathbf{r}_T$ is the from the center of projectile to a nucleon in the target B.

Table 1 Parameter of NN transition amplitude

E(MeV)	**σ(mb)**	**κ**	**B (fm^2)**
30	19.6	0.87	0.685
40	14.4	0.9105	0.462
50	10.4	0.94	0.390
60	9.15	1.173	0.376
70	8.01	1.27	0.354
80	6.79	1.324	0.326
100	5.51	1.37	0.281
160	4.17	1.183	0.173
200	3.405	0.961	0.126
300	3.06	0.476	0.074
425	3.01	0.36	0.741
550	3.47	0.04	0.098
650	3.94	-0.19	0.13
800	4.255	-0.07	0.153
1000	4.52	-00272	0.172

Result and Discussion

The differential cross section for proton- carbon isotopes scattering (^{12,13,14}C) have been calculated by using optical potential. The optical potential depends on parameterization of the harmonic well nuclear matter density and NN transition amplitude. The harmonic well nuclear density parameters used in equation (22)-(23) for carbon isotopes are a=1.67 ϒ= 1.607 (^{12}C), a=1.64 ϒ= 1.432 (^{13}C) and a=1.671 ϒ= 1.26 (^{14}C). The energy dependent parameters of NN transition amplitude are displayed in table 1. In figure 2,3 and 4, the eikonal (position space) refers to the numerical evaluation of the optical potential equation (20), via Gaussian Quadrature Method (six-dimensional integral). Equations (13) and (15) were integrated numerically using Gaussian Quadrature in order to obtain the differential cross section for proton- carbon Isotope. But in eikonal (momentum space) the numerical calculation only required phase shift function equation (13) (one-dimensional integral). So the momentum space eikonal phase shift function was then used directly in equation (15). The calculated differential cross section of carbon isotopes which is various incident energies are shown in figure 2 to 4. That figures show the differential cross section predicted with position space calculation and momentum space calculation agree with experimental data. And also note that position space and momentum space results are good agreement with each other. Comparison of reaction cross section between results which is obtained from the theoretical and experimental calculation is shown in figure 5 in the case of proton carbon scattering. The red dot line represents the currently eikonal calculation. The solid yellow line and solid green line are results from other theoretical calculations of and. The solid black circles are experimental data taken from. It was found that the calculated reaction cross section for p-carbon ^{12}C reaction in eikonal approximation agrees with experimental data as well as other theoretical calculations. Figure 6 shows the reaction cross section for p- ^{13,14}C reaction with respect to energy. According to figure 5 and 6, the reaction cross section of proton carbon isotope increases with increasing mass number of carbon isotope.

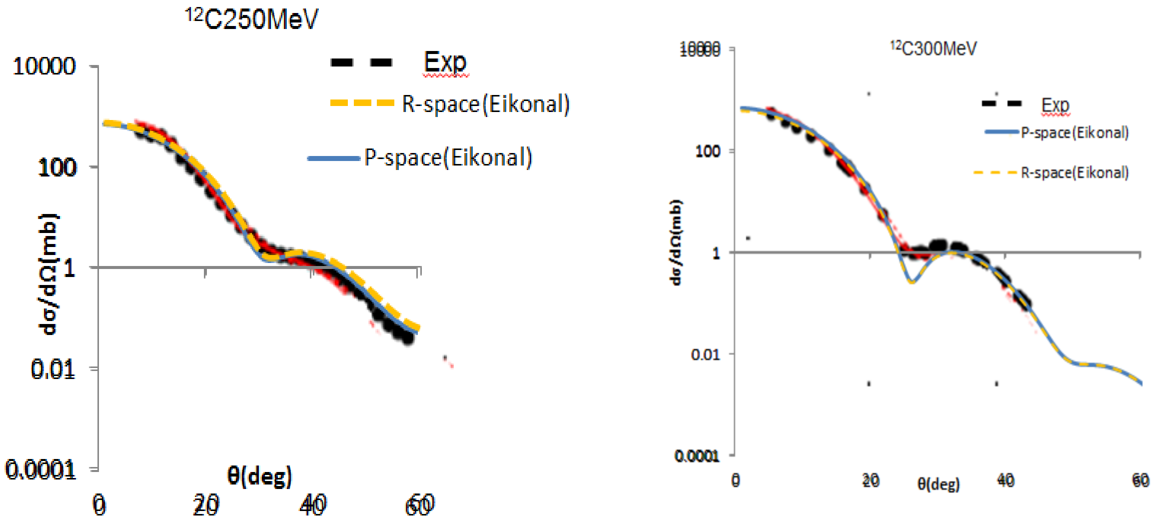

(a) Result for 250MeV (b) Result for 300MeV

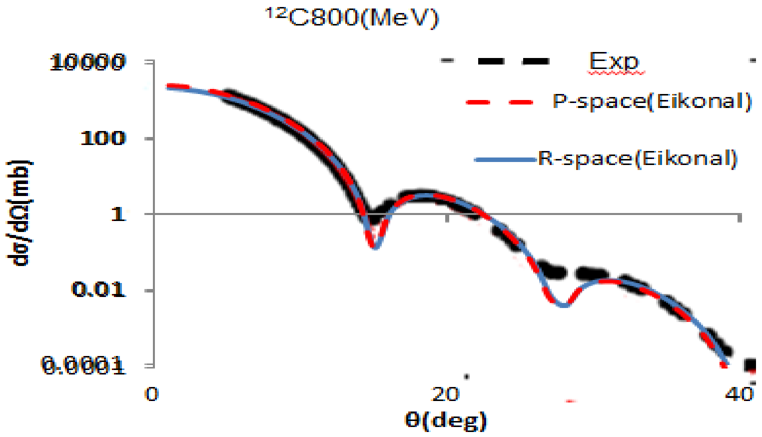

(c) Result for 800MeV

Figure 2 Differential cross section for Carbon ^{12}C target incident on proton at (a) 250MeV, (b) 300Mev and (c) 800MeV. Color lines are p-space and R-space eikonal calculation. Experimental data

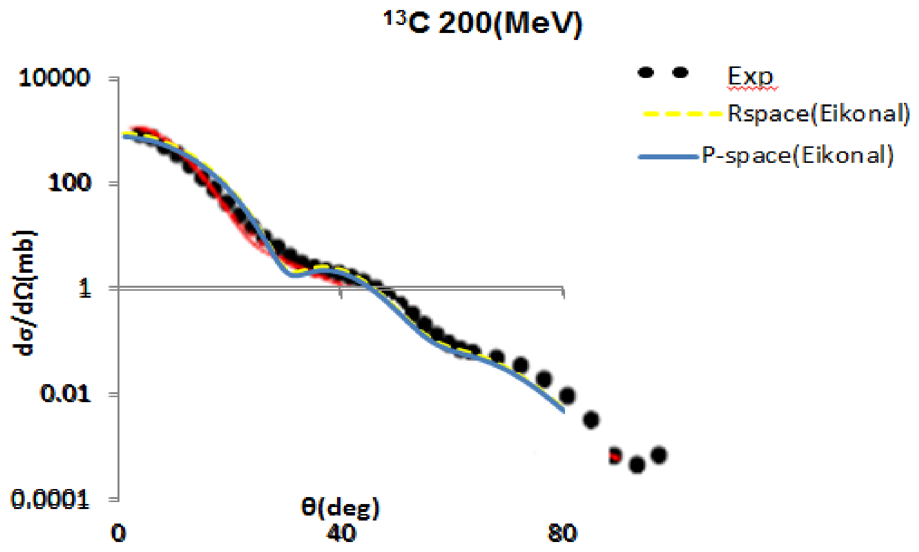

(d)Result for 200MeV

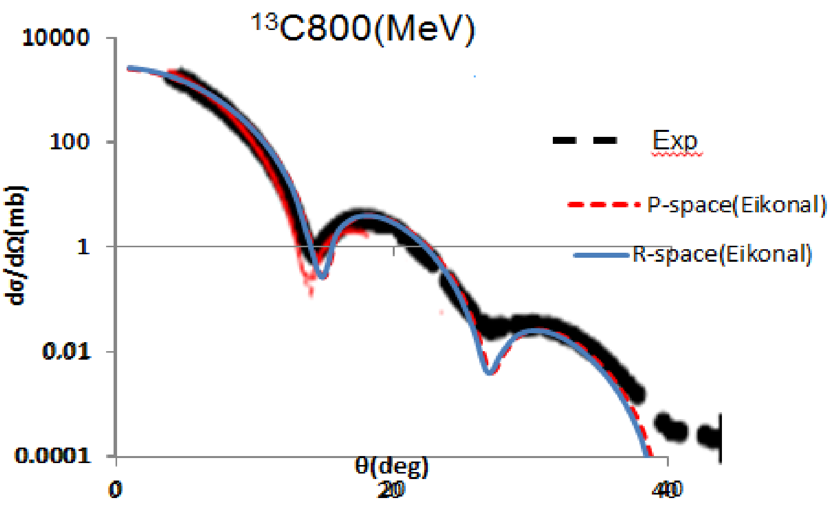

(e) Result for 800MeV

Figure 3 Differential cross section for p-carbon ^{13}C scattering at (d) 200MeV and (e) 800MeV. Experimental data are taken from Ref [4].

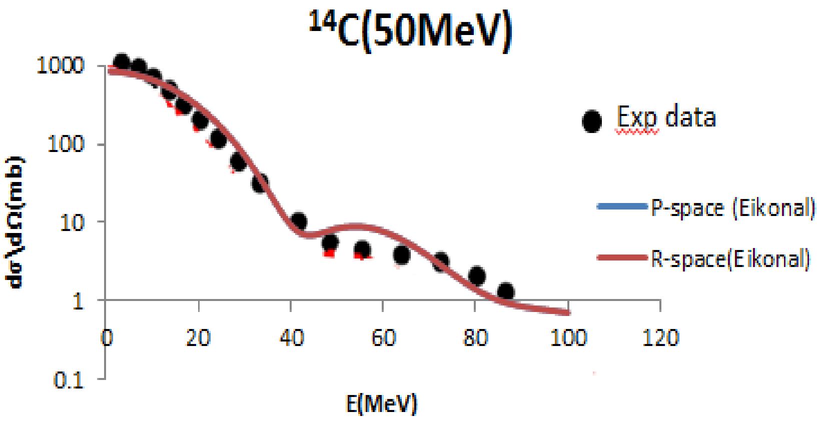

Figure 4 Comparison of numerical results (p-space and R-space) with experimental data [4] for P-Carbon ^{14}C scattering

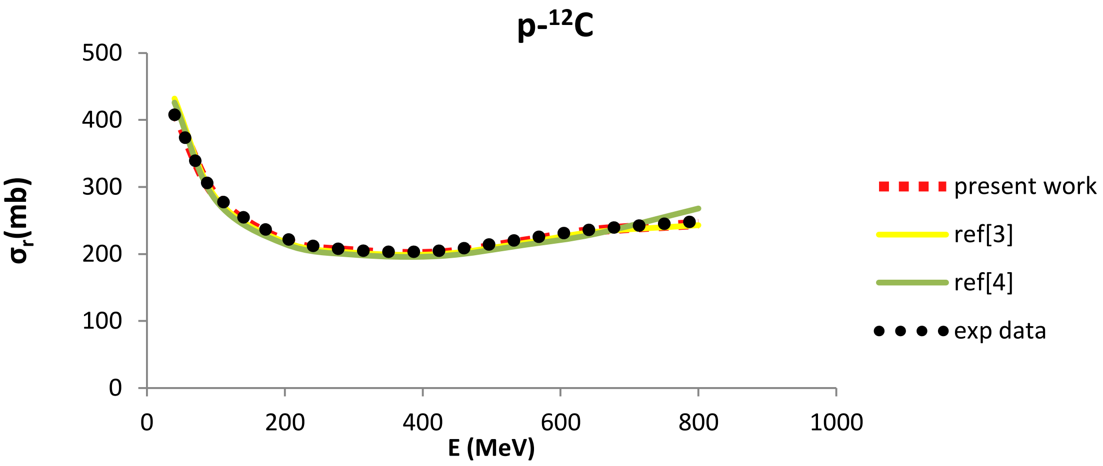

Figure 5 Comparison study of reaction cross section of P-Carbon ^{12}C scattering as a function of energy

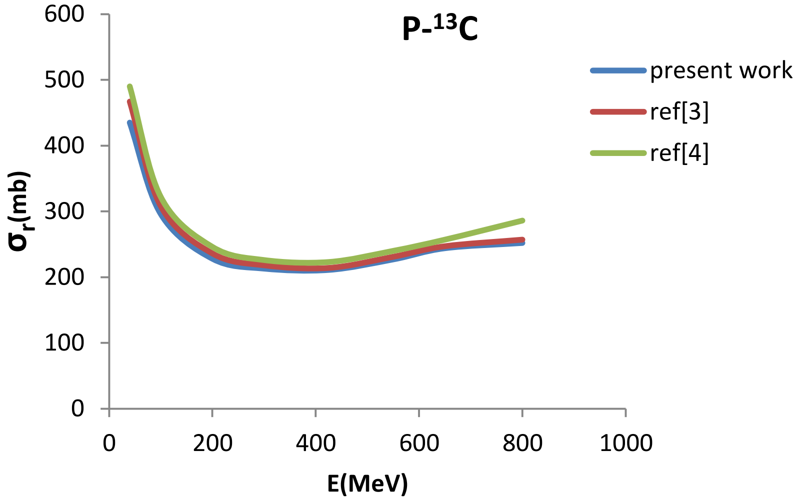

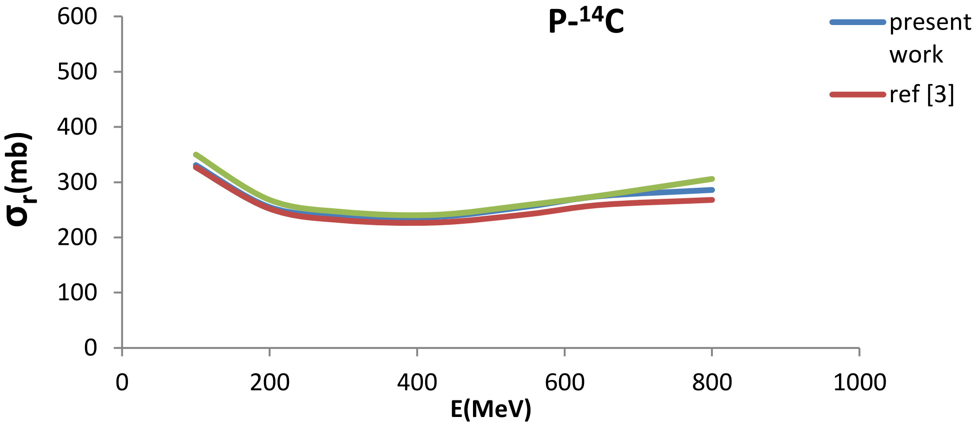

Figure 6 Comparison of reaction cross section for P- Carbon ^{13}C (upper) & ^{14}C(lower) scattering between present work and other theoretical results

Conclusion

The differential cross section of proton carbon scattering is predicted by using NN optical potential. It is obtained by computing a six- dimensional integral over the nuclear matter densities of the target and NN transition amplitude. Consequently, numerical calculation of optical potential is inefficient. According to numerical calculation, the eikonal phase function can be written as a one-dimensional integral by expressing the optical potential as a function of momentum transfer, thereby greatly increasing the efficiency of the numerical evaluation of cross section using eikonal approximation. Moreover, NA optical potential were obtained with harmonic well nuclear matter densities, which are suitable for light nuclei (A<20). The formulas were used to predict the elastic differential cross sections for proton-light nuclei reactions. The results generated from the optical potential were verified with numerical integration, and it was fond that elastic differential cross section are in good agreement with experimental data displayed in figure 2,3 and 4. The momentum-space formulation of the eikonal phase function is used to evaluate the differentisl cross section of proton carbon reaction which utilizes target nuclear matter density parameterization. It was found that the momentum-space phase function agrees exactly with the eikonal approximation computed in position-space and the results of both calculations are in good agreement with experimental data. In present work, the reaction cross sections for proton-elastic scattering from carbon isotopes of A=12-14 calculated in large energy region of 100-1000MeV. The results obtained from eikonal approximation with optical potential compares with other theoretical results as well as experimental results. Their behaviors of reaction cross section with respect to energy are very similar to each other. In figure 5 and 6, the eikonal approximation gives significantly large reaction cross section in energies less than 200MeV, showing minimum values at around 300-425 and after that slightly increasing with increasing energies. This effect is due to attribution of NN transition of amplitudes. The bigger reaction cross section of proton carbon isotope, the more increase mass number of isotope is due to the more present of nucleon inside the nucleus and the interaction between projectile and target becomes snowballing.

Acknowledgements

I am grateful to Professor Dr Khin Maung Maung who gave me advice and guide to do this work. I also acknowledge Associate Professor Dr Thida Wint for her useful comments and discussions. I would to express my gratitude to Professor Dr San San Wai, Head of Department of Physics, Loikaw University, for her approval to carry out this work.

References

Abu-Ibrahim, B., & Horiuchi W., (2008) *Phys. Rev.* ***C*** **77** 034607

Carlson, R.F., (1996) At. Data Nucl, Data Tables 63.93

De Vries., De Jager, C.W., & C. De Vries, C.W., (1987) Nuclear charge density distribution parameter from elastic electron scattering. Atom Data Nuvl. Data, 36, 495-536

Horiuchi W., & Suzuki, Y., (2006) arXiv: 0612029 [nucl-th]

Joachain, C. J., (1983) Quantum Collision Theory. Amsterdam

Kaki, K., (2017) arXiv: 1703. 10733 [nucl-th]

Wernth, C.M., Maung K.M., Vera, M.D., & Townsend, L.W., (2018) Can. J. Phys. **96** 642

J. Myanmar Acad. Arts Sci. 2020 **Vol. XVIII.No.2**B

N-BODY SIMULATIONS OF HOMOGENEOUS GALAXIES

Zaw Shin [1], Htwe Nwe Oo[2], San San Maw[3], Thant Zin Naing[4]

Abstract

N-body simulations of homogeneous galaxies have been made to explore the physical proposal of critical density and mass, angular momentum and so on. Fundamental properties of galactic dynamics and structure formation have also been studied. Mathematica codes and finite element method have been briefly explored. As the situation dictates, Mathematica software is used for some detailed computations and visualization of the results.

Keywords: homogeneous galaxies, galactic dynamics, finite element method.

Introduction

Attempts have been made to investigate the structure formation in the γ gravity f(R) model with N-body simulations. The γ gravity model is a proposal which, unlike other viable f(R) models, not only changes the gravitational dynamics, but can in principle also have signatures at the background level that are different from those obtained in ΛCDM (Cosmological constant, Cold Dark Matter). The aim of this paper is to study the nonlinear regime of the model in the case where, at late times, the background differs from ΛCDM. We quantify the signatures produced on the power spectrum, the halo mass function, and the density and velocity profiles. To appreciate the features of the model, have compared it to ΛCDM and the Hu-Sawicki f(R) models. For the considered set of parameters it was found that the screening mechanism is ineffective, which gives rise to deviations in the halo mass function that disagree with observations. This does not rule out the model per se, but requires choices of parameters such that ($|f_{R0}|$) is much smaller, which would imply that its cosmic expansion history cannot be distinguished from ΛCDM at the background level.

Since the discovery in 1998 that the Universe is speeding up instead of slowing down (as would be expected if gravity is always attractive), considerable effort has been devoted to understanding the physical mechanism behind this cosmic acceleration.(Peebles P.J.E,1970) The two main theoretical approaches considered in the literature to explain this phenomena are (1) to assume the existence of a new component with a sufficiently negative pressure $(p < -\rho/3)$, generically denoted dark energy; and (2) to consider that general relativity has to be modified at large scales, or more accurately, at low curvature (modified gravity). The simplest dark energy candidate is Einstein′s cosmological constant (Λ) with an equation of state $\omega_{DE} \equiv p_{DE}/\rho_{DE} = -1$. However, in spite of its very good accordance with current observations, Λ has some theoretical difficulties such as its tiny value as compared with theoretical predictions of the vacuum energy density, the cosmic coincidence problem, and related fine-tuning. This situation has motivated the search for alternatives like modified-gravity theories. The simplest modified-gravity

---

[1] Dr, Lecturer, Department of Physics, University of Yangon.

[2] Lecturer, Department of Physics, Yangon University of Education.

[3] Assistant Lecturer, Department of Physics, West Yangon University.

[4] Retired Pro-Rector (Admin), International Theravāda Buddhist Missionary University, Yangon.

candidates are the so-called f(R)-theories, in which the Lagrangian density $L = R + f(R)$ is a nonlinear function of the Ricci scalar R.(Planck et al ,2013)

As is well known, metric f (R)-theories can be thought of as a special case of a scalar-tensor theory; a Brans-Dicke model with a coupling constant $\omega_{BD} = 0$. An accelerated expansion appears naturally in these theories. The very first inflationary model, proposed by Starobinsky more than three decades ago, is driven by a term of the type $f(R) = \alpha R^2$ $(\alpha > 0)$ and is still in excellent accordance with observations. More recently, the idea of an acceleration driven by late-time curvature has also been explored. These authors considered a theory in which $f(R) = -\alpha R^{-n}$ $(\mathrm{n} > 0 \text{ and } \alpha > 0)$. However, these models do not have a regular matter dominated era and are incompatible with structure formation.(Amendola et al,2007)

To build a cosmologically viable f(R) theory, some stability conditions have to be satisfied (a) $f_{RR} = d^2 f/dR^2 > 0$ (no tachyons);(b) $1 + f_R \equiv 1 + df/dR > 0$ (the effective gravitational constant $G_{eff} = G_N/(1+f_R)$ does not change sign;(c) after inflation, $\lim_{R\to\infty} = f(R)/R = 0$ and $\lim_{R\to\infty} = f(R) = 0$ (General Relativity is recover at early time); (d) $|f(R)|$ is small in recent times, to satisfy solar system and galactic scale constraints. In addition to those conditions, there are some desirable characteristics that a viable cosmological model has to satisfy. It should have a radiation-dominated era at early times and a saddle point matter-dominated era phase followed by an accelerated expansion as a final attractor.

There are viable f(R) gravity theories that satisfy all the criteria above. However, there is generic difficulty from which all these "viable" f(R) theories suffer: the curvature singularity in cosmic evolution at a finite redshift. It can be shown that this type of singularity problem can be curved, for instant, by adding a high-curvature term proportional to R^2 to the density Lagrangian. Therefore, it is not possible to have cosmic acceleration with totally consistent f(R) theory modifying gravity at low curvatures.

The specific case of a viable f(R) theory called γ gravity. Generally, in almost all viable f(R) theories, structure formation imposes such strong constraints on the parameters of the models that the effective equation of state parameter cannot be distinguished from that of a cosmological constant. In γ gravity the steep dependence on the Ricci scalar R facilitates the agreement with structure formation. The parameter that controls the steepness in γ gravity allows measurable deviation from ΛCDM at both linear perturbation and background levels, while still compatible with both current observations.(Appleby et al,2010) The main goal of this paper is to study the effects of γ gravity on the structure formation at nonlinear scales for choices parameters where the model has observable signature on the background expansion history of our Universe.

γ-Gravity Review

We investigate spatially flat cosmological models in the context of gravity, a viable f (R) theory defined by the following ansatz:

$$f(R) = -\frac{\alpha R_*}{n}\gamma\left[\frac{1}{n},\left(\frac{R}{R_*}\right)^n\right] \tag{1}$$

Where $\gamma(n,x)=\int_0^x t^{n-1}e^{-t}dt$ is the incomplete $\Gamma-$function and α , n and R_* are free positive constants. In reality, γ gravity can be thought of a simple generalization of exponential gravity.

$$f(R)=-\alpha R_*[1-e^{-\left(R/R*\right)}], \tag{2}$$

Obtained by fixing n = 1 in Eq. (1). We emphasize that γ gravity can satisfy all the stability and viability conditions. For fixed n, there is a minimum value ($\gamma_{\min}$) of the parameter α such that for values $\alpha > \alpha_{\min}$ a late-time accelerated attractor is achieved. Consider this case throughout from Eq.(1) ,obtain the following derivatives:

$$f_R=-\alpha e^{-\left(R/R*\right)^n} \tag{3}$$

$$f_{RR}=\frac{\alpha n}{R}\left(\frac{R}{R_*}\right)^n e^{-\left(\frac{R}{R*}\right)^n} \tag{4}$$

Note from Eq.(3) that with increasing n, the steepness of the f (R) function increases. Higher n means smaller $|f_{R0}|$, and the departures from GR will be smaller accordingly. (O′ Dwyer et al, 2013)

Although there is no cosmological constant, f (0) = 0, it follows from Eq. (1) that GR with Λ is recovered at high curvatures. Therefore, for $R>>R_*$ the models behave like $\Lambda\,CDM$. Since interested in phenomena that occurred after the beginning of the matter-dominated era, neglect radiation and write the effective cosmological constant (the cosmological constant of the reference $\Lambda\,CDM$ model) as

$$\tilde{\Lambda}=\frac{\alpha R_*}{2n}\Gamma(1/n)=3\tilde{H}_0^2(1-\tilde{\Omega}_{m0}) \tag{5}$$

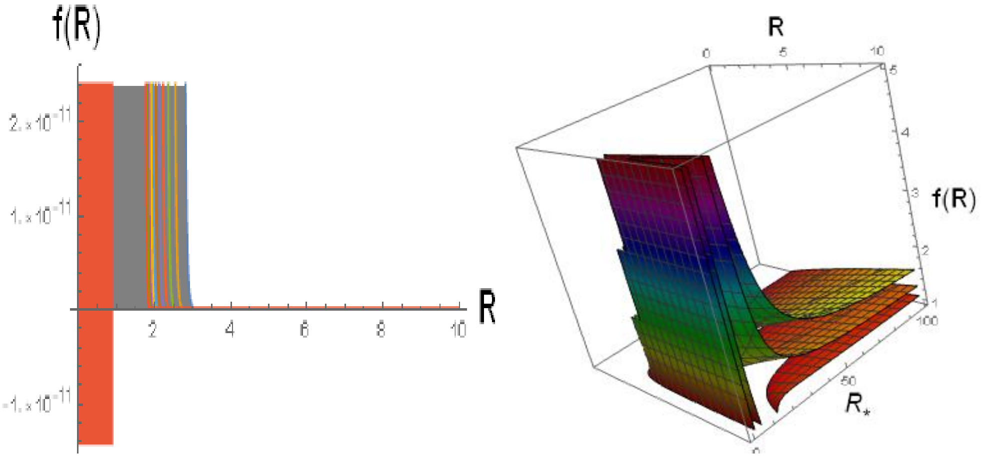

Figure 1 The 2D and 3D profiles of gamma gravity f(R)

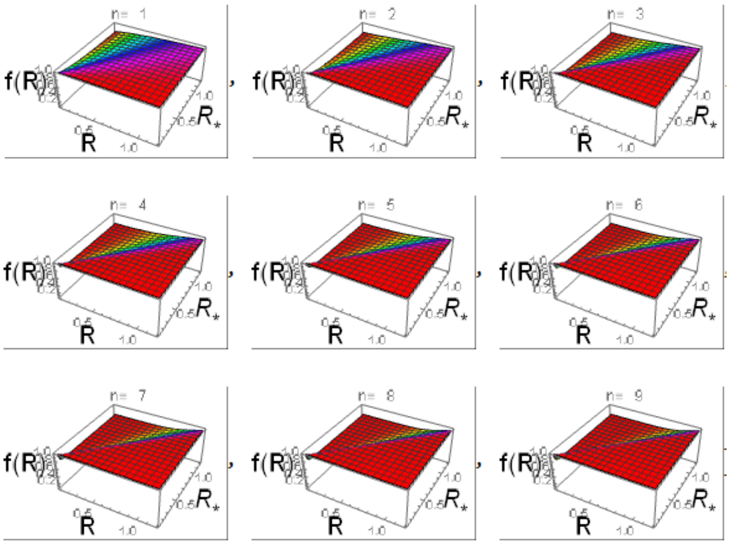

Figure 2 3-D snapshot profiles of gamma gravity f(R)

In the equation above, $\tilde{\Omega}_{m0}$ denotes the present value of the matter density parameter that a $\Lambda\,CDM$ model would have if it had the same matter density today $(\tilde{\rho}_{m0})$ as the modified gravity f(R) model. $\tilde{H}_0$ represents the Hubble constant in the reference $\Lambda\,CDM$ model. Therefore, $m^2 \equiv 8\pi G\tilde{\rho}_{m0}/3 = \tilde{\Omega}_{m0}H_0^2 = \Omega_{m0}H_0^2$, where Ω_{m0} and H_0 are the present value of the matter energy density parameter and Hubble parameter in the f(R) model, respectively. It is useful to rewrite R_* as

$$\frac{R_*}{m^2} = \frac{6nd}{\alpha\Gamma(1/n)} \tag{6}$$

Where $d = (1-\tilde{\Omega}_{m0})/\tilde{\Omega}_{m0}$

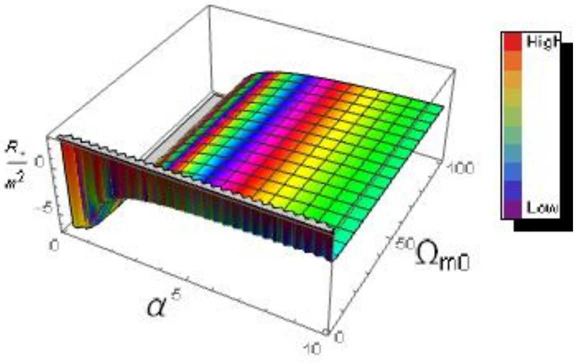

Figure 3 Profile of R_*/m^2 in terms of α and Ω_{m0}.

N-Body Equations

f(R) models are equivalent to a scalar-tensor theory, where the first derivative of the f (R) function, f_R. (Brax et al.2008) This field propagates according the equation

$$\Upsilon\, f_R = \frac{\partial V_{eff}}{\partial f_R} = \frac{(1-f_R)R + 2f + \kappa^2 T}{3} \tag{7}$$

Where $\kappa^2 = 8\pi G/c^4$ and T is the trace of energy-momentum tensor, $T = g_{\mu\nu}T^{\mu\nu}$.In the quasi-static limit, this equation becomes

$$\frac{1}{a^2}\nabla^2 f_R = \frac{R - R(a)}{3} - m^2 a^{-3}\delta_m \tag{8}$$

Where

$$\frac{R(a)}{m^2} = 3(a^{-3} + 4d) + \Delta_R(a), \tag{9}$$

and $\Delta_R(a) = x_2(a) + 12x_1(a)$.The Ricci scalar R in function of f_R is given by inverting Eq. (3)

$$R = R_* \log\left(\frac{a}{|f_R|}\right)^{1/n} \tag{10}$$

The geodesic equation, needed to update the particle positions, reads

$$\ddot{x} + 2H\dot{x} = -\frac{1}{a^2}\nabla\left(\Phi - \frac{f_R}{2}\right), \tag{11}$$

Where Φ is the Newtonian potential, which the dynamics is given by the Poisson equation

$$\nabla^2\Phi = \frac{3m^2}{2}\frac{\delta_m}{a}, \tag{12}$$

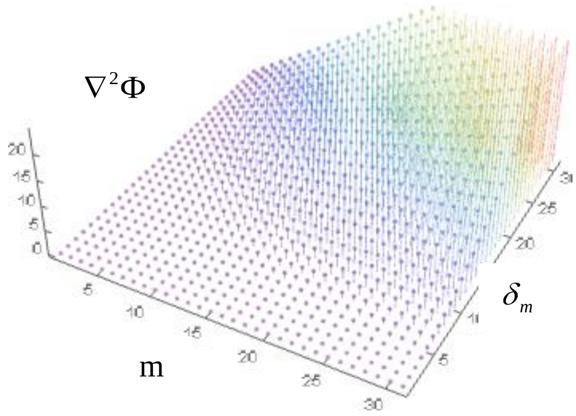

Figure 4 Profile of $\nabla^2\Phi$ in terms of and δ_m

When implementing these equations in the N-body code, need to rewrite them in code-units given by

$$\tilde{x} = \frac{x}{B_0}, \tilde{\Phi} = \frac{\Phi a^2}{(H_0 B_0)^2}$$
$$d\tilde{t} = \frac{H_0 dt}{a^2}, \nabla_{code} = B_0 . \nabla \qquad (13)$$

Here B_0 is the size of the simulation box. In terms of $\tilde{f}_R = -a^2 f_R$, the evolution equation becomes

$$\frac{d^2\tilde{x}}{d\tilde{t}^2} = -\nabla_{code}\Phi - \frac{1}{2(B_0 H_0)^2}\nabla_{code}\tilde{f}_R \qquad (14)$$

$$\nabla^2_{code}\Phi = \frac{3}{2}\Omega_{m0} a \delta_m \qquad (15)$$

$$\nabla^2_{code}\tilde{f}_R = \Omega_{m0}(H_0 B_0)^2 a^4 \times \left\{ -\frac{R_*}{3m^2}\log\left(\frac{aa^2}{\tilde{f}_R}\right)^{1/n} + \left[a^{-3} + 4d + \frac{\Delta_R(a)}{3}\right] + a^{-3}\delta_m \right\} \qquad (16)$$

These are the only equations need to implement and solve in the N-body code. For comparison it also needs the linearized field equation. Simulations with this equation compared to the full f_R equation is a good measure of the amount of screening that takes place in the model. The linearized f_R equation is simply

$$\frac{1}{a^2}\nabla^2 \delta f_R = m^2_{\phi}(a)\delta f_R - m^2 a^{-3}\delta_m \qquad (17)$$

Where $\delta f_R = f_R - f_R(a)$ and $m^2_{\phi}(a) = \frac{1}{3 f_{RR}(a)}$ .In code units, taking $u = -\frac{\delta f_R a^2}{2(H_0 B_0)^2}$, we obtain

$$\nabla^2_{code} u = \left[m_{\phi}(a) a B_0\right]^2 + \delta_m \frac{\Omega_{m0} a}{2} \qquad (18)$$

and the geodesic equation becomes

$$\frac{d^2\tilde{x}}{d\tilde{t}^2} = -\nabla_{code}\Phi - \nabla_{code} u \qquad (19)$$

We have

$$m^2_{\phi}(a) a^2 B_0^2 = \frac{a^2 (H_0 B_0)^2}{3\alpha n}\frac{R(a)}{H_0^2}\left[\frac{R_*}{R(a)}\right]^n e^{[R(a)/R]^{n}} \qquad (20)$$

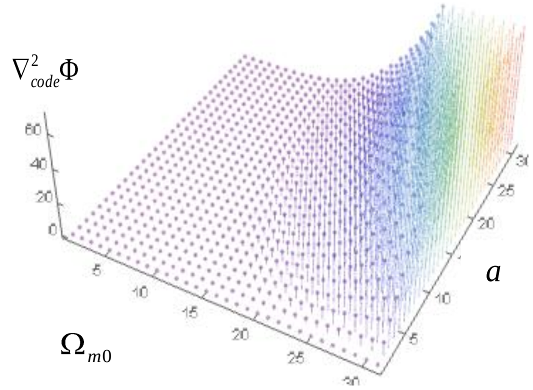

Figure 5 Profile of the $\nabla^2_{code}\Phi$ in terms of Ω_{m0} and a.

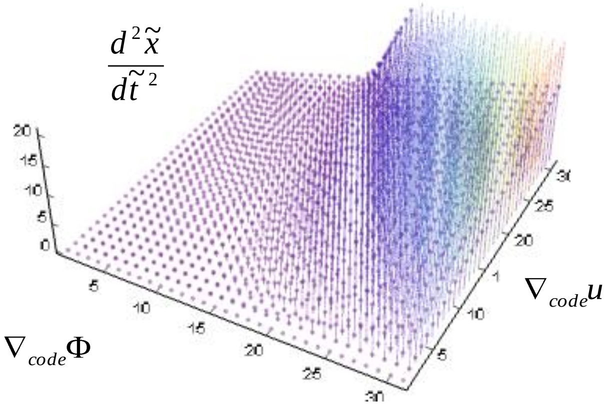

Figure 6 Profile of the $\frac{d^2\tilde{x}}{d\tilde{t}^2}$ in terms of $\nabla_{code}\Phi$ and $\nabla_{code}u$.

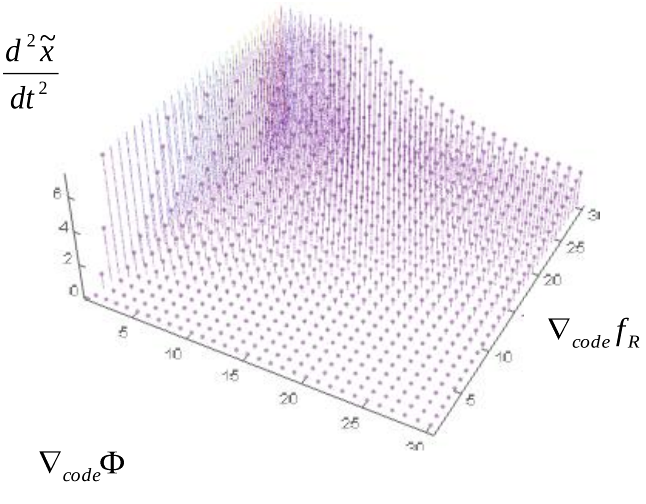

Figure 7 Profile of the $\frac{d^2\tilde{x}}{d\tilde{t}^2}$ in terms of $\nabla_{code}\Phi$ and $\nabla_{code}f_R$.

Result and Conclusions

We have investigated the nonlinear evolution in the γ gravity, the f(R) theory of gravity that is a viable alternative to ΛCDM. In the models under investigation one uses a screening mechanism to suppress the deviations from General Relativity at small and large cosmological scales. Specifically, this is what we called the chameleon screening mechanism. As a result of this screening mechanism, the strongest signatures in these models are expected to occur at the nonlinear regime of structure formation. Therefore, to unveil the imprints of such theories at astrophysical scales, we ran several cosmological N-body simulations. Originally, programmes are ran on highs specially supercomputers. In this paper, we make use of the simple iteration preceding such as Listpointplot3D, BesselJ(2Dand 3D),Contourplot3D, Revolutionplot3D and so on. The interesting point is such that the resulting normalizations are in agreement with the done by the high capacity computers.

Acknowledgements

I am highly grateful to Professor Dr Khin Khin Win, Head of Department of Physics, University of Yangon, for her kind permission to do and her encouragement to carry out this paper.

I would like to thank all the Professors, Department of Physics, University of Yangon, for her valuable guidance, kind encouragement, valuable help, and support in this paper.

Special thanks are due to Professor Dr Thant Zin Naing, Retired Pro-Rector (Admin), International Theravāda Buddhist Missionary University, for his helpful advice to carry out this work.

References

Amendola, L., Gannouji, R., Polarski, D., & Tsujikawa, S (2007), Phys. Rev. D,75, 083504

Appleby, S. A., & Battye, R. A,(2007), Phys. Lett. B, 654, 7

Appleby, S. A., Battye, R. A., & Starobinsky, A. A(2010), J. Cosmol. Astropart. Phys., 1006, 005

Berti, E., Barausse, E., Cardoso, V., et al,(2015), Class. Quant. Grav. 32, 243001

Bouchet, F. R. and L. Hernquist ,(1988), Cosmological simulations using the hierarchical tree method. *Astrophys. J., Suppl. Ser.*, 68, pp. 521–538.

Brax,P., van de Bruck, C., Davis et al,(2008),Phys.Rev.D,78,104021

O’Dwyer et al, (2013), Phys.Rev.D, 89,023521

Peebles P. J. E, (1970), Astro.Phys.J, 75, 13

Planck Collaboration et al,(2013), ArXiv e-prints

J. Myanmar Acad. Arts Sci. 2020 **Vol. XVIII.No.2**B

ESTIMATE OF THE MASS OF DARK MATTER IN INHOMOGENEOUS UNIVERSE

Kyaw Zall Linn[1], Tet Toe[2], Thei Theint Theint Aung[3], Thant Zin Naing[4]

Abstract

Attempts have been made to study the fundamental properties of dark matter and structure formation of the inhomogeneous cosmology. Detailed mechanism of the relation of dark matter candidates in the range of inflation of the universe and axion decay rate at inflation has been investigated and the mass of axion, one of the major candidates of dark matter, has been to estimate in the frameworks of general relativity and elementary particle. As the situation dicates, Mathematica software is utilized for detailed computations and visualization of the results.

Keywords: dark matter, inhomogeneous cosmology, axion

Introduction

The term "dark matter" was first introduced by Fritz Zwicky (1933) in his term paper when he studied the dynamics of galaxy clusters. Several powerful astrophysical and cosmological arguments which dislike "baryonic matter" as a main constituent constrained the physical properties of dark matter. The most popular argument is that of "particle dark matter" which is speculated by Cowski and McClelland (1973) that the new matter appears to hold galaxies and galaxy clusters gravitationally together rather than the baryonic matter.

In the last two decades, new and powerful techniques have emerged that the universe is filled with dark matter. A standard model of cosmology is emerging in which the universe is made of 4.9% of ordinary baryonic matter, nearly 26.8% of dark matter and 68.3% of dark energy according to NASA/WMAP Science Team. Based on the current research, scientists know only that dark matter is cold, slow moving, and interacts weakly with ordinary matter.

The quantity and composition of matter and energy in the universe is a fundamental and important issue in cosmology and also crucial for understanding the past as well as the future of the universe. The growth of small inhomogeneities in the matter and ultimately how large scale structure formed in the present age of the universe, the formation and evolution of individual galaxies, can be determined.

Structural Formation of the Inhomogeneous Universe

From a spatially flat Friedman-Robertson-Walker (FRW) model, it can be induced by the inhomogeneous dark fluids coupled with dark matter in the equation of state. Starting from a universe filled with two interacting ideal fluids, dark energy and dark matter with scale factor. The governing equations are

---

[1] Assistant Lecturer, Department of Physics, University of Yangon

[2] Lecturer, Department of Physics, Pakkoku, University

[3] Assistant Lecturer, Department of Physics, Bago University

[4] Retired, Pro-Rector(Admin), International Theravada Buddhist Missionary University, Yangon

$$\begin{aligned} &\dot{\rho} + 3H(p+\rho) = -Q \\ &\dot{\rho}_m + 3H(p_m+\rho_m) = Q \qquad (1) \\ &\dot{H} = -\frac{k^2}{2}\left(p+\rho+p_m+\rho_m\right) \end{aligned}$$

where, the hubble rate H and $k^2=8\pi G$, G is Newton's gravitational constant and p and ρ are the pressure and the energy density respectively and Q is the function that accounts for the energy exchange between dark energy and dark matter.

Friedman's equation for the Hubble rate is given by

$$H^2 = \frac{k^2}{3}\left(\rho+\rho_m\right)$$

For the case study of nonrelativistic dark matter ($\bar{\omega}=0$), and the consideration the dark matter as a dark, then one obtains $p_m = 0$.

Now the gravitational equation of motion for dark matter becomes

$$\dot{\rho}_m + \sqrt{3}k\rho_m\sqrt{\rho+\rho_m} = Q \qquad (2)$$

The relation between Q and H is

$$Q = \delta H^2$$

Where δ is positive constant and it can be obtained Q for the existence of scaling solutions as

$$Q = \frac{\delta\gamma^2}{3}\rho_m \text{ where } \gamma = \frac{k}{\sqrt{3}}\sqrt{1+\frac{1}{r}} \text{ and } r = \frac{\rho_m}{\rho}.$$

In this situation the energy density of dark matter is given by

$$\rho_m = \left(\frac{C\delta\gamma}{3C+e^{\frac{-\eta^2}{2}}}\right), \qquad (3)$$

where C is an integration constant, $\eta = \delta\gamma^2$.

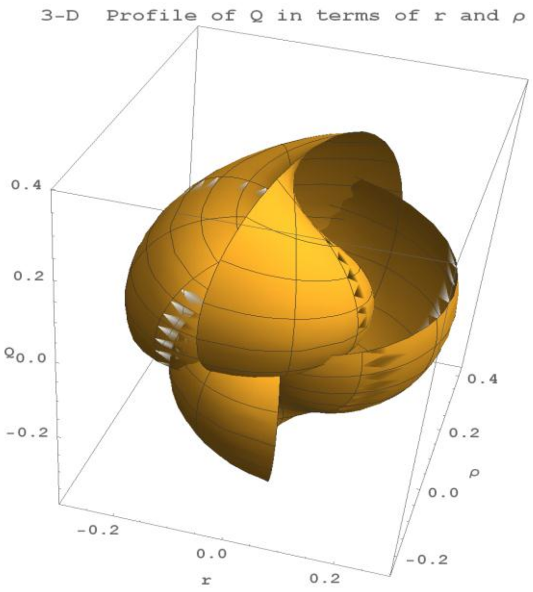

Figure 2 3-D profile of Q in terms of r and ρ

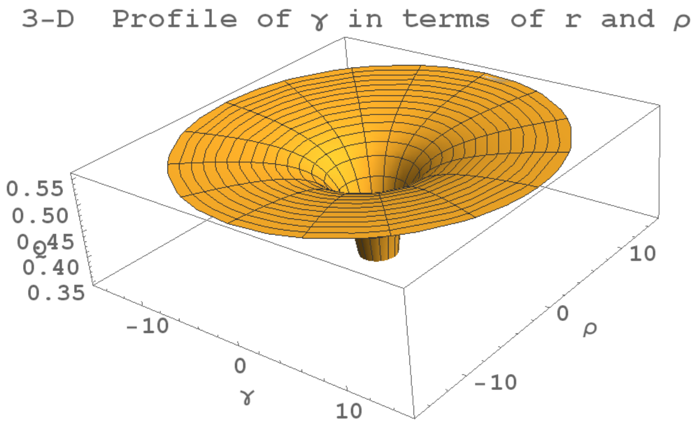

Figure 2 3-D profile of γ in terms of r and ρ

Overview of Dark Matter Candidate

There are many possible candidates of dark matter assuming in modern cosmology ranging the mass from axion with mass 10^{-5} eV to black holes of mass which are 10^{4} times that of solar mass. The first class is to classify the baryonic and non-baryonic. The main baryonic matters are massive compact halo objects (MACHOs) including brown dwarfs, jupiters, stellar black-hole remnants, white dwarfs, and neutron stars, etc. The remaining of the dark matter candidates is non-baryonic which can be in further classification with hot and cold dark matter. The hot dark matter is moving at relativistic speeds when galaxies could just start to form. The major assumption of hot dark matter candidates is neutrino. However, hot dark matter does poorly in reproducing the N body simulations of structure formation in a universe. There have been other suggestions that most of part is cold dart matter.

The non-baryonic cold dark matter candidates can be assumed basically elementary particles although they have not been discovered. The axion and weakly-interacting massive particles (WIMPs) are the leading class in these candidates. There are other pseudo-Nambu-Goldstone bosons which are similar to the axion which have been also proposed as dark matter candidates.

Axion dynamics

In the standard model, the sum of the QCD topological angle and the common quark mass phase $\theta = \theta_0 + \arg\det M$ is experimentally bounded to lie below from the non-observation of the neutron electric dipole moment. Among the known solutions, the QCD axion is probably the most simple and the standard model becomes an argument with an extra pseudo-goldstone boson which only derivative coupling to QCD topological control and repressed by the scale f_A. This coupling permit the effects of θ to be redefined away via a shift of the axion field, whose vacuum expectation value (VEV) is then guaranteed to vanish. It can also produce the mass of the axion. Another model dependent derivative coupling may be present but they do not affect the solution of the strong CP problem, but the mass and couplings of the QCD axion are thus controlled by a single scale f_A.

At energies lower than the PQ and electroweak EW breaking scales, the axion dependent part of the Lagrangian and the weak couplings can be written as

$$\mathcal{L}_{\mathrm{a}} = \frac{1}{2}\left(\partial_\mu a\right)^2 + \frac{a}{f_A}\frac{\alpha_s}{8\pi} G_{\mu\nu}\tilde{G}^{\mu\nu} + \frac{1}{4} a g^0_{a\gamma\gamma} F_{\mu\nu}\tilde{F}^{\mu\nu} + \frac{\partial_\mu a}{2 f_A} j^\mu_{a,0} \tag{4}$$

In the above equation the second term defines f_A with the dual gluon field strength $\tilde{G}_{\mu\nu} = \frac{1}{2} \in_{\mu\nu\rho\sigma}$ colour indices which is implicit and the coupling to the photon field strength $F_{\mu\nu}$ is

$$g^0_{a\gamma\gamma} = \frac{\alpha_{EM}}{2\pi f_A}\frac{E}{N} \tag{5}$$

where $\frac{E}{N}$ is the ratio of electromagnetic EM and the colour incongruity.

The last term of equation(4)

$$j^\mu_{a,0} = c^0_q \bar{q}\, \gamma^\mu \gamma_5\, q \tag{6}$$

is a model dependent axial current made of SM matter fields . The axionic pseudo shift symmetry a→a + δ can remove QCD θ angle.

In particular performing a charge of field variables on top and down quarks

$$q = \begin{pmatrix} u \\ d \end{pmatrix} \rightarrow e^{i\,\gamma_5 \frac{a}{2 f_a} Q_a} \begin{pmatrix} u \\ d \end{pmatrix}, \text{and Tr } \mathrm{Q_a} = 1 \tag{7}$$

Equation (4) becomes

$$\mathcal{L}_{\mathrm{a}} = \frac{1}{2}\left(\partial_\mu a\right)^2 + \frac{1}{4} a g^0_{a\gamma\gamma} F_{\mu\nu}\tilde{F}^{\mu\nu} + \frac{\partial_\mu a}{2 f_a} j^\mu_{a,0} - \bar{a}_L M_a a_R + h.c \tag{8}$$

where ,

$$g_{a\gamma\gamma} = \frac{\alpha_{EM}}{2\pi\, f_a}\left[\frac{E}{N} - 6\, Tr\ \left(Q_a\, Q^2\right)\right] \tag{9}$$

$$j_a^{\mu} = j_{a,0}^{\mu} - \bar{q}\ \gamma^{\mu}\ \gamma_5\ Q_a\, q \tag{10}$$

$$M_a = e^{i\frac{a}{2f_a}Q_a}\, M_q\, e^{i\frac{a}{2f_a}Q_a} \tag{11}$$

$$M_q = \begin{pmatrix} m_u & 0 \\ 0 & m_d \end{pmatrix} \text{ and } Q = \begin{pmatrix} \frac{2}{3} & 0 \\ 0 & -\frac{1}{3} \end{pmatrix} \tag{12}$$

This axion coupling to the axial current only renormalizes multiplicatively and the axion appears through the quark mass terms in this.

The axion can be preserved as an external source by the leading $\frac{1}{f_A}$, and the virtual axions being affected by the tiny coupling. The non-derivative couplings to QCD are programmed in the phase dependence of the quark mass matrix M_a which in the derivative couplings the axion be an external axial current. At the above equation, the choice of axion field allowed to move the non-derivative couplings entirely into the lightest two quarks. From these quarks, it can be integrated out all of the other quarks and directly work in the effective theory with M_a capturing with the whole axion dependence.

In the chiral expansion, all the non-derivative dependence on the axion is contained in the pion mass terms;

$$\mathcal{L}_{p2} \supset 2B_0 \frac{f_\pi^{\ 2}}{4}\left\langle U M_a^{\ +} + M_a U^{+}\right\rangle \qquad \text{c} \tag{13}$$

where, $U = e^{i\beta/f_\pi}$ and $\beta = \begin{pmatrix} \pi^0 & \sqrt{2}\pi^+ \\ \sqrt{2}\pi^- & -\pi^0 \end{pmatrix}$

< > is the traces over flavor indices and B_0 is related to the chiral condensate and determine by the pion mass in terms of quark masses and the pion decay constant is normalized such that $f_\pi \approx 92 MeV$.

In order to derive the leading order effective axion potential, it is required to only consider the neutral pion sector. Choosing Q_a proportional to the identity,

$$V(a,\pi^0) = -B_0\, f_\pi^2\left[m_u \cos\left(\frac{\pi^0}{f_\pi} - \frac{a}{2f_A}\right) + m_d \cos\left(\frac{\pi^0}{f_\pi} + \frac{a}{2f_A}\right)\right]$$

To be solved in all closed form at all $\left(\frac{a}{2f_A}\right)$, it can be considered the case of flavours as

$$\phi_u = \bar{\phi}_u = \arctan \frac{m_d \sin\left(\frac{a}{2f_A}\right)}{m_u + m_d \sin\left(\frac{a}{2f_A}\right)}$$

$$\phi_d = \bar{\phi}_d = \arctan \frac{m_u \sin\left(\frac{a}{2f_A}\right)}{m_d + m_u \sin\left(\frac{a}{2f_A}\right)}$$

and, $\tan\phi_a = \frac{m_u - m_d}{m_u + m_d} \tan\left(\frac{a}{2f_A}\right)$, where $\phi_a = \bar{\phi}_u + \bar{\phi}_d$

$$V(a,\pi^0) = -m_\pi^2 f_\pi^2 \sqrt{1 - \frac{4m_u m_d}{(m_u + m_d)^2} \sin^2\left(\frac{a}{2f_A}\right)} \cos\left(\frac{\pi^0}{f_\pi} - \phi_a\right) \tag{14}$$

On the vacuum π^0 acquires a vacuum expectation value (VEV) proportional to ϕ_a which can be minimized the potential, the last cosine in equation(11) is 1 on the vacuum and π^0 can be trivially integrated out leaving the axion effective potential.

$$V(a) = -m_\pi^2 f_\pi^2 \sqrt{1 - \frac{4m_u m_d}{(m_u + m_d)^2} \sin^2\left(\frac{a}{2f_A}\right)} \tag{15}$$

At the minimum $\langle a \rangle$=0, and mounting to quadratic order, then we have the axion mass equation

$$m_a^2 = \frac{m_u m_d}{(m_u + m_d)^2} \frac{m_\pi^2 f_\pi^2}{f_A^2} \tag{16}$$

Axion Inflation

At the end of the inflation, the axion is to be considered the initial value of $a_0 = f_0\theta_0$, where the angle θ_0 it profits the value in the range of $[0,2\pi)$.When it is considered the PQ symmetry is broken sufficiently at the ahead of inflation, the initial value ends up being constant on super horizon scales, and it can be defined as $a_0 = f_A$ and treat f_A as a free parameter. Predicting that the final baryon asymmetry will depend on a_0, the quantum fluctuations of the axion field during inflation be smaller than the observational upper limit.This implies a constraint on the Hubble rate during inflation,

$$H_{\inf} \le 6 \times 10^{11} GeV \left(\frac{f_A}{10^{15} GeV}\right) \tag{17}$$

The evolution of the homogeneous axion field in effective potential V_{eff} around the origin can be resulting as follow.

The progression of the axion field in the expanding universe is defined as

$$\ddot{a}(x)+3H\dot{a}(x)-\frac{\nabla^2}{R^2(t)}a(x)+\frac{dV(a)}{da}=0 \qquad (18)$$

where, R(t) is the universal scale factor. The effective potential for the axion field is

$$V_{full}(a)=V_{QCD}(a)+V_{Grav}(a)$$

$$=m_a^2F_a^2\left(1-\cos\left(\frac{a}{F_a}\right)\right)+V_{Grav}(a) \qquad (19)$$

$V_{Grav}(a)$ is unknown due because of not having the compressive theory, but it can be supposed that $V_{Grav}(a)$ is not be affected and is to be negligible compared with $V_{QCD}(a)$.

Equation (15) becomes

$$\ddot{a}(x)+3H\,\dot{a}(x)-\frac{\nabla^2}{R^2(t)}a(x)+m_a^2\,F_a^2=0 \qquad (20)$$

assuming a is small compared to F_a.

Let us consider the time t_1 at the following condition

$m_a(T_1)=3H(t_1)$, the Hubble parameter at that time t_1 with the temperature T_1.Using the temperature dependence of $m_a(T_1)$ and for t< t_1, it can be unnoticed the mass term due to $H>>m_a$.

When the axion mass term can be considered, they begin to oscillate with a frequency $\approx m_a$, calling the condition as zero mode and marked as a_0

$$\ddot{a}_0+3H\dot{a}_0+m_a^2a_0=0 \qquad (21)$$

From equation (17) and (18), it is taken as $\frac{a_0}{f_A}$ is 1 in the entire universe at the end of inflation to be reliability .When the inflation is over, the axion field is at rest until the Hubble parameter becomes $H_{osc}=m_a$.

In the early universe, after PQ transition, the axion field grows according to equation (21) $\ddot{a}_0+3H\dot{a}_0+\frac{\chi}{f_A^2}a_0=0$.After the end of inflation, the temperature rises to its maxima value after which it decreases because the energy density is dominant by the inflaton. With the axion decay rate

$$\Gamma_a\approx\frac{\left(\frac{g_2^2}{4\pi}\right)^2}{64\pi^3}\frac{m_a^2}{f_A^2},$$

and then it is recruit that the secondary reheating temperature or axion decay temperature

$$T_{dec} \approx 1\times 10^{4} GeV \left(\frac{m_a}{10^{9} GeV}\right)^{\frac{3}{2}} \left(\frac{10^{15} GeV}{f_A}\right) \tag{22}$$

At temperatures around a GeV, when $\frac{\sqrt{\chi(t)}}{f_A} \approx 3H(t)$, the axion field becomes proposed to the minimum value of the potential and indications to oscillate around CP conserving ground state. Thus, the condition has an equation of state as cold dark matter, $\overline{\varpi} \approx 0$ whereas dark matter is restrained as dust in matter dominant universe. Taking the average values of axion field in that temperature it is initiate as in the vacuum realignment mechanism.

$$\Omega_A^V h^2 \approx 3.8\times 10^{-3} \left(\frac{f_A}{10^{10} GeV}\right)^{1.165} \tag{23}$$

The value 1.165 arises from the temperature dependent of $\chi(t)$ determined from lattice QCD.(Borsanyli,S.,2016)

Axion will also be produced by topological defects and domain walls which are designed at the boundaries of the domains. According the states of this domains, most of the axions produced from strings during the radiation dominated era as (Ballesteros,G.,2016)

$$\Omega_A^S h^2 \approx 7.8\times 10^{-3} \left(\frac{f_A}{10^{10} GeV}\right)^{1.165} \tag{24}$$

Importantly, strings are always attached by N_{DW} domains walls, subsequently the value of phase PQ field around the string core, and then the networks of strings and domain walls called string wall systems are formed. The string wall systems in short-lived (N_{DW}=1), their collapse donates an amount to dark matter as (Kawasaki, M., 2015)

$$\Omega_A^C h^2 \approx 3.9\times 10^{-3} \left(\frac{f_A}{10^{10} GeV}\right)^{1.165} \tag{25}$$

Now, the total abundance of dark matter is

$$\Omega_A h^2 \approx \left(\Omega_A^V h^2 + \Omega_A^S h^2 + \Omega_A^C h^2\right) \approx 15.5\times 10^{-3} \left(\frac{f_A}{10^{10} GeV}\right)^{1.165} \tag{26}$$

The best measurement of matter currently have in the present universe is (Plehn,T.,2017)

$$\Omega_m h^2 \approx 0.1198$$

Then it can be taken as by comparing equation (26),

$$f_A \approx 1.7275\times 10^{9} GeV$$

Inserting this value into equation (16), the mass of axion can be estimated.

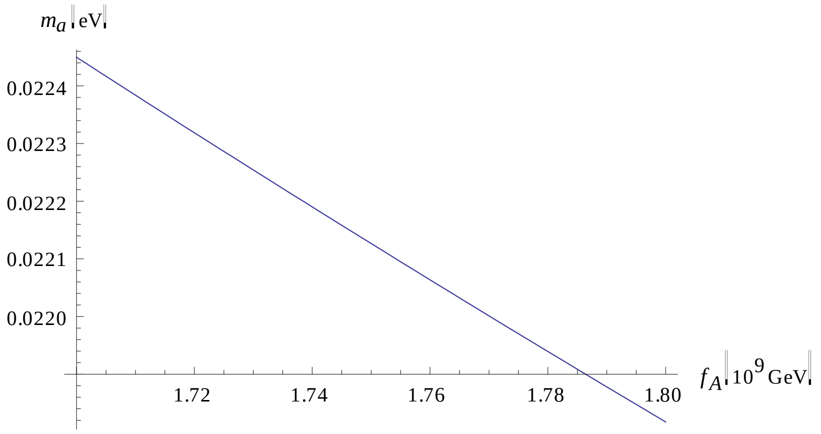

Figure 3 The estimate range of axion mass dependent on f_A in the range of (1.7~1.8) x 10^9GeV

Concluding Remarks

It has been attempted, in this paper, to clarify the basic ideas to understand the axion dark matter and its related ramifications. From the structure formation of the inhomogeneous cosmology, it is observed that the function between matter and energy shows the nature of spiral. The axion dynamics has been investigated using QCD variables with the dependent part of the Lagrangian and the coupling f_a, and the chiral expansion. Detailed mechanism of the relation of dark matter candidate in the range of inflation of the universe and axion decay rate at inflation has been investigated and the mass of axion has also been estimated under the classical motion during inflation and reheating of the universe accompanied with the imposing of scalar field. According to this current research, it is found that the mass of axion is dependent on the scale factor and have the estimate of mass of axion is within the range of < 22.6 meV. This result is in well agreement with the one given in the recent result, 0.56meV < m_a < 130(4.5)meV. (Ringwald A, 2018)

Acknowledgements

I would like to thank Dr Khin Khin Win, Professor and Head, Department of Physics, University of Yangon, for her kind permission and encouragements to carry out this work.

I would like to thank Prof Dr Aye Aye Thant, Prof Dr Myo Lwin, and Prof Dr Yin Maung Maung, Department of Physics, University of Yangon, for their encouragements to carry out this work.

Special thanks are due to Professor, Dr Thant Zin Naing, Retired Pro-rector (Admin), International Theravāda Buddhist Missionary University, for his valuable guidance and helpful advice to carry out this work.

References

Bauesteros, G., etal, (2017), "Neutrio-axion-dilation interconnection", JCAP 1708 (2017) No.08,001

Bertone,G. D.Hooper,., "A History of Dark Matter," arXiv: 1605.04909

Borsnyi et al, (2016), "Calculation of the axion mass based on high-temperature lattice quantum chromodynamics", Nature. 539 (2016) no 7627,69

Cerrilo,A.R.,"Some theoretical and experimental aspects of axion physics", arXiv:1512.03311v2[hep-ph]

Guo R Y, Xin Zhang (2017), "Constraints on inflation revisited: an analysis including the latest local measurement of the Hubble constant", E.Phy. Journal, vol-77, p-1

Jungman,G., M. Kamionkowski, K. Griest,, "Supersymmetric Dark Matter," arXiv:hep-ph/9506380v1

Kawasaki, M., K.Saikawa, T.Sekiguchi, (2014) "Axion dark Matter from topological defects", arXiv:1412.0789 V3[hep-ph]

Khloov,M., (2015), "Fundamentals of Cosmic Particle Physics," Viva Books Private & CISP

Plehn,T.,(2017) "Yet Another Introduction to Dark Matter,"arXiv:1705.01987 [hep- ph]

Ringwald A, (2018), "Axion in the Case of Post-Inflationary Peccei-Quinn Symmetry Breaking", arXiv: 1805.09618v1

Sikivic, P., (1982), "Axions, Domain Walls, and the Early Universe", Phys. Rev.lett 48(1982) 1156

Turner,M.S., (1998)," Dark Matter and Dark Energy in the Universe," arXiv:astro-ph/9811454v1

Wantz, O.,& E.P. Shellaard, (2009), "Axion Cosmology Revisted", arXiv: 0910.1066V3

J. Myanmar Acad. Arts Sci. 2020 **Vol. XVIII.No.2**B

JUNCTION FORMATION AND CURRNET TRANSPORT MECHANISMS IN TIN - DOPED CADMIUM OXIDE FILMS FOR TCO-Si BASED PHOTOVOLTAIC DEVICES APPLICATION

Moht Moht Than[1], Ohn Mar Swe[2], May Kalayar Kyaing[3] and Amy Aung[4]

Abstract

Junction formation and current transport mechanisms of transparent conducting Sn doped CdO thin films on silicon (Si) substrate have been studied as a function of Sn doping concentration (0.15wt%, 0.20wt% and 0.25wt%). The samples have been investigated using current-voltage (I-V) and capacitance voltage (C-V) measurements in order to define the transport mechanisms in heterostructure and basic electronic parameters. From the current density - voltage, illuminated J-V measurement as well as the photovoltaic response extracted the solar cell parameters. The built-in potential, photo and dark saturation current at Sn doped CdO on p-Si interface are monitored varying Sn doping concentration. It is observed that a high built-in potential form at the Sn 0.25wt% doped CdO/p-Si junction. The current voltage characteristics were analyzed using Schottky and abrupt p-n junction models. The open circuit voltage V_{oc} and saturation current density J_o extracted from the illuminated and dark J-V curves as well as calculated assuming a Schottky junction and an abrupt p-n junction for different Sn doping density N_D.

Keywords: Sn doped CdO films, Schottky junction, The open circuit voltage V_{oc}

Introduction

Transparent conducting oxides (TCOs) have been widely used in different areas due to their high optical transparency, low resistivity and wide energy band gap. Hence there has been great deal of work on investigating their preparation process and optimizing their properties [Jeyadheepan K et al 2010]. Among the various TCO materials available, cadmium stannate is one of the potential candidates for solar cell application [Hani Khallaf et al 2012]. Cadmium tin oxide is an n-type semiconductor and has great technological interest due to their high quality electrical and optical properties superior to the conventional transparent conducting oxide materials. In addition, these films have wide applications in photogalvanic cell, liquid crystal displays, heat mirrors, transparent electrode and solar cells [Wu X and Sheldon P et al 1997, Britt J and Ferekides C 1993].

SnO_2 semiconducting transparent thin films have various appealing features for technical applications in solar energy conversion, flat panel displays, electro-chromic devices, invisible security circuits, LEDs etc. The SnO_2 films close to stoichiometric condition have low free carrier concentration and high resistivity, but non-stoichiometric SnO_2 films have high carrier concentration, high conductivity and high transparency [Ginlley D S and Bright C 2000 and Mostafa M et al 2012].

Solar cell is the basic unit of solar energy generation system where electrical energy is extracted directly from light energy without any intermediate process. The working of a solar cell solely depends upon its photovoltaic effect, hence a solar cell also known as photovoltaic cell. A

---

[1] Dr, Associate Professor, Department of Physics, Mohnyin Degree College

[2] Lecturer, Department of Physics, University of Yangon

[3] Assistant Lecturer, Department of Physics, University of Yangon

[4] Assistant Lecturer, Department of Physics, University of Yangon

solar cell is basically a semiconductor p-n junction device. It is formed by joining p-type (high concentration of hole or deficiency of electron) and n-type (high concentration of electron) semiconductor material at the junction excess electrons from n-type try to diffuse to p-side and vice-versa.

In the present study the junction and the device performance of Sn doped CdO thin film on p-Si photovoltaic cell are investigated in great detail. Investigation of junction transport in these devices is essential for understanding the photovoltaic loss mechanism and achieving higher efficiency.

Experimental

The films were deposited on silicon substrates by sol-gel spin coating method. Appropriate proportions of highly pure (99.99%) CdO and SnO_2 powders were ground by agate mortar. Mixture of CdO and SnO_2 have been used to prepare $(CdO)_{1-x}(SnO_2)_x$ with (x = 0.15,0.20 and 0.25 wt %). To increase complete mixing, the mixtures were ground for at least three hours. The mixed powders were annealed at 800˚C for 3 hours. After that, 2-methoxyethanol ($CH_3OCH_2CH_2OH$) is added to the mixture and then stirred and heated upon 100˚C for 30 min. The homogeneous precursor solution or coating solution was obtained and these solutions were used to depose on Si substrates using spin coating technique. After the coating all the films were dried at the room temperature for 1 day in order to diffuse the solvent. Before the spin coating deposition, the silicon substrate was cleaned by standard semiconductor cleaning method.

The cleaning sequences are:

- General clean; The wafer was cleaned by using mixture of Sulfuric Acid and Hydrogen Peroxide for 10 minutes to remove organic and inorganic contamination from the silicon wafer.
- Particle removal; They were cleaned in a ratio of (5:1:1) DI water, Ammonium Hydroxide, Hydrogen Peroxide for 2 minutes to remove silica and silicon particle from the wafer, as well as certain organic and metal surface contamination.
- Oxide removal; The wafer were dipped in (1:20) Hydrofluoric acid, DI water for 60 seconds to remove the native oxide from the wafer surface.
- Metal contamination removal; The wafer were cleaned in a (6:1:1) ratio mixture of DI water, Hydrochloric acid, Hydrogen Peroxide for 10 minutes to remove certain ionic and metal surface contamination. The silicon wafers were rinsed in distilled water for all steps.

Finally the resulting thin films were annealed at 500˚C for 3hours.

The extract junction parameters and solar cell characteristics of TCO devices based on silicon substrates with different doping concentrations. To extract the solar cell parameters, used current density-voltage (dark J-V & illuminated J-V) and small signal capacitance- voltage (C-V) measurements.

Measurement of current- voltage curve, by using Digital multi meter DT 9205 as a voltmeter and DT 9208 A as an ammeter. For illumination, 150 watt Halogen lamp (220V, 50Hz) as a light source and Easy View Digital Light Meter Model EA 30 was used to count the light intensity. Capacitance-voltage characteristics were measured using G$\underline{\text{W}}$InSTEK(LCR-8110G) at 1kH$_z$ and various applied voltage.

Results and Discussion

There are two approaches to describe the junction between Sn doped CdO thin film and p-Si layer. One is based on the Schottky junction theory that explains the interface of semiconductors to a metal. The other is the description of a one-sided abrupt junction between a moderately doped n-type thin film semiconductor region and a highly doped p-type semiconductor region. For both cases the current density - voltage characteristics of such a photovoltaic junction is in the simplest form described by the ideal diode equation under illumination (Equation 1). Rewriting Equation 1 at open circuit conditions (J=0) shows that the open circuit voltage V_{oc} of a solar cell mainly depends on the dark saturation current density J_o and short circuit current density J_{sc} shown in Equation 2.

$$J = J_0\left(\exp\left(\frac{qV}{kT}\right)-1\right)-J_{sc} \qquad (1)$$

$$V_{oc} \approx \frac{kT}{q}\ln\left(\frac{J_{sc}}{J_0}\right) \qquad (2)$$

At a Schottky junction between a metal and high-mobility semiconductor like silicon, the dominating transport mechanism is the thermionic emission of majority carrier over the potential barrier Φ_b that forms at the interface. The J_o for a Schottky junction described in Equation 3,

$$J_0 = A^{**}T^2\exp\left(-\frac{q\phi_B}{kT}\right) \qquad (3)$$

A^{**} denotes the reduced effective Richardson constant including effects of tunneling and scattering of majority carriers at phonons as well as a correction factor for a small contribution of majority carrier diffusion for moderately doped silicon. At room temperature, in a reasonably small applied field, $A^{**}$is about 110 A/(cmK)^2.

If the doping of the p-type semiconductor is substantially larger than that of the n-type semiconductor, the dark saturation current density J_o of the so called one-sided abrupt p+n junction is defined by Equation 4.

$$J_0 = \frac{n_i^2\mu_p kT}{L_p N_A} \qquad (4)$$

where, μ_p = the mobility, L_p = the diffusion length of the minority carriers (electron for p-Si) and n_i = the intrinsic carrier concentration.

Mott-Schottky analysis probes the depletion capacitance at a Schottky or p-n junction which is determined by the width of the bias dependent depletion region. Hence the depletion capacitance “C” is also bias dependent and can be expressed as in equation 5, where, V is the applied bias voltage and V_{bi} is the built-in voltage.

$$\frac{1}{C^2} = \frac{2(V_{bi}-V)}{A^2 q\varepsilon_r\varepsilon_0 N_A} \qquad (5)$$

Figure 1(a ~ c) depicts the characteristics $1/C^2$ versus V plots for Sn doped CdO thin films on Si substrate at frequency range 10 kHz. The so-called Mott-Schottky plot of $1/C^2$ versus applied DC voltage yields a straight line, whose slope yields the doping density and whose extrapolated intersection with the voltage axis yields the built-in voltage. The doping density is given by equation 6.

$$N_A = -\frac{2}{q\varepsilon_s A^2}\left(\frac{d(C)^{-2}}{dV}\right)^{-1} \tag{6}$$

The main parameters obtained from Mott-Schottky analysis for Sn doped CdO/p-Si thin films devices collected in Table 1. The current density - voltage (J-V) curve for dark and under illumination conditions are shown in Figure 2 (a ~ c) and Figure (3). All relevant solar cell parameters extracted from the illumination J-V curves are collected in Table (1).

The open circuit voltage V_{oc} and saturation current density J_o extracted from the illuminated and dark J-V curve, as well as calculated assuming a Schottky junction (Equation 3) and an abrupt junction (Equation 4) for different doping density (N_A). The extracted values are summarized in Table (2).

Table 1 Summary of Sn doped CdO/p-Si thin films devices interface, solar cell parameters for all differently doped Sn concentration from C-V and I-V measurements

Capacitance Measurements				Solar cell parameter			
Sample	***N_A (cm)^3***	***V_{bi} (V)***	**Φ_b(eV)**	**V_{oc}(V)**	**J_{sc} (μA/cm^2)**	**FF**	**PCE (%)**
Sn(0.15wt%) doped CdO/p-Si	6.44 x 10^{13}	0.083	0.42	3.367	9.60	0.419	1.028
Sn(0.20wt%) doped CdO/p-Si	8.20 x 10^{12}	0.148	0.54	4.042	11.1	0.487	1.657
Sn(0.25wt%) doped CdO/p-Si	6.79 x 10^{11}	0.156	0.61	4.729	10.8	0.592	2.295

Table 2 Summary of open circuit voltage V_{oc} and saturation current density J_o extracted from the J-V curve (dark & illumination), calculated Schottky junction and abrupt junction equations

N_A[cm^{-3}]	**J-V curves**		**Schottky junction**		**p^+n-junction**	
	J_o[μA/cm^2]	**V_{oc} [V]**	**J_o[μA/cm^2]**	**V_{oc} [V]**	**J_o[μA/cm^2]**	**V_{oc} [V]**
6.44 x 10^{13}	8.79 x10^{-1}	3.367	8.75x10^{-1}	0.061	1.91x10^{-3}	0.219
8.20 x 10^{12}	8.36 x10^{-1}	4.042	8.40x10^{-3}	0.186	1.50x10^{-2}	0.169
6.79 x 10^{11}	9.24 x10^{-1}	4.729	5.60x10^{-4}	0.255	1.81x10^{-1}	0.106

Conclusion

Tin doped CdO thin films were prepared by sol-gel spin coating method on si substrate. The effect of junction formation and current transport mechanisms of Sn doped CdO/p-Si thin films were investigated by capacitance-voltage and current voltage characteristics under dark and illumination. The doping density obtained from C-V characteristics in the range of (6.79×10^{11} cm^{-3} - 6.44×10^{13} cm^{-3}). The barrier height is in the range of (0.42eV - 0.61eV). The built in voltage range are (0.083V-0.156V) respectively. From the Schottky junction observation, Schottky junction J_o mainly depends on the Schottky barrier height Φ_b. From the abrupt p^+n-junction observation, J_o solely depends on properties of the moderately doped p-type semiconductor and is inversely proportional to its doping concentration N_A. Therefore, it is obvious that the V_{oc} in a p^+n-junction increased with lager N_A. By measuring and modeling, the dark and illuminated current-voltage characteristics, and comparing the extracted open-circuit voltage and dark saturation current density, with value calculated from transport equations based on different junction models. In general, the results corroborate that Sn doped CdO/p-Si thin film devices hetero-interfaces can be great charge carrier selective contacts for photovoltaic and other optoelectronic devices.

Acknowledgements

I wish to express my sincere thanks to Professor Dr Khin Khin Win, Head of Department of Physics, Yangon University, for her kind permission to carry out this research. I also wish to express thanks to Professor Dr Htwe Htwe Yin, Head of Department of Physics, Mohnyin Degree College, for the permission to allow this conference.

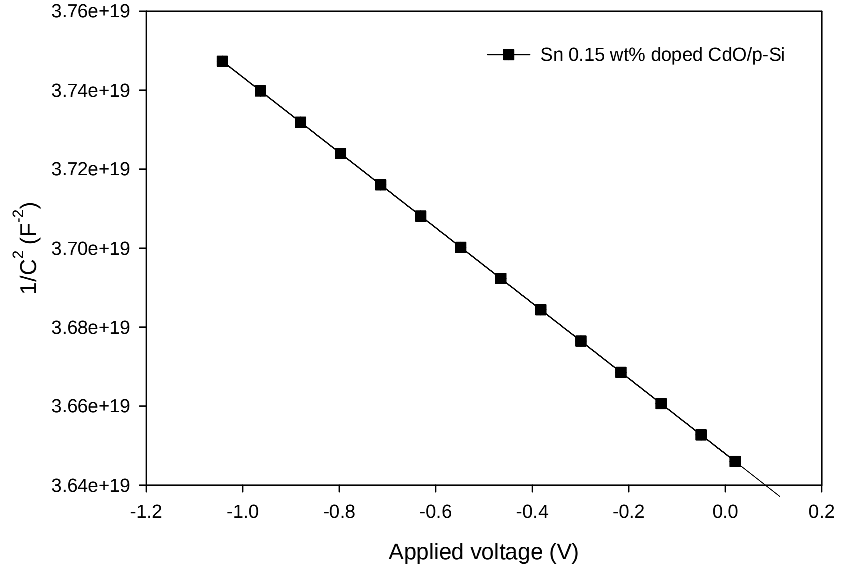

Figure 1 (a) $1/C^2$ versus V plots for Sn 0.15 wt% doped CdO/p-Si thin film device

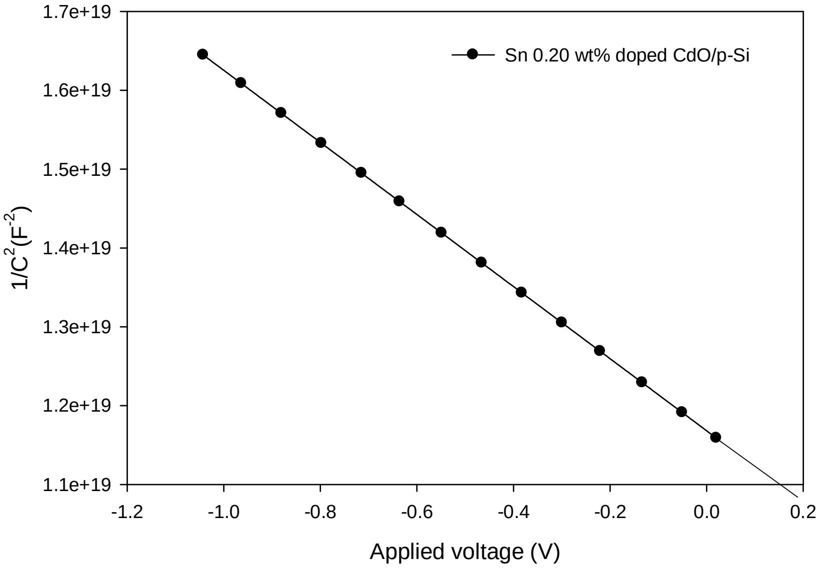

Figure 1(b) 1/C^2 versus V plots for Sn 0.20 wt% doped CdO/p-Si thin film device

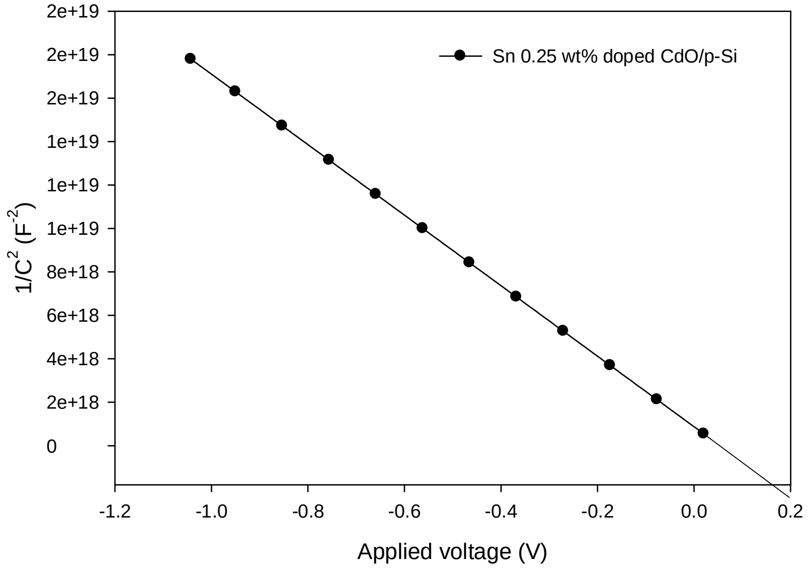

Figure 1(c) 1/C^2 versus V plots for Sn 0.25 wt% doped CdO/p-Si thin film device

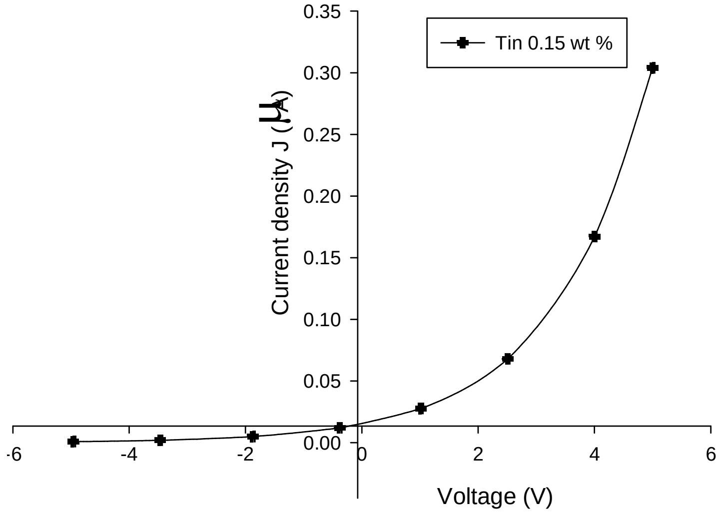

Figure 2(a) The dark J-V plots for Sn 0.15 wt% doped CdO/p-Si thin film device

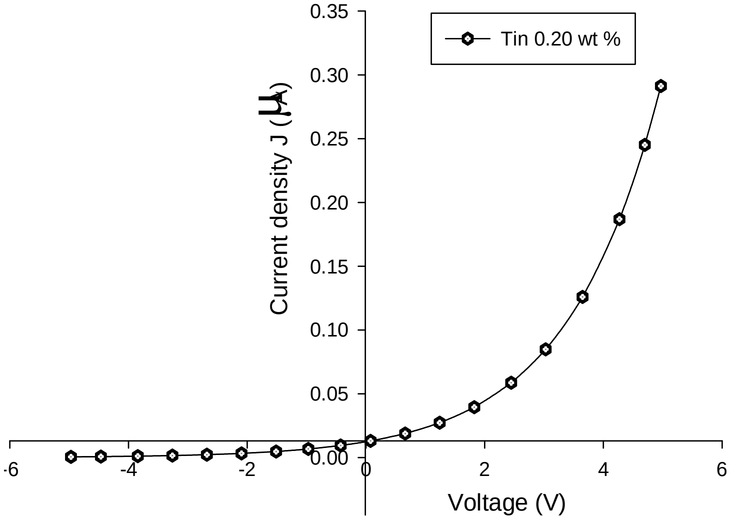

Figure 2 (b) The dark J-V plots for Sn 0.20 wt% doped CdO/p-Si thin film device

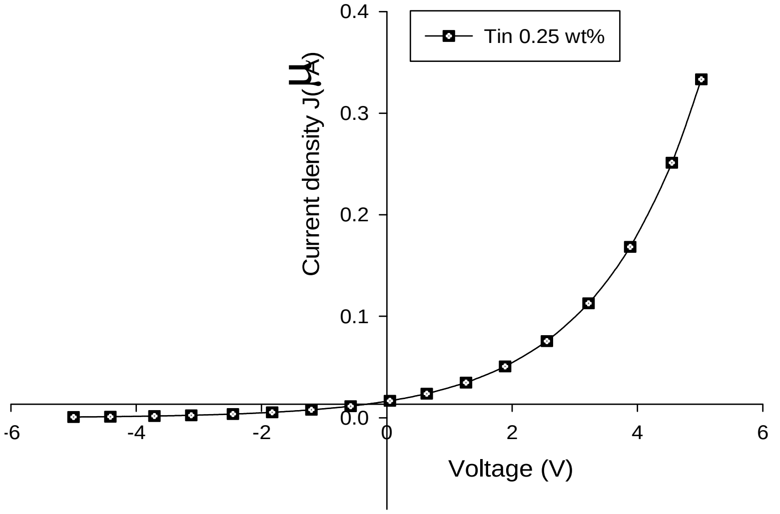

Figure 2(c) The dark J-V plots for Sn 0.25 wt% doped CdO/p-Si thin film device

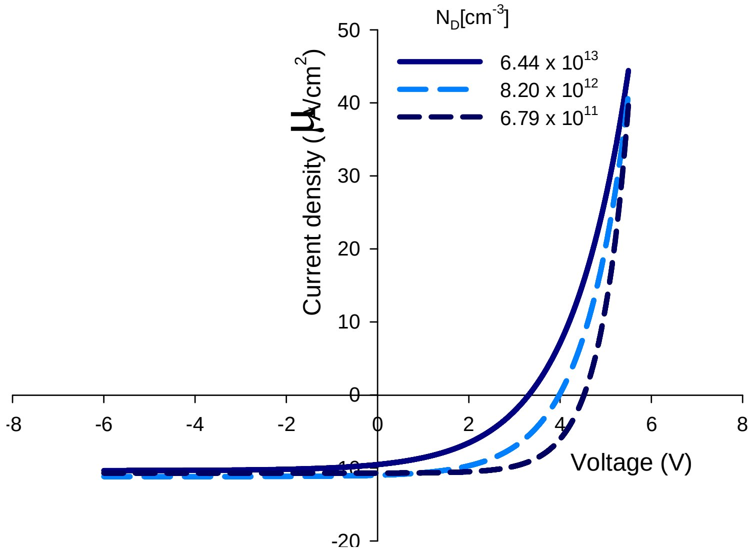

Figure 3 Photovoltaic properties of Sn doped CdO/p-Si thin film device with differently doping density (N_A)

References

Britt J and Ferekides C (1993); Thin-Film CdS/CdTe Solar Cell With a 15.8% Efficiency Applied Physics Letter 62, p2851-2852

Ginlley D S and Bright C(2000); "Transparent Conducting Oxides", Materials Research Society Bulletin 25, p15-18

Hani Khallaf et al (2012); Chemical bath deposition of SnO_2 and Cd_2SnO_4 thin films, Applied Surface Science 258, p 6069-6074

Jeyadheepan K et al (2010); Thermal and optical properties of Cd_2SnO_4 thin films using photoacoustic spectroscopy, Appl Phys A 98, p 919-925

Mostafa M et al (2012); Characterization of Thin Films of Cd doped SnO for Optoelectronic Applications, Advances in Applied Science Research 3, p227-234

Wu X and Sheldon P et al (1997); Application of Cd_2SnO_4 Transparent Conducting Oxides In CsS/CdTe Thin-Film Devices, Presented at the 26th IEEE Photovoltaic Specialists Conference, September29 B October 3, Anaheim, California

J. Myanmar Acad. Arts Sci. 2020 **Vol. XVIII.No.2**B

NONCOMMUTIVITY AND CUTOFF SCALES

Myo Mg Mg[1], Thant Zin Naing[2]

Abstract

Basic ideas and requirements of noncommutative space are presented. Position cutoff and momentum cutoff are calculated by observing the commutation relations. Relation between elements of noncommutative algebra and Dirac operator is also discussed.

Keywords: noncommutative space, position cutoff, momentum cutoff

Introduction

The presence of Plank constant in quantum mechanics and speed of light imply a short wavelength photon will have a high momentum. The proper way to the formalism of quantum mechanics is to define noncommuting operators acting on Hilbert space and a physical state given by a state vector. Restrictions will arise even if momentum is ignored and insert gravitational constant in the formalism of quantum mechanics. There are reasons to believe that problems in unifying quantum mechanics and gravity can be solved by developing the aspects of noncommutative geometry.

A noncommutative algebra is an algebraic structure in which the principle binary operation is not commutative. Additional structures are allowed to carry by the noncommutative algebra of functions.

Noncommutative geometry is a subject of mathematics that concerned with a geometrical approach to noncommutative algebra. It is a system consisting of a Hilbert space, a noncommutative algebra of operators acting on Hilbert space and a self adjoint operator. Noncommutative geometry has been inspired by quantum mechanics and has applications to number theory, deformation theory, quantum field theory, elementary particle physics and solid state physics.

Noncommutivity

A manifold is a locally Euclidean continuous space. It is a space with coordinates that locally looks like Euclidean but globally can bend and distort. Differential manifold is continuous and differentiable. It is a set that can be continuously parameterized. Various objects can exist on a manifold. Infinitely differentiable functions are included in these objects. If M is a manifold, the group of all infinitely differentiable functions is called $C^{\infty}(M)$.These functions can be added and multiplied.

$$(f+g)(x)=f(x)+g(x) \tag{1}$$

$$(fg)(x)=f(x)g(x) \tag{2}$$

Hence, $C^{\infty}(M)$ is a commutative algebra. Geometrical objects, such as, vectors and tensor fields can be defined in terms of the algebra $C^{\infty}(M)$.

For n dimensional manifold, a vector **V** with

---

[1] Candidate, Department of Physics, University of Yangon

[2] Former Professor, Department of Physics, Dawei University

$$\mathbf{V} \to (V^1(x), \dots, V^n(x)) \tag{3}$$

where

$$x = x^1, \dots, x^n \tag{4}$$

will follow local coordinates transformation rules.

If an operator V is defined as

$$\mathrm{V} = V^1 \frac{\partial}{\partial x^1} + \cdots + V^n \frac{\partial}{\partial x^n} \tag{5}$$

then it is clear that V is a linear operator from $C^\infty(M)$ into itself. And it satisfies the Leibniz relation

$$\mathrm{V}(fg) = \mathrm{V}(f)g + f\mathrm{V}(\mathrm{g}) \tag{6}$$

for every f and g.

So, vector fields, differential forms and general tensor fields are derivations of $C^\infty(M)$.

Theorem I Two manifolds M and N are diffeomorphic if and only if the algebra of functions $C^\infty(M)$ and $C^\infty(N)$ are isomorphic.

So, the commutative algebra of the infinitely differentiable functions on M, $C^\infty(M) := A$, encodes all the differential geometric properties of M. And this leads to basic ideas of noncommutative geometry.

The dimension of a space can be derived from the rate of growth of the eigenvalues of D^2. Dimension can be defined if (7) does not diverge for single value of d.

$$\lim_{x\to\infty} \frac{N_x}{x^{0.5d}} \tag{7}$$

Regularity is also required for characteristics of manifolds. That is, a and $[D,a]$ belong to δ^k with

$$\delta(T) = [|D|, T] \tag{8}$$

There should be a J for manifolds, such that

$$[a, Jb^* J^{-1}] = 0 \qquad \forall a, b$$

$$[[D,a], b^0 = Jb^* J^{-1}] = 0 \qquad \forall a, b \tag{9}$$

Noncommutative geometrical objects such as noncommutative vectors, noncommutative differential forms can be defined through a noncommutative algebra. But these noncommutative geometrical objects are only sensible in purely algebrical structure.

Basic ideas lead to noncommutative spaces is based on a theorem which was proved by Gelfand and Naimark.

Theorem II The algebra of continuous functions $C(X)$ of a compact topological space X is a commutative C^* algebra with the complex conjugate $\overline{f}$ is its hermitian adjoint f^*.

Theorem III Given a complex commutative C^* algebra A, one can construct a unique compact topological space X, such that A can be identified with the function algebra $C(X)$.

Topological space is a set of points, along with a set of neighborhood for each point satisfying a set of axioms relating points and neighborhood. Compact topological space means that the topological space is closed and bounded and continuous complex valued functions on a topological space form a commutative algebra.

C^* algebra is an involutive Banach algebra with

$$\left\|a^*a\right\| = \left\|a\right\|^2 \tag{10}$$

for each element a.

Banach algebra is a complete normed algebra and in an involutive algebra, each elements a has properties

$$\left\|a+b\right\| \le \left\|a\right\| + \left\|b\right\| \tag{11}$$

$$\left\|\alpha a\right\| = \left|\alpha\right| \left\|a\right\| \tag{12}$$

$$\left\|ab\right\| \le \left\|a\right\| \left\|b\right\| \tag{13}$$

$$\left\|a^*\right\| = \left\|a\right\| \tag{14}$$

$$\left\|a\right\| = 0 \Leftrightarrow a = 0 \tag{15}$$

Algebra of compact operators on Hilbert space and $n \times n$ matrices are example of C^* algebras. With norm defined as

$$\left\|A\right\|^2 = \max_{eigenvals} A^\dagger A \tag{16}$$

According to theorem of Gelfand and Naimark, there is a one to one correspondence between compact topological spaces and complex commutative C^* algebras. This leads to idea that observing and studying noncommutative C^* algebras amounts to studying noncommutative compact topological spaces.

Momentum and Position Cutoff

To quantize the Minkowski space-time, it will be required that

$$\left[q^\mu, q^\nu\right] = ikq^{\mu\nu} \tag{17}$$

In the limit

$$k \to 0$$

$$q^\nu \to x^\nu$$

And it will be required that q^ν to be Hermitian operators on Hilbert space.

If there is a magnetic field, then the commutation becomes as

$$[p_1, p_2] = i\mathrm{h}eB \tag{18}$$

Points of momentum space is replaced by area $\mathrm{h}eB$. This allows the cutoff as

$$p^2 \geq \mathrm{h}eB \tag{19}$$

Letting $B = 1T$

leads he cutoff scale to $1.7 \times 10^{-53}\left(kgms^{-1}\right)^2$. Let

$$1.7 \times 10^{-53}\left(kgms^{-1}\right)^2 = 1\Gamma \tag{20}$$

And it is postulated that the momentum space exhibits the noncommutative structure under 1Γ. For the position commutation

$$[x_1, x_2] = i\tau \tag{21}$$

then, τ in (21) must have the dimension of area. Which leads to

$$\tau = \mathrm{h}Gc^{-3}$$

$$=2.7\times 10^{-70}m^2 = 1\widehat{M} \tag{22}$$

Again it is postulated that the position space will have the noncommutivity under $1\widehat{M}$.

Operator and Space

The relativistic equation

$$E^2 - p^2 = m^2$$

for a particle with mass m can be quantized into

$$\left(-\frac{\partial^2}{\partial t^2} + \mathrm{V}\right)\Psi = m^2\Psi \tag{23}$$

In order to get a first order, the operator term in (23) must be taken into square root. It will lead to

$$\left(i\varphi - m\right)\Psi = \left(i\gamma^{\mu}\partial_{\mu} - m\right)\Psi = 0 \tag{24}$$

And it is required that

$$\left\{\gamma^{\nu}, \gamma^{\mu}\right\} = 2g^{\nu\mu}$$

to recover (23). And γ^{ν} belongs to $M_4(£)$. Where a matrix representation is

$$\gamma^0 = \begin{pmatrix} \sigma_0 & 0 \\ 0 & -\sigma_0 \end{pmatrix}$$

$$\gamma^i = \begin{pmatrix} 0 & \sigma_i \\ -\sigma_i & 0 \end{pmatrix} \quad , i = 1, 2, 3 \tag{25}$$

Where

$$\sigma_0 = I$$

$$\sigma_1 = \begin{pmatrix} 0 & 1 \\ 1 & 0 \end{pmatrix}$$

$$\sigma_2 = \begin{pmatrix} 0 & -i \\ i & 0 \end{pmatrix}$$

$$\sigma_3 \begin{pmatrix} 1 & 0 \\ 0 & -1 \end{pmatrix} \tag{26}$$

But the Dirac operators that appear in noncommutative geometry should be in the form

$$D\Psi = \sum_{i=1}^{n} e_i . \nabla_{e_i} \Psi \tag{27}$$

with a local orthonormal frame. Then one can defined Hilbert space and the operator will be a symmetric operator on this space. For any

$$f \in A$$

$$\Psi \in H$$

$$[D, f]\Psi = i^{-1}\left(\frac{d}{d\phi}(f\Psi) - f\frac{d}{d\phi}\Psi\right)$$

$$= i^{-1}\frac{df}{d\phi}\Psi \tag{28}$$

Suppose

$$D = \begin{pmatrix} 0 & m \\ m^* & 0 \end{pmatrix} = |m|F$$

$$F = \begin{bmatrix} 0 & e^{i\alpha} \\ e^{-i\alpha} & 0 \end{bmatrix} \tag{29}$$

Then the commutator is

$$[D, a] = (a_2 - a_1)|m|\begin{bmatrix} 0 & e^{i\alpha} \\ e^{-i\alpha} & 0 \end{bmatrix} \tag{30}$$

Thus, it can be seen that (30) is a discrete derivative.

Conclusion

It is postulated that position space will exhibit noncommutative structure under and momentum space will exhibit noncommutative structure under 1Γ. Classical concepts of points and geometry should be replaced by much more general entities.

Acknowledgements

I wish to express my sincere thanks to Professor Dr Khin Khin Win, Head of Department of Physics, University of Yangon, for her kind approval to conduct this work.

My sincere thanks also go to all of the professors, Department of Physics, University of Yangon, for their kind permission to carry out this work.

Special thanks are due to Dr Thant Zin Naing, Pro-rector (retired), International Theravada Buddhist Missionary University for his helpful suggestion and encouraging.

Last but not least, I would like to thank my father, U Mya Than, Former Demonstrator, Department of Physics, University of Yangon, who also helped me with suggestions and ideas for this work.

References

Bongaarts, P., (2004) *A Short Introduction to Noncommutative Geometry*

Connes, A., (1994) *Noncommutative Geometry*

Ray, M., (2010) *Introduction to Vectors and Tensors*

J. Myanmar Acad. Arts Sci. 2020 **Vol. XVIII.No.2**B

LIE DERIVATIVE, KILLING EQUATION AND KILLING VECTOR FIELDS IN SPACETIMES STRUCTURE

Min Thaw Tar[1], Naing Naing Wint Htoon[2], Yee May Thwin[3], Thant Zin Naing[4]

Abstract

Attempts have been made to explore the physical properties of black hole mechanics such as Killing equation and Killing vector fields and its applications to Minkowski spacetime, static spacetimes and spherically symmetric spacetimes. As the situation dictates, Mathematica software is used to utilized for detailed computations and visualization of the results.

Keywords: Killing equation, Killing vector fields, Static spherically symmetric spacetimes.

Introduction

The Lie derivative evaluates the change of a tensor field, along the flow defined by another vector field. This change is coordinate invariant and therefore the Lie derivative is defined on any differentiable manifold. Functions, tensor fields and forms can be differentiated with respect to a vector field.

Killing fields are the infinitesimal generators of isometries; that is, flows generated by Killing fields are continuous isometries of the manifold. More simply, the flow generates a symmetry, in the sense that moving each point on an object the same distance in the direction of the Killing vector field will not distort distances on the object.

The Lie Derivative

With or without the covariant derivative, which requires a connection on all of spacetime, there is another sort of derivation called the Lie derivative, which requires only a curve.

Let $C : R \to M$ be a curve in M with tangent vectors, $\xi = \frac{d}{d\lambda}$, with components

$$\xi = \xi^{\mu}\frac{\partial}{\partial x^{\mu}} = \frac{dx^{\mu}}{\partial\lambda}\frac{\partial}{\partial x^{\mu}} \tag{1}$$

The Lie derivative generalizes the directional derivative of a function,

$$\frac{df}{d\lambda} = \xi^{\mu}\frac{\partial f}{\partial x^{\mu}} \tag{2}$$

to higher rank tensors. First, consider a vector field, v, defined on *M*. One defines the Lie derivative of v at a point *P* along *C* to be

$$L_{\xi}v = \lim_{\varepsilon\to 0}\frac{v(P+\varepsilon\xi)-v(P)}{\varepsilon} \tag{3}$$

where $v(P+\varepsilon\xi)$ is the Lie transport of v along the curve. For simplicity, let $P = C$ ($\lambda = 0$). Lie transport involves taking the value of the vector field at a point on *C*, say, v (λ), and performing a

---

[1] PhD Candidate, Department of Physics , University of Yangon.

[2] Lecturer, Department of Physics, University of Yangon.

[3] Lecturer, Department of Physics, Magway University.

[4] Retired Pro-Rector (Admin), International Theravāda Buddhist Missionary University, Yangon.

coordinate transformation to bring the point C (λ) back to P = C (0) (Adler.R, Bazin.M, Schiffer.M, 1975). The coordinate transformation one require is, for infinitesimal $\lambda = \varepsilon$,

$$y^\alpha = x^\alpha - \varepsilon\xi^\alpha(0) \qquad (4)$$

The components of v^α change as

$$\tilde{v}^\alpha(0) = v^\beta(\lambda)\frac{\partial y^\alpha}{\partial x^\beta} \qquad (5)$$

$$= \left[v^\beta(x^\mu(0) + \varepsilon\xi^\mu)\right](\delta^\alpha_\beta - \varepsilon\partial_\beta\xi^\alpha)$$

$$= \left[v^\beta(0) + \varepsilon\xi^\mu\partial_\mu v^\beta(0)\right](\delta^\alpha_\beta - \varepsilon\partial_\beta\xi^\alpha)$$

$$= v^\alpha(0) + \varepsilon\xi^\mu\partial_\mu v^\alpha(0) - \varepsilon\ \ v^\beta(0)\partial_\beta\xi^\alpha \qquad (6)$$

The derivative is then

$$L_\xi v = \lim_{\varepsilon\to 0}\frac{v(P+\varepsilon\xi) - v(P)}{\varepsilon} \qquad (7)$$

$$L_\xi v = \lim_{\varepsilon\to 0}\frac{v^\alpha(0) + \varepsilon\xi^\mu\partial_\mu v^\alpha(0) - \varepsilon v^\beta(0)\partial_\beta\xi^\alpha - v(0)}{\varepsilon}$$

$$L_\xi v = \xi^\mu\partial_\mu v^\alpha(0) - v^\beta(0)\partial_\beta\xi^\alpha \qquad (8)$$

An easy proof of the covariance of this result is that it equals the commutator of the two vectors,

$$L_\xi v = [\xi, v] \qquad (9)$$

which has the same form when ξ and v are expanded in components,

$$[\xi, v] = [\xi^\alpha\partial_\alpha, v^\beta\partial_\beta] \qquad (10)$$

$$= \xi^\alpha\partial_\alpha v^\beta\partial_\beta - v^\beta\partial_\beta\xi^\alpha\partial_\alpha$$

$$= (\xi^\beta\partial_\beta v^\alpha - v^\beta\partial_\beta\xi^\alpha)\partial_\alpha \qquad (11)$$

The generalization to higher rank tensors is immediate because derivations must satisfy the Leibnitz rule (Hawking S.W, Ellis G.F.R, 1973) .Thus, for an outer product of two vectors,

$$T^{\alpha\beta} = u^\alpha v^\beta \qquad (12)$$

one has

$$L_\xi T^{\alpha\beta} = L_\xi (u^\alpha v^\beta) \tag{13}$$

$$L_\xi T^{\alpha\beta} = (L_\xi u^\alpha) v^\beta + u^\alpha (L_\xi v^\beta)$$

$$L_\xi T^{\alpha\beta} = (\xi^\mu \partial_\mu u^\alpha - u^\mu \partial_\mu \xi^\alpha) v^\beta + u^\alpha (\xi^\mu \partial_\mu v^\beta - v^\mu \partial_\mu \xi^\beta)$$

$$L_\xi T^{\alpha\beta} = \xi^\mu \partial_\mu (u^\alpha v^\beta) - u^\mu v^\beta \partial_\mu \xi^\alpha - u^\alpha v^\mu \partial_\mu \xi^\beta$$

$$L_\xi T^{\alpha\beta} = \xi^\mu \partial_\mu T^{\alpha\beta} - T^{\alpha\beta} \partial_\mu \xi^\alpha - T^{\alpha\beta} \partial_\mu \xi^\beta \tag{14}$$

and so on for higher ranks, with one correction term, $-T^{\alpha\ldots\mu\ldots\beta}\partial_\mu \xi^\nu$, for each index .

For forms, one uses the directional derivative of a scalar,

$$L_\xi \phi = \xi^\mu \frac{\partial \phi}{\partial x^\mu} \tag{15}$$

together with $\phi = v^\alpha w_\alpha$, for arbitrary v^α,

$$\xi^\mu \frac{\partial (v^\alpha w_\alpha)}{\partial x^\mu} = L_\xi (v^\alpha w_\alpha) \tag{16}$$

$$\xi^\mu (\partial_\mu v^\alpha) w_\alpha + v^\alpha \xi^\mu \partial_\mu w_\alpha = (L_\xi v^\alpha) w_\alpha + v^\alpha L_\xi w_\alpha$$

$$\xi^\mu (\partial_\mu v^\alpha) w_\alpha + v^\alpha \xi^\mu \partial_\mu w_\alpha = \xi^\beta (\partial_\beta v^\alpha) w_\alpha - v^\beta (\partial_\beta \xi^\beta) w_\alpha + v^\alpha L_\xi w_\alpha$$

$$v^\alpha \xi^\mu \partial_\mu w_\alpha = -v^\beta (\partial_\beta \xi^\beta) w_\alpha + v^\alpha L_\xi w_\alpha$$

$$v^\alpha L_\xi w_\alpha = v^\alpha \xi^\mu \partial_\mu w_\alpha + v^\alpha (\partial_\alpha \xi^\beta) w_\beta \tag{17}$$

Since this must hold for all v^α,

$$L_\xi w_\alpha = \xi^\mu \partial_\mu w_\alpha + w_\beta \partial_\alpha \xi^\beta \tag{18}$$

Symmetries of Minkowski spacetime

Consider flat spacetime, for which the metric is Minkowski, $\eta_{\mu\nu}$. In Cartesian coordinates,

$$\eta_{\mu\nu} = \begin{pmatrix} -1 & & & \\ & 1 & & \\ & & 1 & \\ & & & 1 \end{pmatrix} \tag{19}$$

and the Christoffel connection vanishes, $\Gamma^\alpha{}_{\mu\nu} = 0$. Then one may replace the covariant derivatives by partial derivatives, and the Killing equation is simply

$$\xi_{\alpha,\beta} + \xi_{\beta,\alpha} = 0 \tag{20}$$

Taking a further derivative, one has

$$\xi_{\alpha,\beta\mu} + \xi_{\beta,\alpha\mu} = 0 \qquad (21)$$

Now, cycle the indices twice, to give

$$\xi_{\alpha,\beta\mu} + \xi_{\beta,\alpha\mu} = 0 \qquad (22)$$

$$\xi_{\beta,\mu\alpha} + \xi_{\mu,\beta\alpha} = 0 \qquad (23)$$

$$\xi_{\mu,\alpha\beta} + \xi_{\alpha,\mu\beta} = 0 \qquad (24)$$

Adding equation (31) and (32) and subtracting equation (33) one finds

$$0 = \xi_{\alpha,\beta\mu} + \xi_{\beta,\alpha\mu} + \xi_{\beta,\mu\alpha} + \xi_{\mu,\beta\alpha} - \xi_{\mu,\alpha\beta} - \xi_{\alpha,\mu\beta}$$

$$0 = \xi_{\beta,\alpha\mu} \qquad (25)$$

so that the second derivative of ξ_β vanishes. This means that ξ_β must be linear in the coordinates,

$$\xi_\alpha = a_\alpha + b_{\alpha\beta} x^\beta \qquad (26)$$

Substituting this into the Killing equation,

$$0 = \xi_{\alpha,\beta} + \xi_{\beta,\alpha} \qquad (27)$$

$$0 = b_{\alpha\beta} + b_{\beta\alpha} \qquad (28)$$

so that a_α is arbitrary while $b_{\alpha\beta}$ must be antisymmetric. One therefore finds exactly 10 isometries in Minkowski space. This is the maximum number of independent solutions to the Killing equation. The static, spherically symmetric Schwarzschild solution had one timelike Killing field and three spatial rotational Killing fields for a total of three. A generic spacetime has no isometries (Schutz. B. F, 2009).

Static, Spherically Symmetric Spacetimes

One may now say what one means by a static, spherically symmetric spacetime. To be static, there must be a timelike Killing vector field; to be spherically symmetric, one require a full set of three rotational (hence spacelike) Killing vectors. one use the Lie derivative to say restrict the form of the metric for a static, spherically symmetric spacetime. If one want a statics spacetime, it means that one want there to exist a timelike Killing vector field. Choosing the time coordinate to be the parameter t = λ, the symmetry condition becomes

$$\begin{aligned} 0 &= L_\xi g_{\alpha\beta} \qquad (29) \\ &= \xi^\mu \partial_\mu g_{\alpha\beta} + \partial_\alpha \xi^\mu g_{\mu\beta} + \partial_\beta \xi^\mu g_{\alpha\mu} \end{aligned}$$

However, with $x^0 = t = \lambda$, the components of ξ are constant, so that

$$\partial_\alpha \xi^\mu = 0 \tag{30}$$

Therefore,

$$\begin{aligned} 0 &= \xi^\mu \partial_\mu g_{\alpha\beta} \qquad (31) \\ &= \frac{\partial}{\partial t}(g_{\alpha\beta}) \end{aligned}$$

and we have a coordinates system in which the metric is independent of the time coordinate.

For the spherical symmetry, we know that we have three rotational Killing vector fields which together generate SO(3). We can pick two of these for coordinates, but they will not commute with one another, so the metric will not be independent of both coordinates. Starting with the familiar form

$$\xi_1 = y\frac{\partial}{\partial z} - z\frac{\partial}{\partial y}$$

$$\xi_2 = z\frac{\partial}{\partial x} - x\frac{\partial}{\partial z}$$

$$\xi_3 = x\frac{\partial}{\partial y} - y\frac{\partial}{\partial x}$$

it is natural to choose one coordinate, φ, such that

$$\frac{\partial}{\partial \varphi} = x\frac{\partial}{\partial y} - y\frac{\partial}{\partial x} \tag{32}$$

is a Killing vector. To describe a second direction, we want a linear combination of the remaining two rotations,

$$\alpha(\varphi)\xi_1 + \beta(\varphi)\xi_2 \tag{33}$$

and we want this to remain orthogonal toξ_3,

$$0 = \langle \xi_3, \alpha\xi_1 + \beta\xi_2 \rangle \tag{34}$$

$$\begin{aligned} &= \left\langle x\frac{\partial}{\partial y} - y\frac{\partial}{\partial x}, \alpha\left(y\frac{\partial}{\partial} - z\frac{\partial}{\partial y}\right) + \beta\left(z\frac{\partial}{\partial x} - x\frac{\partial}{\partial z}\right)\right\rangle \\ &= x\left\langle \frac{\partial}{\partial y}, \alpha\left(y\frac{\partial}{\partial z} - z\frac{\partial}{\partial y}\right) + \beta\left(z\frac{\partial}{\partial x} - x\frac{\partial}{\partial z}\right)\right\rangle \\ &\quad - y\left\langle \frac{\partial}{\partial x}, \alpha\left(y\frac{\partial}{\partial z} - z\frac{\partial}{\partial y}\right) + \beta\left(z\frac{\partial}{\partial x} - x\frac{\partial}{\partial z}\right)\right\rangle \\ &= x\left\langle \frac{\partial}{\partial y}, -\alpha z\frac{\partial}{\partial y}\right\rangle - y\left\langle \frac{\partial}{\partial x}, \beta z\frac{\partial}{\partial x}\right\rangle \\ &= \alpha z x\left\langle \frac{\partial}{\partial y}, \frac{\partial}{\partial y}\right\rangle - \beta z y\left\langle \frac{\partial}{\partial x}, \frac{\partial}{\partial x}\right\rangle \\ &= -z(\alpha x + \beta y) \\ &= -r\, sin\theta z\, (\alpha\cos\varphi + \beta\sin\varphi) \end{aligned}$$

To get zero, one can take

$$\alpha = sin\ \varphi$$

$$\beta = -\cos\varphi$$

Then we have

$$\xi_4 = \xi_1 \sin\varphi + \xi_2 \cos\varphi \tag{35}$$

$$= sin\ \varphi \left(y\frac{\partial}{\partial z} - z\frac{\partial}{\partial y}\right) - \cos\varphi \left(z\frac{\partial}{\partial x} - x\frac{\partial}{\partial z}\right)$$

$$= sin\ \varphi \left(r\ sin\ \theta\ sin\ \varphi\frac{\partial}{\partial z} - r\cos\theta\frac{\partial}{\partial y}\right) - \cos\varphi \left(r\cos\theta\frac{\partial}{\partial x} - r\sin\theta\cos\varphi\frac{\partial}{\partial z}\right)$$

$$= r\sin\theta\sin\varphi\ \frac{\partial}{\partial z} - \mathrm{r}\cos\theta\sin\varphi\frac{\partial}{\partial y} - r\cos\varphi\cos\theta\ \frac{\partial}{\partial x} + r\sin\theta\cos\varphi\ \frac{\partial}{\partial z}$$

$$= -\cos\theta\left(r\cos\varphi\frac{\partial}{\partial x} + r\sin\varphi\frac{\partial}{\partial y}\right) + \mathrm{r}\sin\theta\frac{\partial}{\partial z}$$

$$= -\cos\theta\left(x\frac{\partial}{\partial x} + y\frac{\partial}{\partial y}\right) - \mathrm{r}\sin\theta\ \frac{\partial}{\partial z}$$

Compare

$$\frac{\partial}{\partial x} = \frac{x}{r}\ \frac{\partial}{\partial r} + \frac{1}{\sqrt{x^2+y^2}}\ \frac{xz}{r^2}\ \frac{\partial}{\partial\theta} - \ \frac{y}{x^2+y^2}\ \frac{\partial}{\partial\varphi} \tag{36}$$

$$= \sin\theta\cos\varphi\ \frac{\partial}{\partial r} + \frac{1}{r}\cos\theta\cos\varphi\ \frac{\partial}{\partial\theta} - \frac{1}{r}\frac{sin\varphi}{sin\theta}\frac{\partial}{\partial\varphi}$$

$$\frac{\partial}{\partial y} = \frac{y}{r}\frac{\partial}{\partial r} + \frac{1}{\sqrt{x^2+y^2}}\frac{yz}{r^2}\frac{\partial}{\partial\theta} + \frac{x}{x^2+y^2}\frac{\partial}{\partial\varphi} \tag{37}$$

$$= \sin\theta\sin\varphi\ \frac{\partial}{\partial r} + \frac{1}{r}\cos\theta\sin\varphi\ \frac{\partial}{\partial\theta} + \frac{1}{r}\frac{cos\varphi}{sin\theta}\frac{\partial}{\partial\varphi}$$

$$\frac{\partial}{\partial z} = \frac{z}{r}\frac{\partial}{\partial r} - \frac{\sqrt{x^2+y^2}}{r^2}\frac{\partial}{\partial\theta} \tag{38}$$

$$= cos\theta\frac{\partial}{\partial r} - \frac{sin\theta}{r}\frac{\partial}{\partial\theta}$$

so we have

$$\xi_4 = -cos\theta\left(x\frac{\partial}{\partial x} + y\frac{\partial}{\partial y}\right) + r\ sin\theta\frac{\partial}{\partial x} \tag{39}$$

$$= cos\theta\left(r\sin\theta\ cos^2\varphi\frac{\partial}{\partial r} + cos\ \theta\ cos^2\varphi\frac{\partial}{\partial\theta} + r\ sin\theta\ sin^2\ \varphi\frac{\partial}{\partial\theta} + cos\theta sin^2\varphi\frac{\partial}{\partial\theta}\right)$$
$$- r\ sin\theta\left(cos\theta\frac{\partial}{\partial r} - \frac{sin\ \theta}{\partial r}\frac{\partial}{\partial\theta}\right)$$

$$= r\ sin\theta\cos\theta\frac{\partial}{\partial r} + cos^2\ \theta\frac{\partial}{\partial\theta} - r\sin\theta\cos\theta\ \frac{\partial}{\partial r} + sin^2\ \theta\ \frac{\partial}{\partial\theta}$$

$$= r\, sin\theta\, cos\theta \frac{\partial}{\partial r} + cos^2\theta \frac{\partial}{\partial \theta} - r\, sin\theta\, cos\theta\, \frac{\partial}{\partial r} + sin^2 \frac{\partial}{\partial \theta}$$

$$= cos^2\theta \frac{\partial}{\partial \theta} + sin^2\theta \frac{\partial}{\partial \theta}$$

$$= \frac{\partial}{\partial \theta}$$

We may therefore take two of the Killing vectors to be

$$\xi_4 = \frac{\partial}{\partial \theta} \qquad (40)$$

$$\xi_3 = \frac{\partial}{\partial \varphi} \qquad (41)$$

giving two coordinates, $\theta, \varphi,$ corresponding to symmetry directions. Since these do not commute, the metric cannot be independent of both.

Static, Spherically Symmetric Spacetimes

One may now say what one means by a static, spherically symmetric spacetime. To be static, there must be a timelike Killing vector field; to be spherically symmetric, one require a full set of three rotational (hence spacelike) Killing vectors. one use the Lie derivative to say restrict the form of the metric for a static, spherically symmetric spacetime. If one want a statics spacetime, it means that one want there to exist a timelike Killing vector field. Choosing the time coordinate to be the parameter t = λ, the symmetry condition becomes

$$\begin{aligned} 0 &= L_\xi g_{\alpha\beta} \qquad (36) \\ &= \xi^\mu \partial_\mu g_{\alpha\beta} + \partial_\alpha \xi^\mu g_{\mu\beta} + \partial_\beta \xi^\mu g_{\alpha\mu} \end{aligned}$$

However, with $x^0 = t = \lambda$, the components of ξ are constant, so that

$$\partial_\alpha \xi^\mu = 0 \qquad (37)$$

Therefore,

$$\begin{aligned} 0 &= \xi^\mu \partial_\mu g_{\alpha\beta} \qquad (38) \\ &= \frac{\partial}{\partial t}(g_{\alpha\beta}) \end{aligned}$$

and we have a coordinates system in which the metric is independent of the time coordinate.

For the spherical symmetry, we know that we have three rotational Killing vector fields which together generate SO(3). We can pick two of these for coordinates, but they will not commute with one another, so the metric will not be independent of both coordinates. Starting with the familiar form

$$\xi_1 = y \frac{\partial}{\partial z} - z \frac{\partial}{\partial y}$$

$$\xi_2 = z \frac{\partial}{\partial x} - x \frac{\partial}{\partial z}$$

$$\xi_3 = x\frac{\partial}{\partial y} - y\frac{\partial}{\partial x}$$

it is natural to choose one coordinate, φ, such that

$$\frac{\partial}{\partial\varphi} = x\frac{\partial}{\partial y} - y\frac{\partial}{\partial x} \qquad (39)$$

is a Killing vector. To describe a second direction, we want a linear combination of the remaining two rotations,

$$\alpha(\varphi)\xi_1 + \beta(\varphi)\xi_2 \qquad (40)$$

and we want this to remain orthogonal toξ_3,

$$\begin{aligned}
0 &= \langle \xi_3, \alpha\xi_1 + \beta\xi_2 \rangle \qquad (41)\\
&= \left\langle x\frac{\partial}{\partial y} - y\frac{\partial}{\partial x}, \alpha\left(y\frac{\partial}{\partial} - z\frac{\partial}{\partial y}\right) + \beta\left(z\frac{\partial}{\partial x} - x\frac{\partial}{\partial z}\right)\right\rangle\\
&= x\left\langle\frac{\partial}{\partial y}, \alpha\left(y\frac{\partial}{\partial z} - z\frac{\partial}{\partial y}\right) + \beta\left(z\frac{\partial}{\partial x} - x\frac{\partial}{\partial z}\right)\right\rangle\\
&\quad - y\left\langle\frac{\partial}{\partial x}, \alpha\left(y\frac{\partial}{\partial z} - z\frac{\partial}{\partial y}\right) + \beta\left(z\frac{\partial}{\partial x} - x\frac{\partial}{\partial z}\right)\right\rangle\\
&= x\left\langle\frac{\partial}{\partial y}, -\alpha z\frac{\partial}{\partial y}\right\rangle - y\left\langle\frac{\partial}{\partial x}, \beta z\frac{\partial}{\partial x}\right\rangle\\
&= \alpha z x\left\langle\frac{\partial}{\partial y}, \frac{\partial}{\partial y}\right\rangle - \beta z y\left\langle\frac{\partial}{\partial x}, \frac{\partial}{\partial x}\right\rangle\\
&= -z(\alpha x + \beta y)\\
&= -r\ sin\theta z\ (\alpha\cos\varphi + \beta\sin\varphi)
\end{aligned}$$

To get zero, one can take

$$\alpha = sin\ \ \varphi$$

$$\beta = -\cos\varphi$$

Then we have

$$\begin{aligned}
\xi_4 &= \xi_1\sin\varphi + \xi_2\cos\varphi \qquad (42)\\
&= sin\ \varphi\left(y\frac{\partial}{\partial z} - z\frac{\partial}{\partial y}\right) - \cos\varphi\left(z\frac{\partial}{\partial x} - x\frac{\partial}{\partial z}\right)\\
&= sin\ \varphi\left(r\ sin\ \theta\ sin\ \varphi\frac{\partial}{\partial z} - r\cos\theta\frac{\partial}{\partial y}\right) - \cos\varphi\left(r\cos\theta\frac{\partial}{\partial x} - r\sin\theta\cos\varphi\frac{\partial}{\partial z}\right)\\
&= r\sin\theta\sin\varphi\ \frac{\partial}{\partial z} - \mathrm{r}\cos\theta\sin\varphi\frac{\partial}{\partial y} - r\cos\varphi\cos\theta\ \frac{\partial}{\partial x} + r\sin\theta\cos\varphi\ \frac{\partial}{\partial z}\\
&= -\cos\theta\left(r\cos\varphi\frac{\partial}{\partial x} + r\sin\varphi\frac{\partial}{\partial y}\right) + \mathrm{r}\sin\theta\frac{\partial}{\partial z}\\
&= -\cos\theta\left(x\frac{\partial}{\partial x} + y\frac{\partial}{\partial y}\right) - \mathrm{r}\sin\theta\ \frac{\partial}{\partial z}
\end{aligned}$$

Compare

$$\frac{\partial}{\partial x} = \frac{x}{r}\frac{\partial}{\partial r} + \frac{1}{\sqrt{x^2+y^2}}\frac{xz}{r^2}\frac{\partial}{\partial \theta} - \frac{y}{x^2+y^2}\frac{\partial}{\partial \varphi} \tag{43}$$

$$= \sin\theta\cos\varphi\,\frac{\partial}{\partial r} + \frac{1}{r}\cos\theta\cos\varphi\,\frac{\partial}{\partial \theta} - \frac{1}{r}\frac{sin\varphi}{sin\theta}\frac{\partial}{\partial \varphi}$$

$$\frac{\partial}{\partial y} = \frac{y}{r}\frac{\partial}{\partial r} + \frac{1}{\sqrt{x^2+y^2}}\frac{yz}{r^2}\frac{\partial}{\partial \theta} + \frac{x}{x^2+y^2}\frac{\partial}{\partial \varphi} \tag{44}$$

$$= \sin\theta\sin\varphi\,\frac{\partial}{\partial r} + \frac{1}{r}\cos\theta\sin\varphi\,\frac{\partial}{\partial \theta} + \frac{1}{r}\frac{cos\varphi}{sin\theta}\frac{\partial}{\partial \varphi}$$

$$\frac{\partial}{\partial z} = \frac{z}{r}\frac{\partial}{\partial r} - \frac{\sqrt{x^2+y^2}}{r^2}\frac{\partial}{\partial \theta} \tag{45}$$

$$= cos\theta\frac{\partial}{\partial r} - \frac{sin\theta}{r}\frac{\partial}{\partial \theta}$$

so we have

$$\xi_4 = -cos\theta\left(x\frac{\partial}{\partial x} + y\frac{\partial}{\partial y}\right) + r\;sin\theta\frac{\partial}{\partial x} \tag{46}$$

$$= cos\theta\left(r\sin\theta\;cos^2\varphi\frac{\partial}{\partial r} + cos\;\theta\;cos^2\varphi\frac{\partial}{\partial \theta} + r\;sin\theta\;sin^2\;\varphi\frac{\partial}{\partial \theta} + cos\theta sin^2\varphi\frac{\partial}{\partial \theta}\right)$$

$$- r\;sin\theta\left(cos\theta\frac{\partial}{\partial r} - \frac{sin\;\theta}{\partial r}\frac{\partial}{\partial \theta}\right)$$

$$= r\;sin\theta\cos\theta\frac{\partial}{\partial r} + cos^2\;\theta\frac{\partial}{\partial \theta} - r\sin\theta\cos\theta\;\frac{\partial}{\partial r} + sin^2\;\theta\;\frac{\partial}{\partial \theta}$$

$$= r\;sin\theta\;cos\theta\frac{\partial}{\partial r} + cos^2\theta\frac{\partial}{\partial \theta} - r\;sin\theta\;cos\theta\;\frac{\partial}{\partial r} + sin^2\frac{\partial}{\partial \theta}$$

$$= cos^2\theta\frac{\partial}{\partial \theta} + sin^2\theta\frac{\partial}{\partial \theta}$$

$$= \frac{\partial}{\partial \theta}$$

We may therefore take two of the Killing vectors to be

$$\xi_4 = \frac{\partial}{\partial \theta} \tag{47}$$

$$\xi_3 = \frac{\partial}{\partial \varphi} \tag{48}$$

giving two coordinates, $\theta, \varphi,$ corresponding to symmetry directions. Since these do not commute, the metric cannot be independent of both.

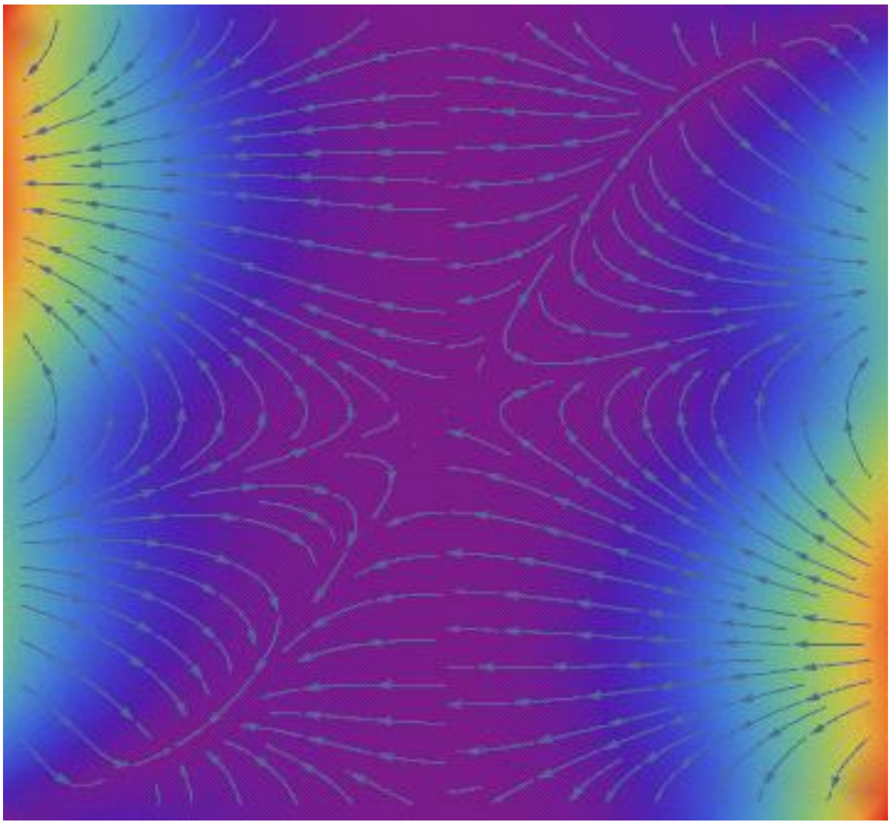

Figure 1 The typical visualization of the gradient of a vector field $\boldsymbol{\xi_1}$

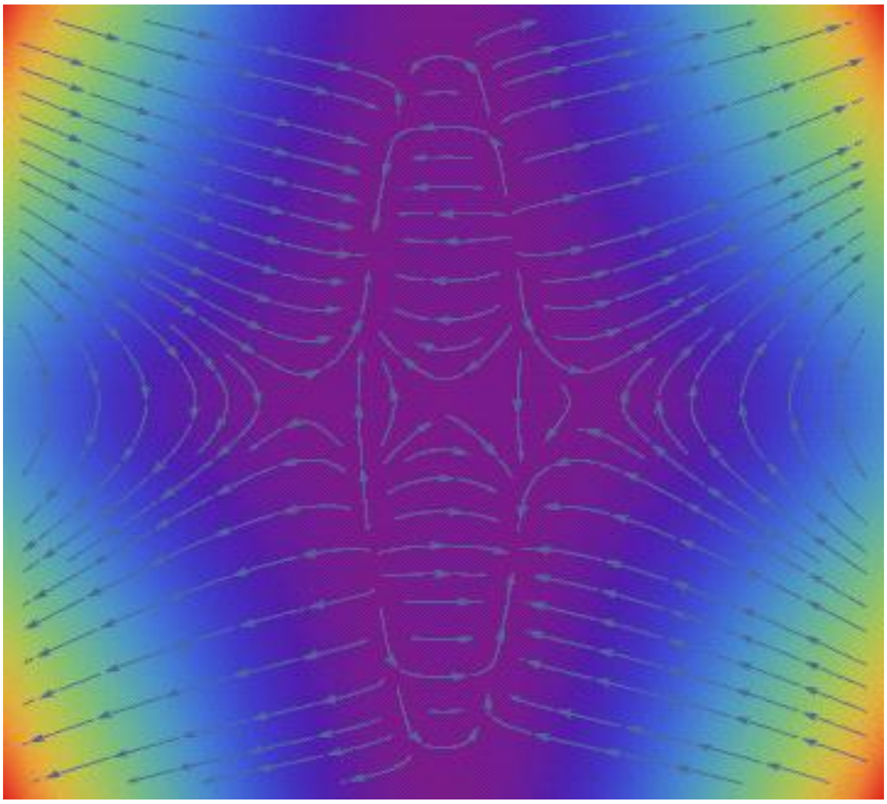

Figure 2 The typical visualization of the gradient of a vector field $\boldsymbol{\xi_2}$

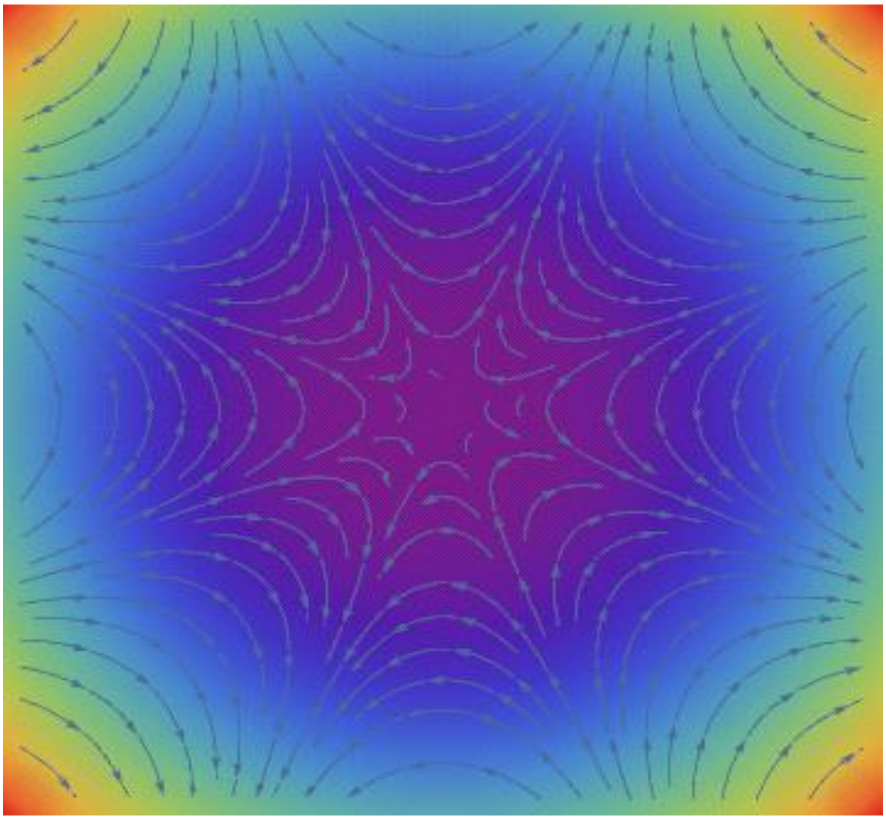

Figure 3 The typical visualization of the gradient of a vector field ξ_3

Concluding Remarks

In this paper, attempts have been made to explore the interesting physical properties of spacetimes structure. Lie derivative , Killing field equations and utilizations of these are also been presented. The symmetry of Minkowki spacetimes, static spacetimes and spherically symmetric spacetimes have been analyzed. The symmetry nature of the vectors fields are visualized with Stream Density Plot by using Mathematica.

Acknowledgements

I would like to thank Dr Khin Khin Win, Professor and Head, Department of Physics, University of Yangon, for her kind permission and encouragements to carry out this work.

I would like to express my gratitude to all of the Professors, Department of Physics, University of Yangon, for their kind permission and encouragemen ts to undertake this research paper.

Special thanks are due to Professor, Dr Thant Zin Naing, Retired Pro-Rector (Admin), International Theravāda Buddhist Missionary University, for his valuable guidance and helpful advice to carry out this work.

References

Adler.R, Bazin. M, Schiffer. M, (1975). *Introduction to General Relativity*. New York: Mc.Graw-Hill.

Carroll, S.M., (2004). *Introduction to General Relativity Spacetime and Geometry*, San Francisco, Addison-Wesley.

Hawking S.W, Ellis G.F.R, (1973). *The large scale structure of space-time*, Cambridge: Cambridge Univ. Press.

Mc Mahon. D, (2006). *Relativity Demystified*, New York: McGraw-Hill.

Misner.C.W, Throne. K.S, Wheeler. J.A, (1973). *Gravitation*, San Francisco: W.H. Freeman and Company.

Stephani.H, (2004). *Relativity: An introduction to Special and General Relativity*, Cambridge: Cambridge University Press.

Schutz. B.F, (2009). *A First Course in General Relativity*, Cambridge: Cambridge University Press.

Weinberg.S, (1972). *Gravitation and Cosmology: Principles and Applications of the General Theory of Relativity,* Hoboken:J. Wiley & Sons.

J. Myanmar Acad. Arts Sci. 2020 **Vol. XVIII.No.2**B

CONTAMINATION ASSESSMENT NEAR PUBLIC DUG WELLS ALONG SHWE-TA-CHAUNG CREEK

Aye Myat Mon[*]

Abstract

Public dug wells are commonly used for drinking, bathing, cleaning and cooking purposes. Two water samples from two dug wells, named Yarma and Cow Lake, along Shwe-Ta-Chaung Creek were examined at Public Health Laboratory in two times to determine the contamination of surface associated with waste water. The first time is October 2017 and second time is March 2018. Four water chemical analysis reports for the two wells are chemically unpotable. The results are compared with the World Health Organization (WHO) standard values to identify the existence of contaminants above the acceptable levels. Also four soil samples near each dug well and related creek were determined with Rigaku EDXRF spectrometer in two times to estimate the elemental pollution in the soil. Contamination factor, modified degree of contamination and pollution load index for soil contamination was calculated. The objective of this research is to determine the environmental pollution on the two public dug wells located adjacent to the Shwe-Ta-Chaung Creek in Tanpawaddy Quarter Mandalay, Myanmar. The water supply wells are impacted by contamination associated with waste water. Yarma Dug Well region adjacent to the rubbish filter site is more polluted than Cow Lake Dug Well region.

Keywords: Yarma Dug Well, Cow Lake Dug Well,Shwe-Ta-Chaung Creek, contamination

Introduction

Water is one of the most vital natural resources for all life on Earth. Water use is the amount of water used by a household or a country, or the amount used for a given task or for the production of a given quantity of some product or crop, or the amount allocated for a particular purpose. The main ways a home has access to water is either through a municipal water supply from a major city or through wells. Wells exist in two forms, dug wells and tube wells. These water supplies can be contaminated through different mechanisms. Water can be contaminated with either chemicals or microorganisms through improper installation of wells, or being in close proximity to sources of pollution such as sewage or lands fills. In this research, the water quality of two dug wells beside Shwe-Ta-Chaung Creek was tested in two times for chemical contamination in Public Health laboratory, Mandalay, Myanmar. Four soil samples near the two dug wells and relevant the creek were determined in two times for elemental contamination by Rigaku EDXRF technique in University Research Centre, Taunggyi University. The main focus of this research is to investigate environmental pollution near two dug wells located adjacent to the Shwe-Ta-Chaung Creek in Mandalay, Myanmar.

Chemical testing of water quality relies on the comparison of the results with WHO drinking water guidelines to identify contaminants. Most of these contaminants are only of concern with chronic exposure (long-term exposure). Some contaminants that occur in water are the matter of concern because of effects arising from acute exposure (short-term exposure). Sewage, garbage and liquid waste of households, agricultural lands and factories are discharged into lakes and rivers. Early types of water pollution were usually due to contamination from human and animal waste, which caused major outbreaks of diseases like cholera. The toxic

---

[*] Dr, Lecturer, Department of Physics, Banmaw University

elements effect on human health including organs, damage respiratory tract disorder, lung diseases, skin diseases and other illnesses.

It is suspected that the waste water from the Shwe-Ta-Chaung Creek may be contaminating the dug wells degrading the water quality. Thus, this research is to determine the impact of the creek on contamination near two public dug wells by the analysis of four water samples and eight soil samples collected at two sites next to the creek in October 2017 and in March 2018.

Materials and Methods

Description of Research Area

Yarma Dug Well and Cow Lake Dug Well are located in the Tanpawaddy, Chanmyatharsi Township, Mandalay district, Myanmar and situated beside Mandalay-Sagaing-Shwebo Road.

Sample Location (Sampling Site) and Collection

Yarma Dug Well lies at approximately 21º 55' 45" north latitude and 96 º 4' 4" east longitudes. The well was constructed over 100 years ago. Typically, the well-base is about 30 feet away from Shwe-Ta-Chaung Creek. A garbage area is about 75 feet away from the well-base. The diameter of the well is 6.5 feet and the thickness of the well is 1 foot, which is constructed with a brick lining. The height of the well base is 1.5 feet above the ground. The depth to water from the top of the well casing is 15.35 feet on 12th October 2017. The depth to water from the top of the well casing is 20.5 feet on 5th March 2018. The photograph of Yarma Dug Well beside the Shwe-Ta-Chaung Creek is shown in Figure (1). The width of the creek near Yarma Dug Well is about 25 feet and it lies approximately at 21º 55' 46" north latitude and 96 º 4' 3" east longitudes. Raw sewage from downtown Mandalay flows into the creek. In this area, the creek is not lined by concrete. Waste water is in direct contact with the ground in the creek. Yarma Dug Well region is located adjacent to the rubbish filter site along the creek. The photograph of trash located near the Yarma Dug Well in the bank of the Shwe-Ta-Chaung Creekis also shown in Figure (2).

Cow Lake Dug Well lies at approximately 21º 56' 19" north latitude and 96 º 4' 21" east longitudes. The well was constructed over 100 years ago. Typically, the well-base is about 45 feet away from the creek. A garbage area is about 95 feet away from the well-base. The diameter of the well is 4 feet and the thickness of the well is 11 inches, which is constructed with a brick lining. The height of the well base is 9 inches above the ground. The depth to water from the top of the well casing is 21 feet on 12th October 2017. The depth to water from the top of the well casing is 14 feet on 5th March 2018. The photograph of Cow Lake Dug Well beside the Shwe-Ta-Chaung Creek is shown in Figure (3).The width of the creek near Cow Lake Dug Well is about 20 feet and it lies approximately at 21º 56'18" north latitude and 96º 4' 21" east longitude. Raw sewage from downtown Mandalay flows into the creek. In this area, the creek is lined by concrete. Waste water is not in direct contact with the ground in the creek. The photograph of trash located near Cow Lake Dug Well in the bank of the Shwe-Ta-Chaung Creek is also shown in Figure (4).The photograph of location map of two research sites in Tanpawaddy is represented in Figure (5).

In this research work, two water samples from Yarma Dug Well and Cow Lake Dug Well were collected first time in 12th October 2017. Also four soil samples were collected. The soil sample near Yarma Dug Well was named as S_1W. The soil sample beside the creek in Yarma Quarter was named as S_1C. The soil sample near Cow Lake Dug Well is represented as S_2W. The soil sample beside the creek in Cow Lake Quarter is represented as S_2C. These soil samples from four research sites were each collected with two inches in diameter PVC pipe which is one feet long. The small trashes in these samples were cleaned and dried under the room temperature. And then it is needed to grind the soil powdered samples and to get very fine powders. The soil powder samples were passed through 325 mesh sieve of the samples. After getting very fine powder, the sample was weighted nearly 5g. Sample preparation is an important role in XRF measurement. Similarly the two water samples and four soil samples were also collected second time in 5th March 2018.

Public Health Laboratory, Ministry of Health and Sports

The water quality parameters (Appearance, Colour, Turbity, pH value, Total Solids, Total Hardness, Total Alkalinity, Ca, Mg, Cl, SO_4 and Fe) in four water samples of Yarma Dug Well and Cow Lake Dug Well were tested at Public Health Laboratory, Ministry of Health and Sports, Mandalay.

Experimental Procedure for Rigaku X-ray Spectrometer

The EDXRF machine (Rigaku) at the University Research Centre, Taunggyi University is used for determination of elemental concentration in the sample of interest in eight soil samples. The photograph of Energy dispersive X-ray fluorescence spectrometer (Rigaku) in University Research Centre, Taunggyi University is shown in Figure (6).

Contamination Factor (CF) and Modified Degree of Contamination (mC_d)

The level of metal contamination was expressed by the contamination status of sediment in the current research. CF and mC_d were calculated according to the equation described as

$$\mathrm{CF} = \frac{\mathrm{MC}}{\mathrm{BC}}$$

$$\mathrm{mC_d} = \frac{1}{\mathrm{N}} \sum_{i=1}^{\mathrm{N}} \mathrm{CF}$$

Four contamination categories are documented on the basis of the contamination factor. CF<1 low contamination; $1 \le \mathrm{CF} < 3$ moderate contamination; $3 \le \mathrm{CF} < 6$ considerable contamination: CF > 6 very high contamination, while the degree of contamination (C_d) was defined as the sum of all contamination factor. The following terms is adopted to illustrate the degree of contamination $C_d < 6$: low degree of contamination; $6 \le C_d < 12$: moderate degree of contamination; $12 \le C_d < 24$: considerable degree of contamination; $C_d > 24$: very high degree of contamination indication serious anthropogenic pollution.

Pollution Load Index (PLI)

Pollution Load Index (PLI) was used to evaluate the extent of pollution by heavy metals in the environment.

$$PLI = (CF_1 \times CF_2 \times CF_3 \times .... \times CF_n)^{1/n}$$

where n is the number of metals and CF is the contamination factor. Five contamination categories are reported on the basis of the pollution load index. A PLI<1 denote perfection, PLI=1 present that only baseline levels of pollutants are present, PLI>1 would indicate deterioration of site quality, PLI≥1 indicates an immediate intervention to ameliorate pollution, 0.5≤PLI<1 suggests that more detailed study is needed to monitor the site.

Figure 1 Yarma Dug Well beside the Shwe-Ta-Chaung Creek

Figure 2 Trash located near the Yarma Dug Well on the bank of the Shwe-Ta-Chaung Creek

Figure 3 Cow Lake Dug Well beside the Shwe-Ta-Chaung Creek

Figure 4 Trash located near Cow Lake Dug Well on the bank of Shwe-Ta-Chaung Creek

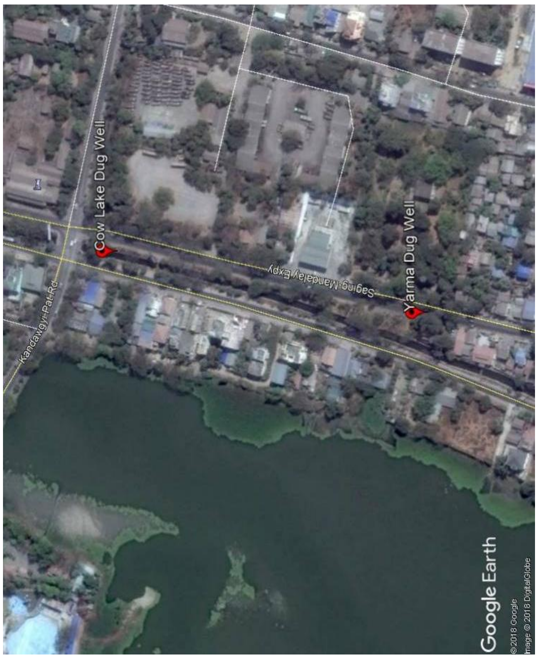

Figure 5 Location Map of two dug wells in Tanpawaddy Township, Mandalay City, Myanmar

Figure 6 Experimental Set-up for Energy dispersive x-ray fluorescence spectrometer (Rigaku) in University Research Centre, Taunggyi University

Results and Discussions

In the research work, the water quality parameters of Yarma Dug Well and Cow Lake Dug Well were tested in two times at Public Health Laboratory. Chemical Analysis of the water in Yarma Dug Well in first time (October 2017) and second time (March 2018) is listed in Table (1).Chemical Analysis of the water in Cow Lake Dug Well in first time (October 2017) and second time (March 2018) is also shown in Table (2).

According to the results, total solids are nearly to the maximum permissible level of WHO in first time and greater than maximum permissible level in second time at the Yarma Dug Well. Total alkalinity is greater than maximum permissible level in both times at the Yarma Dug Well. Other parameters (Colour, pH value, total hardness, Calcium Ca, Magnesium Mg, Chloride Cl and Sulphate SO_4) of Yarma Dug Well are under the level in both times at the Yarma Dug Well. Total Hardness, Calcium Ca and Sulphate SO_4 are nearly to the level in the Cow Lake Dug Well. Total solids and total alkalinity are greater than the level in both times at Cow Lake Dug Well. Other parameters (Colour, pH value, Magnesium Mg and Chloride C1 of Cow Lake Dug Well are under the level in both times. Therefore, the remarks of water chemical analysis reports are chemically unpotable.

Yarma Dug Well base is nearer to the creek than Cow Lake Dug Well base. The disposal area is nearer to the Yarma Dug Well base than the garbage area around Cow Lake Dug Well base. But the height of the Yarma Dug Well base is greater than the Cow Lake Dug Well base above the ground. The width of the creek near Yarma Dug Well is greater than near Cow Lake Dug Well.

The water from Yarma Dug Well and Cow Lake Dug Well are used only for taking baths, washing clothes and cleaning dishes. It is not used for drinking purpose now. Environment around Yarma Dug Well adjacent to the rubbish filter site along the creek is more polluted than Cow Lake Dug Well region because the distance between Yarma Dug Well is close to the creek than Cow Lake Dug Well.

The elemental concentration of elements of four soil samples in the first time and second time is listed in Table (3).These elements are magnesium (Mg), aluminum (Al), silicon (Si), phosphorus (P), sulfur (S), chlorine (Cl), potassium (K), calcium (Ca), titanium (Ti), manganese (Mn), iron (Fe), copper (Cu), zinc (Zn), lead (Pb) and chromium (Cr).The contamination Factor

(CF) for soil pollution near two dug wells in first time and second time is calculated in Table (4). These metals are magnesium (Mg), aluminum (Al), potassium (K), manganese (Mn), iron (Fe), copper (Cu), zinc (Zn), chromium (Cr) and lead (Pb). Modified degree of contamination (mC_d) for soil pollution near two dug wells in first time is calculated in Table (5) and second time is in Table (6).Pollution Load Index (PLI) for soil pollution near two dug wells in first time is listed in Table (7) and second time is in Table (8).Comparison of modified degree of contamination (mC_d)for soil pollution near Yarma Dug Well and Cow Lake Dug Well in first time is shown in Figure (7) and second time is in Figure (11).Comparison of modified degree of contamination (mC_d)for soil pollution in the bank of Shwe-Ta-Chaung Creek near Yarma Dug Well and Cow Lake Dug Well in first time is shown in Figure (8) and second time is in Figure (12).Comparison of pollution load index (PLI)for soil pollution near Yarma Dug Well and Cow Lake Dug Well in first time is represented in Figure (9) and second time is in Figure (13). Comparison of pollution load index (PLI)f or soil pollution in the bank of Shwe-Ta-Chaung Creek near Yarma Dug Well and Cow Lake Dug Well in first time is also shown in Figure (10) and second time is in Figure (14).

The calculated results of modified degree of contamination (mC_d) for soil near Yarma Dug Well are very high degree of contamination and soil in the bank of the creek near Yarma Dug Well are moderate degree of contamination in the first time. Both modified degree of contamination (mC_d) for soil near Yarma Dug Well and soil in the bank of the creek near Yarma Dug Well are moderate degree of contamination in the second time.

The modified degree of contamination (mC_d) results for soil near Cow Lake Dug Well is very low degree of contamination and the soil in the bank of the creek near Cow Lake Dug Well are moderate degree of contamination in the first time. Both modified degree of contamination (mC_d) for soil near Cow Lake Dug Well and soil in the bank of the creek near Cow Lake Dug Well are very low degree of contamination in the second time.

Pollution load index (PLI) for soil near Yarma Dug Well is strongly polluted and for soil in the bank of the creek near Yarma Dug Well is moderately polluted in the first time. Both pollution load indices (PLI) for soil near Cow Lake Dug Well and soil in the bank of the creek near Cow Lake Dug Well are moderately polluted in the first time. Both pollution Load indices (PLI) for soil near the two dug wells and soil in the bank of the creek near the two dug wells are moderately polluted in the second time. The pollution load index (PLI) for soil near Yarma Dug Well would indicate deterioration of site quality. The pollution load index (PLI) for soil near Cow Lake Dug Well presents that only baseline level of pollutants. The pollution load index (PLI) for soil in the bank of the creek near Yarma Dug Well and Cow Lake Dug Well would indicate deterioration of site quality.

According to the results, soil around Yarma Dug Well adjacent to the rubbish filter site along the creek is more polluted than Cow Lake Dug Well region because the distance between Yarma Dug Well is close to the creek than Cow Lake Dug Well. There is more pollution at Yarma Dug Well because there are many trash and garbage near in it.

Table 1 Chemical Analysis of the water in Yarma Dug Well in first time (October 2017) and second time (March 2018)

No.	Parameter	First Result	Second Result	Maximum Permissible Level [WHO]	Unit
1	Appearance	Clear	Slightly Turbid	-	-
2	Colour (Platinum, Cobolot Scale)	5	7	50	Units
3	Turbidity (Silcoda Scale Unit)	-	-	25	NTU
4	PH value	7.3	7.1	6.5 to 9.2	-
5	Total Solids	1482	1571	1500	mg/l
6	Total Hardness (as $CaCO_3$)	290	310	500	mg/l
7	Total Alkalinity (as $CaCO_3$)	1040	1105	950	mg/l
8	Calcium as Ca	80	112	200	mg/l
9	Magnesium as Mg	22	7	150	mg/l
10	Chloride as Cl	120	140	600	mg/l
11	Sulphate as SO_4	157	147	400	mg/l
12	Total Iron as Fe	Nil	Nil	1	mg/l

Table 2 Chemical Analysis of the water in Cow Lake Dug Well in first time (October 2017) and second time (March 2018)

No.	Parameter	First Result	Second Result	Maximum Permissible Level [WHO]	Unit
1	Appearance	Clear	Clear	-	-
2	Colour (Platinum, Cobolot Scale)	5	6	50	Units
3	Turbidity (Silcoda Scale Unit)	-	-	25	NTU
4	PH value	6.9	7.3	6.5 to 9.2	-
5	Total Solids	2100	1808	1500	mg/l
6	Total Hardness (as $CaCO_3$)	400	230	500	mg/l
7	Total Alkalinity (as $CaCO_3$)	1430	1495	950	mg/l
8	Calcium as Ca	128	84	200	mg/l
9	Magnesium as Mg	19	5	150	mg/l
10	Chloride as Cl	160	120	600	mg/l
11	Sulphate as SO_4	314	49	400	mg/l
12	Total Iron as Fe	Nil	Nil	1	mg/l

Table 3 Concentration of elements of four soil samples in the first time and second time

Sr. No	Elements	Concentration (mg/ kg)							
		YarmaDug Well				Cow Lake Dug Well			
		First time		Second time		First time		Second time	
		S_1 W	S_1C	S_1 W	S_1C	S_2 W	S_2 C	S_2 W	S_2 C
1	Mg	9910	10800	8140	8790	7630	10800	9590	11000
2	Al	40800	43200	41000	48000	34800	39400	44000	51800
3	Si	169000	165000	166000	169000	136000	147000	171000	170000
4	P	2080	1860	2060	2050	1370	1330	2020	1060
5	S	819	2410	949	1140	777	1270	989	469
6	Cl	435	151	383	313	179	105	176	127
7	K	16700	16400	16800	17700	13900	15700	16400	18400
8	Ca	54100	52600	50300	40200	34600	56400	50700	38500
9	Ti	2460	2910	1990	2530	1710	2640	2440	2680
10	Cr	74	88	60	75	41	70	44	80
11	Mn	943	536	656	695	639	744	795	790
12	Fe	19100	29100	16300	22800	18800	24800	22000	24000
13	Cu	3080	502	502	748	90	497	145	77
14	Zn	17700	779	2010	792	197	591	330	154
15	Pb	314	217	177	164	113	139	175	91

Table 4 Contamination Factor (CF) for soil pollution near two dug wells in the first time and second time

Sr. No	Symbol	Contamination Factor (CF)							
		Yarma Dug Well				Cow Lake Dug Well			
		First time		Second time		First time		Second time	
		S_1W	S_1C	S_1W	S_1C	S_2W	S_2C	S_2W	S_2C
1	Mg	1.299	1.416	1.006	1.087	1.000	1.416	1.185	1.359
2	Al	1.172	1.241	1.030	1.206	1.000	1.132	1.106	1.302
3	K	1.201	1.180	1.159	1.220	1.000	1.707	1.131	1.269
4	Cr	1.805	2.146	1.364	1.705	1.000	1.707	1.000	1.818
5	Mn	2.235	1.270	1.075	1.139	1.514	1.763	1.303	1.295
6	Fe	1.137	1.732	1.000	1.399	1.119	1.476	1.349	1.472
7	Cu	34.222	5.578	6.519	9.714	1.000	5.522	1.883	1.000
8	Zn	89.848	3.954	13.052	5.143	1.000	3.000	2.143	1.000
9	Pb	2.935	2.028	1.945	1.802	1.056	1.299	1.923	1.000

Table 5 Modified Degree of Contamination (mC_d) for soil pollution near two dug wells in first time

Sample location	S_1W	S_1C	S_2W	S_2C
mC_d	15.095	2.283	1.077	2.049

Table 6 Modified Degree of Contamination (mC_d) for soil pollution near two dug wells in second time

Sample location	S_1W	S_1C	S_2W	S_2C
mC_d	3.128	2.713	1.447	1.279

Table 7 Pollution Load Index (PLI) for soil pollution near two dug wells in first time

Sample location	S_1W	S_1C	S_2W	S_2C
PLI	3.484	1.966	1.067	1.773

Table 8 Pollution Load Index (PLI) for soil pollution near two dug wells in second time

Sample location	S_1W	S_1C	S_2W	S_2C
PLI	1.879	1.941	1.397	1.256

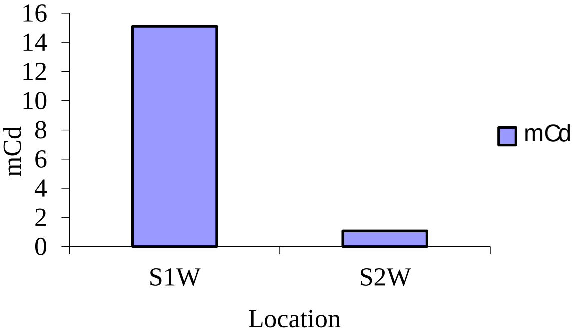

Figure 7 Comparison of modified degree of contamination (mC_d) for soil pollution near Yarma Dug Well and Cow Lake Dug Well in first time

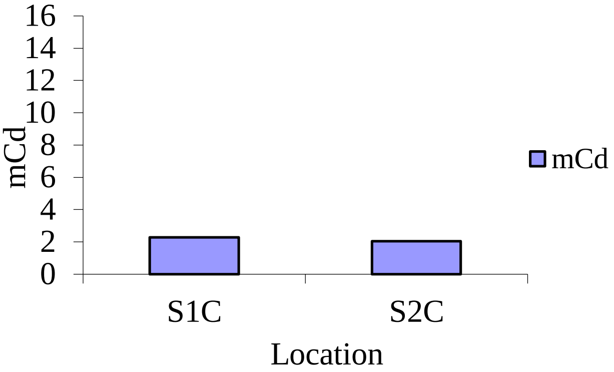

Figure 8 Comparison of modified degree of contamination (mC_d)for soil pollution in the bank of Shwe-Ta-Chaung Creek near Yarma Dug Well and Cow Lake Dug Well in first time

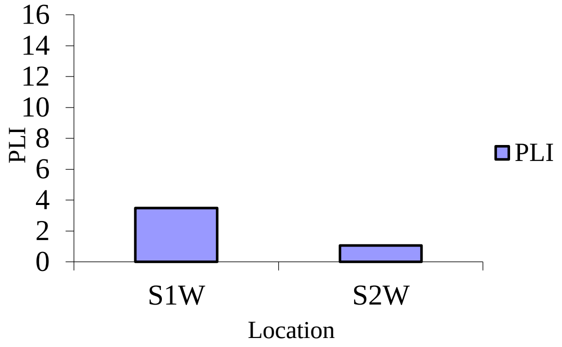

Figure 9 Comparison of pollution load index (PLI) for soil pollution near Yarma Dug Well and Cow Lake Dug Well in first time

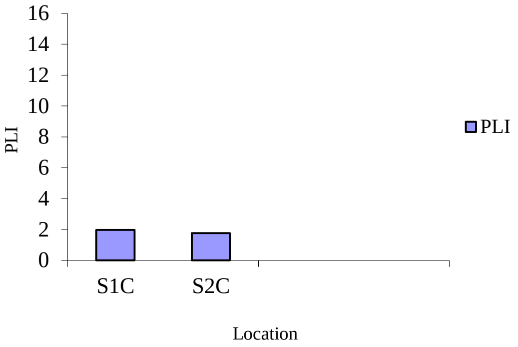

Figure 10 Comparison of pollution load index (PLI) for soil pollution in the bank of Shwe-Ta-Chaung Creek near Yarma Dug Well and Cow Lake Dug Well in in first time

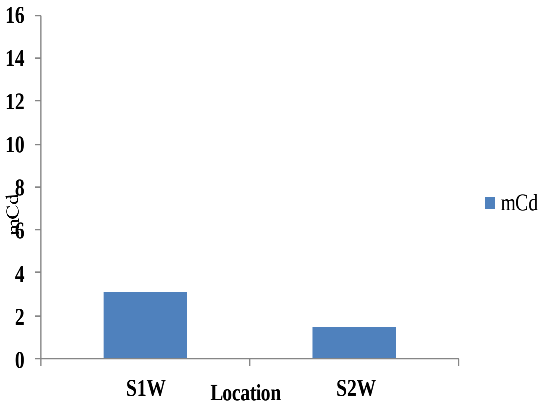

Figure 11 Comparison of modified degree of contamination (mC_d) for soil pollution near Yarma Dug Well and Cow Lake Dug Well in second time

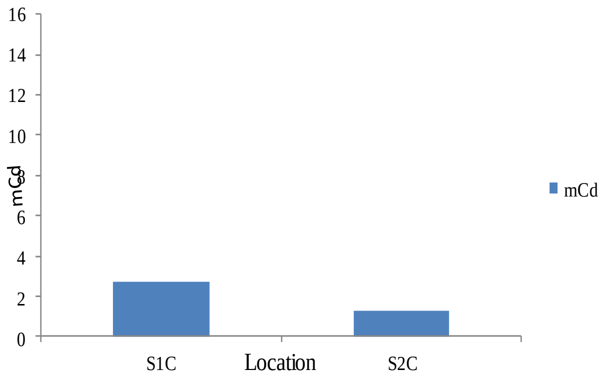

Figure 12 Comparison of modified degree of contamination (mC_d) for soil pollution in the bank of Shwe-Ta-Chaung Creek near Yarma Dug Well and Cow Lake Dug Well in second time

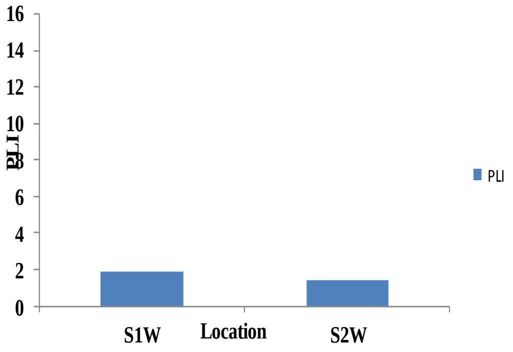

Figure 13 Comparison of pollution load index (PLI) for soil pollution near Yarma Dug Well and Cow Lake Dug Well in second time

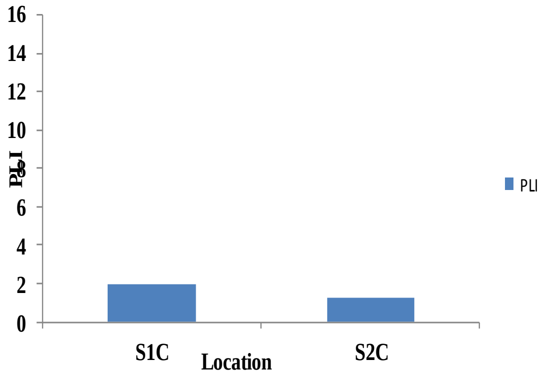

Figure 14 Comparison of pollution load index (PLI)for soil pollution in the bank of Shwe-Ta-Chaung Creek near Yarma Dug Well and Cow Lake Dug Well in second time

Conclusion

Water treatment will be needed to describe those processes used to make water more acceptable for a desired end-use. These can be used to get drinking water and for industrial processes, medical and many other uses. The goal of all water treatment process is to remove existing contaminants in water. Surface water usually needs to be filtered and disinfected, while ground water often needs to have hardness (Ca and Mg) removed before disinfection. Effective municipal wastewater treatment system to human health, ecosystem stability, and water quality will be needed. The results of water samples indicate that water supply wells should not be located near the disposal area. Moreover, garbage should not be dumped near the wells. Although the creek near Yarma Dug Well is not lined by concrete and the creek near Cow Lake Dug Well is lined by concrete. It is indicated that the water supply wells are impacted by contamination associated with waste water.

The waste water creek should be reconstructed with appropriate protection. The creek is too shallow so that it is flooded during the rainy season and the waste water reached to the base of the well. The creek should be constructed with concrete. So the garbage should not be dumped near the well base. Soil around Yarma Dug Well adjacent to the rubbish filter site along Shwe-Ta-Chaung Creek is more polluted than Cow Lake Dug Well region. The pollution around Yarma Dug Well is due to garbage landfills. It is indicated that the water supply wells are impacted by contamination associated with waste water. Humans and animals should not use the wells located near the wastewater creek for any purpose.

Acknowledgements

First and foremost I would like to express my gratitude to Dr Aung Kyaw Tin, Pro-Rector of Banmaw University, for his kind permission to carry out this work. I am also grateful to Professor Dr Than Than Lwin., Head of Physics Department, Banmaw University for her valuable suggestions.

References

Foster S S D & Chilton P J, (2004), Hydrogeology Journal, 12, 15

Lawrence A R et al., (2000), Hydrogeology Journal, 8, 564

Natro J P & Kaper J B, (1998), Clinical Microbiology Reviews, 11, 142

World Health Organization, (2006), Guidelines for Drinking Water Quality [electronic resources]

J. Myanmar Acad. Arts Sci. 2020 **Vol. XVIII.No.2B**

DETERMINATIONOF TYPEOF HYPERNUCLEUSFROMA SINGLE LAMBDA HYPERNUCLEUS EVENT IN NUCLEAR EMULSION OF KEK-E373 EXPERIMENT

Seint Seint Aye[1], KhinThan Tint [2], K. Nakazawa[3]

Abstract

The main aim of this research paper is to determine the type of hypernucleus from a single lambda hypernucleus event, which is an event accompanied by one single Λ hyperfragment and invisible Λ hyperon emitted from a Ξ^- nuclear captured at rest, was found in nuclear emulsion of KEK- E373 experiment . It is interpreted as Ξ^- - ^{14}N system decaying into$^{12}_{\Lambda}B + ^{2}_{1}H + \Lambda$ and hyperfragment decay into$t + d + ^{6}_{3}Li + n$. The type of hypernucleus can be determined as lambda boron 12 hypernucleus ($^{12}_{\Lambda}B$).

Keywords: single lambda hypernucleus, nuclear emulsion, lambda boron 12 hypernucleus.

Introduction

The universe consists of various kinds of materials, which are composed of more fundamental particles. They are cluster of atoms consisting of nucleus and electron. Nuclei formed from nucleons, protons and neutrons, are known for nearly three thousand species, experimentally. At present, we have understood that nucleon would be made of quarks, 'u' (up), 'd' (down), 'c' (charm), 's' (strange), 't' (top) and 'b' (bottom). For each quark there is an anti-quark. Baryon and meson are formed from three quarks and a pair of a quark and an anti-quark, respectively. A proton (uud) consists of two up quarks and one down quark along with short-lived constituent of the strong force field. A neutron (udd) consists of one up quark and two down quarks. A lambda (Λ) consists of one up quark, one down quark and one strange quark.

A hypernucleus is a nucleus which contains at least one hyperon (a baryon carrying the strangeness quantum number) in addition to the normal protons and neutrons. Baryon including "*s"* quark is called hyperon.The first hypernucleus was discovered in Warsaw in September 1952 by the Polish physicists Marian Danysz and Jerzy Pniewski, in a stack of photographic emulsions as shown in Figure 1. A hypernucleus was produced by cosmic ray particle (track p) which interacted with a nucleus in the emulsion at A. The ejected hyperfragment (track f) was brought to rest at B where it decayed into three charged particles (A. Zenoni and P. Gianotti)

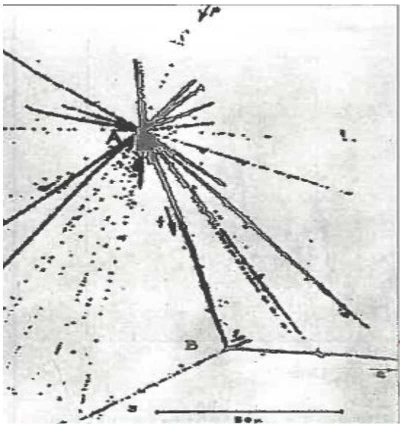

Figure 1 The first hypernuclear event obtained in a nuclear emulsion.

---

[1] Demonstrator, Department of Physics, Technological University(Loikaw), Loikaw, Myanmar

[2] Dr, Lecturer, Department of Physics, University of Mandalay, Mandalay, Myanmar.

[3] Dr, Professor, Physics Department, Gifu University, Gifu, Japan.

KEK-PS E373 Experiment

A hybrid emulsion experiment (E373) was carried out at the KEK proton synchrotron using a 1.66 GeV/c separated K^- beam in 1998, 1999 and 2000. The purpose of the experiment was to study double-strangeness nuclei, such as double-Λ hypernuclei, single Λ hypernucleus , twin Λ hypernuclei and the H dibaryon produced via Ξ^- capture at rest in emulsion with ten times larger statistics than E176 experiment. In this experiment, Ξ^- hyperons were produced in a diamond target via the (K^-, K^+) reaction and were brought to rest in the nuclear emulsion and could form compound nucleus with S = -2 in the emulsion. At the decay of the nucleus, a double-Λ hypernucleus, twin Λ–hypernuclei, single-Λ hypernucleus or *H*- dibaryon (if exist) is emitted, in some case, as shown in Figure (2). The experimental set up of the KEK-PS E373 Experiment and a schematic view at the target region are shown in Figure. 3 and 4, respectively.(H. Takahashi.)

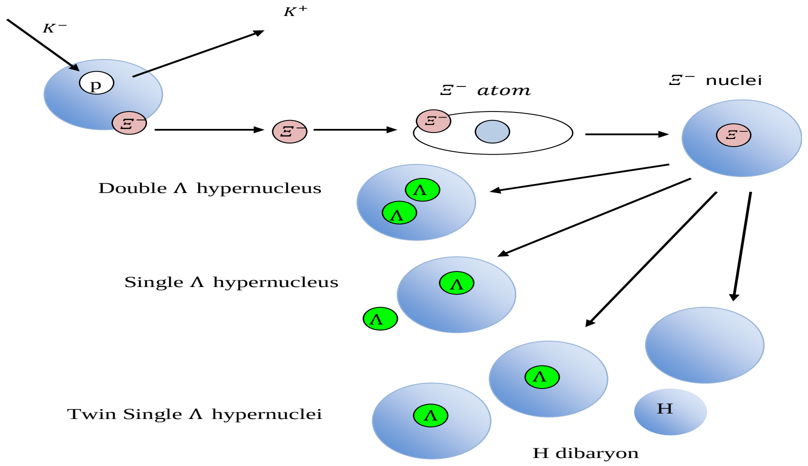

Figure 2 Production process of double-Λ hypernucleus, single Λ hypernucleus, Twin Single Λ hypernuclei and the H dibaryon

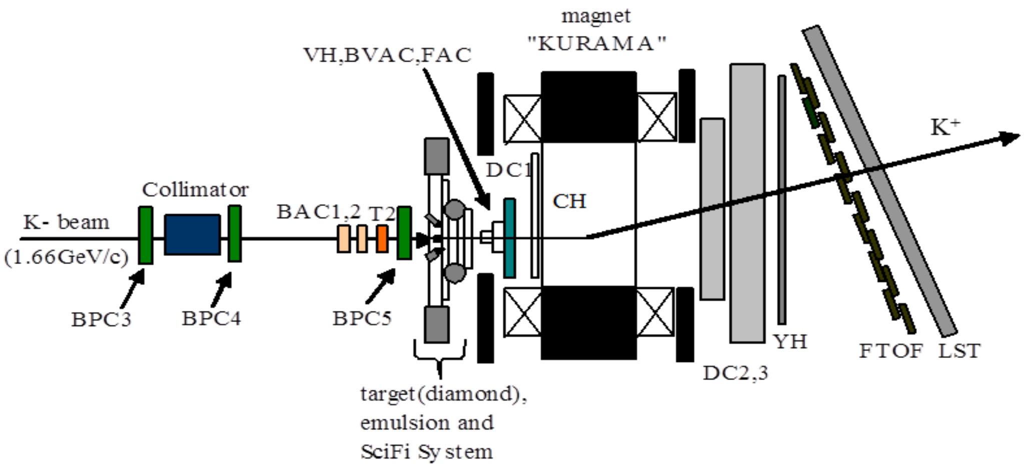

Figure 3 KEK-PS E373 Experiment set up

The Ξ^- hyperon tracks were searched for and followed in the emulsion with an automatic track scanning system guided by the position and angle data of Scintillating-Fiber (Sci-Fi) detector. We have detected 7 double-Λ hypernucleus and 2 twin Λ–hypernuclei events and 35 single Λ hypernucleus events.

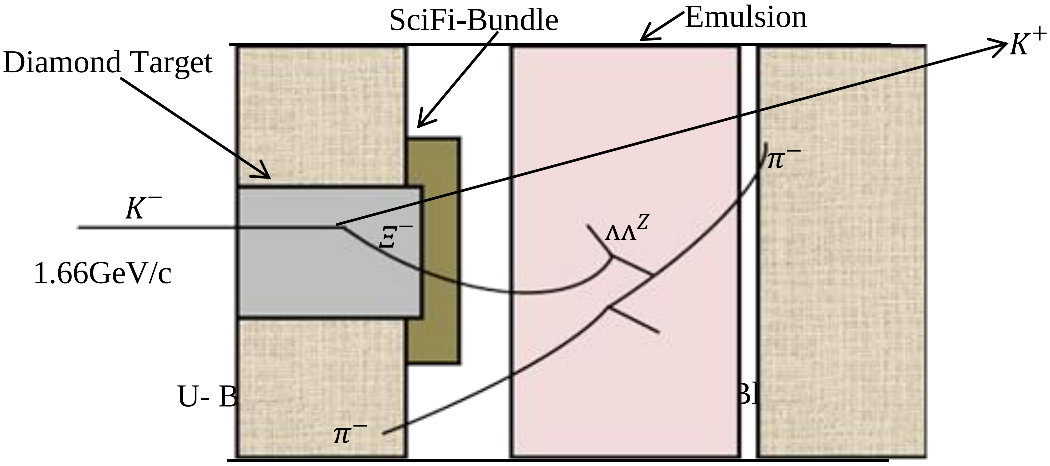

Figure 4 Schematic view at the target region

Nuclear Emulsion

Nuclear emulsion is the key detector to observe the production and decay of S = -2 nuclear system. A nuclear emulsion plate is a photographic plate with a particularly thick emulsion layer and with a very uniform grain size. After exposing and developing the plate, charged particle tracks can be observed and measured using a microscope. The stacks of nuclear emulsion are kept under specific conditions. Thus the photographed events can be preserved for many years.

In E373 experiment, total one hundred stacks made of 69 liters emulsion gel were used. Each stack was composed of eleven (for first ten stacks) or twelve (for the rest stacks) plates with the area of 250×245 mm^2. Figure.5 represents the side view of the constitution of an emulsion stack. Since the first plate was used to connect Ξ^- hyperon tracks from the SciFi-Bundle detector to nuclear emulsion, it was necessary to minimize the distortion of the emulsion gel of the plate.

The emulsion gel was Fuji ET-7C and Fuji-7D, which were developed by Fuji film and Gifu University. All emulsion plates were prepared in Gifu University with the following procedure. First, emulsion gel was poured to one side of the plastic films. They were dried in a drying cabinet which moved emulsion plates automatically so that they were dried uniformly. After drying the emulsion gel, gel was poured to the other side of the plates and dried in the same manner. Then, the emulsion plates were dried again with lower humidity. Each of the emulsion plates was divided to four plates with the size of $24.5 \times 25.0 cm^2$. The density of the emulsion gel can be determined from the volume size and weight measured before and after the beam exposure, the accuracy is not sufficient. The density of the emulsion was 3.60 g/cm^3 on average(A. Ichikawa).

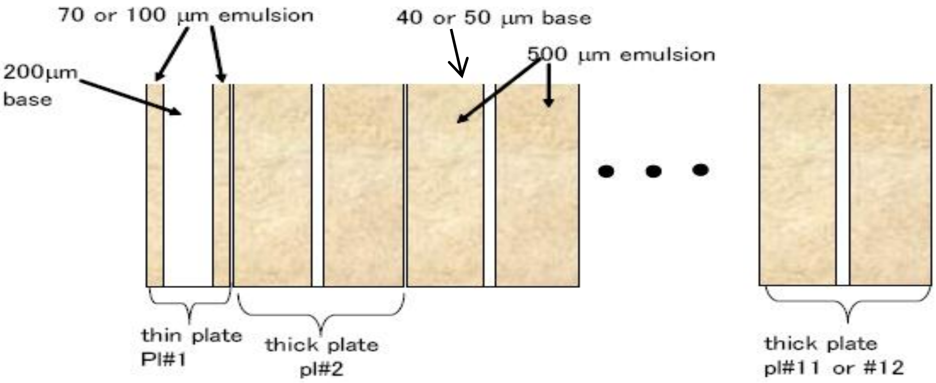

Figure 5 Constitution of an emulsion stack (side view)

Emulsion scanning

The tracks of Ξ^- candidates were searched for the most stream thin-type nuclear emulsion plates (#1) in the area of $24.5 \times 25.0 cm^2$ around the position predicted by the Fiber-bundle.The photograph of the microscope system is shown in Figure (7) for the automatic and semi-automatic scanning system. The thin type emulsions plate is shown in Figure6(a).The events selected by the automatic scanning on the plate #1 were scanned in the remaining thick type plates by the automatic scanning system supported by the human eyes check. Thus, we called the scanning method for thick type emulsion as "semi-automatic". The thick type nuclear emulsions plate is shown in Figure 6(b) (K. T. Tint).

	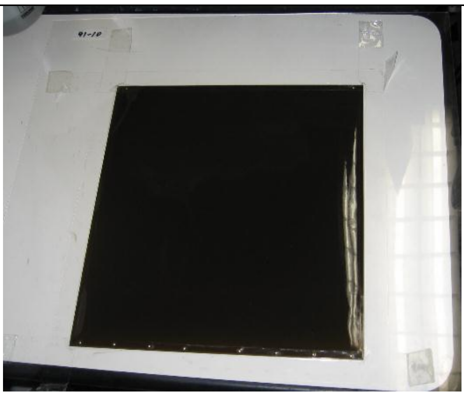
Figure 6(a) Thin type nuclear emulsion plate	**Figure 6(b)**Thicktype nuclear emulsion plate

Figure 7 The Photograph of a microscopic system.

Single Λ Hypernucleus Event

Event Description

A photograph and schematic drawing of a “single Λ hypernucleus” event are shown in Figure 8(a) and (b).A Ξ^- hyperon was captured by a nucleus at point A, from which two charged particles (track #1, #2) and an invisible Λ hyperon were emitted. The particle of track #1 decayed into three charges particles (track #3, #4 and #5) at point B.

Range and Angle Measurement

The range and angles of each track in Single-Λ hypernucleus event were measured by using the microscope system as expressed in Figure 7. The range of the track, R, can be obtained from measured (x, y, z) coordinates which are the clicked points on a track by using the following equation,

$$R = \sqrt{\Delta x^2 + \Delta y^2 + \Delta z^2 \times S^2}$$

where, Δx, Δy and Δz as the lengths in the x, y and z direction respectively. The S is the shrinkage factor for the emulsion gel, defined by the ratio of the original thickness of the plate to the thickness at the time of measurement. The zenith angle ($\boldsymbol{\theta}$) and azimuthal angle (ϕ) of each tracks can be obtained from the coordinates at vertex and suitable click point on track. The imagine range and angles for a track in three dimensional space are shown in Figure.9. The measured lengths and emission angles of these tracks are expressed in Table (1).

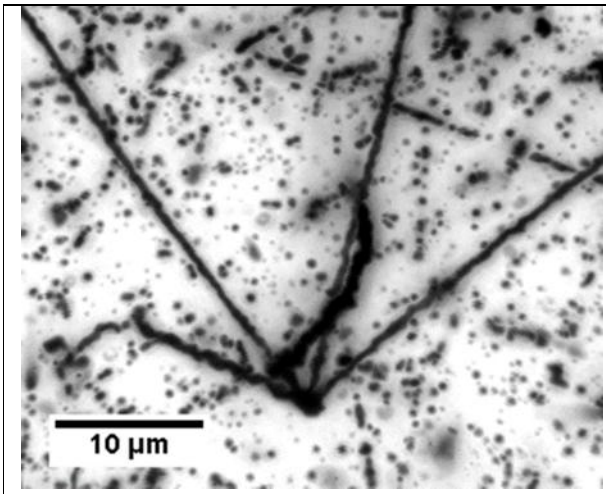

Figure 8(a) Photographic Image of single Lambda hypernucleus

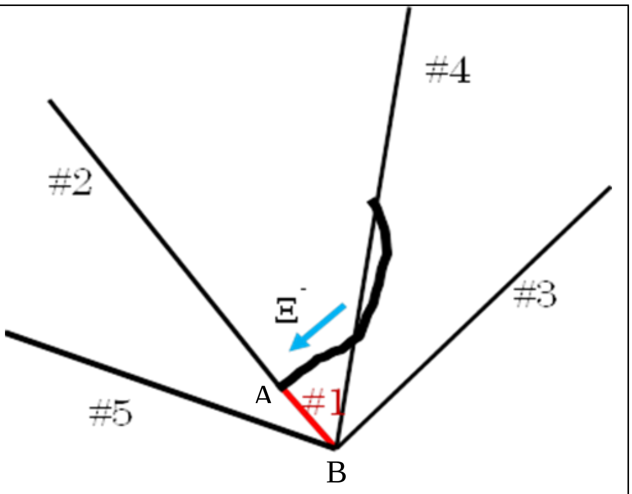

Figure 8(b) Schematic drawing of above single Λ hypernucleus event

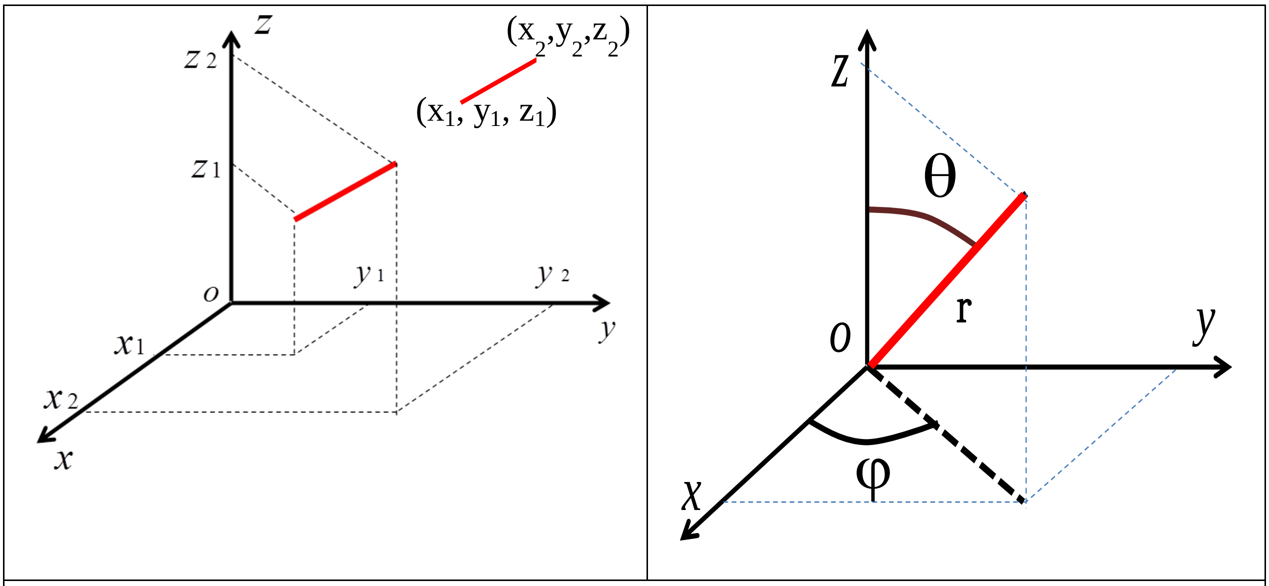

Figure 9 Range and angles of a track in three dimensional space

Table 1 Range and Angle of each track in Single Λ hypernucleus

vertex	Track #	Range(μm)	θ(degree)	ϕ(degree)
A	#1	4.9±0.1	138.2±9.1	139.0±3.6
	#2	47.8±0.4	88.6±1.4	305.8±0.1
B	#3	24.7±0.2	95.2±0.9	221.2±0.4
	#4	475.5±4.1	66.7±0.1	266.2±0.1
	#5	25.4±0.9	97.5±0.3	335.8±1.3

Reconstruction of the event

The event reconstruction in nuclear emulsion is based on the conservation laws of energy and momentum. Once the particle species has been assigned to a track, the kinetic energy of the charged particles can be calculated from their range by means of a range-energy relation. The kinetic energy of neutral particle was calculated from the momentum balance. The errors of kinetic energy come from the errors of range. On the other hand, the errors of total energy were obtained from the errors of range, angles and rest mass.

Firstly, the single Λ hypernucleus (track #1) was identified from its decay point B. The particle species of decay daughters, track #3, #4 and #5, are assigned and considered all the possible decay modes of single Λ hypernucleus. The Q values for each decay mode are obtained and compared with total kinetic energy of track #3, #4 and #5. Since, the total kinetic energies, visible energy E_{visi}, of the three charged particles were smaller than the Q value of the possible decay mode, the total energy for track #1 and decay daughters were considered again and compared. All decay modes of single Λ hypernucleus (track#1) at vertex point B are shown in Table (2). Among them, the most possible decay mode of the single Λ hypernucleus is non-mesonic with neutron emission. Only ${}^{12}_{\Lambda}B$was found to be acceptable for track #1 candidate due to agree their total energy within three standard deviation 3σ.

Secondly, we considered that the Ξ^{-} hyperon was absorbed by a light nucleus $({}^{12}_{6}C, {}^{14}_{7}N, {}^{16}_{8}O)$ in the nuclear emulsion at point A. From which single Λ hypernucleus(track#1), charged particle track (track#2) and invisible Λ hyperon were emitted. The Q value, the kinetic energy of the emitted charged particles (E_{visi}) and the total energy of emitted particles (E_{total}) are calculated and compared. Table (3) summarized the possible decay modes from Ξ^- $+{}^{12}_{6}C/{}^{14}_{7}N/{}^{16}_{8}O$ to a Λ hypernucleus (track#1), track #2 and invisible Λ hyperon. The total rest mass energy (Ξ^- and nuclides of C, N, O) and total energy of (#1 +#2+Λ) were compared.

Results and Discussion

The measured range and angles of all the tracks in single Λ hypernucleus event are described in Table (1). The visible energy E_{visi} is the sum of the kinetic energies of the tracks #3, #4 and #5. The errors of visible energy of the particles of the tracks were obtained from their error of range. We considered not only the total kinetic energy of parent (track #1) and daughters (tracks #3, #4, #5 and n) but also the total energy which includes the kinetic energy and rest mass energy. The errors for total energy of all emitted particles (charged and neutral particles) were obtained from range, angles and mass errors. The some possible decay mode are listed in Table (2).

Table 2 Some possible decay modes of Single lambda hypernucleus (track #1)

Decay mode	**ΔE_{total}(MeV) [$E_{Total\#1}$- $E_{Total\#3+\#4+\#5+n}$]**	**Q-value (MeV)**	**E_{visi}(MeV)**	**Remark**
${}^{7}_{\Lambda}Li \rightarrow$ p + d + t + n	98.23 ±0.47	148.01	15.26±0.45	rejected
${}^{11}_{\Lambda}B \rightarrow$ d + d+ ${}^{6}_{3}Li$ + n	**1.64± 0.69**	**-43.66**	**24.15±0.53**	**rejected**
${}^{12}_{\Lambda}B \rightarrow$ p + t+ ${}^{7}_{3}Li$ + n	-18.64 ±0.70	135.80	26.29±0.53	rejected
${}^{12}_{\Lambda}B \rightarrow$ t + d+ ${}^{6}_{3}Li$ + n	**2.87±0.70**	**130.24**	**24.39±0.53**	**acceptable**

We compared the Q value and E_{visi} for each decay modes. Q-value for all decay modes are greater than the E_{visi}. Since the total energy difference was greater than the three standard deviation, most of the decay modes were rejected. Among all the decay modes of single Λ hypernucleus (track #1), two acceptable decay modes were found. They are, ${}^{11}_{\Lambda}B \rightarrow$ d + d+ ${}^{6}_{3}Li$ + nand ${}^{12}_{\Lambda}B \rightarrow$ t + d+ ${}^{6}_{3}Li$ + n. Q values for these two decay modes are - 43.66 MeV and 130.24 MeV respectively. Since the Q value of 1st decay mode is negative. Therefore, we choose 2nd decay mode as most possible decay mode for single Λ hypernucleus (track #1) for our analyzed event.

The event reconstruction at point A, we considered that the $\Xi-$ hyperon was absorbed by the light nuclei (${}^{12}_{6}C, {}^{14}_{7}N, {}^{16}_{8}O$) in the nuclear emulsion. The results of the possible production modes of the single Λ hypernucleus are listed in Table (3). Among the possible production modes, we choose some decay modes for single Λ hypernucleus which was selected from decay modes. We got two possible production modes, which are described in Table (3). By comparing the total energy differences, the most probable production mode of single Λ hypernucleus (track #1) to be

$${}^{14}_{7}N + \Xi- \longrightarrow {}^{12}_{\Lambda}B + {}^{2}_{1}H + \Lambda.$$

The value of density of emulsion was taken as 3.6 gcm^{-3}. On the other hand, the value of shrinkage factor, 2 was used in the measurement of range.

Table 3 Possible production mode of single lambda hypernucleus (track #2)

Target	**#1**	**#2**		**(total rest mass energy) Ξ⁻ and Target (MeV)**	**#1+#2+ Λ (MeV) Total energy**	**ΔE_{total}**	**Q-value (MeV)**	**E_{visi}(MeV)**
$\mathbf{^{14}_{7}N}$	$\mathbf{^{12}_{\Lambda}B}$	$\mathbf{^{2}_{1}H}$	Λ	**14361.52**	**14436.09**	**74.58**	**13.36**	**7.48±0.44**
$^{16}_{8}O$	$^{12}_{\Lambda}B$	$^{4}_{2}He$	Λ	16216.39	16342.77	126.38	16.47	8.20±0.44

Conclusion

One of the single Λ hypernucleus events has been analyzed based on the conservation laws of energy and momentum. The nuclide of the hypernucleus of the track#1 was selected from its decay point B comparing with production point A. By comparing, the total energy, visible energy and Q value for each decay mode, the possible production event can be interpreted as $^{14}_{7}N + \Xi- \rightarrow {}^{12}_{\Lambda}B + {}^{2}_{1}H + \Lambda$ and $^{12}_{\Lambda}B \rightarrow$ t + d+ $^{6}_{3}Li$ + n. We conclude that the type of hypernucleus of our analyzed event can be determined as lambda boron 12 hypernucleus ($^{12}_{\Lambda}B$).

Acknowledgements

The authors would like to express our profound gratitude to Rectors, Professors from University of Mandalay and Technological University(Loikaw).We also would like to special thanks to the Department of Higher Education, Ministry of Education, Myanmar, for provision of opportunity to do this research and Myanmar Academy of Arts and Science for allowing to present this paper.

References

A. Zenoni, and P. Gianotti (2002), The Physics of Hypernuclei, europhysics news, Features.

A. Ichikawa,(2001),Study of S = -2 Nuclear Systems with Hybrid Emulsion Method, D. Sc. Thesis, Department of physics, Kyoto University, Japan.

H. Takahashi, (2003), Study of Double-Hypernuclei with Hybrid- Emulsion Method, D. Sc. Thesis, Department of Physics, Kyoto University, Japan.

K.T. Tint, (2012),Analysis of Some Hypernucleus Events in Emulsion Counter Hybrid Experiments at KEK(E176 and E373),P.h D. Thesis, Department of Physics, University of Mandalay, Myanmar.

Nicholas T, (1979) “Measurement and Detector of Radiation”, Sec: Edit:, Taylor and Francis.

J. Myanmar Acad. Arts Sci. 2020 **Vol. XVIII.No.2B**

GRAM-SCHMIDT ORTHOGONALIZATION PROCEDURE AND CONSTRUCTION OF TWO-BODY BOUND STATE WAVE FUNCTIONS

Shwe Sin Oo[1], Khin Maung Maung[2]

Abstract

Gram-Schmidt procedure for orthogonalizing vectors or functions is well known. But it is not straight forward to orthogonalize a large set of vectors or functions. We show how this can be accomplished by starting with a set of non-orthogonal set of basis functions. Once orthogonalized, they are normalized so that we have an ortho-normal set of functions. In order to test our functions, they are used as the basis set in expanding the wavefunction of a bound state Schrodinger equation with a specific potential. For test potentials, we use the harmonic oscillator potential and linear potential. The eigen energies and wavefunctions obtained are compared with analytical results for harmonic oscillator potential. For the linear potential, we compare with the standard numerical results. We also compare with the results obtained by using some known ortho-normal basis set of functions.

Keywords: Orthogonalization, basis functions, bound state, wavefunctions

Introduction

Orthogonal set of functions are very useful in many situations. In solving quantum mechanical equations for eigen-energies and eigen-functions, either in position space or in momentum space, basis function expansion methods is commonly applied. If the basis set of functions do not form an orthogonal set, the basis function expansion does not render the eigen-equation into a simple matrix eigen-equation. There are many well known orthogonal set of functions, such as the harmonic oscillator basis, Gauss-Lagauree basis, Jacobi polynomial basis and others, but computational time becomes prohibitively large when we do calculations in three or four body systems. Therefore, in this paper, we study a few simple functions which can be orthogonalized by using Gram-Schmidt orthogonalization procedure.

Gram-Schmidt Orthogonalization Procedure

In this section, we outline the Gram-Schmidt orthogonalization method. We first start with a set of vectors $\{ |g_1>, |g_2>, \ldots, |g_N> \}$. These vectors do not form an orthogonal set, but they are normalized. i.e $< g_i | g_i > = 1$. Next we want to construct an orthonormal set $\{ |f_1>, |f_2>, \ldots, |f_N> \}$ with the property that $< f_i | f_j > = \delta_{ij}$.

We first start by setting $|f_1> = N_1 |g_1>$. Where $N_1 = 1$. Then we define

$$|f_2> = N_2 (\quad |g_2> - C_1 |f_1>)$$

Where C_1 is the constant to be found. We accomplish this by requiring that $|f_2>$ is orthogonal to $|f_1>$.

This gives

$$0 = < f_1 | f_2 > = N_2 (< f_1 | g_2 > - C_1 < f_1 | f_1 >$$

$$C_1 = < f_1 | g_2 >$$

---

[1] Assistant Lecturer, Department of Physics, Mandalay University

[2] Professor, Department of Physics and Astronomy, University of Southern Mississippi, USA

Next we find the normalization constant N_2 by using the normalization condition

$$1 =< f_2| f_2 > = (N_2)^2(< g_2|-< g_2|f_1 >< f_1|)(|g_2 > -|f_1 >< f_1|g_2 >)$$

This gives

$$N_2 = \frac{1}{\sqrt{1-< g_2|f_1 >< f_1|g_2 >}}$$

Continuing in this manner, we obtain

$$|f_N > = N_N(|g_N > -\sum_{i=1}^{N-1} |f_i >< f_i|g_N >)$$

$$N_n = \{ \ 1 - \sum_{i}^{\{n-1\}} < g_n|f_i >< f_i|g_n > \ \}^{-\frac{1}{2}}$$

Now by using the last two equations, we can construct a new ortho-normal set $\{|f_i >\}$.

For practical calculations, it is convenient to derive a recursion relation for

$t_{jn} =< g_j|f_n > = < f_n|g_j >$. By projecting with $< g_j|$ on $|f_n >$ we obtain,

$$< g_j| f_n > = N_n\big(< g_j|g_n > -\sum_{i}^{n-1} < g_j|f_i >< f_i|g_n > \big)$$

or, in terms of t_{jn}

$$t_{jn} = N_n(S_{jn} - \sum_{i=1}^{n-1} t_{ji}t_{in})$$

And the normalization constants are given by

$$N_n = \{ \ 1 - \sum_{i}^{\{n-1\}} t_{in}t_{in} \qquad \}^{-\frac{1}{2}}$$

Note that, here $S_{jn} =< g_j| g_n >$ the overlaps among the original set of vectors $|g_j >$'s. And also note that $j > n > i$ must hold. Now the procedure is clear. First we generate all the overlaps S_{jn} of the non-orthogonal vectors $|g_i >$'s. Then we generate the t_{jn} 's and the normalization constants N_n 's starting with $N_1 = 1$. Then we can generate all the vectors in new orthonormal set $\{ \ |f_i > \}$.

Orthogonalzing functions

Indefining or thogonality of functions, one usually define it with respect to a chosen weight. Let us first define the relation between our vectors and functions on the real line R^1. We will consider the case where both domain and the range of our functions is R^1 . We define our functions by

$$g_n(x) =< x \mid g_n >$$

$$f_n(x) =< x \,|f_n >$$

We demand that our $g_n(x)$ are normalized and our $f_n(x)$ are orthonormal. i.e

$$\int_0^\infty f_n(x) f_m(x)\, w\, dx = \delta_{nm}$$

Here w is the weight function and we choose $w = x^2$. In many physics applications, where the domain of the function is the three dimensional space, the weight function w is x^2 which is part of the volume element in 3-dimensional case. For one-dimensional case, w is usually taken to be unity..i.e w=1.

Example set of functions

The set of functions that we choose to test our Gram-Schmidt procedure is a set of non-orthogonal Gaussian functions which are already normalized. They are given by

$$g_i(x) = \frac{2}{(\pi)^{\frac{1}{4}}}(2A)^{\frac{3}{4}} \exp(-n_i x^2)$$

Where $A = i^2 b$. Here we choose $n_i = i\, b$, where b is a parameter to be chosen. For example b=0.01 . The index iruns from 1 to N, where N is the number of functions to be orthogonalized.

The overlap of these functions $g_i(x)$are

$$S_{ij} = \int_0^\infty g_i(x) g_j(x) x^2 dx = \frac{\sqrt{\pi}}{4}\; 1/(A+B)^{\frac{3}{2}}$$

With $B = j^2 b$. Note that here we are using $w = x^2$ which will be suitable for realistic 3-dimensional quantum mechanical calculations. We can also use w=1 for 1-dimensional problems such as 1-dimensional harmonic oscillator.

Application

We consider two applications. The first one is the 1-dimensional harmonic oscillator problem. The solution is well known and is given as a half-integer multiple of $\hbar\omega$. Since the exact ground state wave function of the harmonic oscillator problem is a simple Gaussian, our calculations yield the exact results with even a few number of basis functions. The interesting one is the Schrodinger equation with linear potential. i.e. $V(r) = Ar$ where A is the strength of the potential. This potential is usually used as the confining potential for the bound states of quarks or in meson spectra where meson are described as bound states of a quark and an anti-quark. Here we choose to solve in momentum space. The Schrodinger equation in momentum space for l^{th} state can be written as

$$\frac{p^2}{2m}\phi_l(p) + \int_0^\infty V_l(p,p')\phi_l(p')p'^2\, dp' \;= E\phi_l(p)$$

Here $V_l(p,p')$ is the l^{th} partial wave component of $< p|\, V|p' >$ which is the Fourier transform of the position space potential $V(r)$. i.e

$$< p|V|p' > = \frac{1}{2\pi^2 q}\int_0^\infty V(r) Sin(qr) r\, dr$$

$$V_l(p,p') = 2\pi \int_{-1}^{1} < p|V|p' > P_l(x)dx$$

For l=0

$$V_{l=0}(p,p') = \frac{1}{\pi pp'}\frac{1}{2}\log(\ |(y+1)/(y-1)| \ )$$

Where $$y = \frac{p+p'}{p-p'}$$

Fourier was done by first introducing a damping factor in the potential i.e$V(r) = A\,r\,exp(-\eta r)$ where η is the damping factor which was taken to be zero later. To take care of the singularity in the potential, the substraction procedure of Maung et al .In order to solve this equation we expand the wave function in our ortho-normalized basis set

$$\phi_l(p) = \sum_i C_i f_i(p)$$

After this expansion, and by projection with $f_j(p)p^2$ and integrating over p we obtain a matrix eigen value equation

$$\sum D_{ji} C_i = E C_j$$

Where the matrix D_{ji} is given by

$$D_{ji} = \int_0^\infty \frac{p^2}{2m} f_i(p) f_j(p) p^2 dp \ + \ \int\int V_l(p,p') f_j(p) f_i(p') p'^2 dp' p^2 dp$$

Now after the matrix D_{ji} is calculated, we can solve the matrix eigenvalue equation. The usual eigen-routines provides us with the energy eigen-values and eigen-vectors whose components are the expansion coefficients $C_i's$. With the strength of the linear potential A=1GeV^2,mass m=1 GeV the exact energies of this eigen-equation are the roots of the Airy's functions. The wave-functions can be constructed once the expansion coefficients $C_i's$ are found.

We present our results in the following table. Here we use b=0.2 Note that b is the variational parameter which is chosen to minimize the eigen energy. As the number of basis function used is increased, the value of b becomes unimportant.

	N=4	**N=10**	**N=18**	**Exact answer [2] Ref. [3,4] 20 functions**
Ground State	2.3506473	2.33810741	2.33810741	2.33810741
1st excited state	4.6909371	4.08794945	4.08794944	4.08794944
2nd excited state	9.8607089	5.52056779	5.52055983	5.52055983
3rd excited state	28.625702	6.79152313	6.78670809	6.78670809
4th excited state		8.09869283	7.94413359	7.94413359

Conclusion

We have presented Gram-Schmidt orthogonalization procedure which is useful in quantum mechanical calculations. We derive a recursion relation for the overlap functions $< g_i|f_j >$which is useful in the calculation. We constructed an orthonormal basis set of functions from a previously defined set of functions which are not mutually orthogonal. We used these orthonormal set of functions in solving the Schrodinger equation in momentum space with linear potential. We obtained very satisfactory results.

Acknowledgement

I would like to thank Dr Thida Win, Rector, Mandalay University and Professor Dr. Lei Lei Win, Head of department of Physics, Mandalay University for their kind permission to carry out this work.

References

B. Keister and W. Polyzou, J. Comp. Phys**. 134,** 231 (1997).

C. Werneth, M. Dhar, K. M. Maung , Euro. J. of Phys. **31**, 693 (2010)

Handbook of Mathematical Functions, by M. Abramowitz and I. E. Stegun, ISBN-0-486-61272-4

Khin Maung Maung, D. E. Kahana, and John W. Norbury, Phys. Rev. D. (**47**) 3, 1182 (1993)

J. Myanmar Acad. Arts Sci. 2020 **Vol. XVIII.No.2B**

GAMMA RAY COMPUTED TOMOGRAPHY (CT) FOR THE INDUSTRIAL APPLICATION

Khin Ye Lwin[1], Moe Phyu Hlaing[2]

Abstract

Radioisotope Techniques have been used as diagnostic tools in various industrial sectors to improve production efficiency and to gain information that cannot be obtained in any other way. The gamma ray computed tomography (CT) is a radioisotope technique largely used for troubleshooting and optimization of the industrial process plants. The experimental research to investigate the interior distribution of density of the different density materials and the phase distribution inside the multiphase system have been carried out using GORBIT - the first generation gamma CT system at the Radioisotope Techniques Laboratory in the Division of Atomic Energy. The GORBIT CT system consists of one collimated radioactive source, one collimated detector, a radiation rate-meter, two servo motors and an electronic control system. The associated GORBIT software was used for controlling the hardware's operations and logging data. The objects were located in the middle of the gantry. The data were collected by measuring the radiation emitted from the radiation source moving around the objects. The radiation source was 50mCi of Co-60 gamma source and the detector was a 2″ × 2″ NaI (TI) gamma scintillation detector. Tomography images were reconstructed from the acquired gamma transmission data by Filter Back Projection (FBP) algorithm using the separate GORBIT software. The experimental results of two dimensional CT images interpreted the cross sectional profiles of the objects and multiphase system and also provided information on the internal structure of the objects including defects and their dimensions. Therefore the gamma computed tomography (CT) has proved a powerful non destructive testing and evaluation tool and has wide range of applications in the petrochemical and chemical process industries: distillation columns, packed beds, risers, fluidized beds and other multiphase processing units.

Keywords: Radioisotope Techniques, Industrial Process Gamma Tomography, Filtered Back Projection, Image Reconstruction, Petrochemical Industry

Introduction

The potentials of imaging with ionizing radiation were discovered almost at the same time as the ionizing radiation itself in the late 1890s.The imaging modality with high interesting is tomographic imaging which is cross-sectional imaging. The computerised tomography (CT) is used worldwide for a large number of applications in medicine as a diagnostic tool for different diseases and in industry for the development of modern engineering materials, a non destructive tool for determining the quality of the materials used in various industrial sectors. Gamma computed tomography for process visualization is a complementary advanced technology for optimizing industrial process design and operation, applicable for many industrial multiphase flow systems: distillation columns, packed beds with two phase flows, risers, fluidized beds, and other multiphase processing units. It is capable of measuring the phase distribution inside multiphase equipment without disturbing normal operations and it provides unique technique for quantification of multiphase opaque flow fields, which cannot be accomplished by any other means. The tomographic technique produces a two dimensional image of the cross-section of an object without physically sectioning and jeopardizing it. The indications revealed in CT images can be readily interpreted in terms of mass density. The CT images also provide information on

---

[1] Dr, Principal Scientist, Division of Atomic Energy, Department of Research and Innovation

[2] Director, Material Science and Research Division, Department of Research and Innovation

the internal structure of the object including defects and their dimensions[IAEA-TECDOC-1589, Ramamoorthy N. et al, Ashraf M. M. et al].

The gamma computed tomography experiments have been carried out at the Radioisotope Techniques Laboratory in the Division of Atomic Energy. The objectives of the experimental researches were to investigate the interior distribution of density of the different density materials, the internal structure of the object and the phase distribution inside the multiphase system using GORBIT-the first generation gamma CT system for the problem-solving application in industries.

Materials and Methods

Gamma Ray Computed Tomography

Computed tomography is a technique aimed to estimate the interior distribution of density of an object by measuring the radiation emitted from a radiation source moving around the object. Tomography refers to the cross-sectional imaging of an object from either transmission or reflection data collected by illuminating the object from many different directions. Gamma ray computed tomography methods measure the attenuation of an incident beam that travels in a straight path through an object. The incident beam is partially absorbed and scattered in the object of interest, with the remaining transmitted radiation traveling in a straight line to the detector. Figure 1 shows schematic principle of gamma computed tomography(CT) system. The amount of attenuation is related to the atomic number of the phases distributed in the object, as well as their density distributions [R. Abdul Rahim]. The data were collected by measuring the radiation emitted from the radiation source moving around the objects.

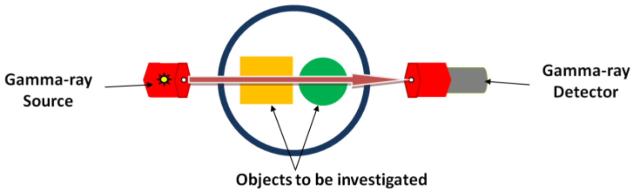

Figure 1 Schematic principle of gamma computed tomography(CT) system

Principle of Computed Tomography

To describe the principle of computed tomography technique, consider a well collimated beam of mono-energetic radiation passing through a homogeneous object. If the intensity of the incident beam of radiation is I_0 and the transmitted intensity through the object in the direction of beam is I, then the attenuation of a well collimated radiation beam through a homogeneous object is given by equation (1).

$$I = I_0 \, exp[-\mu(x,y)x] \; \ldots\ldots\ldots\ldots \; (1)$$

where x is the thickness of object traversed by the radiation and $\mu(x,y)$ is the linear attenuation coefficient within a cross sectional plane of the object. For an inhomogeneous material equation (1) can be rewritten as:

$$ln\frac{I_0}{I} = \int_L \mu(x,y)dx \ldots\ldots\ldots\ldots\ldots (2)$$

The line integral over the path length L, known as the ray sum, is the Radon Transform of μ(x,y).The simplest arrangement for measuring the attenuation coefficients of the first generation transmission CT scanning system is shown in Figure 2.The source and the detector system allow a sequence of discrete transmitted measurements through a defined cross section as it traverses across the object with the source-detector coordinate frame (x, y) and rotated through an angle θ with respect to the object frame (x, y). Since μ (x, y) is a density function of (x, y), replacing μ (x, y) by f(x, y), equation (2) can be rewritten as

$$\ln\frac{I_0}{I} = \int f(x,y)ds \ldots\ldots\ldots\ldots (3)$$

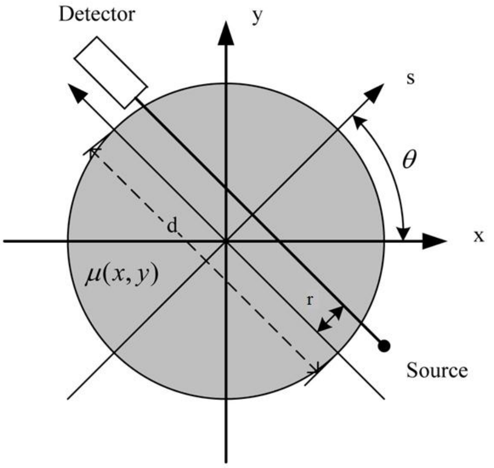

Figure 2 Arrangement of a transmission CT scanning system

Ray paths are described by an (r, S) coordinate system which is rotated by the same angle. Each ray is thus specified by coordinates (r, θ) where θis the angle of the ray with respect to x-axis and r is its distance from the origin. The coordinate S represents the path length along the ray.

$$P(r,\theta) = \int_{r,\theta} f(x,y)ds \ldots\ldots\ldots\ldots (4)$$

For imaging purposes with a radioisotope P(r, θ) , known as ray sum is directly proportional to the detector signal neglecting gamma ray attenuation and changes in the solid angle of the detector [Ashraf M. et al, Avinash C. Kak et al, IAEA-TECDOC-1589].

Image Reconstruction Methods

A number of methods are used for the reconstruction of images in computerized tomography. Two dimensional Fourier reconstruction and Filtered back projection reconstruction are the two analytical reconstruction methods used for image reconstruction. Analytical reconstruction is based on the direct solution of equation (4). The objective of CT algorithms is to inverse a set of equations relating the measurements to the image. The recorded data set are processed by dedicated computer software, which uses mathematic reconstruction algorithms, to generate the cross-sectional images of the object. The process tomography is to provide cross sectional information: spatial resolution, temporal resolution, contrast and linearity. Spatial resolution is strongly linked to the collimation of detectors, the number of steps per projection and the number of projections. Contrast is linked to the energy source, the activity and the detector type[Ashraf M. et al, IAEA-TECDOC-1589].

First Generation Gamma Computed Tomography System (GORBIT)

GORBIT is the first generation of gamma transmission computed tomography system based on the configuration of one source-one detector. The system is operated automatically based on the settings from computer. It consists of two main components: hardware and software. The hardware contains mechanical assembly, one collimated radioactive source and one collimated gamma detector, electronic part includes a radiation rate-meter, two servo motors and an electronic control system. The associated software is used for controlling the hardware's operations and logging data. Tomography images can be reconstructed from the acquired gamma transmission data by using a separate software designing based on Filter Back Projection(FBP), Algebraic Reconstruction Technique (ART) and Expectation Maximization (EM) algorithms.

The GORBIT system is designed to operate under control of an automatic control system (eGORBIT). Typical configuration of the control system would include 2 servo motors (1 for parallel motion, 1 for rotary motion) and their drivers, three photo micro sensors, a central control board and a computer program. Figure 3 illustrates the general arrangement of whole GORBIT system. There are GORBIT gantry, eGORBIT and a personal computer (laptop or desktop). The GORBIT gantry is a flexible design which can be fitted to some kind of object configurations. The Gantry can be set up horizontally, vertically or obliquely. The associated eGORBIT software was used for controlling the hardware's operations and logging data[User Manual of GORBIT].In the experimental research, GORBIT CT system which was provided by IAEA has been used to investigate the interior distribution of density of the objects.

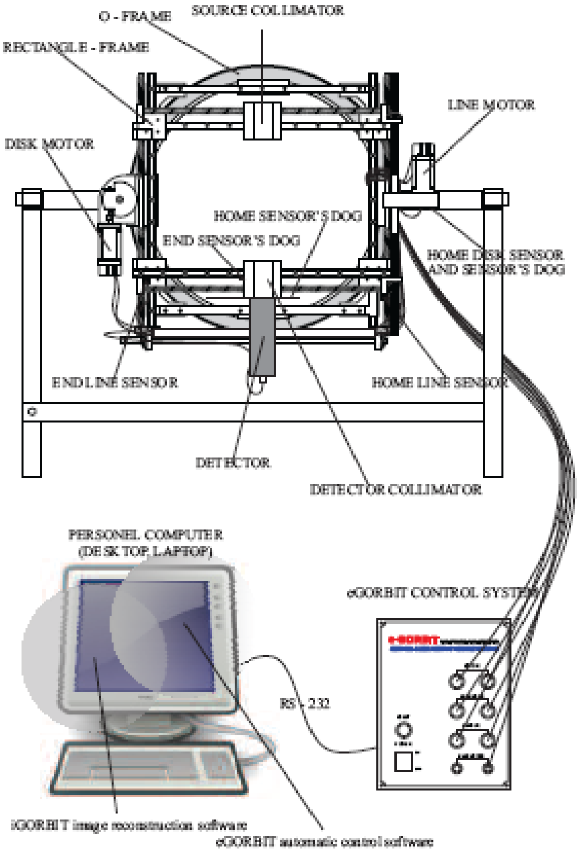

Figure 3. General arrangement of whole GORBIT system

Image Reconstruction

The iGORBIT is an image reconstruction program and used to reconstruct the images from the data set acquired by GORBIT system. The iGORBIT was designed based on four basic algorithms: Back Projection (BP), Filter Back Projection(FBP), Algebraic Reconstruction Technique (ART), and Expectation Maximization (EM). All of these algorithms used in this program to generate the images, which is 256x256 pixels of maximum resolution [User Manual of GORBIT].

Materials

In the gamma ray CT experiments, the blocks of different density materials of wood, polyethylene and concrete were used to investigate the interior distribution of density and a lead block was used to determine the internal structure of the object. 10 inches diameter polyvinyl Chloride (PVC) pipe was used to define the region of interest (ROI) for the CT measurement. For phase distribution experiment, 8 inches diameter of iron pipe partially-filled with crude oil and covered with plastic sheets at both ends was created as the multiphase system.

Figure 4 The horizontal arrangement for the measurements of different density and internal structure of the objects

Figure 5 The vertical arrangement for the measurement of the phase distributionin the pipe

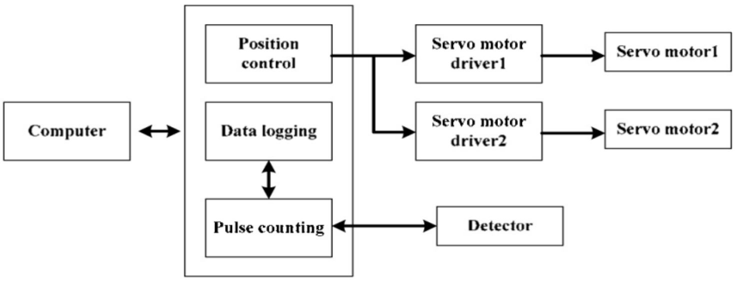

Figure 6 The block diagram of the operation of the CT system

When the experimental setting was completed, the gamma source and the detector were installed in respective containers. The radiation source was 50mCi of Co-60 gamma source and the detector was a 2″ × 2″ NaI (TI) gamma scintillation detector. After the objects to be imaged were located in the middle of gantry, the source and the detector were placed in the initial position. Then set up the parameters for automatic scan by using eGORBIT software installed in the computer.

The resolution of the image is linked to the number of projections and the number of steps per projection. In the experiment, therefore firstly, three different parameter sets of view (number of projections) and trays (number of steps per projection) were used to compare the resolution of the images. Table 1 shows the required parameters for three different scans of an object and figure 7 shows the parameters for automatic scan in eGORBIT software.

Table 1 Three different parameter sets for three scans of an object

Scan	Number of views	Number of rays
Scan 1	16	32
Scan 2	32	64
Scan 3	64	128

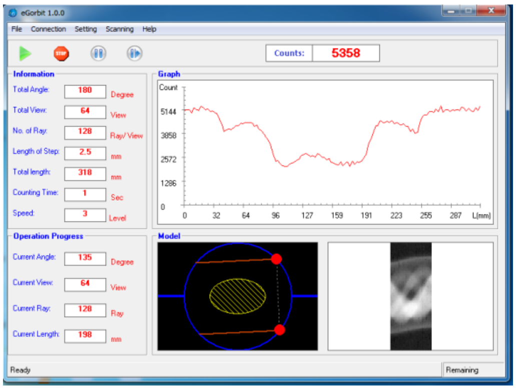

Counts: 5358

Information
Total Angle: 180 Degree
Total View: 64 View
No. of Ray: 128 Ray/ View
Length of Step: 2.5 mm
Total length: 318 mm
Counting Time: 1 Sec
Speed: 3 Level

Operation Progress
Current Angle: 135 Degree
Current View: 64 View
Current Ray: 128 Ray
Current Length: 198 mm

Ready
Remaining

Figure 7 The parameters for automatic scan by using eGORBIT software

To scan the object, the source and the detector were moved according to preset steps simultaneously by one motor for a parallel beam scanning, whereas the other motor rotated the gantry at the preset projection angles within 180°. The motors were controlled through a driver linked to a data logger for PC control. The driver makes the motor finish the motion by the input pulses. The input pulse was generated from the data logger. The data logger transmitted the acquired data to a PC and controlled the two servo motor drivers for the rotating and scanning motions. It processed the measured radiation counts as two-dimensional data, the rows and columns which indicate the index for the location of a detector bin and the projection angle, respectively.

Tomography images were reconstructed from the acquired gamma transmission data by Filter Back Projection (FBP) algorithm using the separate iGORBIT software. The comparison of the reconstructed images of three different scans of an object are shown in figure 8.

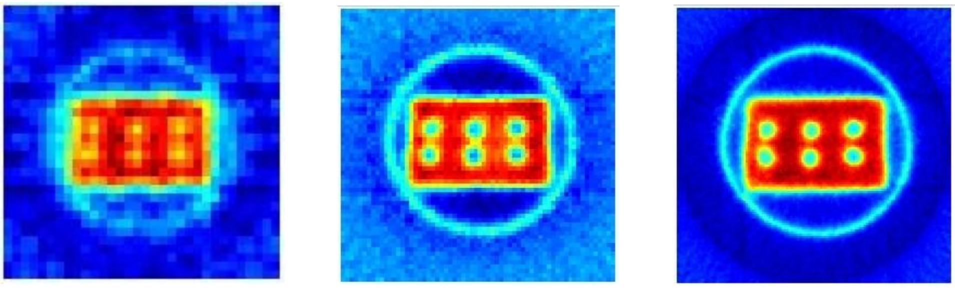

(a) Scan 1 (16x32) (b) Scan 2 (32x64) (c) Scan 3 (64x128)

Figure 8 The comparison of reconstructed images of three different scans of an object

These images can be determined that the image of Scan 3 with the parameters 64x128 is with the highest resolution. Therefore the gamma ray computed tomography automatics cans for the different density materials (wood, polyethylene and concrete), the lead block and the multiphase system pipe performed with 64 projections and 128 rays (64 x 128 pixels)for 180°.

Results and Discussion

Tomography images of the blocks of different density materials of wood, polyethylene and concrete, the lead block and the multiphase system pipe were reconstructed from the acquired gamma transmission data by Filter Back Projection (FBP) algorithm using the separate iGORBIT software. The reconstructed cross-sectional images were compared with the optical camera images. The comparison for the interior density distribution of different density objects is shown in figure 9, for the internal structure of lead block is shown in figure 10 and for the phase distribution in the pipe is shown in figure 11.

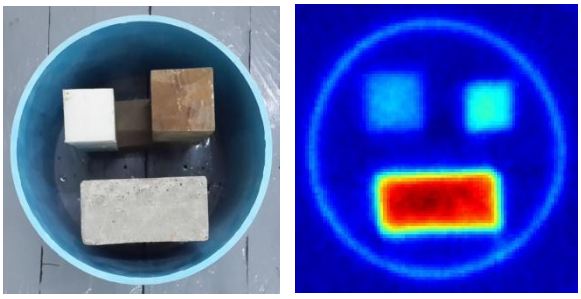

(a) (b)

Figure 9 The comparison of(a) the optical camera image and (b) the reconstructed cross-sectional image of the interior density distribution of different density objects

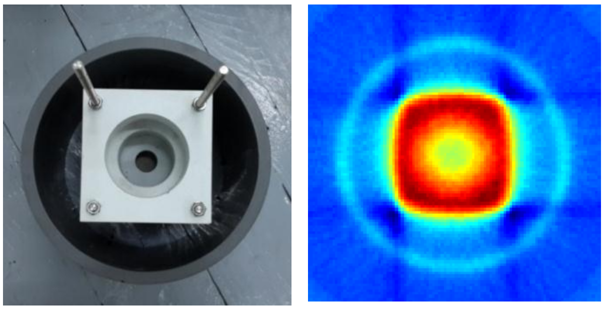

(a) (b)

Figure 10 The comparison of (a) the optical camera image and (b) the reconstructed cross-sectional image of the internal structure of the lead block

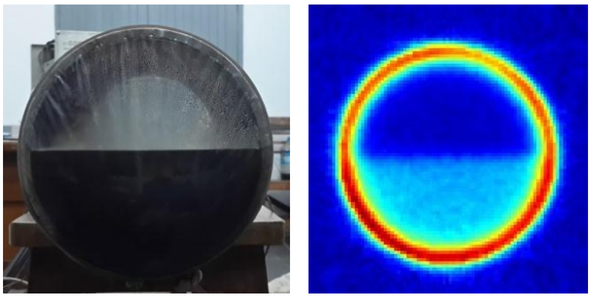
(a) (b)

Figure 11 The comparison of (a) the optical camera image and (b) the reconstructed cross-sectional image of the phase distribution in the pipe

The reconstructed images measured by the different scan parameters can be compared the resolution of the images. The resolution of the tomography image scanned with the highest number of parameters (64x128) is the highest resolution. The experimental results of two dimensional CT images revealed the cross sectional profiles of the objects and multiphase system. The reconstructed images also provided information on the internal structure of the objects including defects and their dimensions. The tomography images can be determined the dimension of the object and the attenuation coefficient of materials by using reconstructed software.

Conclusion

Gamma ray computed tomography system was used to look the interior of the different density materials, the lead block and the multiphase pipe. The experimental results of two dimensional CT images interpreted the cross sectional profiles of the objects and multiphase system and also provided information on the internal structure of the objects including defects and their dimensions. The resolution of the image is linked to the scan parameters. The higher the number of parameters (projections and steps) was used, the higher the resolution of the reconstructed image can be got.

Gamma transmission tomography allows measuring spatial distributions of material based on its attenuation properties. The attenuation properties take into account the nature of material (atomic number) and the density. It means that transmission CT can distinguish phases with significant different attenuation properties due to density (liquid-gas or solid-gas) and/or atomic number. Therefore the gamma computed tomography (CT) has proved a powerful non-destructive testing and evaluation tool and has wide range of applications in the petrochemical and chemical process industries. The success of radioisotope industrial application is due to primarily to the ability, conferred by the unique properties of radioactive materials, to collect data which cannot be obtained by other investigative techniques.

Acknowledgements

The authors acknowledge International Atomic Energy Agency (IAEA) for technical co-operating, providing equipments and transferring technology. The author also thank to Director General and Deputy Director General of Division of Atomic Energy for their supporting. Deeply thank to our team members of Radioisotope Techniques Laboratory for co-operation and successful implementation of research work.

References

Ashraf M. M, Peter Well, "Computerized Industrial Tomography", Report of Non Destructive Testing Group, Radiation and Isotope Application Division, Islamabad, Pakistan, January, 1999

Avinash C. Kak, Malcolm Slaney. "Principles of Computerized Tomographic Imaging", Electric Copy. IEEE PRESS (1999).

IAEA-TECDOC-1589, "Industrial Process Gamma Tomography", Final report of a coordinated research project2003–2007, IAEA, Vienna, May 2008

R. Abdul Rahim, Y. Shaan-Li Susiapan, R. Mohd. Zain, "Introduction to Gamma-Ray Transmission Tomography", Progress in Process Tomography and Instrumentation System: Series 2, Cybernetics, UTM, 2010

Ramamoorthy N., Haji-Saeid M, "Industrial Applications of Radioisotopes and Radiation Technology and Agency's Role", Proceedings of theThird Eurasian Conference on Nuclear Science and its Application, International Atomic Energy Agency,Vienna, Austria, October 5 - 8 , 2004

User Manual of GORBIT First Generation Gamma Computed Tomography System, Centre for Applications of Nuclear Technique in Industry, Da Lat, Vietnam

J. Myanmar Acad. Arts Sci. 2020 **Vol. XVIII.No.2B**

SYNTHESIS AND CHARACTERIZATION OF NICKEL FERRITES PREPARED BY DIFFERENT METHODS FOR HUMIDITY SENSOR APPLICATION

Aung Ye Htun[1], Aye Aye Lwin[2] and Win Kyaw[3]

Abstract

Nickel ferrites, $NiFe_2O_4$, were prepared by three different preparation methods; solid state reaction (SSR) method, chemical co-precipitation (CCP) method and auto-combustion (AC) method. XRD technique was used to investigate the crystalline phase formation and to examine the lattice parameters of the samples. From XRD patterns, the samples analogous to cubic structure and the lattice parameters were found with small variation. The average crystallite sizes were obtained as 74.11 nm (solid state reaction method), 85.31 nm (chemical co-precipitation method) and 49.04 nm (auto-combustion method). Morphological features and porosities of the samples were examined by SEM. The samples were made into circular shaped pellets and their humidity sensitive electrical properties were investigated in the relative humidity range of 50 RH% - 99 RH% with the step of 1 RH% for humidity sensor application.

Keywords: $NiFe_2O_4$, solid state reaction, chemical co-precipitation, auto-combustion, XRD, SEM, humidity sensor application.

Introduction

The increased concern about environmental protection led to the development in sensors field [Patil, (2013)]. Apart from the technological importance ferrite materials have shown advantages in the field of sensors due to its mechanical strength, resistance to chemical attack and stability [Gadkari, (2013)]. Ferrites have spinel structure, which is mainly used in gas, stress and humidity sensors [Ahmad, (2012); Rezlescu, (2002)].

Humidity sensors are potentially in demand in industries like cloth driers, air coolers, broiler forming, cereal stocking and medical field. Humidity sensors based on the metal oxide materials have advantages such as low cost, simple construction and ease of placing the sensor in the operating environment [Attia, (2006)]. The ability of a metal oxide to sense the presence of water molecules depends on the interaction between water molecules and surface of the metal oxide i.e. the reactivity of its surface [Brito, (2010)]. The reactivity depends on the composition and morphological structure, which depends on the preparation procedure.

A large number of methods have been developed to prepare $NiFe_2O_4$ (NFO), such as the standard solid-state reaction method, co-precipitation method, auto-combustion method, solvothermal method and hydrothermal method [Fawzi, (2010); Vagolu, (2013)]. In this work, $NiFe_2O_4$ were prepared by the standard solid-state reaction (SSR) method, chemical co-precipitation (CCP) and auto-combustion (AC) method. The obtained Nickel ferrites were characterized by XRD and SEM to investigate the structural and microstructural characteristics of the samples. Furthermore, humidity sensitive electrical resistance was investigated in this work.

---

[1] Dr, Assistant Lecturer, Department of Physics, Pathein University

[2] Dr, Associate Professor, Department of Physics, Loikaw University

[3] Dr, Associate Professor, Department of Physics, Pyay University

Materials and Method

Preparation of Nickel Ferrites using Three Different Methods

Nickel ferrites, $NiFe_2O_4$, have been prepared by the standard solid state reaction method, co-precipitation method and auto-combustion method. The chemical reagents used were as follows:

(1) Nickel Oxide [NiO] and Ferric Oxide [Fe_2O_3] for standard solid-state reaction method,

(2) Nickel Sulphate Hexahydrate [$NiSO_4.6H_2O$], and Ferrous Sulphate Heptahydrate, [$FeSO_4.7H_2O$] in which Sodium Hydroxide [NaOH] as an agent for co-precipitation method and

(3) Nickel Nitrate Hexahydrate [$Ni(NO_3)_2.6H_2O$] and Ferric Nitrate Nonahydrate [$Fe(NO_3)_3.9H_2O$] in which Urea [$CO(NH_2)_2$] as a fuel for auto-Combustion method.

For solid state reaction method, Nickel Oxide (NiO) and Ferric Oxide (Fe_2O_3) were used. For co-precipitation method, Nickel Sulphate Hexahydrate [$NiSO_4.6H_2O$], and Ferrous Sulphate Heptahydrate, [$FeSO_4.7H_2O$] were used. For auto-combustion method, the stoichiometric ratio of metal nitrates and Urea were used. Flow diagrams of the experimental procedures of the sample processes of three different preparation methods are shown in Figure 1.

XRD and SEM Measurements

The X-ray diffraction measurement was carried out by using RIGAKU MULTIFLEX X-ray diffractometer [Universities' Research Centre (URC), University of Yangon]. Morphological features of the samples prepared by three different methods were investigated by JEOL JSM-5610LV Scanning Electron Microscope (SEM) [Universities' Research Centre (URC), University of Yangon] with the accelerating voltage of 15 kV, the beam current of 50 mA and 5500 times of photo-magnification.

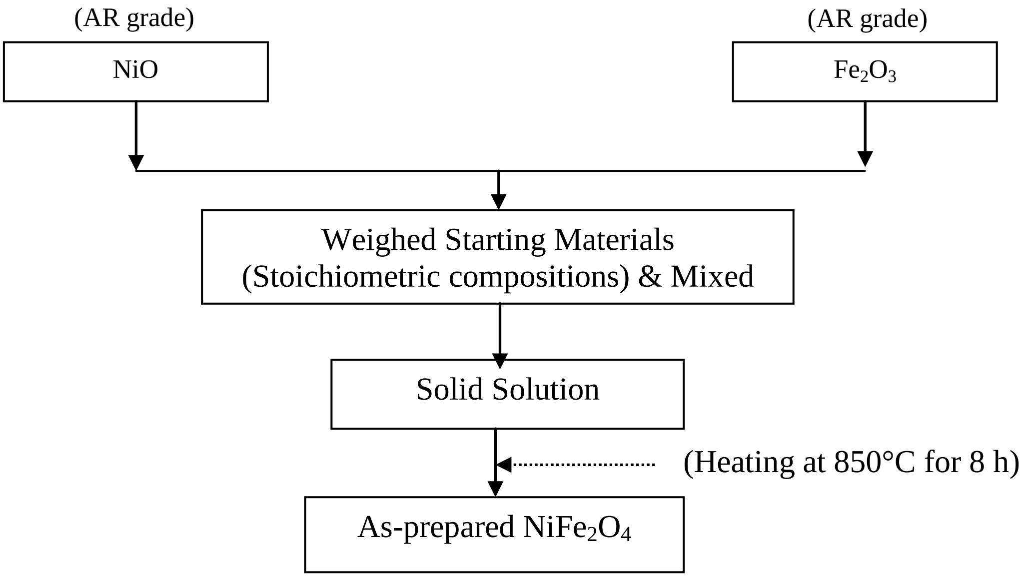

Figure 1(a) Preparation procedure of $NiFe_2O_4$ using solid state reaction method

Humidity Sensitive Electrical Resistance Measurement

Humidity sensitive electrical resistance of the $NiFe_2O_4$ pellets were investigated in the relative humidity range of 50 RH% - 99 RH%. Firstly, the samples were made into circular shape pellets by using SPECAC hydraulic press with the pressure 5 ton (~70 MPa). Thickness and area of the each of the sample were as 2.5 mm and 1.14×10^{-4} m^2 respectively. In this measurement, XSW TDK 0302 Humidity Meter was used as the humidity sensing element. Humidity sensitive electrical resistance was observed by two probe method by using FLUKE 189 digital multimeter. The refrigerator (Haier) was used as the humidity generator. Photographs of the experimental setup of humidity sensitive electrical resistance measurement are shown in Figure 2.

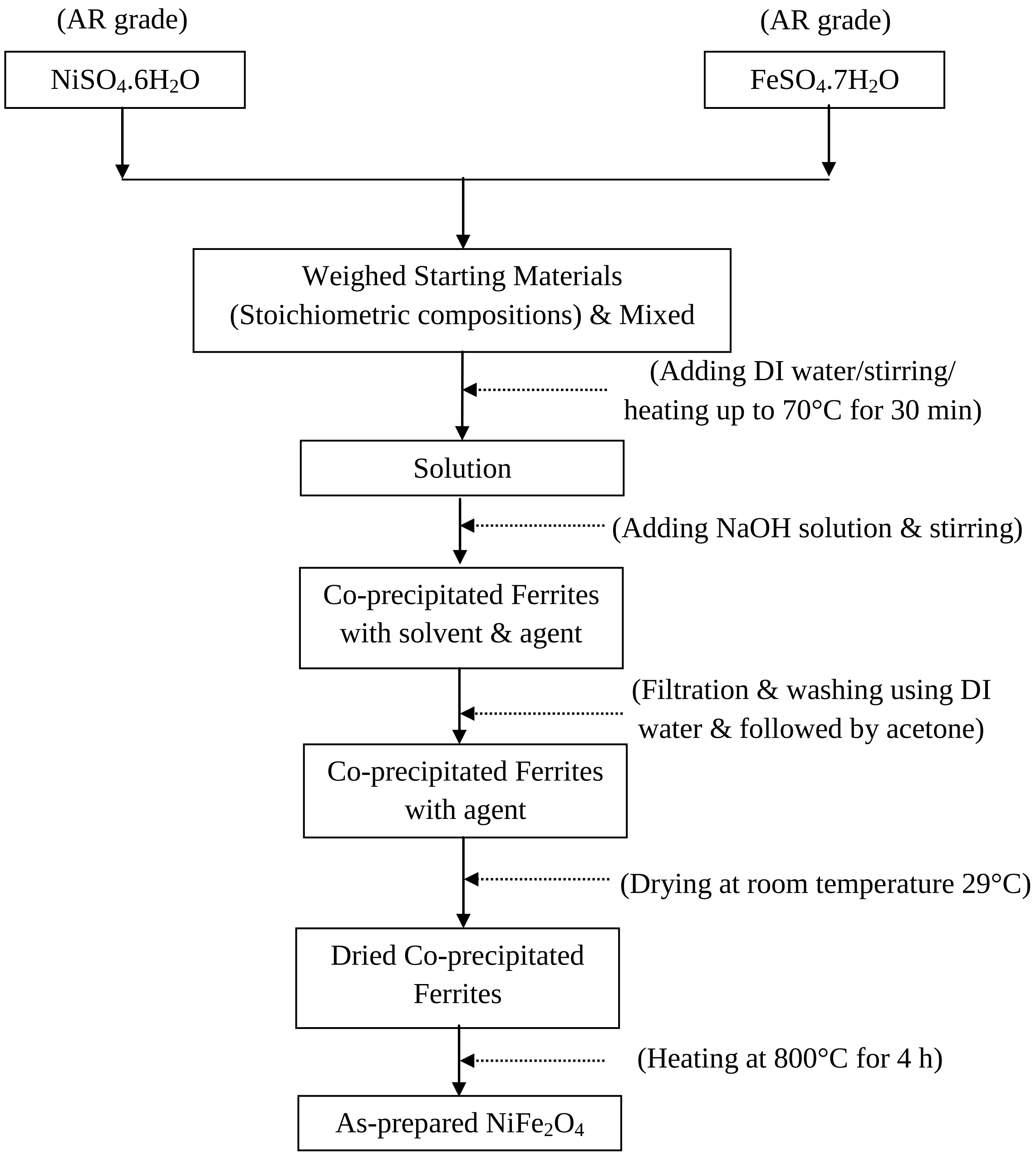

Figure 1(b) Preparation procedure of $NiFe_2O_4$ using co-precipitation method

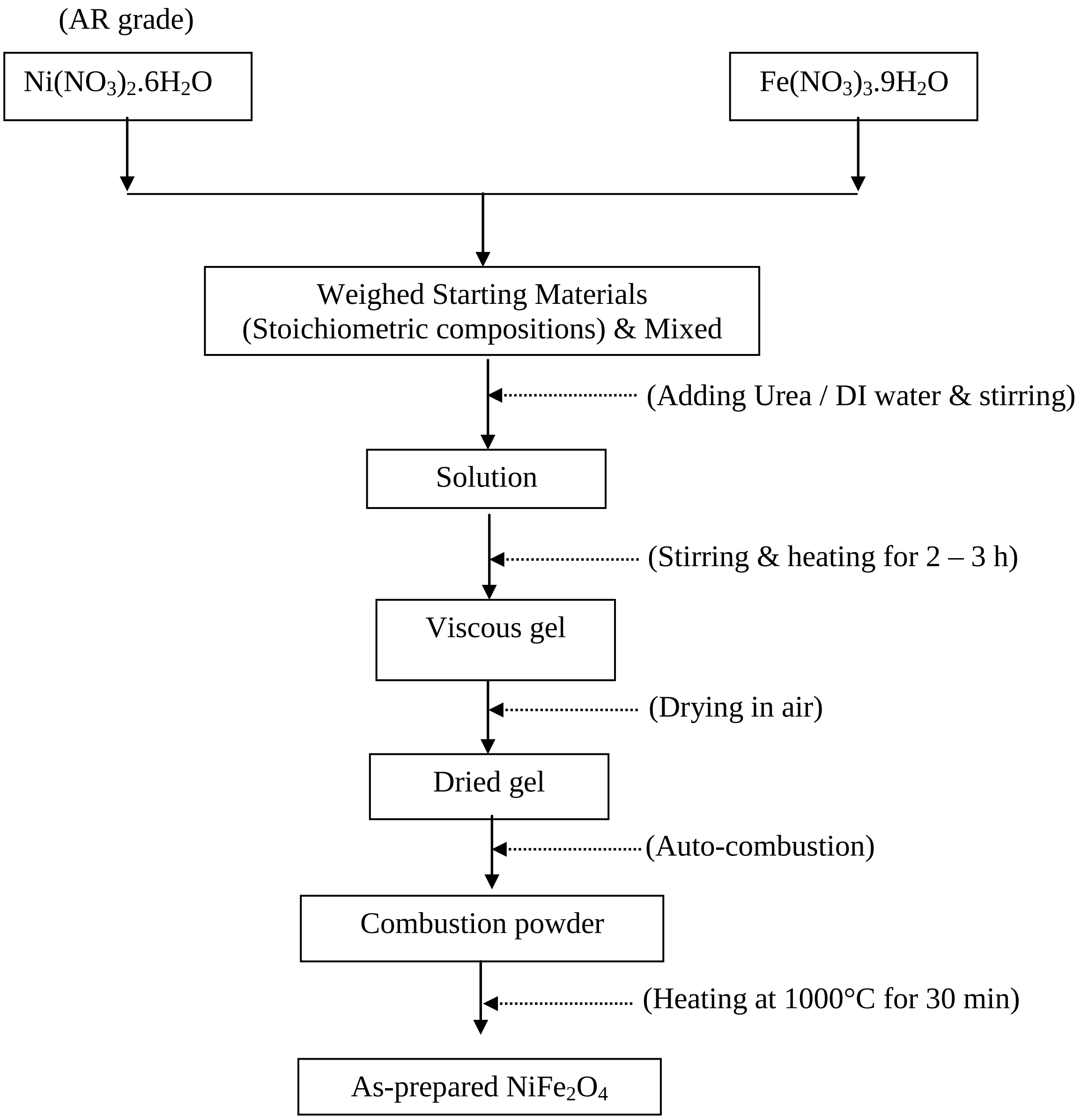

Figure 1(c) Preparation procedure of $NiFe_2O_4$ using auto-combustion method

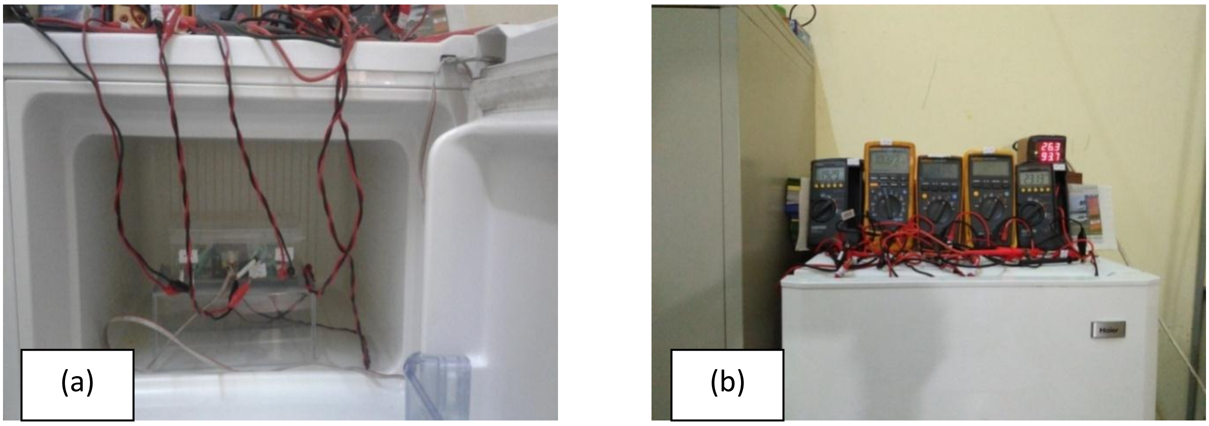

Figure 2 Photographs of the experimental setup of humidity sensitive electrical properties measurement, (a) the sample and sensor placed in the same condition and (b) the wiring connection of sample and meter

Results and Discussion

XRD Investigation

XRD patterns of Nickel ferrites, $NiFe_2O_4$, prepared by the standard solid state reaction method, co-precipitation and auto-Combustion method are shown in Figure 3. The collected diffraction lines were identified by using JCPDS data files of Cat. No. 89-4927> Trevorite, syn - $NiFe_2O_4$ for the sample prepared by standard solid state reaction method and auto-combustion method and Cat. No. 89-4927> Trevorite, syn - $NiFe_2O_4$ for the sample prepared by co-precipitation method respectively. As shown in observed XRD patterns, the collected diffraction lines were assigned with standard JCPDS data library files.

As shown in Figure 3(a), the collected peaks of the $NiFe_2O_4$ sample prepared by standard solid state reaction method are (220), (311), (222), (400), (511) and (440) respectively. In Figure 3(b), the collected peaks of the $NiFe_2O_4$ sample prepared by co-precipitation method are (220), (311), (400), (422), (511) and (440). As depicted in Figure 3(c), the collected peaks of the $NiFe_2O_4$ sample prepared by auto-combustion method are (220), (311), (400), (511) and (440). As shown in XRD patterns, the diffraction line of (311) plane is found to the strongest in intensity (I = 100%).

XRD patterns indicate the samples belong to cubic structure. In the present work, the calculated and observed lattice parameters of the samples are obtained as 8.33 Å for the $NiFe_2O_4$ sample prepared by standard solid state reaction method, 8.34 Å for the $NiFe_2O_4$ sample prepared by co-precipitation method and 8.31 Å for the $NiFe_2O_4$ sample prepared by auto-combustion method. The standard lattice parameters of the $NiFe_2O_4$ sample are $a = b = c = 8.32$ Å. Thus, the obtained lattice parameters in this work of different preparation methods are good agreement with the standard values. The crystallite sizes of the samples have been estimated by using the Scherrer formula, $D = \frac{0.9\lambda}{B \cos\theta}$, where D is he crystallite size nm, λ is the wavelength of incident X-ray (nm), θ is diffraction angle of the peak under consideration at FWHM (°) and B is observed FWHM (radian). In the present work, the average crystallite sizes were calculated and obtained as 74.11 nm for the sample prepared by solid state reaction method, 85.31 nm for the sample prepared by co-precipitation method and 49.04 nm for the sample prepared by auto-combustion method respectively. The crystallite size of the sample prepared by auto-combustion method was the smallest one among in the investigated samples using three different preparation methods. The obtained crystallite sizes showed the nanosized materials.

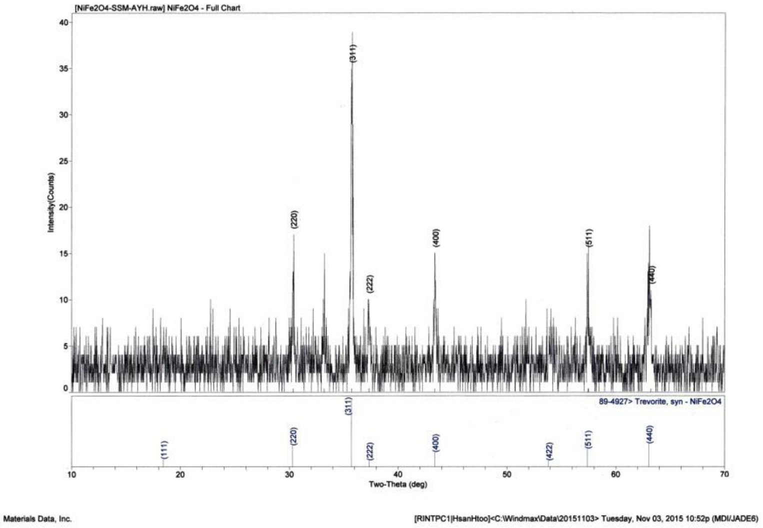

Figure 3(a) XRD pattern of $NiFe_2O_4$ prepared by solid state reaction method

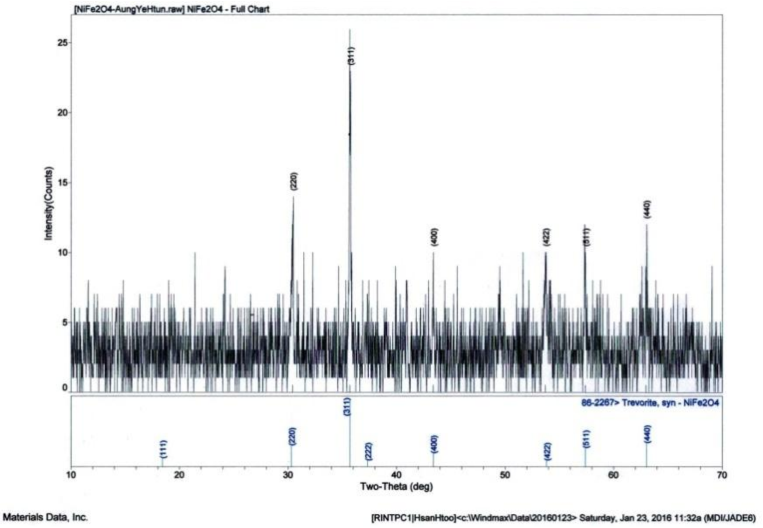

Figure 3(b) XRD pattern of $NiFe_2O_4$ prepared by co-precipitation method

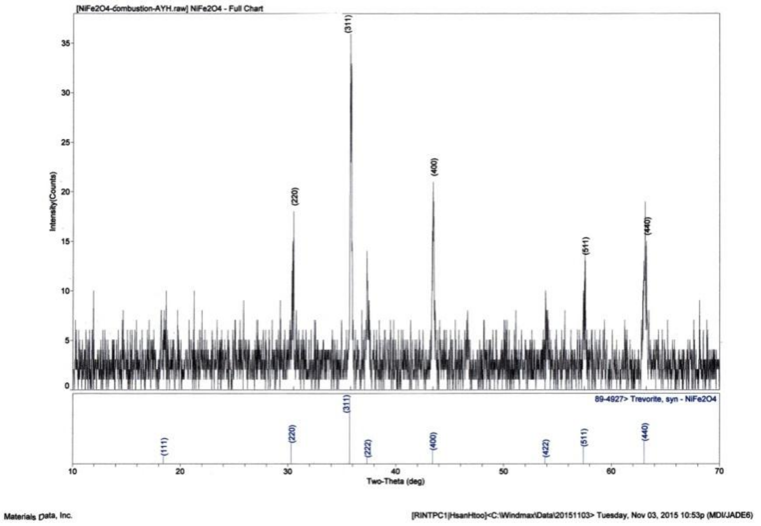

Figure 3 (c) XRD pattern of $NiFe_2O_4$ prepared by auto-combustion method

SEM Investigation

SEM images of Nickel ferrites, $NiFe_2O_4$, prepared by the standard solid-state reaction method, co-precipitation method and auto-combustion method are shown in Figure 4. As shown in figures, the grain shapes of the samples are spherical shapes and the samples from the standard solid-state reaction method and co-precipitation method are found to be similar. In Figure 4(a) and (b), the grain sizes are obtained as 0.25 – 0.40 μm and 0.15 – 0.25 μm respectively. The grains from co-precipitation method are found to be more homogeneous and smaller than that of solid state reaction method. The grain boundaries from solid state reaction method and co-precipitation method are clear than auto-combustion method. The grain shape of the sample from the auto-combustion method is the spherical with poor grain boundary. The sample composed of agglomerated particles. The obtained grain sizes are tabulated in Table 1.

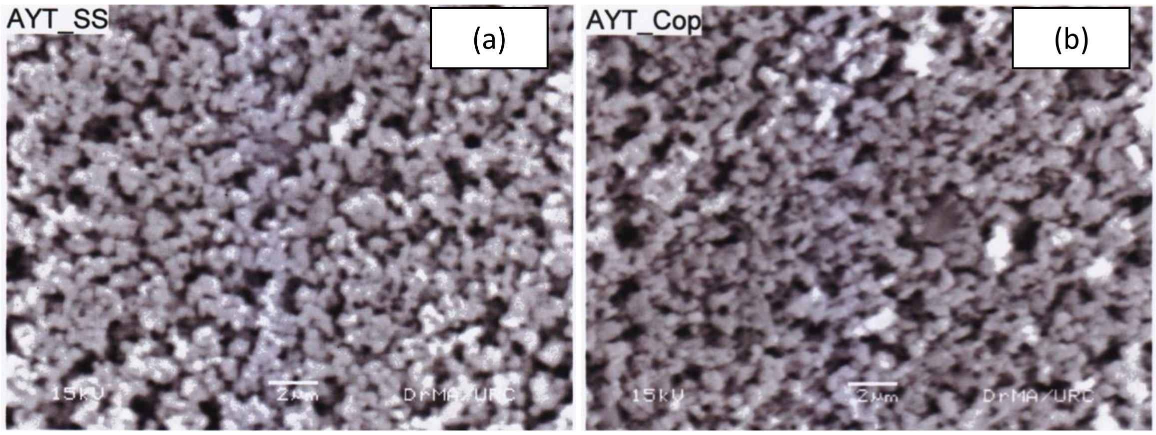

Figure 4 SEM images of $NiFe_2O_4$ prepared by (a) solid state reaction and (b) co-precipitation method

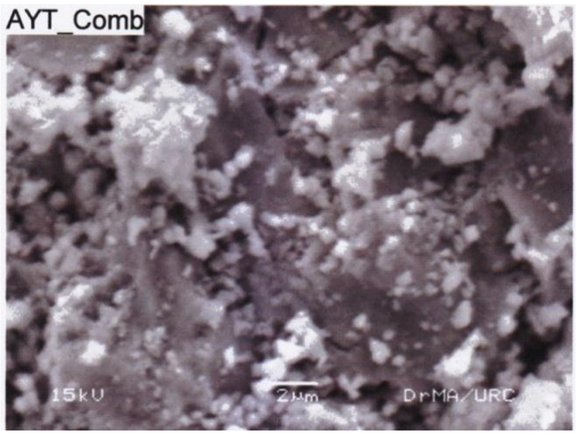

Figure 4(c) SEM image of $NiFe_2O_4$ prepared by auto-combustion method

Table 1 The grain sizes of Nickel ferrites, $NiFe_2O_4$

Method	**Grain size (μm)**
Solid state reaction	0.25 – 0.40
Co-precipitation	0.15 – 0.25
Auto-combustion	0.20 – 1.00

Humidity Sensitive Electrical Properties Study

The electrical resistance versus relative humidity (R vs. RH%) characteristic curves of the $NiFe_2O_4$ samples are shown in Figure 5. As shown in Figures, the electrical resistance decreased with increase in humidity because of capillary condensation of water vapours in all the pores that composed in the samples. In the observed (R vs. RH%) relationships, it is generally found that the decreasing of electrical resistances are varied with the observed corresponding humidity ranges.

The sensitivity factor "S_f" of the sample can be estimated by using the following relation; $S_f = R_{50\%}/R_{99\%}$, where $R_{50\%}$ and $R_{99\%}$ are the electrical resistances of the samples at the relative humidity 50 RH% (start point) and 99 RH% (end point) respectively. According to above relation, the sensitivity factors were calculated and obtained as follows.

For $NiFe_2O_4$ prepared by SSR method,
$S_{f\_SSR} = R_{50\%}/R_{99\%} = 60.77$
For $NiFe_2O_4$ prepared by CCP method,
$S_{f\_CCP} = R_{50\%}/R_{99\%} = 14.44$
For $NiFe_2O_4$ prepared by AC method,
$S_{f\_AC} = R_{50\%}/R_{99\%} = 18.81$

The sensitivity factor of the sample prepared by SSR method was the largest one because the microstructure (porosity, grain size, structural defects) has a great role on the electrical resistivity. Smaller grains imply an increase of the grain boundary surface which normally account for high resistivity of a polycrystalline material. The larger the specific surface area and porosity of the specimens the more water vapors can be physically adsorbed, resulting in a larger decrease of the resistivity.

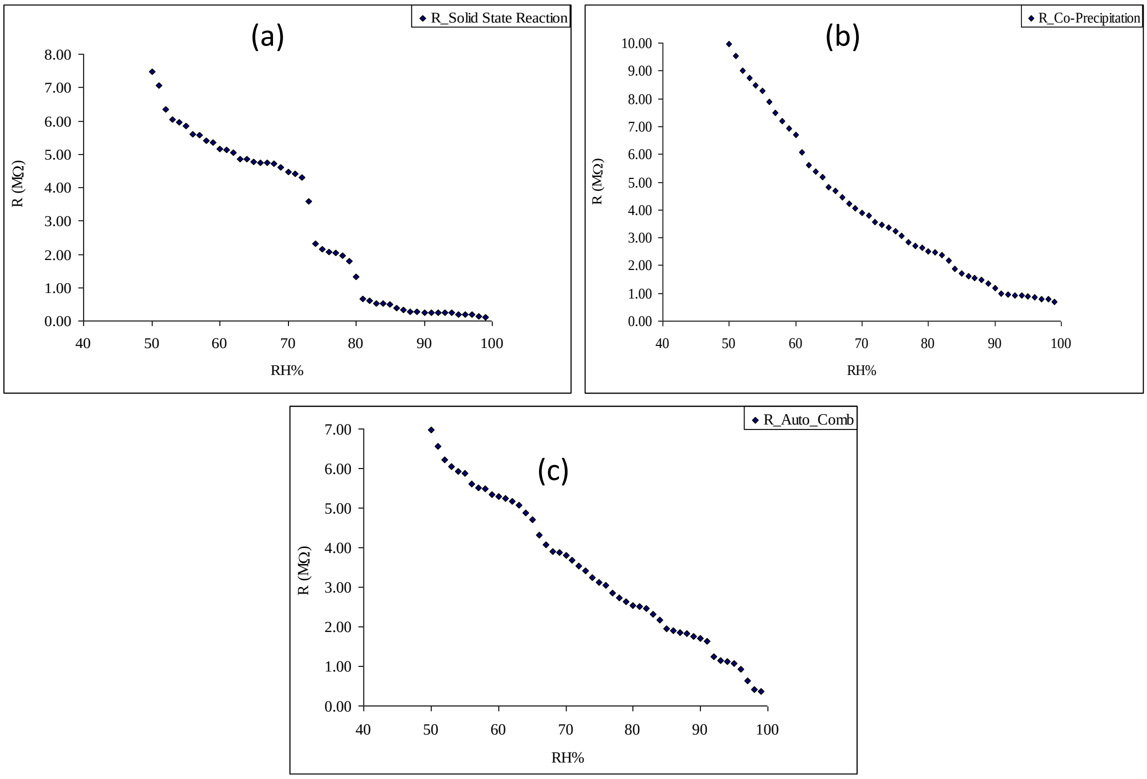

Figure 5 Electrical resistance versus relative humidity (R vs. RH%) characteristic curves of $NiFe_2O_4$ prepared by (a) SSR, (b) CCP and (c) AC method

Conclusion

Nickel ferrites, $NiFe_2O_4$ were successfully prepared by solid state reaction (SSR) method, chemical co-precipitation (CCP) method and auto-combustion (AC) method. Structural and microstructural characteristics of the samples were studied by XRD and SEM. Humidity sensitive electrical resistance was also investigated in this work. The X-ray diffraction confirmed the presence of spinel phase cubic crystalline as major phase of the as-prepared Nickel ferrite samples. The obtained lattice parameters and crystallite sizes were found to be small variation each other. It can be said that physical properties of the samples depend on the preparation techniques. From the observed SEM micrographs, the grain shapes of the samples are spherical. Due to the obtained grain sizes, the sample prepared from CCP method is the smallest and homogeneous among the investigated samples. The porosity (defect area) of the samples from SSR method and CCP method are larger than that of AC method. It indicated that the grain sizes and porosity depend on the preparation technique of the desired materials. From the humidity sensitive electrical properties measurement, the electrical resistances of the samples decreased with increase in humidity. The samples can be used as the humidity sensing materials in the relative humidity range of 50 RH% – 99 RH%. Due to the obtained sensitivity factor, the sample prepared by SSR method is the most suitable for the application of humidity sensing material among the investigated samples of different preparation methods.

Acknowledgement

The authors would like to acknowledge Professor Dr Khin Khin Win, Head of Department of Physics, University of Yangon, for her valuable suggestion and comments for this work.

References

Ahmad, I. & Farid, M.T. (2012).Characterization of Cobalt Based Spinel Ferrites with Small Substitution of Gadolinium. *World Applied Sciences Journal*, 19, 464–469.

Attia, S.M. (2006). Study of Cation Distribution of Mn-Zn Ferrites. *Egypt Journal of Solids*, 29(2), 329–340.

Brito, V.L.O. (2010). EVALUATION OF A Ni-Zn FERRITE FOR USE IN TEMPERATURE SENSORS. *Progress in Electromagnetic Research Letters*, 13, 103–112.

Fawzi, A.Z., Sheikh, A.D. & Mathe, V.L. (2010). Structural, Dielectric Properties and AC Conductivity of $Ni_{(1-x)}Zn_xFe_2O_4$ Spinel Ferrite. *Journal of Alloys and Compounds*, 502, 231-237.

Gadkari, A.B., Shinde, T.J. & Vasambekar, P.N. (2013). Liquid petroleum gas sensor based on nanocrystallite $Mg_{0.6}Cd_{0.4}Fe_2O_4$. *Advanced Materials Letters*, 4(7), 573–576.

Patil, S.N. & Ladgaonkar, B.P. (2013). Synthesis and Implementation of $NiZnFe_2O_4$ Ferrites to Design Embedded System for Humidity Measurement. *International Journal of Advanced Research in Electrical, Electronics and Instrumentation Engineering*, 19, 3813-3821.

Rezlescu, N., Rezlescu, E., Popa, P. & Tudorache, F. (2002). ON THE HUMIDITY SENSITIVITY OF A CERAMIC ELEMENT. STRUCTURE AND CHARACTERISTICS. *Journal of Institute of Technical Physics*, 8, 89-97.

Vagolu, V.K. & Samatha, K. (2013). Studies on Structural and Electrical Properties of Cobalt Substituted Nickel-Zinc Ferrites Prepared from Soft Chemical Method. *International Journal of Innovative Research and Studies*, 2(8), 99-113.

J. Myanmar Acad. Arts Sci. 2020 **Vol. XVIII.No.2B**

EXPERIMENTAL CHARACTERIZATION OF INDEX-COUPLED AND GAIN-COUPLED DISTRIBUTED FEEDBACK (DFB) LASERS

Ei Ei Minn[1], Jochen Kreise[2] and Kyaw Zwa Soe[3]

Abstract

For WDM or dense WDM communication systems, long FP lasers (cavity length> 200µm) are not useful because of their many-modes and strong thermal dependent system. The development of high-power, single mode lasers is needed. In this paper, we investigated the characteristics of the lasing mode spectra of the Index –Coupled and Gain-Coupled DFB lasers before and after AR coating.

Keywords : WDM (Wavelength-Division Multiplexing), FP (Febry-Perot) Laser, Gain-Coupled DFb Laser, Index-Coupled DFB Laser, DFB (Distributed Feedback) Laser, RW (Ridge Waveguide) DFB Laser .

Introduction

Wavelength Division Multiplexing (WDM) is quickly becoming a critical technology for many high speed communication systems. The operation of a WDM system begins with the conversion of each input data stream into separate wavelengths. In the case of optical communication, the wavelengths are grouped in transmission windows around 850, 1300 and 1500nm (the available hardware for optical communications is typically centered around these wavelengths). Each application creates a channel that operates at a separate wavelength. The WDM system then combines and simultaneously transmit the channels through the same optical fiber. Since each wavelength is completely isolated from the other, protocols can be mixed within the same link. The combined signals are then separated by the WDM at the other side and converted back to their original wavelength. Essentially, WDM systems create multiple virtual fiber pairs from one. Since light of different wavelengths do not interfere with each other, multiple wavelength signals can be transmitted through the same optical fiber without error. WDM begins to capture the true

Bandwidth potential of fiber optics by allowing multiple high speed communication applications to simultaneously share the same fiber.

Photonic Integrated Circuit (PICs) for WDM communication system require the integration of high performance 1.55µm DFB-Lasers : high single mode output power, small line widths and good high temperature behavior are demanded. Ridge-Waveguide (RW) type DFB-lasers are favorable compared with buried heterostructure (BH) lasers, because they show an unproblematic ageing behavior and only two epitaxial steps are needed for fabrication. However. High power performance of RW-laser is often limited by lateral mode instability leading to undesirable lasing action of a second lateral mode. So the hetero structure layout and stripe width has to be designed to provide lateral single mode emission particularly at high injection currents.

---

[1] Dr, Professor & Head, Department of Physics, University of Computer Studies (Mandalay), Myanmar.

[2] Heinrich-Hertz Institute für Nachrichtentechnik GmbH Berlin, Germany.

[3] University of Computer Studies (Mandalay), Myanmar.

Experimental Measurement On Index-Coupled DFB Laser

The Index-Coupled DFB laser is based on a ridge waveguide structure. The active region consists of an In_{1-x} Ga_x As_{1-y} P_y strained layer multi-quantum well (MQW) embedded between quaternary waveguides. A rectangular grating without a phase shift was etched into the upper waveguide layer before processing the p-InP ridge. The etch depth was calculated to achieve a coupling strength κ larger than $100cm^{-1}$.The length and the width of the laser ridge were 400 µm and 2.4 µm, respectively. The name of the laser structure is Clock 09 C 20.

First the pulsed light current characteristics of the Index-Coupled DFB laser with cleaved facets was measured. Figure-1 shows the typical light output power versus current characteristics under temperature 20°C pulsed operation.

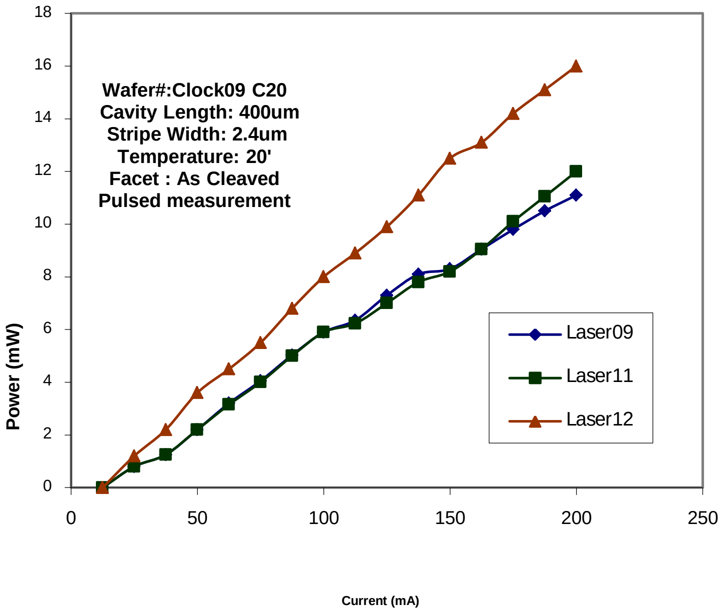

Figure 1 Light output versus current characteristics of Index-Coupled DFB laser with cleaved facets.

In these DFB lasers, low threshold current and high light output power have been achieved. The threshold current was about 10 mA. The corresponding lasin spectra of the Index-Coupled DFB laser under temperature 20°C CW operation at different currents was also measured. The lasing spectrum is changed depends on the injected current. Figure-2 shows the spectrum characteristics of the Index-Coupled DFB laser with cleaved facets.

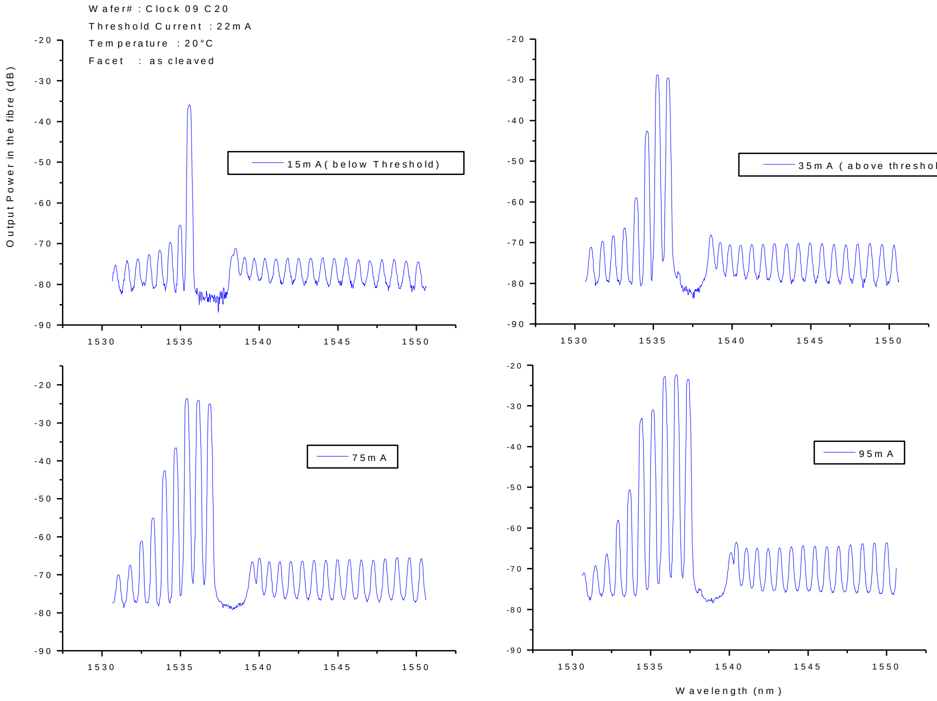

Figure-2 Lasing spectra of Index-Coupled DFB laser with cleaved facets.

In order to get the stable single- mode lasers, the facets of the laser have been AR coated. Anti-reflection (AR) films have been deposited on both facets so that their reflectivity was reduced to $\leq 1*10^{4}$. The light current characteristics and the corresponding lasing spectra of the Index-Coupled DFB laser with AR-coated facets at different currents were measured again.

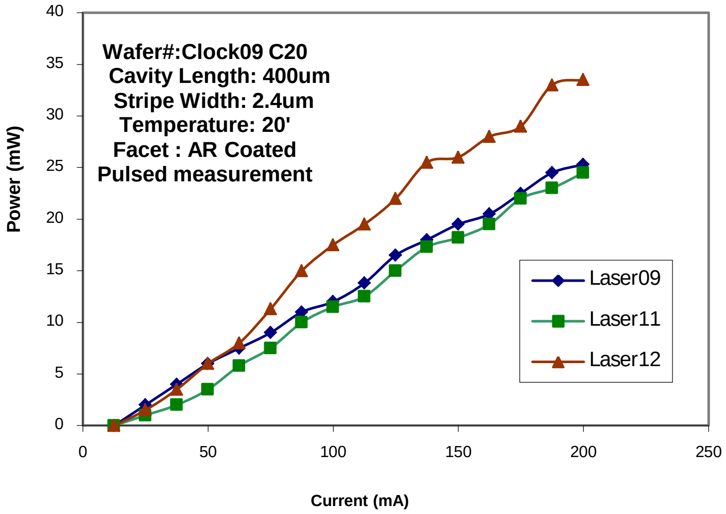

Figure 3 Light output versus current characteristic of Index-Coupled DFB laser with AR-coated facets.

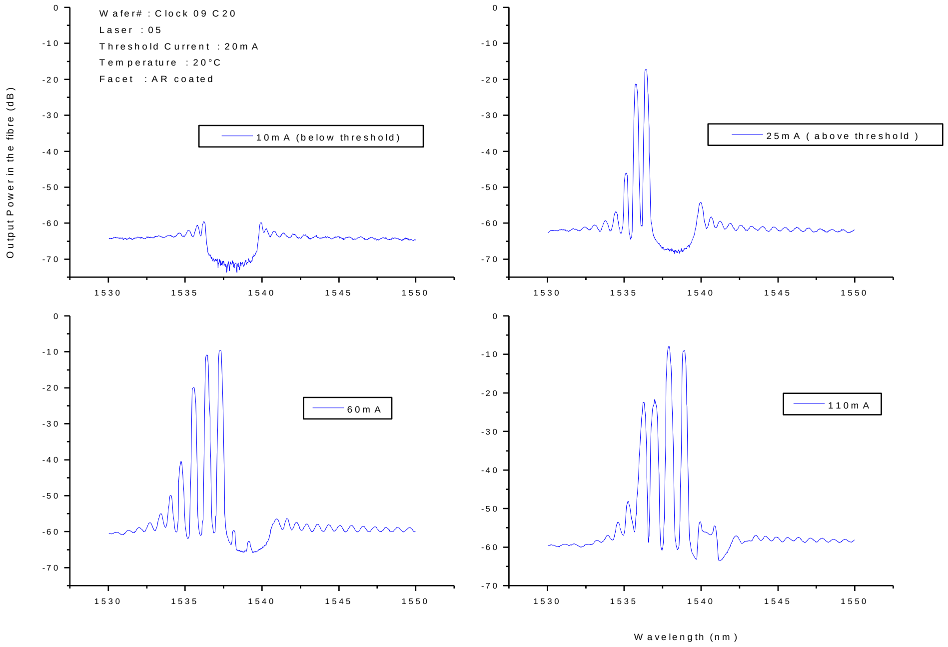

Figure 4 Lasing spectra of Index-Coupled DFB laser with AR-coated facets.

Results

Table 1 The results of the threshold current and output power before and after AR-coating.

Facet	I th (Threshold Current)	Power at 100mA (Output Power)
As cleaved	10mA	17mW
AR coated	10mA	34 mW

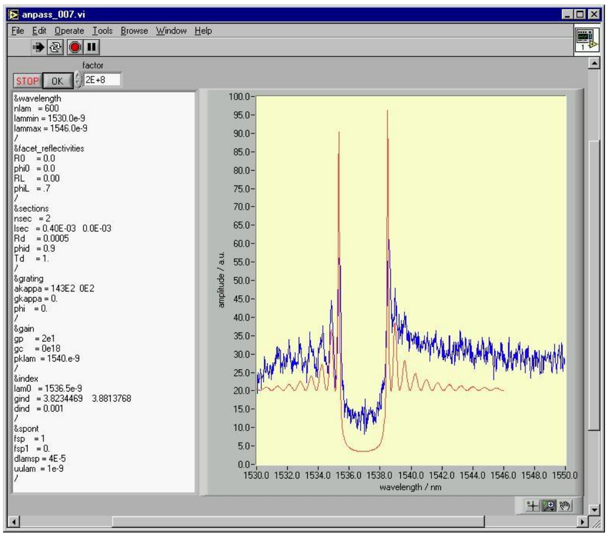

factor 2E+8

```
&wavelength
nlam   = 600
lammin = 1530.0e-9
lammax = 1546.0e-9
/
&facet_reflectivities
R0     = 0.0
phi0   = 0.0
RL     = 0.00
phiL   = .7
/
&sections
nsec   = 2
lsec   = 0.40E-03   0.0E-03
Rd     = 0.0005
phid   = 0.9
Td     = 1.
/
&grating
akappa = 143E2  0E2
gkappa = 0.
phi    = 0.
/
&gain
gp     = 2e1
gc     = 0e18
pklam  = 1540.e-9
/
&index
lam0   = 1536.5e-9
gind   = 3.8234469   3.8813768
dind   = 0.001
/
&spont
fsp    = 1
fsp1   = 0.
dlamsp = 4E-5
uulam  = 1e-9
/
```

Figure 5 Theoretical curve fitting with the experimental result of the Index-Coupled DFB laser.

It can be seen that, there is no change of I_{th} after AR coating because of the large κ-value. K is about $143cm^{-1}$. Spectra are characterized by the spatial hole burning effect. In large κ values spatial hole burning occurs and led to the dominant lasing of the mode at the low wavelength stop band side. In most of the cases no single mode behavior could be measured. Further studies are necessary to find the optimum coupling strength which is needed for mode selection of the one hand and prevailing many mode behavior of the other hand.

Experimental Measurement on Gain-Coupled DFB Laser

An alternative approach for feedback insensitive single mode lasers is the introduction of gain coupling. At least different principles of a complex-coupling are known : first the grating is etched in the active layer, second an absorption layer is structured as a grating, third the grating is build by inverse pn diode modulating the carrier concentration and fourth a modulated lattice damage by ion implantation in the active layer is realized. If the real part and the imaginary part of the refractive index are in phase, the stop band mode of the longer wavelength side is dominant in opposite to the antiphase case where the modes in the smaller wavelength side have low threshold values. Purely gain-coupled lasers were treated theoretically. They have a lasing mode exactly at the Bragg frequency. The example that should be discussed in the following is a complex coupled DFB laser realized by a loss grating. In that case real and imaginary part of the refractive index is in antiphase. The Gain-Coupled DFB laser is based on ridge waveguide lasers. The active region consists of an $In_{1-x} Ga_x As_{1-y} P_y$ strained layer multi-quantum well (MQW) embedded between quaternary waveguides. A rectangular grating was deeply etched into a In GaAs absorption layer placed above the quaternary waveguide before processing the p-InP ridge. The length and the width of the laser ridge were 400 µm and 2.4 µm, respectively. The name of the laser structure is gl02.

First the light current characteristics of the Gain-Coupled DFB laser with cleaved facets was measured. Figure-6 shows the typical light output power versus current characteristics under temperature 20°C pulsed operation.

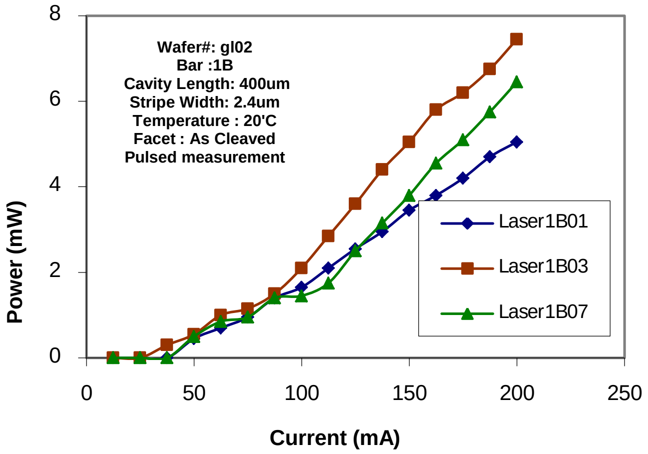

Figure 6 Light output versus current characteristic of Gain-Coupled DFB laser with cleaved facets.

The threshold current of the Gain-Coupled DFB laser is higher than that of the Index-Coupled DFB laser and the optical output power is lower than that of the Index-Coupled DFB laser.

The corresponding lasing spectra of the Gain-Coupled DFB laser under temperature 20°C CW operation at different currents was also measured. The lasing spectrum is changed depends on the injected current. Figure-7 shows the spectrum characteristics of the Gain-Coupled DFB laser with cleaved facets. For injection currents below and slightly above threshold the expected dominance of the smaller wavelength stop band mode could be observed.

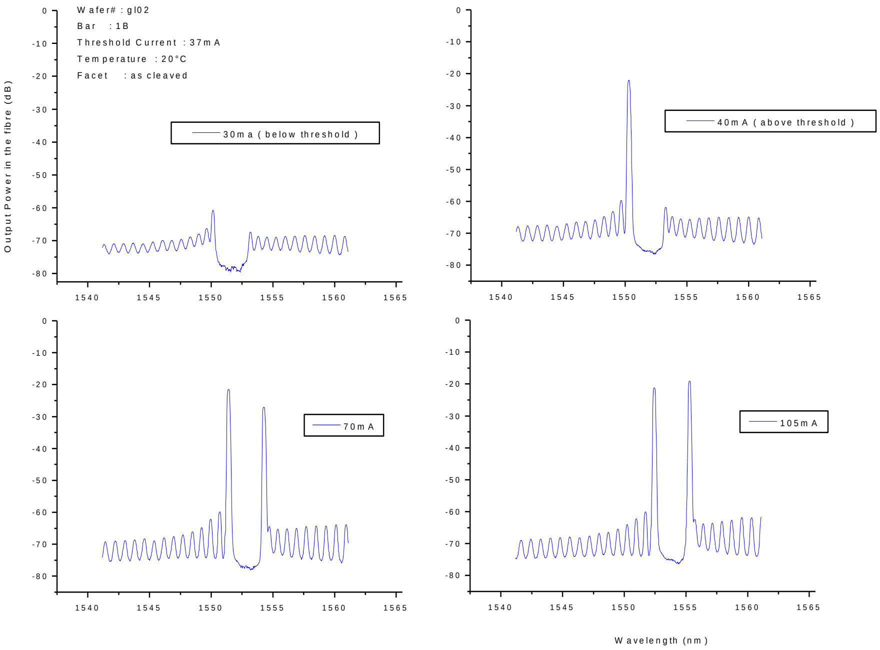

Figure 7 Lasing spectra of Gain-Coupled DFB laser with cleaved facets.

In order to get stable single- mode lasers, the facets of the laser have been AR coated. Anti-reflection (AR) films have been deposited on both facets so that their reflectivity was reduced to ≤ $1*10^4$. The light current characteristics and the corresponding lasing spectra of the Gain-Coupled DFB laser with AR-coated facets at different currents were measured again.

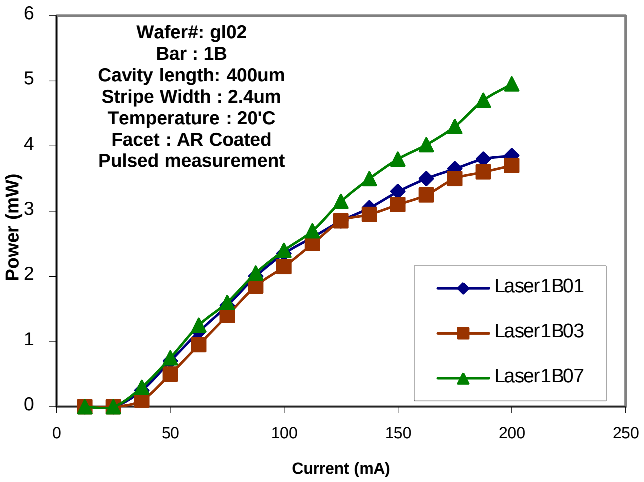

Figure 8 Light output versus current characteristics of Gain-Coupled DFB laser with AR-coated facets.

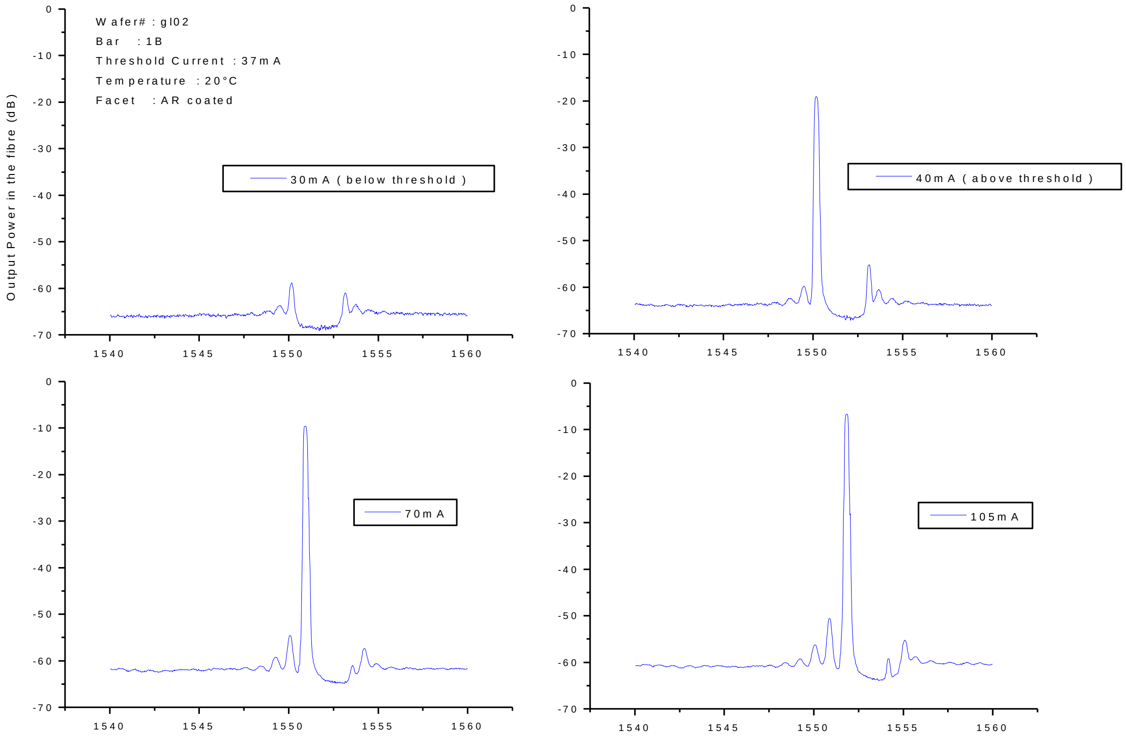

Figure 9 Lasing spectra of Gain-Coupled DFB laser with AR-coated facets.

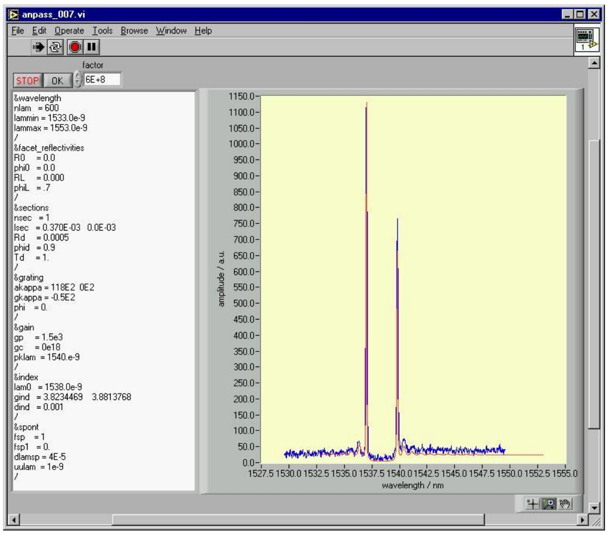

```
&wavelength
nlam   = 600
lammin = 1533.0e-9
lammax = 1553.0e-9
/
&facet_reflectivities
R0     = 0.0
phi0   = 0.0
RL     = 0.000
phiL   = .7
/
&sections
nsec   = 1
lsec   = 0.370E-03   0.0E-03
Rd     = 0.0005
phid   = 0.9
Td     = 1.
/
&grating
akappa = 118E2  0E2
gkappa = -0.5E2
phi    = 0.
/
&gain
gp     = 1.5e3
gc     = 0e18
pklam  = 1540.e-9
/
&index
lam0   = 1538.0e-9
gind   = 3.8234469   3.8813768
dind   = 0.001
/
&spont
fsp    = 1
fsp1   = 0.
dlamsp = 4E-5
uulam  = 1e-9
/
```

Figure 10 Theoretical curve fitting with the experimental result of the Gain-Coupled DFB laser.

Most of the lasers show single mode behavior over the whole current range (up to 100mA). In agreement with the theoretical predictions the smaller wavelength stop band mode dominates. The coupling parameters were determined using a fit program write by Hans Wenzel. For a spectrum below threshold we drive coupling strength values $\kappa_I = 118 \text{cm}^{-1}$ and $\kappa_G = 0.5 \text{cm}^{-1}$. The gain part of the coupling is rather small. This might be responsible to the double mode behaviour in the case of as cleaved lasers, that is very similar to pure Index-Coupled lasers.

Conclusion

In experiment on Index-Coupled DFB laser, firstly the light current characteristic and the lasing spectrum of the Index-Coupled DFB laser with cleaved facets have been measured. The mode spectrum of the laser is changed depending on the injected current. And then the facets of the Index-Coupled DFB laser are AR coated and the light current characteristic and the lasing spectrum have been measured again.

In experiment on Gain-Coupled DFB laser, by measuring the light current characteristic of the Gain-Coupled DFB laser, it can be seen that the threshold currents of the Gain-Coupled DFB lasers are higher than that of the Index-Coupled DFB laser and the output power is lower than that of the Index-Coupled DFB laser. By measuring the lasing spectrum of the Gain-Coupled DFB laser with cleaved facets and with AR coated facets, it can be seen the changes of the mode spectrum of the laser depending on the injected currents.

Acknowledgement

Thanks are due to Dr Ronald Kaiser, Section Head, Mode-Locked Laser Section, for his supervision, guidance and comments on the resulting data, and to Dr Herbert Venghaus, Head, Integration Technology Department and all members of Integration Technology Department, Heinrich-Hertz Institute für Nachrichtentechnik, Berlin, who helped in many ways during the fellowship training period.

References

Arahira S., Matsui Y. and Ogawa Y (2001):, " Mode-Locking at very high repetition rates more than Terahertz in Passively Mode-Locked Distributed-Bragg-Reflector laser diodes", *IEEE Journal of Quantum Electronics.*, vol. 32, No. 7, pp1211-1224.

Arahira S., Matsui Y., Kunii T., Oshiba S. and Ogawa Y (1998), " Transform-limited optical short-pulse generation at high repetition rate over 40GHz from a Monolithic Passive Mode-Locked DBR laser diode", *IEEE Journal of Quantum Electronics*., vol.5, No.12, pp1362-1365.

Garmire E. and Kost A (1999), *Nonlinear Optic in Semiconductors II* , New York, Academic Press.

Hofmann M., Fröjdh K., Brorson S.D.and J. Mφrk J (1999), "Temporal and Spectral Dynamics in Multiquantum Well Semiconductor Saturable Absorbers", *IEEE Photonics Technology Letters,* vol.9, No.5, pp622-624.

Kamiya T., Saito F., Wada O. and Yajima H (1999): *Femtosecond Technology*, Berlin, Heidelberg Press.

Miller D., Weiner J. and Chemla D.S (1994), "Electric-field dependence of linear optical properties in quantum well structures: waveguide electroabsorption and sum rules", *IEEE J Quantum Electron.*, vol. QE-22, No.9, pp1816-1830.

Ramaswami R., Sivarajan K.N (1999): *Optical Networks*, London, Academic Press.

Weber H.G., Ludwig R (2002): " Ultrafast OTDM Transmission Technology with Advanced Optical Devices." *The 9th International Workshop on Femtosecond Technology June 27-28, 2002. Tuskuba, Japan .*

STRUCTURAL CHARACTERIZATION AND NON-OHMIC PROPERTIES OF AL DOPED ZNO VARISTORS

Win WinYee[1], Pwint Hlaing Ni[2], Zin Oo Hlaing[3], May Aye Khine[4] and PwintYi Thein[5]

Abstract

Al (0 mol%,1 mol% & 2 mol%) doped ZnO ceramics are prepared by using solid state reaction method. Samples are heat treated at 500ºC for 3 hrs. After pre-heat treatment schedule, samples are heated treatment again temperature 1100ºC for 2 hrs respectively. Structural characterization of the samples are investigation by using XRD. From the XRD analysis, structural properties such as, lattice parameters, crystallite size and micro stain are evaluated. Energy gaps of the samples are studied by using UV Vis spectrometer. Non-Ohmic behavior of the Al doped ZnO ceramics varistors are also determined.

Keywords: XRD,ceramics & varistor.

Introduction

Varistors are used to protect a circuit from high voltage surges. When a voltage surge is applied to s circuit, the outcome is usually catastrophic to the circuit. A capacitor may be installed across the signal lines. However, this capacitor cannot suppress voltage surge. Therefore, when circuit protection from voltage surge is required, a varistor is used as a voltage protection device. When a voltage surge exceeding a specified value (varistor voltage) is applied, the varistor suppresses the voltage to protect the circuit. When voltage surge does not exceed the varistor voltage, the varistor works as a capacitor.

The varistor is composed of ZnO with small addition of Bi, Co, Mn and other metal oxides. The structure of the body consists of a matrix of conductive ZnO grains separated by grain boundaries providing P - N junction semiconductor characteristics. These boundaries are responsible for blocking conduction at low voltages and are the source of the nonlinear conduction at higher voltages.

It is well known that, the performance of ZnO varistor is controlled by the dopant additives, usually metal oxides and the dopants are responsible for the formation of varistor behavior. It is believed that, dopants play an important role to modify the defect concentrations at the ZnO grain and /or of grain boundary where the performance of ZnO is sensitive to the some additives even when their amount is very small. Among the additives, Al is widely used as grain growth enhancer and ZnO conductivity enhancer in ZnO based ceramics.

In this research work, the introduction of Al doped ZnO ceramics samples were prepared by solid state sintering method. X - rays diffraction is used to characterize the structural properties of the ceramics samples. ln I – ln V characteristics of the samples are studied. From the I (V) data, varistor behavior of the samples are evaluated. Bandgaps of the prepared ceramics samples are examined by UV Vis spectrometer.

---

[1] Lecturer, Department of Physics, University of Computer Studies, Yangon.

[2] Lecturer, Department of Physics, University of Information Technology, Yangon.

[3] Dr, Lecturer, Department of Physics, University of Maubin.

[4] Dr, Associate Professor, Department of Physics, University of Kyaing Tong.

[5] Dr, Professor, Department of Physics, Nationalities Youth Resources Development Degree College, Yangon.

Experimental Procedure

Al doped ZnO samples were mixed, according to (1 - x) ZnO + (x) Al_2O_3, where, x = 0, 1 mol %, 2 mol % respectively. Analar grade ZnO and Al_2O_3 were mixed with agate mortar for 2 hrs. After mixing the specimen, the mixture was heat treated at 500°C for 3 hrs. After that, the mixture was grinded with ball milling for 6 hrs. Then, the mixture was heat treated again at 1100°C for 2 hrs.

Structural characteristics of the ceramics were investigated from the XRD spectra. Samples were scanned from 10° to 70° in diffraction angle, 2Θ, with scanning speed 0.01 degree / sec. The diffraction patterns were recorded at room temperature, using CuK_α (λ = 1.5408 Ȧ) radiation, and voltage and current were 40 kV and 50 mA respectively.

Optical characteristics of the ceramic samples were examined in the wavelength 190 nm to 700 nm, using UV Vis spectrometer ,(SHIMADZU UV-1800). From the optical absorption spectra, band gaps of the samples were studied.

The mixture powder were uniaxially pressed into circular shape disc of 20 mm in diameter and 3.5 mm in thickness at a pressure of 19.5 tons. Silver paste was coated on the both surfaces of the samples and the electrodes were formed by heating at 600°C for 15 min.The nonlinear behavior of the ceramic samples were measured using high voltage DC power supply. The threshold voltage (V_{1mA}) was measured at current 1mA, and the leakage current was studied at 0.8 V_{1mA}. From the lnV - lnI characteristics, nonlinear coefficient of the ceramics was examined.

Results and Discussion

XRD spectra of Al (0 mol %,1 mol % and 2 mol %) doped ZnO ceramic samples are depicted in figure (1). It is obvious that, only diffraction peaks of hexagonal wurtize ZnO (075 - 0576 > JPDCS library file) are observed, as seen in figure (1). Furthermore, (101) peak is the most intense peak and a little shift of (101) peak is found in all spectra. Atomic radius of Al atoms are slightly smaller than Zn atoms and the covalent bond length of Al - O is estimated to be shorter than Zn - O. Al has solid solubility limit of about 2~3 % in ZnO . These results can interpret as Al ions are possibly diluted in the ZnO host matrix. Lattice parameters ‘a’, ‘c’ and lattice tetragonality c/a are listed in table (1).Crystallize size and micro stain, derived from Debye-Sherrer equation , are also listed in table (1).The ‘a’ and ‘c’ parameters of the ceramic samples are very little change, as listed in table (1), it may be due to the unchanged of hexagonal wurtize ZnO structure.

Table 1 Structural properties of ZnO : Al ceramics.

Molar concentration	lattice parameter “a(A°)”	lattice parameter “c(A°)”	lattice distortion	crystallize size (nm)	micro strain	FWHM of (101) peak(°)
Pure ZnO	3.2484	5.2056	1.6027	86.173	2.6377x 10^{-3}	0.097
Al 1mol%	3.2497	5.2049	1.6017	55.370	1.2928 x 10^{-3}	0.151
Al 2mol%	3.2438	5.2031	1.6045	42.219	2.0100 x 10^{-3}	0.198

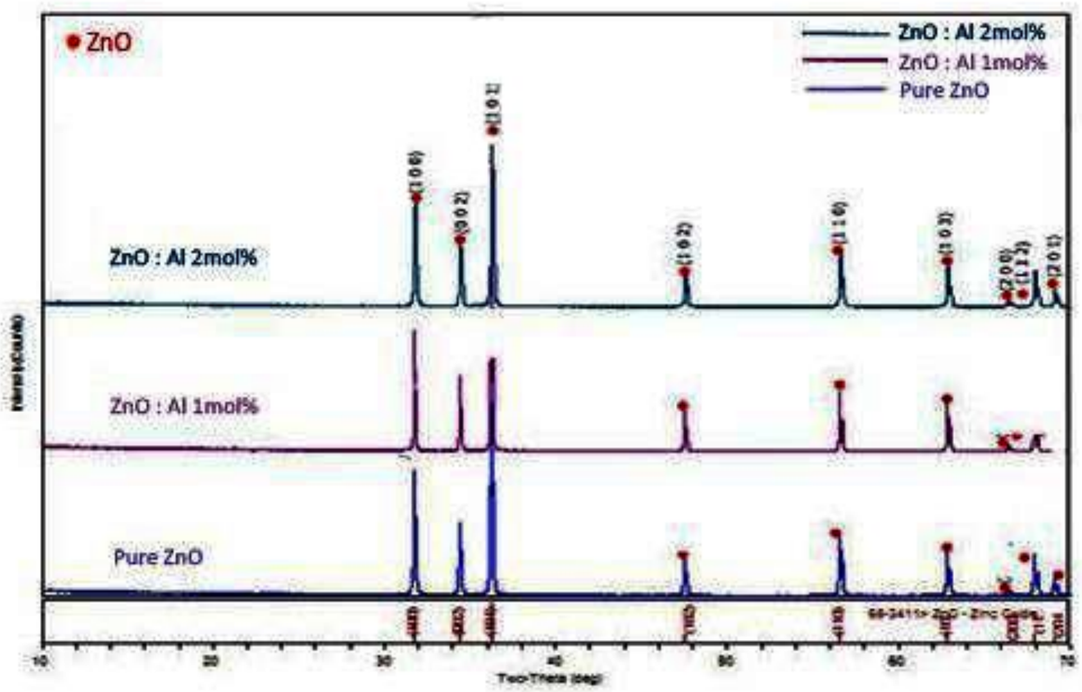

Figure 1 XRD spectra of Al doped ZnO ceramics with different Al contents.

Nonlinear properties of the ceramic samples are studied from the lnV vs lnI curves, as seen in figure (2). Nonlinear coefficients are obtained from the slopes of the ln V vs ln I curves. Threshold voltages (V_{1mA}) which are measured at current 1mA and leakage currents are examined at 0.8 V_{1mA}.Data are collected and listed in table (2). The ZnO grains themselves are highly conductive, while the intergranular boundary formed of other oxides is highly resistive. Only at those points where ZnO grains meet does sintering produce microvaristors, comparable to symmetrical back-to-back Si Zener diode. The nonlinear behaviour of the varistor results from the number of microvaristors connected in series or in parallel.

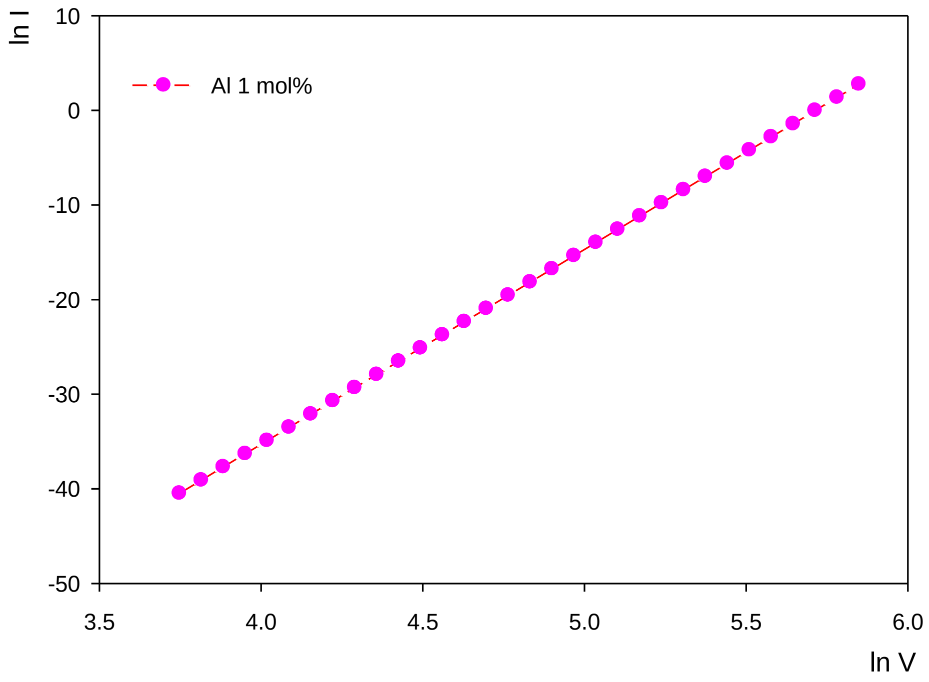

Figure 2 (a) Non- linear behavior of Al 1 mol % doped ZnO ceramics.

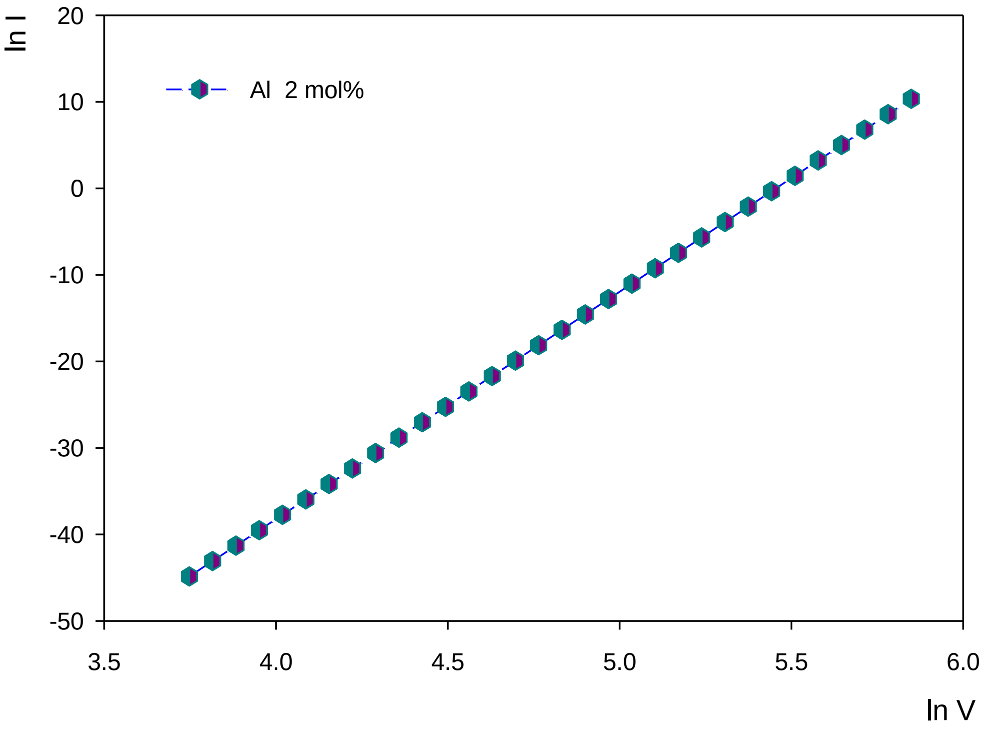

Figure 2 (b) Non- linear behavior of Al 2 mol % doped ZnO ceramics.

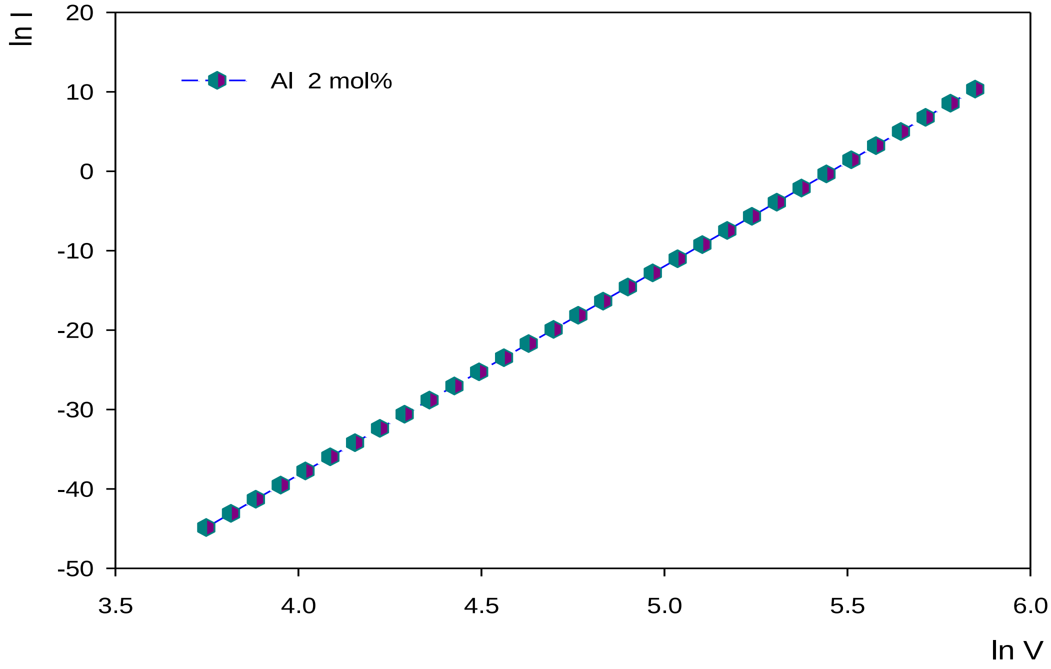

Figure 2 (c) Non- linear behavior of Al 2 mol % doped ZnO ceramics.

Table 2 Varistor Properties of ZnO : Al Ceramics.

Al concentration	**Th Threshold Voltage V_{th}(V)**	**Leakage Current I_L(mA)**	**Non-linear coefficient**
Al 1mol%	215.1	0.011219	20.15
Al 2mol%	213.4	0.011156	20.18

It is obvious that the nonlinear coefficient increases with increasing Al content, as listed in table (2). It is believed that after doping Al in to ZnO ceramics, there were be good grain boundaries in host ZnO ceramics. From the ln V vs ln I curves, nonlinear coefficients of the samples are obtained by the following relation.

$$\propto = \frac{\log({}^{I_2}/_{I_1})}{\log({}^{V_2}/_{V_1})}$$

where, I_1= 1 mA and I_2 = 10 mA and, V_1 and V_2 are the voltages corresponding to $I_1$and I_2Threshold voltages ($V_{1\ mA}$), which are measured at current 1 mA and leakage currents are studied at 0.8 $V_{1\ mA}$. Data are collected and listed in table (2).

Threshold voltage and leakage current decrease when Al content is raised, as listed in table (2).It may be due to increase of grain size that leads to lower the threshold voltage. The substitution of Zn^{2+} ions with Al^{3+} in ZnO lattice causes the increase of electrical conductivity, due to increase of charge carrier .This result can interpret as a decrease of leakage current.

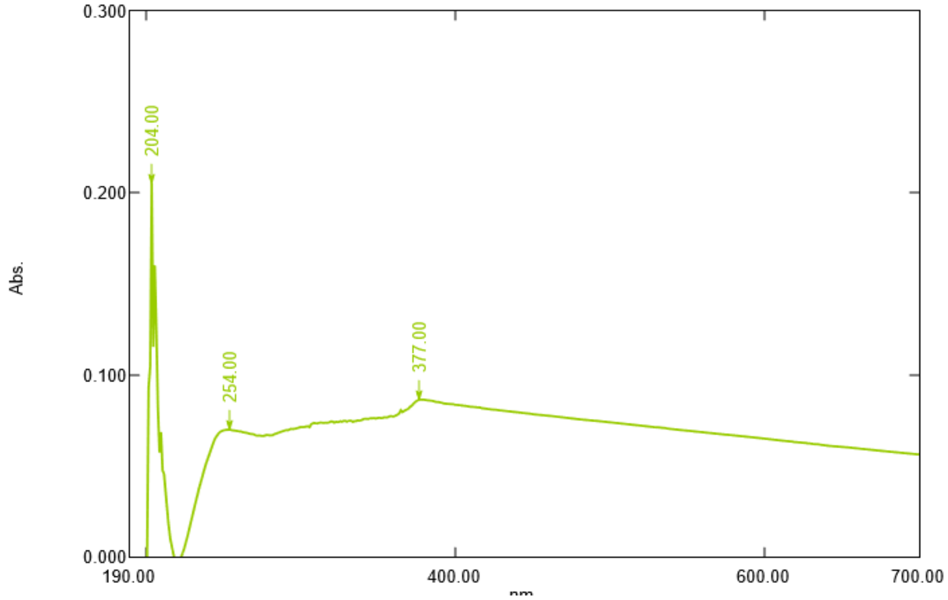

Figure 3 (a) Optical absorbance spectrum of pure ZnO

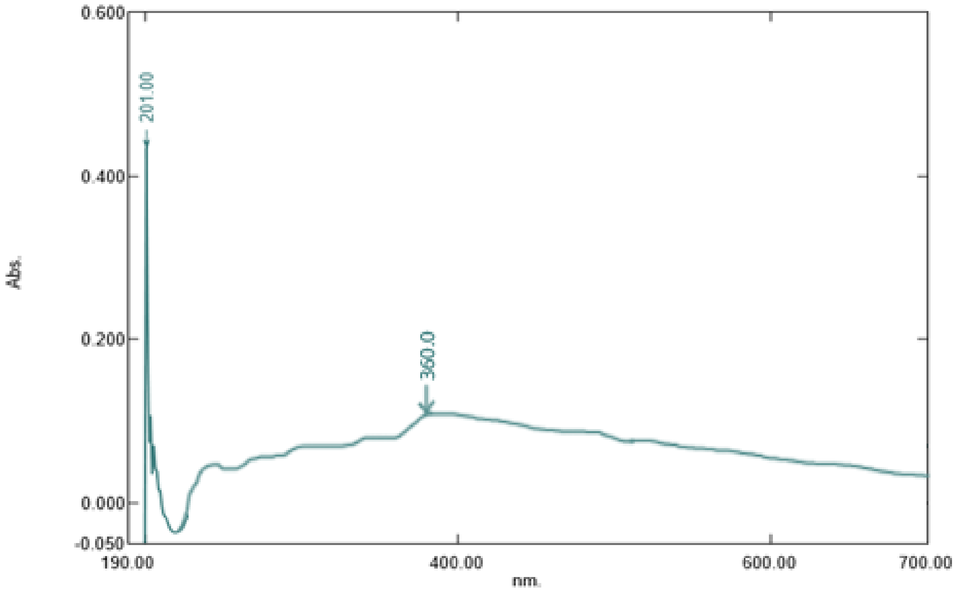

Figure 3 (b) Optical absorbance spectrum of Al 1 mol % doped ZnO ceramics

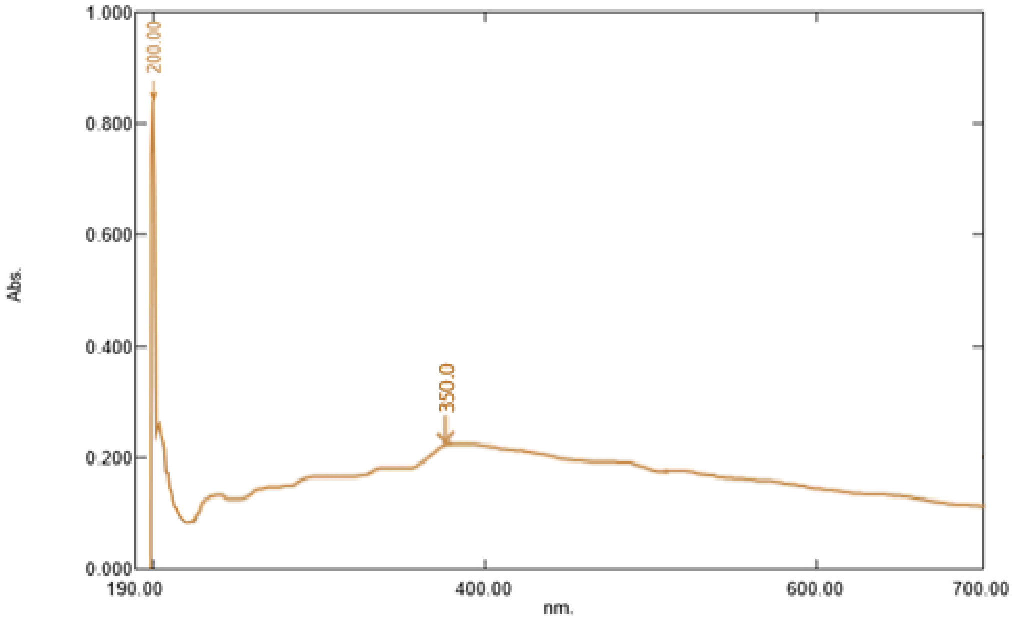

Figure 3 (c) Optical absorbance spectrum of Al 2 mol % doped ZnO ceramics

Figure (3) depicts the optical absorption spectra of ZnO : Al ceramics in the wavelength 190 nm to 700 nm. It is obvious that ,absorbance increases with Al content. The optical bandgaps of the ceramic samples were examined by applying Tauc - Mott relation and listed in table (3). It is noted that bandgap varies with dopant Al content. It is probably due to the quantum confinement effect in compound semiconductors.

Table 3 Band gaps of Al doped ZnO ceramics.

Al concentration	**Energy gap (eV)**
Pure ZnO	3.274
Al 1mol%	3.429
Al 2mol%	3.527

Conclusion

Al (1 mol % , 2 mol %) doped ZnO ceramic samples were prepared by applying solid state reaction method in this research. Structural properties of the samples were characterized by using XRD technique. Influence of Al concentration on lattice parameters, lattice distortion, crystallite size and lattice micro strain were determined. Ceramic samples were prepared with standard varistor preparation process and varistor behaviour of the samples were examined. From the V (I) data, threshold voltage, leakage current and nonlinearity factor were studied. Furthermore, optical bandgaps of the samples were evaluated.

Acknowledgements

The authors would like to acknowledge the Universities Research Centre (URC) , University of Yangon, for XRD measurements.

References

Akdag A, Budak H F, Yilmaz M, Efe A, Biiyiikaydin M, Can M, Turgut G and Sonmez E (2016) : " *Structural and Morphological Properties of Al Doped ZnO Nanoparticles* " , J.Phy.Conf.Ser.707, 012020.

Buneo P R, Varela J A and Longo E (2008) : " *SnO2, ZnO and Related Polycrystalline Compound Semiconductors : An Overview and Review Voltage Dependent Resistance (Non - Ohmic) Feature* ", J.Eur.Cer.Soc., 28(3), 505 – 529.

Chou Y H, Chau J L H, Wang Y L, Chen C S,Wang S H and Yang C C (2011) : " *Preparation and Characterization of Solid - State Sintered Al doped ZnO with Different Alumina.*

Clarke D R (1999): " *Varistor Ceramics* " , J.Am.Cer.Soc., 82(3), 485 - 492.

Gupta T K (1990): " *Application of ZnO Varistors* " , J.Am.Cer.Soc., 71(3), 1817 - 1840.

Helene Serier, Gaudon M and Menetrier M (2009) : *" Al doped ZnO Powdered Material : Al Solubility Limit and IR Absorption Properties* ".Solid State Sciences, 21, 1192 – 1.

Hng H H and Knowles K M (2002) : " *Microstructure and Current - Voltage Characteristics of Praseodymium Doped ZnO Varistor Containing* MnO_2, Sb_2O_3 *and* Co_3O_4 "J.Mat.Sci., 37(6), 1143 - 1154.

Jood P et al. (2011) :" *Al Doped ZnO Nanocomposite with Enhanced Thermoelectric Properties* " , Nano Lett., 11, 4337 - 4342

Khan W, Khan Z A, Saad A A, Sherrani S, Saleen S and Naqvi A H (2013) : "*Synthesis and Characterization of Al doped ZnO Nanoparticles* " , Int.J.Mod.Phy.Conf.Ser., 22, 630 - 636.

Leite E R, Varela J A and Longo E (1992) : " *A New Interpretation for the Degradation of Phenomenon in ZnO Varistor* " , J.Mat.Sci., 27, 5527 - 5529.

Levine J D (1975) : " *Theory of Varistor Electronic Properties* " , Critical Review of Solid State Science, 5,597- 608.

Martzloff F D and Levinson L M (1998) : " *Surge Protective Devices : Electronic Ceramic Properties, Devices and Applications* " , Marcel Dekker Inc., NewYork. of Materials, Faculty of Engineering and Physical Sciences, University of Manchester,

Onreaboy W and Sirikulart N (2006) : "*Effect of Co Doping on Nonlinearity of ZnO*", Mat.Sci.Engg., B 150, 32 -37.

Poonsuk Poosimma (2014) : " *Stability of Zinc Oxide Varistors* ", PhD dissertation, School

Sinha A and Sharma B P (1997) : " *Novel Route for Preparation of High VoltageVaristor Powder* " , Mat.Res.Bull., 32, 1571 - 1579.

U K.(Unpublished)

Wang Y G, Lau S P, Lee H W, Yu S F, Tay B K, Zhang X H and Hng H H (2003) : " *Photoluminescence Study of ZnO Films Prepared by Thermal Oxidation of Zn Metallic in Air* " , J.Appl.Phys., 94., 354 - 359.

Yang W, Liu Z, Peng D L, Zhang F, Hung H, Xie Y and Wu Z (2009) : " *Room Temperature Deposition of Transparent Conducting Al Doped ZnO Films by RF Magnetron Supttering Method* " , Appl. Sur. Sci. , 255, 5669 - 5673 .

Yoon M H, Lee S H, Park H L, Kim H K and Jang M S (2002) : " *Solid Solubility Limits of Ga and Al in ZnO* " , J.Mater.Sci. Lett., 21, 1703 - 1704 .

J. Myanmar Acad. Arts Sci. 2020 **Vol. XVIII.No.2B**

AN EXISTENCEOF HYPERONIN HYDROGEN-LIKE ATOM FORΞ PbSYSTEM

Yin Yin Nu*

Abstract

The purpose of our research is to calculate the energy of hydrogen-like Ξ Pb atom for various states by solving the Schrödinger equation. We assumed as Ξ Pb atom is liked an ordinary hydrogen atom in which the electron is replaced by a negative xi hyperon. By assuming above approximation, we also calculated the energy of hydrogen-like Pb^{81} ionized atom. And then, we determined the radius of hydrogen-like Ξ Pb atom to know about their structure. We found that the energy of hydrogen-like Ξ Pb atom is greater than Pb^{81} ionized atom for various orbits and the inclusion of xi reduces the size of the atom in such a way the smaller radius is obtained. In addition, we observed that the radius of Ξ Pb atom is less than nuclear radius for lower orbits. It is found that the existence of atomic state and nuclear state cannot be distinguished in lower orbits. In this way, the existence of atomic and nuclear hybrid state can be found in lower orbits of Ξ Pb atom.

Keywords: energy of hydrogen-like atom, radius of hydrogen-like atom.

Introduction

The hydrogen atom is a simple mathematical problem in quantum mechanics, but any atom with more than one electron is difficult that an exact solution is impossible. For the two-electron atom, helium, very elaborate approximate solution have been set up by Hylleraas, which gives result agreeing with experimental error. This agreement has convinced physicists that Schrödinger's equation for the many-body problem provides the correct starting point for a study of more complicated atoms. But the method used for helium is too complicated to apply to atoms with more than two electrons and the approximations must be made for many electron atoms. A good starting point is provided by assuming that each electron moves in a central or spherically symmetrical, force field, produced by the nucleus and other electrons.

The Hydrogenic Core Model for Atoms with One-Valence Electron

The alkali atoms are approximately hydrogen like. They all have one valence electron. It will suffice to say that (Z-1) of the electrons are arranged in closed shells. So far as the electric field outside the closed shells is concerned, the nuclear charge +Ze, shielded by the (Z-1) electron carrying a charge of –(Z-1)e, is equivalent to +e, the same as the hydrogen atom. Thus the valence electron is essentially in a hydrogen-like field. However, inside the closed shells the shielding effect of (Z-1) electrons becomes less and less as we approach the centre and eventually becomes zero in the region just outside the nucleus. For large r the valance electron has an electrostatic potential $\frac{e^2}{r}$, this expresses the fact that the nuclear charge +Ze is screened by the core of (Z-1) electrons. For small r, potential approaches $\frac{Ze^2}{r}$ corresponding to an unscreened nucleus. Overall, the electrostatic attraction towards the nucleus is always greater than for hydrogen.

---

[*] Dr, Lecturer, Department of Physics, Banmaw University

Hydrogen-Like Atom

The spectra of all atoms or ions with only one electron should be the same expect for the factor Z^2 and the Rydberg number. The spectrum of hydrogen should thus explain those of the ions He , Li^2 , Be^3 or any other ions which have only one electron. For Li^2 , Be^3 and still heavier highly ionized atoms, spectral lines have been observed which can be calculated by multiplying the frequencies of the lines of the H atom by Z^2 and insertion of the corresponding Rydberg constant. In 1916, the collected spectroscopic experience concerning the hydrogen-similarity of these spectra was generalized in displacement theorem of Sommerfeld and Kossel, which states: the spectrum of any atom is very similar to the spectrum of the singly charged positive ion which follows it in the periodic table.

Hydrogen-like heavy atoms are the heavy atoms from which all the electrons expect one have been removed. Hydrogen-like heavy atoms can be prepared by accelerating the singly-ionized atoms to high energies and passing them through a thin foil; their electrons are "stripped off" on passing through the foil. For example, in order to strip all the electrons from a uranium atom and produce U^{92} ions, they must be accelerated to energies greater than 10 GeV. By permitting the U^{92} ions to recapture one electron each, one can then obtain hydrogen-like ion U^{91} .The corresponding spectral lines are emitted as the captured electron makes transitions from orbits of high n to lower orbits. In present work, we assumed above approximation, a Ξ Pb atom is like an ordinary hydrogen atom in which the electron is replaced by a negative xi. We calculated the energy of hydrogen-like Pb^{81} ionized atom and Ξ Pb atom forvarious states by solving the Schrodinger equation. And then, we also calculated the radii of Ξ Pb atom to know about their structure.

Solving the Schrödinger Equation for Hydrogen Atom

The Schrödinger equation for the hydrogen atom is

$$\frac{\hbar^2}{2\mu}\quad {}^2\psi \quad V\psi \quad E\psi \tag{1}$$

$$^2 \quad \frac{2\mu}{\hbar^2}\, E \quad V \quad \psi \quad 0 \tag{2}$$

Where the potential energy V of the electron in the hydrogen atom is

$$V(r) \qquad \frac{Ze^2}{4\pi\varepsilon_0 r} \tag{3}$$

$$^2 \quad \frac{1}{r^2}\frac{}{r}\; r^2\frac{}{r} \quad \frac{1}{r^2}\frac{1}{\sin\theta}\frac{}{\theta}\; \sin\theta\frac{}{\theta} \quad \frac{1}{r^2\sin^2\theta}\frac{^2}{\varphi^2} \tag{4}$$

Substitution equation (4) into equation (2)

$$\frac{1}{r^2}\frac{}{r}\; r^2\frac{\psi}{r} \quad \frac{1}{r^2}\frac{1}{\sin\theta}\frac{}{\theta}\; \sin\theta\frac{\psi}{\theta} \quad \frac{1}{r^2\sin^2\theta}\frac{^2\psi}{\varphi^2} \quad \frac{2\mu}{\hbar^2}\, E \quad V\; r \quad \psi \quad 0 \tag{5}$$

The wave function ψ is variable-seperable, i.e, ψ can be written as

$$\psi\ r,\theta,\varphi \qquad P\ \theta\ Q\ \varphi\ R\ r \qquad (6)$$

where $P\ \theta$ is a function of θ only, $Q\ \varphi$)of φ only and $R\ r$ of r only.

Substitution equation (6) into equation (5)

$$\frac{P\ \theta\ Q\ \varphi}{r^2}\frac{}{r}\ r^2\frac{}{r}R\ r \qquad \frac{R\ r\ Q\ \varphi}{r^2\sin\theta}\frac{}{\theta}\ \sin\theta\frac{}{\theta}P\ \theta \qquad \frac{P\ \theta\ R\ r}{r^2\sin^2\theta}\frac{{}^2}{\varphi^2}Q\ \varphi$$

$$\frac{2\mu}{\hbar^2}E \quad V\ r\ \ P\ \theta\ Q\ \varphi\ R\ r \quad 0 \qquad (7)$$

Dividing by $P\ \theta\ Q\ \varphi\ R\ r$ on both sides,

$$\frac{1}{R\ r\ r^2}\frac{}{r}\ r^2\frac{}{r}R\ r \qquad \frac{1}{P\ \theta\ r^2\sin\theta}\frac{}{\theta}\ \sin\theta\frac{}{\theta}P\ \theta \qquad \frac{2\mu}{\hbar^2}E \quad V\ r$$

$$\frac{1}{Q\ \varphi\ r^2\sin^2\theta}\frac{{}^2}{\varphi^2}Q\ \varphi \qquad (8)$$

Multiplying equation (8) by $r^2\sin^2\theta$, we get

$$\frac{\sin^2\theta}{R\ r}\frac{d}{dr}\ r^2\frac{d}{dr}R\ r \qquad \frac{\sin\theta}{P\ \theta}\frac{d}{d\theta}\ \sin\theta\frac{d}{d\theta}P\ \theta \qquad \frac{2\mu\, r^2\sin^2\theta}{\hbar^2}E \quad V\ r$$

$$\frac{1}{Q\ \varphi}\frac{d^2}{d\varphi^2}Q\ \varphi \qquad (9)$$

According to equation (9), the R. H. S and L. H. S should equal to some arbitrary constant and we use m_ℓ^2.

Therefore R. H. S of equation (9) becomes

$$\frac{1}{Q\ \varphi}\frac{d^2}{d\varphi^2}Q\ \varphi \qquad m_\ell^2 \qquad (10)$$

Similarly, L. H. S of equation (9) becomes

$$\frac{\sin^2\theta}{R\ r}\frac{d}{dr}\ r^2\frac{d}{dr}R\ r \qquad \frac{\sin\theta}{P\ \theta}\frac{d}{d\theta}\ \sin\theta\frac{d}{d\theta}P\ \theta \qquad \frac{2\mu r^2\sin^2\theta}{\hbar^2}E \quad V\ r \qquad m_\ell^2 \qquad (11)$$

Dividing equation (11) by $\sin^2\theta$, we get

$$\frac{1}{R\ r}\frac{d}{dr}\ r^2\frac{d}{dr}R\ r \qquad \frac{2\mu r^2}{\hbar^2}E \quad V\ r \qquad \frac{m_\ell^2}{\sin^2\theta} \quad \frac{1}{P\ \theta\ \sin\theta}\frac{d}{d\theta}\ \sin\theta\frac{d}{d\theta}P\ \theta \qquad (12)$$

Similarly, L. H. S and R. H. S should equal to some arbitrary constant.

Therefore, the R. H. S of equation (12) becomes

$$\frac{m_\ell^2}{\sin^2\theta} \quad \frac{1}{P\ \theta\ \sin\theta}\frac{d}{d\theta}\ \sin\theta\frac{d}{d\theta}P\ \theta \qquad L^2 \qquad (13)$$

and L. H. S becomes

$$\frac{1}{R\ r}\frac{d}{dr}\ r^2\frac{d}{dr}R\ r \qquad \frac{2\mu r^2}{\hbar^2}\ E \quad V\ r \qquad L^2 \tag{14}$$

Substitution the potential term

$$V\ r \qquad \frac{Ze^2}{4\pi\varepsilon_0 r} \tag{15}$$

We obtain the equation

$$\frac{1}{R\ r}\frac{d}{dr}\ r^2\frac{d}{dr}R\ r \qquad \frac{2\mu r^2}{\hbar^2}\ \frac{Ze^2}{4\pi\ {}_0r} \quad E \quad L^2 \tag{16}$$

By multiplying with $\frac{R\ r}{r^2}$, equation (16) becomes

$$\frac{1}{r^2}\frac{d}{dr}\ r^2\frac{d}{dr}R\ r \qquad \frac{2\mu}{\hbar^2}\ \frac{Ze^2}{4\pi\varepsilon_0 r} \quad E \quad \frac{\ell(\ell \quad 1)}{r^2}\ R\ r \quad 0$$

Since the reduce mass $\mu \quad m$, multiplying with $\frac{\hbar^2}{2m}$, we get

$$\frac{\hbar^2}{2m}\frac{1}{r^2}\frac{d}{dr}\ r^2\frac{dR}{dr} \qquad \frac{Ze^2}{r} \quad E\ R \quad \frac{\hbar^2}{2m}\frac{\ell(\ell \quad 1)}{r^2}R \quad 0 \tag{17}$$

where $4\pi\varepsilon_0 \quad 1$ in atomic unit.

After solving mathematical steps,we obtain the energy of electron for the n^{th} orbit.

$$E_n \qquad \frac{Z^2me^4}{2\hbar^2}\frac{1}{n^2} \tag{18}$$

where, E_n = the total energy of the electron

m = mass of electron

$\hbar \quad \frac{h}{2\pi}$ (h=Planck constant)

e = electron charge

n = 1, 2, 3…

We calculated the energy levels of hydrogen-like Pb^{81} ionized atom and $\Xi^- \quad Pb$ atom by using the above equation.

Calculation of the Radius for Hydrogen Atom

The Coulomb force between a stationary nucleus with charge +Ze and an orbiting electron with charge –e is

$$F \qquad \frac{kZe^2}{r^2} \tag{19}$$

From Newton's second law of motion, the centripetal force

$$F \quad \frac{mv^{2}}{r} \tag{20}$$

From equation (19) and equation (20)

$$mv^{2} \quad \frac{kZe^{2}}{r} \tag{21}$$

But, from Bohr's postulate

$$mvr \quad n\hbar$$

$$v^{2} \quad \frac{n^{2}\hbar^{2}}{m^{2}r^{2}} \tag{22}$$

Substituting the equation (22) into equation (21) we getthe radius of electron for the n^{th} orbit.

$$r_{n} \quad \frac{n^{2}\hbar^{2}}{mkZe^{2}} \tag{23}$$

Where, r_{n} the radius of the circular orbit

m = mass of electron

v = velocity of electron

k = constant = $9 \quad 10^{9}\,\mathrm{Nm}^{2}\mathrm{C}^{\;2}$

$\hbar \quad \frac{h}{2\pi}$ (h=Planck constant)

e = electron charge

n = 1, 2, 3 ….

By using the above equation, we calculated the radius of hydrogen-like Pb^{81} ionized atom and $\Xi \quad Pb$ atom for various orbits.

Results and Discussions

The Energy of Hydrogen-Like Pb^{81} ionized atom and $\Xi \quad Pb$ atom

Hydrogen-like heavy atoms are the heavy atoms from which all the electrons except one have been removed. We assumed as $\Xi \quad Pb$ atom is like an ordinary hydrogen atom in which the electron is replaced by a negative xi hyperon. And then we calculated the energy of hydrogen-like Pb^{81} ionized atom and $\Xi \quad Pb$ atom for various states by solving the Schrödinger equation. From these results, we observed that the energy of $\Xi \quad Pb$ atom is greater than Pb^{81} ionized atom for each orbits. The higher the orbit, the greater the energy for these atoms. The calculated energy for these atoms is given in Table (1) and the energy levels of Pb^{81} ionized atom as shown in Figure (1). Then the energy levels $\Xi \quad Pb$ atom as shown in Figure (2).

The Radius of Hydrogen-Like Pb^{81} ionized atom and $\Xi \quad Pb$ atom

And then we also calculated the radius of hydrogen-like Pb^{81} ionized atom and $\Xi \quad Pb$ atom as given in Table (2). In our calculation, the radius of $\Xi \quad Pb$ atom is very smaller than Pb^{81} ionized atom for each orbit. The higher the orbits, the greater the size of these atoms. The inclusion of xi reduces the size of the atom in such a way the small radius is obtained. Moreover, we found that the radius of Ξ Pb atom is less than the nuclear radius for lower orbit. Therefore, the existence of atomic state and nuclear state are mixture. The mixture of the atomic state and nuclear state is called hybrid state. So we cannot distinguish the existence of the atomic state or the nuclear state of hydrogen-like Ξ Pb atom for lower orbits.

Table 1 Comparison between energy of Hydrogen–like Pb^{81} ionized atom and Ξ Pb atom for various orbits

Orbital quantum number	**Energy (MeV)**	
	Hydrogen-like Pb^{81} ionized atom	**Hydrogen-like Ξ Pb atom**
1	- 0.0911624	- 236.4217125
2	- 0.0227906	- 59.1054281
3	- 0.0101292	- 26.2690792
4	- 0.0056976	- 14.7763570
5	- 0.0036465	- 9.4568685
6	- 0.0025323	- 6.6572698

Table 2 Comparison between radii of Hydrogen–like Pb^{81} ionized atom and Ξ Pb atom for various orbits

Orbital quantum number	**Radius (fm)**	
	Hydrogen – like Pb^{81} ionized atom	**Hydrogen – like Ξ Pb atom**
1	647. 6339	0.2497
2	2590.5356	0.9988
3	5828.7051	2.2473
4	10362.1424	3.9952
5	16190.8475	6.2425
6	23314.8204	8.9892

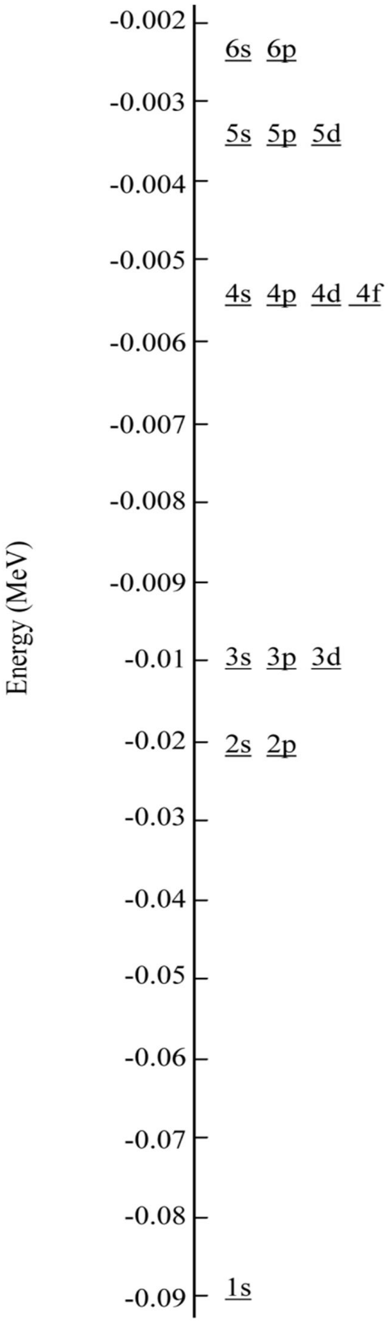

Figure 1 Energy levels of the Pb^{81+} ionized atom

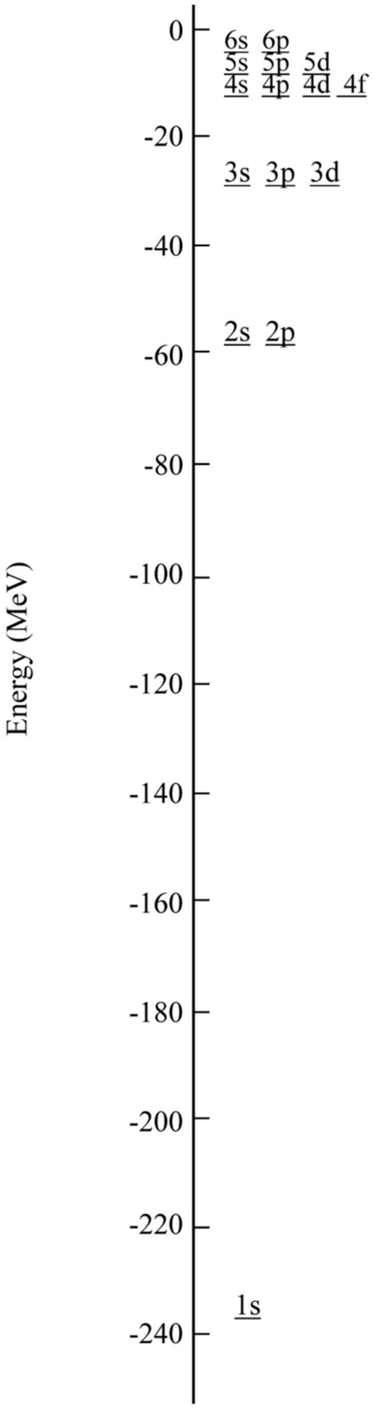

Figure 2 Energy levels of the Ξ Pb atom atom

We calculated the energy of hydrogen-like Pb^{81} ionized atom and $\Xi \quad \mathrm{Pb}$ atom for various states by solving the Schrödinger equation. And then, we also calculated the radii of hydrogen-like Pb^{81} ionized atom and $\Xi \quad \mathrm{Pb}$ atom to know about their structure. In our calculation, we assumed as $\Xi \quad \mathrm{Pb}$ atom is liked an ordinary hydrogen atom in which the electron is replaced by a negative xi hyperon. From the calculations, we concluded that the radius of $\Xi \quad \mathrm{Pb}$ atom is less than nuclear radius and we cannot distinguish the existence of atomic state and nuclear state (hybrid state).

Acknowledgement

The author would like to thank Dr Than ThanLwin, Professor, Head of Physics Department, Banmaw University for her encouragement.

References

Bransen, B.H. & C. J. Joachain, (2007) Quantum Mechanics, Dorling Kindersley Pvt. Ltd., New Delhi, India.

French, A.P., (1958) Principles of Modern Physics, John Wiley & sons, Inc., New Yorky.

Haken, H., & H. C. Wolf, (2005) The Physics of Atom and Quanta, Springer Berlin Heidelberg, New York .

J. Myanmar Acad. Arts Sci. 2020 **Vol. XVIII.No.2B**

ENHANCEMENTOF MRI BRAINIMAGESUSING MATLAB

Thazin Khaing[1 2] & Khin Khin Win[3]

Abstract

Image enhancement aims to increase the visibility of original input images and to convert them into a better form with detail information. Images enhancement is a vital role in image processing because of the poor contrast depending on the nature of the images. In this research, a total of 100 test grayscale images which are normal and abnormal MRI brain (512×512) pixels images have been processed by using enhancement techniques. This research described the methods of enhancement of magnetic resonance imaging (MRI) brain images in spatial domain by using MATLAB. Image data used in this research were obtained from No (2) military hospital 500 bedded, Dagon Township, Yangon (Myanmar). The best technique to be applied for MRI brain images has been identified by comparing the result of peak signal to noise ratio (PSNR). Based on the result obtained, it has been confirmed that the combination of spatial filtering and histogram equalization technique is more suitable for enhancement of the MRI brain images.

Keywords: Image Enhancement, Filtering, Histogram Equalization, Magnetic Resonance Imaging (MRI), Matrix Laboratory (MATLAB)

Introduction

Image processing is a method to perform some operations on an image, in order to get an enhanced image or to extract some useful information from it. It is the most popular field for image analysis (Gonzalez, R.C.,& R. E. Woods, 2002).The purpose of image processing is divided into five groups. They are visualization, image sharpening and restoration, retrieval, measurement of pattern and image recognition. This paper will present medical image enhancement techniques. Image enhancement is to increase the quality of an image so that the result is clearer and clean than the original image for a specific application. Medical images are a special kind of image that can be used for the diagnostics of diseases in the patients. A number of modalities like Magnetic resonance imaging (MRI), Computed Tomography (CT) and X-rays exit for obtaining these images. MRI is a popular technique to analyze human brain soft tissue because it gives detailed information about the diseases (Cheruku, K. S., R. Ratnadeep, K. P. Archek, and Y. K. Ashwani, 2015). In this paper, normal and abnormal original MRI brain T2-weighted images which having low contrast depending on the MRI machine are applied to get the more detailed information of MRI images. One of the most important stages in medical images detection and analysis is image enhancement techniques which improve the quality of images for human vision, removing blurring and noise, increasing contrast, and revealing details. The techniques of image enhancement can be classified into two broad categories: Spatial Domain Methods and Frequency Domain Methods. This paper describes the methods of enhancement of brain MRI images in spatial domain by using MATLAB. Image data used in this work were obtained from No (2) military hospital 500 bedded, Dagon Township, Yangon (Myanmar).

---

[1] Assistant Lecturer, Department of Engineering Physics, Technological University (Banmaw)

[2] Third Year PhD Student, Department of Physics, University of Yangon

[3] Professor and Head, Department of Physics, University of Yangon

Materials and Methods

Frequency Domain Methods

Frequency domain image enhancement is a term used to describe the analysis of mathematical functions or signals with respect to frequency and operate directly on the transform coefficients of the image such as Fourier transform, discrete wavelet transform, discrete cosine and sine transform. The quality of the respective image can improve by making changes in the transform coefficient functions. The advantages of frequency domain image enhancement include low complexity of computations, manipulating the frequency coefficient of an image and the applicability of improved version of domain properties. The major drawback of frequency domain method is it cannot produce clear picture of background and it cannot enhance all the parts of the image. It can focus only on particular parts(Gonzalez, R.C.,& R. E. Woods, 2002).

Spatial Domain Methods

Spatial domain techniques directly deal with the image pixels. The pixel values are manipulated to achieve desired enhancement. The main advantage of spatial based domain technique is conceptually simple to understand and the complexity of these techniques is low which favors real time implementations. But they usually enhance the whole image in a uniform manner which in many cases produces undesirable results. The approaches can be classified into two categories: Point processing operation and Spatial filter operations. Point processing operations is the simplest spatial domain operation as operations are performed on single pixel only. Pixel values of the processed image depend on pixel values of original image. The point processing approaches can be classified into four categories as negative transformation, thresholding transformation, log transformation and power law transformations. Spatial filter operations are performed on a pixel along with its immediate neighbors; this is also called as neighborhood operations. Based on type of operations performed on the pixels spatial filters are classified into two categories: Linear and Nonlinear spatial filters. Linear spatial filter process involves convolving a mask with an image that is passing a weighted mask over the entire image. Mask is also referred as window, template, or kernel. Non-linear spatial filter are those filters in which enhanced image is not linearly related to pixels in the neighborhood of original image (Uday, K., P. Vishal, and R.Shekhar, 2013).

Spatial Filtering

Filtering is a neighborhood operation, in which the value of any given pixel in the output image is determined by applying some algorithm to the values of the pixels in the neighborhood of the corresponding input pixel. A pixel's neighborhood is some set of pixels, defined by their locations relative to that pixel. Filtering is a technique for modifying or enhancing an image. Filtering an image is to emphasize certain features or remove other features. Image processing operations implemented with filtering include smoothing, sharpening, and edge enhancement. *Linear filtering* is filtering in which the value of an output pixel is a linear combination of the values of the pixels in the input pixel's neighborhood. Mean and median filters are effective for reducing different types of noise. The effect of low pass filtering in the spatial domain is to blur the sharp edges, and therefore increase the uncertainty about the location of the edges. A high pass filtering technique is to increase the contrast of the edges. As mention above there are a lot of techniques used in image enhancement. The enhancement techniques differ from one field to another according to its objectives and requirements. Depending on nature of an image, appropriate method should be used for enhancement purposes. This paper proposed that the combination of spatial filtering and histogram equalization technique. It is consists of three steps. They are median filter for noise reduction, Contrast Limited Adaptive Histogram Equalization technique for improving the local contrast of images and average filter for smoothing images data (Gonzalez, R. C.,& R. E. Woods, 2002).

Median Filter

Median filtering preserves edges while removing noise. It is a nonlinear operation. To compute the output of a median filter, an odd number of sample values are ranked and the median value is used as the filter output.

For example,

$$\begin{bmatrix} 10 & 20 & 20 \\ 20 & 15 & 20 \\ 20 & 25 & 100 \end{bmatrix}$$

Sort them $\longrightarrow$ 10, 15, 20, 20, 20, 20, 20, 25, 100 then median value = 20.

Histogram Equalization

In an image histogram, the *x* axis shows the gray level intensities and the y axis shows the frequency of these intensities. Numerous spatial domain processes consider histogram as the efficient technique for pre-processing. Histogram equalization is a common technique for enhancing the appearance of images. Suppose an image which is predominantly dark. Then its histogram would be skewed towards the lower end of the grey scale and all the image detail is compressed into the dark end of the histogram. If we could `stretch out' the grey levels at the dark end to produce a more uniformly distributed histogram then the image would become much clearer. The goal in histogram equalization is to approximate the grayscale-value distribution of an image to the uniform distribution (Hardeep, K., and R. Jyoti, 2016). Histogram equalization is useful because it helps in spreading the grayscale values and allows us to see a larger range of grayscale values. The histogram of an image mostly represents the comparative frequency of occurrence of the different grey levels in the image. The advantage of histogram equalization is in full automation and its results are very similar to linear contrast stretching. Histogram equalization automatically computes a transformation function to give a new image with uniform histogram (Gonzalez, R.C.,& R. E. Woods, 2002).

Contrast Limited Adaptive Histogram Equalization

Contrast limited adaptive histogram equalization proposed to improve the over amplification of noise problem present in the histogram equalization technique. It is different from standard histogram adjustment in which it works on small regions in the image are called as tiles and computes several histograms, each compared to a particular area of the picture and use them to redistribute the brightness or contrast estimation of the image. Contrast limited adaptive histogram equalization improves contrast of an image more than standard histogram equalization in which it gives more detail but still has tendency to amplify noise (Cheruku,K. S., R. Ratnadeep, K. P. Archek, and Y. K. Ashwani, 2015).

Average Filter

The average (mean) filter smoothen image data, thus eliminating noise. The filter performs spatial filtering on each individual pixel in an image using the gray level values in a square or rectangular window surrounding each pixel. The average filter computes the sum of all pixels in the filter window and then divides the sum by the number of pixels in the filter window.

$$1/9 * \begin{bmatrix} 1 & 1 & 1 \\ 1 & 1 & 1 \\ 1 & 1 & 1 \end{bmatrix} \longrightarrow 3 \times 3 \text{ filter window}$$

The essential idea of this method is to replace grayscale value of the center pixel by average value of neighborhood pixel grayscale.

PSNR

The following equation is to calculate the Peak Signal-to-Noise Ratio (PSNR):

$$PSNR = 10log_{10}\left(\frac{peakval^2}{MSE}\right)$$

Where peakvalue is either specified by the user or taken from the range of the image data type (e.g. for uint8 image it is 255). MSE is the mean square error, i.e. MSE between A and ref.MSE measures the average squared difference between actual and ideal pixel values.

Results and Discussion

Image data used in this work were obtained from No (2) military hospital 500 bedded, Dagon Township, Yangon (Myanmar). The normal and abnormal original MRI brain (512×512) pixels images have been enhanced with various methods. By using thresholding method, the region of interest of abnormal MRI brain image could be isolated from background. The flaw of the abnormal part of MRI brain image could be seen very clearly by using gray level slicing method. Histogram equalization stretches the contrast by redistributing the gray-level values uniformly. It is found that histogram equalization technique is not very effective for MRI brain images used in this work although it is popular for poor contrast images. The result of enhanced original images using the combination of spatial filtering and histogram equalization method is illustrated in figure 1(b) and figure 2(b). The effective enhanced images are obtained by using these algorithms. According to the human vision, the quality of the enhanced images is found to be better than that of the original images because the internal structure of the image become clearer. The region of interest was appeared as shown in figure 2(b). The simplest and most widely used performance measure is peak signal to noise ratio (PSNR). The value of PSNR obtained by using the combination method is found to be higher than those obtained via the others techniques applied in this research. The higher PSNR indicates the better the MRI brain image results. The measurements of the normal and abnormal MRI brain grayscale images using the three techniques are described in Tables 1 and 2. All of the MRI images are processed through MATLAB code.

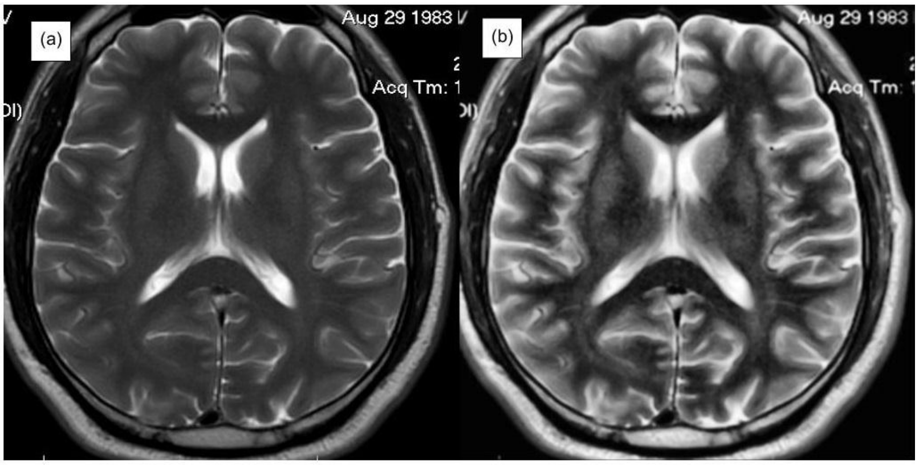

Figure 1 (a) Input MRI normal brain (512×512) pixels image
(b) Enhanced image after using the combination of spatial filtering and histogram equalization

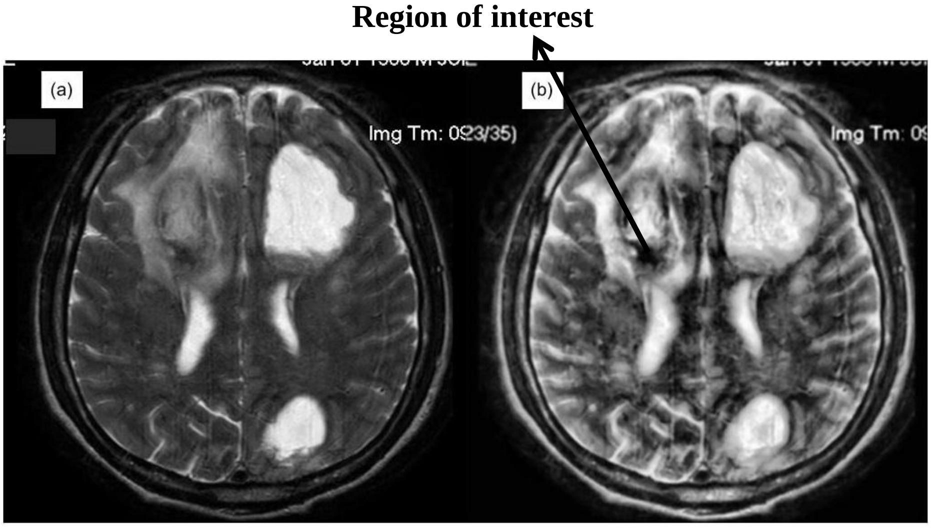

Figure 2 (a) Input MRI abnormal brain (512×512) pixels image
(b) Enhanced image after using the combination of spatial filtering and histogram equalization

Table 1 PSNR values of normal brain (512×512) pixels images

Input images name	Thresholding method PSNR(dB)	Histogram equalization PSNR(dB)	Combination method PSNR(dB)
N1	11.04	14.36	18.53
N2	9.70	17.02	19.07
N3	10.79	13.95	19.49
N4	10.80	14.48	19.97
N5	10.66	12.89	20.19
N6	10.47	12.54	19.49
N7	10.81	12.44	19.58
N8	10.72	12.93	17.23
N9	10.60	14.05	18.79
N10	12.42	10.98	18.47

Table 2 PSNR values of abnormal brain (512×512) pixels images

Input images name	Thresholding method PSNR(dB)	Histogram equalization PSNR(dB)	Combination method PSNR(dB)
Ab1	10.32	12.73	16.80
Ab2	10.77	15.33	20.21
Ab3	10.81	14.68	21.36
Ab4	11.68	10.60	20.79
Ab5	11.15	13.20	18.67
Ab6	10.85	13.15	21.83
Ab7	11.29	11.92	16.94
Ab8	11.39	12.28	19.78
Ab9	13.44	10.12	16.85
Ab10	12.55	10.59	17.20

Conclusion

Normal and abnormal MRI brain images have been applied by the various image enhancement techniques in spatial domain. The techniques like thresholding transformation and intensity level slicing have been analyzed. These techniques are found to be suitable for the brain images used in this paper. The performance of enhancement techniques has been measured using peak signal to noise ratio (PSNR). Based on calculation, the combination of spatial filtering and histogram equalization method could provide the better results with large PSNR value comparable to other methods. It is concluded that the combination of spatial filtering and histogram equalization method are preferable to apply on the original MRI brain images with the poor contrast. Other methods such as negative transformation, log transformation and power law transformation have also been applied to the MRI brain images. Negative transformation is suited for enhancing white detail embedded in dark regions and has applications in medical imaging. Therefore, image enhancement techniques can be used particularly for medical image enhancement to obtain potential results. However, log transformation technique is suitable for security surveillance applications. Besides, power law transformation can be useful for general purpose contrast manipulation. The enhancement techniques differ from one field to another according to its objectives and requirements. Depending on nature of an image, appropriate method should be used for enhancement purposes.

Acknowledgements

First and foremost my profound thanks go to my supervisor Professor Dr Khin Khin Win, Head of Department of Physics, University of Yangon, who gave me the opportunity to carry out this work and for her guidance, encouragement, helpful discussions and valuable suggestions.

I wish to show my sincere thanks to all the Professors in Department of Physics, University of Yangon, for their discussion, valuable suggestions and for allowing presenting this paper.

The authors would like to express their thank to the Department of Higher Education (Lower Myanmar), Ministry of Education, Yangon, Myanmar, for provision of opportunity to do this research.

References

Cheruku,K. S., R. Ratnadeep, K. P. Archek, and Y. K. Ashwani, (2015), “Analysis of Histogram Processing for Brain MRI using MATLAB”, International Journal of Innovative Research in Engineering & Science, Vol. 3, pp1-6

Gonzalez, R. C.,& R. E. Woods, (2002), “Digital Image Processing*”*, 2nd Edi, Upper Saddle River, NJ: Prentice-Hall

Hardeep, K., and R. Jyoti, (2016), “MRI brain image enhancement using Histogram equalization techniques”, IEEE WiSPNET conference, pp770-773

Uday, K., P. Vishal, and R.Shekhar, (2013), “Enhancement of Medical Images using Image Processing in Matlab”, International Journal of Engineering & Technology, Vol. 2, pp2359-2364

J. Myanmar Acad. Arts Sci. 2020 **Vol. XVIII.No.2B**

PREPARATION OF CALCIUM PHOSPHATE BIOMATERIALS BY USING MICROWAVE–ASSISTED CO-PRECIPITATION

Seinn New Aung [1],Aye Aye Thant[2], Nwe Ni Hlaing[3], Than Htike Win[4]

Abstract

The calcium phosphate-based biomaterials have been synthesized by microwave assisted co-precipitation method. The calcium nitrate tetrahydrate and diammonium hydrogen phosphate have been used as calcium and phosphorus sources. The pH regulation has been performed by using two types of inorganic bases; sodium hydroxide and ammonium hydroxide during processing. The phase formation of the synthesized biomaterials with two different inorganic bases has been compared in this work. The synthetic samples have been characterized by using X-ray diffractrometry (XRD), Fourier Transform-Infrared Spectroscopy (FTIR) and Scanning Electron Microscopy(SEM). These results show that crystallized monetite phase and biphasic calcium phosphate (20% of Apatite &80% of Beta tricalcium phosphate)have been obtained via sodium hydroxide assisted synthesis. Crystallized hydroxyapatite (HA) phase and biphasic calcium phosphate (23% of Apatite &97% of β-tricalcium phosphate) have been obtained via ammonium hydroxide assisted synthesis at calcination temperature of 900ºC.

Keywords: biomaterials, precipitation, microwave, XRD, FTIR, SEM.

Introduction

Calcium Phosphate based biomaterials play a pivotal role as scaffolds for tissue regeneration and drugdelivery due to their chemical similarity to the inorganic phase of bone. Biomaterials are not only biocompatible but also non-toxic, immune agent, bioactive and osteoconductive. CaPfamily includes four main categories: Hydroxyapatite (HAP), calcium deficient Hydroxyapatite (CDHAP) (tetracalcium phosphate or octacalcium phosphate), biphasic calcium phosphate(BCP) and tricalcium phosphate (α or β-TCP).When precipitating CaP in basic aqueous solutions, three main different solid phases could be formed; either amorphous calcium phosphates, Octate calcium phosphates or HAP(Behzad and Gholam, 2015).

These phases are different by increasing in their thermodynamic order and decreasing on the time scale. Although being similar chemically, their crystal structure, mechanical, physical and biological differ according to the processing parameters temperature, pH, partial pressure of water, aging time and the presence of impurities) (I Y.J.Zhu, F, 2014).

Materials and Method

Materials

In this study, calcium nitrate tetrahydrateand ammonium hydrogen phosphate were used as calcium and phosphorus sources. The pH regulation has been performed by using two types of inorganic bases; sodium hydroxide ands ammonium hydroxide during processing.Distilled water (H_2O) was used as solvent.

---

[1] PhD candidate, Assistant Lecture, Department of Physics, University of Dagon

[2] Dr, Professor, Department of Physics, University of Yangon.

[3] Dr, Lecturer, Department of Physics, University of Taunggyi.

[4] Dr, Lecturer, Department of Physics, University of Mandalay.

Method

There are various methods of CaP synthesis such as precipitation technique, sol-gel approach, hydrothermal technique, multiple emulsion technique, biomimetic deposition technique, electrode position technique, etc. Each employs various process parameters. In this research, microwave-assisted precipitation method has been used to provide enhanced reaction rate and improved product field in chemical synthesis (E.Lerner, S. Sarig, 1991)

Result and Discussion

The synthetic samples have been characterized by X-ray diffractrometry (XRD), Fourier Transform-Infrared Spectroscopy (FTIR) and Scanning Electron Microscopy (SEM).

XRD Analysis of Calcium Phosphate Sample by Using Sodium Hydroxide before and after calcination

The XRD pattern of Calcium Phosphate sample by using sodium hydroxide(inorganic base)has been shown in Figure 1. Figure 1 (a) showsthe XRD pattern of of synthetic Calcium Phosphate sample by using sodium hydroxide before calcination. The monetite($CaHPO_4$) hexagonal, space group of P63/m(ICDD-00-009-0432) has been observed as a major phase. The sharp intensity peak at 26.45°indicated that monetitephase could be attained by simple precipitation method at room temperature.

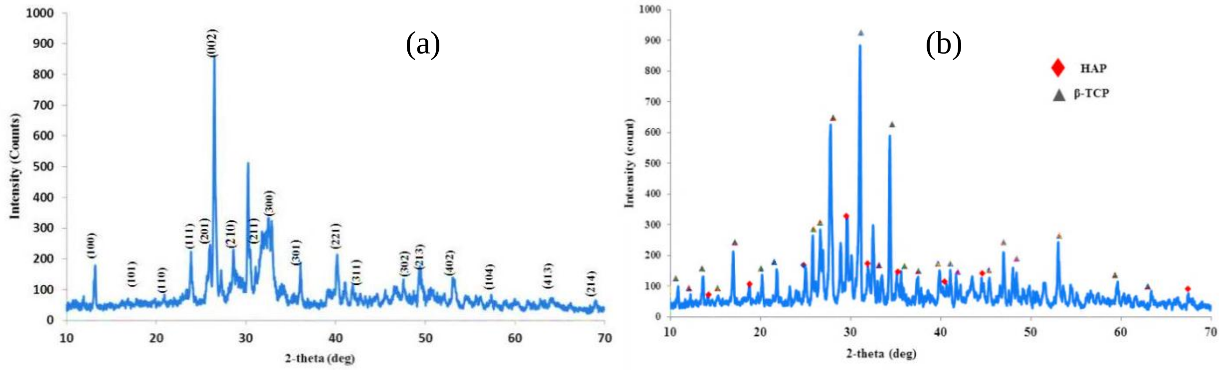

Figure 1 XRD pattern of synthetic Calcium Phosphate sample by using sodium hydroxide (a) before calcination (b) after calcination at 900ºC

Figure 1 (b) shows the XRD pattern of synthetic Calcium Phosphate sample by using sodium hydroxide at 900ºC. The formation of biphasics hydroxyapaitite (trigonal (H),R3c) with beta tricalcium phosphate with (hexagonal, P63/m) have been reported in (ICDD-00-009-0432).

XRD Analysis of Calcium Phosphate Sample by Using Ammonium Hydroxide before and after calcination

The XRD pattern of calcium phosphate sample by using Ammonium hydroxide(inorganic base) is hown in Figure 2. Figure 2 (a) shows the hydroxyapatite(hexagonal,P63/m) reported in (ICDD-00-009-0432). The sharp intensity peak at 2θ value of 32.22° corresponding to (211) plane indicated that hydroxyapatite phase could be attained by simple precipitation method at room temperature.

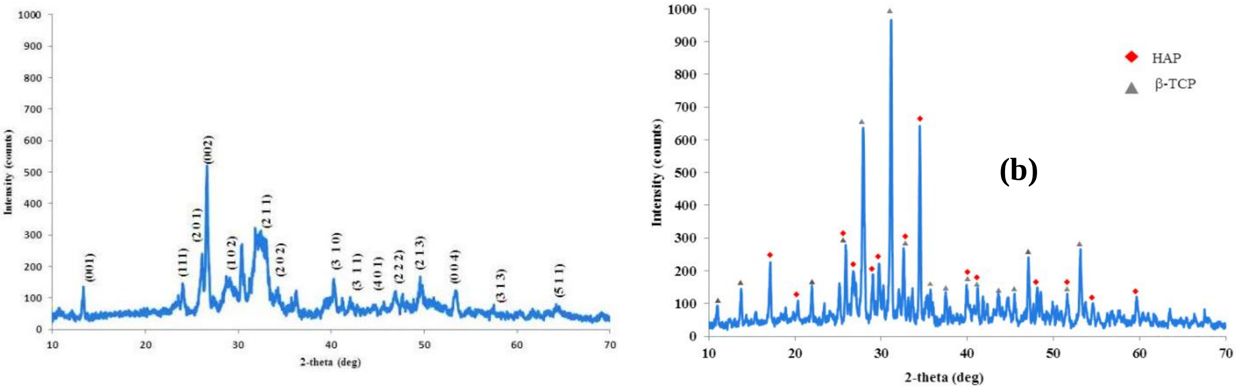

Figure 2 XRD pattern of synthetic Calcium Phosphate sample by using ammonium hydroxide (a) before calcination (b) after calcination at 900ºC

XRD Analysis of Calcium Phosphate Sample by Using ammonium hydroxide after calcination

The XRD pattern of calcium phosphate sample at 900ºC is shown in Figure 2 (b), the formation of biphasics; hydroxyapaitite (trigonal, R3c) with betatricalcium phosphate (hexagonal, P63/m) reported in ICDD-00-009-0432 (Baradaran S, 2013).

Crystallite Size

The crystallite size can be estimated using the Scherer's equation:

$$D = \frac{0.9\lambda}{B\cos\theta}$$

where, B = full width at the half maximum (radian)

λ is the wavelength (Å), θ is diffraction angle

Table 1 Results of nano-sized Calcium Phosphate powders from(XRD)

Inorganic bases	Condition	Crystallite size (nm)
NaOH	before calcination	33.24
	after calcination	41.98
NH_4OH	before calcination	17.18
	after calcination	36.09

Reference Intensity Ratio (RIR) Value and Weight Percentage

Reference Intensity Ratio (RIR) value and weight percentage of constituent of the sample has been calculated by using following formula(I Y.J. Zhu, F.)

$RIR_{HAP} = I_{HA} / (I_{HAP} + I_{\beta\text{-TCP}})$

$RIR_{\beta\text{-TCP}} = I_{\beta\text{-TCP}} / (I_{\beta\text{-TCP}} + I_{HAP})$

Weight % = (RIR ×100)%

where, I_{HAP} = maximum intensity of HAP phase

$I_{\beta\text{-TCP}}$= = maximum intensity of β-TCP phase

Comparison of RIR Value and Weight % of Calcium Phosphate by Using Sodium Hydroxide and Ammonium Hydroxide after Calcination at 900ºC

Table 2 Comparison of RIR Value and Weight % of Calcium Phosphate by using sodium hydroxide and ammonium hydroxide after calcination

Inorganic bases	Phase	2 (deg)	Plane	Relative Intensity	RIR value	Weight(%)
NaOH	β-TCP	31.50	(0210)	149	0.80	80
	HAP	33.00	(112)	38.30	0.20	20
NH_4OH	β-TCP	27.87	(214)	168	0.97	97
	HAP	34.50	(202)	38.30	0.03	3.0

FT-IR analysis

FT-IR Analysis of Calcium Phosphate by using sodium hydroxide before and after calcination

The functional groups generally observed in the FT-IR spectra of calcium phosphate based materials are PO_4^{3-}, OH^-, CO_3^{2-}, P_2O_7 and HPO_4^{2-} groups in the range around 4000–400 cm^{-1}.

Figure 3 shows FTIR spectrum of Calcium Phosphate by using sodium hydroxide (before calcination). The characteristic bands of phosphate groups have been appeared around 560–613 cm^{-1} and 1100–1000cm^{-1}. There are sharp and well-separated peaks at 431.1 cm^{-1}, 560.97 cm^{-1}, 601.49 cm^{-1} and 1026 cm^{-1} have been all attributed to the PO_4^{3-}group of monetite. The peak 3571 cm^{-1} has been attribute to OH- group and 861.80 cm^{-1} has been attribute to $CO_3^{2-.}$

Figure 4 shows FTIR spectrum of Calcium Phosphate by using sodium hydroxide (after calcination). The sharp and well-separated peaks at 542.61 cm^{-1}, 589.85cm^{-1}, 945.25 cm^{-1}, 971.61 cm^{-1} and 1023.63 cm^{-1} have been assigned to biphasics (β-TCP and HAP)groups. These results are in good agreement with the X-ray diffraction analysis.

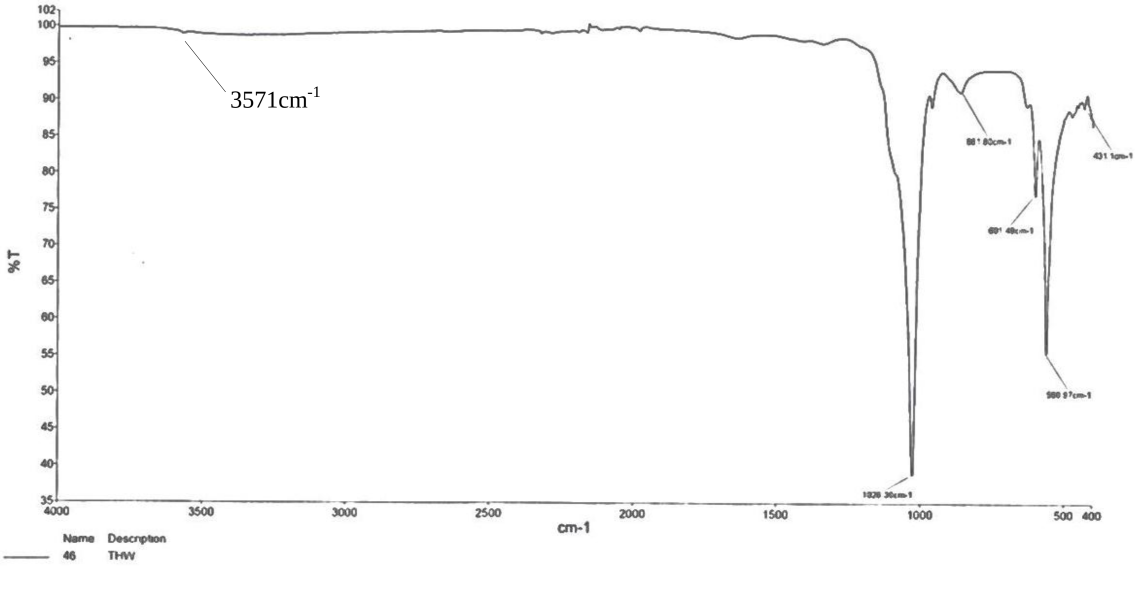

Figure 3 FT-IR spectrum of CaP sampleby using sodium hydroxide(before calcination)

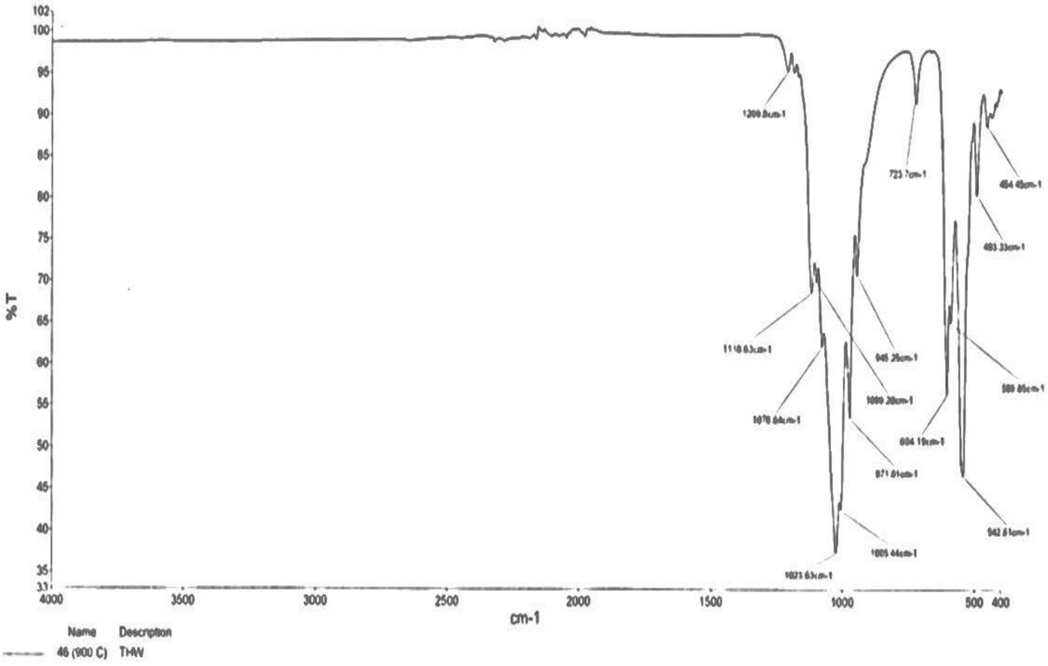

Figure 4 FT-IR spectrum of CaP sample by using sodium hydroxide (after calcination at 900°C)

Table 3 The FT-IR transmission bands of CaP sample using sodium hydroxide before and after calcination

Calcination condition	Transmission Bands(cm^{-1}) of Chemical groups					
	PO_4^{3-}				OH-	CO_3^{2-}
	ν1 symmetric (P-O) stretching	ν2 (O-P-O) bending	ν3 asymmetric (P-O) stretching	ν4 (P-O) bending	Stretching	
before calcination	`	431.10	1026.30	560.97 691.40	3571.00	861.80
900°C	493.83 542.61 589.85 945.25 971.61	451.45	1018.63 1005.44 1118.63 1209.80	- - 604.19	-	-

FT-IR Analysis of Calcium Phosphate by using ammonium hydroxide before and after calcination

Figure 5 shows FT-IR spectrum of Calcium Phosphate by using ammonium hydroxide (before calcination). There are sharp and well-separated peaks at 560.94 cm^{-1}, 601.01 cm^{-1}, 962.45 cm^{-1} and 1025.23 cm^{-1} have been all attributed to the hydroxyapatite group.

Figure 6 shows FT-IR spectrum of Calcium Phosphate by using ammonium hydroxide (after calcination). The sharp and well-separated peaks at 493.83 cm^{-1}, 542.65 cm^{-1}, 603.98 cm^{-1}, 970.56cm^{-1} and 1015.68 cm^{-1} have been assigned to biphasic (hydroapatite and β- TCP) group. These results are in good agreement with the X-ray diffraction analysis (M. Sadat-Shojai, M.T, 2013).

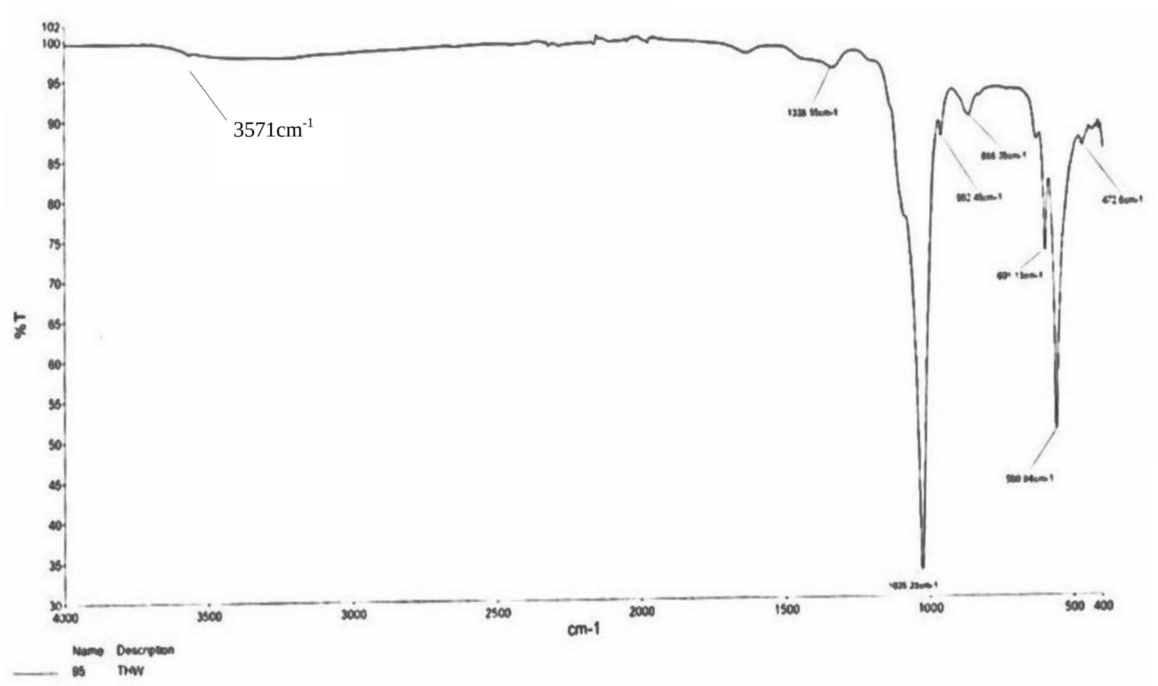

Figure 5 FT-IR spectra of CaP sample by using Ammonium hydroxide (before calcination)

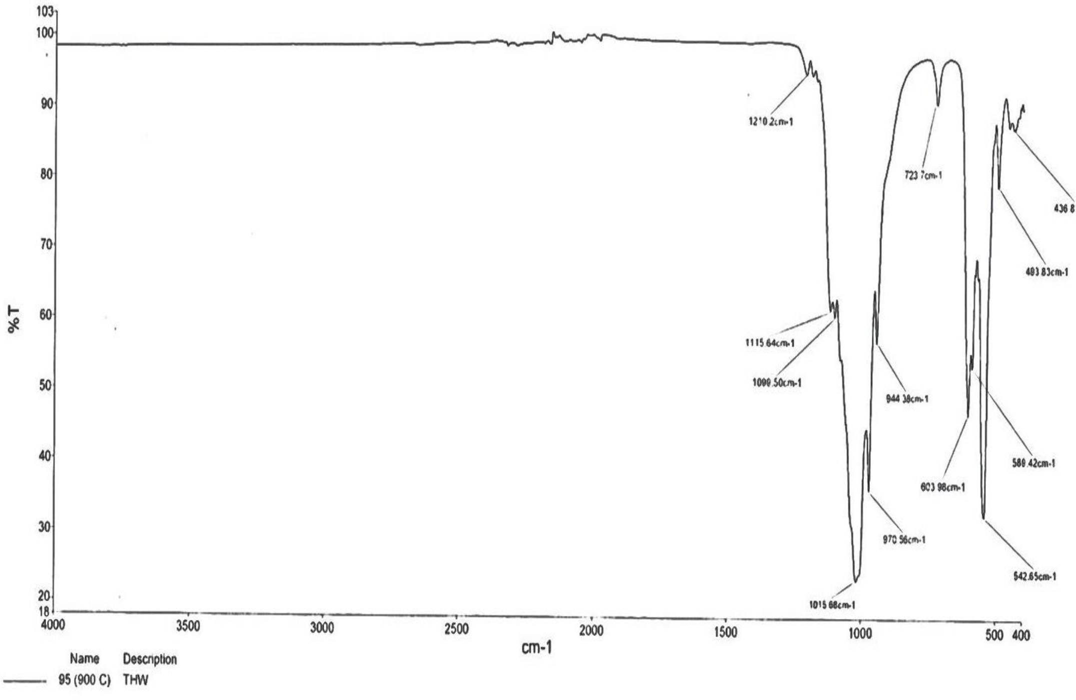

Figure 6 FT-IR spectra of CaP sample by using Ammonium hydroxide (after calcination at 900ºC)

Table 4 The FT-IR transmission bands of CaP sample by using ammonium hydroxide before and after calcination

Calcination condition	Transmission Bands(cm^{-1}) of Chemical groups					
	PO_4^{3-}				OH-	CO_3^{2-}
	ν_1 symmetric (P-O) stretching	ν2 (O-P-O) bending	ν_3 asymmetric (P-O) stretching	ν_4 (P-O) bending	Stretching	
before calcination	962.45	472.6	1025.23	560.94 601.13	1338.55 3571.00	868.05
900ºC	493.83 542.62 589.42 944.38 970.56	436.81	1015.98 1099.50 1115.64 1210.2	- - 603.98 723.7	-	-

Scanning Electron Microscopy (SEM) Analysis

(SEM) Analysis of Calcium Phosphate powdersby using sodium hydroxide and Ammonium hydroxide before and after calcination

Figure (7) shows SEM micrographs of the CaP powders by using sodium hydroxide before and after calcination. Figure 7(a) shows the monetite microparticles which were highly agglomerated. Figure 7(b) shows biphasics microsturcutre has been found. The grain size for the samples (after heating) have been estimated by using image J software and it is found to be 1.20 µm (E. Lerner, S. Sarig) .

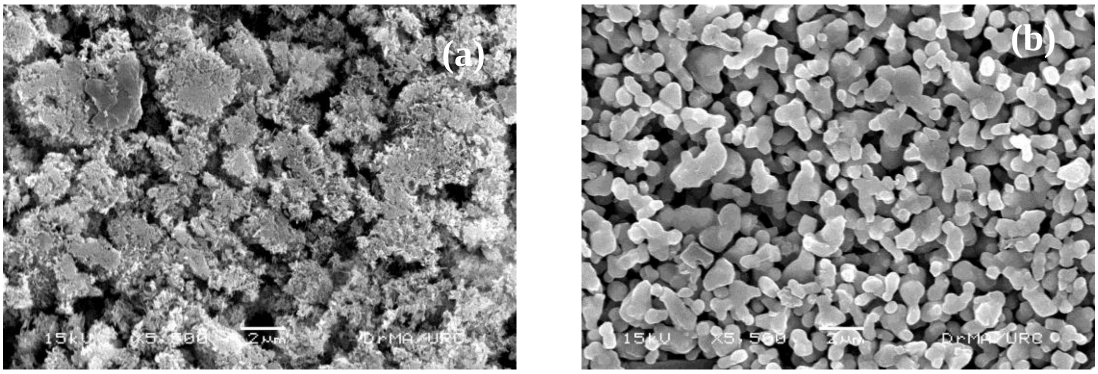

Figure7 SEM micrographs of CaP powders by using sodium hydroxide: (a) before calcination (b) after calcination at 900ºC.

Figure (8) shows SEM micrographs of the CaP powders by using ammonium hydroxide before and after calcination. Figure 8 (a) shows the formation and agglomeration of small irregular particles in the sample. Figure 8(b) shows homogenous microstructure and interconnected micropores. The grain size for the sample after calcination have been estimated by using image J software and it is found to be 0.56 µm.

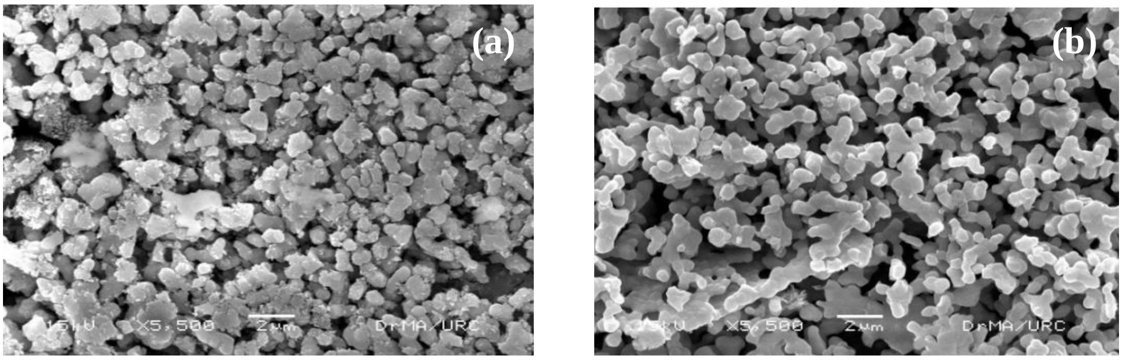

Figure 8 SEM images of CaP powders by using Ammonium hydroxide: (a) before calcination (b) after calcination at 900ºC.

Conclusions

The synthesis of calcium phosphate biomaterials powder via microwave-assisted precipitation method has been reported. Two types of inorganic bases; Sodium hydroxide and Ammonium hydroxide have been used for the pH regulation. The XRD analysis proved that the well crystallized monetite phase was formed with sodium hydroxide where as hydroxyapatite phases with Ammonium hydroxide before calcination. The formation of biphasics (hydroxyapapite & beta-tricalcium Phosphate) after calcination has been identified by XRD and FTIR analyses. The biphasic biomaterials with different phases involving different RIR values could be obtained by assisting different types of inorganic base. Note worthily, Observation on morphology proved that the formation of agglomeration of small particles(before calcination)and microstructures (after calcination)have been obtained by using sodium hydroxide. The formation of irregular particles(before calcination), homogenous microstructure and interconnected micropores could be obtained by using ammonium hydroxide in this research. In this study, when comparison of sodium hydroxide and ammonium hydroxide, smaller crystalline size, more percentage weight of TCP groups and homogeneous microstucture have been obtained via ammonium hydroxide.

Acknowledgements

The authors are grateful to the Department of Physics, University of Yangon and University of Taunggyi for the supports with research facilities.

References

Asmae Massit et al (2014) “Synthesis and characterization of nano-sized β-Tricalcium phosphate: Effects of the aging time”, IOSR Journal of Applied Chemistry (IOSR-JAC),**7**(7), pp. 57-61.

Baradaran S. (2013). “Synthesis and Characterization of Monetite Prepared Using a Sonochemical Method in a Mixed Solvent System of Water/Ethylene Glycol/N,N-Dimethylformamide”, The Minerals, Metals & Materials Society and ASM International.

Behzad Mehdikhania, and Gholam Hossein Borhani. (2015) “Synthesis nano bio-ceramic powderβ-$Ca_2P_2O_7$”, Journal of Ceramic Processing Researchy, **16**(3), pp. 308-312.

E. Lerner, S. Sarig, Enhanced maturation of hydroxyapatite from aqueous solutions using microwave irradiation, J. Mater. Sci. Mater. Med. 2 (1991) 138–141.

I Y.J. Zhu, F. (2014).“Microwave-assisted preparation of inorganic nanostructures in liquid phase, Chem. Rev. 114, pp.6462–6555.

M. Sadat-Shojai, M.-T. Khorasani, E. Dinpanah-Khoshdargi, A. Jamshidi, Synthesis methods for nano-sized hydroxyapatite with diverse structures, ActaBiomater.9 (2013) 7591–7621, http://dx.doi.org/10.1016/ j.actbio.2013.04.012.

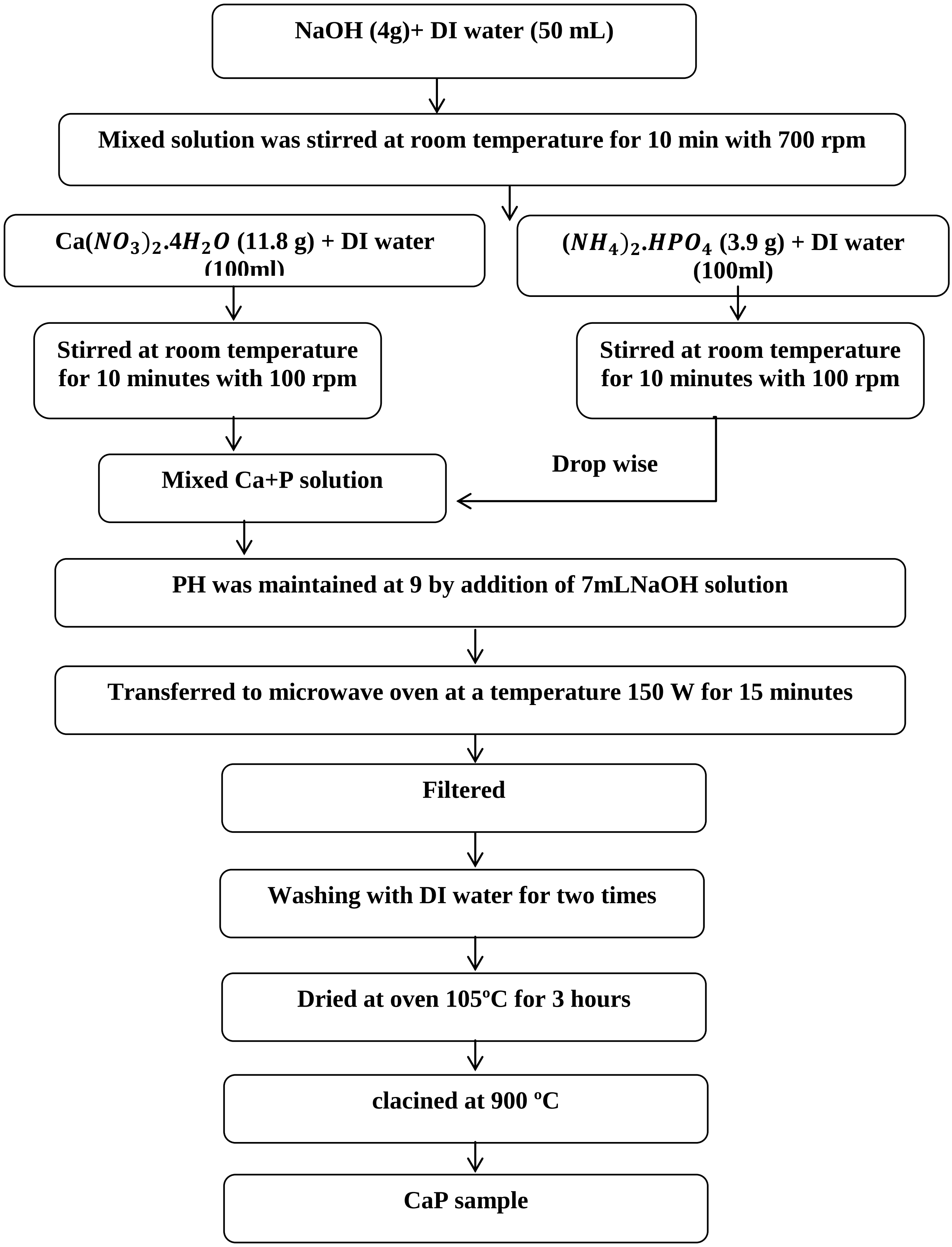
NaOH (4g)+ DI water (50 mL)
Mixed solution was stirred at room temperature for 10 min with 700 rpm
Ca(NO_3)$_2$.4H_2O (11.8 g) + DI water (100ml)
(NH_4)$_2$.HPO_4 (3.9 g) + DI water (100ml)
Stirred at room temperature for 10 minutes with 100 rpm
Stirred at room temperature for 10 minutes with 100 rpm
Drop wise
Mixed Ca+P solution
PH was maintained at 9 by addition of 7mLNaOH solution
Transferred to microwave oven at a temperature 150 W for 15 minutes
Filtered
Washing with DI water for two times
Dried at oven 105ºC for 3 hours
clacined at 900 ºC
CaP sample

J. Myanmar Acad. Arts Sci. 2020 **Vol. XVIII.No.2B**

PREPARATION AND CHARACTERIZATION OF COPPER SUBSTITUTED MAGNESIUM-ZINC FERRITES

San Htar Oo[1], Aye Aye Lwin[2], Zune Hnin Pwint[3] and Win Kyaw[4]

Abstract

A series of Copper substituted Magnesium-Zinc ferrites, $Mg_{0.5}Zn_{0.5-x}Cu_xFe_2O_4$ (where x = 0.0 – 0.5 with the step of 0.1) were prepared by solid state reaction method. Stoichiometric compositions of MgO, ZnO, CuO and Fe_2O_3 were used. XRD patterns indicated that the samples were cubic structure and the crystallite sizes were estimated by using the observed XRD spectral lines. Microstructural properties of the samples were investigated by Scanning Electron Microscope (SEM). It was found that the grain sizes of the samples depend on the concentration of Cu. Some pores were found in the observed SEM images. Vibrational characteristics of the samples were investigated by Fourier Transform Infrared (FTIR) spectroscopic method. The collected spectral lines were identified by using molecular vibrational theory and standard data (wavenumbers). The observed wavenumbers showed that the stretching vibrations of tetrahedral site atoms (υ_1-mode) and octahedral site atoms (υ_2-mode) that composed of the samples.

Keywords: $Mg_{0.5}Zn_{0.5-x}Cu_xFe_2O_4$, XRD, SEM, FTIR.

Introduction

Ferrite materials have been under intense research for so long due to their useful electromagnetic characteristics for a large number of applications [Marial, (2013)]. The performance of these materials in their bulk form where the grain dimensions are in micrometer scales is limited to a few megahertz frequency due to their higher electrical conductivity and domain wall resonance [Fawzi, (2010)]. However, the recent technological advances in electronics industry demand even more compact cores for work at higher frequencies. One way to solve this problem is by synthesizing the ferrite particles in nanometric scales before compacting them for sintering. When the size of the magnetic particle is smaller than the critical size for multidomain formation, the particle is in a single domain state. Domain wall resonance is avoided, and the material can work at higher frequencies [IIslam, (1998); Son, (2002)].

This work preferred the Mg based ferrite from the following reasons: it is a slight porous ceramic and the stability of Mg^{2+} ions avoid the appearance of Fe^{2+} ions (essential require to obtain high resistivity) [Pathan, (2010); Patil, (2013)]. In the present work, Copper substituted Magnesium-Zinc ferrites, $Mg_{0.5}Zn_{0.5-x}Cu_xFe_2O_4$ (where x = 0.0 – 0.5 with the step of 0.1) were prepared by solid state reaction method. The as-prepared samples were characterized by XRD, SEM and FTIR spectroscopy to study the structural, microstructural and vibrational characteristics.

---

[1] Dr, Associate Professor, Department of Physics, University of Computer Studies (Pyay)

[2] Dr, Associate Professor, Department of Physics, Loikaw University

[3] Dr, Assistant Lecturer, Department of Physics, Pyay University

[4] Dr, Associate Professor, Department of Physics, Pyay University

Experimental Details

Preparation of the Samples

Copper substituted Magnesium-Zinc ferrites, $Mg_{0.5}Zn_{0.5-x}Cu_xFe_2O_4$ (where x = 0.0 – 0.5 with the step of 0.1) were prepared by solid state reaction method. Analytical Reagent (AR) grade Magnesium Oxide (MgO), Zinc Oxide (ZnO), Copper Oxide (CuO) and Iron Oxide (Fe_2O_3) were used to prepare the samples. Flow diagram of the sample preparation process is shown in Figure 1.

XRD, SEM and FTIR Measurements

Powder XRD patterns of the samples were observed by RIGAKU MULTIFLEX Powder X-Ray Diffractometer [Universities' Research Centre (URC), University of Yangon]. Microstructural characteristics of the samples were studied by using JEOL JSM-5610LV Scanning Electron Microscope (SEM) [Universities' Research Centre (URC), University of Yangon] with the accelerating voltage of 15 kV, the beam current of 50 mA and 10,000 times of photo magnification. FTIR spectra were observed by PC-controlled FTIR-8400 SHIMADZU Spectrophotometer [Universities' Research Centre (URC), University of Yangon].

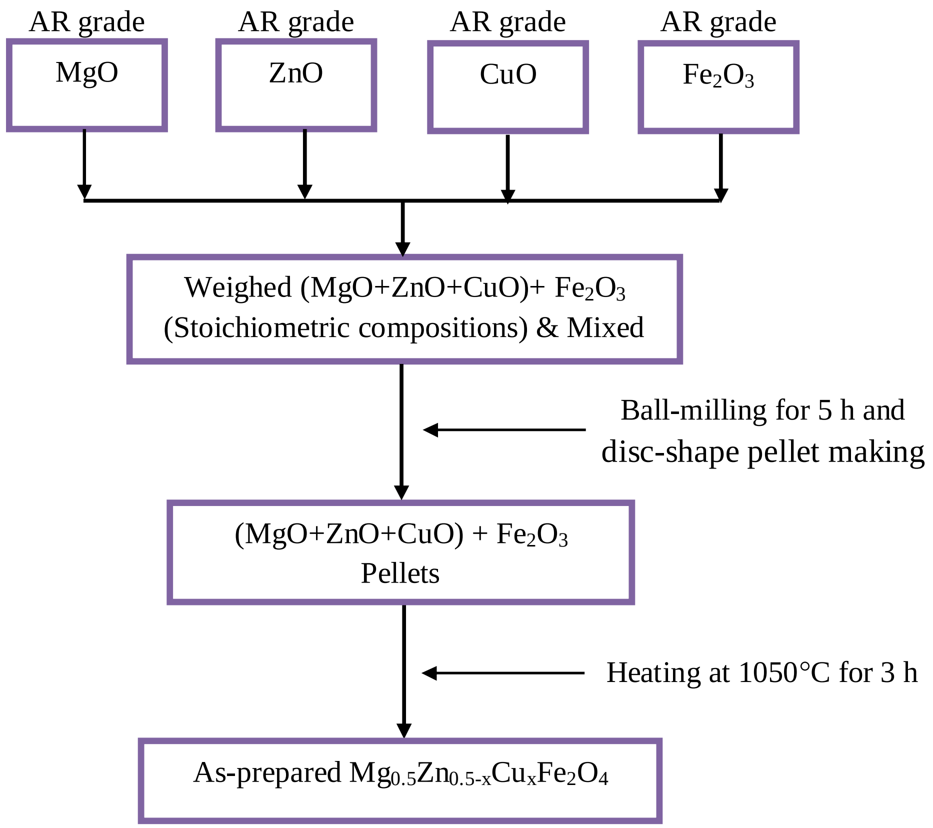

Figure 1 Flow diagram of the sample preparation procedure of $Mg_{0.5}Zn_{0.5-x}Cu_xFe_2O_4$

Results and Discussion

XRD Study

Powder XRD patterns of the samples are shown in Figure 2. The observed diffraction lines were identified by using JCPDS data files. As shown in XRD patterns, most of the collected diffraction lines were assigned with standard JCPDS (Joint Committee on Powder Diffraction Standards) data library files. Some of the lines were not assigned with standard files due to the difference between the standard JCPDS data library files and substitution of materials deviation of diffraction angles of collected lines with standard data files. In the observed XRD patterns, the diffraction line of (311) plane is found to the strongest in intensity (I = 100%) among the diffraction lines.

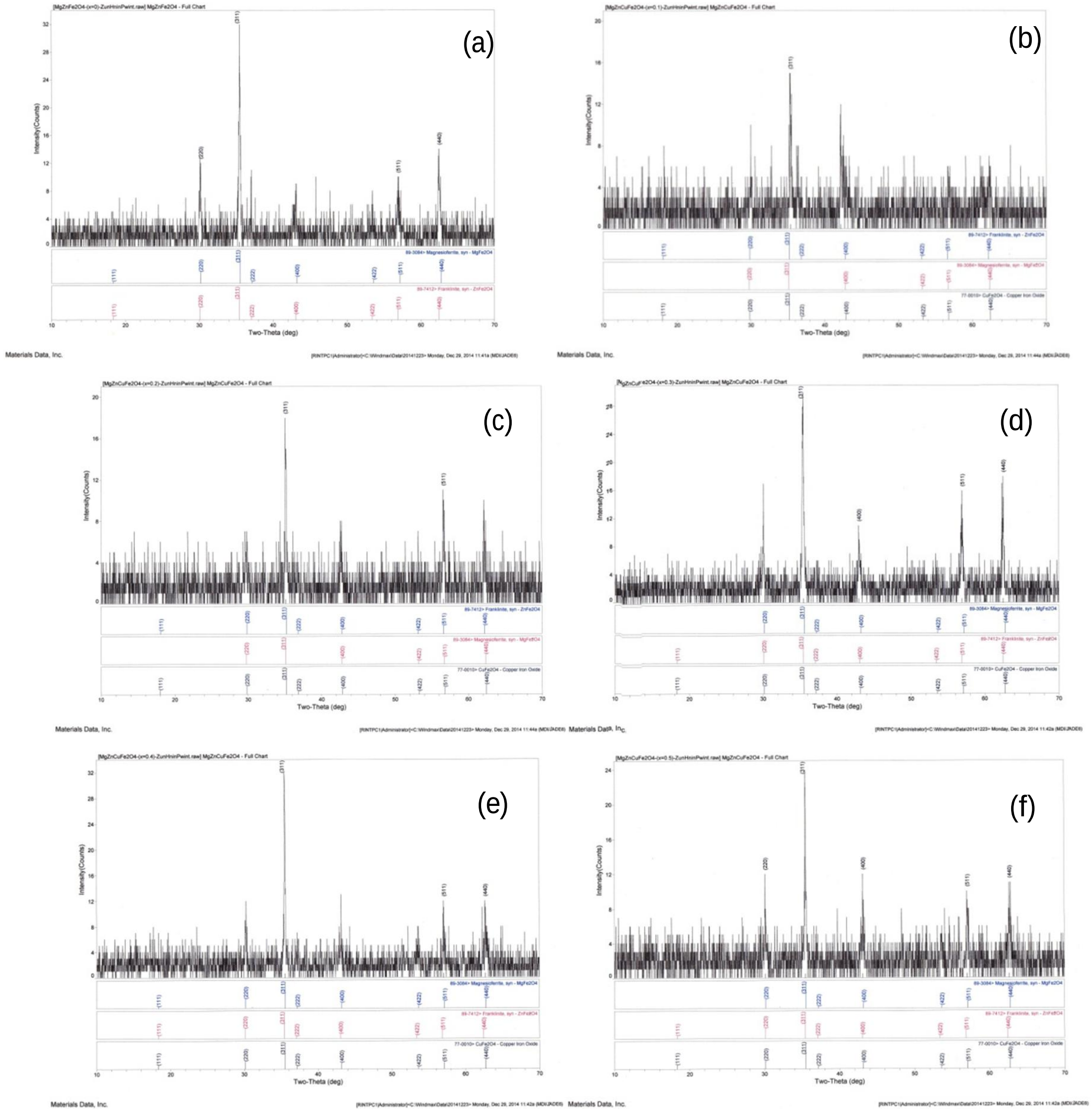

Figure 2 XRD patterns of $Mg_{0.5}Zn_{0.5-x}Cu_xFe_2O_4$ where (a) x = 0.0, (b) x = 0.1, (c) x = 0.2, (d) x = 0.3, (e) x = 0.4 and (f) x = 0.5

XRD patterns indicate the samples belong to cubic structure. For cubic crystals, it is then possible to use $a=\frac{\lambda}{2\sin\theta}\sqrt{h^2+k^2+l^2}$ to convert each interplanar spacing into a lattice parameter, *a*. The indexing is consistent if all peaks provide the same lattice parameter(s). In the present work, the calculated and observed lattice parameters of the samples are tabulated in Table 1. Rezlescu, N. et. al. (2002) has reported that the lattice parameters of the $Mg_{0.5}Zn_{0.5}Fe_2O_4$ or x = 0.00 sample are a = b = c = 8.4060 Å [Rezlescu, (2002)]. In this work, the obtained lattice parameters are compatible with the result of Rezlescu, N. et. al.. The lattice parameters of the samples were varied with increased in concentration of Cu due to the atomic substitution of Cu on Zn in the lattice sites.

The crystallite sizes of the $Mg_{0.5}Zn_{0.5-x}Cu_xFe_2O_4$ samples have been estimated by using the Scherrer formula, $D=\frac{0.9\lambda}{B\cos\theta}$, where *D* is the crystallite size (nm), λ is the wavelength of incident X-ray (Å), θ is diffraction angle of the peak under consideration at

FWHM (°) and B is observed FWHM (radian). In the present work, the average crystallite sizes were calculated and the obtained crystallite sizes are also presented in Table 1. The crystallite sizes of the samples were found to vary with increased in concentration of Cu.

Table 1 The observed and calculated lattice parameters and the crystallite sizes of $Mg_{0.5}Zn_{0.5-x}Cu_xFe_2O_4$

Sample (Contents x of Cu)	Obs. *a*=*b*=*c* (Å)	Cal. *a*=*b*=*c* (Å)	*D* (nm)
0.0	8.3897	8.3897	52.44
0.1	8.4225	8.4224	86.81
0.2	8.4413	8.4413	108.84
0.3	8.4035	8.4035	44.44
0.4	8.3781	8.3781	40.42
0.5	8.3837	8.3837	92.66

SEM Analysis

Figure 3 shows the SEM micrographs of the samples prepared at 1050°C for 3 h. As shown in SEM micrographs, the grains are small, below 4 µm, and the ceramic bodies are porous. It was found that the grain size ranges from 0.10 µm to 3.20 µm. The porosity within the matrix is relatively cleared. Also, all porosity is distributed along the grain boundaries through the image (except x = 0.5 sample). This structure indicates that the porous ceramic can easily exhibit absorption and condensation of water vapour.

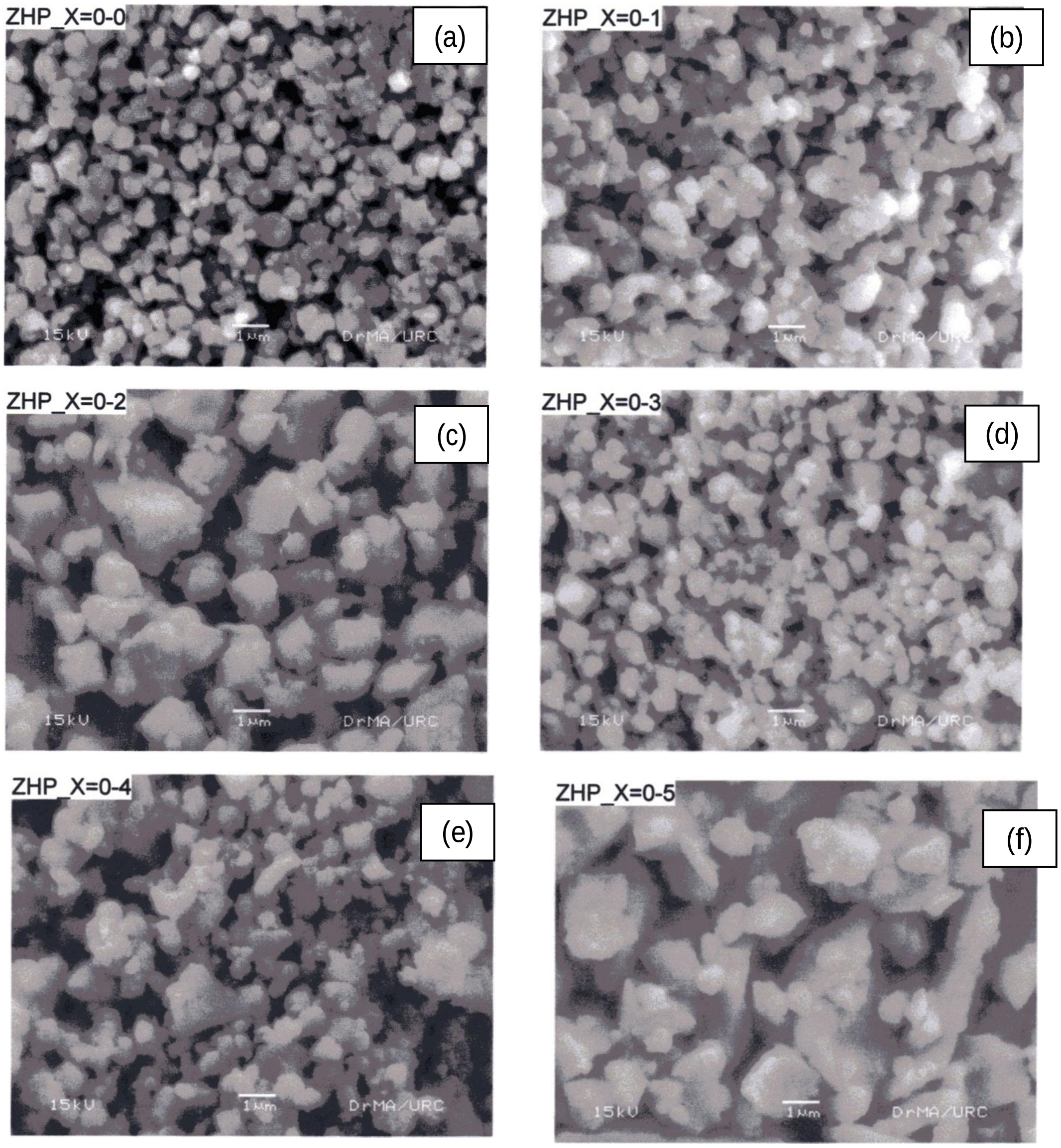

Figure 3 SEM micrographs of $Mg_{0.5}Zn_{0.5-x}Cu_xFe_2O_4$ where (a) x = 0.0, (b) x = 0.1, (c) x = 0.2, (d) x = 0.3, (e) x = 0.4 and (f) x = 0.5

Furthermore, the porous structure is an advantage in discouraging fracture due to thermal shock. The grain shapes were found to be clearly difference in the samples of Cu contents and no-contents. In the most Cu concentration of the sample (x = 0.5), the largest grain size and poor grain boundary. In Figure 3(a), (b), (d) and (e) of x = 0.0, x = 0.1, x = 0.3 and x = 0.4 samples, the grains shapes are nearly spherical but in Figure 3(c) and (f) of x = 0.2 and x = 0.5, the grains shapes are flake. The obtained grain sizes of the samples are tabulated in Table 2. The grain size of the un-substituted (x = 0.0) sample is the smallest one with clearly grain boundary and it is the most homogeneity among the investigated samples.

Table 2 Grain sizes of $Mg_{0.5}Zn_{0.5-x}Cu_xFe_2O_4$

Sample (Contents x of Cu)	Grain size (μm)
0.0	0.10 – 0.80
0.1	0.35 – 1.10
0.2	0.55 – 2.50
0.3	0.25 – 1.20
0.4	0.40 – 1.80
0.5	0.75 – 3.20

FTIR Spectroscopic Analysis

Spinels are generally formulated as AB_2X_4 that formally consider the structure as consisting of isolated ion of B and isolated AX_4 molecules. The so-called normal spinel structure is cubic, space group O_h^7, with eight molecules in the unit cell, and has the B atoms on octahedral sites D_{3d} symmetry, and the A atoms on tetrahedral sites of T_d symmetry. The oxygen atoms occupy C_{3v} sites. The coordination polyhedron around B is a regular octahedron. The vibrational frequencies (wavenumbers) of undoped Zinc Ferrite, $ZnFe_2O_4$, are mainly 550 cm^{-1} and 555 cm^{-1} for A atoms on tetrahedral sites and 415 cm^{-1} for B atoms on octahedral sites. Also, vibrational frequencies of undoped $MgFe_2O_4$ are mainly 565 cm^{-1} and 581 cm^{-1} for A atoms on tetrahedral sites and 406 cm^{-1} and 433 cm^{-1} for B atoms on octahedral sites. Vibrational frequencies of undoped $CuFe_2O_4$ are mainly 592 cm^{-1} for A atoms on tetrahedral sites and 420 cm^{-1} for B atoms on octahedral sites. The frequencies for A-atoms (tetrahedral site) assigned as υ_1-mode and for B-atoms (octahedral site) assigned as υ_2-mode [Ross, (1972)].

In the present work, FTIR transmission spectra of the Copper substituted Magnesium-Zinc ferrites, $Mg_{0.5}Zn_{0.5-x}Cu_xFe_2O_4$ (where x = 0.0 – 0.5 with the step of 0.1) samples are shown in Figure 4. The observed spectral lines (wavenumbers) and the corresponding vibrational mode assignments of molecules are listed in Table 3. Furthermore, the collected wavenumbers and their corresponding vibrational properties (wavelength, frequency, oscillation time and energy) of constituent molecules of the samples are also tabulated in Table 3. As shown in Tables, the obtained data (observed wavenumbers or emitted frequencies with $\bar{\lambda} = \bar{\nu}$ = wavenumbers are found experimentally that the vibrational frequencies of tetrahedral site and octahedral site molecular networks in the samples. The obtained frequencies ($>10^6$ Hz) indicate the samples composed of high frequency oscillators.

As shown in figures, some of the absorption bands observed in the wavenumber ranges of round about 1600 cm^{-1} and 3400 cm^{-1} represent the vibrational characteristics of water (H_2O) and the band observed at about 2300 cm^{-1} represents the vibrational characteristic of carbon dioxide (CO_2) molecules. These two molecules of water and carbon dioxide distributed as the moisture in the atmosphere (surrounding) of FTIR spectrophotometer. Normally, their vibrational modes appeared in a FTIR spectrum of KBr pellet.

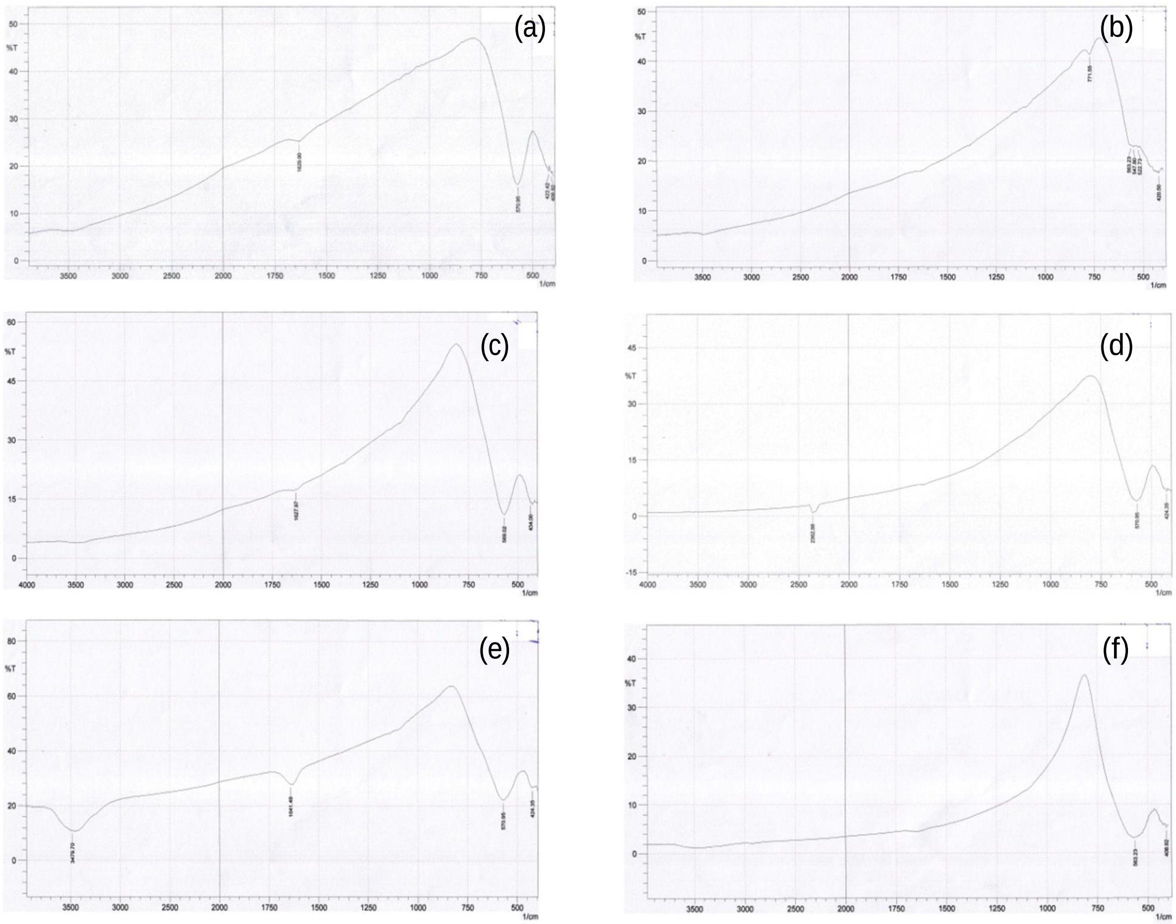

Figure 4 FTIR transmission spectra of $Mg_{0.5}Zn_{0.5-x}Cu_xFe_2O_4$ where (a) x = 0.0, (b) x = 0.1, (c) x = 0.2, (d) x = 0.3, (e) x = 0.4 and (f) x = 0.5

Table 3 (a) Wavenumbers and corresponding vibrational modes and vibrational properties of $Mg_{0.5}Zn_{0.5-x}Cu_xFe_2O_4$ (where x = 0.0)

$\bar{V}$ (1/cm)	Mode	Molecule	λ(nm)	υ (Hz)	τ (s)	E(eV)
409, 422	υ_2-mode (stretching)	B atoms on octahedral site	24450, 23697	1.226E+13, 1.265E+13	8.156E-14, 7.904E-14	0.0508, 0.0524
571	υ_1-mode (stretching)	A atoms on tetrahedral site	17513	1.712E+13	5.842E-14	0.0709

Table 3. (b) Wavenumbers and corresponding vibrational modes and vibrational properties of $Mg_{0.5}Zn_{0.5-x}Cu_xFe_2O_4$ (where x = 0.1)

$\bar{V}$ (1/cm)	Mode	Molecule	λ(nm)	υ (Hz)	τ (s)	E(eV)
421	υ_2-mode (stretching)	B atoms on octahedral site	23753	1.262E+13	7.923E-14	0.0523
523, 548, 563	υ_1-mode (stretching)	A atoms on tetrahedral site	19120, 18248, 17762	1.568E+13, 1.643E+13, 1.688E+13	6.378E-14, 6.087E-14, 5.924E-14	0.0649, 0.0680, 0.0699
772	υ-Combination	A atoms +B atoms	12953	2.314E+13	4.321E-14	0.0958

Table 3 (c) Wavenumbers and corresponding vibrational modes and vibrational properties of $Mg_{0.5}Zn_{0.5-x}Cu_xFe_2O_4$ (where x = 0.2)

$\bar{v}$ (1/cm)	Mode	Molecule	λ(nm)	υ (Hz)	τ (s)	E(eV)
434	υ_2-mode (stretching)	B atoms on octahedral site	23041	1.301E+13	7.686E-14	0.0539
569	υ_1-mode (stretching)	A atoms on tetrahedral site	17575	1.706E+13	5.862E-14	0.0706
1628	υ_2-mode (bending)	H_2O	-	-	-	-

Table 3 (d) Wavenumbers and corresponding vibrational modes and vibrational properties of $Mg_{0.5}Zn_{0.5-x}Cu_xFe_2O_4$ (where x = 0.3)

$\bar{v}$ **(1/cm)**	**Mode**	**Molecule**	λ**(nm)**	υ **(Hz)**	τ **(s)**	**E(eV)**
424	υ_2-mode (stretching)	B atoms on octahedral site	23585	1.271E+13	7.867E-14	0.0526
571	υ_1-mode (stretching)	A atoms on tetrahedral site	17513	1.712E+13	5.842E-14	0.0709
2363	υ_2-mode (bending)	CO_2	-	-	-	-

Table 3 (e) Wavenumbers and corresponding vibrational modes and vibrational properties of $Mg_{0.5}Zn_{0.5-x}Cu_xFe_2O_4$ (where x = 0.4)

$\bar{v}$ **(1/cm)**	**Mode**	**Molecule**	λ**(nm)**	υ **(Hz)**	τ **(s)**	**E(eV)**
424	υ_2-mode (stretching)	B atoms on octahedral site	23585	1.271E+13	7.867E-14	0.0526
571	υ_1-mode (stretching)	A atoms on tetrahedral site	17513	1.712E+13	5.842E-14	0.0709
1641	υ_2-mode (bending)	H_2O	-	-	-	-
3480	υ_3-mode (asymmetric-stretching)	H_2O	-	-	-	-

Table 3. (f) Wavenumbers and corresponding vibrational modes and vibrational properties of $Mg_{0.5}Zn_{0.5-x}Cu_xFe_2O_4$ (where x = 0.5)

$\bar{v}$ **(1/cm)**	**Mode**	**Molecule**	λ **(nm)**	υ **(Hz)**	τ **(s)**	**E (eV)**
409	υ_2-mode (stretching)	B atoms on octahedral site	24450	1.226E+13	8.156E-14	0.0508
563	υ_1-mode (stretching)	A atoms on tetrahedral site	17762	1.688E+13	5.924E-14	0.0699

Conclusion

Copper substituted Magnesium-Zinc ferrites, $Mg_{0.5}Zn_{0.5-x}Cu_xFe_2O_4$ (where x = 0.0, 0.1, 0.2, 0.3, 0.4 and 0.5) were prepared by solid-state reaction method. Structural, microstructural and vibrational characteristics of the samples were reported by XRD, SEM and FTIR spectroscopic methods. XRD patterns showed that the samples analogous to cubic structure. The lattice parameters and the crystallite sizes of the as-prepared samples were varied with increase in concentration of Cu on the atomic sites of Zn. SEM micrographs showed that the grain shape and size were generally varied with the concentration of Cu in the samples. Some pores appeared in the observed SEM micrographs and they showed that the sample may be sensitive material for the application of environmental effect sensors, such as humidity and gas sensors. According to FTIR spectra, the υ_1-mode of tetrahedral site atoms and the υ_2-mode of octahedral site atoms were appeared and assigned by using standard wavenumbers. The appearance of the lines in the FTIR spectra showed that the vibrational characteristics of the samples. It showed that phase formation of the samples was valid or the phase formation from the XRD results well confirmed by FTIR spectroscopy.

Acknowledgement

The authors would like to acknowledge Professor Dr Khin Khin Win, Head of Department of Physics, University of Yangon, for her valuable suggestion and comments for this work.

References

Fawzi, A.Z., A.D. Sheikh, & V.L. Mathe, (2010) “Structural, Dielectric Properties and AC Conductivity of $Ni_{(1-x)}Zn_xFe_2O_4$ Spinel Ferrite.” *Journal of Alloys and Compounds*, vol. 502, pp. 231-237.

IIslam, M.U., M.U. Rana, & Abbas, (1998) “Study of Magnetic Interactions in Co-Zn-Fe-O System.” *Materials Chemistry and Physics*, vol. 57, pp. 190-193.

Maria1, K.H., S. Choudhury, & M.A. Hakim, (2013) “Structural Phase Transformation and Hysteresis Behavior of Cu-Zn Ferrites.” *International Nano Letters*, vol. 3, pp. 2-10.

Pathan, A.N., K. Sangshetti, & A.A.G. Pangal, (2010) “Synthesis and Moussbauer Studies on Nickel-Zinc-Copper Nanoferrites.” *Nanotechnology and Nanoscience*, vol. 1, pp. 13-16.

Patil, S.N., & B.P. Ladgaonkar, (2013) “Synthesis and Implementation of $NiZnFe_2O_4$ Ferrites to Design Embedded System for Humidity Measurement.” *International Journal of Advanced Research in Electrical, Electronics and Instrumentation Engineering*, vol. 2, pp. 3813-3821.

Rezlescu, N., E. Rezlescu, P. Popa, & F. Tudorache, (2002) “On the Humidity Sensitivity of a Ceramic Element. Structure and Characteristics.” *Journal of Institute of Technical Physics*, vol. 8, pp. 89-97.

Ross, S.D., (1972) *Inorganic Infrared and Raman Spectra*. London, McGraw-Hill.

Son, S., & M. Taheri, (2002) “Synthesis of Ferrite and Nickel Ferrite Nanoparticles Using Radio-Frequency Thermal Plasma Torch.” *Journal Apply Physics*, vol. 91, pp. 7589-7591.

J. Myanmar Acad. Arts Sci. 2020 **Vol. XVIII.No.2B**

INFLUENCE OF DEPOSITION TIME ON THE PROPERTIES OF CHEMICAL BATH DEPOSITED NICKEL OXIDE THIN FILMS

Thet Mar Win[1] and Pho Kaung[2]

Abstract

Nickel Oxide (NiO) thin films were synthesized on glass substrates from aqueous solution of nickel chloride hexahydrate ($NiCl_2.6H_2O$), potassium persulfate ($K_2S_2O_8$), ammonia in which ammonia was employed as complexing agents in the presence of hydroxyl solution. NiO thin films were prepared by Chemical Bath Deposition (CBD) method at different deposition time (60, 75 and 90) min. The structural, surface morphological and optical properties of 450 ºC- annealed NiO thin films were investigated. The XRD studies revealed that NiO thin films were polycrystalline nature with cubic structure. Surface morphology, average grain size and thickness of NiO thin films were estimated from different SEM micrographs. The optical absorbance and transmittance spectra of NiO thin films were recorded in the wavelength range 200 nm - 1100 nm. The sharp absorption peaks of all NiO films were observed at below 400 nm. It was found that NiO thin films with high transmittance in visible region. The refractive index, extinction coefficient and optical conductivity were calculated from the optical measurements. The direct optical energy band gap of 450ºC –annealed NiO films was found to be in the range 3.43 eV-3.76eV.

Keywords: Chemical Bath Deposition method, Deposition time, NiO thin films, Refractive index, Optical energy band gap

Introduction

Nickel oxide (NiO) is a versatile wide band gap semiconductor material. At present, transparent conducting oxide films, such as indium oxide, tin oxide and zinc oxide, are routinely used as transparent electrodes and window coatings for opto-electronic devices [Gopchandran K G et al., 1997 and Benny J et al., 1999]. These films are n-type. However p-type conducting films are required as optical windows for devices where hole injection is required. NiO is a p-type semiconductor with a band gap ranging from 3.6 eV to 4.0 eV, transparent to ultraviolet (UV), visible and near infrared radiation and consequently has the potential to address this need [Sasi B et al., 2003].

There are several methods for synthesis of NiO thin films on various substrates including physical as well as chemical deposition methods. The physical methods used are DC reactive magnetron sputtering and RF sputtering while chemical methods used to deposit NiO thin films are vapor deposition, chemical bath deposition, sol-gel, electro deposition and spray pyrolysis [**Chena H L et al., 2005].**The optical properties of thin films are very important for many applications including interference devices such as antireflection coatings, laser mirrors and monochromatic filters as well as optoelectronics, integrated optics, solar power engineering, microelectronics and optical sensor technology depending on the reflectance and transmittance properties of the films during their preparation. The optical constants of thin films provide us the information concerning with microscopic characteristics of materials [Safwat A M et al., 2011].

---

[1] Dr, Associate Professor, Department of Engineering Physics, Technological University (Thanlyin)

[2] Dr, Rector, University of Yangon

The chemical bath deposition (CBD) method was used in this work to deposit NiO thin films on the glass substrate due to its simplicity and versatility. The effect of deposition time on the structural, surface morphology and optical properties of NiO thin films was evaluated.

Experimental Procedure

The phase formation of chemically deposited NiO thin films for different deposition time were characterized by X- ray diffraction technique using Rigaku Smart Lab X-ray Diffractometer with Cu-K_α radiation (λ = 1.5404 Å) operating at 40 kV and 40 mA. Surface morphology and thickness of NiO thin films were examined by Scanning Electron Microscopy (SEM) taken by JEOL- JCM 6000 Plus. The optical properties of the films were recorded by Schimadzu UV-Vis (UV-1800) spectrophotometer in the wavelength range of 200 nm-1100 nm.

Preparation of the Glass Substrates

The microscopic glass substrates (2.54 cm × 2.54 cm) were put into a beaker containing distilled water and kept for 10 minutes to remove contaminants such as dust on their surfaces. Then the substrates were degreased by hydrochloric acid for 1 hour and rinsed with distilled water and dried in air for a few minutes. Then, the glass substrates were slid into paper-poster plastic hangers.

Nickel Oxide Thin Films Grown by CBD Method

To synthesis the NiO thin films, high purity nickel chloride hexahydrate ($NiCl_2.6H_2O$) is used as source of Ni. A precursor solution is prepared by using 80 ml of 1M $NiCl_2.6H_2O$, 60 ml of 0.1M $K_2S_2O_8$, and 20 ml of aqueous ammonia (25-28%) in 200 ml beaker. The substrates were kept vertically in the deposition bath with constant stirring at 70°C. The deposited films are extracted from deposition bah after 60 min, 75min and 90 min. Then washed with distilled water in order to remove loosely bounded particles and further annealed at 450 °C in air for 2 hour to be uniform and well adherent to the substrate.

Results and Discussion

Structural Analyses

The X- ray diffractograms of 450 ºC -annealed NiO thin films for different deposition time were shown in Fig 1. The peaks (111), (200) and (220) were observed at 2θ values 37.238°, 43.310° and 62.851° for film NiO-1 (60 min), 37.191°, 43.337° and 63.029° for the film sample NiO-2 (75 min) and 37.224°, 43.301° and 62.795° for NiO-3 (90 min) films, respectively. All NiO films were found to have polycrystalline nature and bunsenite phase with cubic structure with the preferential orientation along the (200) plane. This conforms to standard card number JCPDS 71-1179.

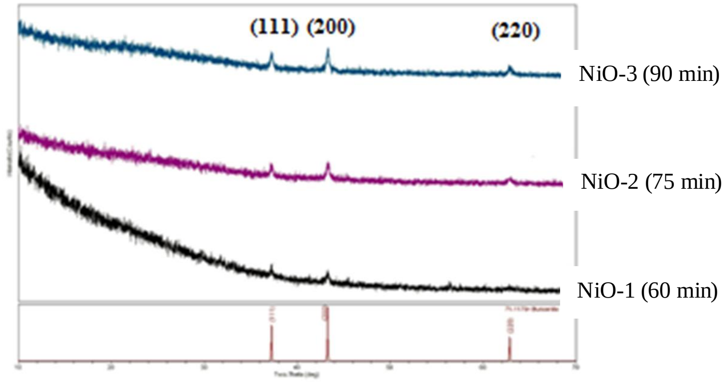

Figure 1 XRD patterns of 450 ºC -annealed NiO thin films for different deposition time

The average crystallite sizes (D) were determined Debye Scherrer’s formula,

$$D = \frac{K\lambda}{\beta\cos\theta}$$

where, the constant K is a dimensionless constant often called the shape factor with a value of 0·94, λ the wavelength of X-ray used which is CuK_α radiation (λ = 1.54 Å), β the full width at half maximum of the diffraction peak and θ is the diffraction angle. It was observed that the crystallite size of the NiO film was improved with increasing deposition time. The dislocation density (δ) which represents the amount of defects in the film was determined from the formula,

$$\delta = \frac{1}{D^2}$$

where “δ” the dislocation density and “D” is the crystallite size.

The micro strain (μ) produced in the NiO thin films was calculated by using the formula,

$$\mu = \frac{\beta\ \cos\theta}{4}$$

The occurrence of micro strain may be attributed to stretching and compression in the lattice. The lattice constant “a” for the cubic structure is given by the relation,

$$\frac{1}{d^2} = \frac{(h^2+k^2+l^2)}{a^2}$$

where “d” is the inter-planer distance and (hkl) are the Miller indices. Structural parameters of 450 ºC - annealed NiO thin films for different deposition time were presented in Table 1. The peak broadening decreases and the sharpness of the peak increases which clearly denote the reduction of lattice strain and increase in crystallinity of 450 ºC - annealed NiO films.

Surface Morphology and Thickness Measurement of NiO Thin Films

The SEM micrographs of 450 ºC -annealed NiO thin films for different deposition time were depicted in Fig 2. There was a distinct change in surface morphology for films by increasing deposition time. Flake surface morphology was observed in NiO-1 (60 min) film. The surface of NiO-2 (75 min) film sample was evenly covered with homogeneous grains with little pores. The SEM micrograph of NiO-3 (90 min) film revealed inhomogeneous cellular like morphology. The surface morphology strongly depends on deposition time, concentration, orientation of grain growth and nucleation process.

Thickness of the film plays an important role in determining the film properties. Thickness of the NiO thin films were measured by SEM through the cross- section of the sample using imaging software. The average grain size and estimated thickness values are presented in Table 1.

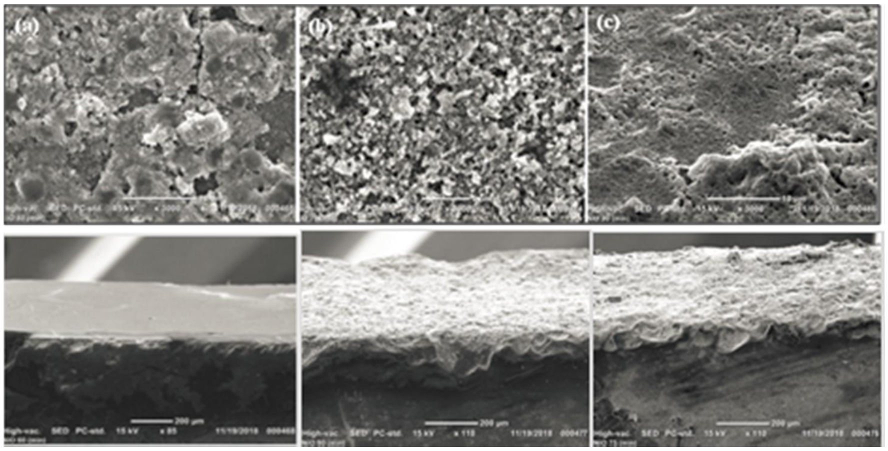

(a) (b) (c)

Figure 2 Surface morphology (upper) and cross sectional view (lower) SEM images of 450ºC - annealed NiO thin film for deposition time (a) 60 min (b) 75 min and (c) 90 min

Table 1 Structural parameters of 450 ºC - annealed NiO films for different deposition time

Sample	NiO-1	NiO-2	NiO-3
Deposition Time (min)	60	75	90
Film Thickness (µm)	264	353	378
Average Lattice Constants (a=b=c)(Å)	4.1774	4.1747	4.1793
System	Cubic	Cubic	Cubic
Intense Peak (hkl)	(200)	(200)	(200)
FWHM (× 10^{-3} rad)	7.69	6.82	5.22
Crystallite Size from XRD(nm)	20.2	22.8	29.9
Dislocation density (× 10^{16} lines/ m^2)	0.24	0.19	0.11
Microstrain (× 10^{-3})	1.79	1.59	1.21
Average Grain Size from SEM(µm)	0.77	0.23	0.12

Optical Properties

Energy band gap and index of refraction are the two fundamental properties that determine the optical and electrical and electronic properties of semiconductors. The energy gap is determined by threshold of photon absorption while refractive index is a measure of transparency of the material to the incident light. The variation of absorbance and transmittance spectra with wavelength of annealed NiO films for different deposition time 60 min, 75 min and 90 min was shown in Fig 3(a) and 3(b), respectively. The absorbance decreases rapidly at short wavelengths corresponding to the energy gap of the film. This evident increase of energy is due to the interaction of the material electrons with the incident photons which have enough energy for the occurrence of electron transitions. The sharp absorption edges were observed at 297 nm, 298 nm and 303 nm for NiO-1 (60 min), NiO-2 (75 min) and NiO-3(90 min) films. For a transmittance study, all NiO thin films showed transmittance of ~ 84 %, ~27 % and ~19 %, in the wavelength range of visible region, respectively.

The energy band gap value of NiO thin films was determined using the absorbance spectra in the wavelength range 300 nm- 900 nm. Absorption coefficients (α) have been evaluated using absorbance (A) data and following equation:

$$\alpha = 2.303\frac{A}{t}$$

where "t"is film thickness (µm). The optical absorption gives the relationship between the absorption coefficient "α" and the photon energy "hν" as

$$\alpha = \frac{B(h\nu\text{-}E_g)^{\frac{1}{2}}}{h\nu}$$

where “B” is a constant called the band tailing parameter. The band gap values were determined from the intercept of the straight line portion of the square of absorption coefficient $(\alpha h\nu)^2$ is plotted as a function of photon energy (hν) were shown in Fig 4. The direct energy band gap value of NiO-1 (60 min), NiO-2 (75 min) and NiO-3 (90 min) found to be 3.43 eV, 3.62 eV and 3.76 eV, respectively.

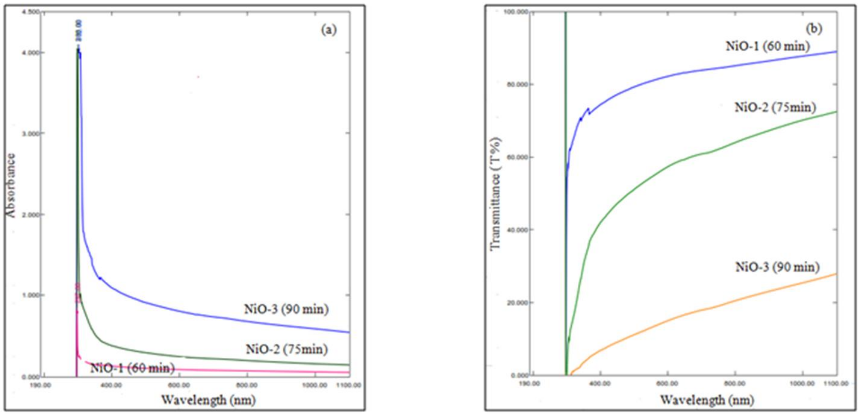

Figure 3 (a) The absorbance and (b) transmittance spectra of NiO films for deposition time (60,75 and 90) min

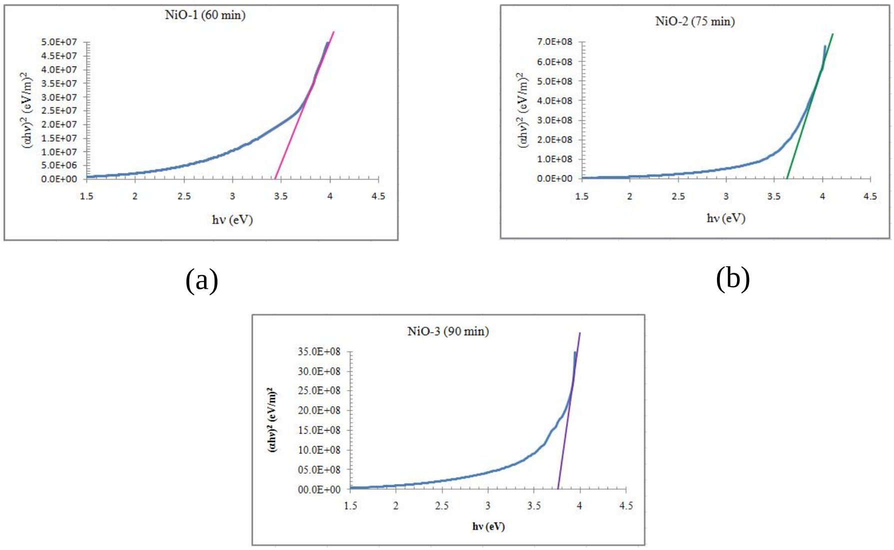

(a) (b)

(c)

Figure 4 Variation of $(\alpha h\nu)^2$ with photon energy of 450ºC -annealed NiO thin film for deposition time (a) 60 min (b) 75 min(c) 90 min

The optical constants such as refractive index (n) and the extinction coefficient (k) and optical conductivity (σ) were evaluated from the reflectance data over the spectral range from 300 to 1100 nm.

The reflectance has been found by using the relationship:

$$R + T + A = 1$$

The "n" and "k" have been and using the following relations,

$$n=\frac{1+\sqrt{R}}{1-\sqrt{R}}$$

$$k=\frac{\alpha\lambda}{4\pi}$$

The optical conductivity "σ" was determined using the following equation

$$\sigma=\frac{\alpha n c}{4\pi}$$

where "c" is the velocity of light. The variation of refractive index with wavelengths of the NiO films for different deposition time is shown in Fig 5(a). NiO-1 thin film, it can be seen that the maximum index of refraction (n = 2.49 at λ = 302 nm, strong absorption region) and the n values between 2.49 and 1.82 was observed in the visible region. The NiO-2 thin film sample showed an anomaly. It was observed that the value of refractive index 1.29 - 3.53 at the wavelength range 308 nm - 334 nm. The n value drastically increased in the wavelength range 380 nm - 660 nm and then abruptly decreases in the wavelength range 680 nm -1100 nm. For NiO-3 thin film, the index of refraction (n= 1.021 at λ=570 nm) was observed. And then the n value is gradually increasing and reaching to the value of 1.71- 2.33 in the wavelength range 700 nm- 1100 nm.

Fig.5 (b) shows the variation of extinction coefficient (*k*) as a function of wavelength (λ) of NiO films for various deposition time. It was observed that the *k* value 0.62×10^{-4}, 4.95×10^{-4} and 5.83×10^{-4} at λ =300 nm for NiO-1, NiO-2 and NiO-3 thin films. The *k* value decreases rapidly at short wavelength 300 nm- 400 nm and after that the value of *k* remains almost constant. The rise and fall in the value of *k* is directly related to the absorption of light. The variation of optical conductivity (σ) with wavelengths of NiO films for different deposition time was shown in Fig 5 (c). It was noticed that the σ value increases rapidly beyond absorption edge region because of the high increase of the absorbance in this region.

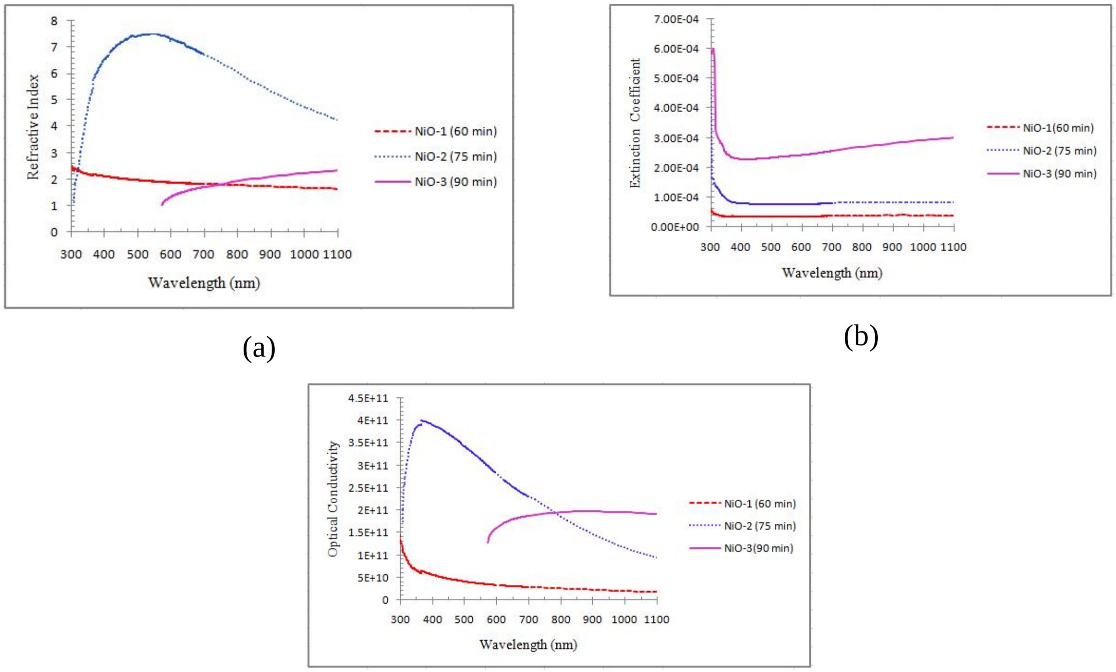

(a) (b)

(c)

Figure 5 Variation of (a) refractive index (b) extinction coefficient (c) optical conductivity with wavelength of NiO thin films for different deposition time

Conclusions

The role of deposition time in NiO thin films were prepared by CBD method and all these films were annealed at 450 ºC for 2 h. The XRD studies revealed that NiO-1(60 min), NiO-2 (75 min) and NiO-3 (90 min) thin films were polycrystalline nature with cubic structure. Defects decreases by the increasing of thickness which means the increasing of crystallite size of NiO thin films. From SEM micrographs, the surface morphologies were transformed from flake shaped morphology to homogeneous grains and to inhomogeneous cellular like morphology. It was found that the grain sizes were decreased as deposition time increased.

The refractive index (*n*) value of NiO-1 film tends to decrease with increasing the wavelengths. The *n* values were observed between 2.49 and 1.82 in the visible region. This is due to the influence of lattice absorption. It was observed that the index of refraction increased with wavelength of visible region in NiO-2 and NiO-3 thin films. It is due to the anomalous dispersion. The extinction coefficient value varies in UV range and it is almost constant in the visible and NIR range for all NiO films. The optical conductivity value of NiO films increases rapidly beyond absorption edge region because of the high increase of the absorbance in this region. The transmittance of NiO thin film decreases from 84 % to 19 % with increasing film thickness in the visible region. The direct energy band gap increases from 3.43 eV to 3.76 eV with deposition time, which is due to the smaller grain size. Having wide band gap and high transmittance, NiO thin films make them promising candidate for optoelectronic devices as well as window layer in solar cell applications.

Acknowledgements

We are grateful to Professor and Head Dr Khin Hla Hla Win and Professor Dr Cho Cho Moe, Department of Engineering Physics, Technological University (Thanlyin) for their kind permission to carry out this work.

References

Benny J, Gopchandran KG, Thomas PV, Koshy P, Vaidyan VK.(1999) Optical and electrical properties of zinc oxide films prepared by spray pyrolysis. Mater Chem Phys. 58, 71.

Chena H L, Lub Y M, Hwanga WS (2005) Characterization of sputtered NiO thin films. *Surf. Coat. Tech.* 198,138-142.

Gopchandran KG, Joseph B, Abraham JT, Koshy P, Vidyan VK. (1997) The preparation of transparent electrically conducting indium oxide films by reactive vacuum evaporation. Vacuum. 48, 547.

Safwat A M, Shereen A and Mou’ad A T (2011). Structural, Optical Dispersion characterization of Sprayed Nickel Oxide Thin films. Journal of Modern Physics, 2, 1178-1186

Sasi B, Gopchandran KG, Manoj PK, et al.(2003) Preparation of transparent and semiconducting NiO films. Vacuum. 68, 149–154.

J. Myanmar Acad. Arts Sci. 2020 **Vol. XVIII.No.2B**

GEOCHEMICAL CHARACTERISTIC OF HEAVY METAL CONTAMINATION IN SURFACE SEDIMENTS ALONG THE UPPER AYEYARWADDY RIVER BANK OFMYITKYINA, KACHIN STATE

Khin Mar Wai[1], Su Su Win[2], Lei Lei Win[3]

Abstract

Ayeyarwaddy River is the country’s largest river and Myanmar’s most important commercial waterway. Gold mining is taking place in the headwaters of the Ayeyarwaddy, and sewage from the mining sites contaminates the rivers. The main objective of the present study is to assess heavy metal contamination in sediments from Ayeyarwaddy River. Surface sediments (0-60 cm) from 4 stations along river bank near Myitkyina region were sampled for metal concentration. The concentration of metals (mg/kg) was as follows: 0-670 Cr; 1000-7020 Mn; 4.28-15.99 (%) Fe; 0.446-1.445 (%) Ti and 0-920 Ni. The degree of sediment contaminations were computed using an enrichment factor (EF), geo-accumulation index (Igeo) and pollution load index (PLI). In this work, average EF of the heavy metals were between 0 and 5, therefore the river sediments were between no enrichment and moderate enrichment. The average Igeo values of these metals except Cr, Mn and Ni were less than zero (Igeo< 0), that the river sediments were not polluted by these metals. Therefore, the surface sediments are uncontaminated to moderately contaminated with Cr, Mn and Ni.PLI value of sampling point C was 2.79 indicating that Ayeyarwaddy River was polluted with the heavy metals. The PLI values of other sampling points were greater than 1 (PLI > 1) which would indicate deterioration of site quality. The study revealed that on the basis of computed indexes, the river is classified uncontaminated to moderately contaminated.

Keywords: Ayeyarwaddy River; heavy metals; indixes; surface sediment; contamination

Introduction

The Ayeyarwaddy River is the country’s largest river and Myanmar’s most important commercial waterway. Hydrological, ecological, anthropogenic pressures and socio-economic factors vary along the length of the Ayeyarwaddy River. Gold mining is taking place in the headwaters of the Ayeyarwaddy, the lifeline of the country and one of the greatest Asian rivers. It threatens the ecosystem of the entire river basin and along with it the livelihoods of about 20 million people. Gold mining is becoming an issue of debate in Kachin State as it has been expanding rapidly in the middle of 1990.It has resulted in serious social and environmental problems not only for those living in gold mining area but also the larger Kachin population.

Gold mining companies operate along all the major rivers and also on-land where gold yielding sediments are found. The main mining centers appear to be along the Ayeyarwaddy River north of the state capital Myitkyina. On land, more and more areas are deforested in order to make way for mining and to build the necessary infrastructure. Together with the mining activities, the use of the mining agent mercury has increased. The logging and gold mining has already caused incalculable loss of biodiversity in the riverine and forest ecosystems. Discarded engines are simply left behind whenever a mining operation moves on. Engine oil used to run machines and waste from mining camps all add to the pollution. Bioaccumulation of mining chemicals will continue to take its toll on species diversity and human health. Aside from the obvious pollution, mining causes structural changes to rivers which can cause severe ecological damage. Rivers are diverted for riverbed mining operations, while water blasting of sediments destroys riverbanks. These structural changes result in the loss of many riverine habitats for endemic fish species. They also affect the direction and speed of the water flow which reportedly has already led to unusually low water levels in some areas and increased flooding in others.

---

[1] Lecturer, Department of Physics, Monywa University

[2] Dr, Lecturer, Department of Physics, University of Mandalay

[3] Dr, Professor, Department of Physics, University of Mandalay

The Mali Hka River is one of the main centres of mining activities in Kachin State. In contrast to the N'MaiHka River, most of the mining on the Mali Hka is done with floating dredges scooping up sediments from the bottom of the river. At some places the river is wide enough to allow river bank mining. Deforestation is a major concern since the trees of the surrounding forests are being cut to clear land, for the construction of mining camps, fuel wood or simply to make space for mining. Waste from the mining sites contaminates the rivers.

Literature Review

Calculation of Pollution Indices

In an attempt to understand the pattern of metal contamination in the study area, useful tools including pollution indices such as; enrichment factor (EF), geo-accumulation index (Igeo) and pollution load index (PLI) were used to calculate heavy metal concentration in sediments.

2.1 Enrichment Factor (EF)

The enrichment factor is established on the bases of standardization of a tested element against a reference one. A reference element is the one characterized by low occurrence variability such as Al, Fe, or Zn. In this study Al was used as a reference element since its concentration in earth's crust is low. Also, Al is a major constituent of clay mineral and has been used as a reference element to assess the status of heavy metals pollution.

EF was calculated using the relation as

$$EF = \left[\frac{C_n / C_{ref}}{B_n / B_{ref}} \right]$$

Where $C_n$is content of the examined element in the examined environment, $C_{ref}$is content of the examined element in the reference environment, $B_n$is content of the reference element in the examined environment and B_{ref} is content of the reference element in the reference environment. Classification of enrichment factor is shown in Table (2.1).

Table 2.1 Classification of enrichment factor

EF	Classification
EF < 1	No enrichment
EF < 3	Minor enrichment
EF = 3-5	Moderate enrichment
EF = 5-10	Moderately severe enrichment
EF = 10-25	Severe enrichment
EF = 25-50	Very severe enrichment
EF > 50	Extremely severe enrichment

2.2 Geo- accumulation Index (Igeo)

Geo-accumulation index serves to assess contamination by comparing current and preindustrial concentration of heavy metals (**Muller, 1981**). Background concentration of heavy metals in the earth's crust was used as a reference value implicating pre-industrial environment. Igeo is calculated through the following equation:

$$I_{geo} = \log_2 [C_n/1.5B_n]$$

Where $C_n$is concentration of the element (n) in the sediment sample and $B_n$is geochemical background value. The constant 1.5 helps to analyze natural fluctuation between a content of a given substance in environment and very small anthropogenic influences. Six classes of geochemical index are shown in Table (2.2).

Table 2.2 Classification of geo-accumulation index

Class	Value	Description of sediment quality
0	Igeo< 0	Practically uncontaminated
1	0 <Igeo< 1	Uncontaminated to moderately contaminated
2	1 <Igeo< 2	Moderately contaminated
3	2 <Igeo< 3	Moderately to heavily contaminated
4	3 <Igeo< 4	Heavily contaminated
5	4 <Igeo< 5	Heavily to extremely contaminated
6	5 <Igeo< 6	Extremely contaminated

2.3 Pollution Index (PI)

The assessment of the sediment contamination was also carried out using the pollution index PI and Pollution Load Index PLI. The contamination factor or pollution index was calculated using the relation described by Hakanson (1980);

$$PI = C_n / C_b$$

Where C_n is the mean content of metals from at least five sampling sites and $C_b$is the pre-industrial concentration of individual metal. Four categories of pollution index were defined by (Hakanson, 1980) as given in Table (2.3).

Table (2.3) Categories of pollution index

PI	Category
PI < 1	Low contamination factor
1 < PI < 3	Moderate contamination factor
3 < PI < 6	Considerable contamination factor
6 < PI	Very high contamination factor

2.4 Pollution Load Index(PLI)

Each sampling site was evaluated for the extent of the metal pollution by employing the method based on the pollution load index (PLI) developed by Tomlinson et al. as follows:

$$PLI = \left(PI_1 * PI_2 * PI_3 * .....PI_n\right)^{1/n}$$

Where n is the number of metals studied and PI is the pollution index as mentioned above. The PLI provides simple but comparative means for assessing a site quality, where a value of PLI < 1 denotes perfection; PLI = 1 denotes that only baseline levels of pollutants are present and PLI > 1 would indicate deterioration of site quality.

Material and Methods

3.1 Study Area and Sampling Points

The Ayeyarwaddy River is named from the confluence of the N'maiH’ka and MaliH’ka Rivers in Kachin State. The upper part from the headwaters of the Ayeyarwaddy river, NmaiH’ka and Mali H’ka rivers that join about 50 km north of Myitkyina. The four sampling points were selected for the present study. In NmaiH’ka , sampling point (A) is 1.6 km upstream north of the confluence. In Mali H’ka, sampling point (B) is situated about 1.6 km upstream north of confluence. Confluence lies 28 miles (45 km) north of Myitkyina, capital of the Kachin State. In Ayeyarwaddy River, sampling point (C) is located on 1.6 km and sampling point (D) is 3.6 km downstream south of confluence. Map of study area showing sampling sites A, B, C and D is as shown in Fig. (3.1). Coordinate of each sampling site is shown in Table (3.1).

3.2 Sample Collection and Preparation

Freshly deposited sediments from shallow water near the banks of Ayeyarwaddy River at different sites were collected with the help of PVC pipe during the month of July 2016 from the river bed where flow rates were low and sedimentation was assumed to occur. Collected samples were air dried at room temperature. From the bulk sediment, a representative sub sample was powdered and sieved through 100 mesh. After getting the fine powder of sediment samples, they were analysed by EDXRF technique.

Figure 3.1 Map of study area showing sampling sites A, B, C and D

Table 3.1 Coordinates of each sampling site

Sites	Latitude	Longitude	Sample Code	Depth(cm)
Maykha (A)	25° 42.55′ N	97°31.57′ E	MK1	60
			MK2	45
			MK3	30
			MK4	15
Malikha (B)	25 ° 45.42′ N	97° 29.95′ E	ML1	60
			ML2	45
			ML3	30
			ML4	15
Ayeyarwaddy 1 (C)	25 ° 41.57′ N	97° 29.95′ E	A 1,1	60
			A 1,2	45
			A 1,3	30
			A 1,4	15
Ayeyarwaddy 2 (D)	25 ° 41.23′ N	97° 31.38′ E	A 2,1	60
			A 2,2	45
			A 2,3	30
			A 2,4	15

3.3 Elemental Analysis Using EDXRF System

The X-ray fluorescence spectrometer used for heavy metal analysis is HORIBA XGT 5200 at Suranaree University of Technology, Thailand. It is a high purity Si detector and the sample is simply placed in the sample chamber and analysed at normal atmospheric pressure.

Results and Discussion

From the results, the mean concentrations of heavy metals found in the samples collected from the sampling point C: Ti, Mn, Fe and Ni were higher than in the samples from the sampling points A, B and D. The mean concentrations of heavy metals in sediments collected from the sampling point B: Cr was higher than in the samples collected from other sampling points. The mean concentrations of the heavy metals collected from the sampling point A: Ti, Cr, Mn, Fe and Ni were the lowest.

Average shale value was used as reference baseline in this study to provide elemental background concentration. Comparison of the values obtained in this study with global reference value indicates that the concentration of Ti, Cr, Mn, Fe and Ni were higher than the reference baseline of average shale shown in Fig. (4.1).

The EF was calculated for a better assessment of anthropogenic input for each metal. In sampling point A, average EF values of Ti, Cr, Fe and Ni were found to be no enriched (EF< 1) and Mn was minor enriched (EF<3). In sampling point B, average EF values of Ti, Mn, Fe and Ni were minor enriched (EF<3) and Cr was moderate enrichment (EF<5). In sampling point C, average EF values of Ti, Cr, Mn and Fe were minor enriched (EF<3) and Ni was moderate enrichment. In sampling point D, average EF values of Ti, Cr, Mn, Fe and Ni were minor enriched (EF<3).The EF value above 1.5 indicates an anthropogenic contribution and if EF is less than 1.5, the metal concentration is considered crustal or natural weathering origin. The higher the EF values is, the more severe the anthropogenic contribution. In this study, the studied heavy metals were proven to be between no enrichment and moderate enrichment. Comparison of average EF for each heavy metal in difference sites is shown in Fig.(4.2).

Based on the average values of Igeo, the ranking of intensity of heavy metal pollution of surface sediments is as follow: Ni>Cr>Mn>Ti>Fe. The average Igeo value of Cr and Mn are between zero and one (0<Igeo< 1) indicating that surface sediments are uncontaminated to moderately contaminated. The average Igeo value of Ni is between one and two (1<Igeo<2) indicating that surface sediments are moderately contaminated. Other heavy metals showed an Igeo of less than 0, indicating that the river sediments are not polluted by these metals. Therefore, the surface sediments are uncontaminated to moderately contaminated with Cr, Mn and Ni. Average Igeo values of each heavy metal in different sites is shown in Fig.(4.3).

PLI value of sampling point C was 2.79 indicating that Ayeyarwaddy River was polluted with the heavy metals. The PLI values of other sampling points were greater than 1(PLI > 1) which would indicate deterioration of site quality. The study revealed that on the basis of computed indexes, the river is classified uncontaminated to moderately contaminated. Comparison of average PLI values in difference sites is shown in Fig.(4.4).

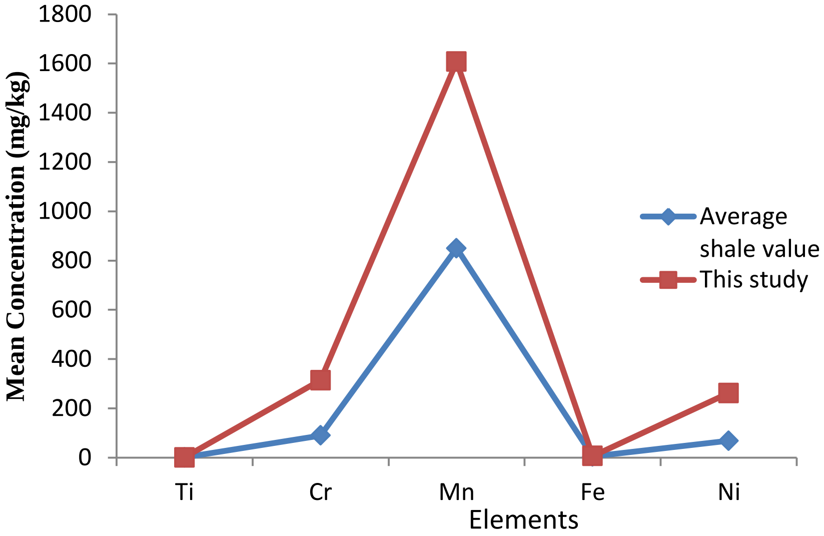

Figure 4.1 Mean concentrations of sampling sites compared with average shale values

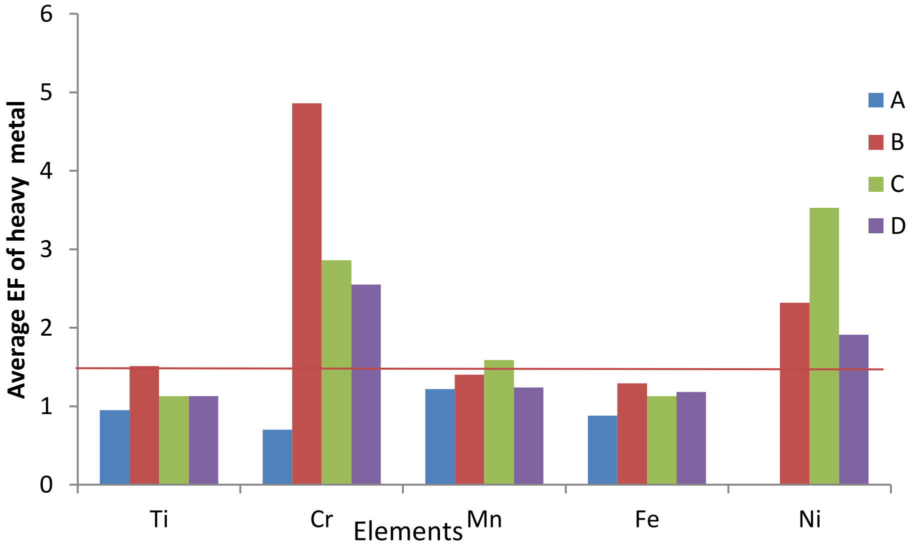

Figure 4.2 Comparison of average EF for each heavy metal in difference sites

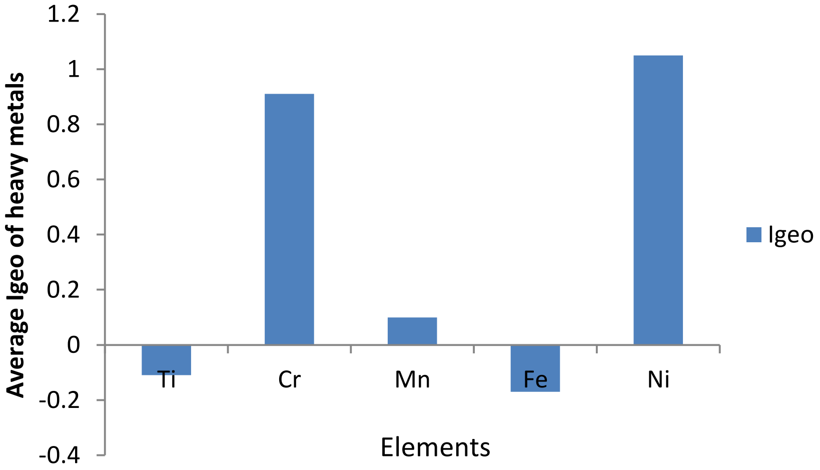

Figure 4.3 Average Igeo values of each heavy metal in different sites

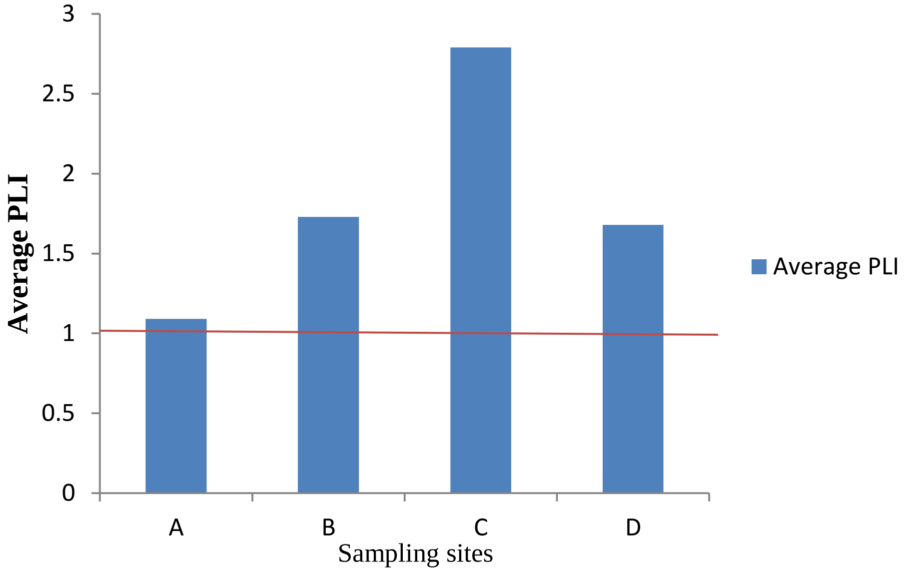

Figure 4.4 Comparison of average PLIvalues in difference sites

Acknowledgements

I would like to express our gratitude and sincere thanks to Rector Dr Thura Oo, Monywa University for his permission to do this work. I would like to thank Dr Khin Khin Win, Professor and Head, Department of Physics, University of Yangon for her precious advice and guidance. I wish to thank Dr Shwe Zin Aung, Professor and Head, Department of Physics, Monywa University for her exhortation.

References

Asibor Godwin, Edjere Oghenekohwiroro, Adeniyi Funsoand Ogundele Olaniyi, (2015) " Using EF, PLI and IGEO for the assessment of heavy metal pollution and sediment quality of Asejire Reservoir."Southwest Nigeria vol.3, No.4, pp.77-90.

F. Moore, G. Forghani and A. Qishlaqi, (2009) "Assessment of heavymetal contamination in water andsurfaces of the Maharlu Saline Lake, SW Iran." Iranian Journal of Science & Technology, vol.33, No A1.

H. Sharri, Siti Nurul Hidayu Mohamad Azmi, Khawar Sultan, Joseph Bidai and Yuzwan Mohamad (2015)"Spatial distribution of selected heavy metal in surface sediments of the east coast of Peninsular Malaysia", International Journal of Oceanography, vol. 15.

Thabet A. Mohamed, Mohamed Abuel-Kassem Mohamed, Ragab Rabeiy Mohmoud A. Ghandour "Application of pollution indices for evaluation of heavy metals in soil close to fertilizer plant, Assiut, Egypt."Assiut

J. Myanmar Acad. Arts Sci. 2020 **Vol. XVIII.No.2B**

DETERMINATION OF RADON CONCENTRATION IN THE STALACTITE WATER FROM MAHAR SADAN CAVE, KAW KA THAUNG CAVE AND EAIK SA TA YA CAVE IN KAYIN STATE, MYANMAR

Win Win Mon[1], Kywe Kywe Aung[2], May Zin[3], Khin Yu Mon[4]

Abstract

The pure of drinking water is very important for health of our human beings. The water form stalactite can be used as drinking water. Radon gas involvement is a part of the fact that caused water pollution. Using RAD 7 nuclear radiation detector, we tried to test the stalactite water to know how much the level of radon gas involves in it. The following three caves from Kayin State have been experiment; Mahar Sadan cave, Kaw Ka Thaung cave and Eaik Sa Ta Ya cave. Review the results of the radon concentration are as follow; Mahar Sadan cave has 10.7 ± 11 pCi/L, Kaw Ka Thaung cave has 24.9 ± 13 pCi/L and Eaik Sa Ta Ya cave has 29.3 ± 18 pCi/L.According to measurement, the extent of radon concentration in the cave cannot cause danger to human life that is why the stalactite water can be used.

Keywords: Radon concentration, stalactite water, RAD 7.

Introduction

Two major chains of initial radioactive nuclear decay associated with the earth are Th-232 and U-238. Among the radioactive nuclear produced in the two mentioned chains,Radiom-226 is a product of the U-238 radioactive decay series with half-life about 1600years that emits alpha particle is very important. Radon 222,the most stable isotope in its family which is used in radio therapy and special properties as odourless, colourless, water-soluble and radioactive like-in other 20 isotopes, is the daughter of alpha disintegration from Ra-226 with a half-life about 92 hours, can then enter the human body through the respiratory. The total amount of annual effective dose of natural radioactive sources is 2.4msv and1.2 msv nearly belongs to radon and its daughters. Radon-222 and its decay products are the most important source of human exposures. The second natural Radon isotope is Radon 219 which has a half-life 3.9 seconds and is produced from U 235 decay serie. The third natural isotope located in the The 232 decay chain is called Thorium with half-life 55.6 seconds. When the radon gas to be cooled below the freezing point it has a bright phosphoric color and in the lower temperature has yellow color. In normal temperature its color goes to be red orange. The average concentration of radon in the atmosphere is about one molecule of radon in molecule of air, and it is estimated that every square mile of soil to a depth of 6 inches contains approximately one gram of radium which decays to radon 222. At least 50percent of natural exposures are due to radon gas and its corresponding decay products.

Radon in water and its hazards

Once radon in water supply reaches people, it may produce human exposure via inhalation and direct digestion. Radon in water transfers into the air during showers, flushing

---

[1] Assistant Lecturer, Department of Physics, Hpa-an University
[2] Associate Professor, Department of Physics, Hpa-an University
[3] Professor, Department of Physics, Hpa-an University
[4] Professor and Head, Department of Physics, Hpa-an University

toilets, washing dishes and washing clothes. The aerosols tend to deposit into the lungs where they release radiation that has been shown to increase the likelihood of lung cancer. Radon can also reach other body tissues through ingestion resulting in radiation exposure to the internal organs. Ingestion of radon is believed to increase the risk of stomach cancer. As stated one kinds of water contamination is due the existence of radon and this is very important in the quality of water.

Table 1 A Save Level of Radon Gas for Public Area

Radon concentration	Recommended Remedial Action Time
Less than 100 pCi/L	No action required
100 – 300 pCi/L	Save Level
greater than 300 pCi/L	Action required

Measurement of radon in water samples

The concentration of radon in stalactite water is more than of spring waters and also deep wells, however if the water is moving more and more the concentration of radon is expected to be further reduced. The investigated water samples are collected from three caves in Kayin State. By keeping the samples in a cold place and at the least time the samples have been transported to laboratory.

Figure 1 Location map of Kayin State

Radon measurement system

In this research to determine the concentration of radon in stalactite water the RAD 7 Professional Electronic Radon Detector has been used. This system has suitable features to measure the concentration of radon gas in the water. The most important characteristics of this system is the high sensitivity and short time response. The detection system has RAD H_2O accessory, RAD AQUA accessory and Water Probe accessory. RAD H_2O accessory enables to measure collected water samples to detect radon with high accuracy over a wide range of concentrations, obtain data within an hour of taking sample. RAD AQUA accessory handles the continuous monitoring of radon in water, offering accurate results in as little as half an hour. Water Probe accessory is used to collect radon samples from large bodies of water. The probe consists of a semi-permeable membrane tube mounted on an open wire frame. The tube is placed in a closed loop with the RAD7. When the probe is lower into water , radon passes through the membrane until the radon concentration of air in the loop is in equilibrium with that of water. As with the RAD AQUA, the RAD7 data and water temperature data are collected simultaneously and accessed by capture to determine the final result. RAD H_2O accessory and RAD AQUA accessory are shown in figure 2 and figure 3.

Figure 2 The RAD H_2O Accessory

Figure 3 The RAD AQUA Accessory

Measurement results

In this research, radon concentrations in stalactite water samples from three cave of Kayin State is measured. The radon concentration in each sample has shown in table 2. In Figure4, 5 and 6 the spectrum of radon concentration of each sample are shown respectively.

Table 2 Specific Activity of Samples

Samples No	Caves Name	Specific Activity
1	Mahar Sadan Cave	10.7 ± 11 pCi/L
2	Kaw Ka Thaung Cave	24.9 ± 13 pCi/L
3	Eaik Sa Ta Ya Cave	29.3 ± 18 pCi/L

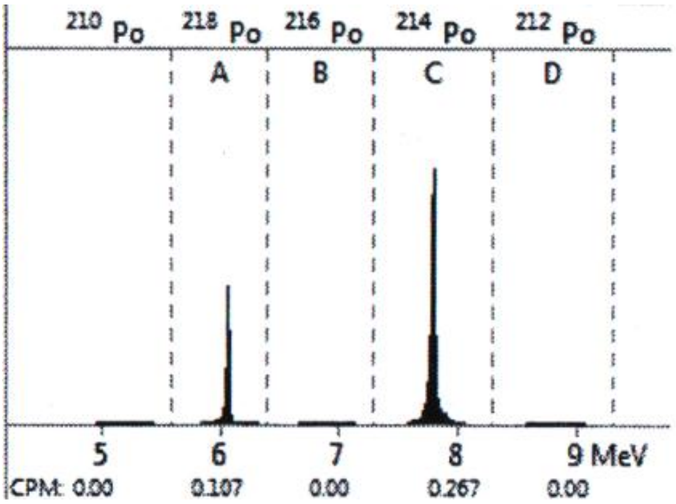

Figure 4 The Spectrum of stalactite water sample in Mahar Sadan Cave

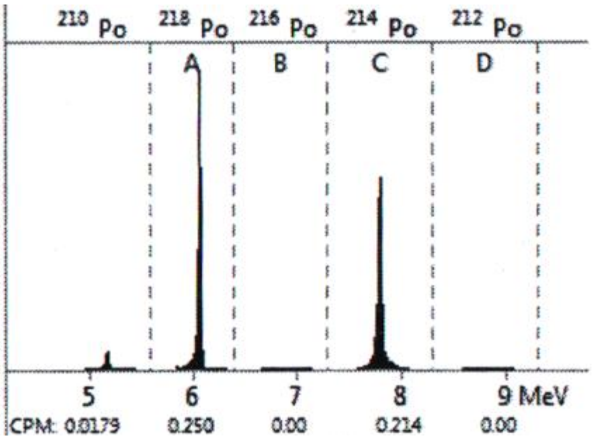

Figure 5 The Spectrum of stalactite water sample in Kaw Ka Thaung Cave

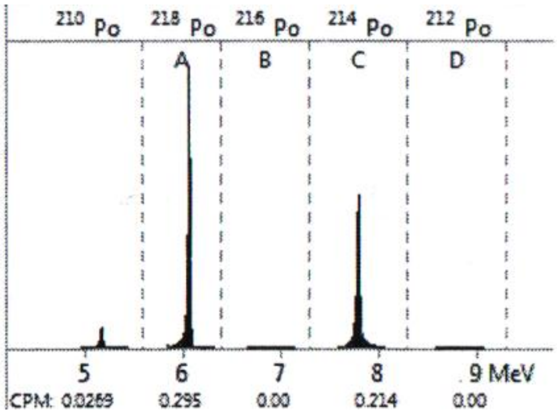

Figure 6 The Spectrum of stalactite water sample in Eaik Sa Ta Ya Cave

Discussion

When analyses the synthetic spectra for water samples of Mahar Sadan Cave, Kaw Ka Thaung Cave and Eaik Sa Ta Ya Cave, the following peaks are observed. At 5.3 MeV, a persistent peak will be developed as resultant of Polonim-210 build up. At 6.00 MeV, after less than one hour of exposure to radon (new radon) Po-218 peak A. At 6.78 MeV, the RAD 7 spectrum while continuous sampling thoron laden air (new thoron) Po-216 peak B. At 7.69 MeV, the RAD 7 spectrum after purging the instrument with radon-free air for more than 10 minutes (old radon) following exposure to radon,Po-214 peak C. At 8.78 MeV, the spectrum after discontinuing a length (old thoron) sampling of thoron laden air, Po 212. Peak D.

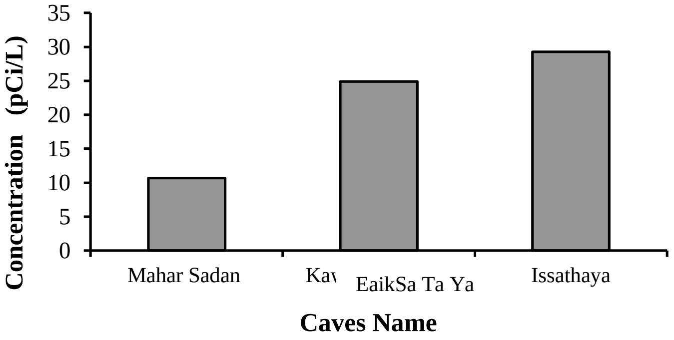

Figure 7 The histogram of radon concentration (pCi/L) of each sample

Conclusion

From the public health point of view, if we breathe radon gas, it tends to suffer from cancer, stomach (ingestion) cancer and skin allergy. As our study on three natural caves, we have observed as below: Mahar Sadan cave was low radon concentration in air. The reason was the size of the cave is larger enough and it also has good ventilation to reduce the concentration of radon gas. Although, Kaw Ka Thaung cave was large, it has poor ventilation, so the radon concentration was higher than the Mahar Sadon cave. For Eaik Sa Ta Ya cave, the size is smaller than Mahar Sadan cave and Kaw Ka Thaung. Its' ventilation is worse than the previous two.

Therefore, this one is the obviously highest radon concentration in water sample. According to measurement, the extent of radon concentration in the cave cannot caused danger to human life that is why the stalactite water can be used.

Acknowledgements

I would like to express our gratitude to Dr Mya Mya Aye, Rector and Dr Than Than Myint, Pro-Rector, Hpa-an University for their permission to conduct this research.

References

A. El-Sersy, M Mansy and A Hussein, (2003), Effect of environment conditions on radon concentration-track density calibration factor of soil statenuclear track detectors

T. Ren, B. Shang, Y. Yu, H. Guo, Radon-222 concentration in water and the exposure ofthe public. IRPA 9, April (1996), Vienna, Austria

Webb,G.A.M. (1992),"Exposureto radon", Radiation Protection Dosimetry, 42(1992)191-195.

http://www.epa.gov/radiation/radionuclides /radon.html

http:/www.radon gas.org

J. Myanmar Acad. Arts Sci. 2020 **Vol. XVIII.No.2B**

RADON MEASUREMENTS IN AND AROUND SOME GOLD MINES IN SHWE KYIN

Hein Nay Zar Wann[1], Tin Tin Phyo Lwin[2], Yin Maung Maung[3], Kyi Thar Myint[4]

Abstract

The aim of this paper is to carry out the radon concentration. In this research, radon concentration in five soil samples collected from different depths at Kalain Ravine are recorded by RAD 7 radon detector as 415, 8.20, 16.4, 13.1 and10.9Bq/m^3 respectively. At5 ft depth, the recommended remedial action has to perform in less than 3 years and underneath this depth, there is no action required. Collected soil samples were also examined with energy dispersive X-ray fluorescent spectrometer. In addition to the standard feature of identification of all elements sodium (Na) to Uranium in a sample, quantitative information is provided. In these samples, it was observed that the main constituents in all samples Si, Al, Fe, K and S. Potassium was detected in all samples which can contribute to K^{40} activity. The pore space in soil grains might contain water and if the radon atom terminates its recoil in the water, the radon might be transported to water around mining sites (mine dump, mine tailings or ravine). Water samples were collected and analysed in laboratory to record radon concentration also with RAD7 detector. It was found that the radon concentration in water samples from Kanni tailing dam and Kyet Khat Kali spring were 4.84 pCi/L and 2.68 pCi/L respectively. The water samples were analysed with Atomic Absorption Spectrometer (AAS) to be see the concentration of particular hazardous elements (Pb and K). It has been obtained that in water samples from both sites no trace of lead was found. Potassium contents in water samples from KyetKhatKali site is 1.53 mg/L and that from Kannitwin is 0.99 mg/L.

Keywords : Radon Concentration; RAD 7; EDXRF; AAS

Introduction

Radon is a radioactive gas that is formed naturally by the radioactive breakdown of uranium in soil, rock and water. It cannot be detected by the senses, i.e, it is colour less and odourless however, it can be detected with special instruments. Radon usually escapes from the ground into outdoor air where it mixes with fresh air resulting in concentration too low to be of concern. Radon gas breaks down or decays to form radioactive elements that can be inhaled into the lungs. In the lungs, decay continues, creating radioactive particles that release small bursts of energy. Radon is a inert, water soluble gas produced by the decay series of radium (^{226}Ra) which is also a decay product of uranium (^{238}U) decay series. Radon further decays into Polonium (^{218}Po) which emits an alpha particle of energy 5.5 MeV. Radon is present in trace amount almost everywhere on earth being distributed in the soil, groundwater and in the lower levels of the atmosphere. Radon which is present everywhere on the earth surface reaches by different processes and accumulates in the houses and underground mine. In order to measure the radon concentration which would not exceed the safe level, the investigation can be taken out by appropriate instruments. In this research work, RAD 7 solid state detector was used to determine the radon concentration in soil samples and water samples from Shwe Kyin Gold mines, Bago Region.

---

[1] U, Assistant Lecturer, Department of Physics, Hpa-An University

[2] Dr, Assistant Lecturer, Department of Physics, University of Yangon

[3] Dr, Professor, Department of Physics, University of Yangon

[4] Dr, Professor (Retd:), Department of Physics, West Yangon University

Natural Decay Series

Radioactive decay occurs when an unstable (radioactive) isotope transforms to a more stable isotope, generally by emitting a subatomic particle such as an alpha or beta particle. Radionuclides that give rise to alpha and beta particles are shown in this figure.

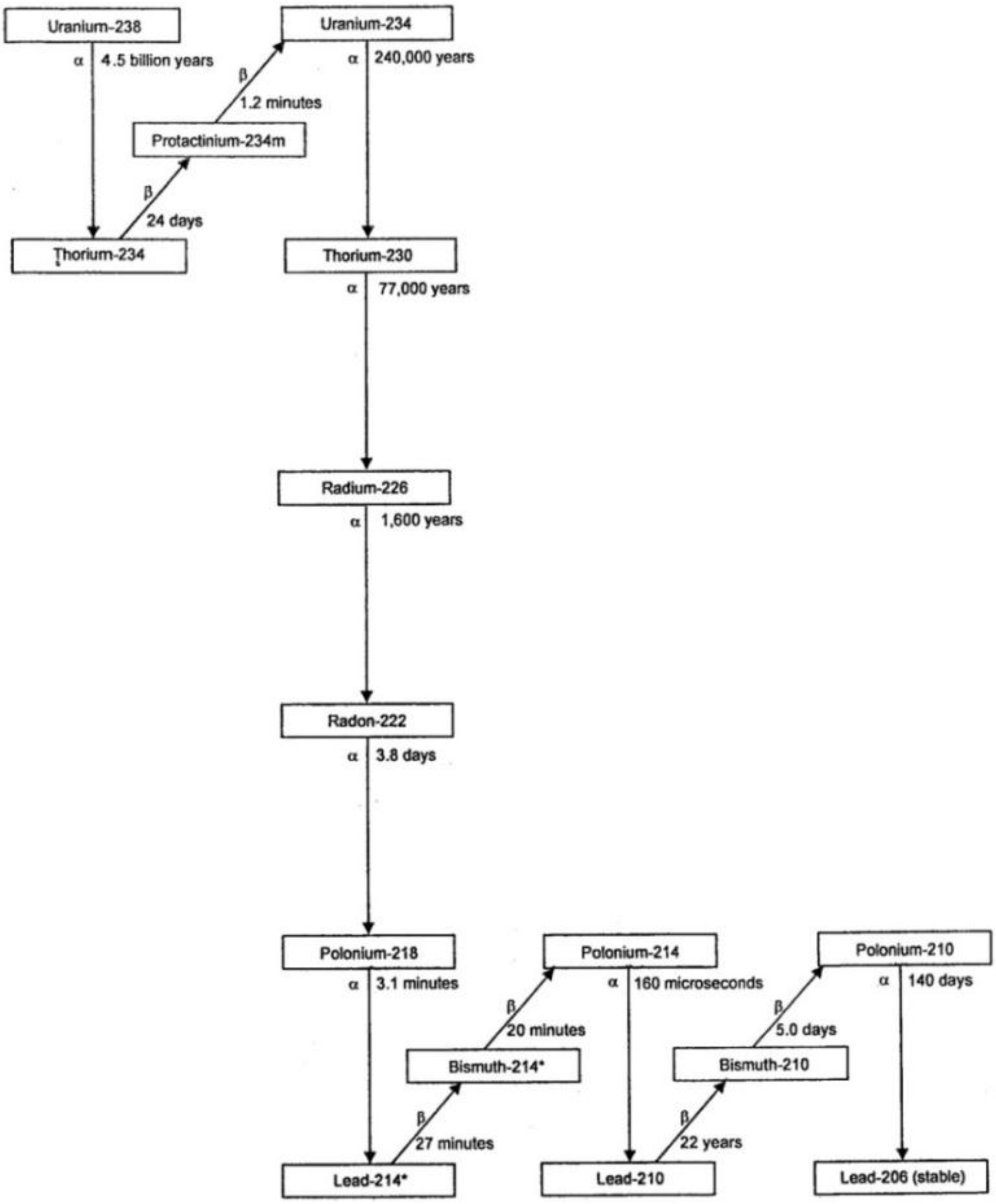

Natural Decay Series: Uranium – 238

A Safe Level of Radon Gas

Radon gas braks down or decays to form radioactive elements that can be inhaled into the lungs. In the lungs, decay continues, creating radioactive particles that release small bursts of energy. This energy is absorbed by nearby lung tissue, damaging the lung cells. When cells are damaged, they have the potential to result in cancer when they reproduce.

The construction of new dwellings should employ techniques that will minimize radon entry and will facilitate post-construction radon removal, should this subsequently prove necessary.

Radon concentration	**Recommended Remedial Action Time**
Greater than 600 Bq/m^3	In less than 1 year
Between 200 Bq/m^3 and 600 Bq/m^3	In less than 3 years
Less than 200 Bq/m^3	No action required

ICRP recognizes that an action level can have two distinct purposes:

(a) to define workplaces either in which intervention should be undertaken, or

(b) to identify where the system of protection for practice should be applied.

Radon concentrations in water samples are below the WHO recommended permissible level (100 pCi/L) and much lower than WHO action level (300 pCi/L) [ICRP, 2007].

Material and Methods

Sample collection

The RAD 7 detector was performed on soil samples at ByutMyaung Site on the mine dump of ShweKyin gold mines at 284 ft above sea level.

The samples are collected the location at 17° 50' 46.08' north latitude, 96° 57' 46.80' east longitude and Kalain, Byut Myaung site with GPSMAP 62 S.

The collected soil samples at depths with five feet and two feet variations are shown in figures1, 2 and tables 1, 2.

Water samples were collected from two different sites with clean litre polythene bottles. One of the samples was collected from Kanni tailing dam and another from the Kyet Khut Kali spring as show in figure 3 and table 3.

Figure 1 Soil samples at depths with five feet variations

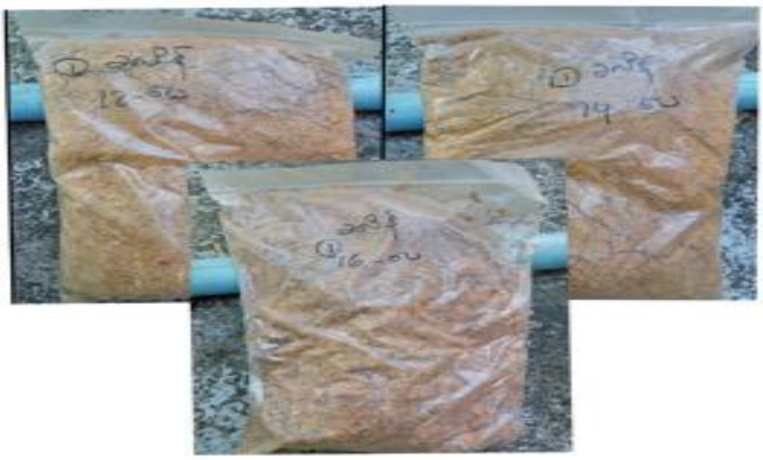

Figure 2 Soil samples at depths with two feet variations

Table 1 Collected soil samples from different depths with five feet variations

Samples No:	Location	Depth
1	Kalain Ravine ByutMyaung gully	1.524 m (5 ft)
2		3.048 m (10 ft)

Table 2 Collected Soil sample from different depths with two feet variations

Sample	Location	Depths
1	Kalain Ravine ByutMyaung gully	3.6576m (12ft)
2		4.2672m (14ft)
3		4.8768 m (16ft)

Ravine – Deep narrow valley groge, mountain cleft.
Gully – A channel worn by running water deep artificial channel.

Figure 3 Water samples from Kanni tailing dam and Kyet Khat Kali spring

Table 3 **Collected water samples from different depths and locations**

Sample No	Location	Depth
1	KyetKhat Kali	0.9144 m (3ft)
2	Kannitwin	5.7912 m (19 ft)

Figure 4 Photo graph of taking the sample of the soil and water on various depths

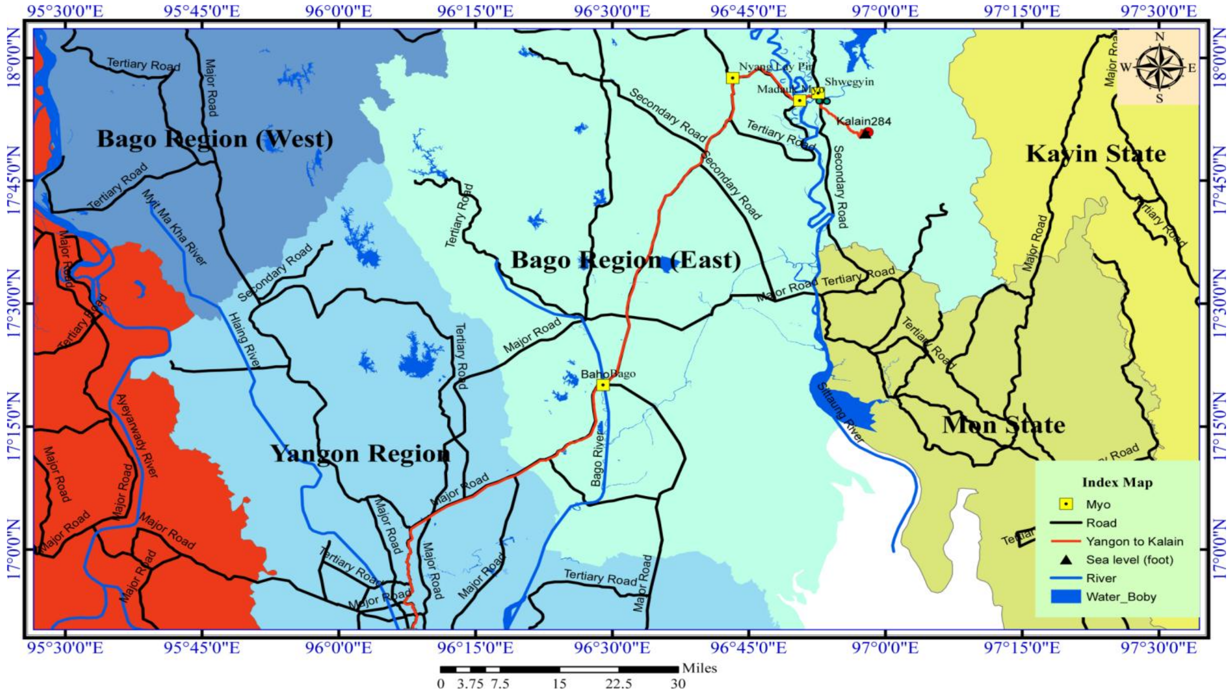

Figure 5 Location Map of Shwe Kyin Goldmine from Yangon Region

Measurement Procedure

After taking arrangement consists of RAD professional 7 Durridge and small drying tube filled with fresh (blue) descendant $(\mathrm{CaSO_4})$ positioned vertically, soil gas sample plastic can was filled through sampling point. The soil gas probe should be inserted into the soil sample up to depth about 15cm. Make sure that there is a reasonable seal between the probe shaft and the lid of can, so that ambient air does not descend around the probe and dilute the soil gas sample. Soil gas is normally so high in radon that it is not necessary to use long cycle times to gain precision. Five minute cycle times (pumping 5 minutes, waiting 5 minutes, counting 5 minutes) are sufficient. In total, each set of readings included four 5 minute cycles that took 1 half hour. Running the test and interpretation of the data were also taken out.

The Water Probe is used to collect radon samples from large bodies of water. The probe consists of a semi-permeable membrane tube mounted on an open wire frame. The tube is placed in a closed loop with the RAD 7.

When the probe is lowered into water, radon passes through the membrane until the radon concentration of the air in the loop is in equilibrium with that of the water. As with the RAD AQUR, the RAD7 data and water temperature data are collected simultaneously and accessed by CAPTURE Software of RAD 7 to determine the final result.

The study on soil samples are conducted at Universities' Research Centre (URC) Monywa University. A Shimadzu Co. X-ray fluorescence spectrometer, model EDX-700, was used, following the operating condition; X-ray tube; Rh (3.0 KW); Excitation; 50 KV for NaKα and 50 KV for ULα; Current: 1-50 μA, maximum; Collimator; 10 mm; Detector: Si (Li) cooled with LN_2 (liquid nitrogen); Measurement time: Live-60 s.

Atomic absorption spectrometry (AAS) is an analytical technique that measures the concentrations of elements. Atomic absorption is so sensitive that it can measure down to parts per billion of a gram (μgdm^{-3}) in a sample. The technique make use of the wavelengths of light specifically absorbed by an element. They correspond to the energies needed to promote electrons from one energy level to another, higher, energy level. The concentrations to toxic elements such as Pb and K in two water samples from mining sites were analyzed by AA-6300 SHIMADZU at AMTT analytical laboratory.

Results

Table 4 Specific activity of soil samples with five feet variations

Samples No:	Depth	Specific Activity (Bqm^{-3})
1	1.524 m (5 ft)	415
2	3.048 m (10 ft)	8.20

Table 5 Specific activity of soil samples with two feet variations

Samples No:	Depth	Specific Activity (Bqm^{-3})
1	3.6576 m (12 ft)	16.4
2	4.2672 m (14 ft)	13.1
3	4.8768 m (16 ft)	10.9

Table 6 Concentration of elements contained in soil samples from different depths

Elements	**% Concentration of Elements at the depth(ft)**				
	5ft	**10ft**	**12ft**	**14ft**	**16ft**
AL	27.879	19.814	22.377	18.689	26.946
Si	**41.537**	**33.895**	**65.831**	**60.005**	**48.139**
S	0.576	0	0	0.705	0.739
K	5.161	2.306	3.671	2.695	0.301
Ti	4.154	5.118	0.635	0.735	6.968
V	0.144	0.135	0.038	0	0
Cr	0.087	0.110	0	0.019	0.100
Mn	0.061	0.097	0.022	0.047	0.035
Fe	20.080	38.106	7.284	16.987	16.293
Ni	0.037	0.066	0.020	0	0.067
Cu	0.063	0.080	0.052	0.055	0.053
Zn	0.029	0.077	0.040	0.048	0.060
Ga	0	0	0	0	0.024
Rb	0	0	0.006	0	0
Sr	0.025	0.035	0.025	0.016	0.063
Y	0.013	0	0	0	0
Zr	0.099	0.137	0	0	0.180
Nb	0.016	0.023	0	0	0.031
Ir	0.040	0	0	0	0

Table 7. Specific activity of water samples from different locations

Samples No:	**Location**	**Specific Activity (pCi/L)**
1	KyetKhat Kali	2.68
2	Kannitwin	4.84

Table 8 Atomic Absorption Spectroscopy data for water samples from different locations.

Samples No:	**Name**	**Lead (mg/L)**	**Potassium (mg/L)**
1	KyetKhat Kali	ND	1.53
2	Kannitwin	ND	0.99

ND = not detected (< LOD), Pb< 0.006 mg/L , LOD = limit of detection

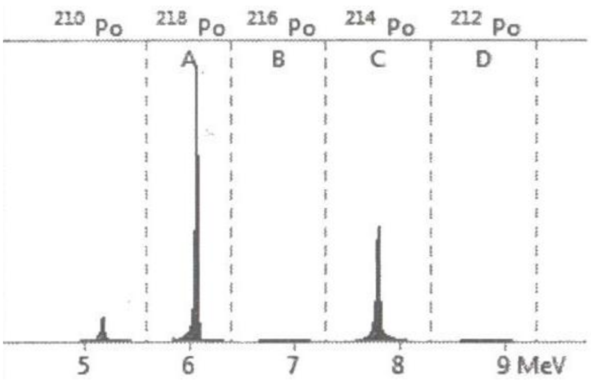

Figure 6 5 ft depth Spectrum for soil sample

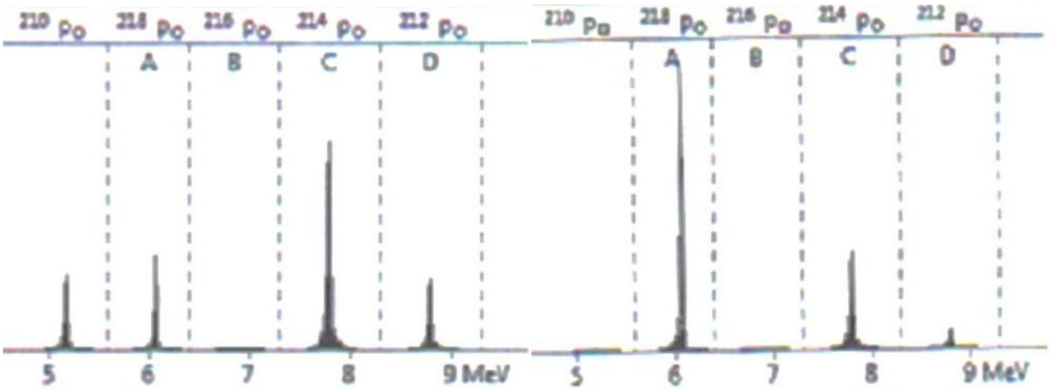

Figure 7 Operational Radon Spectra for water samples from different locatoins

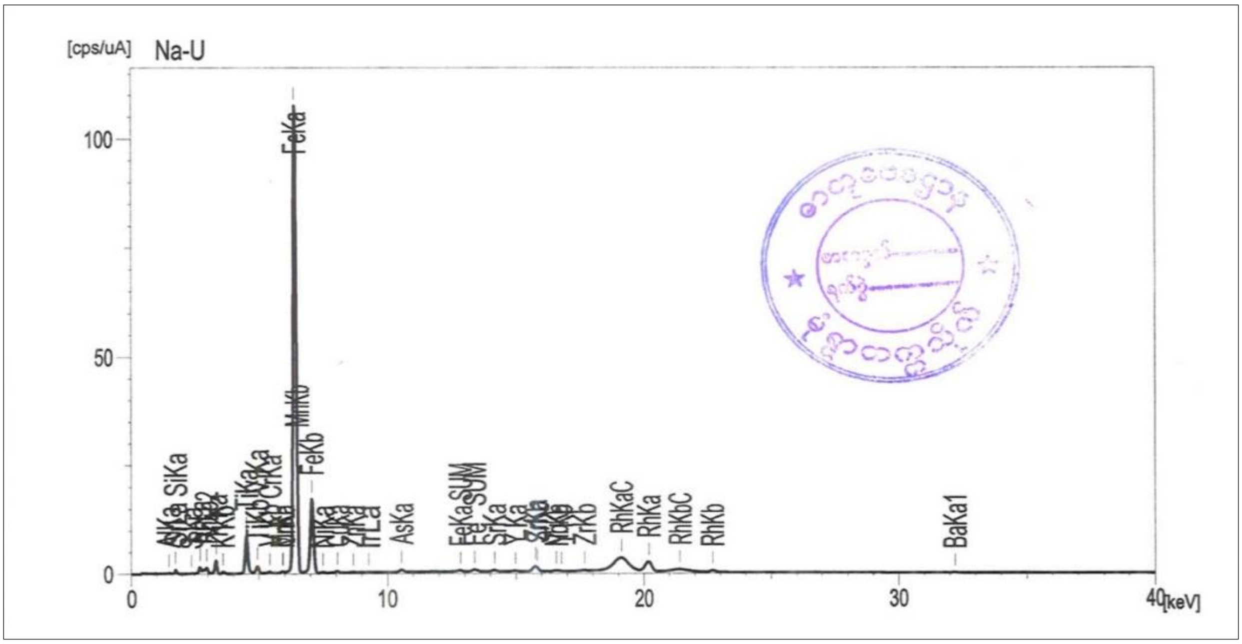

Figure 8 EDXRF spectrum of 5ft depth variation

Discussion

When analyses the synthetic spectra for soil samples at 5ft, 10ft, 12ft, 14ft and 16ft depths, the following peaks are observed. At 5.3 MeV, a persistent peak will be developed as resultant of Polonium-210 buildup. At 6.00MeV, after less than one hour of exposure to radon (new radon) Po-218 peak A. At 6.78MeV, the RAD7 spectrum while continuous sampling thoron laden air (new thoron) Po-216 peak B. At 7.69MeV, the RAD7 spectrum after purging the instrument with radon-free air for more than 10 minutes (old radon) following exposure to radon. Po-214 peak C. At 8.78MeV, the spectrum after discontinuing a lengthy (old thoron) sampling of thoron laden air, Po 212. Peak D.

In water samples from Kyatkatkale spring and Kanni tailing dam, the contents of lead are not detected because those are lower than the limit of detection (Pb< 0.006 mg/L). The potassium contents for these samples are 1.53 mg/L and 0.99 mg/L. The Analytical report described lead concentration for safety limit and monitor potassium for K^{40} activity. This result showed that these in low risk of radon exposure due to K^{40} which contribute only 0.012 % to natural potassium.

Conclusion

For the depths less than 5ft the recoil radon transported more easily to the air, so the activity should be less. In the depths more than 5ft the rocks soil grains constituted more compact with small or without pore space. The recoil radon at that depths should embedded in the grains, then the radon activity may decrease. The height of the peaks on the spectrum depend on the concentration of the radon and to which radon had exposed. According to the results, the depth 5ft has the highest specific activity and the depth 10ft has the lowest specific activity. The radon level of the depth 12ft, 14ft and 16ft are lower than the ICRP (International Commission on Radiological Protection) recommendation level. The qualitative results indicated the highest silicon content is in soil from 12ft depth as 65.83 %. But specific activity at the depth 5ft is higher than the ICRP recommendation level. It may cause health risks to the mine workers in less than 3 years. It is not seriously effect to the workers because the workers isn't stay longer at this depth.However, continuous monitoring of radon concentration of water from other hilly region and mining area is need for radiation safety as radon can cause some malignancies in human. Radon is believed to be the second largest cause of lung cancer, after smoking.

Acknowledgements

I am greatly indebted to Professor Dr Khin Khin Win, Head of Department of Physics, University of Yangon, for her kind permission to carry out my research work. I also would like to thank Professor Dr Myo Lwin, Department of Physics and Professor Dr Aye Aye Thant, Department of Physics, University of Yangon for their valuable suggestion. I am deeply grateful to my supervisor, Dr Yin Maung Maung, Professor, Department of Physics, University of Yangon, for his valuable guidance and helpful advice to carry out this research work. I also thank to my Co-Supervisor, Dr Tin Tin Phyo Lwin, Assistant Lecturer, Department of Physics, University of Yangon, for her helpful guidance and suggestion throughout this work. I also deeply thank to Dr Kyi Thar Myint, Professor (Retd), Department of Physics, West Yangon University for her valuable advice and guidance in carry out this research.I would like to thank all people who encourage and support me during the undertaking of this work.

References

A. El-Sersy, M Mansy and A Hussein, (2003), Effect of environmental conditions on radon concentration-track density calibration factor of solid state nuclear track detectors.

ICRP : The (2007) Recommendations of International Commission on Radiological Protection. ICRP Publication 103.

W.J. Speelman, R-Lindsay, R.T. Newman, R.J.de Meijer, (2006) TA-6 Radiation Protection of the Public and the Environment. Radon Generation And Transport In And Around A Gold-Mine Trilings Dam In South Africa.

http://www.epa.gov/radiation/radionaclides/radon.html
http://www.radongas.org/

J. Myanmar Acad. Arts Sci. 2020 **Vol. XVIII.No.2B**

STRACTURAL AND OPTICAL CHARACTERIZATION OF SENSITIZED ZnO POWDER BY CHEMICAL REACTION METHOD

Moh Moh Lwin[1], Myint Kalyar[2], Than Than Win[3], Yin Maung Maung[4] and Khin Yu Mon[5]

Abstract

Prepared ZnO powder has been successfully synthesized by chemical reaction method. The calcination of ZnO powder has been characterized by number of techniques such as X-ray diffraction (XRD), Scanning Electron Microscopy (SEM) and Ultraviolet and Visible spectrophotometry (UV-Vis) at room temperature. The structural characteristic was examined using XRD and the surface morphology of ZnO powder was analyzed by Scanning Electron Microscopy (SEM). XRD analysis revealed that the sample crystallite in polycrystalline nature with wurtzite hexagonal structure and average crystallite was 30.50 nm at 500 °C. The microstructural of SEM result was observed that hexagonal shape and granular in nature. The absorption spectrum indicated that the energy band gap of ZnO powder. The optical property of the ZnO powder was determined by UV-Vis absorption spectrophotometry. The energy band gap of sensitized powder was examined to be equal to 3 eV. Taking into account the results obtained, ZnO powder has been reported for photoanode of solar cell applications.

Keywords: chemical reaction method, ZnO powder, XRD, SEM, UV-Vis

Introduction

Nanotechnologies are the design, characterization, production and application of structures, devices and systems by controlling shape and size at the nanometer scale. Two approaches for the building up nanoscopic features have been investigated: the so-called top down method and bottom up method. In the top down methods, the features are written directly onto a substrate, for example, by electron beams, and then by applying appropriate etching and deposition processes, the nanoscopic features are engraved. In the bottom-up approach, nanocomponents are made from precursor in the liquid, solid or gas phase employing either chemical or physical deposition processes that are integrated into building blocks within the final material structure [Filipponi L. and D. Sutherland, 2013].

ZnO is an important II-VI compound semiconductor material due to its novel properties like large direct energy gap (3.37 eV), high melting point (2248 K) high refractive index, and large exit on binding energy of (60 meV) at room temperature. This semiconductor also exhibit several favorable properties like good transparency, high electron mobility, wide band gap, strong room temperature luminescence, high thermal conductivity, antibacterial and UV protection [Taunk, P. B. et al, 2015], [Vanaja, A. and K. S. Rao, 2016].

ZnO has attracted much interest as one of the multifunction inorganic nanoparticles due to its unique combination of superior physical, chemical, biological, electrical, optical, long-term environmental stability, biocompatibility, low cost and non-toxic properties. Therefore, nano-ZnO can potentially be applied to gas sensors, photo catalyst for degradation of waste water pollutants, catalysts, semiconductors, varistors, piezoelectric devices, field emission displays,

---

[1] Dr, Lecturer, Department of Physics, Hpa-an University

[2] Dr, Lecturer, Department of Physics, Hpa-an University

[3] Dr, Professor, Department of Physics, Pang Long University

[4] Dr, Professor, Department of Physics, University of Yangon

[5] Dr, Professor, Head of Department of Physics, Hpa,-an University

ultraviolet (UV) photodiodes, surface acaustic wave (SAW) devices, UV shielding materials, rubber, medical and dental materials, pigments and coating, ceramic, concrete, antibacterial and bactericide and composites [Nehal, S. A. et al, 2015].

Many techniques are nature used to synthesize ZnO nanoparticles via precipitation method, spray pyrolysis method, microemulation method, hydrothermal method and sol-gel method [Kulkarni, S. S. & D. S. Mahendra, 2015]. The process parameters for the preparation of the ZnO nanoparticle, by CBD include deposition temperature, deposition time, concentration ratio of the reaction solution, types of chelating compounds and additives, pH values, and so on [Wen-Yao, H., 2012]. Chemical bath deposition is one of the useful solution methods for the preparation of such as semiconductors from aqueous solution, with advantage such as low processing temperature, allowing growth variety of substrates and easy adaptation to large area processing at low fabrication cost [Wallace, I. et al, 2015]. The adopted ZnO nanoparticles CBD approach, requiring low temperature treatments, is suitable for integration will colloidal lithography [Kathalingam, A. et al, 2010].

In the present work, ZnO *nanoparticles powder was prepared by chemical* reaction method. The structural powder was characterized by XRD and SEM. The optical property was investigated by UV-Vis spectrophotometer.

Experimental Procedure

Zinc sulphate, ethylenediamine and sodium hydroxide were used as the starting materials for the preparation of the ZnO nanoparticles by chemical reaction method. Deionized (DI) water (80 mL) was added to the solid materials of zinc sulphate (0.02 M) and ethylenediamine (1 mM), to prepare the reaction solution. After the solution was prepared, it was stirred with magnetic stirrer to maintain at temperature (50 ˚C - 55 ˚C). Then, NaOH (0.045 M) was added to the homogeneous solution and the pH value of the solution was controlled the range of 13. Next, the obtained solution was heating in oven at 50 ˚C for 8 h. And then, the homogenous powder was annealed in furnace at 500 ˚C for 1 h. The annealed powder was grinding with mortar and pestle for 3 h to obtain ZnO nanoparticles. The parameter of annealed ZnO nanoparticles was determined from the X-ray diffraction (XRD) measurement using (Multiflex - 700) with CuK$_\alpha$ (λ = 1.54056 Å) radiation operation at 40 kV and 40 mA. Scanning Electron Microscopy (SEM) was conducted with a JEOL, Japan JSM-(5610 LV) operated at 15 kV to determine the morphological changes as a function of annealing temperature. The optical absorption spectrum was recorded in the range of 300-800 nm using UV-Vis spectrophotometer (UV-1800, Shimadzu, Japan). Synthesis and characterization flow chart of ZnO nanoparticles at 500 ˚C were shown in Figure 1.

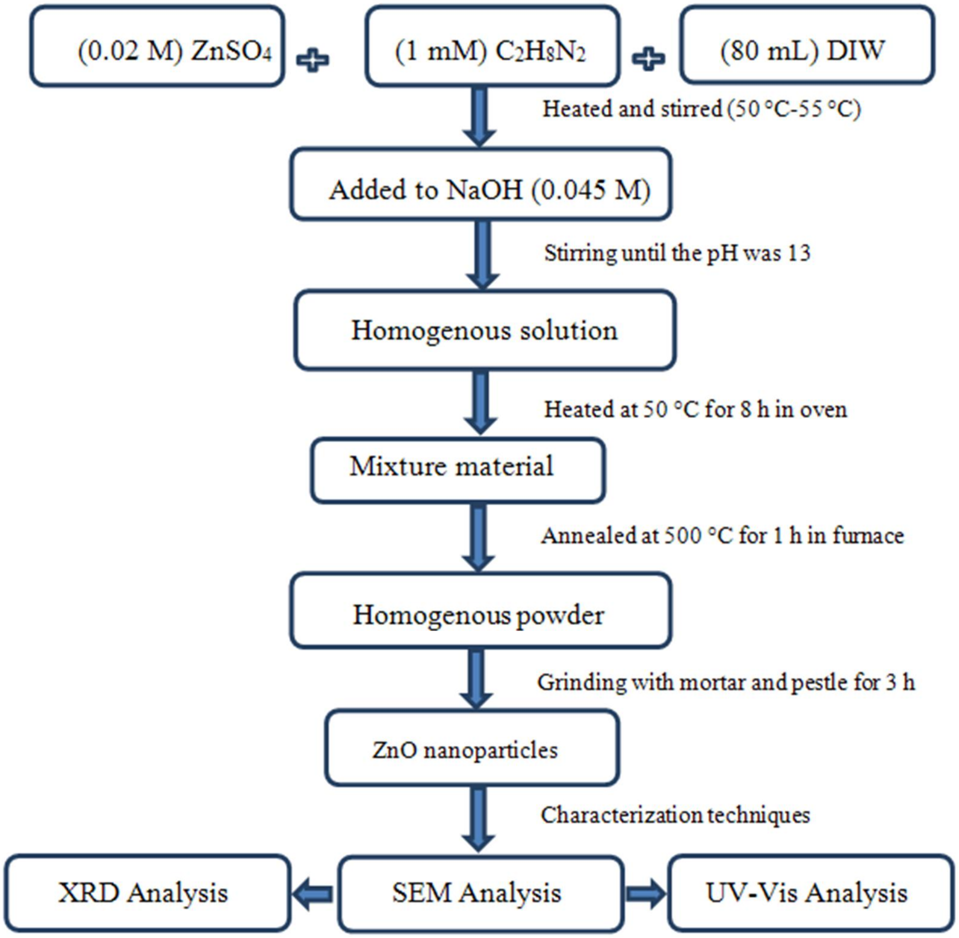

Figure 1 Synthesis and characterization flow chart of ZnO nanoparticles at 500 ˚C

Results and Discussion

XRD Analysis

The X-ray diffraction data was recorded by using $\mathrm{CuK_{\alpha}}$ radiation (1.54056 Å). The intensity data was collected over a 2θ range of 10-70. X-ray diffraction studied confirm that the synthesized materials was ZnO with wurtzite phase and all the diffraction peaks agreed with the reported JCPDS (Joint Committee on Powder Diffraction Standards) data and no characteristics peaks were observed other than ZnO. The average crystallite size D was determined from the XRD line broadening measurement using Scherrer equation.

$$D = \frac{0.9\,\lambda}{\beta\cos\theta}$$

where, λ is the wavelength ($\mathrm{CuK_{\alpha}}$), β is the full width at half maximum (FWHM) of the ZnO and θ is the diffraction angle.

Figure 2 showed XRD diffraction pattern of ZnO nanoparticles. The detected peaks corresponded with those of hexagonal phase zinc oxide were found at the lattice plains of (100), (002), (101), (102), (110), (103), (200), (112), (201) in the 2 theta values: 31.58˚, 34.223˚, 36.034˚, 47.350˚, 56.371˚, 62.661˚, 66.173˚, 67.701˚, 68.901˚ respectively. All diffraction peaks of sample corresponded to the characteristics hexagonal wurtzite structure of zinc oxide nanoparticles (a = 3.2676 Å and c = 5.2266 Å). The diffraction peaks related to the impurities were not observed in the XRD pattern, confirming the high purity of the synthesized powder. Diffraction angles, crystallite sizes and lattice parameters data of ZnO nanoparticles powder was summarized in Table (1-3).

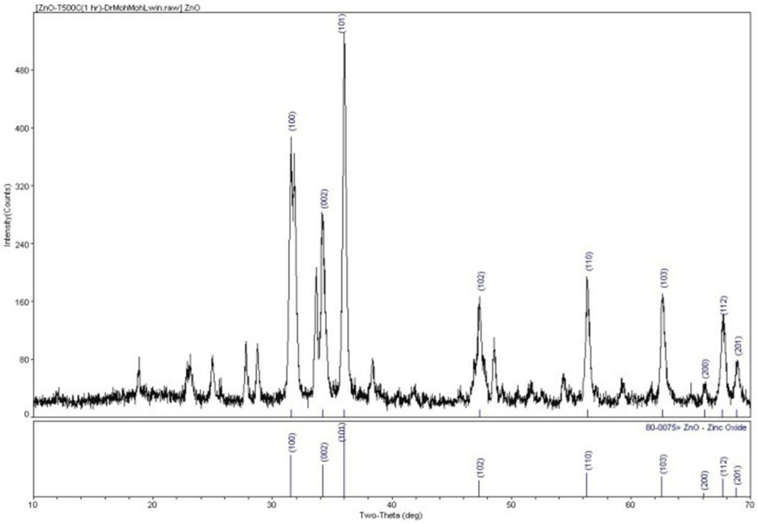

Figure 2 XRD pattern of ZnO nanoparticles at 500 ˚C

Table 1 Diffraction angles of all identified peaks for ZnO nanoparticles at 500˚C

No	Peaks	2θ (deg)	
		Observed values	Standard values
1	(100)	31.580	31.537
2	(002)	34.223	34.210
3	(101)	36.034	36.021
4	(102)	47.350	47.303
5	(110)	56.371	56.327
6	(103)	62.661	62.611
7	(200)	66.173	66.091
8	(112)	67.701	67.674
9	(201)	68.901	68.800

Table 2 Crystallite sizes of ZnO nanoparticles at 500˚C

No	Peak	FWHM (deg)	Crystallite size (nm)
1	(100)	0.496	14.9233
2	(002)	0.441	29.7784
3	(101)	0.302	17.2563
4	(102)	0.468	26.0518
5	(110)	0.370	17.0916
6	(103)	0.398	21.5713
7	(200)	0.321	33.2406
8	(112)	0.419	32.3068
9	(201)	0.338	82.3077
Average crystallite size			30.5031

Table 3 Lattice parameters of ZnO nanoparticles at 500˚C

No	**Peak**	**Lattice parameter (Å)**		
		a	**c**	**c/a**
1	(101)	3.2687	5.2382	1.6025
2	(102)	3.2687	5.2170	1.5960
3	(103)	3.2687	5.2153	1.5955
Average c/a ratio				1.598

SEM Analysis

The grain size, shape and surface properties like morphology were investigated by Scanning Electron Microscopy (SEM). Figure 3 represents the SEM image of ZnO nanoparticles synthesized by CBD annealed at 500 °C for 1 h. The SEM image was observed with the magnification of 2 µm, the ZnO nanoparticles were uniform, crack free and they formed hexagonal shape. Few particles were granular in shape and aggregation.

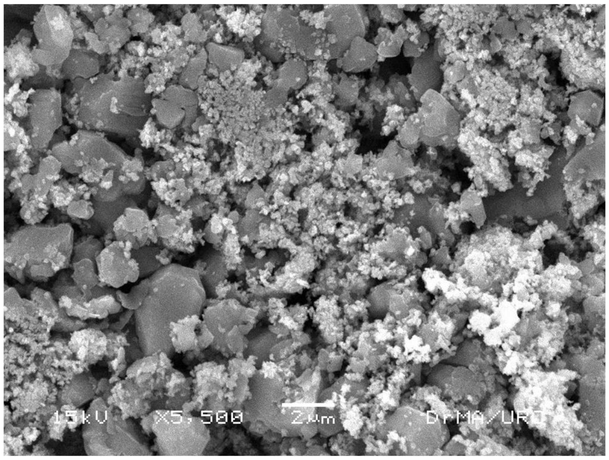

Figure 3 SEM image of ZnO nanoparticles at 500 ˚C

UV-Vis Analysis

UV absorption was related to the electronic transition from filled valence states to empty conduction states. Therefore, the optical band gap can be defined as the difference between the valence band and conduction band in momentum space. The optical band gap is dependent upon the particle shape, particle size and defect concentration in the crystal. The band gap energy can be determined by substituting the value of the cutoff wavelength in the following equation.

$$E_g = hc/\lambda$$

where, $h = 6.63\text{x}10^{-34}$ Js, $c = 3\ \text{x}10^{8}\ \text{ms}^{-1}$, λ = cutoff wavelength (388 nm). The absorption coefficient (α) as a function of photon energy ($h\upsilon$) can be expressed by the Tauc equation,

$$\alpha h\upsilon = B\,(h\upsilon - E_g)^n$$

where, $h\upsilon$ is the incident photon energy, B is the edge width parameter and n is an exponent that determines the type of electronic transition causing absorption, which is $^1/2$ or 2 for direct or indirect transition, respectively.

The UV-Vis absorption spectra and optical band gap of ZnO nanoparticles at 500˚C annealing temperature with different powder concentration were shown in Figure 4 & 5. A broad absorption peak was observed in each spectrum at 375.5 nm which is a characteristics band for the pure ZnO. No other peak was observed in the spectrum confirmed that the synthesized product was ZnO only. Interestingly, an obvious red shift in the absorption edges were observed for the product annealed at 500˚C. This red shift of the band gap energy was due to aggregation of nanocrystallites into larger grains as reported by various authors in different literatures. The direct energy band gap was calculated to be nearly equal to 3 eV and the large band gap clearly the wide transparency of the crystal.

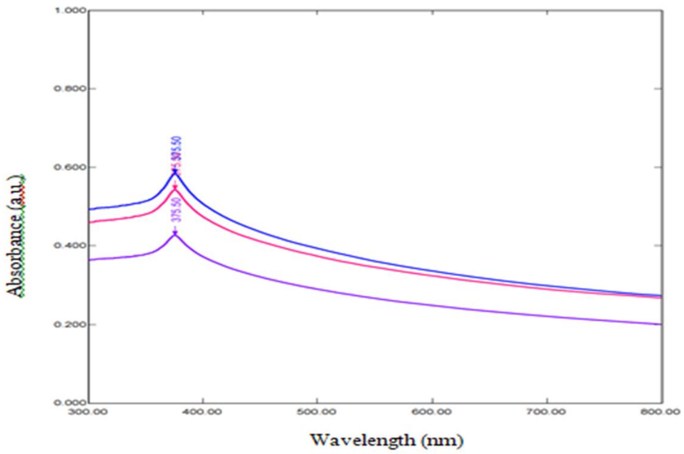

Figure 4 Absorption spectrum of ZnO nanoparticles with different powder concentration at 500 ˚C

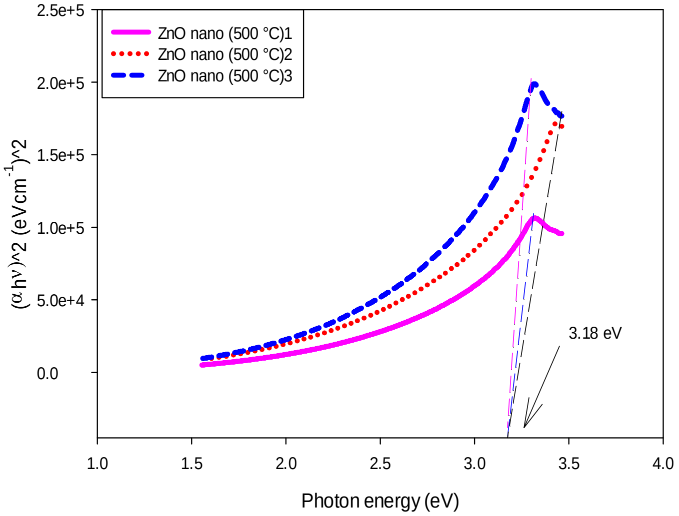

Figure 5 Optical band gap of ZnO nanoparticles with different powder concentration at 500˚C

Conclusion

ZnO powder has been successfully synthesized via direct precipitation route using wet chemical reaction method. XRD analysis confirmed the formation of polycrystalline nature of ZnO nanoparticles. The analysis of XRD pattern showed only the presence of pure wurtize crystal structure with average crystallite size of about 30.502 nm. The microstructural properties of ZnO nanoparticles were uniform in hexagonal shape. Few particles were granular nature of aggregation. A broad absorption peaks were observed in each spectrum at 375.5 nm. The band gap of the ZnO nanoparticles was calculated from the UV-Vis absorption, and it was stably observed spectra that there were red shifts in the absorption edges of different powder concentration compared with bulk material (3.3 eV). The energy band gap of sensitized nanoparticles was obtained to be approximately equal to 3 eV. ZnO is a wide band gap semiconductor having high optical transparency in visible and near ultraviolet range of spectrum. Therefore, it would be a promising candidate for solar cell applications.

Acknowledgements

The authors would like to thank Dr Mya Mya Aye, Rector and Dr Than Than, Pro-Rector, Hpa-an University, for their permission and encouragement on this research work. The authors also would like to acknowledgements to Professor Dr Khin Yu Mon, Head of Department of Physics and Professor Dr May Zin, Hpa-an University, for their valuable guidance and suggestion.

References

Filipponi, L. & D. Sutherland, (2013) *Nanotechnologies: Principles, Applications, and Hands on Activities.* Europe, European Union Press.

Kathalingam, A. et al, (2010) "Chemical Bath Deposition and Characterization of Nanocrystalline ZnO Thin Films" *Journal of Material Science,* Poland, vol. 28, No. 2, pp. 513-522.

Kulkarni, S. S. and D. S. Mahendra, (2015) "Optical and Structural properties of ZnO Nanoparticles" *International Journal of Advanced Research in Physical Science,* India, vol. 2, No. 1, pp. 14-18.

Nehal, S. A. et al, (2015) "Synthesis and Characterization of ZnO Nanoparticles Precipitation Method Effect of Annealing Temperature on Particle Size" *Nanoscience and Nanotechnology,* Egypt, vol. 5, No. 4, pp. 82-88.

Taunk, P. B. et al, (2015) "Synthesis and Optical Properties of Chemical Bath Deposition ZnO Thin Film" *Kerbala International Journal of Modern Science,* Kerbala, vol. 1, pp.159-165.

Vanaja, A. and K. S. Rao, (2016) "Precursors and Medium Effect on Zinc Oxide Nanoparticles Synthesized by Sol-gel Process" *International Journal of Applied and Natural Sciences,* India, vol. 5, Issue 1, pp. 53-62.

Wallace, I. et al, (2015) "Synthesis and Characterization of Zinc Oxide (ZnO) Nanowire" *J Nanomed Nanotechnol,* Nigeria, vol. 6, Issue 5, 1000321.

Wen-Yao, H. et al, (2012) "Preparation of ZnO Membrance by Chemical Bath Deposition Method via Regulated Acidity" *Journal of Information Engineering and Applications,* Taiwan, vol. 2, No. 5, pp. 27-34.

J. Myanmar Acad. Arts Sci. 2020 **Vol. XVIII.No.2B**

CHARACTERIZATION OF DIFFERENT BATH MOLARITY DEPENDENT ZINC OXIDE NANOPARTICLES BY HYDROTHERMAL SYNTHESIS

Myint Kalyar[1], Moh Moh Lwin[2], Than Than Win[3] and Yin Maung Maung[4]

Abstract

Synthesis of Zinc Oxide nanoparticles (ZnO NPs) were made by using the prepared precursor solution of zinc nitrate hexahydrate ($Zn(NO_3)_2 .6H_2O$) and different molarity of sodium hydroxide (NaOH) (1 M, 1.5 M) with solvent deionized water through the hydrothermal synthesis. The hydrothermal reaction was carried out at the temperature range (100°C – 150°C) for 7h. After the hydrothermal reactor was naturally cooled to room temperature, the obtained product was filtered and annealed at 200°C for 1h. The obtained Zinc Oxide (ZnO) nanoparticles were characterized by X-ray Diffraction (XRD), Scanning Electron Microscopy (SEM) and UV-Vis spectroscopy**.** The hexagonal wurtzite structure of good crystallinity of ZnO NPs was revealed through the XRD patterns and the crystallite sizes were 29.72 nm and 28.60 nm. The two morphologies of spherical and rod-like structures were found in SEM micrograph. The estimated energy band gaps were 3.06 eV and 3.08 eV obtained through the Tauc' s plot method.

Keywords: Hydrothermal Synthesis, Zinc Oxide, XRD, SEM, UV-Vis

Introduction

Semiconductor nanomaterials have been received great attentions. Among these various semiconductor nanomaterials zinc oxide is a versatile material because of its physical-chemical properties such as mechanical, electrical, optical, magnetic and chemical sensing properties. Zinc oxide a chemical compound found naturally in the mineral called zincite has attracted much attention in recent times due to its low cost and because it can be obtained by simple techniques [S. S. Kumar,2013]. Chemical synthesis is one of the important techniques which can be performed by using a range of precursors and different conditions like temperature, time, concentration of reactants, and so forth. Various chemical synthetic methods have been developed to prepare such nanoparticles [S.R.Brintha,2015].

Hydrothermal technique is a promising alternative synthetic method because of the low process temperature and very easy to control the particle size. The hydrothermal process has several advantages over other growth processes such as use of simple equipment, catalyst-free growth, low cost, ease of large scale production, eco-friendly and less hazardous [S.R.Brintha,2015]. The low reaction temperature makes this method attractive for microelectronics and plastic electronics. This method has also been successfully employed to prepare nano scale ZnO and other luminescent materials [A. Ramar Chandra Reddy, 2015]. This work intended to investigate the formation and characterization of ZnO nanoparticles depending upon the different bath molarity of NaOH solution.

---

[1] Dr, Lecturer, Department of Physics, Hpa-an University
[2] Dr, Lecturer, Department of Physics, Hpa-an University
[3] Dr, Professor, Department of Physics, Pang Long University
[4] Dr, Professor, Department of Physics, University of Yangon

Experimental Procedure

ZnO nanopowders were synthesized by hydrothermal method using the starting materials zinc nitrate hexahydrate ($Zn(NO)_3.6H_2O$) and sodium hydroxide (NaOH). Zinc nitrate hexahydrate ($Zn(NO)_3.6H_2O$) aqueous solution of 0.5 M was firstly prepared using the solvent deionized water (DIW).An aqueous solution of 0.5 M zinc nitrate hexahydrate ($Zn(NO)_3.6H_2O$) were mixed with different molarity of NaOH (1 M and 1.5 M) solution. The mixture solution of zinc nitrate hexahydrate ($Zn(NO)_3.6H_2O$) and sodium hydroxide (NaOH) were stirred at 80°Cfor 20 minutes by magnetic stirrer. The final pH of the mixed solution was highly basic with pH of 14. The mixture solution was put into a Teflon-lined stainless steel bomb for hydrothermal reaction at 100°C -150°C for 7 h. After hydrothermal reaction, the reactor was naturally cooled to room temperature. The obtained product was filtered and washed with de-ionized water till the pH of the final solution was 7.Finally, the as-prepared sample was calcined at 200°C for 1h.

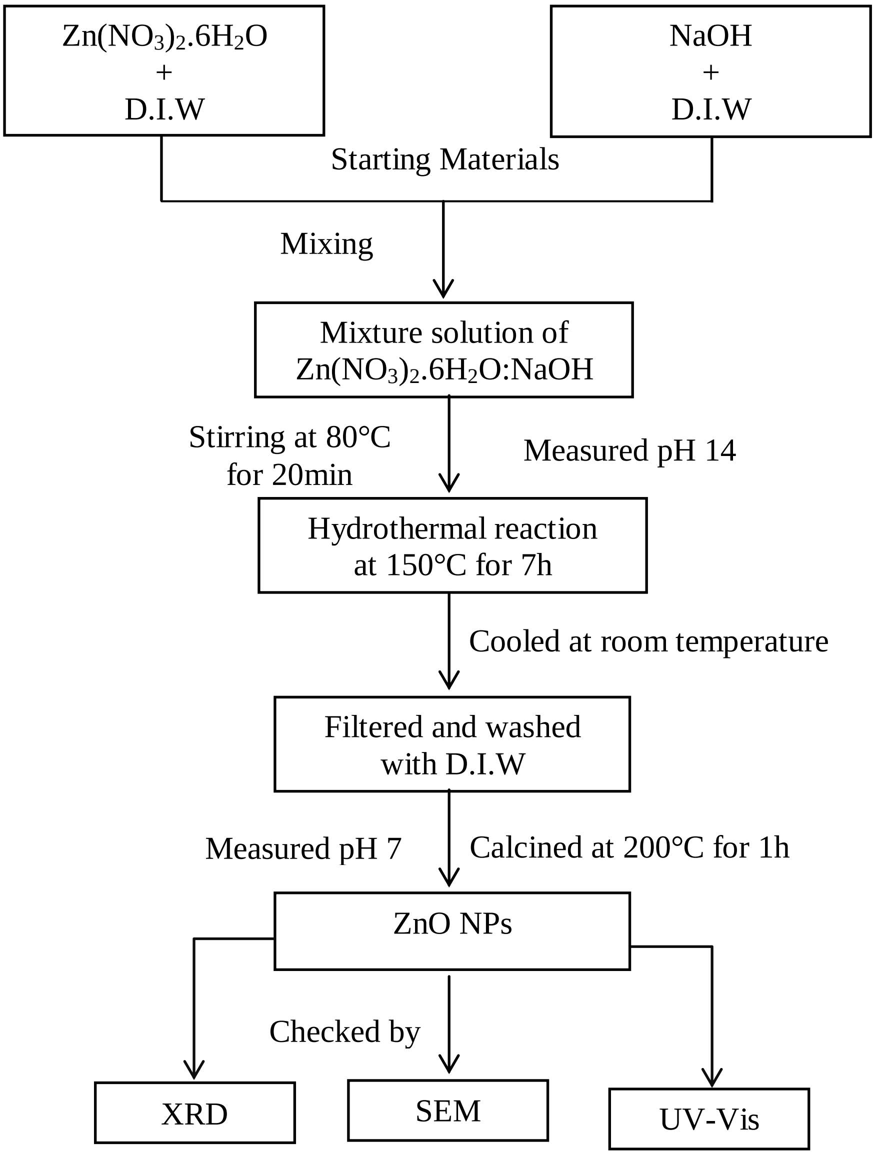

Figure 1 The block diagram for the preparation ZnO nanoparticles

Figure 2 Schematic diagram of home made Teflon-lined stainless steel vessel

Results and Discussion

XRD Analysis

Experimentally obtained diffraction patterns of the sample were compared with the standard powder diffraction files JCPDS (Joint Committee on Powder Diffraction Standard) (79-0206 > Zincite, syn-ZnO).The reflection planes (100), (002),(101), (102),(110) (103),(200),(112) and (201) of ZnO hexagonal wurtzite structure were occurred at the corresponding 2θ value. The most intense diffraction peak (101) plane was found at 2θvalue of 36.242 (deg). All the resulting diffraction peaks were coincideed with those of the standard library file (79-0206 > Zincite, syn-ZnO). The crystallite size of (101) plane was 29.72 nm. The lattice parameters of the ZnO hexagonal crystal were a=b= 3.2514 Å, and c=5.2046 Å.

Fig.2. showed the XRD patterns of ZnO particles with NaOH 1.5 M. It is cleared that the intensity of (101) plane was higher than that of ZnO with NaOH 1 M. All the resulting peaks were coincident with those of the standard library file (79-0206 > Zincite, syn-ZnO).The most intense (101) peak was formed at 2θ value of 36.291(deg). The crystallite size of ZnO hexagonal crystal structure was 28.6 nm with lattice parameters a=b= 3.2460 Å and c=5.2043Å. The crystallographic properties of the obtained ZnO NPs were compared with the standard library file and shown in Table (1) and (2).

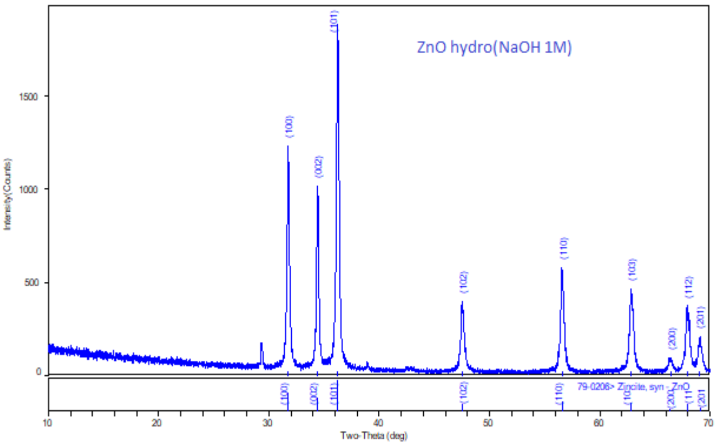

Figure 1 XRD patterns of ZnO NPs by hydrothermal synthesis with (1M NaOH)

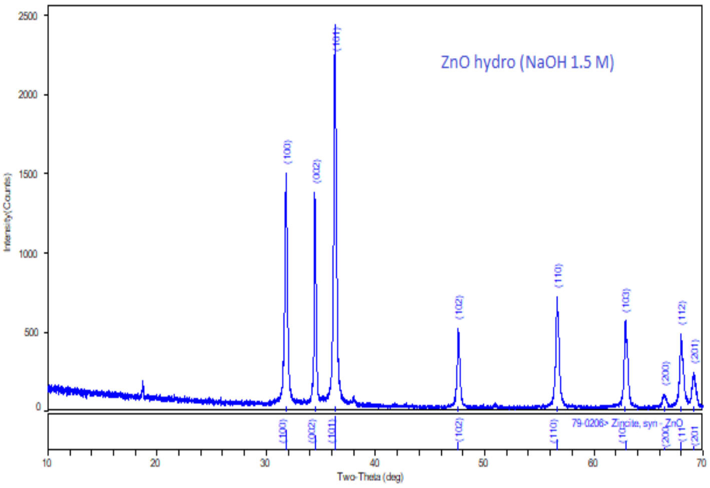

Figure 2 XRD patterns of ZnO Nps by hydrothermal synthesis with (1.5 M NaOH)

Table 1 Comparison of the standard and observed values of crystalline ZnO

Sample	**The most intense peak**	**2θ value(degree)**		**FWHM(rad)**	**Crystallite Size (nm)**
		Observed	Standard		
ZnO (1M NaOH)	101	36.242	36.251	0.281	29.72
ZnO (1.5 M NaOH)	101	36.291	36.292	0.292	28.60

Table 2 Comparison of standard and observed values of the lattice parameters and hexagonality of the ZnO Nps

Lattice parameter (Å)	**Standard (Å)**	**Observed values**	
		ZnO (1M NaOH)	**ZnO (1.5 M NaOH)**
a	3.2495	3.2514	3.2460
c	5.2069	5.2046	5.2043
c/a	1.6330	1.600	1.603

SEM Analysis

The micrograph of ZnO particles were examined by Scanning Electron Microscopy (SEM). SEM micrographs of hydrothermal synthesized ZnO particles were shown in figure.4&5.The granular morphology of the ZnO NPs with (1M NaOH) were both the spherical and rod like structure in figure.4. The estimated granular sizes were in the range of (0.28- 0.48 µm) range. The SEM images of the ZnO NPs with (1.5 M NaOH) revealed that the rod-liked structures of ZnO NPs granules were abundantly found and which were exhibited with different orientations. The estimated granular sizes were between the range of 0.16 µm to 0.32µm.

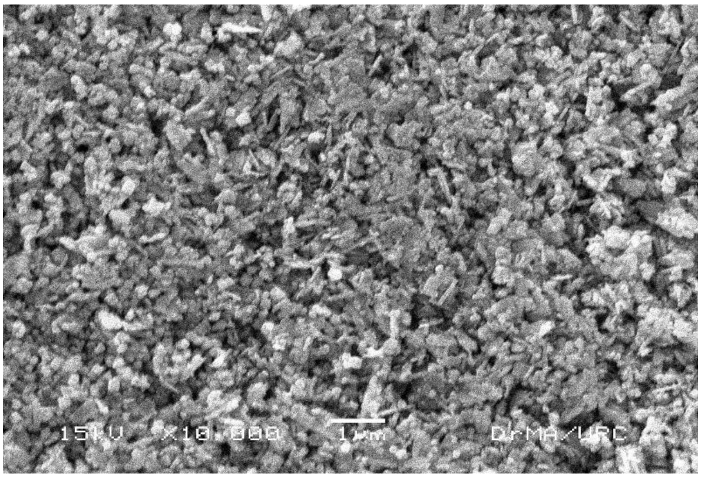

Figure 3 SEM micrograph of ZnO crystals with bath molarity of NaOH (1 M)

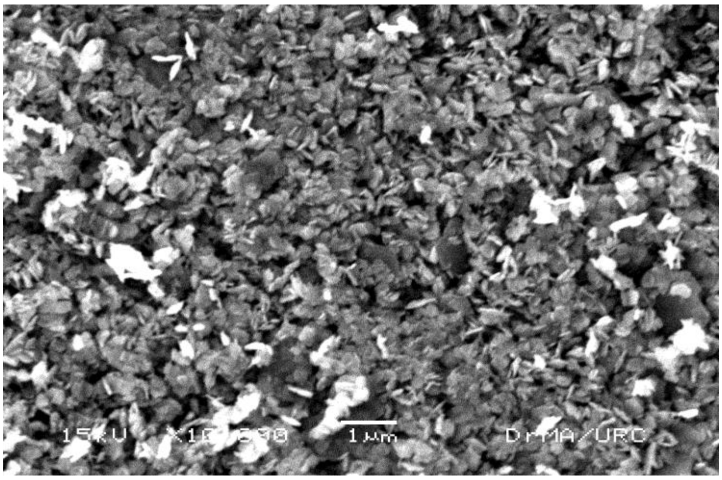

Figure 4 SEM micrograph of ZnO crystals with bath molarity of NaOH(1.5 M)

UV-Vis Analysis

The optical properties of the ZnO were determined by UV-Vis Spectrophotometer. The optical band gap was determined by using Tauc's plot method. The absorbance spectrum of the ZnO NPs with NaOH 1 M and 1.5M including Tauc's plot were shown in Fig.5(a), (b) and Fig.6 (a), (b).The absorption wavelength was 375 nm and 377nm for ZnO NPs. Tauc's plot showed the variation of $(\alpha h\nu)^2$ with the photon energy ($h\nu$) in eV. The E_g can be obtained by extrapolating the linear portion to the photon energy axis. The obtained optical band gaps values were 3.06 eV and 3.08 eV.

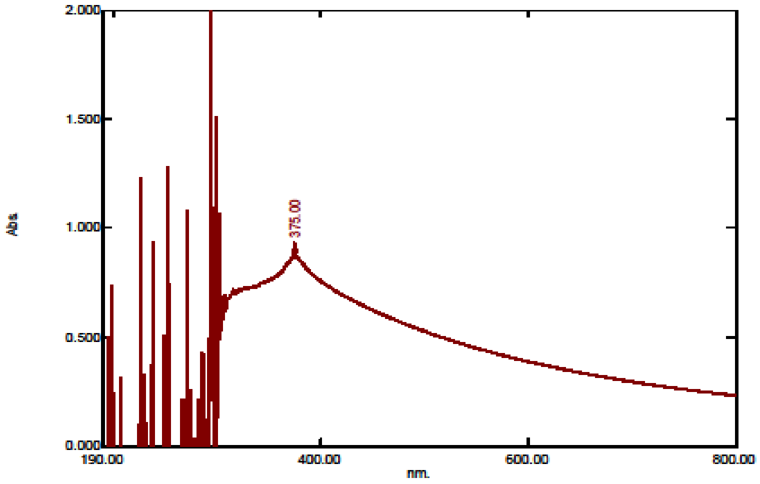

Figure 5(a) Absorption spectrum of ZnO NPs with (1 M NaOH)

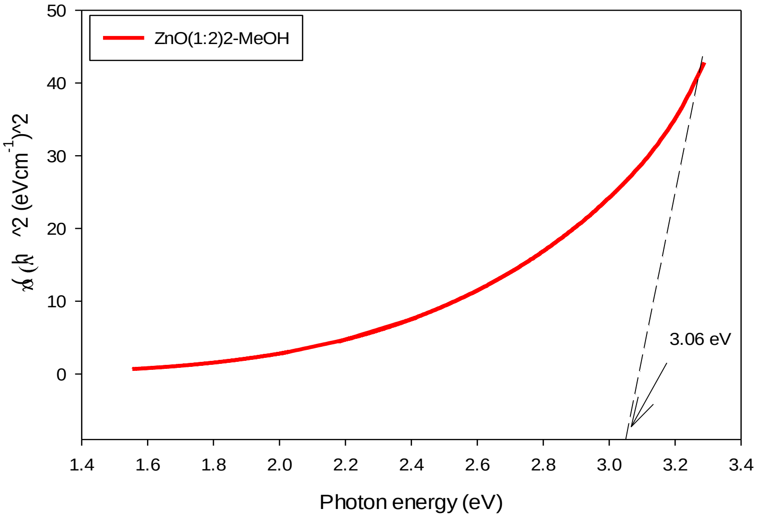

Figure 5(b) Tauc's plot of ZnO NPs with (1 M NaOH)

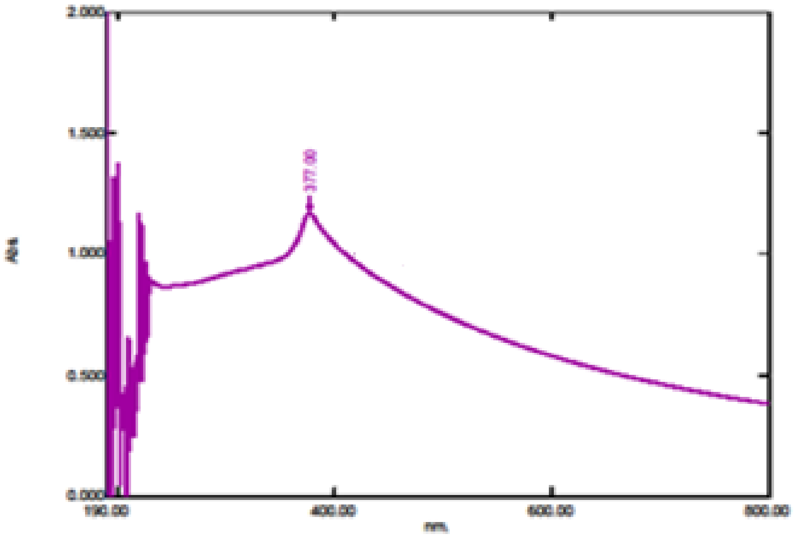

Figure 6 (a) Absorption spectrum of ZnO NPs with (1.5 M NaOH)

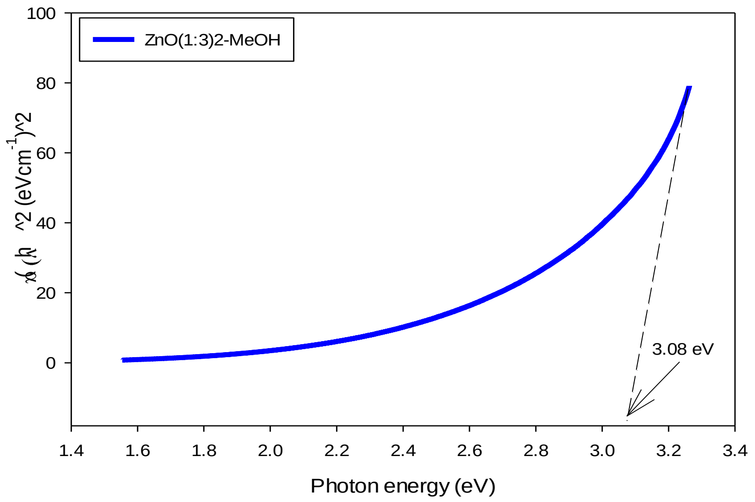

Figure 6 (b) Tauc's plot of ZnO NPs with (1.5 M NaOH)

Conclusion

Zinc oxide ZnO nano particles were successfully synthesized with the hydrothermal synthesis with different bath molarity of NaOH concentration. The XRD patterns confirmed that the crystal structure was wurtzite hexagonal ZnO and the crystallite sizes were 29.72 nm and 28.60 nm which were in the range of nanoscale. The good crystallinity of ZnO nanoparticles were apparently found through the XRD results.The two different morphologies of SEM micrographs were in accordance with the different bath molarity. The rod like structures of the ZnO NPs resulted in the strong enhancement of the electric field. The estimated granular sizes of the ZnO NPs were consistent with the crystallite size obtained from XRD results. The optical band gaps obtained from Tauc's plot were 3.06 eV and3.08 eV. These values were approximately equal to the typical value of wide band gap ZnO (3.3 eV).Moreover, the smaller the crystallite size, the greater the optical band gap. The results obtained from all the characterization techniques: XRD, SEM and UV-Vis were well consistent with each other. It was concluded that ZnO nano particles were successfully synthesized by a promising versatile hydrothermal synthesis.

Acknowledgements

The authors would like to thank Dr Mya Mya Aye, Rector and Dr Than Than Myint, Pro-Rector, Hpa-an University, for their permission and encouragement on this research work. The authors also would like to acknowledgements to Professor Dr Khin Yu Mon, Head of Department of Physics and Professor Dr May Zin, Hpa-an University, for their valuable guidance and suggestion.

References

A.Ramachandra Reddy, A.N.Malika,et al. “Hydrothermal Synthesis and Characterization of ZnO Nano Crystals”, J (IJMMME) Volume 3, Issue 2 (2015) ISSN 2320-4060

D.A.M. Osman, M.A Mustafa “ Synthesis and Characterization of Zinc Oxide Nanoparticles using Zinc Acetate Dhihydrate and Sodium Hydroxide”. The journal of Nanoscience and Nanoengineering (2015) 1(4) 248-251

D.SIBERA, R.JEDRZEJEWSKI et al, “ Synthesis and Characterization of ZnO Doped with FE_2O_3 Hydrothermal Synthesis and Calcination Process”. Proceedings of the III Conference on nanotechnology NANO (2009) Vol.116.

Nehal A. Salahuddin, Maged El-Demary and Ebtisam M.Ibrahim. “Synthesis and Characterization of ZnO Nanotubes by Hydrothermal Method”. Internation journal of scientific and Research publications, (2015) 5(9) ISSN 2250-3153.

P.M. Aneesh, K.A.Vanaja, M.K.Jayaraj, “ Synthesis of ZnO nanoparticles by hydrothermal method”. Proc.of SPIE Vol.6639 66390J-1.

S.R.Brintha, M.Ajitha “Synthesis and characterization of ZnO nanoparticles via aqueous solution, sol-gel and hydrothermal methods”. (IOSR-JAC) e-ISSN: 2278-5736. (2015) 8(11) 66-72.

Sunandan Baruah and Joydeep Dutta “ Hydrothermal growth of ZnO nanostructures”, J.Sci. Technol.Adv.Mater 10 (2009) 013001(18pp).

Surabhi Siva Kumar, Putcha V, et al “Synthesis , characterization and optical properties of zinc oxide nanoparticles”. The journal of International Nano letters (2013)

Thanakorn W, Narongchai O-C,and Sorapong P. “Simple Hydrothermal Preparaion of Zinc Oxide Powders Using Thai Autocalve Unit”, J. Sciverse Science Direct 807- 809

J. Myanmar Acad. Arts Sci. 2020 **Vol. XVIII.No.2B**

OPTICAL AND ELECTRICAL PROPERTIES OF (Cu, Al, In) DOPED SnO_2 THIN FILMS ON GLASS SUBSTRATE

Ohn Mar Swe[1], Zin Mar Win[2], Amy Than[3] and Moht Moht Than[4]

Abstract

The undoped SnO_2, Cu, Al and In (5mol%) doped SnO_2 thin films were deposited on glass substrates by sol-gel and spin coating technique. The effect of Cu, Al and In doping on the optical and electrical properties of the SnO_2 thin films were studied. The optical transmittance of thin films was measured and the optical band gap E_g values of the films were obtained in the range of 3.4 - 4.00 eV using the Tauc relation. The electrical transport properties of undoped, Cu, Al and In doped SnO_2 thin films were investigated by mean of current-voltage (I-V) measurement using simple diode model. The important diode parameters such as ideality factor, saturation current, and barrier height are also calculated.

Keywords: Cu, Al and In doped SnO_2, optical band gap E_g, current-voltage (I-V)

Introduction

Tin dioxide (SnO_2) has been intensively investigated because of its rich physical properties and large applications in commercial devices. The SnO_2 with a wide-band-gap (E_g = 3.6-4.0eV) is one of the excellent semiconductors which can be applied to solid state gas sensors, sensing arrays, solar cells, photovoltaic cells, organic light emitting diodes, touch sensitive screens and thin film transistors. [Bagheri Mohaghegi M M et al (2008), Bagheri Mohagheghi MM et al 2008, Khan AF et al (2010), Khan Af et al 2010, Moharrami F et al (2012)]. The SnO_2 thin films can be fabricated by a number of techniques such as chemical vapour deposition (CVD), metalorganic deposition, rf sputtering, sol-gel dip coating, spin coating and spray pyrolysis. [Maekava T et al (2001), Yin LT et al (2000), Yin LT et al (2000), Ouerfelli J et al (2008).] It was clearly established spin coating that structural, electronic transport and optical properties of SnO_2 films are very sensitive to preparation method, deposition conditions, dopant atoms and amount of dopant atoms.

Experimental

The glass substrates were ultrasonically cleaned by keeping in ethanol and in the distilled water, for ten minutes, respectively. Then the glass substrates were dried. The films were deposited on the glass substrates by spin coating technique. In order to prepare the coating solution, firstly, Cu, Al and In (5 mol%) doped SnO_2 powder mixed by conventional stoichiometric composition. The mixture powder is ground by agate mortor to obtain the homogeneous and uniform grain size of powder. This powder is heat treated at 500° C for 1 hr. The crystalline powder, were mixed with 2-methoxgethanol solution by using sol-gel method. And then these pastes were coated on glass substrates and annealed at 400°C for 1 hr, respectively.

[1,2,3.] Dr, Lecturer, Department of Physics, University of Yangon

[4.] Associate, Professor, Department of Physics, Mohnyin Degree College.

Results and Discussion

Figure 1 (a ~ d) shows the optical transmittance spectra of the SnO_2 films for various dopant atoms (Cu, Al, In). The transmittances of all the films were increased in an apparent way with wavelength near the IR region. It was seen that the transmittance has the lowest value for the film doped with Cu.

The absorption coefficients (α) were determined by means of the optical transmittance spectra using the relation, $\alpha = (1/d)\ln(1/T)$ where d is the thickness and T is the transmittance of the film at a particular wavelength. The optical band gap E_g of the film was calculated using the Tauc relation, which is given as $\alpha h\nu = \alpha_o (h\nu - E_g)^n$, where hν, α_o and n = 0.5, 1.5, 2.0 and 3.0 are the photon energy, a constant and for allowed direct, forbidden direct, allowed indirect and forbidden indirect electronic transitions, respectively. The plot of $(\alpha h\nu)^2$ versus hν is shown in Figure 2 (a ~ d). It was seen that the band gap energy E_g obey to the allowed direct transition (1/2) model. The optical energy band gap was obtained by extrapolating the linear portion of $(\alpha h\nu)^2$ versus hν plot to $(\alpha h\nu)^2 = 0$ as 3.4eV for undoped SnO_2, 4eV for Cu-doped SnO_2, 3.89eV for Al-doped SnO_2 and 3.8eV for In-doped SnO_2. The similar values for the optical energy band gaps were also reported by many researches.

Current-voltage (I-V) data of undoped SnO_2, (Cu, Al, In) doped SnO_2 thin films were measured in the forward and reverse directions using a DC power supply. Figure 3 (a ~ d) show the current – voltage characteristics of undoped SnO_2, (Cu, Al, In) doped SnO_2 thin films. From the ln I-V characteristics, the ideality factor (η) and the saturation current (I_s) are carried out. The saturation current (I_s) obtained from the ln I versus V characteristics. The diode ideality factor (η) is calculated by equation (1).

$$I = I_s \exp\left[\frac{V_a}{\eta V_T}\right] \quad (1)$$

where, I_s is the saturation current, V_a is the applied voltage, V_T is the threshold voltage (0.02586V) for room temperature. The zero-bias barrier height (ϕ_{bo}) can be obtained by using the area "A" (0.03 cm^2) and the Richardson constant R* (8.16 $AK^{-2}cm^{-2}$) from the equation (2),

$$I_s = AR^*T^2 \exp\left[-\frac{q\phi_{bo}}{KT}\right] \quad (2)$$

The values of ideality factor, saturation current and zero bias barrier height of undoped SnO_2, (Cu, Al, In) doped SnO_2 thin films are described in Table (1).

Table 1 Ideality factor (η), saturation current (I_s) and zero bias barrier height for undoped SnO_2, (Cu, Al, In) doped SnO_2 thin films

Samples	Saturation current I_s (A)	Zero bias barrier height Φ_{bo} (eV)	Ideality factor (η)
Undoped SnO_2	2.02×10^{-03}	0.4190	1.124
Cu doped SnO_2	4.04×10^{-03}	0.4011	1.118
Al doped SnO_2	4.08×10^{-03}	0.3832	1.112
In doped SnO_2	4.21×10^{-03}	0.3727	1.109

From the current-voltage characteristics, it was observed that the current flow through the samples exponentially increased with an increase in potential in forward bias region, it shows an exponential growth of the current that is main characteristics of a diode. In the reverse bias, the reverse breakdown voltage increase with increasing reverse-biasing voltage.

Conclusion

The undoped SnO_2, Cu, Al and In doped SnO_2 thin films on glass substrates were successfully investigated. The transmittances of all the films were apparently increased with increasing wavelength near the IR region and the transmittance has the lowest value for the film doped with Cu. The forbidden band-gap energy value for Cu doped SnO_2 was found as 4eV. The E_g was determined as 3.8eV and 3.89eV, having the nearly same result for In and Al-doped SnO_2 films. The electrical transport mechanism of the undoped, Cu, Al and In doped SnO_2 films was determined by means of the simple diode model. The zero bias barrier height and the ideality factor was determined the range of 0.37 – 0.42 eV and 1.109-1.124, respectively.

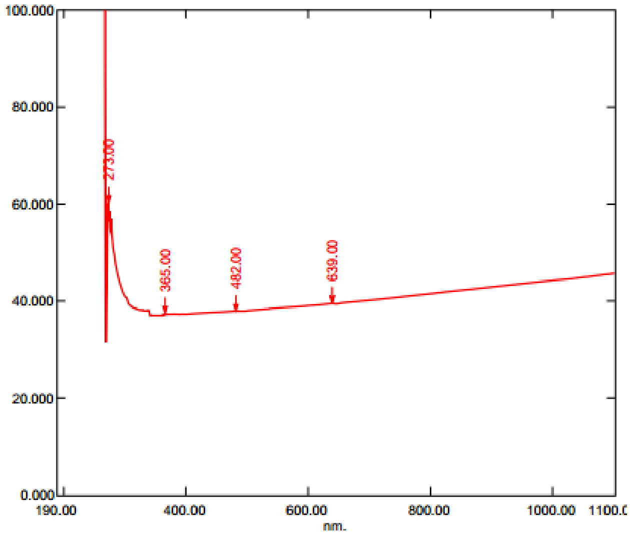

Figure 1 (a) Transmittance (T%) spectra for undoped SnO_2 thin film on glass

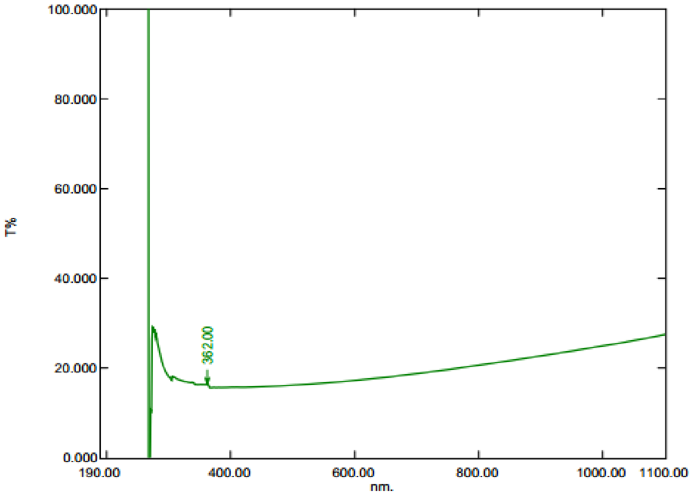

Figure 1 (b) Transmittance (T%) spectra for Cu doped SnO_2 thin film on glass

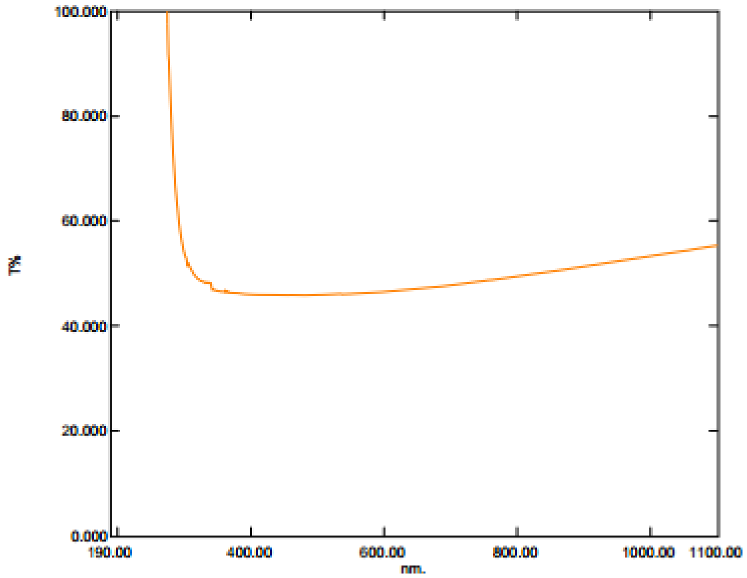

Figure 1 (c) Transmittance (T%) spectra for Al doped SnO_2 thin film on glass

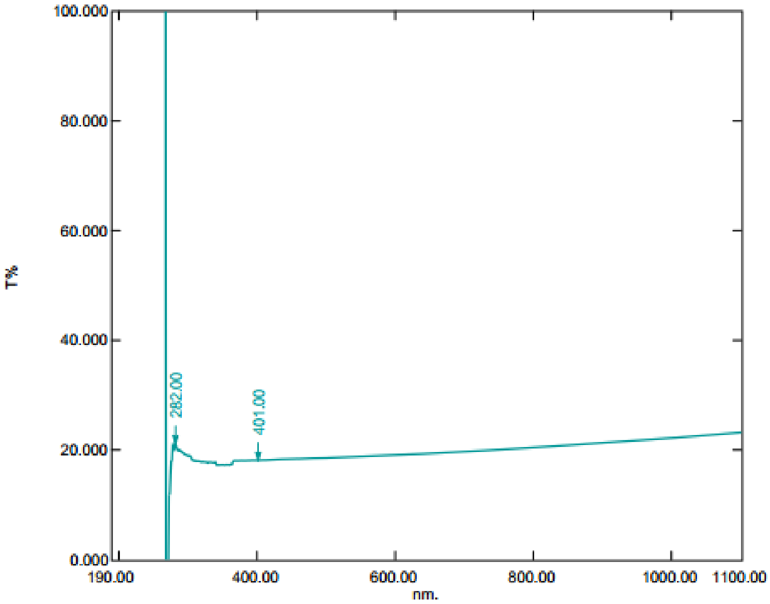

Figure 1 (d) Transmittance (T%) spectra for In doped SnO_2 thin film on glass

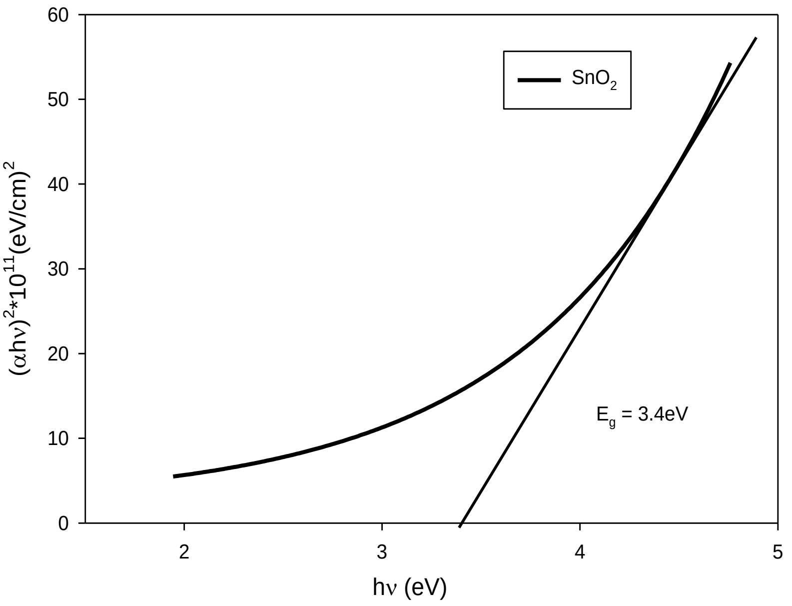

Figure 2 (a) Plot of $(\alpha h\nu)^2$ versus hν (undoped SnO_2)

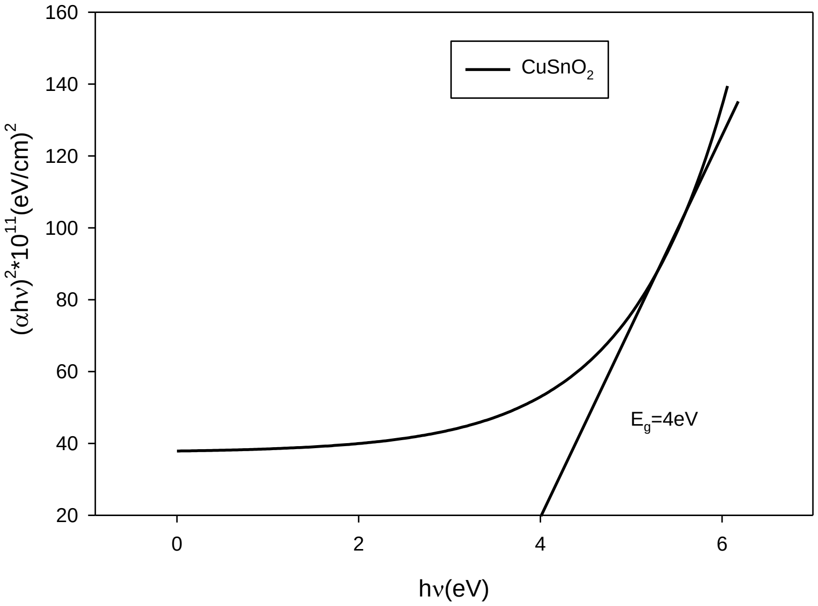

Figure 2 (b) Plot of $(\alpha h\nu)^2$ versus hν (Cu doped SnO_2)

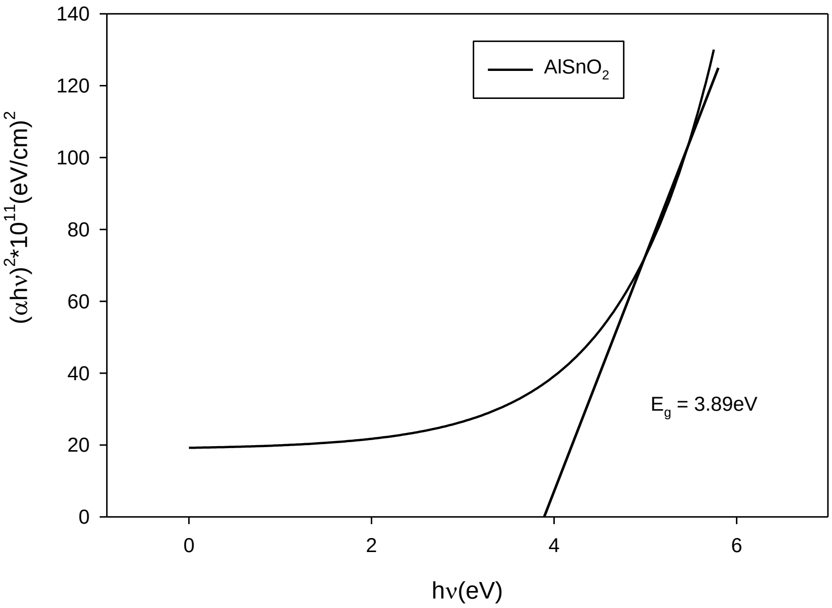

Figure 2 (c) Plot of $(\alpha h\nu)^2$ versus hν (Al doped SnO_2)

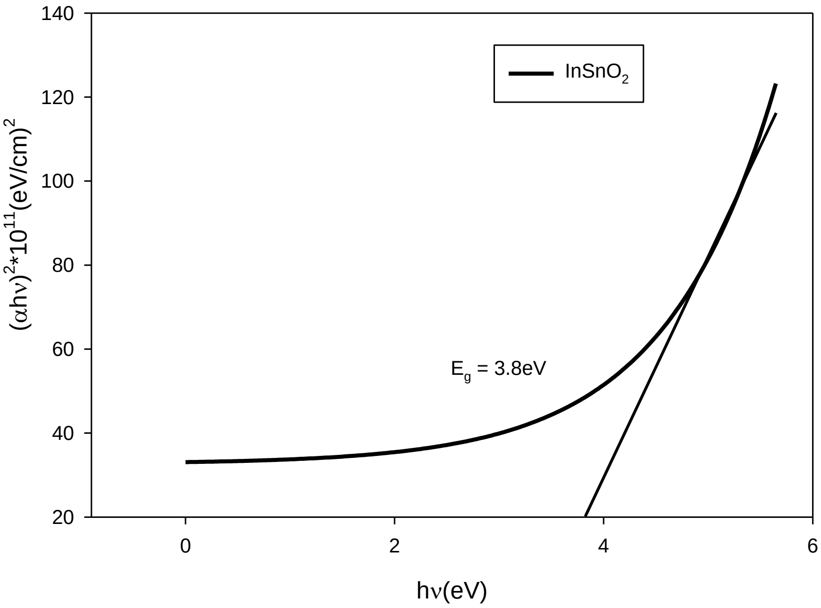

Figure 2 (d) Plot of $(\alpha h\nu)^2$ versus hν (In doped SnO_2)

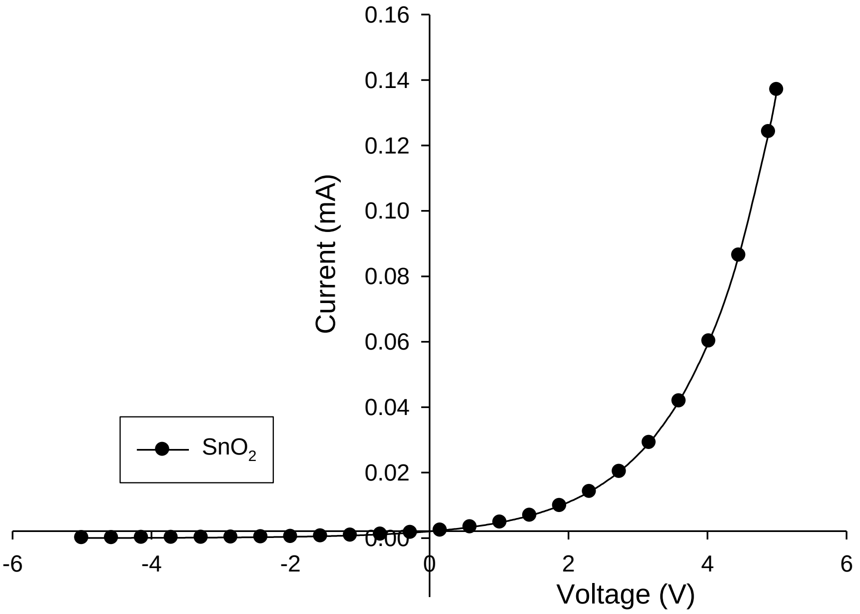

Figure 3 (a) I-V characteristics of (Undoped SnO_2)

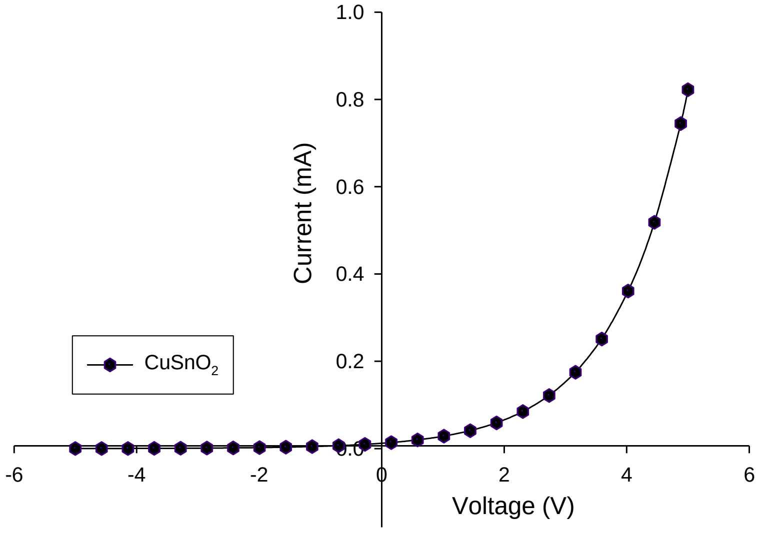

Figure 3 (b) I-V characteristics of (Cu doped SnO_2)

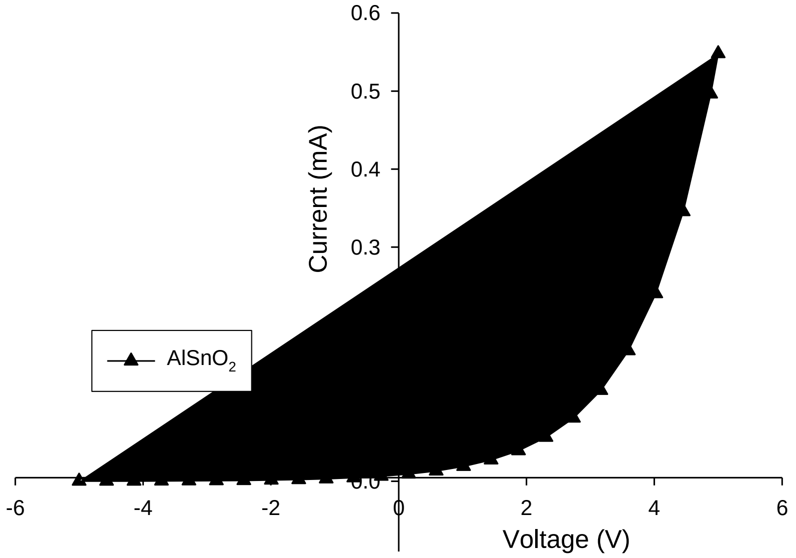

Figure 3 (c) I-V characteristics of (Al doped SnO_2)

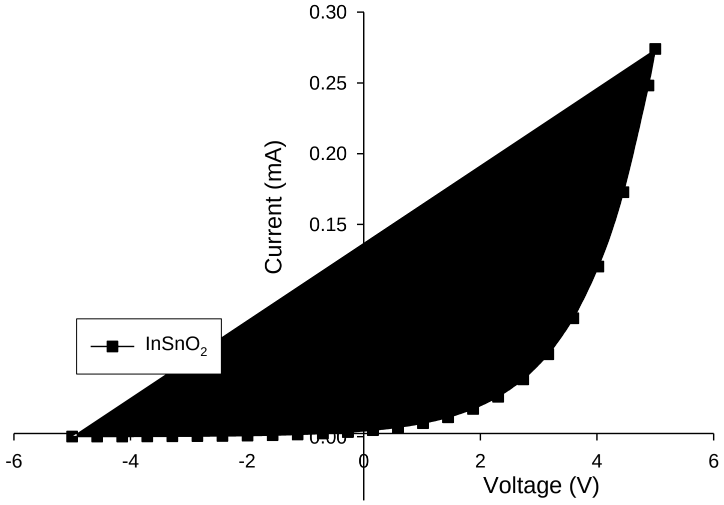

Figure 3 (d) I-V characteristics of (In doped SnO_2)

Acknowledgements

I would like to thank Professor Dr Khin Khin Win, Head of department of Physics, University of Yangon for her kind permission to carry out this research.

I would like to express my sincere thanks to Dr Myo Lwin, Professor, Dr Ye Chan, Professor and Head, Universities' Research Center, Dr Aye Aye Thant, Professor, Department of Physics, Dr Yin Maung Maung, Professor, Department of Physics, Department of Physics and Dr Than Zaw Oo, Professor Universities' Research Center, University of Yangon, for their suggestion and comments for this work.

References

Agashe C et al (2009); Solar Energy Materials and Solar Cells 93, P 1256-1253

Bagheri Mohaghegi MM et al (2008); Physica B 403, P 2431-2437

Khan AF et al (2010); Applied Surface Science 256, P 2252-2258,

Kikuchi N et al (2002); Vacuum, 66 P 365-371

Moharrami F et al (2012); Solid films, 520, P 6503-6509

Maekava T et al (2001); Sensors and Actuators, B 80, P 51-58

Ouerfelli J et al (2008); Materials Chemistry and Physics, 112, P 198-201

Rani S et al (2007); Sensos and Actuators, B 122, P 204-210

Yin LT et al (2000); Sensors and Actuators, B 71, P 106-111

J. Myanmar Acad. Arts Sci. 2020 **Vol. XVIII.No.2B**

SINGLE-PARTICLE ENERGY STATES FOR ${}^{208}_{\Lambda}\mathrm{Pb}$ and ${}^{208}_{82}\mathrm{Pb}$

Yin Mar Aung[*]

Abstract

Single-particle energy states in lambda hypernuclei and ordinary nuclei are calculated to study the structures of ${}^{208}_{82}\mathrm{Pb}$ and ${}^{208}_{\Lambda}\mathrm{Pb}$ nuclei. The phenomenological Woods-Sexon central potential and Woods-Sexon lambda-core nucleus potential including spin orbit interaction are used. Single-particle energy levels are investigated by solving one-body Schrodinger equation with the Gaussian basis treatment.

Keywords: single –particle energy states, Gaussian basis wave function, Woods-Sexon potential, Woods-Sexon lambda-core nucleus potential including spin orbit interaction. *FORTRAN program, Gaussian basis wave function, Woods-Saxon potential*

Introduction

In nuclear physics, the nuclear shell model is a model of the atomic nucleus which uses the Pauli exclusion principle to describe the structure of the nucleus in terms of energy levels. The study of low-lying excited states of closed shell and near-closed shell provide information about specific nuclear orbital nucleus. The purpose of this paper is to determine the energy levels of ${}^{208}_{82}\mathrm{Pb}$ and to use the phenomenological Woods-Saxon potential with spin-orbit interaction. It is to concentrate on${}^{208}_{82}\mathrm{Pb}$ nucleus which describes the binding energies with low-lying levels schemes. This determination is the fundamental importance for explaining the structure of nuclei.

The energy levels are found by solving the Schrödinger equation for a single nucleon moving in the average potential generated by all other nucleons. Each level may be occupied by a nucleon, or empty. Some levels accommodate several different quantum states with the same energy, they are said to be degenerate [Greiner, W., A.M. Joachim, 1996].

Some nuclei are bound more tightly than others. This is because two nucleons of the same kind cannot be in the same state. So the lowest energy state of the nucleus is one where nucleons fill all energy levels from the bottom up to some level. The energy levels increase with the orbital angular quantum number l, and s, p, d, f ... symbols are used for l = 0, 1, 2, 3, ... The value of total angular momentum is j and the spin orbit interaction depresses the state with total angular momentum j = l + ½ and rises the one j = l - ½[Frauenfelder, H. and M. H. Ernest, 1972].

Calculation of Single Particle Energy Levels

The time-independent Schrödinger equation for potential well is as follows.

$$\left[\left(-\frac{\hbar^2}{2M}\nabla^2\right)+\mathrm{v(r)}\right]\Psi(\mathrm{r})=\mathrm{E}\Psi(\mathrm{r}) \qquad (1)$$

So, the radial part of Schrödinger equation is as follows.

---

[*] Dr, Lecturer, Department of Physics, Monywa University

$$-\frac{\hbar^2}{2M}\left[\frac{d^2}{dr^2}-\frac{l(l+1)}{r^2}\right]u(r)+V(r)u(r)=Eu(r) \qquad (2)$$

The Gaussian basis wave function is used

$$u(r)=r^{l+1}N\sum_i c_i e^{-(\frac{r}{b_i})^2} \qquad (3)$$

These linear equations can be solved by using Gauss elimination method which is the fundamental one for solving linear systems. And so norm matrix elements, kinetic energy matrix element and potential energy matrix elements and root-mean-square distance are analytically obtained by using Gaussian standard integral form. By diagonalzing the Hamiltonian matrix, the energy eigen-value is obtained with the help of FORTRAN PROGRAM.

Normalization Constant, Kinetic Energy, Centrifugal Potential Energy

To solve the physical quantities of $^{208}_{82}\mathrm{Pb}$ nuclei, the normalization constant is calculated. The normalized condition is as follows;

$$\int_0^\infty u^*(r)\,u(r)\,dr=1 \qquad (4)$$

The normalized Gaussian basis wave function is defined as follows;

$$u(r)=A\sum_i c_i\, e^{-(\frac{r}{b_i})^2}\, r^{l+1} \qquad (5)$$

By using standard Integral, the normalized constant is obtained.

$$A=\frac{1}{\left[\sum_i\sum_j c_i c_j \frac{(2l+1)!!}{2^{l+2}}\frac{1}{(\frac{1}{b_i^2}+\frac{1}{b_j^2})^{l+1}}\left(\frac{\pi}{\frac{1}{b_i^2}+\frac{1}{b_j^2}}\right)^{1/2}\right]^{1/2}} \qquad (6)$$

The kinetic energy is calculated as follows;

$$\hat{T}(r)u(r)=\frac{\hbar^2}{2\mu}A\sum_i c_i\, e^{-(\frac{r}{b_i})^2}\left[l(l+1)r^{l-1}-\frac{2}{b_i^2}(2l+3)r^{l+1}+\frac{4}{b_i^4}r^{l+3}\right] \qquad (7)$$

The average kinetic energy is as follows.

$$\left\langle\hat{T}(r)\right\rangle=\frac{\hbar^2}{2\mu}A^2\sum_i\sum_j c_i c_j\left[(\ell^2+\ell)\frac{(2\ell-1)!!\sqrt{\pi}}{2^{\ell+1}}\frac{1}{(\frac{1}{b_i^2}+\frac{1}{b_j^2})^{\ell+0.5}}\right. \qquad (8)$$

$$\left.-\frac{2}{b_j^2}(2\ell+3)\frac{(2\ell+1)!!\sqrt{\pi}}{2^{\ell+2}}\frac{1}{(\frac{1}{b_i^2}+\frac{1}{b_j^2})^{\ell+1.5}}+\frac{4}{b_j^4}\frac{(2\ell+3)!!\sqrt{\pi}}{2^{\ell+3}}\frac{1}{(\frac{1}{b_i^2}+\frac{1}{b_j^2})^{\ell+2.5}}\right]$$

The centrifugal potential energy is follows;

$$\hat{F}(r)u(r) = \frac{\hbar^2}{2\mu}\left[\frac{l(l+1)}{r^2}u(r)\right] \tag{9}$$

By using wave function, the centrifugal potential energy is described as follows;

$$\hat{F}(r)u(r) = \frac{\hbar^2}{2\mu}\left[\frac{l(l+1)}{r^2}\, A\sum_i c_i e^{-(\frac{r}{b_i})^2} r^{l+1}\right] \tag{10}$$

The average centrifugal potential energy is calculated.

$$\left\langle \hat{F}(r) \right\rangle = \frac{\hbar^2}{2M} A^2 \sum_i \sum_j c_i c_j (\ell^2 + \ell) \frac{(2\ell-1)!!\sqrt{\pi}}{2^{\ell+1}} \frac{1}{(\frac{1}{b_i^2} + \frac{1}{b_j^2})^{\ell+0.5}} \tag{11}$$

The Lambda-Core Nucleus Interaction

The interactions between nuclei are commonly described by using phenomenological Woods-Saxon potential that plays a great role in nuclear physics. Woods-Saxon potential is based on the sum of a spin-independent central potential and a spin-orbit potential.

$$V(r) = V_0(r) + V_{ls}(r)\ \vec{l}.\vec{s} \tag{12}$$

The form of the generalized spin-independent central Woods-Saxon potential is as follows.

$$V_0(r) = -\frac{V_0}{1+e^{(r-R)/a}} \tag{13}$$

$R = r_0 A^{1/3}$ is the nuclear radius where r_0 = 1.25 fm and A is the mass number.

Typical values for the parameters are: $V_0 \approx 50\,\mathrm{MeV},\ a \approx 0.53\,\mathrm{fm}$ [Woods, R.D. and D.S. Saxon, 1954].

For lambda particle, $V_0 \approx 30\,\mathrm{MeV}$, $a \approx 0.6\,\mathrm{fm}$ and r_0 = 1.1 fm are used [M. Wang, et al., 2014].

The potential strength depends upon the number of proton and neutron. It is represent by,

$V_0 = \left[50 - 32\frac{N-Z}{A}\right]$ and the nuclear density, $\rho(r) = \frac{1}{1+e^{r-R/a}}$.

Woods-Saxon potential including spin-orbit interaction is

$$V(r) = V_0(r) + V_{ls}(r) \tag{14}$$

The spin-orbit interaction is described as follows.

$$V_{ls}(r) = V_{so}(\frac{\hbar}{Mc})^2(l.s)\,\frac{1}{r}\frac{d\rho}{dr} \tag{15}$$

The total angular momentum is $\vec{j} = \vec{l} + \vec{s}$ and the spin of a nucleon is $\frac{1}{2}\hbar$.

For $\quad j = l + \frac{1}{2}\,,\ l.s = \frac{1}{2}l$

$$\therefore\ V(r) = V_0(r) + V_{ls}(r) \tag{16}$$

$$= \frac{-V_0}{1+e^{r-R/a}} + V_{so}(\frac{\hbar}{Mc})^2(\frac{1}{2}l)\left[\frac{1}{r}\,\frac{e^{r-R/a}}{1+e^{r-R/a}}\,\frac{1}{a}\right]$$

For $j = l - \frac{1}{2}\,,\ l.s = -\frac{1}{2}(l+1)$

$$\therefore V(r) = \frac{-V_0}{1+e^{r-R/a}} - V_{so}(\frac{\hbar}{Mc})^2(\frac{1}{2}(l+1))\left[\frac{1}{r}\,\frac{e^{r-R/a}}{1+e^{r-R/a}}\,\frac{1}{a}\right] \tag{17}$$

So, the average Woods-Saxon potential with spin orbit interaction, for $j = l + \frac{1}{2}$ state is as follow,

$$\begin{aligned}\langle V(r)\rangle &= \langle V_{W-S}(r)\rangle + \langle V_{\ell s}(r)\rangle \\ &= A^2\sum_i\sum_j c_i c_j\left[r^{2\ell+2}\,e^{-(\frac{r^2}{b_i^2+b_j^2})}\left(\frac{-V_0}{1+e^{(r-R)/a}}\right)\right. \\ &\left.\quad - V_{so}\left(\frac{\hbar^2}{m_\pi c}\right)\frac{1}{a}r^{2\ell+1}\,e^{-(\frac{r^2}{b_i^2+b_j^2})}\,\frac{1}{2}\ell\,\frac{e^{(r-R)/a}}{(1+e^{(r-R)/a})^2}\right]\end{aligned} \tag{18}$$

So, the average Woods-Saxon potential with spin orbit interaction, for $j = l - \frac{1}{2}$ state is as follow,

$$\begin{aligned}\langle V(r)\rangle = {} & A^2\sum_i\sum_j c_i c_j\left[r^{2\ell+2}\,e^{-(\frac{r^2}{b_i^2+b_j^2})}(-\frac{V_0}{1+e^{(r-R)/a}})\right. \\ & \left. -V_{so}(\frac{\hbar}{m_\pi c})^2\,\frac{1}{a}r^{2\ell+1}\,e^{-(\frac{r^2}{b_i^2+b_j^2})}\,\frac{1}{2}(-\ell-1)\,\frac{e^{(r-R)/a}}{(1+e^{(r-R)/a})^2}\right]\end{aligned} \tag{19}$$

Root-Mean Square Distance

The root-mean square distance of a particle is as follows.

$$\langle r^2\rangle = \int \psi(r)^*\, r^2\, \psi(r)\, dr \tag{20}$$

By using normalized wave function, the root-mean square distance is described as follows.

$$\langle r^2\rangle = A^2\sum_i c_i\sum_j c_j\,\frac{(2l+3)(2l+3-2)!!}{2^{l+2}\times 2}\,\frac{1}{(\frac{1}{b_i^2}+\frac{1}{b_j^2})^{l+1}}\,\frac{1}{(\frac{1}{b_i^2}+\frac{1}{b_j^2})}\,(\frac{\pi}{\frac{1}{b_i^2}+\frac{1}{b_j^2}})^{1/2} \tag{21}$$

Results

The calculated results of energy levels of ${}^{208}_{82}Pb$ and ${}^{208}_{\Lambda}Pb$ are shown in Table 1 and Table 2 and then the corresponding energy shell levels are shown in Fig. 1 and Fig. 2 respectively. In these figures, the innermost level $1s_{1/2}$ has the highest binding energy. The binding energy of the single particle $1s_{1/2}$ state is gradually decreased to $1i_{11/2}$ levels away from the ${}^{208}_{82}\mathrm{Pb}$ nucleus. The values of total energy decrease with the increasing of orbital angular momentum. In spin-orbit interaction, a single particle has a doublet state. The splitting of a single particle has $\mathrm{j}=l+\frac{1}{2}$ and $\mathrm{j}=l-\frac{1}{2}$. It is found that $l+\frac{1}{2}$ state is the lower state and more bounds than the upper level, $l-\frac{1}{2}$ state.

Discussion

By comparing the calculated results of energy levels of ${}^{208}_{\Lambda}\mathrm{Pb}$ and ${}^{208}_{82}\mathrm{Pb}$, the energy levels of $\wedge$-hypernucleus is smaller than the ordinary nuclei and the energy of ${}^{208}_{\Lambda}\mathrm{Pb}$ nuclei is looser than the ${}^{208}_{82}\mathrm{Pb}$ nuclei. Then, the level splitting between $1p_{1/2}$ and $1p_{3/2}$ for ${}^{208}_{\Lambda}\mathrm{Pb}$ is 0.66 MeV and that for ${}^{208}_{82}\mathrm{Pb}$ is 0.28 MeV respectively.

The energy of ${}^{208}_{\Lambda}\mathrm{Pb}$ nucleus at s-state is calculated and it is -25.29MeV and it is nearly equal to experimental result, -26.3 MeV [Chhanda ,S., and A.Thomas, 2018].

The values of root-mean-square distances decrease with the total binding energies of ${}^{208}_{\Lambda}\mathrm{Pb}$ and ${}^{208}_{82}\mathrm{Pb}$ nucleus due to the $\vec{l}$ and $\vec{s}$ interaction. The innermost portion of these two nuclei has zero potential and the higher binding energy of $l+\frac{1}{2}$ state is the outer side of the lower binding energy of $l-\frac{1}{2}$ state. So, the root-mean-square distance of $l+\frac{1}{2}$ state is greater than that of $l-\frac{1}{2}$ state.

Conclusion

The Woods-Saxon potential is a convenient phenomenological choice for the one body potential. It provides a model for the properties of bound-state and continuum single-particle wave functions.

Table 1 The Physical Quantities of $^{208}_{82}\mathrm{Pb}$

Single-Particle State of $^{208}_{82}\mathrm{Pb}$	**Total Energy (MeV)**	**Root-Mean-Square Distance(fm)**
$1s_{1/2}$	-46.09	3.94
$1p_{3/2}$	-42.25	4.63
$1p_{1/2}$	-41.97	4.56
$1d_{5/2}$	-37.64	5.11
$1d_{3/2}$	-36.93	4.99
$1f_{7/2}$	-32.37	5.48
$1f_{5/2}$	-30.99	5.32
$1g_{9/2}$	-26.50	5.79
$1g_{7/2}$	-24.21	5.58
$1h_{11/2}$	-20.11	6.07
$1h_{9/2}$	-16.67	5.82
$1i_{13/2}$	-13.26	6.32
$1i_{11/2}$	-8.43	6.05

Table 2 The Physical Quantities of $^{208}_{\Lambda}\mathrm{Pb}$

Single-Particle State of $^{208}_{\Lambda}\mathrm{Pb}$	**Total Energy (MeV)**	**Root-Mean-Square Distance(fm)**
$1s_{1/2}$	-25.29	3.60
$1p_{3/2}$	-20.97	4.39
$1p_{1/2}$	-20.32	4.20
$1d_{5/2}$	-15.99	4.94
$1d_{3/2}$	-14.43	4.76
$1f_{7/2}$	-10.54.	5.40
$1f_{5/2}$	-7.68	5.19
$1g_{9/2}$	-4.64	5.85
$1g_{7/2}$	-0.35	5.79

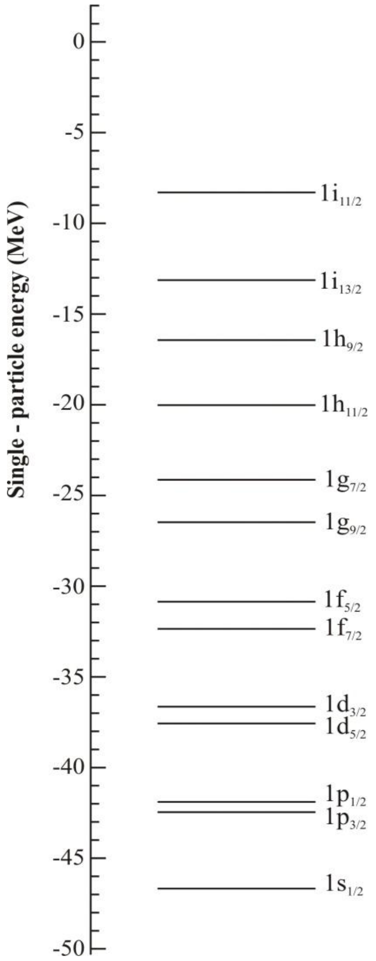

Figure 1 Single-particle energy levels of ${}^{208}_{82}\mathrm{Pb}$

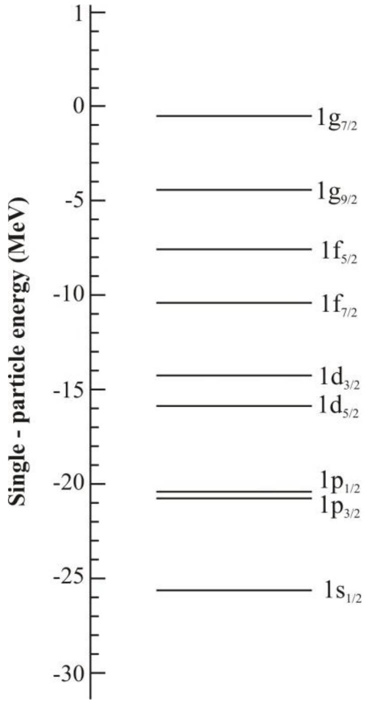

Figure 2 Single-particle energy levels of ${}^{208}_{\Lambda}\mathrm{Pb}$

Acknowledgements

I would firstly thank Professor Dr Khin Khin Win, Head of Department of Physics, Yangon University for her permission to present our research work. I would sincere thank to Rector Dr Thura Oo, Monywa University for his permission to do this work. I wish to thank Dr Shwe Zin Aung, Professor and Head, Department of Physics, Monywa University for her exhortation. I would like to thank Dr Khin Swe Myint, Rector (Rtd.), emeritus Prefessor, Department of Physics, Mandalay University for her precious advice, discussions and guidance.

References

Chhanda, S., and A. Thomas, (2018), "Bonding, Bonding and Charge Symmetry Breaking in ∧–Hypernuclei", vol.2, pp.4-6.

Frauenfelder, H. and M. H. Ernest, (1972), *Subatomic Physics*, Prentice-Hall, Inc Englewood Cliffs, New Jersey.

Greiner, W., A. M. Joachim, (1996), *Nuclear Models,* Springer- Verlag Berlin Heidelberg .

M. Wang, et al., (2014), "The AME2012 Atomic Mass Evaluation", vol. 120, pp. 1-5.

Woods, R.D. and D.S. Saxon, (1954), "Diffuse Surface Optical Model for Nucleon-Nuclei Scattering", vol. 95, pp. 577-578.

J. Myanmar Acad. Arts Sci. 2020 **Vol. XVIII.No.2B**

ACCESSING PAIRING CORRELATION FROM AVERAGE PARING GAPS ALONG POTENTIAL ENERGY SURFACES

Khaing Pwint Wai[1], Nyein Wint Lwin[2]

Abstract

In this work, the paring correlation along the energy surfaces for some light nuclei has been investigated. To this end, constrained Hartree-Fock+BCS method with Skyrme interaction is employed. Variation of average paring gaps along with the Nilsson single- particle levels at each constrained nuclear shapes shows the relation between nuclear shapes, paring correlation and nature of single particle levels. The calculated results indicate that the effect of paring depends on the level density in the vicinity of highest occupied level.

Keywords: Skyrme Hartree-Fock + BCS method

Introduction

Pairing correlations, which play not only a crucial role in superconducting solids but also contribute an important complement of nuclear shell structure (Bardeen, J., L. N. Cooper, and J. R. Schrieffer, 1957). The key feature of pairing correlations is the occurrence of an energy gap in the excitation spectrum.This gap manifests itself in two different kinds of energetic observables: first, there is a gap in the excitation spectra of even-even nuclei, which does not appear in the spectra of odd-mass number or odd-odd nuclei, and second, there occurs a shift between the interpolation curves of the ground-state binding energies of even-even as compared to odd-mass nuclei, which is called the odd-even mass staggering (Bender, M. et al, 2000). For light and medium-mass nuclei, the staggering has two components. The first one originates from pairing while the second, comparable in magnitude, has its roots in the deformed mean-field (Satula, W., J. Dobaczewski and W. Nazarewicz, 1998). Most often, pairing correlations are described within the Hartree-Fock framework by generalizing the mean-field concept to include a pairing field with the use of the BCS (Bardeen, Cooper, and Schrieffer) approximation by employing a self-consistent approach. We employ Skyrme interaction which can simplify the calculations with its zero-range form to successfully describe the masses, charge radii and excited states of finite nuclei. In this work, we will investigate the effects of pairing correlation in some selected even-even nuclei (^{28}Si, ^{22}Ne, ^{36}Mg) with the calculated potential energy surfaces by employing the Ev8 code (Ryssens, W. et al, 2014).

Theoretical Framework

The full many-body Hamiltonian can be written as follows

$$H = \sum_{i=1}^{N} \hat{t}_i + \frac{1}{2}\sum_{i\neq j}^{N} \hat{V}(r_i,\ r_j) \qquad (1)$$

where the first term is the one-body kinetic energy, and the second term represents the two-body force with the Coulomb interaction. The simplified expression for the Hatree-Fock equation is obtained as

---

[1] Assistant Lecturer, Department of Physics, Monywa University.

[2] Professor, Department of Physics, University of Mandalay.

$$\left(-\frac{\hbar^2}{2\mathrm{m}}\nabla^2+\int d\mathbf{r}'\rho\ \mathbf{r}'\ \mathrm{V}(\mathbf{r},\mathbf{r}')\right)\varphi_i\ \mathbf{r}\ -\int d\mathbf{r}'\rho\ \mathbf{r},\mathbf{r}'\ \mathrm{V}(\mathbf{r},\mathbf{r}')\varphi_i\ \mathbf{r}'\ =\varepsilon_i\varphi_i\ \mathbf{r}\ . \qquad (2)$$

This equation is known as the Hartree-Fock equation which looks like the regular one-body Schrödinger equation, with the extra non-local term. The Skyrme interaction is one of the most widely used energy functional for nuclear structure calculations. In the Skyrme-Hartree-Fock approach, the total binding energy of the system is given by the sum of the kinetic and Coulomb energies as well as the Skyrme energy functional that models the effective interaction between nucleons is shown in the following equation (Bender, M., and P. H. Heenen, 2003),

$$\mathrm{E}=\mathrm{E}_{\mathrm{Coulomb}}+\mathrm{E}_{\mathrm{kin}}+\mathrm{E}_{\mathrm{Sk}}\ . \qquad (3)$$

The Skyrme energy (E_{Sk}), is derived by evaluating,

$$E_{Sk}=\frac{1}{2}\sum_{i,j}^{A}\int\phi_i^*(\mathbf{r}')\phi_j^*(\mathbf{r}')\hat{V}_{sk}(\mathbf{r},\mathbf{r}')(1-\hat{P}_M\hat{P}_\sigma\hat{P}_q)\phi_i(\mathbf{r})\phi_j(\mathbf{r})d\mathbf{r}\ d\mathbf{r}'\Big|_{\mathbf{r}=\mathbf{r}'}\ . \qquad (4)$$

The Hartree-Fock equations with Skyrme interaction is given by

$$\begin{aligned}E_{Sk}=\ &B_1\rho^2\ \mathbf{r}\ +B_2\sum_q\rho_q^2\ \mathbf{r}\ +B_3\ \rho\ \mathbf{r}\ \tau\ r\ -j^2\ \mathbf{r}\ \ +B_4\sum_q\ \rho_q\ \mathbf{r}\ \tau_q\ \mathbf{r}\ -j_q^2\ \mathbf{r}\\ &+B_5\rho\ \mathbf{r}\ \nabla^2\rho\ \mathbf{r}\ +B_6\sum_q\rho_q\ \mathbf{r}\ \nabla^2\rho_q\ \mathbf{r}\ +B_7\rho^\alpha\ \mathbf{r}\ \rho^2\ \mathbf{r}\ +B_8\rho^\alpha\ \mathbf{r}\ \sum_q\rho_q^2\ \mathbf{r}\\ &+B_9\left[\rho\ \mathbf{r}\ \nabla.J\ \mathbf{r}\ +S\ \mathbf{r}\ .\ \nabla\times j\ \mathbf{r}\ \ +\sum_q\ \rho_q\ \mathbf{r}\ \nabla.J_q\ \mathbf{r}\ +S_q\ \mathbf{r}\ .\ \nabla\times j_q\ \mathbf{r}\right]\\ &+B_{10}S^2\ \mathbf{r}\ +B_{11}\sum_q S_q^2\ \mathbf{r}\ +B_{12}S^2\ \mathbf{r}\ \rho^\alpha\ \mathbf{r}\ +B_{13}\rho^\alpha\ \mathbf{r}\ \sum_q S_q^2\ \mathbf{r}\ \rho_q^\alpha\ \mathbf{r}\\ &+B_{14}\ S\ \mathbf{r}\ .T\ \mathbf{r}\ -J^2\ \mathbf{r}\ \ +B_{15}\ S\ \mathbf{r}\ \nabla^2 S\ \mathbf{r}\\ &+B_{16}\sum_q\ S_q\ \mathbf{r}\ .T_q\ \mathbf{r}\ -J_q^2\ \mathbf{r}\ \ +B_{17}\sum_q S_q\ \mathbf{r}\ \nabla^2 S_q\ \mathbf{r}\ .\end{aligned} \qquad (5)$$

The formulation of BCS theory and gap equation will be solved in pairing problems with the use of Hamiltonian that contains a single-particle part and residual interaction acting on the states k and –k. It has the form

$$\hat{H}=\sum_k\varepsilon_k^0\hat{a}_k^\dagger\hat{a}_k+\sum_{kk'>0}\langle k,\text{-}k|v|k',\text{-}k'\rangle\hat{a}_k^\dagger\ \hat{a}_{\text{-}k}^\dagger\hat{a}_{\text{-}k'}\hat{a}_{k'} \qquad (6)$$

where $\hat{a}_k^\dagger\hat{a}_k$ is the creation operator of each pair. For the simple case, the matrix element $\langle k,\text{-}k|v|k',\text{-}k'\rangle$ is assumed to be independent of the state k and is given by a constant number, $-G$. The Hamiltonian then becomes

$$\hat{H}=\sum_k\varepsilon_k^0\hat{a}_k^\dagger\hat{a}_k-G\sum_{kk'>0}\hat{a}_k^\dagger\ \hat{a}_{-k}^\dagger\hat{a}_{-k'}\hat{a}_{k'}\ . \qquad (7)$$

The approximate BCS ground state wave function of the Hamiltonian is

$$|BCS\rangle=\prod_{k>0}^{\infty}(u_k+v_k\,\hat{a}_k^\dagger\,\hat{a}_{-k}^\dagger)|0\rangle\ . \qquad (8)$$

We have to use the variational principle with a constraint to the particle number.

$$\hat{H}' = \hat{H} - \lambda N \ . \tag{9}$$

The Lagrange multiplier λ is determined by the condition that the expectation value of the particle number operator with respect to the BCS state must be the particle number N of the system,

$$\langle BCS | \hat{N} | BCS \rangle = 2\sum_{k>0} v_k^2 = N, \tag{10}$$

and the expectation value of the constrained Hamiltonian leads to

$$\langle BCS | \hat{H} - \lambda\hat{N} | BCS \rangle = 2\sum_{k>0} (\varepsilon_k^0 - \lambda) v_k^2 - G\left(\sum_{k>0} u_k v_k\right)^2 - G\sum_{k>0} v_k^4 \ . \tag{11}$$

The occupation probability of each paired state can be calculated by solving the gap equation iteratively.

This obtained

$$\begin{pmatrix} u_k^2 \\ v_k^2 \end{pmatrix} = \frac{1}{2}\left[1 \pm \frac{\varepsilon_k^0 - \lambda}{\sqrt{(\varepsilon_k^0 - \lambda)^2 + \Delta^2}}\right] \tag{12}$$

where, v_k^2 and u_k^2 are occupation and inoccupation probabilities of the single particle levels k or –k. The gap equation becomes

$$\Delta_k = \frac{G}{2}\sum_{k>0} \frac{\Delta_k}{\sqrt{{\varepsilon_k^0 - \lambda}^{\;2} + \Delta_k^2}} . \tag{13}$$

The energy of the system in equation (7) becomes

$$E = 2\sum_{k>0} v_k^2 \, \varepsilon_k^0 - \frac{\Delta^2}{G} \tag{14}$$

where, $\frac{\Delta^2}{G}$ is called the pairing energy.

These occupation probabilities v_k^2 are used in replacing all the sums over the occupied orbital by a sum over all orbital multiplied with the corresponding occupation probabilities:

$$\sum_{i=1}^{A} .... \Rightarrow \sum_{k} v_k^2 \ . \tag{15}$$

If the sum over k is unrestricted, the sums in equation (13) diverge. One has to introduce cut-off energy in these sums. Therefore, in the calculations including pairing interaction; an additional parameter such as the pairing cut-off or the size of the pairing window is needed.

Results and Discussion

The occurrence of gaps or regions of the low single particle level density around the Fermi surface is correlated with the deformed ground state energies. Thus, it is necessary to calculate the potential energy surfaces to predict the shape of the nucleus whether it has stable or deformed nature. In this framework, the constrained quadrupole moment is added to the Hamiltonian to generate energy surfaces. We calculate the potential energy surfaces as a function of quadrupole deformation parameter using constrained Hartree-Fock method as follows

$$\left\langle H' \right\rangle = \left\langle H \right\rangle - \lambda \left\langle \hat{Q} \right\rangle, \tag{16}$$

The deformation parameter $\beta_{\ell m}$ is related to the total mass of the moment which can be seen as follows

$$\beta_{\ell m} = \frac{4\pi}{3R_0^{\ell} A} \left\langle \hat{Q}_{\ell m} \right\rangle \tag{17}$$

The connections between q_i and the Cartesian quadrupole moments are given by the following equations

$$\left\langle \hat{Q}_x \right\rangle = -\frac{1}{2} \; q_1 - q_2 \tag{18}$$

$$\left\langle \hat{Q}_y \right\rangle = -\frac{1}{2} \; q_1 + \;\; 2q_2 \tag{19}$$

$$\left\langle \hat{Q}_z \right\rangle = \frac{1}{2} \; 2q_1 + \;\; q_2 \;\; . \tag{20}$$

An alternate representation is given in terms of the deformation parameter (q) and the triaxiality angle (γ). Their relationship can be represented by

$$q_1 = q \cos \;\gamma\; - \frac{1}{\sqrt{3}} q \sin \;\gamma \tag{21}$$

$$q_2 = \frac{2}{\sqrt{3}} \, q \sin \;\gamma\; . \tag{22}$$

In this work, Ev8 code is used to solve the mean-field equations for the Skyrme energy density functional. The single particle wave functions are discretized on a 3-dimensional (3D) Cartesian mesh to solve the mean-field equations (Ryssens, W. et al, 2014). There are many sets of the Skyrme parameters which have been generated to reproduce the nuclear matter properties. In this work, the Sly4 and SGII parameter sets are chosen because they are powerful to investigate neutron-rich nuclei. The Sly4 parameter set provides more consistent binding energies with experimental data than the SGII parameter set as shown in Table 1.1. These experimental data are reported by the National Nuclear Data Center (https://www.nndc.bnl.gov/nudat2/). For this reason, Sly4 parameter set will be used in this work.

Table 1.1 Comparison of ground state minimum energies for each parameter set and experimental data.

Nucleus	SGII	Sly4	Experimental data
^{28}Si	243.49 MeV	234.56 MeV	236.54 MeV
^{22}Ne	187.91 MeV	177.45 MeV	177.77 MeV
^{36}Mg	283.63 MeV	263.08 MeV	260.78 MeV

The calculated potential energy surfaces (PES) are depicted in Fig. 1(a) for (i)^{28}Si, (ii)^{22}Ne and (iii)^{36}Mg. In general, the nuclei having minimum energy located at the positive deformation parameter describes the prolate shape whereas the minimum energy with negative deformation parameter stands for the oblate shape. The energy surface for ^{28}Si shows a deep oblate minimum, while that for ^{22}Ne and ^{36}Mg show prolate minimum. As can be seen in Fig 1, ^{28}Si nucleus has energy minimum of oblate configuration which has the ground state energy of -234.56 MeV at $\beta_2 = -0.32$. Next to ^{28}Si, the PES of ^{22}Ne nucleus shows the prolate configuration with ground state energy (-177.45 MeV) and its quadrupole deformation is 0.42. The potential energy surface of ^{36}Mg nucleus shows the prolate configuration ($\beta_2 = 0.39$) with the ground state minimum of nearly -263 MeV.

It is well known that pairing plays a decisive role in the open shell nuclei. The energy gap is a measure of the width of the transition between highly occupied states and unoccupied ones. The appropriate pairing strength (G) is considered to reproduce ground state binding energies. The paring strength $G = 410\,\mathrm{MeVfm}^3$ is used for both protons and neutrons in this calculation. A smooth pairing energy cut-off of 5 MeV around the Fermi level is also used to overcome the divergence case. The zero-range density-dependent pairing force is employed for the pairing interaction as follows

$$V(r_1, r_2) = -g\frac{1-\hat{P}_\sigma}{2}\left(1-\frac{\rho\;\bar{r}}{\rho_0}\right)\delta\;r_1 - r_2 \qquad (23)$$

where $\hat{P}_\sigma$ is the spin-exchange operator, $\rho_0 = 0.16\ \mathrm{fm}^{-3}$ and $r = \frac{r_1 - r_2}{2}$.

The corresponding average neutron pairing gaps as a function of quadruple deformation for ^{28}Si, ^{22}Ne and ^{36}Mg are depicted in Fig. 1 (b). In ^{28}Si and ^{22}Ne, there is no pairing gap at the absolute minimum; it can be assumed that there is no pairing effect at these regions. It is predicted that the energy spacing between next unoccupied level and last occupied one is larger than the energy available from pairing of nucleons in the last occupied levels. For ^{36}Mg nucleus, the effect of pairing correlation becomes weaker as the paring gap decreases near the deformed ground state.

The formation of deformed minima can be related to the occurrence of gaps or regions of low single particle level density around the highest occupied level. To illustrate the effect of pairing correlation and the level density, the neutron single-particle energy levels versus quadruple deformation for the selected nuclei are depicted in Fig. 1 (c). For deformed nuclei such as ^{28}Si, ^{22}Ne and ^{36}Mg; the deformation removes the degeneracy of energy levels at spherical shape and energy levels split-up according to their angular momentum. Solid curves correspond to levels with positive parity whereas short-dashed curves denote levels with negative parity. The red circles indicated the magic number. From these figures, it can be seen that the lower level density leads to smaller pairing gaps (or pairing correlation) near local minima, on the other hand, denser level density to larger pairing effects.

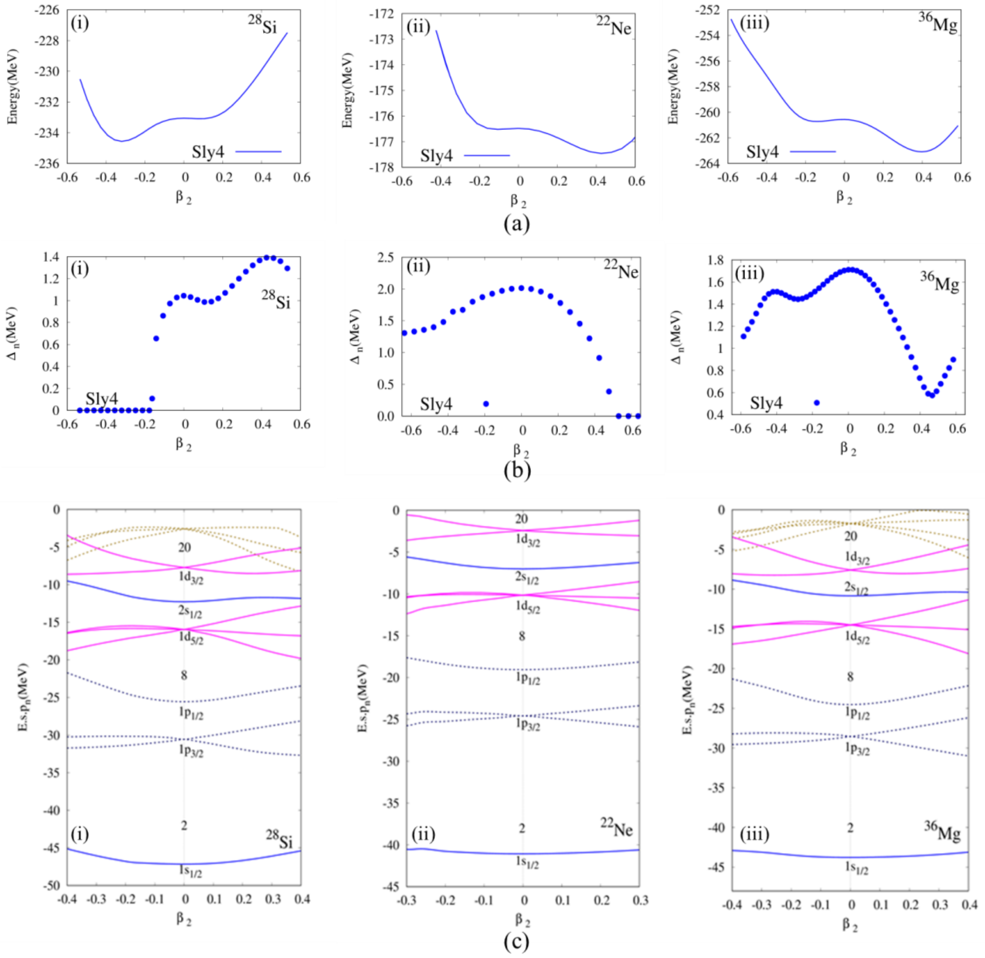

Figure 1 (a) Potential energy surfaces (b) Average neutron pairing gaps Δ_n and (c) Neutron single-particle energy levels versus quadruple deformation β_2 for (i) ^{28}Si, (ii) ^{22}Ne and (iii) ^{36}Mg obtained with Sly4 parameter set.

Summary and Conclusion

In this work, we have compared the potential energy surfaces as a function of deformation parameters for some selected nuclei, namely, ^{28}Si, ^{22}Ne and ^{36}Mg using the two Skyrme parameter sets (Sly4, SGII). From these results, the energy surface for ^{28}Si shows a deep oblate minimum meanwhile ^{22}Ne and ^{36}Mg show prolate minimum. Then we calculate the corresponding average neutron pairing gaps and neutron single particle levels as a function of quadrupole deformation with the choice of the Sly4 parameter set to provide the fact that pairing plays an important role in determining the shapes of nuclei. It is found that the lower level density leads to smaller pairing gaps (or pairing correlation) near local minima, on the other hand, denser level density to larger pairing effects. At spherical shapes, pairing correlation becomes strongest due to dense level density. It can be concluded that the effect of paring depends on the level density in the vicinity of the Fermi surface.

Acknowledgements

I am grateful to the respectable person who is devoted their efforts and time for holding the seminar of Myanmar Academy of Arts and Science hosted at the University of Yangon. I would like to express my sincere gratitude to Dr.Khin Khin Win, Professor and Head of Physics Department at the University of Yangon for supporting this seminar. I also thank Dr.Shwe Sin Aung, Professor, and Head of Physics Department at Monywa University for giving enthusiasm and permission.

References

Bardeen, J., L. N. Cooper, and J. R. Schrieffer, (1957) "Theory of Superconductivity." Phys. Rev, vol. 108, pp. 1175.

Bender, M., K. Rutz, P.G. Reinhard, and J. A. Maruhn, (2000) "Pairing Gaps from Nuclear Mean–Field Models." arXiv: nucl-th **0005028v1**, pp. 4.

Bender, M., and P. H. Heenen (2003) "Self-consistent mean-field models for nuclear structure." Rev. Mod. Phys. vol. 75, pp. 121.

https://www.nndc.bnl.gov/nudat2/.

Ryssens, W., V. Hellemans, M. Bender and P.H. Heenen, (2014) "Solution of the Skyrme HF+BCS equation on a 3D mesh: II. A new version of the Ev8 code." arXiv: nucl-th **1405.1897v2**, pp. 1.

Satula, W., J. Dobaczewski and W. Nazarewicz, (1998) "Odd-Even Staggering of Nuclear Masses: Pairing or Shape Effect?" arXiv: nucl-th **9804060v1**, pp. 1.

J. Myanmar Acad. Arts Sci. 2020 **Vol. XVIII.No.2B**

FABRICATION OF MEH-PPV:PCBM BASED ORGANIC SOLAR CELLS

Thet Thet Naing[1] , Nyein Wint Lwin[2], Than Zaw Oo[3]

Abstract

For the fabrication of MEH-PPV:PCBM solar cells, the bulk heterojunction blend solutions of MEH-PPV:PCBM (1:2 wt%) were prepared in chloroform, dichlorobenzene, toluene and xylene. A thin layer of poly (3,4-ethylenedioxythiophene):poly(styrenesulfonate) or (PEDOT:PSS) was spin-coated on pre-cleaned ITO glass plates. Then the PEDOT: PSS coated substrate was annealed at 100ºC for 15 min. Subsequently, MEH-PPV:PCBM photoactive layer was spun-coat at 1000 rpm for 60 s on the top of PEDOT:PSS layer. After annealing at 130°C for 8 min, the devices were completed by deposition of cathode aluminum through a mask by thermal evaporation at a pressure of 10^{-6} Torr. The I-V curves of the devices were recorded under illumination of light intensity (100 mWcm^{-2}). The photovoltaic efficiency of organic solar cells were evaluated from the J-V characteristics of the device. It was measured using a computer-controlled digital source meter (Keithley 2420) with a Newport solar simulator (A.M. 1.5, 100 mWcm^{-2}). Light intensity was calibrated with a National Renewable Laboratory (NREL)-calibrated monocrystalline Silicon solar cell.

Keywords: MEH-PPV:PCBM solar cells.

Introduction

Photovoltaic (PV) cells convert solar energy into electrical energy. Solar cells are usually divided into three main generations. The first generation solar cells are mainly based on silicon (Si) wafers. The silicon-based photovoltaics have outstanding advantages in both efficiency and lifetime with power conversion efficiencies (PCE) in excess of 25% [K.Wu *et al.,* (2010)]. Second generation solar cells are thin-film solar cells which include amorphous silicon (a-Si), and cadmium telluride (CdTe), and copper indium gallium selenide (CIGS). Their typical performance is 10-15% [X. Wang *et al.*, (2010)]. Third generation solar cells are organic heterwwwojunction solar cells, dye sensitized solar cells (DSSC) and organic/inorganic hybrid solar cells. Organic solar cells have received attention due to their low-cost, easy processability, low weight, and mechanical flexibility. Their power conversion efficiencies have increased considerably from 0.001% in 1975 to 1% in 1986 and more recently to 8.13% in 2010 [C. Tang *et al*., (2007)].

The choice of solvent for polymeric blends is one of the major factors which have influence on the performance of the polymer solar cell. To provide effective donor- acceptor charge transfer and transport in bulk heterojunction solar cells, the photoactive layar has to demonstrate the right morphology, which means appropriate domain size, crystallinity and vertical distribution of both components [B. Chung *et al*., (2007)]. The choice of solvent, annealing temperature and time are the most critical factors determining the final morphology. The effect of morphology can be described by the formation of an effective network between donor and acceptor which creates effective routes for separated charge transport. The properties of the solvents, such as boiling point, solubility and surface tension have a considerable impact on the final morphology of the photoactive layer, thereby determining the device performance. It

---

[1] Dr, Lecturer, Department of Physics, Monywa University.

[2] Dr, Professor, Department of Physics, University of Mandalay.

[3] Dr, Professor, Department of Physics, University of Yangon.

is thus crucial to explore a suitable solvent for the particular polymeric material that yields the preferable morphology of photoactive layer [J. Kim *et al*., (2007)].

Several attempts have being implemented in order to achieve the higher device efficiency. The choice of solvent for polymeric blends is a major factor which influences on the performance of the polymer solar cells. To provide effective donor-acceptor charge transfer and transport in bulk heterojunction solar cells, the photoactive layar has to demonstrate the right morphology, which means appropriate domain size, crystallinity and vertical distribution of both components. The properties of the solvents, such as boiling point, solubility and surface tension have a considerable impact on the final morphology of the photoactive layer, thereby determining the device performance. It is thus crucial to explore a suitable solvent for the particular polymeric material that yields the preferable morphology for photoactive layer.

Experimental Details

This section details about device fabrication and efficiency measurement.

Device Fabrication and Efficiency Measurement

The fabrication steps for organic photovoltaic device are depicted in Fig.(1). The devices were fabricated on indium tin oxide (ITO) coated glass substrates which are used as the transparent electrodes. The indium tin oxide (ITO) glasses were cleaned by sequential ultrasonification in acetone, distilled water and isopropyl alcohol (IPA) for 15 min consecutively and dried by nitrogen blow. Since ITO was coated throughout the glass substrate, etching had to be carried out to remove the ITO at the sides, leaving the only ITO in the center region as shown in Fig. 2(a). ITO surfaces were then treated by UV light in order to remove the organic contamination on the ITO surface. Fabricated OPV devices are shown in Fig.(2)(b). The ultrasonic cleaner and UV chamber used in our ITO cleaning processes are shown in Fig.(2)(c) and (d) respectively. For the fabrication of MEH-PPV:PCBM solar cells, the bulk heterojunction blend solutions of MEH-PPV:PCBM (1:2 wt%) were prepared in chloroform, dichlorobenzene, toluene and xylene. A thin layer of poly (3, 4- ethylenedioxythiophene):poly (styrenesulfonate) or (PEDOT:PSS) (Sigma Aldrich) was spin-coated at 3000 rpm for 60 s on pre-cleaned ITO glass plates. Then the PEDOT:PSS coated substrate was annealed at 100 °C for 15 min. Subsequently, MEH-PPV:PCBM photoactive layer was spun-coat at 1000 rpm for 60 s on the top of PEDOT:PSS layer. The active layer thicknesses were in the range of 80 nm-100 nm as determined by a surface profiler (Tencor Alpha-Step IQ). After annealing at 130 °C for 8 min, the devices were completed by deposition of cathode aluminum (Al) (~ 100 nm) through a mask by thermal evaporation at a pressure of 10^{-6} Torr. The device active area was around 0.07 cm^2. Fig.(4)(a) shows thermal evaporator (NTE 1000) for the deposition metal (Al) cathode. The I-V curves of the devices were recorded under illumination of light intensity (100 mW/cm^2). The photovoltaic efficiency of organic solar cells were evaluated from the J-V characteristics of the device. It was measured using a computer-controlled digital source meter (Keithley 2420) with a Newport solar simulator (A.M. 1.5, 100 mW/cm^2). Light intensity was calibrated with a National Renewable Laboratory (NREL)-calibrated monocrystalline Silicon solar cell. Fig.(3)(b) shows the experimental setup for the efficiency measurement of OPV devices.

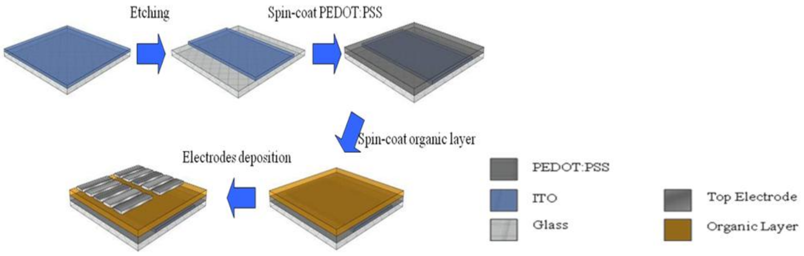

Figure 1 Fabrication steps for organic photovoltaic device

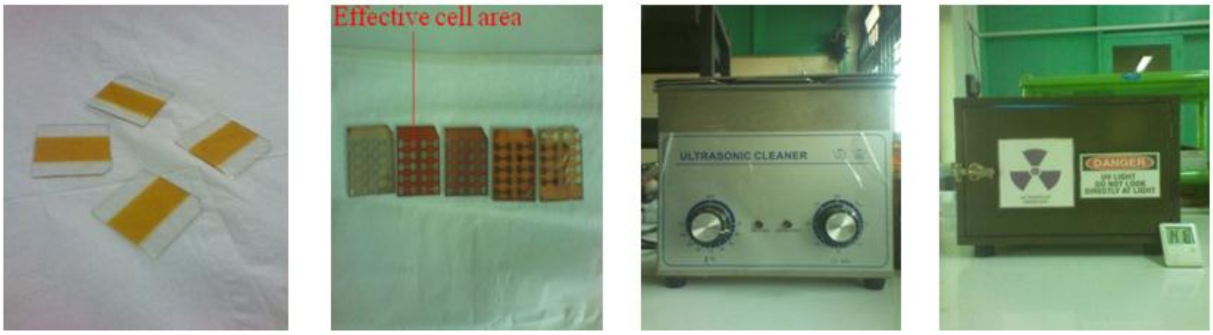

(a) (b) (c) (d)

Figure 2 Illustrations of (a) etched ITO pattern on glass substrate, (b) fabricated OPV devices, (c) ultrasonic cleaner and (d) UV chamber

(a) (b)

Figure 3(a) Thermal evaporator (NTE 1000) for the deposition metal (Al) cathode and (b) Experimental setup for the measurement of device efficiency (Newport Solar simulator and Keithley source meter)

Results and Discussion

This section discusses the photovoltaic performance of MEH-PPV:PCBM based organic solar cells.

Photovoltaic Performance of MEH-PPV:PCBM Devices: Correlating the Properties and Performance

The device performances of MEH-PPV:PCBM solar cells using four different solvents (chloroform, dichlorobenzene, toluene and xylene) were evaluated under A.M 1.5 solar irradiation of intensity 100 mW/cm^2. The current-voltage (J-V) characteristics of these devices are shown in Fig. (4)(a). Dichlorobenzene based device showed the highest J_{sc} of 0.66 mA/cm^2 and FF of 26.40. Its power conversion efficiency (PCE) is as high as 0.112%. The power conversion effeciencies of chloroform and toluene based devices are 0.0067% and 0.0080% two orders lower than that of dichlorobenzene. The PCE of xylene based device is as low as 0.0003%. In order to understand more about the system, it is crucial to correlate the optical, electrical and morphological properties of the photoactive layer with each and every device parameters (V_{oc}, J_{sc} and FF) which determine the device efficiency. The open circuit voltages (V_{oc}) of the devices are 0.82 V, 0.63 V, 0.70 V and 0.43 V for toluene, dichlorobenzene, chloroform and xylene respectively. It is well accepted that the V_{oc} in organic solar cell is determined by the energy level difference between highest occupied molecular orbital (HOMO) of p-type donor material and lowest unoccupied molecular orbital (LUMO) of n-type acceptor material. Higher V_{oc} of 0.82 V is produced in the device with toluene while lower V_{oc} of 0.43 V in the device with xylene. In Fig. 4(b), we can see that there is a change in optical band gap energy of the active layer with toluene and xylene.

The short circuit current (J_{sc}) of dichlorobenzene based device is 0.66 mA/cm^2 which is higher than those of chloroform, toluene, xylene based devices (0.10, 0.07 and 0.04 mA/cm^2). The photocurrent generation (J_{sc}) in organic solar cells is related to the number charge carriers and carrier mobility. The number of carrier generated is in turn related to the absorption (electron excitation) properties of photoactive materials. The absorption spectra (Fig. 4(b)) shows that the dichlorobenzene and chloroform offers the higher absorption properties as compared to those of others. It suggests that higher absorption with dichlorobenzene and chloroform would generate the higher current. However, only dichlorobenzene device generates higher current. As mentioned earlier, the current generation is also related to the carrier mobility. It seems that the mobility of the chloroform based photoactive layer would be poor, resulting in the lower current in the devices. Another possibily of lower J_{sc} in chloroform, toluene and xylene based devices is that the ionization of excitons is insufficient in the devices with chloroform, toluene and xylene due to the less exciton ionization interfaces [N. Shaheen *et al.*, (2001)].

The fill factor (FF) in the devices is very sensitive to the surface mophology/roughness of the active layer and series resistance of the device. The FF of the device is 26.40 for dichlorobenzene, 14.10 for toluene, 13.46 for xylene and 9.84 for chloroform. The series resistance of the devices is calculated from the slope of the J-V curves at the open-circuit point (Fig. 5(a)). The R_s is 0.87 Ωcm^2, 32.32 Ωcm^2, 58.99 Ωcm^2 and 467.28 Ωcm^2 for the device with dichlorobenzene, toluene, xylene and chloroform respectively. It is obvious that the highest FF in the dichlorobenzene device would be due to the lowest R_s and the lowest FF in chloroform device would be due to the highest R_s. Since the FF of the devices is also related to the surface roughness/morphology of the films, the roughness profiles of the photoactive layers with various solvents are generated and depicted in Fig. (5)(b). The lowest surface roughness (R_a) achieved in the active layer with dichlorobenzene leads to higher FF in the device with dichlorobenzene.

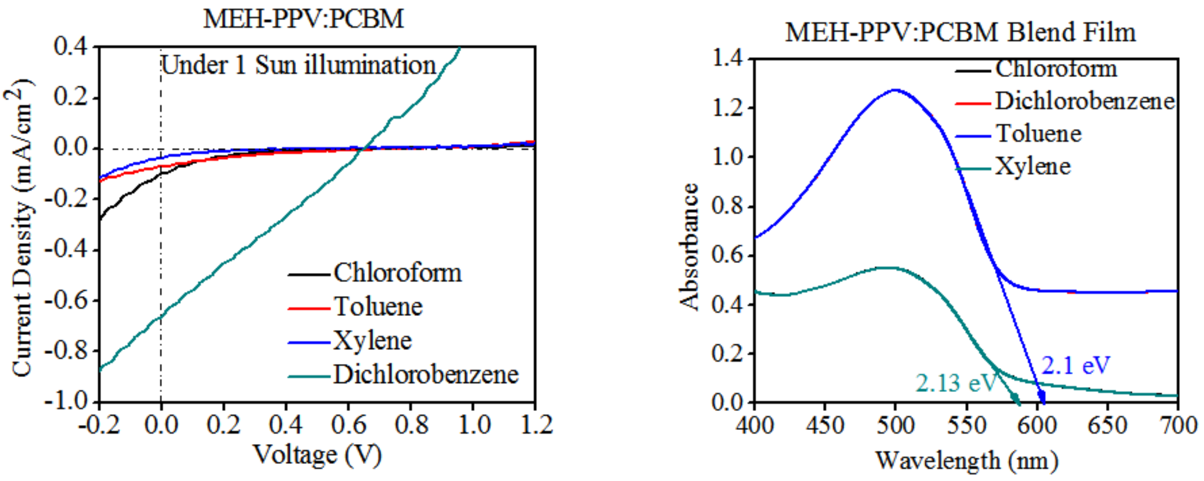

(a) (b)

Figure 5 (a) J-V characteristics of MEH-PPV:PCBM devices using four different solvents. and (b) Absorption spectra of MEH-PPV:PCBM blend films using four different solvents

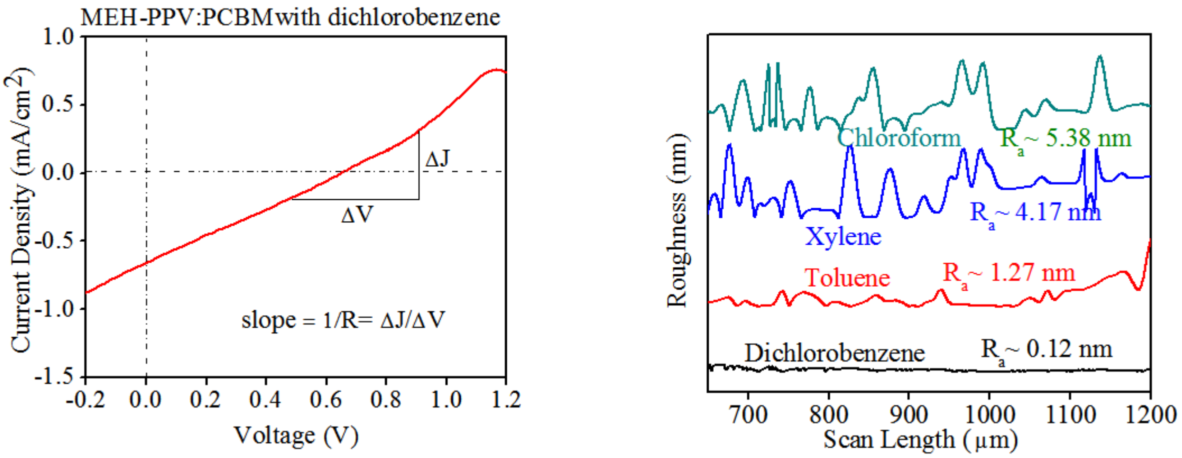

(a) (b)

Figure 5 (a) Estimation of series resistance (R_S) from the J-V curve and (b) Roughness profiles for the MEH-PPV:PCBM films with different solvents

Conclusion

The optical properties of MEH-PPV:PCBM devices were investigated. The solvents used were chloroform, dichlorobenzene, toluene and xylene. The solvent "dichlorobenzene" provides the highest absorption intensity and lowest band gap energy of 2.1 eV. Achieving the high optical absorption and low band gap energy is requisite for photoactive layers in solar cells. The fabrication of organic solar cells using MEH-PPV:PCBM polymer blend film as photoactive layer. The device using "dichlorobenzene" produced the efficiency as high as 0.112% (open circuit voltage 0.63 V, short circuit current density 0.67 mAcm^{-2} and fill factor 26.40).

Acknowledgements

I would like to express my deepest gratitude to Dr Thura Oo, Rector, Monywa University, for his invaluable guidance. I am thankful to Dr Khin Khin Win, Professor and Head, Department of Physics, University of Yangon, for her help and kind encouragement. I am also gratefully thanks Professor Dr Shwe Zin Aung, Professor and Head, Department of Physics, Monywa University, for her permission and valuable suggestions.

References

Chung B, D. Yanfei, L.Ping and C. Qiying, (2007) Appl. Phys. Lett. Vol.**55**, pp-1741.

Kim J and G. Weihao, (2007) "An Overview on MEH-PPV:PCBM", J.Sci. Vol **45**, pp- 222.

Shaheen N, C.Markus and J. Christoph, (2001) "Polymer- Fullerene Bulk Heterojunction Solar Cells", Appl. Phys. Lett. Vol. **78**, pp-98.

Tang C, B.Minnaert and M. Burgelman, (2007) "Modelling MEH-PPV:PCBM (1:4) Bulk Heterojunction Solar Cells", Appl. Phys. Lett. Vol. **91**, pp-143.

Wu K and J. deBoisblanc, (2010) "Synthesis and Charactreization of MEH-PPV:PCBM Organic Solar Cells", Master Thesis.

Wang X, D.Lui and L.Jiuyan, (2010) "Orgnic Photovoltaic Materials and Thin Film Solar Cells", Front. Chem. Lett. Vol. **5**, pp-45.

J. Myanmar Acad. Arts Sci. 2020 **Vol. XVIII.No.2B**

COMPARATIVE STUDY OF CONTACT ANGLE MEASUREMENTS ON POLYMERMDMO-PPV COMPOSITE NIO AND AG/NIOFILMS

Yin Yin Kyi[1], Win Win Aye[2], Than ZawOo[3]

Abstract

The wettability behavior of MDMO-PPV solution on NiO and Ag/NiO substrates was investigated by contact angle measurement. The present study focuses on the effect of polymer solution concentration (6-10-14 mg/ml) and solvent (dichlorobenzene) on the wettability of substrate surface. The measured contact angles are 12°, 11° and 10°on NiO films and 22°, 17°, 12° on Ag/NiO films, 14°, 11°, 10° on Ag/NiO films, 19°, 16°, 14° on Ag/NiO films at different silver concentrations (2.5, 5, 10 mM) for polymer concentration of 6, 10 and 14 mg/ml. There is no significant changes in contact angle measurements of MDMO-PPV on NiO and Ag/NiO films.

Keywords: wettability, MDMO-PPV polymer, contact angle.

Introduction

Recently, the electron donating p-type and electron accepting n-type polymer solar cells are produced commercially and its cell efficiency is around 10% [Jingbi, You *et al.,* (2013)]. Substrate treatment and wetting behaviors are good tools for increasing cell efficiency in semiconducting polymers.Thin film solar cells technology and nanoparticles exhibit unique physical and chemical properties which have a significant effect on wettability [Rafal, Sliz, (2014), Richard, Magdalena Mandoc M *et al.,* (2007)and Hansson, (2015)]. Wettability provides quantitative data describing the behaviour of liquid droplets on substrate surfaces [Harald, Hoppe *et al.,* (2006)]. Controlling the hydrophobicity or hydrophilicity of a substrate surface is of crucial importance for solar cell device fabrication. In everyday life applications, it is desirable to have highly hydrophilic surfaces in wallpaper painting, biomedical applications such as tissue reconstruction.

In wallpaper painting, the interface between the substrate (wall) and solution (ink) drop is much studied, as it is considered the most critical factor for achieving high printing quality. Polymer solar cell used printing process like printing newspapers and coating technologies [K. Jeroen Van Duren *et al.,* (2004)]. Charge transportation can be improved through the roughness, chemistry of the surface and surface energy, boiling point of liquid.

Surface of a material is a region where phase is transformed one state to another. The energy required to form a surface is called surface energy and it is an important property of every surface. Surface science plays an important role in surface morphology and surface chemical properties [Jan Anton Koster L. *et al.,* (2012)]. Studies of surface roughness, surface energy and contact angle values are important factors for polymer thin films. The study of wetting phenomena at polymer surfaces and interfaces is of interest in the many industrial processes, such as oil recovery, lubrication, liquid coating, printing and spray quenching. The importance of substrate surface energy for polymer thin films is rapidly growing in cell device performance.

---

[1] Ph.D. Student, Lecturer, Department of Physics, University of Monywa.
[2] Assistant Lecturer, Department of Physics, Hakha College.
[3] Professor, Department of Physics, Yangon University.

Experiment

Preparation of Solutions

In the polymer synthesis, 6, 10 and 14 mg of MDMO-PPV were dissolved in 1 ml of dichlorobenzene (DCB). The resulting solutions were stirred vigorously for 15 min at RT. In the synthesis of nickel oxide (NiO) sol-gel, the nickel acetate Ni $(CH_3COO)_{2.4H2O}$ was used as a source of nickel (Ni). 4.42 g of nickel acetate was added to 50 ml of ethanol and 0.5 ml of HCl. The resulting solution was stirred vigorously for 90 min at 60°C forming a clear light green solution. In the silver nanoparticle synthesis,$AgNO_3$ (metal salt precursor), PVP (stabilizing agent) and $NaBH_4$ (reducing agent) were used. 5.6mgof $NaBH_4$ were added to 3ml of distilled water to create a 50mMsolution. 2.4mg, 4.8mg, 9.6mg of $AgNO_3$ were added to 6ml of distilled water to create a 2.5mM, 5mM, 10mM solutions. And then $AgNO_3$ solutions were added to the $NaBH_4$(50 mM) solutions using a dropper, at about one drop per second. The color of solution was immediately changed into light yellow. The resulting solution was stirred vigorously for 20 min at RT. Upon the complete addition of the $AgNO_3$, stirring were stopped. Next, polyvinylpyrrolidone (PVP) (dissolving 1mMofPVP in 3 ml distilled water) solutions were added immediately to the resulting solutions in order to prevent nanoparticles aggregation. The synthesis steps are illustrated in Fig. 1.

Formation of Polymer Composite NiO and Ag/NiO Films

NiO sol-gel solution was spun-coat on glass substrate by spin coating with five deposition cycles forming NiO films. Then NiO films were annealed at 700°C on the temperature controlled hot plate. Then silver nanoparticle solutions were deposited on NiO films by spin coating with three deposition cycles and annealed at 100°C for 10 min to get Ag NPs/NiO films. Subsequently, MDMO-PPV solutions were then spun-coat at 1000 rpm for 60 s on the top of NiO and Ag/NiO layers.

Contact Angle Measurement

The wetting properties of polymer MDMO-PPV films on underlying NiO were determined based on measurement of contact angle. The cross-section images of polymer MDMO-PPV liquid drop on glass substrates and on NiO underlying layer were captured by a video camera which is attached with Digital Microscope (U500X). The experimental step up for contact angle measurement is shown in Fig. 2. The video camera performs its digitalization in ranging from 320x230 to 1600x1200 pixels images. The image analysis was performed by using the Axisymmetric Drop Shape Analysis (FTÅ 32) software. Using the profile of the liquid drop recorded by digital camera with a resolution of 640x480 pixels, then the contact angle between the liquid and substrate is measured. At least three measurements are taken for each target drop in order to obtain average contact angle values.

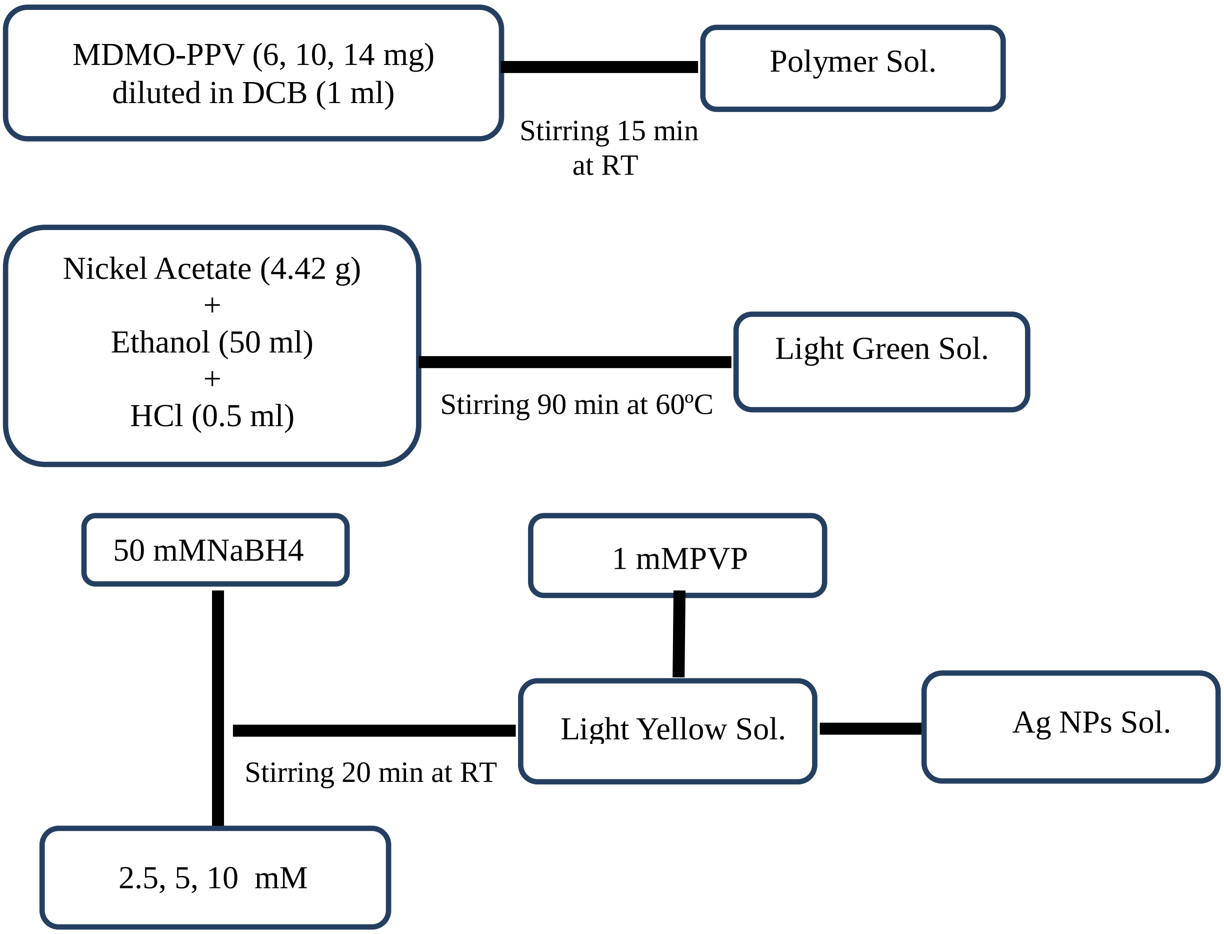

Figure 1 Synthesis steps for polymer, NiO and Ag NPs solutions.

Figure 2 The experimental setup for contact angle measurement.

Results and Discussion

Surface Wettability of MDMO-PPVon NiO Film

Wettability involves the interaction between liquid and solid in contact. The wetting behavior of thin film is characterized by the value of contact angle. The contact angle is an important parameter in surface science and its measurement provides a simple and reliable technique for the interpretation of surface energies. The value of contact angle is directly correlated with the surface structure of the film. The contact angles for MDMO-PPV on NiOfilm annealed at 700 °C were investigated and the photographs of the cross-sectional view of a drop of MDMO-PPV solution (solvent: dichlorobenzene) on NiOfilms areshown in Fig. 3. The contact angle values are listed inTable1.

The contact angles seem to be insensitive to the changes in polymer concentration for the MDMO-PPV on NiO. It is also observed that the contact angles were smaller than on NiO films. It indicates that the higher polymer concentrations on NiO films lead to a better wetting behavior.

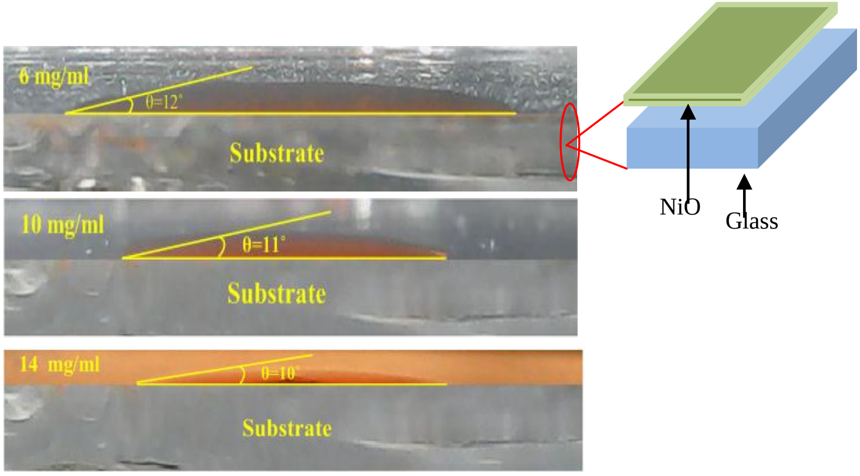

Figure 3 Contact angles of polymer MDMO-PPV solution on NiO film at 700˚C.

Table 1 Contact angle values

MDMO-PPV/NiO			
Temp. (˚C) of NiO	**Polymer Concentration (mg/ml)**	**Solvent**	**Contact Angle (degree)**
700	**6**	**Dichlorobenzene**	**12**
	10		**11**
	14		**10**

Surface Wettability of MDMO-PPV on Ag/NiO Films

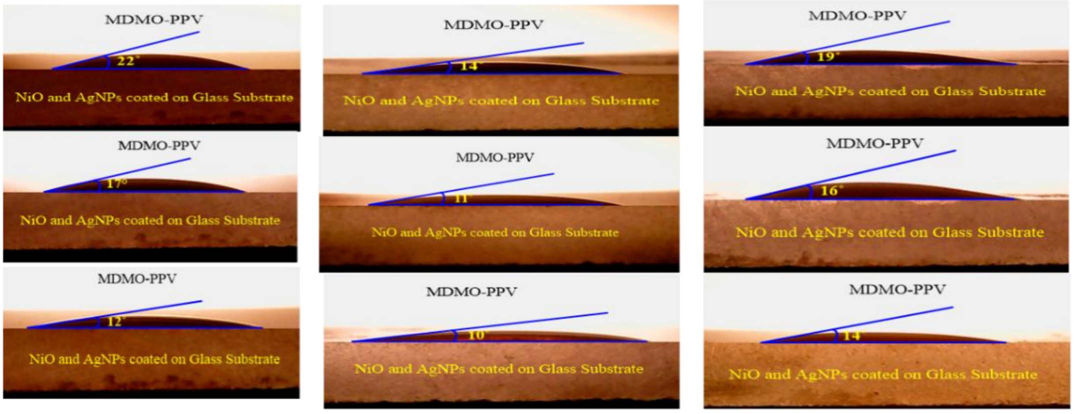

(a) 2.5 mM Ag (b) 5 mM Ag (c) 10 mM Ag

Figure 4 Contact angles of polymer MDMO-PPV solution on Ag/NiO films.

The value of contact angle is directly correlated with the surface structure of the film. The contact angle values are shown in Fig. 4and listed in Table 2. The contact angles seem to be insensitive to the changes in polymer concentration for the MDMO-PPV on Ag/NiO film. Especially, we found that contact angle of MDMO-PPV on 5mM Ag/NiO concentration was less than other two concentrations.

Table 2 Contact angle values

MDMO-PPV/Ag/NiO				
Ag NPs Concentration (mM)	**Polymer Concentration (mg/ml)**	**Temp. (°C) Of NiO**	**Solvent**	**ContactAngle (degree)**
2.5	**6 10 14**	**700**	**Dichlorobenzene**	**22° 17° 12°**
5	**6 10 14**	**700**	**Dichlorobenzene**	**14° 11° 10°**
10	**6 10 14**	**700**	**Dichlorobenzene**	**19° 16° 14°**

Conclusion

The surface wettability of MDMO-PPV on NiO and Ag/NiO films was examined by contact angle measurement. Contact angles values decreased with increasing polymer concentrations for all films. Thus, the contact values ranging from 10° to 22° confirmed that there is a good wetting at interface of polymer and substrate surface.The wetting behaviours are good tools for increasing cell efficiency in polymer films and solar cell.

Acknowledgement

The authors would like to acknowledge Professor, Dr Khin Khin Win, Head of Department of Physics, Yangon University for her effort to MAAS program and Professor Dr Kathi New, Department of Physics, Mandalay University of Distance Education for her permission and encouragement to carry out this work.

References

Harald, Hoppe *et al.*,(2006)"Morphology of Polymer/Fullerene Bulk Heterojunction Solar Cells."*Journal of Materials Chemistry,* Italy,vol. 16, pp.46-49.

Jan Anton Koster L. *et al.,* (2012)"Device Model for the Operation of Polymer/Fullerene Bulk Heterojunction Solar Cells." *Advanced Energy Materials*, Romania, vol. 12, pp. 1-4.

K. Jeroen Van Duren *et al.*,(2004)"Synthesis and Characterization of a Low Bandgap Conjugated Polymer for Bulk Heterojunction Photovoltaic Cells." *Advanced Functional Materials.* Rome, vol. 14, pp.1-5.

Magdalena Mandoc M *et al.*,(2007)"Charge Transport in MDMO-PPV:PCNEPV All-Polymer Solar Cells." *Journal of Applied Physics,* Italy,vol. 101, pp. 104-105.

Magdalena Mandoc M *et al.*,(2007)"Origin of the Reduced Fill Factor and Photocurrent in MDMO-PPV:PCNEPV All-Polymer Solar Cells." *Advanced Functional Materials,* Italy, vol. 17, pp.2165-2167.

Richard, Hansson, (2015) "PhD Thesis", Morphology and Materials Stability in Polymer Solar Cells, University of Karlstad.

Rafal, Sliz, (2014) "PhD Thesis", Analysis of Wetting and Optical Properties of Materials Developed for Novel Printed Solar Cells, University of Oulu.

Jingbi, You *et al.*,(2013)"A Polymer Tandem Solar Cell with 10.6 % Power Conversion Efficiency." *Nature Communications,* China,vol. 15, pp.1.

J. Myanmar Acad. Arts Sci. 2020 **Vol. XVIII.No.2B**

CALCULATION OF HEAVY-ION FUSION CROSS SECTIONS USING DIFFERENT NUCLEAR POTENTIALS

Aye Myat Wai[1], Nyein Wint Lwin[2]

Abstract

The fusion cross sections and fusion barrier distributions of ^{16}O + ^{148,154}Sm systems have been calculated using different types of nuclear potentials. Simple one-dimensional potential model and coupled-channels method have been applied. The calculated results are compared with the experimental data. The calculated fusion cross sections using one-dimensional potential model disagree with the experimental data. The improvements have been made by inclusion of channel coupling effects. The calculated fusion cross sections are also analyzed by calculating the fusion barrier distributions which is sensitive to details structure of the colliding nuclei.

Keywords: different potentials, one-dimensional potential model, coupled-channels method

Introduction

In nuclear physics, heavy-ion is any particle with a mass exceeding that of the helium-4 nucleus (α-particle). Fusion is a process in which two or more nuclei combine to form a compound nucleus. The simplest approach to heavy-ion fusion reactions is to use a one-dimensional potential model. This model deals with only the relative distance between a target and a projectile [Hagino, 1998]. For reactions involving heavy-ions, the fusion cross sections were found to be significantly different from the expectations of such a model, particularly at energies below the barrier where enhancement of several orders of magnitude was observed.

Couplings of the relative motion to nuclear shape deformations and vibrations lead to an enhancement of the sub-barrier fusion cross section in comparison with the predictions of one-dimensional potential model. The couplings produce some interesting features in the barrier distribution for fusion. The fusion barrier distribution is defined as the second derivative of the energy-weighted fusion cross sections with respect the centre-of-mass energy E, that is, $d^2(E\sigma_f)/dE^2$. The barrier distribution has been shown to be sensitive to the data related to the nuclear structure, such as the nuclear shapes, the multiple excitations and the nuclear surface vibrations etc.

In order to make a systematic study of many systems, the choice of the potential is one of the most challenging aspects to compare theory with experimental fusion data both below and above the barrier. The scope of this work is to investigate the fusion cross sections and the corresponding fusion barrier distributions by using different nuclear potentials in the interaction and also take into account the channel coupling effects.

Theoretical framework

A simple estimate of the fusion cross section is obtained by the one dimensional potential model, where one considers the degree of freedom only of the relative motion between the colliding nuclei.

---

[1] Dr, Assistant Lecturer, Department of Physics, Monywa University

[2] Professor, Department of Physics, University of Mandalay

In this model, the fusion cross section for the compound nucleus formation, σ_F, is obtained from the standard formula:

$$\sigma_F(E) = \frac{\pi}{k^2} \sum_l (2l+1)\, P_l(E) \quad , \tag{1}$$

where $P_l(E)$ is the penetrability for the *l*-wave scattering.

The couplings of the relative motion between the colliding nuclei to other degrees of freedom, e.g. their intrinsic excitations, nuclear transfer, can be caused the large enhancement of fusion cross section against predictions of the potential model. They are called channel coupling effects. The coupled-channels calculation is a standard theoretical approach to describe heavy-ion fusion reactions by taking the effects of nuclear intrinsic degrees of freedom into account. The full coupled-channels calculations quickly become very difficult to handle if many physical channels are included. The dimension of the resulting of coupled-channels problem is in general too large if several important intrinsic degrees of freedom exit simultaneously. For this reason, one often introduces the so called the no-Cariolis approximation to avoid these difficulties. In the no-Coriolis approximation, the angular momentum of the relative motion in each channel has been replaced by the total angular momentum J. The coupled-channels equations read

$$\left[-\frac{\hbar^2}{2\mu}\frac{d^2}{dr^2} + \frac{J\,(J+1)\,\hbar^2}{2\mu\, r^2} + V_N(r) + \frac{Z_P Z_T e^2}{r} - E + \varepsilon_n \right] \Psi_n(r) + \sum_m V_{nm}(r)\,\Psi_m(r) = 0, \tag{2}$$

where Vnm are the matrix elements of the coupling Hamiltonian including the Coulomb and nuclear coupling components. E and ε_n are the bombarding energy in mass center frame and the n-th channel excitation energy, respectively. The coupled equations are solved by using the boundary conditions of the ingoing waves at a radius inside the barrier, and to be matched to appropriate the Coulomb waves at a radius outside the range of the nuclear potential. The minimum position of the Coulomb pocket inside the barrier r_{min}, and the finite distance r_{max} which is the position where both the nuclear and the Coulomb coupling are relatively sufficient small, are adopted by the program. Then the wave functions within r_{min} and beyond r_{max} can be expressed as

$$\Psi_n(r) = T_n \exp\left(-i \int_{r_{min}}^{r} k_n(r')\, dr' \right) r \le r_{min}\,, \tag{3}$$

$$\Psi_{nm}(r) = C_{nm}\, H_J^{(-)}(k_m r) + D_{nm}\, H_J^{(+)}(k_m r) \quad r \ge r_{max}\,, \tag{4}$$

with

$$k_n(r) = \sqrt{\frac{2\mu}{\hbar^2}\left(E - \frac{J(J+1)\hbar^2}{2\mu r^2} - V_N(r) - \frac{Z_P Z_T e^2}{r} - \varepsilon_n - V_{nn}(r) \right)} \tag{5}$$

which is the local wave number for the n-th channel and $K_n = K_m$ if r is beyond r_{max} to the infinite. $H_J^{(-)}$ and $H_J^{(+)}$ are the incoming and the outgoing Coulomb functions, respectively.

In order to get the wave functions between r_{min} and r_{max}, the modified Numerov methods have been employed to solve the second order differential equations with setting the conditions at the boundary position r_{min}

$$\Psi_n(r_{min}) = 1, \quad \frac{d}{dr}\Psi_n(r_{min}) = -iK_n(r_{min}). \tag{6}$$

With Eq. (6), the recurrence relation related to wave functions at r_{i+1}, r_i and r_{i-1} are obtained as

$$\Psi^{i+1} = \left(1-\frac{h^2}{12}A^{i+1}\right)^{-1}\left\{\left[\left(\frac{h^2}{\sqrt{12}}A^i+\sqrt{3}\right)^2-1\right]\left(1-\frac{h^2}{12}A^i\right)\Psi^i-\left(1-\frac{h^2}{12}A^{i-1}\right)\Psi^{i-1}\right\}, \tag{7}$$

with

$$A_{nm}(r) = \frac{2\mu}{\hbar^2}\left[\left(\frac{J(J+1)\hbar^2}{2\mu r^2}+V_N(r)+\frac{Z_P Z_T e^2}{r}+\varepsilon_n-E\right)\delta_{n,m}-V_{nm}(r)\right]. \tag{8}$$

And h is the radial step for integrating the equations. By matching the ratio of the wave functions at $r_{max}-h$ to those at $r_{max}+h$, the coefficients C_{nm} and D_{nm} in Eq. (4) then can be determined. With the above, the solution of the coupled-channels equation can be naturally given by a linear combination of Ψ_{nm}

$$\Psi_m(r) = \sum_n T_n \Psi_{nm}(r). \tag{9}$$

With Eq. (9), the transmission coefficients can be easily obtained. Taking into account all the possible intrinsic states, the inclusive penetrability can be calculated by

$$P^J(E) = \sum_n \frac{k_n(r_{min})}{k}\left|T_n\right|^2. \tag{10}$$

Then, the fusion cross section can be given by

$$\sigma_F(E) = \frac{\pi}{k^2}\sum_J (2J+1)P^J(E). \tag{11}$$

Results and discussion

We investigate the fusion cross sections and fusion barrier distributions by taking the different nuclear potentials in the inter-nuclear interaction. In this work, we use CCFULL code which solves the coupled-channels equations in computing the fusion cross sections, taking the relative motion and the intrinsic degrees of freedom [Hagino *et al*, 1999]. In the original code, Woods-Saxon potential is used as the entrance and coupling potentials. We substitute the original potential in the program with AW, BW, Prox-77 and Prox-88 potentials. These potentials are used as the entrance and coupling potentials in the calculations. We will describe the different nuclear potentials in the following.

A refined version of the Woods-Saxon potential was derived by Broglia and Winther. This refined potential resulted in

$$V_N(r) = -\frac{V_0}{1+\exp[(r-R_0)/a]}, \tag{12}$$

where $V_0 = 16\pi \frac{R_1 R_2}{R_1 + R_2} \gamma a$, a =0.63 fm and $R_0 = R_1 + R_2 + 0.29$. (13)

Here radius R_i has the form $R_i = 1.233 A_i^{1/3} - 0.98 A_i^{-1/3}$ fm $(i = 1, 2)$ and

$$\gamma = \gamma_0 \left[1 - k_s \left(\frac{N_1 - Z_1}{A_1} \right) \left(\frac{N_2 - Z_2}{A_2} \right) \right], \tag{14}$$

where γ_0= 0.95 MeV/fm^2 and k_s= 1.8. We label this potential as BW.

The parameters "a" and "R_i" of the above potential were further refined by Winther to a modified form Aage Winther 1995.

$$a = \left[\frac{1}{1.17 \left(1 + 0.53 \left(A_1^{\frac{-1}{3}} + A_2^{\frac{-1}{3}} \right) \right)} \right] \text{fm}, \tag{15}$$

$$R_i = 1.20 A_i^{1/3} - 0.09 \,\text{fm} \qquad (i=1,2). \tag{16}$$

Here, $R_0 = R_1 + R_2$ only. We label this potential as **AW**.

According to the original version of proximity potential 1977, the interaction potential $V_N(r)$ between two surfaces can be written as;

$$V_N(r) = 4\pi \gamma b \bar{R} \Phi \left(\frac{r - C_1 - C_2}{b} \right) \text{MeV}. \tag{17}$$

Where, $C_i = R_i \left[1 - \left(\frac{b}{R_i} \right)^2 + \dots \right]$, $\bar{R} = \frac{C_1 C_2}{C_1 + C_2}$ and b has the approximate value of 1 fm.

The effective sharp radius, R_i, reads as $R_i = 1.28 A_i^{1/3} - 0.76 + 0.8 A_i^{-1/3}$ fm $(i=1, 2)$.

$\Phi\left(\xi = \frac{r - C_1 - C_2}{b} \right)$ is a universal function which is parameterized with the following form;

$$\begin{aligned} \Phi(\xi) &= -\frac{1}{2}(\xi - 2.54)^2 - 0.0852\,(\xi - 2.54)^3, \text{for } \xi \le 1.2511, \\ &= -3.437 \exp\left(-\frac{\xi}{0.75} \right), \text{for } \xi \ge 1.2511 \end{aligned} \tag{18}$$

and the surface energy coefficient is $\gamma = \gamma_0 \left[1 - k_s \left(\frac{N - Z}{N + Z} \right)^2 \right]$. (19)

Where, N and Z are the total number of neutrons and protons. In the present version, γ_0 and k_s were taken to be 0.9517 MeV/fm^2 and 1.7826, respectively [Blocki *et al*, 1977]. We label this potential as **Prox-77**. Later on, using the more refined mass formula due to Möller and Nix, the value of coefficients γ_0 and k_s were modified yielding the values of 1.2496 MeV/fm^2 and 2.3, respectively. We label this potential as **Prox-88**.

We calculate the fusion cross sections for ^{16}O + ^{148}Sm and ^{16}O +^{154}Sm systems with these different nuclear potentials by using 1-D potential model and coupled-channels method.

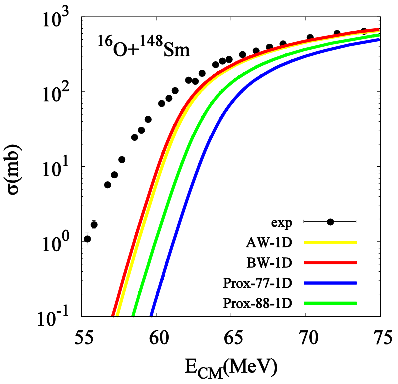

Figure 1 The fusion cross sections for the reaction of ^{16}O + ^{148}Sm system as a function of centre-of-mass energy E$_{cm}$ (MeV). The experimental data are taken from Ref. [Leigh *et al*, 1995].

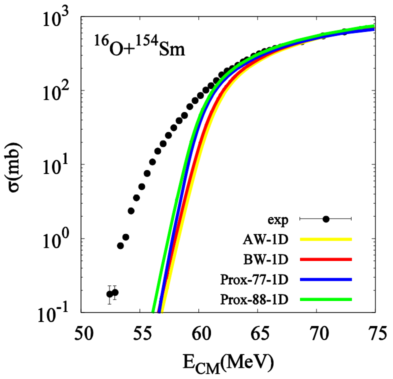

Figure 2 The fusion cross sections for the reaction of ^{16}O + ^{154}Sm system as a function of centre-of-mass energy E$_{cm}$ (MeV). The experimental data are taken from Ref. [Leigh *et al*, 1995].

Fig. 1 and Fig. 2 display the results of fusion cross sections using AW, BW, Prox-77 and Prox-88 potentials for ^{16}O + ^{148}Sm and ^{16}O + ^{154}Sm systems in 1-D potential model. We can see that the results of fusion cross sections for all potentials in one dimensional potential model cannot explain the fusion reactions used in this work. All nuclei considered here are assumed to be spherical in nature; however, deformation as well as orientation of the nuclei (that is channel coupling) can affect the fusion cross sections.

Therefore, we investigate the fusion cross sections and fusion barrier distributions of the same systems using the coupled-channels method. We categorize these systems into two groups having different excitation nature:

(i) Spherical projectile and vibrating target (^{16}O + ^{148}Sm) and

(ii) Spherical projectile and deformed rotating target (^{16}O + ^{154}Sm).

(i) The ^{16}O + ^{148}Sm System

We consider ^{16}O + ^{148}Sm system, ^{148}Sm is considered as vibrating nuclei. In the calculations, we include the quadrupole triple phonon $(2^{+})^{3}$ and octupole triple phonon $(3^{-})^{3}$ states of ^{148}Sm. The excitation energies and the deformation parameters of ^{148}Sm are E_2 = 0.55 MeV, β_2 = 0.182 for 2^{+} state and E_3 = 1.16 MeV, β_3 = 0.236 for 3^{-} state.

Fig. 3 (a) and (b) show the fusion cross sections and the fusion barrier distributions obtained by using AW, BW, Prox-77 and Prox-88 potentials. The results of fusion cross sections with AW and BW potentials slightly underestimate with the experimental data. All potentials can reproduce similar peak character of fusion barrier distributions with the experimental barrier distribution of this system. Prox-77 and Prox-88 potentials give better agreement compared to AW and BW potentials for fusion cross sections as well as the fusion barrier distributions. Interestingly, fusion barrier distribution extracted from the results obtained with Prox-77 potential well reproduces the second peak character in experimental barrier distribution at high energy region (see Fig. 3 (b)).

(ii) The ^{16}O + ^{154}Sm System

In this subsection, the fusion reaction of ^{16}O projectile on ^{154}Sm target has been considered. It is known from the excitation spectra of ^{154}Sm that this nucleus is deformed. Thus, in the calculations it is taken as a well deformed nuclei with deformation parameters $\beta_2 = 0.330$, $\beta_4 = 0.050$ and excitation energy is E = 0.080 MeV. The fusion cross sections and the corresponding fusion barrier distributions are depicted in Fig. 4 (a) and (b), respectively. The fusion cross sections calculated with Prox-77 and Prox-88 potentials show nearly the same result with the experimental data than that of AW and BW potentials. Concern with fusion barrier distributions, all potentials can reproduce the gross structure of the experimental barrier distribution as shown in Fig. 4 (b). It can be seen that Prox-77 and Prox-88 potentials give better results than AW and BW potentials especially at low energies.

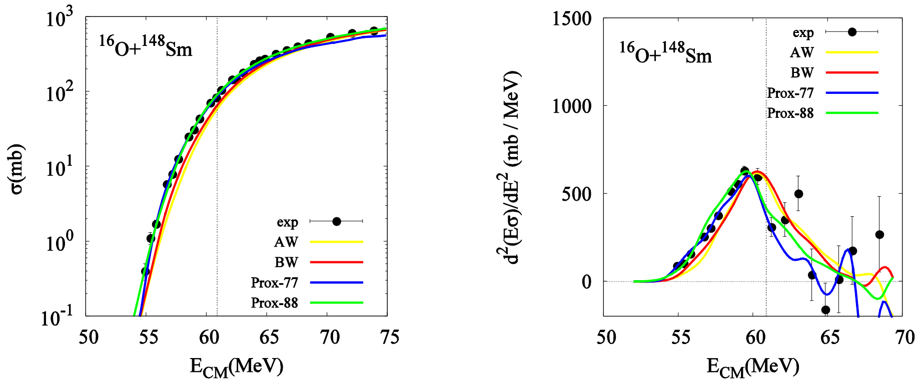

(a) (b)

Figure 3 The comparison of (a) fusion cross sections and (b) the corresponding fusion barrier distributions using different nuclear potentials along with experimental data for ^{16}O + ^{148}Sm system. The vertical line represents the experimental Coulomb barrier height.

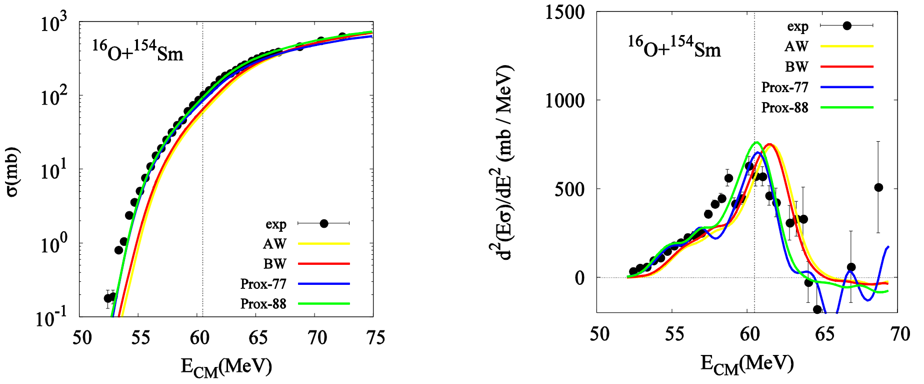

(a) (b)

Figure 4 The comparison of (a) fusion cross sections and (b) the corresponding fusion barrier distributions using different nuclear potentials along with experimental data for ^{16}O + ^{154}Sm system. The vertical line represents the experimental Coulomb barrier height.

Conclusion

We have performed the calculation of fusion cross sections with one dimensional potential model and coupled-channels method for ^{16}O + ^{148}Sm and ^{16}O + ^{154}Sm systems with four different nuclear potentials, namely, AW, BW, Prox-77 and Prox-88. The improvements of fusion cross sections have been made by inclusion of channel coupling effects for all potentials used in this point. According to the calculated fusion cross sections and the corresponding fusion barrier distributions, proximity type potentials give better results than AW and BW potentials and it can be used to make systematic study of heavy-ions fusion reactions.

Acknowledgement

I am grateful thanks to Dr Khin Khin Win, Professor and Head of the Department of Physics, University of Yangon for her kind permission to carry out this work.

I also thank to Professor Dr Shwe Zin Aung, Head of Department of Physics, Monywa University, for her encouragement and permission.

References

Blocki, J. *et al* (1977), “Proximity Forces”, Annals of Physics. **105**, pp.427-462.

Hagino, K. (1998), “Multi-Dimensional Quantum Tunneling in Heavy-Ion Fusion Reactions”, Tohoku University.

Hagino, K. *et al* (1999), “A Program for Coupled-Channel Calculations with All Order Couplings for Heavy-Ion Fusion Reactions ”, vol. **123,** pp.143-152.

Leigh, J. R. *et al* (1995), “Experimental data on HI fusion cross sections”, Physical Review, **C 52,** pp.3151.

J. Myanmar Acad. Arts Sci. 2020 **Vol. XVIII.No.2B**

NEUTRON SINGLE PARTICLE ENERGY STATES IN ^{118}Sn BY APPLYING WOODS-SAXON POTENTIAL WITH SPIN ORBIT INTERACTION

Yin Min Kyaw*

Abstract

The purpose of this research work is to analyze the neutron single particle energy levels of ^{118}Sn in non-relativistic shell model. The single particle energy levels and wave function of ^{118}Sn nucleus are obtained by solving one body Schroedinger equation numerically with Numerov Method. Numerov method is one of the methods which can give the energy and wave function simultaneously. In our calculation, the Woods-Saxon potential with spin orbit term is used for interaction between core and single nucleon. . In our calculation of ^{118}Sn, the calculated shell structure of neutron single particle are $1s_{1/2}$, $1p_{3/2}$, $1p_{1/2}$, $1d_{5/2}$, $1d_{3/2}$, $2s_{1/2}$, $1f_{7/2}$, $1f_{5/2}$, $2p_{3/2}$, $2p_{1/2}$, $1g_{9/2}$, $1g_{7/2}$, $2d_{5/2}$, $2d_{3/2}$, $3s_{1/2}$, and $1h_{11/2}$.

Keywords: single particle energy, spin-orbit interaction, angular momentum

Introduction

The determination of the single particle energies of the atomic nuclei is an important problem in nuclear physics. An analytic expression for single-particle energy levels in the nucleus is based on a phenomenological behavior of main feature of shell model. The nuclear shell model is founded on the principle that neutrons and protons can move as independent in orbitals with discrete quantum numbers. In a physics of nuclear structure, a single particle state is assumed as an excitation state that one proton or one neutron jumped to a higher orbit. The term single particle state is usually used in the analysis of non-interacting or weakly interacting particles.

In our research work, the neutron single particle energy levels and wave function of the ^{118}Sn (Tin) nucleus are obtained by solving one body Schrödinger equation numerically with Numerov method. Tin has the largest number of stable isotopes. We have investigated the single particle levels of ^{118}Sn by using Woods-Saxon potential with spin orbit term for interaction between core and single nucleon.

Theoretical framework

In order to investigate the nucleon single-particle energy levels in^{118}Sn, we firstly solved one-body Schroedinger equation by applying Numerov method.

The Schroedinger radial equation is

$$\frac{d^2u(r)}{dr^2}+\frac{2m}{\hbar^2}\left[(E-V(r)-\frac{\hbar^2}{2m}\frac{l(l+1)}{r^2}\right]u(r)=0 \tag{1}$$

We can integrate equation (1) by means of the Numerov method.

In Numerov method, the forward and backward recursive relations are examined by using Taylor series expansion method.

---

[*] Dr, Assistant Lecturer, Department of Physics, Monywa University

Firstly it is split that the ‘r’ range into N points according to “$r_n = r_{n-1} + h$”

By using Taylor series expansion,

$$f(x) = f(a) + (x-a)f'(a) + (x-a)^2 \frac{f''(a)}{2!} + - - - + \frac{(x-a)^{n-1} f^{n-1}(a)}{(n-1)!} \tag{2}$$

(i) forward recursive relation

$$[1 + \frac{h^2}{12} k(r_{n-1})]u(r_{n-1}) = 2[1 - \frac{5h^2}{12} k(r_n)]u(r_n) - [1 + \frac{h^2}{12} k(r_{n+1})]u(r_{n+1}) \tag{3}$$

(i) backward recursive relation

$$u(r_{n-1}) = \frac{2[1 - \frac{5h^2}{12} k(r_n)]u(r_n) - [1 + \frac{h^2}{12} k(r_{n+1})]u(r_{n+1})}{[1 + \frac{h^2}{12} k(r_{n-1})]} \tag{4}$$

According to the properties of wave function, u_{out} and u_{in} must be homogeneous at a point r_c called matching point. According to continuity equation

$$(u_{out})_{r_c} = (u_{in})_{r_c} \tag{5}$$

$$(u'_{out})_{r_c} = (u'_{in})_{r_c} \tag{6}$$

We can define a function Match (E) at r_c whose zeros correspond to the energy eigen values as

$$\text{Match }(E) = \left[\frac{u'_{out}}{u_{out}}\right]_{r_c} - \left[\frac{u'_{in}}{u_{in}}\right]_{r_c} \tag{7}$$

$$E_n = E_{n-1} + \Delta E \tag{8}$$

For each E_n, we have to calculate their Eigen function u_{out} and u_{in} at r_c point. Then the match point, r_c, have been defined and this matching point is within the N points which covered the interaction range. The matching point was selected at N/3. The trial energy range splitting have been set into N points according to $E_n = E_{start} + E$. For each E_n, the Eigen function u_{out} (r) and u_{in} (r) have been calculated at the r_c point. We build a “Match (E)” function based on continuity condition. Finally, the correct energy Eigen value (E) and Eigen function have been searched simultaneously.

In order to calculate nucleon single particle energy levels in ${}_{50}Sn^{118}$ for different angular momentum states, phenomenological Woods-Saxon potential is used. It is based on the sum of spin independent-central potential and a spin orbit potential.

Woods-Saxon potential with spin-orbit coupling term is express as follows.

$$V_{so}(r) = V_{so} \frac{1}{r} \frac{d}{dr} f_0(r)(\vec{l}.\vec{s}) = -V_{so} \frac{1}{r} \frac{1}{a_0} \frac{\exp[(r-R_0)/a_0]}{\left[1 + \exp\left[\frac{(r-R_0)}{a_0}\right]\right]^2} (\vec{l}.\vec{s}) \tag{9}$$

where, V_{so} = the strength of Woods-Saxon spin-orbit coupling potential term

Results and discussion

We have investigated the neutron single-particle energy levels of ^{118}Sn by solving one-body Schroedinger radial equation with the use of phenomenological Woods-Saxon central potential including spin-orbit interaction. According to our results, the calculated shell levels for neutron single particle in ^{118}Sn are $1s_{1/2}$, $1p_{3/2}$, $1p_{1/2}$, $1d_{5/2}$, $1d_{3/2}$, $2s_{1/2}$, $1f_{7/2}$, $1f_{5/2}$, $2p_{3/2}$, $2p_{1/2}$, $1g_{9/2}$, $1g_{7/2}$, $2d_{5/2}$, $2d_{3/2}$, $3s_{1/2}$, and $1h_{11/2}$. Table (1) is the calculated results for neutron single-particle energy levels in ^{118}Sn. The systematic energy level diagrams for neutron is displayed in Fig. (1). The corresponding wave functions for various states are described in Fig. (2), (3) and (4) respectively.

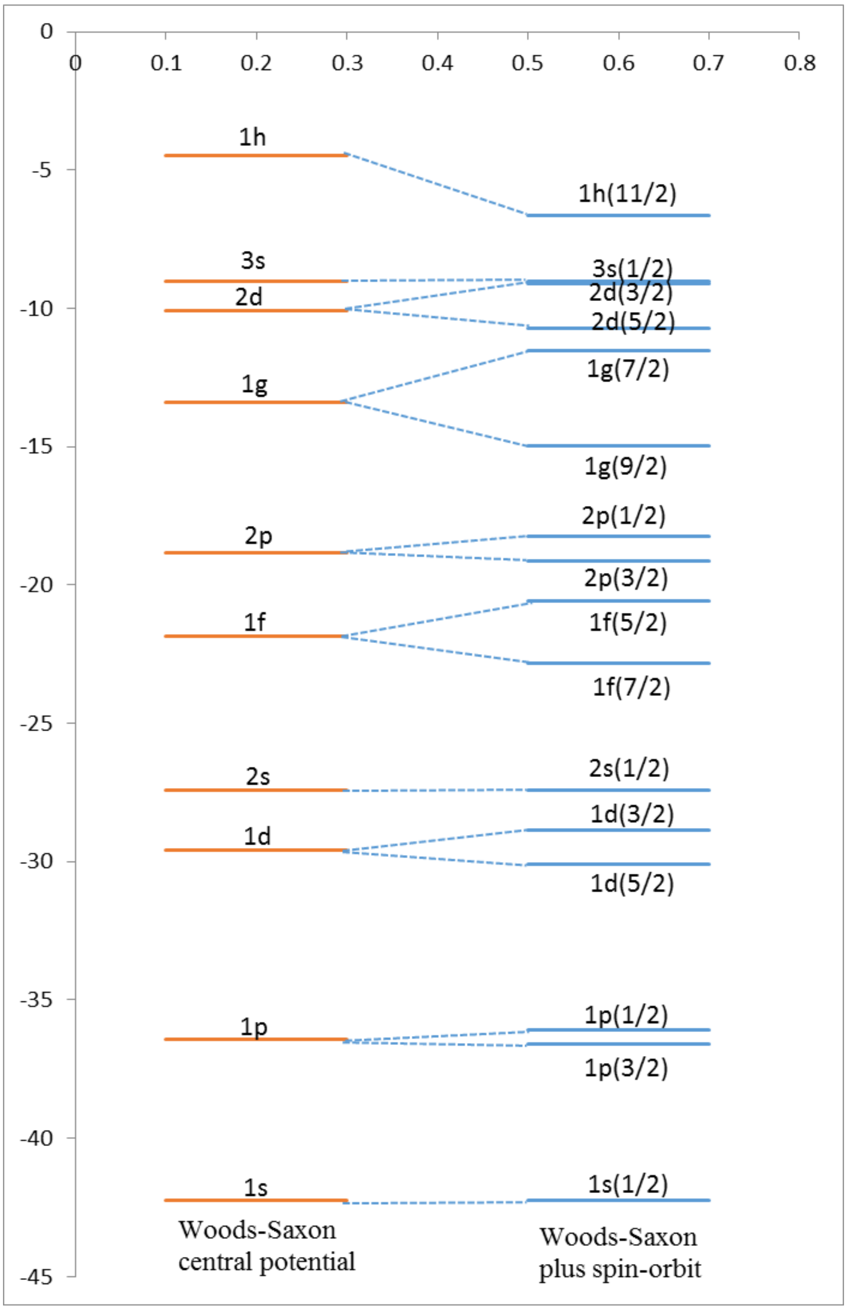

Figure 1 Neutron single-particle energy levels in ^{118}Sn

According to our results, it is found that the attractive interaction strength for the higher orbital angular momentum in each particle state is weaker. It is also known that the attractive interaction strength which possess the total spin J=l+s is stronger than that having J=l-s. We also found that the wave functions of higher orbital angular momentum states shift to the horizontally right. Thus it is also seen that the single-neutron wave functions for J=l+s are more shifted to the outer region than that having spin state J=l-s. Therefore, it can be said that the grater angular momentum, the probability of find the nuclear bound state becomes smaller. From this calculation, we can know the last neutron state which can be bound in the nucleus. In^{118}Sn, nuclear bound states may exist in $1s_{1/2}$, $1p_{3/2}$, $1p_{1/2}$, $1d_{5/2}$, $1d_{3/2}$, $2s_{1/2}$, $1f_{7/2}$, $1f_{5/2}$, $2p_{3/2}$, $2p_{1/2}$, $1g_{9/2}$, $1g_{7/2}$, $2d_{5/2}$, $2d_{3/2}$, $3s_{1/2}$, and $1h_{11/2}$ .So it can be said that no neutron can exist upper $1h_{11/2}$ state in ^{118}Sn nucleus.

Table 1 Neutron single particle energy levels by Woods-Saxon potential

Single-particle state	Single-particle energy(MeV) (central term)	Single-particle state	Single-particle energy(MeV) (central term+ L-S coupling term)	Experimental Results(1)
1s	-42.258	$1s_{1/2}$	-42.26	
1p	-36.4415	$1p_{3/2}$	-36.61	
		$1p_{1/2}$	-36.098	
1d	-29.576	$1d_{5/2}$	-30.08	
		$1d_{3/2}$	-28.848	
2s	-27.4145	$2s_{1/2}$	-27.4145	
1f	-21.845	$1f_{7/2}$	-22.81	
		$1f_{5/2}$	-20.598	
2p	-18.823	$2p_{3/2}$	-19.12	
		$2p_{1/2}$	-18.235	
1g	-13.415	$1g_{9/2}$	-14.969	
		$1g_{7/2}$	-11.539	9.92±1
2d	-10.09	$2d_{5/2}$	-10.736	9.61±0.96
		$2d_{3/2}$	-9.11	7.57±0.80
3s	-9.026	$3s_{1/2}$	-9.026	8.39±0.84
1h	-4.4665	$1h_{11/2}$	-6.664	7.13±0.71

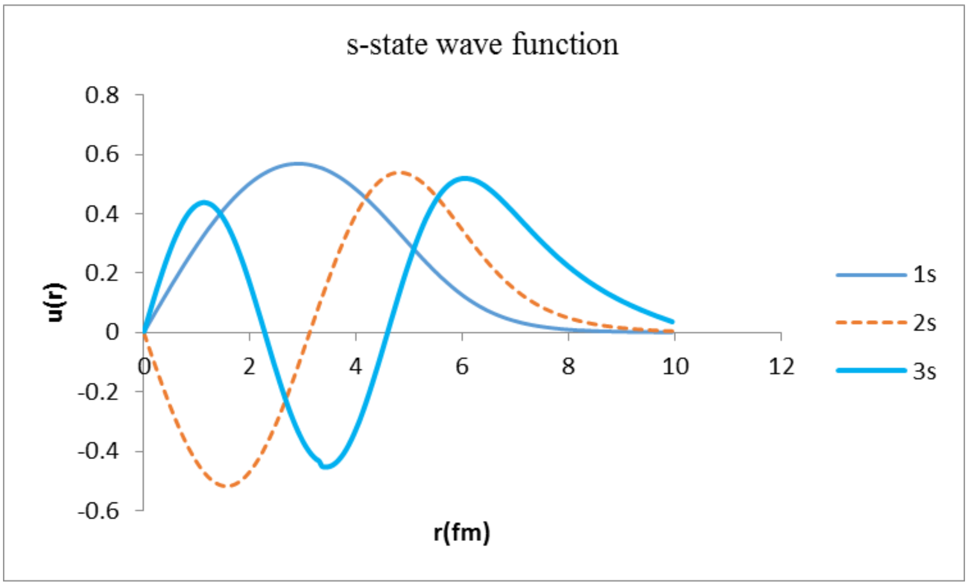

Figure 2 Neutron s-states wave function with Woods-Saxon spin-orbit potential for^{118}Sn

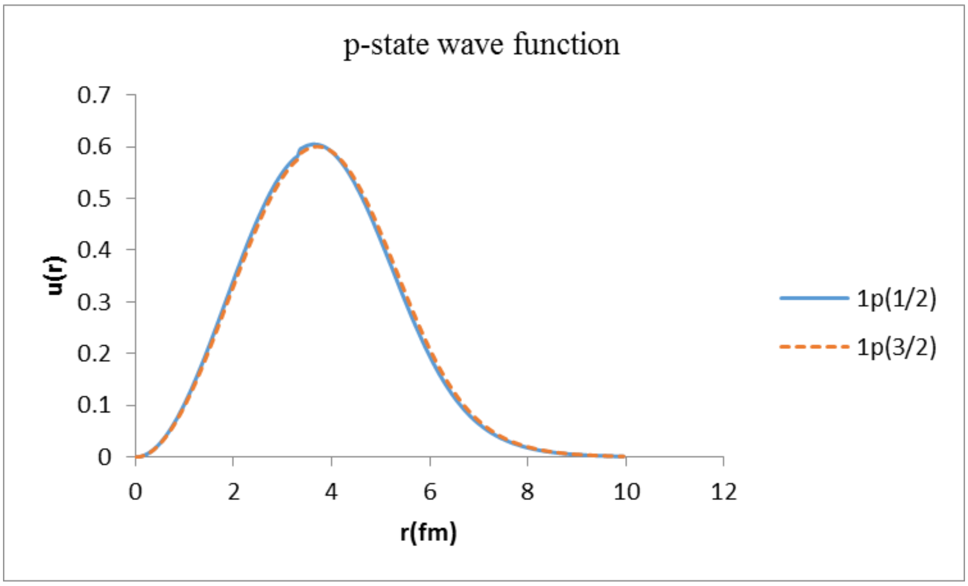

Figure 3 Neutron p-states wave function with Woods-Saxon spin-orbit potential for^{118}Sn

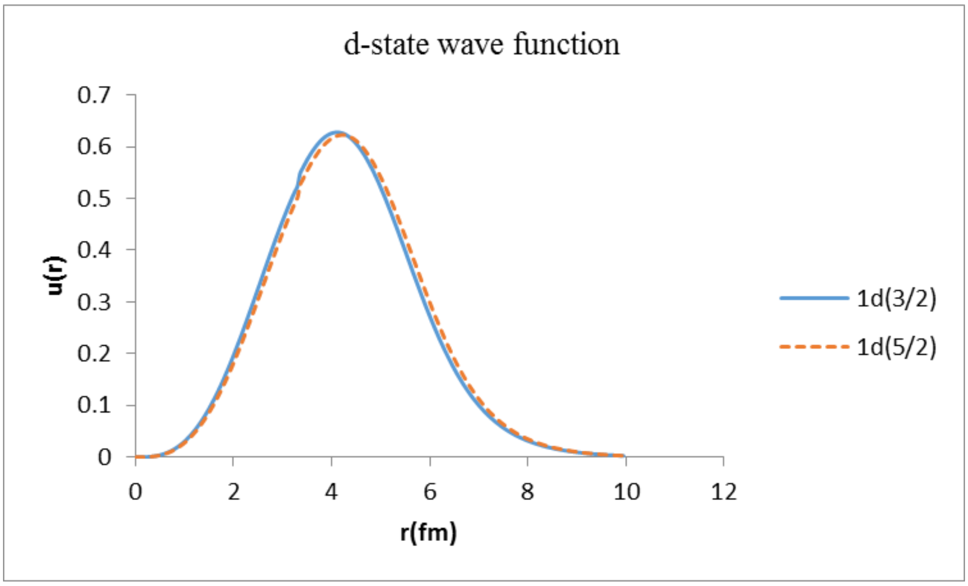

Figure 4 Neutron d-states wave function with Woods-Saxon spin-orbit potential for^{118}Sn

Conclusion

Our calculated neutron single particle energy of ^{118}Sn are a little smaller than the experimental results (1). One reason of this case is that the imaginary potential that was taken from the systematic of global parameter of conventional optical model potential and the force parameters of its volume and surface parts are neglected in our calculation. For large even-even nuclei, the paring interaction in nuclei for different subshells and the core excitation potential should be taken into account in the interaction term. If we would consider this system by including these factors in the interaction, it will be suggested that more accurate value of the neutron single particle energy of ^{118}Sn which would be fit to the experimental data.

Acknowledgement

I thank to Professor Dr Shwe Sin Aung, Head of Department of Physics, Monywa University, for her encouragement and permission. I would like to thank Dr khin Khin Win, Professor and Head, Department of physics, University of Yangon, for her permission and edition for this paper. I am grateful to Dr Theingi, Associate Professor, Department of Physics, University of Distance Education, Mandalay, for her advice and useful discussions.

References

Bespalova, O. V. et al., (2007) **“**Analysis of Single-Particle Energies of Doubly Magic ^{100,132}Sn nuclei within the Dispersive Optical Model.” Vol. 71. No. 3, pp. 448-450

Bespalova, O.V. et al., (2007) “Calculation of Single-particle Energies of bound Nucleon States in Nuclei with 40 ≤A≤ 208 Using Global Parameters of Dispersive Optical Model Potential.” Bulletin of the Russian Academy of Sciences: Physics, 2007, Vol. 71, No. 3, pp. 423-427.

Imasheva, L .et al., (2016) “Nucleon pairing in Sn isotopes” EPJ Web of Conferences **107**, 0 04 05

Schubart, R. et al., (1995) “Shell model structure at ^{100}Sn-The nuclides ^{98}Ag, ^{103}In, and ^{104,105} Sn.” Z. Phys.A, vol. 352, p.385

Smith, A.B., (1995) “Fast-neutron scattering at Z=50: tin.” Nucl. Phys. A,vol. 589, p. 201.

J. Myanmar Acad. Arts Sci. 2020 **Vol. XVIII.No.2B**

NATURAL RADIONUCLIDES IN AGRICULTURAL SOIL IN MANDALAY AREA

Thet Thet Cho[1], Kalyar Thwe[2], Kathi Nwe[3]

Abstract

Natural radionuclides are present in every human environment such as earth crust, water, air, foods and even our own body contains naturally occurring radioactive materials. In this study, the radioactivity levels of ^{226}Ra,^{232}Thand ^{40}K in the agriculturalsoil samples in Mandalay area were determined by using HPGe detector at Department of Physics, University of Mandalay. The activity concentration were found in the range of 8.329 Bq/kg to 33.42 Bq/kg for ^{226}Ra, 16.25Bq/kg to 72.38Bq/ kg for ^{232}Th and 363.4 Bq/kg to 488.3 Bq/kg for ^{40}K, respectively. The radiological hazard parameters for ^{226}Ra, ^{232}Th and ^{40}K in were also evaluated. The radium equivalents activity (Ra_{eq}) and the absorbed dose rate (D) are 107.9Bq/kg and 50.72nGy/h. Obtained results were compared and discussed with internationally recommend values.

Keywords: Radionuclides, Soil, Gamma Ray Spectroscopy, radiological hazard parameters.

Introduction

Radioactive elements occur naturally in the earth's rocks, soils, and water in varying concentrations. Naturally occurring radionuclides contribute to a major portion to the effective dose of the worldwide population. Natural radionuclides in soil generate a significant component of the background radiation exposure of the population. The natural radioactivity in soil mainly comes from the uranium and thorium decay series and potassium. Radiation has always been present and is all around us in many forms. Life has evolved in a world with significant levels of ionizing radiation, and our bodies have adapted to it.

Many radioisotopes are naturally occurring, and originated during the formation of the solar system and through the interaction of cosmic rays with molecules in the atmosphere. The earth’s outer atmosphere is continually bombarded by cosmic radiation. Usually, cosmic radiation consists of fast moving particles that exist in space and originate from a variety of sources, including the sun and other celestial events in the universe. Some ionizing radiation will penetrate the earth’s atmosphere and become absorbed by humans which results in natural radiation exposure. The composition of the earth’s crust is a major source of natural radiation. The main contributors are natural deposits of uranium, potassium and thorium which, in the process of natural decay, will release small amounts of ionizing radiation. Uranium and thorium are found essentially everywhere. Trace amounts of radioactive minerals are naturally found in the contents of food and drinking water. For instance, vegetables are typically cultivated in soil and ground water which contains radioactive minerals. Once ingested, these minerals result in internal exposure to natural radiation.

Detection of radioactivity, analysis of radioactive samples, and deciphering data require sophisticated devices and techniques. One of the popular techniques being used today for low-background radio-analysis is the gamma-ray spectrometry. Three types of gamma ray detectors can be used for gamma ray analysis: thallium doped sodium iodide crystal NaI(Tl) scintillation

---

[1] Dr, Assistant Lecturer, Department of Physics, University of Mandalay

[2] Dr, Professor, Department of Physics, University of Mandalay

[3] Dr, Professor, Department of Physics, Mandalay University of Distance Education.

detector, lithium drifted crystal of purified germanium detector, and High-Purity Germanium (HPGe) detector. Among them, HPGe- detector is the most sensitive and efficient device which is widely used in determining activity of radionuclides from higher order down to pCi level. Assessing the effects of radiation exposure based on the knowledge of radionuclide distribution and radiation levels in the environment is important for public health protection. M. S. Jaffar *et al.*, were studied the specific activities of different natural radio nuclides in the soil samples from different locations in the middle and northern parts of Iraq by using gamma-ray spectrometry. In 2016, G. Alzubaidi *et al* .,were determined the activity concentrations of naturally occurring radio nuclides ^{226}Ra, ^{232}Th, and ^{40}K in agricultural and virgin soil samples randomly collected from Kedah, north of Malaysia. In this study, the radioactivity levels and radiation hazard of ^{226}Ra, ^{232}Th and ^{40}K in the agricultural soil samples in Mandalay area were determined by using aHPGe detector at Department of Physics, University of Mandalay.

Material and Method

2.1 Sample Collection and Preparation

Soil is not only the key nutrient bearing environment for plant life but also a supplier of many pollutants to plants because plants can uptake toxic substances through their roots from soils. In this experiment twelve samples of soil samples were collected from different agricultural fields in Mandalay Division. All soil samples were collected from top 0 to 5cm deep soil layer. Collected soil samples were purified by removing all contaminants such as rocks, woods, metals, dry roots, grasses, vegetation residual parts. The map of sampling area was shown in Fig. (1). Table (1) shows the sample codes and location of analyzed soil samples. The collected samples were put in vacuum black plastic bags directly after collection to prevent from atmospheric humidity. And then all these samples were dried at room temperature about two weeks. After drying all collected soil samples were powdered by using a pestle and mortar prior to analysis. Fine quality of the sample is obtained by using 200 mesh sieves. Then 500 grams of each sample were weighed and transferred in sealed cylindrical containers to analysis.

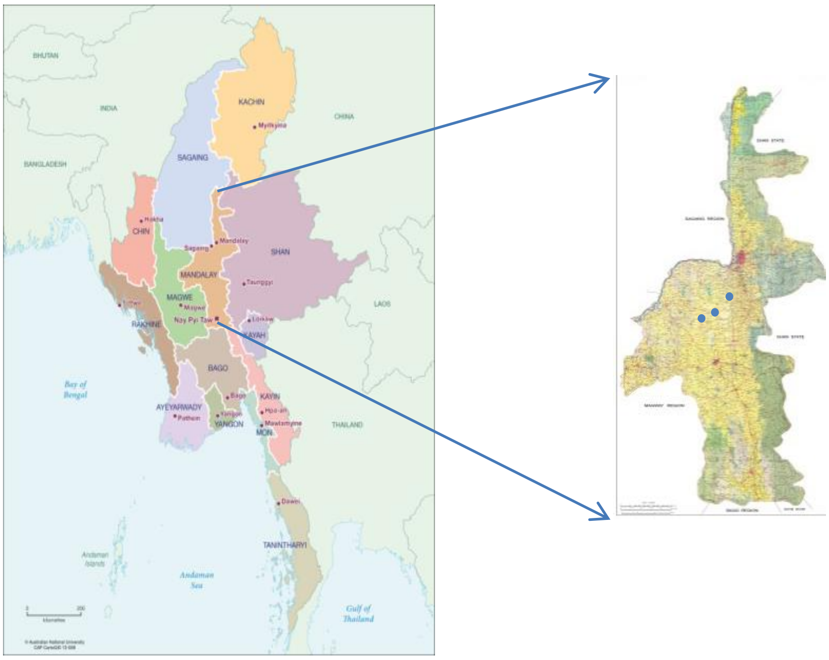

Figure 1 The photograph of map of sampling area.

Table 1 The sample codes and sample location of analyzed soil samples

Sr No	Sample Code	Sample Name
1	RSS1	Soil sample from rice field near Myotha
2	RSS2	Soil sample from rice field near Shan Lay Kyun
3	RSS3	Soil sample from rice field near Latt Kaung
4	BSS1	Soil sample from bean field near Myotha
5	BSS2	Soil sample from bean field near Shan Lay Kyun
6	BSS3	Soil sample from bean field near Latt Kaung
7	SSS1	Soil sample from spinach field near Myotha
8	SSS2	Soil sample from spinach field near Shan Lay Kyun
9	SSS3	Soil sample from spinach field near Latt Kaung
10	PSS1	Soil sample from peanut field near Myotha
11	PSS2	Soil sample from peanut field near Shan Lay Kyun
12	PSS3	Soil sample from peanut field near Latt Kaung

2.2 Radioactive Measurement

Radioactivity in soil samples were measured by gamma ray spectrometry system from University of Research Center in Mandalay University. Gamma-ray spectrometry is one of the most accepted and widely used techniques for the detection and analysis of radioactive materials for a wide range of activity. The gamma ray spectrometry system consists of a High Purity Germanium (ORTEC model GMX10P4-70-RB-SMN) detector, detector shield with lead, high voltage power supply, cooling system (electrically cooled by X COOLER 3), a preamplifier, digital signal processor, a multichannel analyzer system with Gamma Vision-32 software installed in PC and data readout devices. Before the measurement, the energy calibration for the detection system was done using the standard sources (^{133}Ba, ^{60}Co, ^{22}Na and ^{137}Cs) of known energies. The energy calibration for the HPGE detector is shown in Table (2) and the energy calibration curve is also shown in Fig.(3).The efficiency calibration curve was used by using standard reference material IAEA 448 in this measurement. All each samples and background measurements were taken 10800 s for analysis measurements. The photograph of HPGe detector was shown in Fig.(3).

Table 2 Energy calibration for HPGE detector.

Radionuclides	Channel No.	Energy (keV)
^{133}Ba	427.8	81
^{133}Ba	1459.84	276.39
^{133}Ba	1599.6	302.73
^{133}Ba	1880.78	356.02
^{133}Ba	2028.2	383.85
^{22}Na	2700.82	511
^{137}Cs	3497.26	661.66
^{60}Co	6201.54	1173.23
^{22}Na	6737.18	1274.54
^{60}Co	7043.38	1332.5

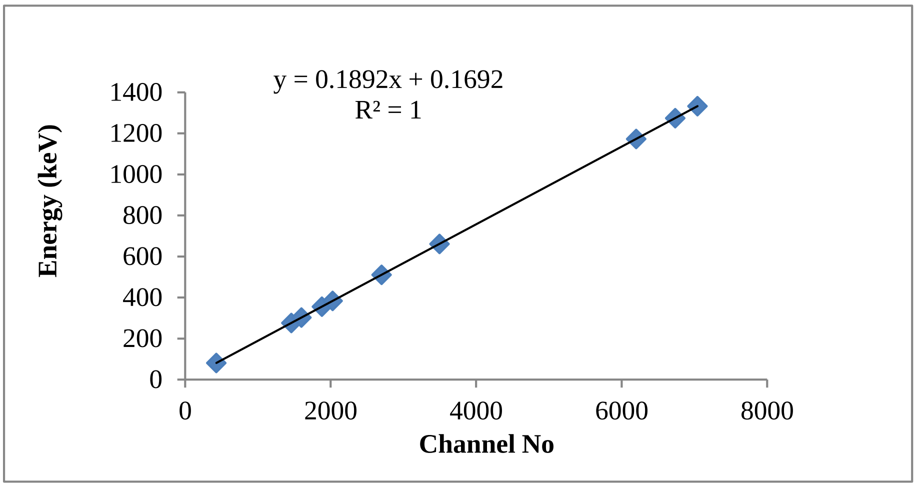

Figure 2 Energy calibration curve for HPGe detector

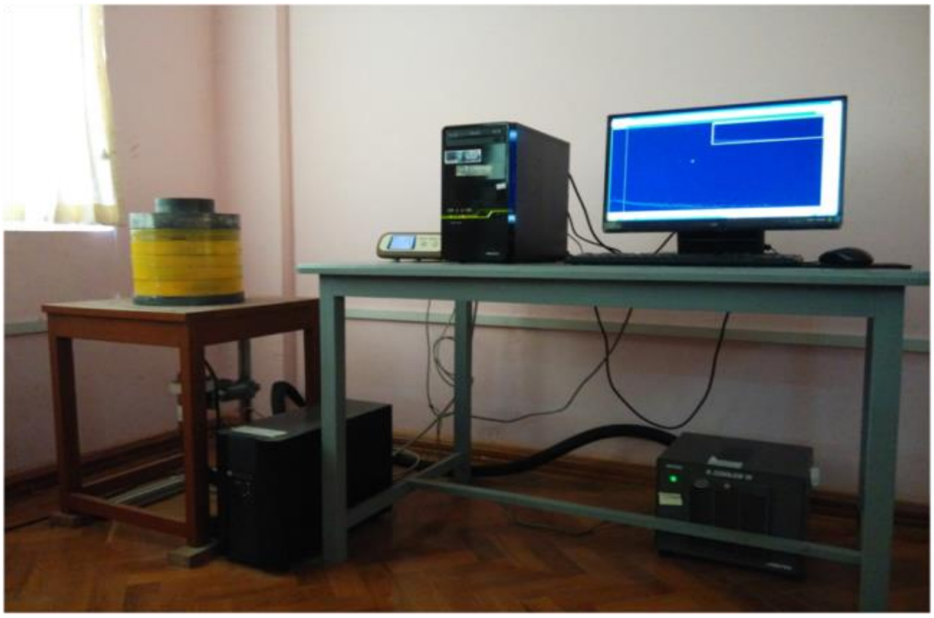

Figure 3 The photograph of HPGe detector

2.2.1 Analytical Methods

The gamma activity was calculated based on the measured efficiency of the detector from the following equation.

$$A = \frac{C}{\varepsilon(E) \times P_\gamma \times W}$$

where, A is the activity in $Bqkg^{-1}$; C is the net gamma counting rate in countper second (cps); ε(E) is the efficiency of the detector at energy E (keV); Pγ is the photon emission probability at energy E (keV) intensity of the radionuclide and W is the dry mass of the sample.

2.2.2 Radium Equivalent Activity

It is significant to evaluate the gamma-ray radiation hazards of soil to human beings. The gamma-ray radiation hazards due to the natural radionuclides ^{226}Ra, ^{232}Th, and ^{40}K were assessed by various radiation hazard indices. Uniformity with respect to exposure to radiation has been defined in terms of radium equivalent activity (Ra_{eq}) in Bq kg^{-1} to compare the specific activity of materials containing different amounts of ^{226}Ra,^{232}Th and ^{40}K. It is calculated through the following relation

$$Ra_{eq} = A_{Ra} + 1.43\, A_{Th} + 0.077 A_{K}$$

where, A_{Ra}, A_{Th} and A_{K} are the activity concentrations of ^{226}Ra, ^{232}Th and ^{40}K in Bq kg^{-1}, respectively.

2.2.3 Absorbed Dose Rates

The external outdoor absorbed gamma dose rates due to terrestrial γ- rays from the nuclides ^{226}Ra, ^{232}Th and ^{40}K at 1 m above the ground level was calculated as

$$D= 0.461\, A_{Ra}+0.623\, A_{Th}+0.0414\, A_{K}$$

where, A_{Ra}, A_{Th} and A_{K} are the activity concentrations of ^{226}Ra, ^{232}Th and ^{40}K in Bq kg^{-1}, respectively[4].

Result and Discussion

Soil samples collected from the different agricultural soil were analyzed by using aHPGe-gamma-ray spectrometer to determine the activity concentration for natural radionuclides ^{226}Ra, ^{232}Th and ^{40}K.The background spectrum and gamma ray spectrum were shown in Fig. (4) to Fig. (7).The average activity concentrations of natural radionuclides in the soil samples in different location are shown in Table (3).The average concentrations in the soil samples in different crop soil sample were shown in Fig. (8) to Fig. (11). According our results, the activity concentration values are (8.329, 8.532, 10.55, 12.47, 12.69, 14,20, 17,69, 26.95, 27.72, 28,02, 28.12 and 33.42) $Bqkg^{-1}$ for ^{226} Ra, (16.25, 20.00, 23.87, 28.22, 35.11, 36.49, 36.82, 43.35, 44.17, 57.88, 65.30 and 72.38) $Bqkg^{-1}$ for ^{232}Th and (363.4, 367.8, 370.9, 379.4, 400.1, 406.7, 408.7,408.7, 439.0 447.9, 453.0 and 488.3) $Bqkg^{-1}$ for ^{40}K in rice soil, bean soil, spinach soil and peanut soil samples, respectively. The average activity concentrations are 19.06± 9.11 $Bqkg^{-1}$ for ^{226}Ra, 39.98 ± 17.70$Bqkg^{-1}$ for^{232}Th, 411.2 ± 39.04$Bqkg^{-1}$ for^{40}K, respectively. The variation of activity concentration with location was presented in Table (4). The variation of average activity concentration with location was presented in Fig. (12). In order to assess the health effects, the radiation hazards such as radium equivalent activity (Ra_{eq}), absorbed dose rate (D), have been calculated from the activity of nuclides ^{226}Ra, ^{232}Th, ^{40}K. The calculated radium equivalent activity data and the absorbed dose rates values are shown in Table (5). The radium equivalent values for the soil samples varied in the range from 72.32$Bqkg^{-1}$ to 165.43$Bqkg^{-1}$. The radium equivalent values in different soil sample were shown in Fig. (13). The absorbed dose rate in different soil samples were shown in Fig. (14).In the present study, the absorbed dose rates due to ^{226}Ra, ^{232}Th and ^{40}K in the soil samples varied from 35.13 $nGyh^{-1}$ to 76.23$nGyh^{-1}$. Comparison of absorbed dose rate in different location are shown in Table (6).

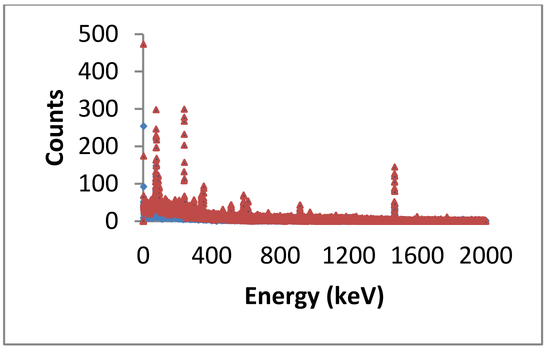

Figure 4 The gamma ray spectrum of soil RSS1 sample with background.

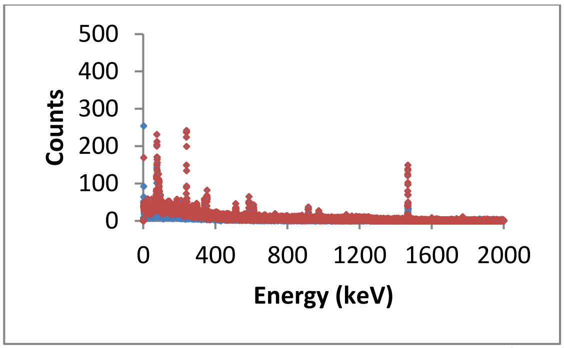

Figure 5 The gamma ray spectrum of soil BSS12 sample with background

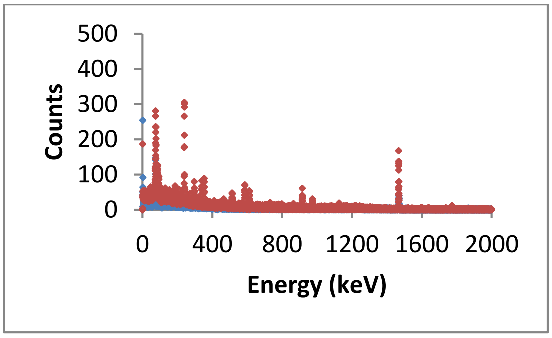

Figure 6 The gamma ray spectrum of soil SSS1sample with background

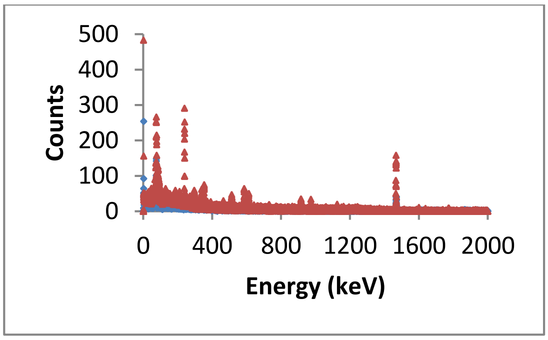

Figure 7 The gamma ray spectrum of soil PSS1 sample with background

Table 3 Activity concentration of natural radionuclide in the soil sample

Sample Name	**Code**	**Activity Concentration (Bq/kg)**		
		^{226}Ra	**^{232}Th**	**^{40}K**
Rice soil	RSS1	12.69	35.11	363.4
	RSS2	10.55	43.35	367.8
	RSS3	28.12	72.38	439
Bean soil	BSS1	8.329	28.22	370.9
	BSS2	28.02	57.88	488.3
	BSS3	12.47	20.00	408.7
Spanisch soil	SSS1	33.42	36.49	406.7
	SSS2	26.95	23.87	408.7
	SSS3	27.72	65.3	400.1
Peanut soil	PSS1	14.2	16.25	453.0
	PSS2	17.69	36.82	379.4
	PSS3	8.532	44.17	447.9

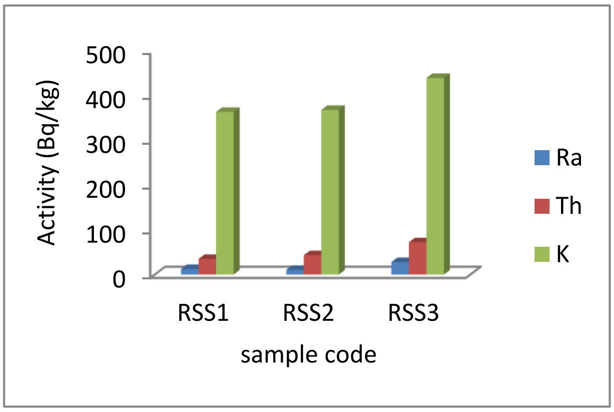

Figure 8 Activity concentration of radionuclide in the rice soil sample

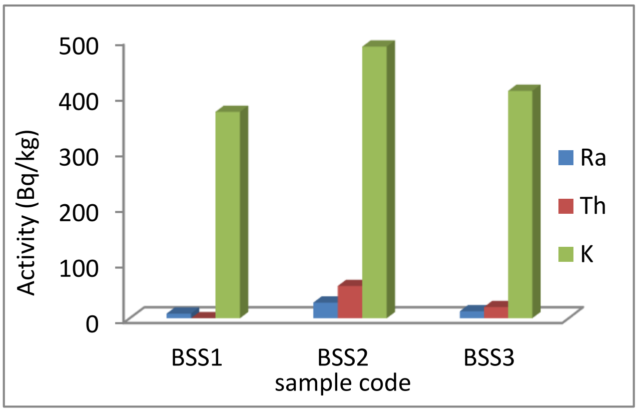

Figure 9 Activity concentration of radionuclide in the bean soil sample

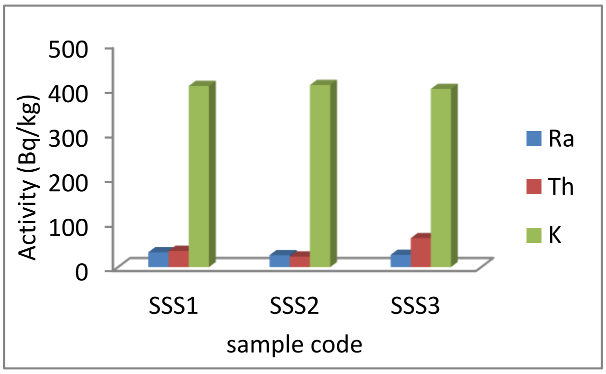

Figure 10 Activity concentration of radionuclide soil sample

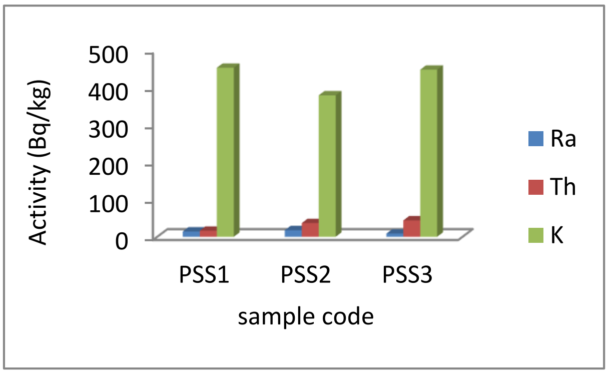

Figure 11 Activity concentration of in the spinach radionuclide in the peanut soil

Table 4 Average activity concentration in different location.

Sample location	**Average activity concentration (Bq/kg)**		
	^{226}Ra	**^{232}Th**	**^{40}K**
S1	17.16±11.10	29.02±9.248	398.5±40.95
S2	20.8±8.26	40.48±14.14	411.1±54.29
S3	19.21±10.18	50.46±23.58	423.9±23.10

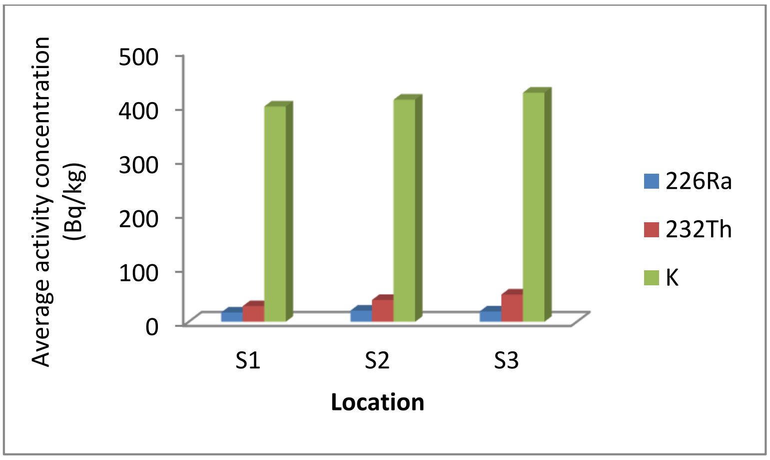

Figure 12 Average activity concentration in different location.

Table 5 Radium equivalent activities and absorbed dose rate in soil samples

Sample Name	Ra_{eq}(Bq/kg)	D (nGy/h)
RSS1	90.88	42.77
RSS2	100.86	47.10
RSS3	165.43	76.23
BSS1	77.24	36.78
BSS2	148.39	69.19
BSS3	72.54	35.13
SSS1	116.92	54.98
SSS2	92.55	44.22
SSS3	151.91	70.02
PSS1	72.32	35.42
PSS2	99.56	46.80
PSS3	106.18	49.99

Table 6 Comprison of absorbed dose rate in different location.

Countries	Absorbed dose rate ($nGyh^{-1}$)	Methodology
Romania[5]	81	Soil analysis using gamma spectrometry
Nigeria[6]	128	Analysis of rocks using gamma spectrometry
China[5]	69	Soil analysis using gamma spectrometry
Chittagong (Bangladesh)[7]	75	Soil analysis using gamma spectrometry
India[8]	95.2	Soil analysis using gamma spectrometry
World average[5]	55	-
Present Study	50.72	Soil analysis using gamma spectrometry

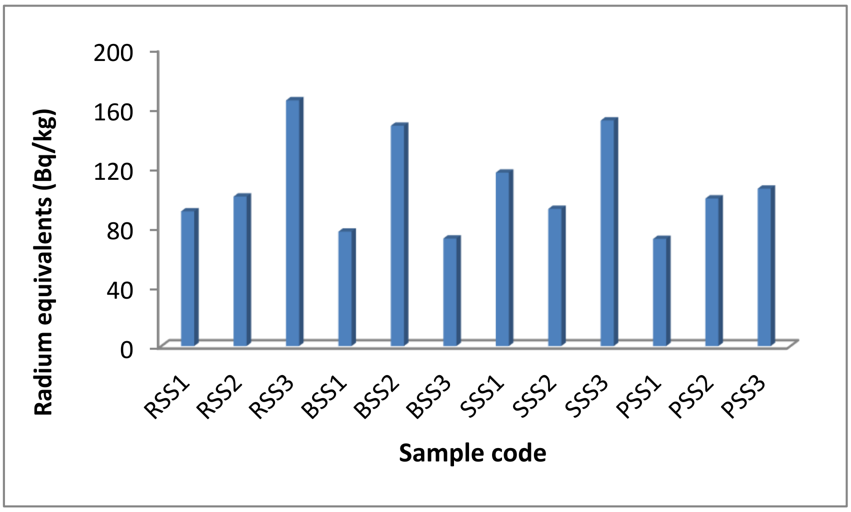

Figure 13 Radium equivalents activity in different soil samples.

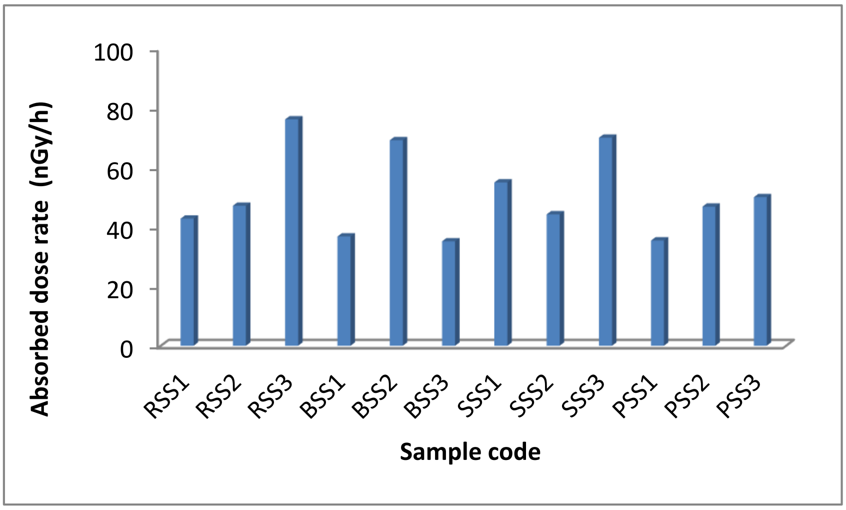

Figure 14 Absorbed dose rate in different soil samples.

Conclusion

In conclusion, the average activity concentrations are 19.06± 9.1 Bqkg^{-1} for ^{226}Ra, 37.64 ± 18.1 Bqkg^{-1} for ^{232}Th, 411.2 ± 39.0 Bqkg^{-1} for ^{40}K. This study observed that the average ^{40}K activity concentration obviously exceeds the values of ^{226}Ra and ^{232}Th in the study places. The average natural activity values of all analysis samples were less than the world average value for ^{226}Ra, ^{232}Th and ^{40}Kactivity. The calculated average radium equivalent activity value is 107.9 Bqkg^{-1}. This average value is below the allowable limit 370 Bqkg^{-1}recommended by the International Atomic Energy Agency (IAEA). The average absorbed dose rate value is 50.72 nGyh^{-1}in this study. These values are comparable to the world average of 55 nGyh^{-1}. The reported data in the present work can be considered as base values for distribution of natural radionuclides in the studied region.

Acknowledgements

We express our thanks to Dr Thida Win, Ractor, University of Mandalay, her permission and encouragement to conduct this research work.

References

Canadian Nuclear Safety commission “ Introduction to Radiation ”,2012.

G.Alzubaidi et al., J. Sci. World. **26**(2016)

M. I. Chowdhury et al., Appl. Radiat. Isot.,**51** (1999) 747-755.

M.S.Jaafar et al., Elixir Chem. Phys.**53** (2012) 12079-12081

O.S. jayi et al ., Health Phy.. **79** (2000)74-78.

S.Selvasekarapandian et al., J.Radional. Nucl. Chem., **252** (2002) 74-78

UNSCEAR, Explosure from natural sources of radiation. New York (1988)

UNSCER, Sources and Effects of Ionizing Radiation. (2000)

J. Myanmar Acad. Arts Sci. 2020 **Vol. XVIII.No.2B**

INVESTIGATION ON MISSING MASS SPECTRUM OF D (K^-, n) Λ (1405) REACTION

Win Win Maw[1], Thida Wint[2], Khin Swe Myint[3], Yoshinori Akaishi[4],
Toshimitsu Yamazaki[5]

Abstract

The aim of this research work is to investigate the missing mass spectrum of D (K^-, n) Λ (1405) reaction process of J-PARC (Japan Proton Accelerator Research Complex) E31 experiment. This experiment which was conducted at J-PARC with 1.0 GeV/c incident momentum of K^- on target deuterium. This reaction is expected to enhance a virtual $\bar{K}N$ scattering process, where a K^- beam kicks a neutron out of the deuteron target in a forward angle and is slowing down to form a Λ(1405) with a residual nucleon. We have calculated the missing mass spectrum of D (K^-, n) Y reaction with Green's function method by using YA (Yamazaki and Akaishi) potential for $\bar{K}N$ interaction. It is observed that the missing mass spectrum of the D (K^-, n) Y reaction at a neutron forward angle has two peaks, one below the K^-p threshold and another above the threshold. The former peak represents Λ (1405) quasi-bound state while the latter is a quasi-free K^-p peak.

Key words: virtual $\bar{K}N$ scattering, missing mass, threshold, quasi-free, quasi-bound.

Introduction

An antikaon ($\bar{K}$) and a nucleus may form a bound state (a kaonic nucleus), due to the strong attraction between $\bar{K}$ and nucleon in an isospin, I = 0 state. Λ (1405) resonance state is nominally accepted as a bound state of K^-p system which lies in the continuum region of π Σ, having strangeness, S = -1, total charge, Q = 0, isospin, I = 0 and spin parity, $J^p = 1/2^-$.

The PDG value of the mass and width of this Λ (1405) resonance state or often known as Λ* is $1405.1^{+1.3}_{-1.0}$ MeV/c^2 and 50.5 ± 2.0 MeV (Particle Data Group K. A. Olive *et al.*, (2014)) with 27 MeV binding energy with respect to $\bar{K}N$ threshold.

However, chiral unitary model claims that Λ (1405) may have two pole structure; one is mainly coupled to πΣ state and the other is to $\bar{K}N$ state which are located at different positions, (1390-132i) MeV and (1426-32i) MeV, respectively (T. Hyodo and A. Weise, (2008)). As a consequence, the resonance position of the Λ (1405) is 1420 MeV/c^2 and the binding energy is as shallow as 15 MeV.

In K^-p reactions at 4.2 GeV/c, the mass and width of Λ (1405).resonance were obtained to be 1400.5 ± 4.0 MeV/c^2 and 50.0 ± 2.0 MeV from production of Λ (1405) (R. J. Hemingway, (1985)) by Dalitz and Deloff (R. H. Dalitz and A. Deloff, (1991)). It is interpreted as a quasi-bound state of $\bar{K}N$ coupled with continuum stat of πΣ. Esmaili *et al.*,(J. Esmaili, Y. Akaishi and T. Yamazaki, (2010), (2011)) analyzed old bubble-chamber of stopped-K^- on ^{4}He (B. Riley *et al.*,

---

[1] Dr, Assistant lecturer, Physics Department, Mandalay University, Mandalay, Myanmar

[2] Associate Professor, Physics Department, University of Distance Education Mandalay, Mandalay, Myanmar

[3] Emeritus Professor, Physics Department, Mandalay University, Mandalay, Myanmar

[4] Dr, Professor, College of Science and Technology, Nihon University, Chiba, Japan and RIKEN Nishina Center, Saitama, Japan

[5] Professor, Department of Physics, University of Tokyo, Bunkyo-ku, Tokyo 113-0033, Japan

(1975)) with a resonance capture process, and found the best-fit value of mass and width for the Λ (1405) are $1405.1^{+1.3}_{-1.0}$ MeV/c^2 and $24.0^{+4.0}_{-3.0}$ MeV.

Maryam *et al*. (M. Hassanvand, Y. Akaishi, T. Yamazaki, (2015)) have calculated the $\Lambda(1405) \to (\pi\Sigma)^0$ invariant mass spectra produced in the reaction $K^- + p \to \Sigma^+(1660) + \pi^-$, followed by $\Sigma^+(1660) \to \Lambda(1405) + \pi^+ \to \Sigma\pi + \pi^+$, processes at p(K$^-$) = 4.2 GeV/c.

An experiment which has reported Λ (1405) resonance state in the reaction $K^- p \to \Sigma\ 3\pi$ at 1.15 GeV/c was conducted by Alston *et al*., (R.H. Alston *et al*., (1961)). The values of mass and width of this resonance state are 1405 MeV/c^2 and 20 MeV, respectively.

Another experiment in the reaction of $\pi^- p \to \Sigma\ \pi\ K$ at 1.69 GeV/c π$^-$ beam has been reported for searching Λ (1405) resonance state by Thomas *et al.*, (D.W. Thomas *et al.*,(1977)). The mass and width of this resonance state from this experiment are ~1405 MeV/c^2 and 45 to 55 MeV, respectively.

Momentum Transfer of Emitted Neutron

First, the momentum transfer of the emitted neutron which is an important for Λ (1405) formation processes are calculated. The momentum transfer of emitted neutron (n$_1$) and product kaon (K_1^-) from the elementary process n (K$^-$, n$_1$) K_1^- are calculated by using Newton-Raphson method. Then, the missing mass of $K^- p$ is calculated after having obtained the momentum transfer of neutron (n$_1$).

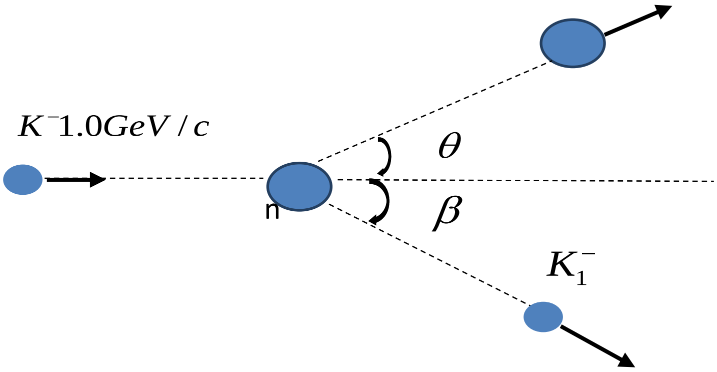

Figure 1 Schematic diagram of the elementary process

Elementary process is

$$K^- + n \to n_1 + K_1^- \qquad (1)$$

By the law of conservation of energy, we have

$$E_{K^-} + E_n = E_{n_1} + E_{K_1^-}$$

where,

$$E = \sqrt{p^2c^2 + m^2c^4} \qquad (2)$$

Equation (2) becomes,

$$\sqrt{p_{K^-}^2 c^2 + m_{K^-}^2 c^4} + \sqrt{p_n^2 c^2 + M_n^2 c^4} = \sqrt{p_{n_1}^2 c^2 + M_n^2 c^4} + \sqrt{p_{K_1^-}^2 c^2 + m_{K^-}^2 c^4} \tag{3}$$

By the law of momentum conservation,

$$\vec{p}_{K^-} + \vec{p}_n = \vec{p}_{n_1} + \vec{p}_{K_1^-} \tag{4}$$

$$\vec{p}_{K_1^-} = \vec{p}_{K^-} - \vec{p}_{n_1}$$

$$p_{K_1^-}^2 = p_{K^-}^2 + p_{n_1}^2 - 2p_{K^-} p_{n_1} \cos(\theta) \tag{5}$$

By substituting equation (5) in to equation (3), we obtain

$$\sqrt{p_{K^-}^2 + m_{K^-}^2} + M_n = \sqrt{p_{n_1}^2 + M_n^2} + \sqrt{(p_{K^-}^2 + p_{n_1}^2 - 2p_{K^-} p_{n_1} \cos(\theta)) + m_{K^-}^2}\ .$$

$$\sqrt{p_{n_1}^2 + M_n^2} + \sqrt{(p_{K^-}^2 + p_{n_1}^2 - 2p_{K^-} p_{n_1} \cos(\theta)) + m_{K^-}^2} - \sqrt{p_{K^-}^2 + m_{K^-}^2} - M_n = 0 \tag{6}$$

The momentum of emitted neutron (n_1) can be obtained by solving the equation (6) by using Newton-Raphson Method. This method is numerical method applied to find the root of a function f (p_{n1}) equal to zero.

Missing mass formula for D (K^- , n) Y

The missing mass formula for D (K^-, n) Y reaction is calculated. If we know the emitted neutron momentum, we can get the missing mass spectrum.

$$K^- + D \rightarrow n + Y \qquad (Y = \Lambda^* \text{ or } K^- + p) \tag{7}$$

$$E_Y^2 = P_Y^2 c^2 + M_Y^2 c^4 \tag{8}$$

$$M_Y^2 c^4 = E_Y^2 - P_Y^2 c^2 \tag{9}$$

For a system Y, missing mass is defined as

$$M_Y c^2 = \sqrt{E_Y^2 - P_Y^2 c^2} \tag{10}$$

By the law of conservation of energy,

Let $E_{init} = E_{K^-} + E_D$ and $E_n = E_{obs}$ (11)

$$E_{init} = E_{obs} + E_Y \tag{12}$$

$$E_Y = E_{init} - E_{obs} \tag{13}$$

By the law of conservation of momentum,

$$\vec{P}_{K^-} + \vec{P}_D = \vec{P}_n + \vec{P}_Y \tag{14}$$

Let $\vec{p}_{init} = \vec{p}_{K^-} + \vec{p}_D$ and $\vec{p}_n = \vec{p}_{obs}$

$$\vec{p}_{init} = \vec{p}_{obs} + \vec{p}_Y \tag{15}$$

$$\vec{p}_Y = \vec{p}_{init} - \vec{p}_{obs} \tag{16}$$

By substituting equation (13) and equation (16) into equation (10), the equation (10) becomes

$$M_Y c^2 = \sqrt{(E_{init} - E_{obs})^2 - (p^2_{init} + p^2_{obs} - 2P_{init}p_{obs}\cos(\theta))c^2} \tag{17}$$

We can get the missing mass spectrum by using the above formula.

Differential cross section for D (K$^-$, n) Λ (1405)

The differential cross section is the most important factor to determine the probability of the reaction. Therefore, we are going to determine the differential cross section and spectral function for D (K$^-$, n) Λ (1405) reaction. The differential cross section is defined as the transition rate per incident flux. According to the Fermi's Golden Rule, the transition rate W_{fi},

$$W_{fi} = \frac{2\pi}{\hbar}\left|T_{fi}\right|^2 \delta\left(E_i - E_f^{(n)}\right)\rho(E). \tag{18}$$

where, T_{fi} is the transition matrix element, $\delta\left(E_i - E_f^{(n)}\right)$ is the energy conservation term and $\rho(E)$ is the density of allowed states.

The expression for differential cross section with neutron momentum between $\vec{k}_n$ and $\vec{k}_n + d\vec{k}_n$ and with Λ (1405) momentum between $\vec{K}$ and $\vec{K} + d\vec{K}$ is written as follows:

$$d^6\sigma = \frac{L^3}{v_0}\frac{2\pi}{\hbar}\sum_n \delta(E_i - E_f^{(n)})(\frac{L}{2\pi})^3 d\vec{k}_n (\frac{L}{2\pi})^3 d\vec{K}\left|T_{fi}^{(n)}\right|^2. \tag{19}$$

where, $\frac{v_0}{L^3}$ = incident flux, incident kaon velocity, $v_0 = \frac{\hbar k_0 c^2}{E_0}$ and $\left(\frac{L}{2\pi}\right)^3 d\vec{k}_n \left(\frac{L}{2\pi}\right)^3 d\vec{K}$ = phase space.

The differential cross section contains per incident flux, energy conservation term, phase space and transition matrix element. First, we will calculate the transition matrix element.

Transition matrix element

We considered the elementary process of reaction $K^- + D \to n + \Lambda(1405)$

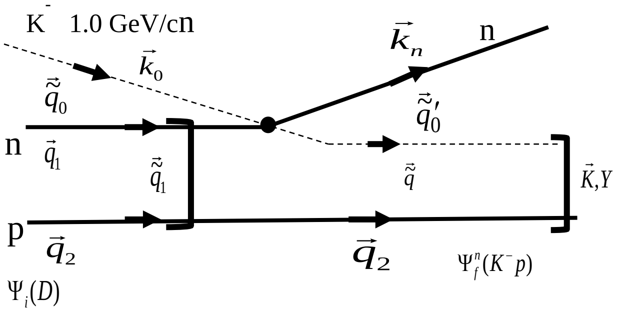

Figure 2 Schematic diagram of the reaction D (K$^-$, n) Λ (1405)

Transition matrix for D (K^- , n) Λ (1405) reaction can be described as follows:

$$T_{fi}^{(n)} = \left\langle \text{final state} \middle| T \middle| \text{initial state} \right\rangle . \tag{20}$$

$$T_{fi}^{(n)} = \left\langle \Psi_f^n \left(K^- p\right), \vec{K}, \vec{k}_n \middle| T \middle| \Psi_i (D), \vec{0}, \vec{k}_0 \right\rangle \tag{21}$$

where, T = transition operator, $\Psi_f^n(K^- p)$ involves $\vec{q}_2$ and $\vec{q}_0'$, $\Psi_i(D)$ involves $\vec{q}_1$ and $\vec{q}_2$.

Relation between $\left\langle \vec{r} \middle| \vec{k} \right\rangle$ and $\left\langle \vec{r} \middle| \vec{k} \right]$ is $\left\langle \vec{r} \middle| \vec{k} \right\rangle = \left(\frac{L}{2\pi} \right)^{\frac{3}{2}} \left\langle \vec{r} \middle| \vec{k} \right]$.

Equation (21) is rewritten in terms of internal coordinates with the aid completeness relation.

$$T_{fi}^{(n)} = \left(\frac{L}{2\pi} \right)^9 \iiint d\vec{q}_1 d\vec{q}_2\, d\vec{q}_0' \left\langle \Psi_f^n (K^- p), \vec{K} \middle| \vec{q}_0', \vec{q}_2 \right] \left[\vec{q}_0', \vec{k}_n \middle| T_{K^- n} \middle| \vec{k}_0, \vec{q}_1 \right] \left[\vec{q}_1, \vec{q}_2 \middle| \vec{0}, \Psi_i (D) \right\rangle \tag{22}$$

where, $$\int d\vec{q} \left| \vec{q} \right\rangle \left\langle \vec{q} \right| = \int d\vec{q} \left(\frac{L}{2\pi} \right)^3 \left| \vec{q} \right] \left[\vec{q} \right| = 1 .$$

By solving equation (21), he final expression of transition matrix element as follows.

$$T_{fi}^{(n)} = \int d\vec{q}_1 \left\langle \Psi_f^{(n)} (K^- p) \middle| \vec{\tilde{q}} \right] \delta(\vec{K} + \vec{k}_n - \vec{k}_0)\ [\vec{\tilde{q}}_0' \left| t_{K^- n} \right| \vec{\tilde{q}}_0][\vec{\tilde{q}}_1 \left| \Psi_i (D) \right\rangle . \tag{23}$$

After calculating the transition matrix element, we will be calculated the differential cross section for this reaction. After that, by substituting the transition matrix element into equation (19), the differential cross section for this reaction becomes,

$$d^6\sigma = \frac{L^3}{v_0} \frac{2\pi}{\hbar} \sum_n \delta (E_i - E_f^{(n)}) (\frac{L}{2\pi})^3 d\vec{k}_n (\frac{L}{2\pi})^3 d\vec{K} \delta^2 (\vec{K} + \vec{k}_n - \vec{k}_0)$$

$$\times \left| \int d\vec{q}_1 \left\langle \Psi_f^{(n)}) (K^- p) \middle| \vec{\tilde{q}} \right] \left[\vec{\tilde{q}}_0' \middle| t_{K^- n} \middle| \vec{\tilde{q}}_0 \right] \left[\vec{q}_1 \middle| \Psi_i (D) \right\rangle \right|^2 . \tag{24}$$

By integrating the above equation (24) with $d\vec{K}$, .

$$d^3\sigma = \frac{L^3}{v_0} \frac{2\pi}{\hbar} \sum_n \delta (E_i - E_f^n) (\frac{L}{2\pi})^9 d\vec{k}_n \left| \int d\vec{q}_1 \left\langle \Psi_f^n (K^- p) \middle| \vec{\tilde{q}} \right] \left[\vec{\tilde{q}}_0' \middle| t_{K^- n} \middle| \vec{\tilde{q}}_0 \right] \left[\vec{q}_1 \middle| \Psi_i (D) \right\rangle \right|^2 . \tag{25}$$

$v_0 = \frac{\hbar k_0 c^2}{E_0}$ is substituted into equation (25). The equation (27) becomes

$$d^3\sigma = \frac{L^3 E_0}{\hbar k_0 c^2} \frac{2\pi}{\hbar} \sum_n \delta (E_i - E_f^{(n)}) (\frac{L}{2\pi})^9 d\vec{k}_n$$

$$\times \left| \int d\vec{q}_1 \left\langle \Psi_f^{(n)} (K^- p) \middle| \vec{\tilde{q}} \right] \left[\vec{\tilde{q}}_0' \middle| t_{K^- n} \middle| \vec{\tilde{q}}_0 \right] \left[\vec{q}_1 \middle| \Psi_i (D) \right\rangle \right|^2 . \tag{26}$$

Equation (26) can be expressed in terms of delta function normalization. The equation (26) becomes

$$d^3\sigma = \frac{(2\pi)^4}{\hbar^2 k_0 c^2} E_0 \sum_n \delta(E_i - E_f^{(n)}) d\vec{k}_n \left|\langle t_{K^-n}\rangle\right|^2 \left|\int d\vec{q}_1 \langle \Psi_f^{(n)}(K^-p)|\vec{\tilde{q}}\rangle\langle\vec{q}_1|\Psi_i(D)\rangle\right|^2 \tag{27}$$

$$\because \left\langle t_{K^-n}\right\rangle = \left\langle \vec{\tilde{q}}'\middle| t_{K^-n}\middle|\vec{\tilde{q}}_0\right\rangle .$$

Calculation of Energy Conservation Term

Energy of initial state, E$_i$, $E_i = E_0 + M_n c^2 + M_p c^2 - BE$

(28)

where, BE is the binding energy of deuteron.

Energy of final state, E$_f$

$$E_f^{(n)} = E_n + (m_{K^-}c^2 + M_p c^2) + \left\langle \Psi_f^{(n)}\middle|H_{K^-p}\middle|\Psi_f^{(n)}\right\rangle + \frac{\hbar^2\vec{K}^2}{2(m_{K^-} + M_p)} \tag{29}$$

$$E = E_0 + M_n c^2 + M_p c^2 - BE - E_n - (m_{K^-}c^2 + M_p c^2) - \frac{\hbar^2(\vec{k}_0 - \vec{k}_n)^2}{2(m_{K^-} + M_p)} \tag{30}$$

where, $\frac{\hbar^2(\vec{k}_0 - \vec{k}_n)^2}{2(m_{K^-} + M_p)}$ is the recoil energy and $\left\langle \Psi_f^{(n)}\middle|H_{K^-p}\middle|\Psi_f^{(n)}\right\rangle$ is the excitation energy of final state.

$$\delta(E_i - E_f^{(n)}) = \left\langle \Psi_f^{(n)}\middle|\delta\left(E - H_{K^-p}\right)\middle|\Psi_f^{(n)}\right\rangle \tag{31}$$

To obtain the $\delta(E_i - E_f^{(n)})$, the Cauchy's principle is used.

$$\frac{1}{x + i\varepsilon} = \frac{p}{x} - i\pi\delta(x)$$

where, P is the principle value.

$$\delta(x) = -\frac{1}{\pi}\,\mathrm{Im}\frac{1}{x + i\varepsilon}$$

And then, we can expressed the energy conservation term as follows:

$$\delta(E_i - E_f^{(n)}) = -\frac{1}{\pi}\,\mathrm{Im}\frac{1}{E - H_{K^-p} + i\varepsilon} \tag{32}$$

The equation (27) becomes

$$d^3\sigma=\frac{(2\pi)^4}{\hbar^2c^2}\frac{E_0}{k_0}d\vec{k}_n\left|\left\langle t_{K^-n}\right\rangle\right|^2\times-\frac{1}{\pi}\mathrm{Im}\sum\nolimits_n\left\langle\Psi_f^{(n)}\right|\frac{1}{E-H_{K^-p}+i\varepsilon}\left|\Psi_f^{(n)}\right\rangle$$

$$\times\int d\vec{q}_1\int d\vec{q}_1'\left\langle\Psi_f^{(n)}\middle|\vec{\tilde{q}}\right\rangle\left\langle\vec{\tilde{q}}'\middle|\Psi_f^{(n)}\right\rangle\left\langle\vec{q}_1\middle|\Psi_i\right\rangle\left\langle\Psi_i^*\middle|\vec{q}_1'\right\rangle. \qquad (33)$$

where, $\sum_n\left|\Psi_f^{(n)}\right\rangle\left\langle\Psi_f^{((n))}\right|=1.$

$$d^3\sigma=\frac{(2\pi)^4}{\hbar^2c^2}\frac{E_0}{k_0}d\vec{k}_n\left|\left\langle t_{K^-n}\right\rangle\right|^2(-\frac{1}{\pi}\mathrm{Im}\int d\vec{q}_1\int d\vec{q}_1'\left\langle\Psi_i^*\middle|\vec{q}_1'\right\rangle\left\langle\vec{q}_1\middle|\Psi_i\right\rangle\left\langle\vec{\tilde{q}}'\right|\frac{1}{E-H_{K^-p}+i\varepsilon}\left|\vec{\tilde{q}}\right\rangle) \qquad (34)$$

where, $\int d\vec{r}\left|\vec{r}\right\rangle\left\langle\vec{r}\right|=1.$

The equation (34) can be expressed coordinate representation by using completeness relation. It can be expressed as follows

$$\frac{d^2\sigma}{d\cos(\theta)}=\frac{(2\pi)^5}{\hbar^2c^2}\frac{E_0}{k_0}k_n^2dk_n\left|\left\langle t_{K^-n}\right\rangle\right|^2(-\frac{1}{\pi})\mathrm{Im}\int d\vec{r}'d\vec{r}f^*(\vec{r}')\left\langle\vec{r}'\right|\frac{1}{E-H_{K^-p}+i\varepsilon}\left|\vec{r}\right\rangle f(\vec{r}) \qquad (35)$$

In equation (35) contains dk$_n$. To get dk$_n$, the energy conservation law and momentum conservation law are used.

$$dk_n=\frac{Yc^2dY}{\hbar^2[(1+\frac{E_Y}{E_n})k_n-k_0\cos(\theta)} \qquad (36)$$

By substituting equation (36) into equation (35), the equation (35) becomes

$$\frac{d^2\sigma}{dY d\cos(\theta)}=\frac{(2\pi)^5}{\hbar^4}\frac{E_0}{k_0}k_n^2\left|\left\langle t_{K^-n}\right\rangle\right|^2\frac{Y}{(1+\frac{E_Y}{E_n})k_n-k_0\cos(\theta)}(-\frac{1}{\pi})\mathrm{Im}\int d\vec{r}'d\vec{r}$$

$$\times f^*(\vec{r}')\left\langle\vec{r}'\right|\frac{1}{E-H_{K^-p}+i\varepsilon}\left|\vec{r}\right\rangle f(\vec{r}) \qquad (37)$$

In equation (37) contains two terms. The first term is kinematical factor and the other one is spectral function.

In this spectral function equation, $\left\langle\vec{r}'\right|\frac{1}{E-H_{K^-p}+i\varepsilon}\left|\vec{r}\right\rangle$ is the Green's function.

The energy conservation term will be solved by using Green's function method.

Numerical Calculation of Green's Function

Green’s function can be expressed by coordinate representation as follows;

$$G(\vec{r}',\vec{r}) = \langle \vec{r}' | \frac{1}{E - H_{K^-p} + i\varepsilon} | \vec{r} \rangle . \tag{38}$$

It is satisfies the following equation,

$$\left(E - H_{K^-p}\right) G^+\left(\vec{r}',\vec{r}\right) = \left\langle \vec{r}' | 1 | \vec{r} \right\rangle = \delta\left(\vec{r}' - \vec{r}\right) \tag{39}$$

Green’s function and delta function are expressed partial wave expression as

$$G\left(\vec{r}',\vec{r}\right) = \Sigma_{\ell=0}^{\infty} \Sigma_M Y_{\ell M}(\hat{\vec{r}}') \frac{G_\ell^{\,+}(r',r)}{r'r} Y^*{}_{\ell M}(\hat{\vec{r}}) \tag{40}$$

$$\delta\left(\vec{r}' - \vec{r}\right) = \Sigma_{\ell=0}^{\infty} \Sigma_M Y_{\ell M}(\hat{\vec{r}}') \frac{\delta(r' - r)}{r'r} Y^*{}_{\ell M}(\hat{\vec{r}}) \tag{41}$$

Radial part of Green’s function $G_\ell^{\,+}(r',r)$ satisfies the following equation,

$$[k^2 + \frac{d^2}{dr^2} - \frac{\ell(\ell+1)}{r^2} - \tilde{U}(r)] G_\ell^{\,+}(r',r) = \frac{2\mu}{\hbar^2} \delta\left(r' - r\right) \tag{42}$$

$k = \sqrt{\dfrac{2\mu E}{\hbar^2}}$, $\tilde{U}\left(r\right) = \dfrac{2\mu}{\hbar^2} V_{K^-p}\left(r\right)$ is the potential of K^-p system.

In our calculation, we have constructed YA (T. Yamazaki and Y. Akaishi (2007))) potential for $\overline{K}N$ interaction.

Integrating equation (44) with $\int dr$ from $r' - \varepsilon$ to $r' + \varepsilon$ will give,

$$\int_{r'-\varepsilon}^{r'+\varepsilon} [k^2 - \frac{\ell(\ell+1)}{r^2} - \tilde{U}\left(r\right)] G_\ell^{\,+}\left(r',r\right) dr + \int_{r'-\varepsilon}^{r'+\varepsilon} \frac{d^2}{dr^2} G_\ell^{\,+}\left(r',r\right) dr = \frac{2\mu}{\hbar^2} \int_{r'-\varepsilon}^{r'+\varepsilon} \delta\left(r' - r\right) dr$$

(43)

The first term of left hand side vanishes since it is continuous. The second term gives

$$\frac{d}{dr} G_\ell^{\,+}\left(r',r\right)\Big|_{r'+\varepsilon} - \frac{d}{dr} G_\ell^{\,+}\left(r',r\right)\Big|_{r'-\varepsilon} = \frac{2\mu}{\hbar^2} . \tag{44}$$

Green’s function $G_\ell^{\,+}\left(r',r\right)$ is divided into two regions $G_{\ell 1}^{\,+}\left(r',r\right)$ and $G_{\ell 2}^{\,+}\left(r',r\right)$ with

$$G_{\ell_1}^{+}\left(r',r\right) = C_1 u_\ell^{(0)}\left(r\right) \qquad \left(0 \langle r \langle r'\right)$$

$$G_{\ell_2}^{(+)}\left(r',r\right) = C_1 u_\ell^{(+)}\left(r\right) \qquad \left(r' \langle r \langle \infty\right).$$

$u_\ell^{(0)}(r)$ and $u_\ell^{(+)}(r)$ satisfies

$[k^2+\frac{d^2}{dr^2}-\frac{\ell(\ell+1)}{r^2}-\tilde{U}(r)]u_\ell^{(0)}(r)=0$ with boundary condition at original $u_\ell^{(0)}(0)\xrightarrow{r\to 0}0$.

$[k^2+\frac{d^2}{dr^2}-\frac{\ell(\ell+1)}{r^2}-\tilde{U}(r)]u_\ell^{(+)}(r)=0$ with boundary condition at asymptotic region, $u_\ell^{(+)}(r)\xrightarrow{r\to\infty}krh_\ell^{+}(kr)$ (45)

where, $h_\ell^{+}(kr)$ is the spherical Hankel function.

According to the continuity of Green's function,

$$C_1u_\ell^{(0)}(r)\Big|_{r'}=C_2u_\ell^{(+)}(r)\Big|_{r'}. \tag{46}$$

Discontinuity of $\frac{dG}{dr}$ gives

$$C_1u_\ell^{(0)'}(r)\Big|_{r'}-C_2u_\ell^{(+)'}(r)\Big|_{r'}=\frac{2\mu}{\hbar^2}. \tag{47}$$

By solving equation (48) and (49), the values of C_1 and C_2 are obtained.

$$C_1=\frac{\begin{vmatrix}0 & -u_\ell^{(+)}(r')\\ \frac{2\mu}{\hbar^2} & -u_\ell^{(+)'}(r')\end{vmatrix}}{\begin{vmatrix}u_\ell^{(0)}(r') & -u_\ell^{(+)}(r')\\ u_\ell^{(0)'}(r') & -u_\ell^{(+)'}(r')\end{vmatrix}}=\frac{2\mu}{\hbar^2}\times\frac{u_\ell^{(+)}(r')}{W\left(u_\ell^{(0)},u_\ell^{(+)}\right)} \tag{48}$$

$$C_2=\frac{\begin{vmatrix}u_\ell^{(0)}(r') & 0\\ u_\ell^{(0)'}(r') & \frac{2\mu}{\hbar^2}\end{vmatrix}}{\begin{vmatrix}u_\ell^{(0)}(r') & -u_\ell^{(+)}(r')\\ u_\ell^{(0)'}(r') & -u_\ell^{(+)'}(r')\end{vmatrix}}=\frac{2\mu}{\hbar^2}\times\frac{u_\ell^{(0)}(r')}{W\left(u_\ell^{(0)},u_\ell^{(+)}\right)},$$

where, $W\left(u_\ell^{(0)},u_\ell^{(+)}\right)$ is Wronskian. (49).

After comparing the value of r and r ', we used the smaller part is $r_<$ and the larger one is $r_>$.

The final expression of the differential cross section for missing mass spectrum by using Green's function method as shown bellows,

$$\frac{d^2\sigma}{dYd\cos(\theta)} = \frac{(2\pi)^5}{\hbar^4}\frac{E_0}{k_0}k_n^2\left|\left\langle t_{K^-n}\right\rangle\right|^2 \frac{Y}{(1+\frac{E_Y}{E_n})k_n - k_0\cos(\theta)}$$

$$\times\frac{2\mu}{\hbar^2}\left(\frac{-1}{\pi}\right)\mathrm{Im}[\sum_{\ell}(2\ell+1)\int drdr' j_{\ell}^{*}(Qr')u_i^{*}(r')] \qquad (50)$$

YA Potential for $\overline{K}N$ Interaction

The radial form of YA potential for $\overline{K}N$ interaction is as follows:

$V_{\overline{K}N}^{I=0}(r) = (V_0 + i\,W_0)e^{-\left(\frac{r}{b}\right)^2}$, where, V_0 = -597.0 MeV, W_0 = -140.0 MeV, b = 0.66 fm.

It is a Gaussian type complex potential with strength parameters (V_0 and W_0) and range parameter (b), where imaginary part represents decay into Σπ channel.

Results and Discussion

Missing Mass Spectrum of D (K⁻, n) Λ (1405) Reaction

We have calculated the differential cross section for the missing mass spectrum of the $D(K^-,n)$ Λ (1405) reaction (J-PARC E31) (Noumi *et al.,*) by using Green's function method. In our calculation, we used the YA potential for K^-p interaction which reproduced the binding energy and the level width of Λ (1405) quasi-bond state.

By using equation (50), we have analyzed the missing mass spectrum of Λ (1405) for various angular momentum contributions. The calculated missing mass spectrum of $D(K^-,n)\Lambda(1405)$ reaction for individual angular momentum contributions for $\ell = 0$, $\ell = 1$, $\ell = 3$ and $\ell = 8$ are shown in Figure (3). In the energy region below the K^-p threshold, it can be seen that $\overline{K}N$ bound state is mainly contributed by $\ell = 0$. In the continuum region, the higher angular momenta dominantly contribute to the quasi-free peaks. The total angular momentum contributions to the missing mass spectrum converge at $\ell_{max} = 8$ as shown in Figure (4). According to these two figures, it can be concluded that the peak position is found to be clearly dominant at $\ell = 0$. The mass and level width of Λ (1405) is 1407.9 MeV/c^2 and 48 MeV, respectively. The updated PDG value of the mass and width of this Λ (1405) resonance state or often known as Λ* is $1405.1^{+1.3}_{-1.0}$ MeV/c^2 and 50.5 ± 2.0 MeV (Particle Data Group K. A. Olive *et al*., (2014)). The calculated result of the mass and level width of Λ (1405) is nearly consistent with that of the updated PDG (2016) data.

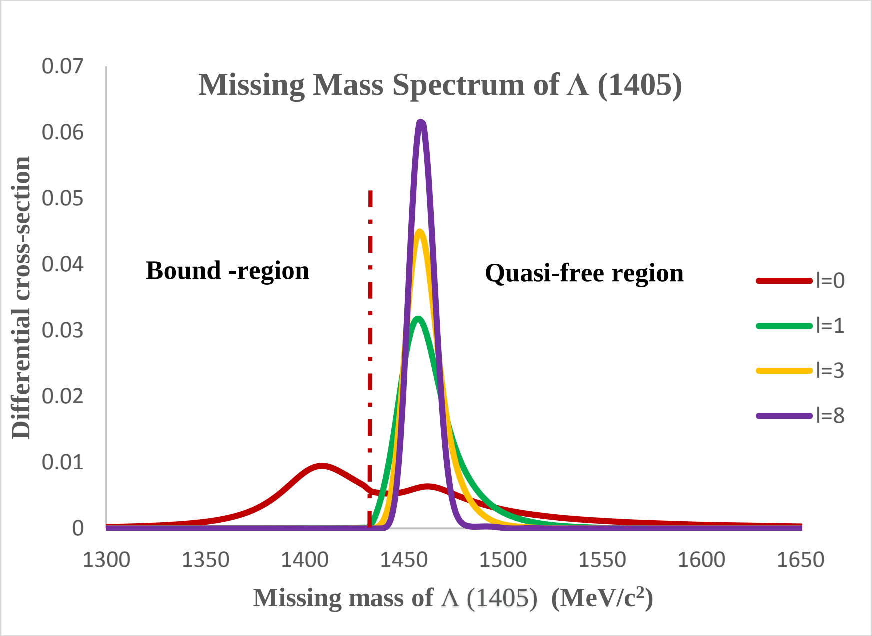

Figure 3 Missing mass spectrum of Λ (1405) with individual angular momentum; the red color solid curve represents $\ell = 0$ only; the green color solid curve represents $\ell = 1$ only; the orange color solid curve represents $\ell = 3$ only; The violet color solid curve represents $\ell = 8$ only

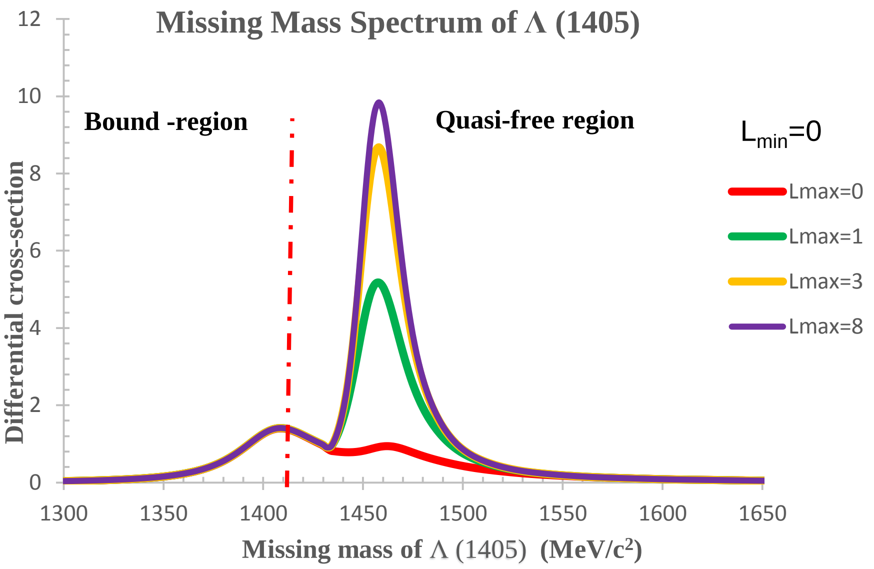

Figure 4 Missing mass spectrum of Λ (1405) with total angular momentum the violet color solid curve represents the summation of total angular momentum $\ell = 0$ to 8; the green color solid curve represents the summation of total angular momentum $\ell = 0$ to 1; the orange color solid curve represents the summation of total angular momentum $\ell = 0$ to 3; the red color solid curve represents the angular momentum $\ell = 0$ only

Conclusion

We have analyzed the missing mass spectrum of D (K^- , n) Λ (1405) reaction at the incident momentum of K^- 1.0GeV/c. The calculated result of the mass and level width of Λ (1405) is nearly consistent with that of the updated PDG (2016) data.

Acknowledgements

I would like to specially thank to my supervisor, Dr Khin Swe Myint, Emeritus Professor, Rector (Rt.d), University of Mandalay, for her invaluable advices and enthusiastic guidance throughout this work.

I do thank Dr Lei Lei Win, Professor and Head of Physics Department, University of Mandalay, for her encouragement and permission.

I also thank my co-supervisor, Dr Thida Wint, Associate Professor, Physics Department, University of Distance Education Mandalay, for her discussions and collaborations.

References

D.W. Thomas *et al*., (1977), Nucl. Phys. **B 129 1**.

H. Noumi *et al*., Spectroscopic study of hyperon resonances below $\overline{K}$N threshold via the (K^-, n) reaction on deuteron (J-PARC E31), http://j-parc. jp/researcher/Hadron/en/pac_1207/pdf/E31_1202-9.pdf.

J. Esmaili, Y. Akaishi and T. Yamazaki, (2010), Phys. Lett. **B 686 23**.

J. Esmaili, Y. Akaishi and T. Yamazaki, (2011), Phy. Rev. **C 83 055207**.

M.H. Alston et al., (1961), Phys. Rev. Lett. **6 689.**

Maryam Hassanvand, Yoshinori Akaishi, Toshimitsu Yamazaki, (3 Oct 2015), arXiv;**1510.00870v1** [hep-ph].

Particle Data Group K. A. Olive *et al*., (2016), Chin. Phys. **C 40 100001**.

R. H. Dalitz and A. Deloff, (1991), J. Phys. G: Nucl. Part. Phys. **17 289**.

R. J. Hemingway, (1985), Nucl. Phys. **B 253 742**.

T. Hyodo and A. Weise, (2008), Phys. Rev. **C 77 035204**..

T. Yamazaki and Y. Akaishi (2007), Phys. Rev. **C 76 045201.**

ရက်စွဲ။ ၂၄-၇-၂၀၂၀

မြန်မာနိုင်ငံ ဝိဇ္ဇာနှင့်သိပ္ပံပညာရှင်အဖွဲ့မှ ကြီးမှူးကျင်းပခဲ့သော (၁၉) ကြိမ်မြောက် သုတေသန ညီလာခံတွင် မန္တလေးတက္ကသိုလ်၊ ရူပဗေဒဌာန၊ ကထိက၊ ဒေါက်တာ မြတ်မွန်သင်း ဖတ်ကြား တင်သွင်းခဲ့သော **Speciation and Distribution of Phosphorus in Sediments at Inle Lake (Southern Shan State, Myanmar)** သုတေသနစာတမ်းကို ကာယကံရှင်၏ တင်ပြလျှောက်ထားချက်အရ The Journal of the Myanmar Academy of Arts and Science Vol. XVIII, No.2B, July 2020, Sr. No(41), Pages (355–366) တွင် ဖော်ပြခဲ့သည့် စာတမ်းကို ရုပ်သိမ်းပယ်ဖျက်လိုက်သည်။

Date 24–7–2020

The Research paper entitled **Speciation and Distribution of Phosphorus in Sediments at Inle Lake (Southern Shan State, Myanmar**) Submitted by Dr Myat Mon Thin, Lecturer, Department of Physics, the University of Mandalay at the 19th Research Conference of the Myanmar Academy of Arts and Science is hereby withdrawn from The Journal of the Myanmar Academy of Arts and Science Vol. XVIII, No.2B, July 2020, Sr. No(41), Pages (355–366) and Website www.maas.edu.mm at the request of the author in her letter dated 21st July 2020 to the President of the Myanmar Academy of Arts and Science.

INFLUENCE OF Al DOPING ON THE MICROSTRUCTURAL AND OPTICAL PROPERTIES OF CdSe THIN FILMS

Aye Aye Thandar Naing[1], Mar Mar Swe[2], and Moht Moht Than[3]

Abstract

Al doped CdSe films were deposited on glass substrate using rolling method. Difference concentrations of Al (10 mol%, 20 mol% & 30 mol%) were introduced into the CdSe matrix. The deposited thin films were annealed at 300˚C for 1 hour. The microstructural properties such as lattice parameters, microstrain and dislocation density of the thin films were characterized by X-ray diffraction. Grain size and crystallite variation were studied for Al doping effect. The UV-Vis spectrometer used to determine optical band gap of thin films.

Keywords : Al doped CdSe, optical band gap E_g, Grain size

Introduction

CdSe is II-IV n-type semiconductor and is taken into consideration as an essential material for the advance of different optoelectronic devices. It has inherent band energy of 1.74 eV that makes it an attractive materials for different applications consists of light emitting diodes, solar devices, photodectors and other optoelectronic gadgets.

A proficient manner to decrease the resistivity and to get better properties of semiconducting substance is to dope with an appropriate impurity such as copper, silver, aluminium and indium. The dopant has revealed to improve properties in number of host crystal lattices. The electronic and optical properties of semiconductors are strongly influence via the doping technique that provides the origin for tailoring the preferred carrier density and, therefore, the absorption, emission and transport characteristic as well.

Optical and electrical characteristic of semiconducting films are necessary obligation for proper application in a variety of optoelectronic tools. These characteristic of such films are adequately structure responsive. Consequently, proper structural description of the films is essential. It can be well-known that the structural parameters which include crystal phase, crystallinity, grain size, lattice constant are strongly depending on the deposition situation. The structure of the films is possibly relies upon at the preparative parameters.[Chate P A,2016]

Experimental Details

Aluminum(10 mol%, 20 mol% & 30 mol %)doped CdSe were prepared by using rolling method. The row materials of CdSe and Aluminum were weighted by digital balance to get desire composition. The two powder were mixed with appropriate ratio. Appropriate proportions of highly pure (99.99%) CdSe and Al powders were ground separately by mean of an agate mortar and pestle. The specific weight from CdSe powder and 10%,20% and 30%from this weight of aluminum powder must be taken and put it into starting materials. To increase complete mixing, the mixtures were ground for at least three hours. The stirring speed was 500 rpm. After stirring, the mixing powder were heated at 100□C for 1h for doping. After that,2

---

[1] Dr, Lecturer, Department of Physics, University of Yangon

[2] Lecturer, Department of Physics, University of Yangon

[3] Associate Professor, Department of Physics, Mohnyin Degree College

methoxy ethanol ($CH_3OCH_2CH_2OH$) is added to the mixture and rolling on glass substrates. For deposition of the films, the glass substrate choosing is very important. Indium Tin Oxide glass (ITO) slides of dimension 1.5 cm x 1.5 cm with a sheet resistance of 18W are used. After the coating all the films were dried at room temperature for 1 day in order to diffuse the solvent. After that, the glass substrates were heated with the temperature 300°C for 1 h. Figure 1 shows that flow chart for sample preparation of Al doped CdSe thin films.

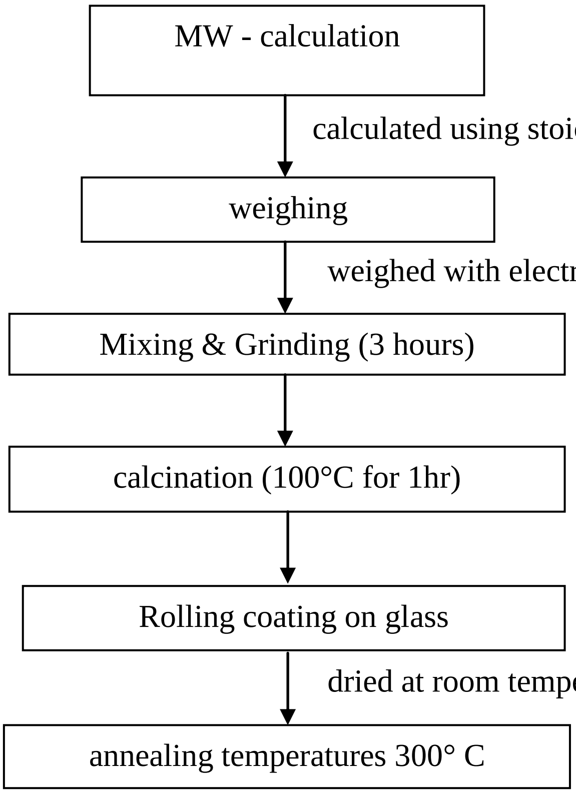

Results and Discussions

XRD Analysis of Al Doped CdSe Thin Films

Al doped CdSe thin films were characterized by using monochromatic Cu-$K_\alpha$radiation (λ= 1.54056Å) operated at 40 kV (tube voltage) and 30 mA (tube current). Specimen was scanned from 10º to 70º in diffraction angle, 2 θ with step-size of 0.02. The upper site of XRD spectrum was represented the observed profile while the lower site indicated the standard CdSe library file. The X-ray diffraction (XRD) spectra of pure CdSe as shown in figure 2.They can be form hexagonal structure. The upper site of XRD spectrum was represented the observed profile while the lower site indicated the standard CdSe of JCPDS library file. From figure 2, three peaks such as (100),(002)and (110) were performed on XRD profile of CdSe. All peaks were well matched with standard profile of JCPDS library file. The structure for pure CdSe were used for identification purpose.

The XRD pattern shows a large number of peaks indicating the polycrystalling character of the films. The examination of spectrum indicated that all the films have hexagonal structure in the whole range of composition studied. The cubic phase of CdSe has not been observed. Figrue 3 shows that the comparison between three XRD results for three different ratios of Al doped CdSe thin films.

The crystallite size of the particle can be calculated from the XRD peak broadening of the peaks using the Scherrer's formula.

$$g_{\text{crystallite}} = \frac{0.9\lambda}{D\cos\theta} \qquad \text{.........(1)}$$

where, ' s the size of the crystallites, 'λ' is the wavelength of the x-ray used, '*D*' is the full width at half maximum height and 'θ'is the angle of diffraction. In this research, we used Cu K_α radiation in which λ = 1.54056 Å.The analysis of XRD patterns in terms the values of hkl ,lattice parameter, crystallite size, Dislocation Density, Microstrain of the Al (10%, 20%,30%) doped CdSe thin films have been done by considering hexagonal structure and is displayed in table 1. Figure 4 shows Crystallite size vs dislocation density plot for CdSe:Al(10%) thin film. Figure 5 shows Crystallite size vs dislocation density plot for CdSe:Al(20%) thin film at 300°C. Figure 6 shows Crystallite size vs dislocation density plot for CdSe:Al(30%) thin film at 300°C.

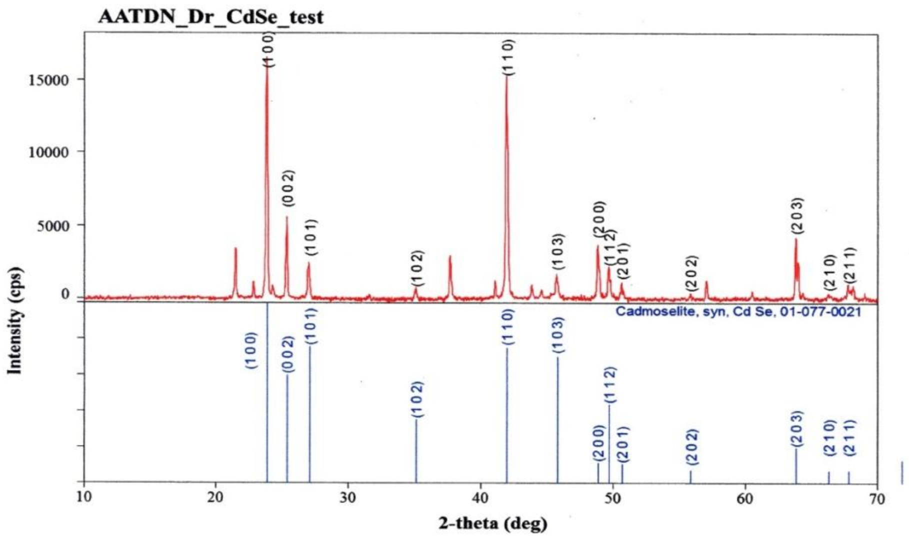

Figure 2 XRD spectrum of pure CdSe powder

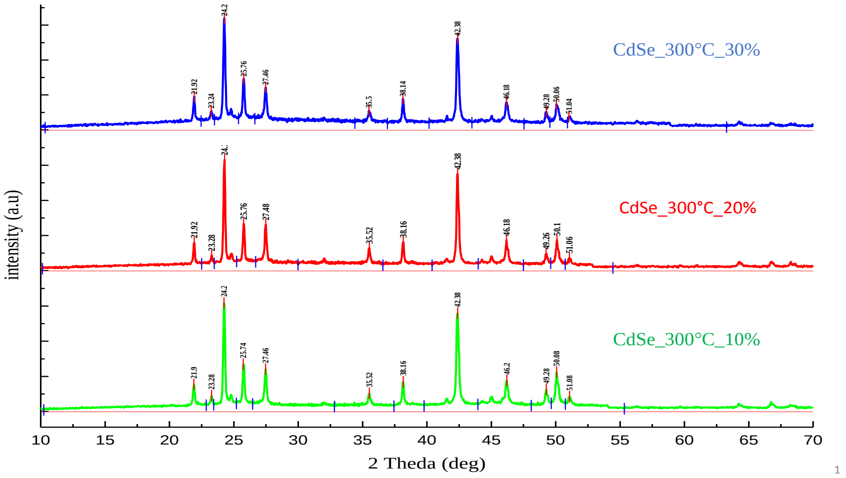

Figure 3 X-ray diffraction pattern of CdSe: Al(10%,20%,30%) thin film

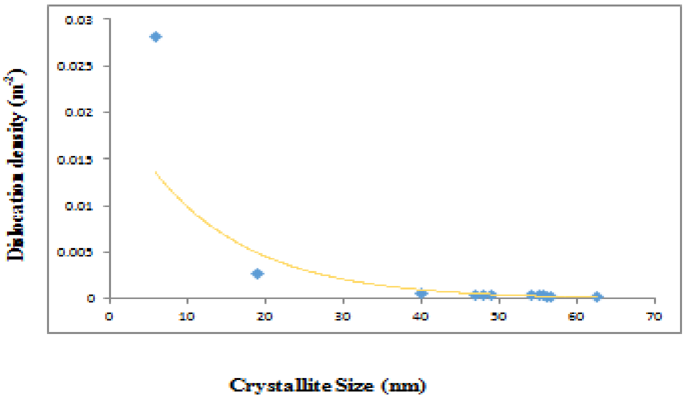

Figure 4 Crystallite size vs dislocation density plot for CdSe: Al(10%) thin film at 300°C

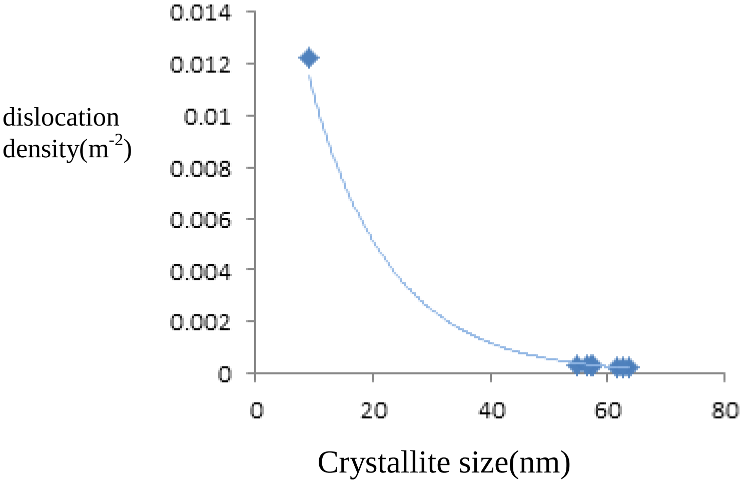

Figure 5 Crystallite size Vs dislocation density plot for CdSe:Al(20%) thin film at 300°C

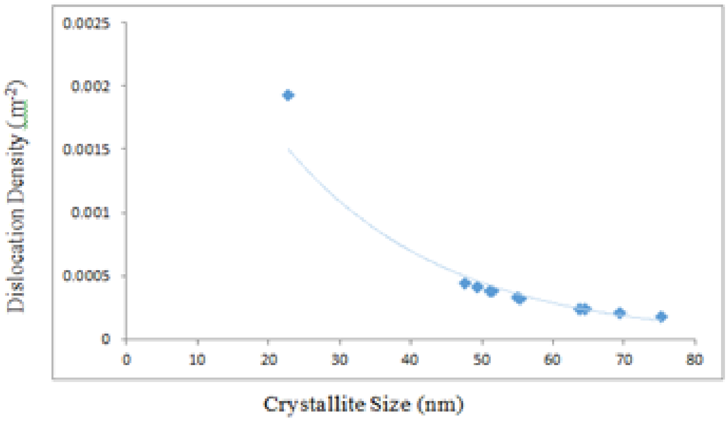

Figure 6 Crystallite Size Vs dislocation density plot for CdSe:Al(30%) thin film at 300°C

Table 1 The value of hkl, lattice parameter, crystallite size, disolcation density and microstrains of the Al doped CdSe thin films

Ddoping Conc (mol)	**Plane (hkl)**	**lattice paremeter(A)**	**2-theta (deg)**	**FWHM (deg)**	**Crystallite size(nm)**	**Dislocation Density $(m^{-2})x10^{14}$**	**Microstrain (10^{-4})**
10%	(100)	a = 4.2600	24.241	0.146	55.652	3.228	6.228
	(002)	c = 6.9402	25.74	0.13	62.683	2.545	5.529
	(110)		42.346	0.154	55.319	3.268	6.265
20%	(100)	a = 4.2590	24.259	0.136	57.108	3.066	5.79
	(002)	c = 6.9409	25.772	0.132	61.737	2.623	5.614
	(110)		42.367	0.136	62.645	2.548	5.533
30%	(100)	a = 4.2624	24.252	0.159	51.102	3.829	6.78
	(002)	c = 6.9398	25.739	0.126	64.672	2.39	5.359
	(110)		42.347	0.154	55.319	3.267	6.265

SEM Analysis of Al Doped CdSe Thin Films

The study of scanning electron micrographs, this can be shown that the presence of non homogeneous grains and having different sizes. Figure 7 (a),(b) and (c) shows that SEM image of Al (10%,20%,30%)doped CdSe with thin films at 300°C. The grain sizes are expressed with table 2.

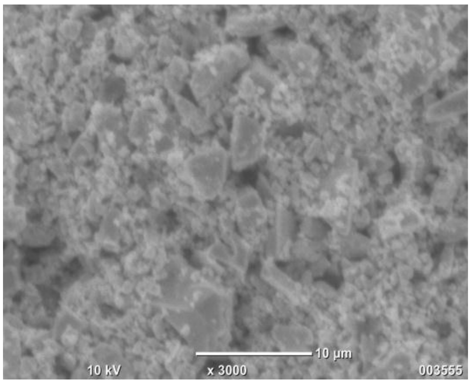

Figure7 (a) The SEM image of CdSe:Al(10%) thin film at 300°C

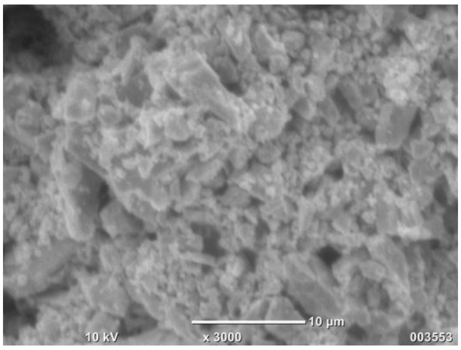

Figure7 (b) The SEM image of CdSe:Al(20%) thin film at 300°C

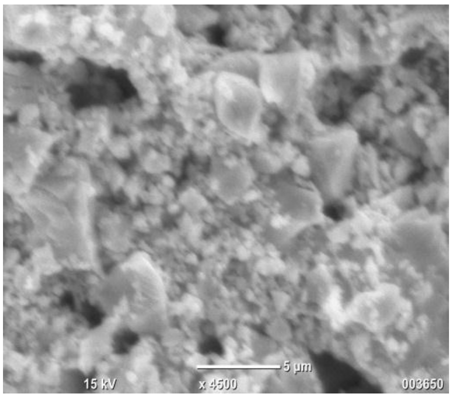

Figure7(c) The SEM image of CdSe:Al (30%) thin film at 300°C

Table 2 The value of grain size for Al doped CdSe thin films

Doping Conc (mol)	Grain Size (µm)
10%	3.2806
20%	3.0026
30%	1.8632

UV-Vis Analysis of Al Doped CdSe Thin Films

The optical absorption spectrum are measure by UV-Vis spectrometer as shown in figure 8(a),9(a) and 10(a). The plot of $(\alpha h\upsilon)^2$vs$h\upsilon$ is shown in figure 8 (b),9(b),10(b). The value of band gap for three ratios of Al(10%,20% and 30%) doped CdSe thin film at 300°C are 1.0938 eV, 2.2062eV and 2.87 eV.

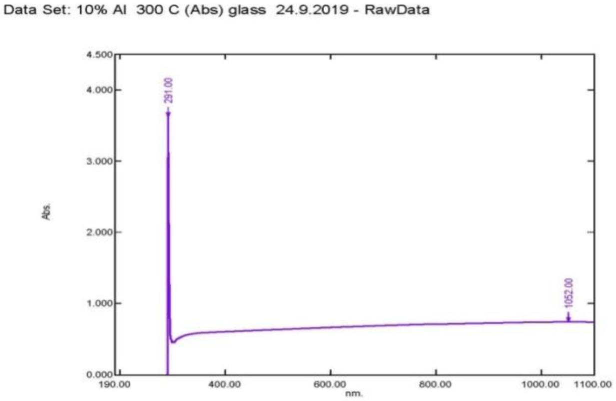

Figure 8(a) Optical absorption spectrum of Al(10%) doped CdSe thin film at 300°

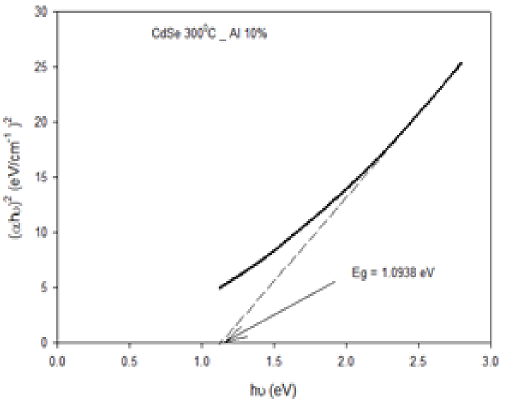

Figure 8 (b) Plot of α^2vshυ in curve of Al 10% doped CdSe thin film at 300°C

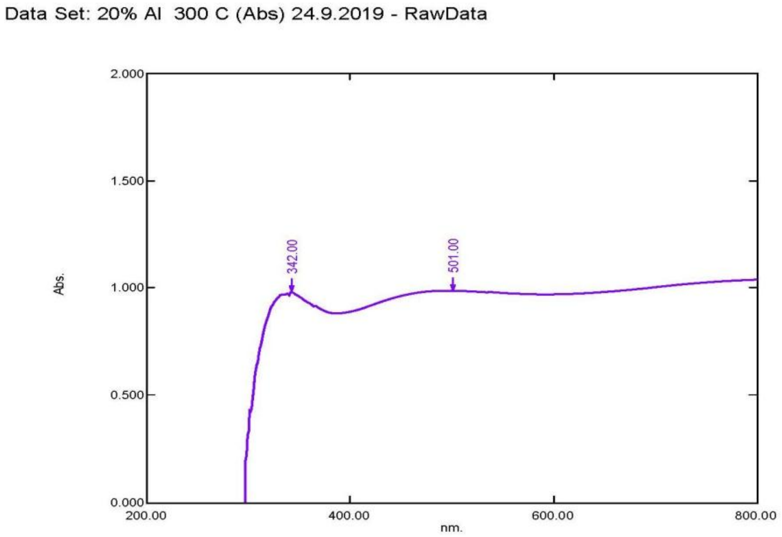

Figure 9(a) Optical absorption spectrum of Al(20%) doped CdSe thin film at 300°C

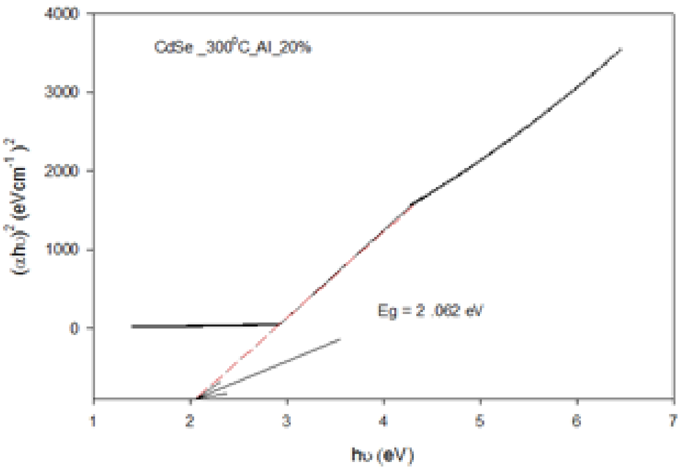

Figure 9 (b) Plot of α^2vshυ in curve of Al 20% doped CdSe thin film at 300°C

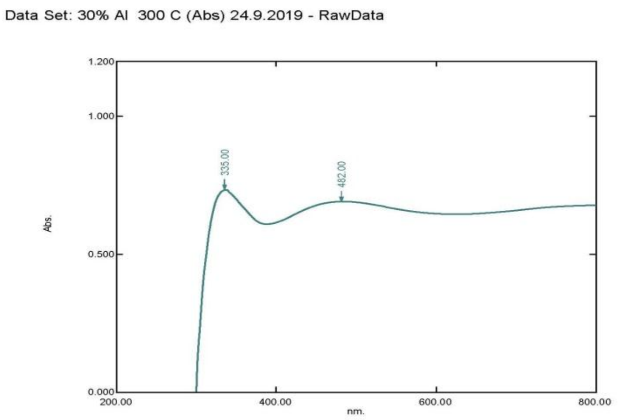

Figure 10(a) Optical absorption spectrum of Al(30%) doped CdSe thin film at 300°C

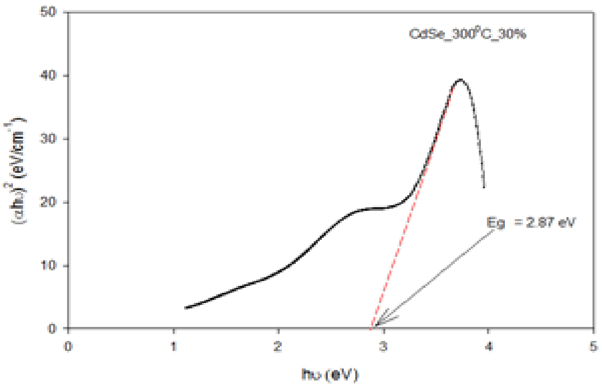

Figure 10 (b) Plot of α^2vshυ in curve of Al 30% doped CdSe thin film at 300°C

Conclusion

Aluminium doped CdSe thin films have been synthesized by using rolling method. The varying concentration of aluminium (10 %, 20 % & 30 %) was used. The structural studies was done using X-ray diffraction pattern. Polycrystalline character as well as a hexagonal structure having (100) plane as the preferred orientation was observed. The average grain size of three sample is found 2.715µm. The direct optical band gap of three samples are 1.903eV, 2.062 eV and 2.87eV. The study of these results shows that the Al doped CdSe thin films can be suitable for optoelectronic application.

Acknowledgements

I would like to thank Professor Dr Khin Khin Win, Head of department of Physics, University of Yangon for her kind permission to carry out this research.

I would like to express my sincere thanks to Dr Myo Lwin, Professor, Dr Ye Chan, Professor, Universities' Research center, Dr Aye Aye Thant, Professor, Department of Physics, Dr Yin Maung Maung,Professor, Department of Physics and Dr Than Zaw Oo, Professor, Universities' Research Center, University of Yangon, for their suggestion and comments for this work.

References

Chate P A, Bhabad V D, (2016), “Aluminum Doped CdSe Thin Films: Structural Characterization” *International Journal for Trends in Science and Technology*, Department of Chemistry, JSM College, b Alibag, M.S, India .Vol.2, Issue 10, ISSN: 2445-3778

Mahawela P,Jeedingunto S, Vakkalanka S, Ferekides C S, Morel D L, (2005) "Transparent high-performance CdSe thin-film solar cells", Thin Solid Films, vol. 480-481, pp. 466-470.

Murali K, Sivaramamoorthy K, Kttaisamu M, Bahadur S, (2009), Physics B 404-2449

Padmanbhassrma H, Subramanian V, Rangarajan V, Murali Bull K, (1995), Master, Sci 18 - 875.

Pawar S M,moholkar AV, Rajpure KY, Bhosale C H, (2008)"Photoelectrochemical investigations on electrochemically deposited CdSe and Fe-doped CdSe thin films", Sol.Energy Mater, Sol, Cells, vol. 92, pp45-49,

Patel K, Jani M, Pathak V, Srivastava R, Chalcogen, (2009), Lett, 6, 279.

Sathyalatha K,Uthanna S, Reddy P, (1989), *Thin Solid Films* 174 - 233.

Shreekanthan K, Rajendra B, Kasturi V, Shivkumar G, (2003), Crst, Res, Technol,38 – 30.

J. Myanmar Acad. Arts Sci. 2020 **Vol. XVIII.No.2B**

INTERNET OF THINGS (IOT) BASED HEART BEAT MONITORING SYSTEM

Tin Tin Nyo[1], Zin Zin Naing[2], Nu Nu Lwin[3]

Abstract

The system implemented in this research is an advanced solution for monitoring the heart beat of a patient at a particular place and makes the information visible anywhere in the world. The technology behind this is Internet of Things (IoT), which is an advanced and efficient solution for connecting the things to the internet and to connect the entire world of things in a network. Here things might be whatever like electronic gadgets, sensors and automotive electronic equipment. The system deals with monitoring heart beat with sensor and send the information to the web page of" thingspeak" server and then plot the sensor data as graphical statistics. "ThingSpeak" has integrated support from the numerical computing software MATLAB from MathWorks. The data updated from the implemented system can be accessible in the internet from anywhere in the world.

Keywords: Internet of Things (IoT), ThingSpeak, Embedded Computing System, Arduino Software, ESP8266.

Introduction

Health monitoring is the major problem in today's world. Due to lack of proper health monitoring, patient suffer from serious health issues. There are lots of internet of thing (IoT) devices now days to monitor the health of patient over internet. Health experts are also taking advantage of these smart devices to keep an eye on their patients. IoT is rapidly revolutionizing the healthcare industry.

Materials and Methods

In this research, Pulse rate are recorded over ThingSpeak and Google sheets so that patient health can be monitored from anywhere in the world over internet. Materials used in the heart beat monitoring system composes of two sections; hardware and software. In hardware section, Arduino uno, NodeMCU and heart rate sensor are essential parts. The <ESP8266WiFi.h>,"software Serial.h" Pulse Senor Playground.h", and ThingSpeak.h" library are required for this IoT work.

Pulse Sensor SEN11574 in figure 1 is a well-designed plug-and-play heart-rate sensor for Arduino. The sensor clips onto a fingertip or earlobe and plugs right into Arduino. The front of the sensor is the side with the Heart logo. This is the side that makes contact with the skin. On the front side, there is a small round hole, which is where the LED shines through from the back, and there is also a little square just under the LED. The square is an ambient light sensor, exactly like the one used in cellphones, tablets, and laptops, to adjust the screen brightness in different light conditions. The LED shines light into the fingertip or earlobe, or other capillary tissue, and sensor reads the light that bounces back. The back of the sensor is where the rest of the parts are mounted.

---

[1] Dr, Associate Professor, Department of Physics, Taungoo University.

[2] Dr, Lecturer, Department of Physics, Taungoo University.

[3] Dr, Associate Professor, Department of Physics, TU Mawlamyaing.

Node MCU is an open source IoT platform.[4] It includes. The firmware which runs on the ESP8266 Wi-Fi SoC from Espressif Systems, and hardware which is based on the ESP-12 module. The term "NodeMCU" by default refers to the firmware rather than the development kits.

ThingSpeak is an IoT platform for data collection and analytics that serves as a bridge connecting edge node devices such as temperature, humidity, pressure etc. sensors to collect data and data exploratory analysis software to analyze data. ThingSpeak serves as the data collector which collects data from edge node devices (Nodemcu/ESP8266 is this case) and also enables the data to be pulled into a software environment for historical analysis of data.

The primary element of ThingSpeak activity is the channel, which contains data fields, location fields, and a status field. After creating a ThingSpeak channel, data can be written to the channel, the data can be processed and viewed with MATLAB code, and react to the data with tweets and other alerts.

The Arduino Uno is a microcontroller board based on the ATmega328. The board carries an 8-bit microcontroller, and it comes with 14 digital input/output pins and 6 analog inputs. Six of the digital pins can be programmed to send pulse width modulation (PWM). The Uno board also comes with internal peripherals able of running the UART, SPI, and I2C communication protocols. Programs using the Arduino Uno board (Figure 2.1) can be as big as 30 Kbytes and run at 16 MHz.

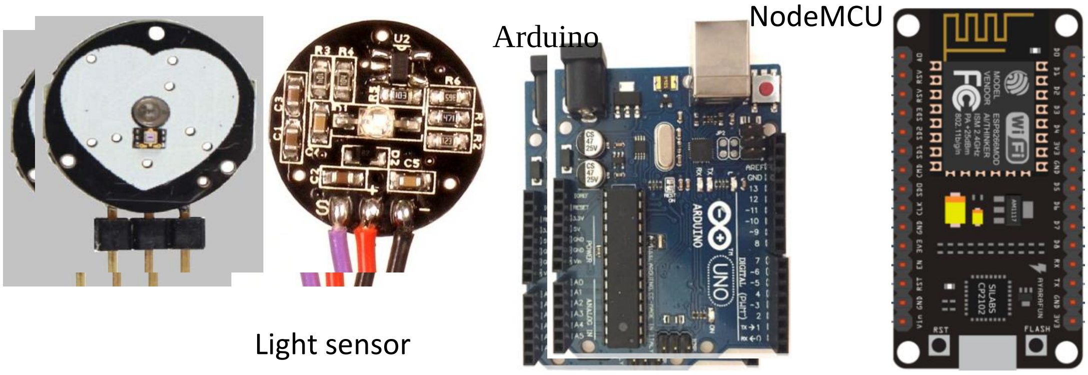

Figure 1 Components used in IoT heart rate monitoring sytem

The sensor data are received by Arduino uno. And then, Arduino sends these data to Node MCU ESP826612E which sends data to thingspeak cloud. The analog output of light sensor is connected to analog pin A0 of Arduino. Digital pin D2 and D3 are defined as the receive and transmit pin of Arduino. The transmit pin D3 of Arduino is connected to the receive pin of Node MCU as shown in figure 2.

Three programs are used in IOT based heart beat monitoring system. One is sketch for Arduino sending the data to Node MCU. Second is to upload the data to the thingspeak server via Node MCU. The data are down loaded to PC or smart phone The block diagram of communication to and from thingspeak is illustrate in figure 3. Third program is to visualize the heart beat using processing software.

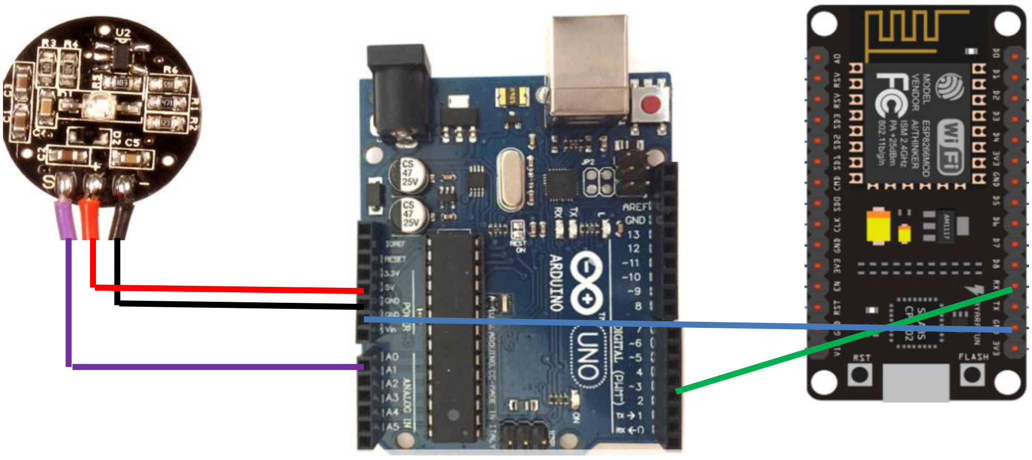

Figure 2 Cicuit connection of monitoring system of IoT

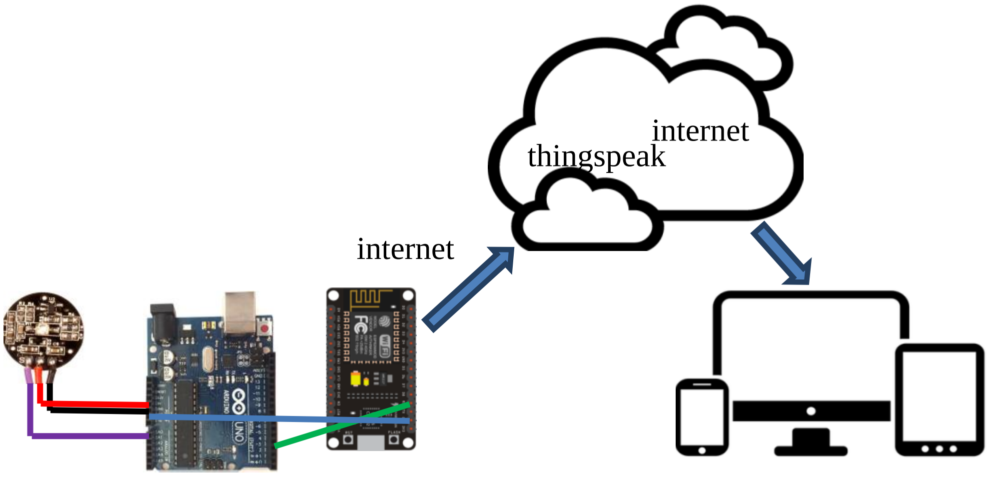

Figure 3 Block diagram of IoT communication

The following part of program is data sending from Arduino to NodeMCU.

```
serial Output() ;
 if (QS == true){
       digital Write(blinkPin,HIGH);
       fadeRate = 255
       serialOutputWhenBeatHappens();
       QS = false;
       ESPSerial.write(BPM);
      }
     else {
     digitalWrite(blinkPin,LOW);
     }
       ledFadeToBeat();
 delay(20);
```

The following is sending data from Node MCU to thingspeak;

```
while(!Serial.available()){}
        int BPM = Serial.read();
        sendDataThingSpeak(BPM);
        Serial.print("BPM is ");
        Serial.println(BPM);
```

And then, select the channel in thingSpeak window.

```
int x = ThingSpeak.writeField(my Channel Number, 1, number, my WriteAPIKey);
```

Results

Firstly, the output data from the sensor is examined by Arduino. The graph shown in figure 4 is drawn with data received by Arduino and it is displayed by serial plotter which is built-in Arduino IDE.

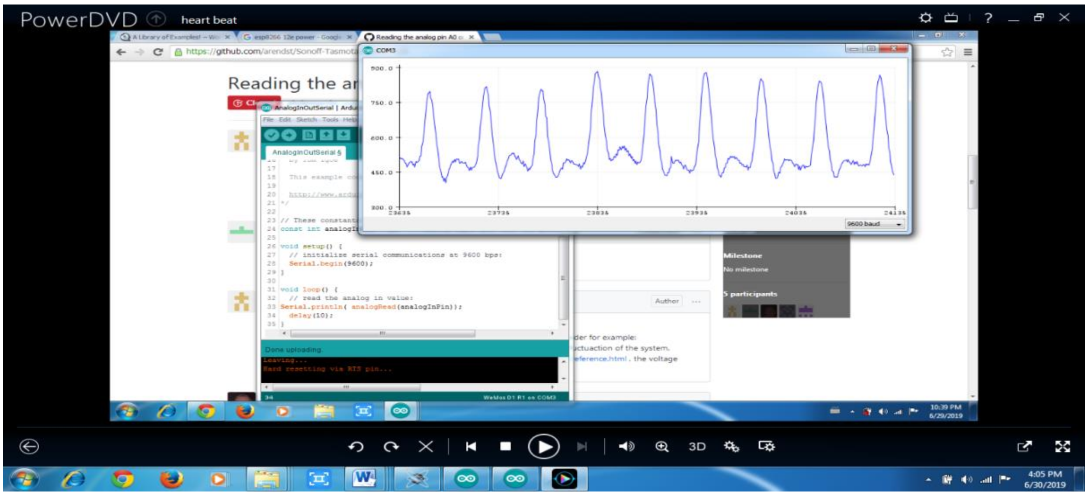

```
  This example co

  http://www.ardu
*/

// These constant
const int analogI

void setup() {
  // initialize serial communications at 9600 bps:
  Serial.begin(9600);
}

void loop() {
  // read the analog in value:
Serial.println( analogRead(analogInPin));
  delay(10);
}
```

```
Done uploading.
Leaving...
Hard resetting via RTS pin...
```

Figure 4 Heart rate by Arduino IDE

According to the waveform, the sensor has Good sensitivity. After testing sensor, it is connected to NodeMCU through Arduino. The heart beat wave form can be visualized by using the processing software. The heart rate – time graph, the sending heart rate data on serial monitor and pulse rate wave form are illustrated together in the figure 5.

```
Got 20s
Channel update successful.
BPM is 74
Got 20s
Channel update successful.
BPM is 82
Got 20s
Channel update successful.
BPM is 78
Got 20s
Channel update successful.
BPM is 77
Got 20s
Channel update successful.
BPM is 76
```

Figure 5 Heart rate monitoring on PC.

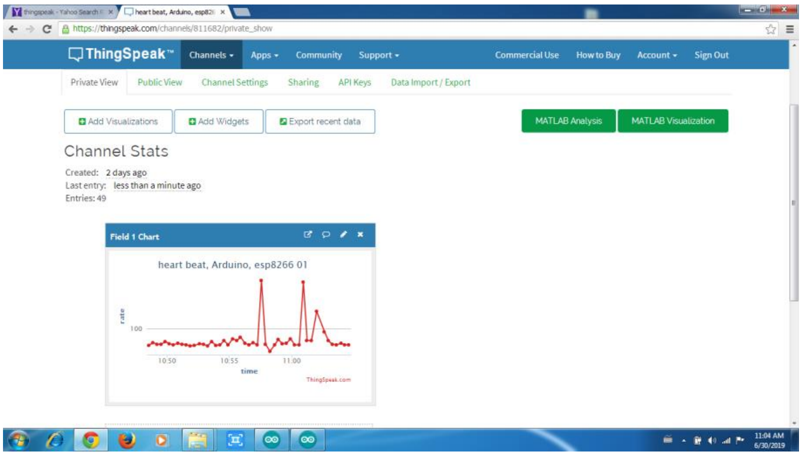

Channel Stats

Created: 2 days ago

Last entry: less than a minute ago

Entries: 49

Figure 6 Heart rate displayed on thingSpeak

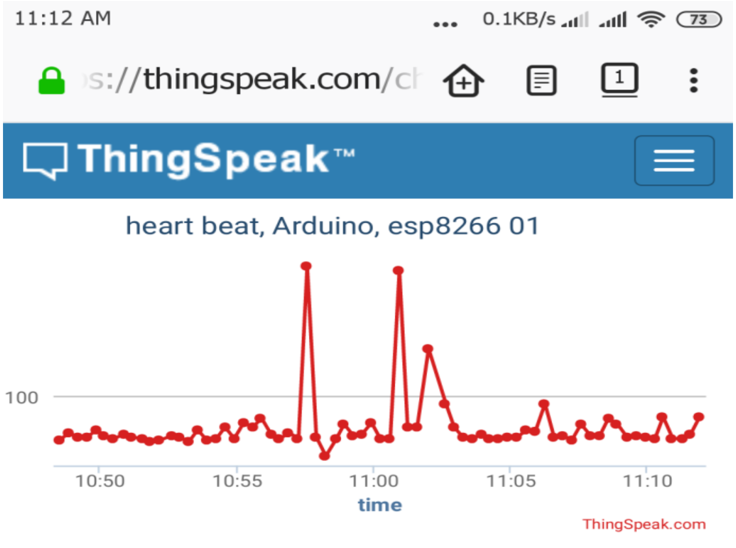

Figure 7 Heart beat display on phone

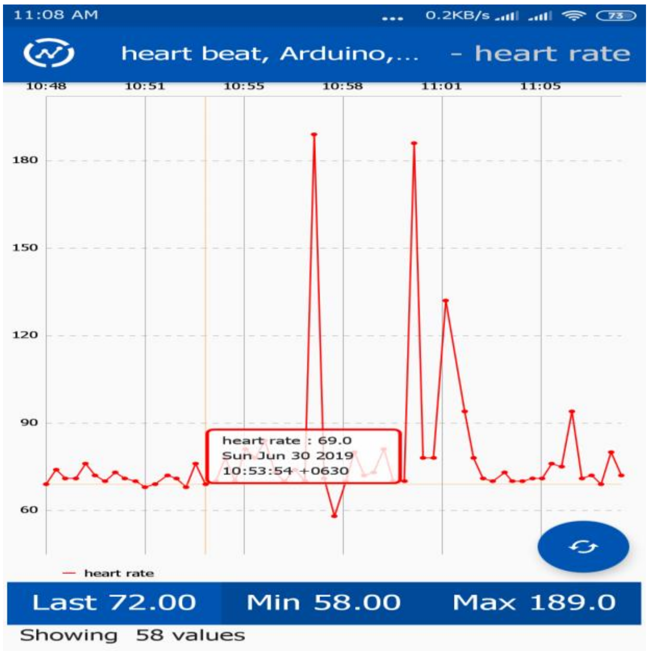

Last 72.00 Min 58.00 Max 189.0

Showing 58 values

Figure 8 Analysis of heart rate

The heart rate can be received by smart phone, tablet which has internet accessibility as well as PC. Figure 7 and figure 8shows the heart rate and Matlab analysis on phone respectively.

Conclusion

This is an important sensor based system which has the latest technology implemented in it. And it has many applications & advantages. IoT Healthcare is the most demanding field in the medical area. Patient health parameter data is stored over the cloud. So it is more beneficial than maintaining the records on printed papers kept in the files. Or even the digital records which are kept in a particular computer or laptop or memory device like pen-drive.

Acknowledgements

The authors would like to acknowledge Professor Dr Khin Khin Win, Head of Department of Physics, University of Yangon, for her valuable suggestion and comments for this work. I would like to thank Associate Professor Dr Than Nwet, Head of Department of Physics(Acting), Taungoo University, for her kind permission to carry out this work.

References

Banzi M, 2009“Getting Started with Arduino” U.S.A.

Boxall J, 2013 “ Arduino Workshop”, No Starch Press, San Fransisco.

Monk S, 2010“Arduino™ + Android™ Projects for the Evil Genius” Tab.5. Purdun J,2012 “Beginning C for Arduino” Apress, NY

https://en.wikipedia.org/wiki/NodeMCU

www.projectsof8051.com/arduino-and-iot-based...

en.wikipedia.org/wiki/ThingSpeak

J. Myanmar Acad. Arts Sci. 2020 **Vol. XVIII.No.2B**

DATA ACQUISITION OF SOLAR RADIATION AND ULTRA-VIOLET (UV) INTENSITY

Zin Zin Naing[1], Tin Tin Nyo[2], Hla Hla Htoo[3]

Abstract

The intensity of solar radiation and UV radiation are measured using BH1750 by BH1750 sensor and light sensor and ML 8511 UV sensor respectively. The process is implemented by using microcontroller. As BH 1750 light sensor is inter- integrated circuit (I2C) device, it is connected to microcontroller with I2C mode. The data from each sensor are sent to Arduino microcontroller and then, data are displayed on LCD. Simultaneously, the intensity of light and UV radiation are logged in excel spreadsheet directly using the parallex data acquisition (PLX-DAQ) software. These data are uploaded directly to Microsoft(MS) excel spreadsheet directly with the accompanying the current date and time.

Keywords: UV radiation, I2C, data acquisition, MS excel

Introduction

The Sun also emits light across a broad spectrum. At the low end is the Infrared light (which is perceived as heat), followed by the visible light that are all familiar with living and non-living things. And then there is Ultraviolet light at the high end. Ultraviolet or UV light is filtered to a large degree by the Earth's Ozone layer, a protective layer of gas in the upper atmosphere that absorbs UV radiation. But the ozone layer is not a perfect filter and as a consequence some of the UV makes it through. The visible light is detected by BH1750 light sensor and UV radiation is detected by ML8511 sensor. Since BH1750 is inter-integrated circuit (I2C) device, "wire" library is included in Arduino integrated development and Environment (IDE) software. Arduino microcontroller can detected the output voltage of two sensors and these are converted to the intensity value by using respective equation. These data are directly transferred to the Microsoft(MS) excel spreadsheet using the parallex data acquisition (PLX_DAQ) software.

Materials and Methods

In this research, Arduino microcontroller, BH 1750 light sensor, ML8511 UV sensor and LCD are required as the hardware. BH1750 library is downloaded from website. "wire" and" Liquid Crystal" library is built- in library in Arduino IDE. The circuit diagram is illustrated in figure 1.BH1750 is I2C device which has serial data and serial clock line. Analog pin A4 and A5 are serial data and serial clock pin for Arduino uno, SDA and SCL are connected to A4 and A5 of Arduino, respectively.

---

[1] Dr, Lecturer, Department of Physics, Taunggoo University

[2] Dr, Associate Professor, Department of Physics, Taunggoo University

[3] Dr, Associate Professor, Department of Physics, Taunggoo University

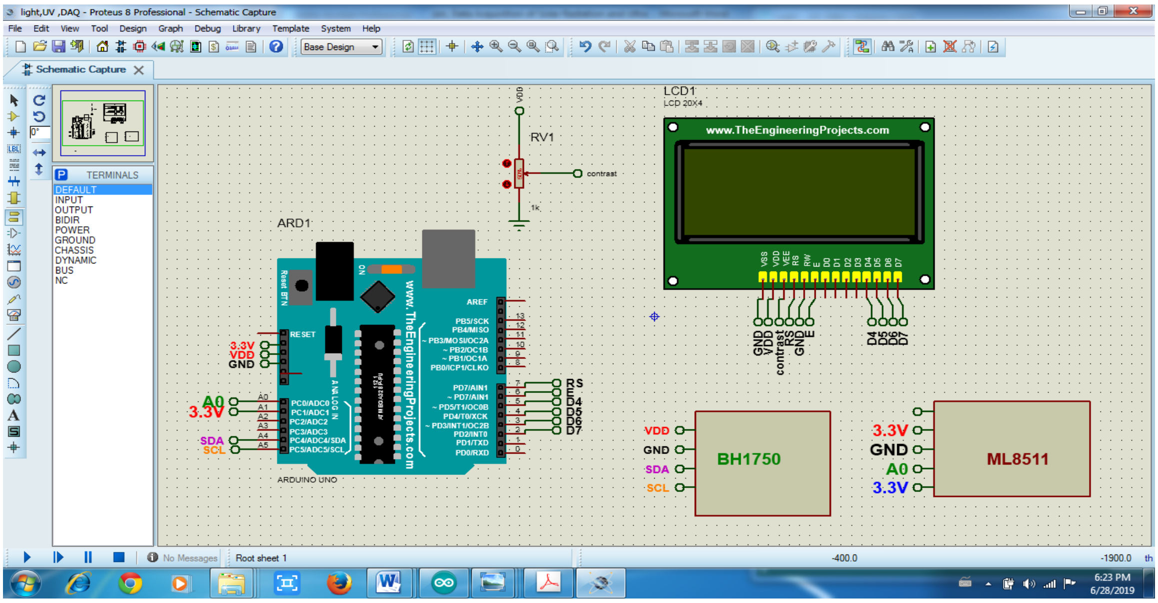

Figure 1 Schematic circuit diagram of light meter

BH1750 light sensor

BH1750 light intensity sensor breakout board(figure.2) consists of a 16 bit AD converter built-in which can directly output a digital signal; there is no need for complicated calculations. With the BH1750 Light Sensor intensity can be directly measured by the lux meter, without needing to make calculations. The data which is output by this sensor is directly output in Lux (Lx). By connecting the BH1750 with I2C bus interface it can determine the light intensity with illuminant to digital converter. It is possible to detect with wide range and high resolution 1 up to 65535 lx with low current power down function.

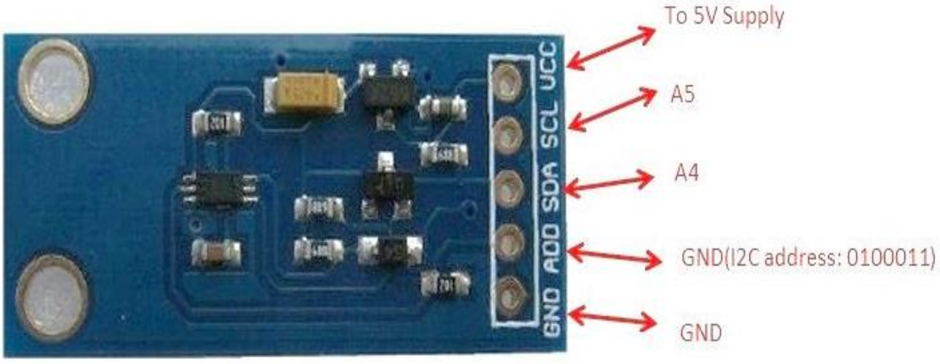

Figure 2 BH1750 light sensor

ML 8511 UV Sensor

The MP8511 UV (ultraviolet) Sensor works by outputting an analog signal in relation to the amount of UV light that’s detected. This sensor detects 280-390nm light most effectively. This is categorized as part of the UVB (315nm- 280nm) spectrum and most of the UVA (400nm-

315nm) spectrum. It outputs a analog voltage that is linearly related to the measured UV intensity (mW/cm2). The sensor ML8511 has a UV photodiode and Internal Amplifier which will converts photo current to voltage output depending on the UV light intensity. Through the voltage output it is easy to interface with external micro controllers and ADC.

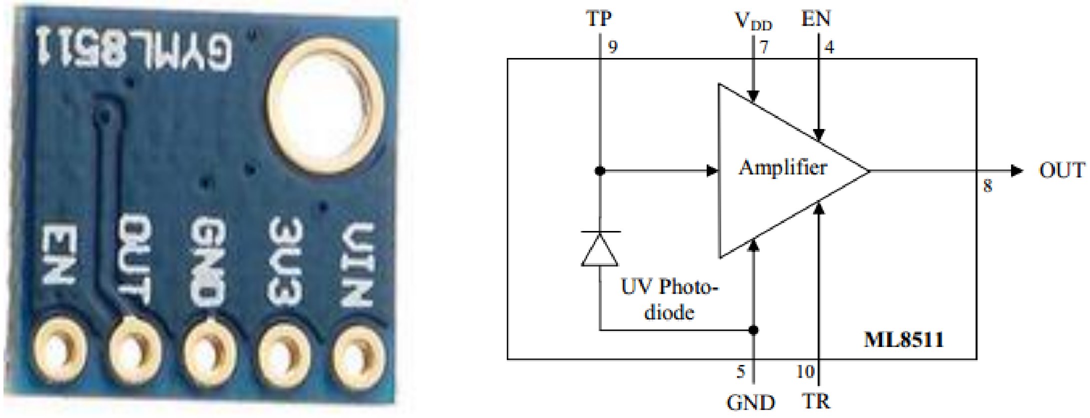

Figure 3 UV sensor and its block diagram

The UV Index scale was developed by Canadian scientists in 1992, then adopted and standardized by the WHO in 1994. In most areas of the world the UV Index ranges from 0 to 10, but it can get a lot higher than that. Locations in the tropics often have UV levels exceeding 12 and high altitudes like mountaintops routinely register a UV Index of 20.UV index is illustrated in figure 4. UV intensity is directly proportional to the output voltage of ML 8511 sensor as shown in figure.

Figure 4 UV index level

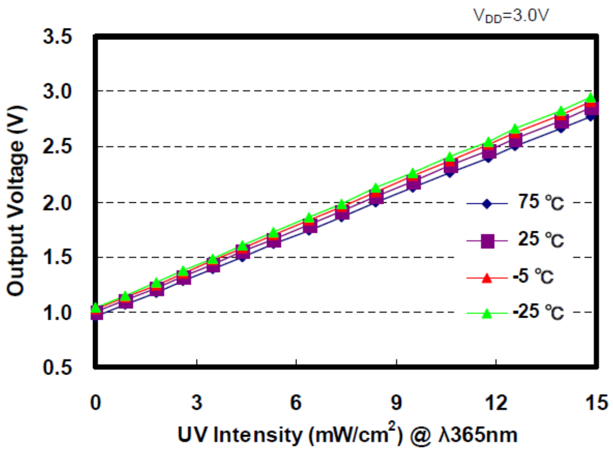

Figure 5 Output voltage dependency on UV radiation

Program Explanation

- Address and Library file for BH 1750 are included in Arduino IDE.

```
#include <LiquidCrystal.h>
#include <Wire.h>
#include <BH1750.h>
LiquidCrystallcd(7, 6, 5, 4, 3, 2);
```

To obtain the light intensity

```
Wire.beginTransmission(BH1750address);
Wire.write(0);
Wire.endTransmission();
Wire.requestFrom(BH1750address, 1);
while(Wire.available() == 0);
 uint16_t lux = lightMeter.readLightLevel();
```

To get UV intensity, floatmap() function is used . From figure 5, output voltage is extended from 0.99V to 2.9 V while the UV intensity is varied from 0 to 15mW/m^2. Since the reference level is 3.3V, firstly output voltage is determined and then, transform to UV intensity by mapping.

```
float outputVoltage = 3.3 / refLevel * uvLevel;
float uvIntensity = mapfloat(outputVoltage, 0.99, 2.9, 0.0, 15)
```

Light intensity and UV intensity are displayed on LCD and are sent to excel sheet simultaneously.

For data logging in excel, firstly , data are clear and make the heading line of table as follows;

```
Serial.println("CLEARDATA");
Serial.println("LABEL,Date,Time,Intesity(lux),Intesity(FtCd),Intesity(W/m^2),UVIntensity(mW/cm^2)");
```

And then, data sent from microcontroller are filledin the excel table.

```
Serial.print("DATA,DATE,TIME,");
Serial.print(lux);
Serial.print(",");
Serial.print(lux/10.764);
Serial.print(",");
Serial.print(lux/683.0);
Serial.print(",");
Serial.println(uvIntensity);
```

Results

Light intensity is measured in “lux”, “foot candle”(ft-cd) and W/m^2. UV intensity is measured in mW/cm^2.Figure 7 shows the Light intensity and UV intensity of phone flash light on LCD at the distance 2cm to 10 cm variation. Light intensity is varied with distance but UV intensity is small and almost same. So, phone flash light emits the low level UV radiation. Data are sent to excel via PLX_DAQ software in figure 8. When UV light falls on sensor, UV level are changed with distance between source and sensor as shown in figure 9.

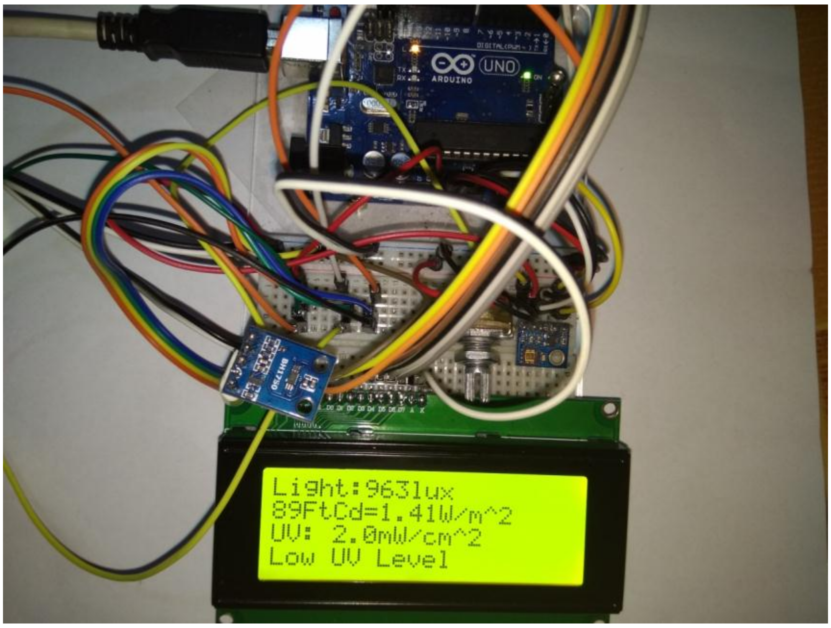

```
Light:963lux
89FtCd=1.41W/m^2
UV: 2.0mW/cm^2
Low UV Level
```

Figure 6 Experimental setup

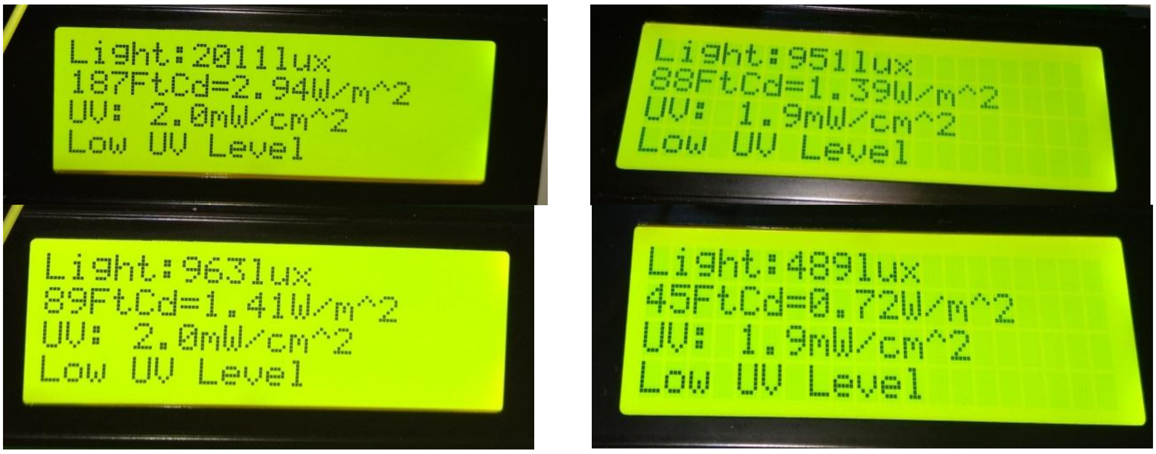

```
Light:2011lux
187FtCd=2.94W/m^2
UV: 2.0mW/cm^2
Low UV Level
```

```
Light:951lux
88FtCd=1.39W/m^2
UV: 1.9mW/cm^2
Low UV Level
```

```
Light:963lux
89FtCd=1.41W/m^2
UV: 2.0mW/cm^2
Low UV Level
```

```
Light:489lux
45FtCd=0.72W/m^2
UV: 1.9mW/cm^2
Low UV Level
```

Figure 7 Light intensity of Phone Flash light

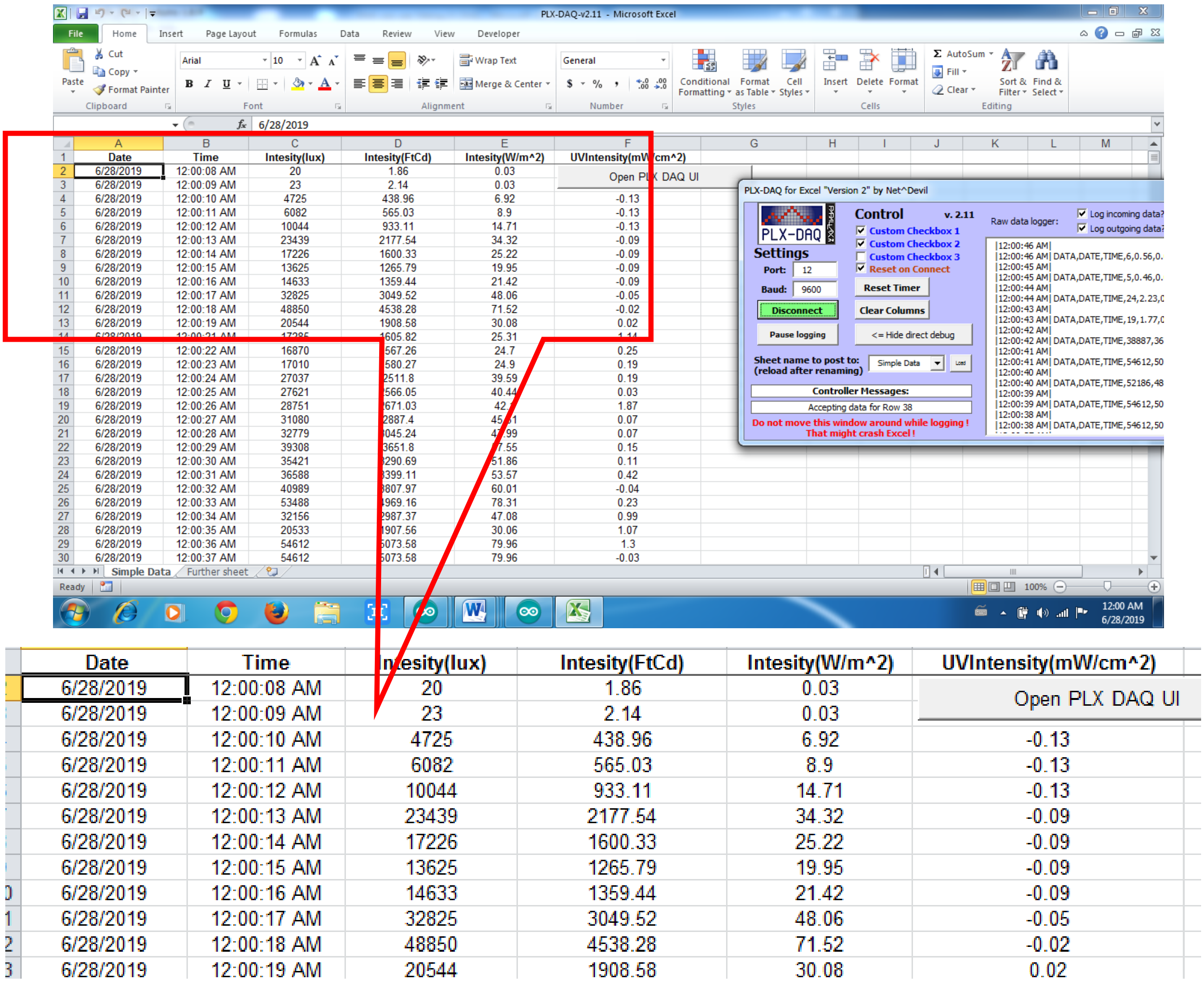

	A	B	C	D	E	F
1	Date	Time	Intesity(lux)	Intesity(FtCd)	Intesity(W/m^2)	UVIntensity(mW/cm^2)
2	6/28/2019	12:00:08 AM	20	1.86	0.03	
3	6/28/2019	12:00:09 AM	23	2.14	0.03	
4	6/28/2019	12:00:10 AM	4725	438.96	6.92	-0.13
5	6/28/2019	12:00:11 AM	6082	565.03	8.9	-0.13
6	6/28/2019	12:00:12 AM	10044	933.11	14.71	-0.13
7	6/28/2019	12:00:13 AM	23439	2177.54	34.32	-0.09
8	6/28/2019	12:00:14 AM	17226	1600.33	25.22	-0.09
9	6/28/2019	12:00:15 AM	13625	1265.79	19.95	-0.09
10	6/28/2019	12:00:16 AM	14633	1359.44	21.42	-0.09
11	6/28/2019	12:00:17 AM	32825	3049.52	48.06	-0.05
12	6/28/2019	12:00:18 AM	48850	4538.28	71.52	-0.02
13	6/28/2019	12:00:19 AM	20544	1908.58	30.08	0.02
14	6/28/2019	12:00:21 AM	17285	1605.82	25.31	1.14
15	6/28/2019	12:00:22 AM	16870	567.26	24.7	0.25
16	6/28/2019	12:00:23 AM	17010	580.27	24.9	0.19
17	6/28/2019	12:00:24 AM	27037	2511.8	39.59	0.19
18	6/28/2019	12:00:25 AM	27621	566.05	40.44	0.03
19	6/28/2019	12:00:26 AM	28751	671.03	42.[illegible]	1.87
20	6/28/2019	12:00:27 AM	31080	2887.4	45.[illegible]1	0.07
21	6/28/2019	12:00:28 AM	32779	045.24	4[illegible].99	0.07
22	6/28/2019	12:00:29 AM	39308	3651.8	[illegible]7.55	0.15
23	6/28/2019	12:00:30 AM	35421	290.69	51.86	0.11
24	6/28/2019	12:00:31 AM	36588	399.11	53.57	0.42
25	6/28/2019	12:00:32 AM	40989	807.97	60.01	-0.04
26	6/28/2019	12:00:33 AM	53488	969.16	78.31	0.23
27	6/28/2019	12:00:34 AM	32156	2987.37	47.08	0.99
28	6/28/2019	12:00:35 AM	20533	1907.56	30.06	1.07
29	6/28/2019	12:00:36 AM	54612	073.58	79.96	1.3
30	6/28/2019	12:00:37 AM	54612	073.58	79.96	-0.03

PLX-DAQ for Excel "Version 2" by Net^Devil

Control v. 2.11

☑ Custom Checkbox 1
☑ Custom Checkbox 2
☐ Custom Checkbox 3
☑ Reset on Connect

Settings

Port: 12
Baud: 9600

Disconnect
Reset Timer
Clear Columns
Pause logging
<= Hide direct debug

Sheet name to post to: (reload after renaming) Simple Data

Raw data logger: ☑ Log incoming data? ☑ Log outgoing data?

```
|12:00:46 AM|
|12:00:46 AM| DATA,DATE,TIME,6,0.56,0.
|12:00:45 AM|
|12:00:45 AM| DATA,DATE,TIME,5,0.46,0.
|12:00:44 AM|
|12:00:44 AM| DATA,DATE,TIME,24,2.23,0
|12:00:43 AM|
|12:00:43 AM| DATA,DATE,TIME,19,1.77,0
|12:00:42 AM|
|12:00:42 AM| DATA,DATE,TIME,38887,36
|12:00:41 AM|
|12:00:41 AM| DATA,DATE,TIME,54612,50
|12:00:40 AM|
|12:00:40 AM| DATA,DATE,TIME,52186,48
|12:00:39 AM|
|12:00:39 AM| DATA,DATE,TIME,54612,50
|12:00:38 AM|
|12:00:38 AM| DATA,DATE,TIME,54612,50
```

Controller Messages:
Accepting data for Row 38

Do not move this window around while logging !
That might crash Excel !

Date	Time	Intesity(lux)	Intesity(FtCd)	Intesity(W/m^2)	UVIntensity(mW/cm^2)
6/28/2019	12:00:08 AM	20	1.86	0.03	Open PLX DAQ UI
6/28/2019	12:00:09 AM	23	2.14	0.03	
6/28/2019	12:00:10 AM	4725	438.96	6.92	-0.13
6/28/2019	12:00:11 AM	6082	565.03	8.9	-0.13
6/28/2019	12:00:12 AM	10044	933.11	14.71	-0.13
6/28/2019	12:00:13 AM	23439	2177.54	34.32	-0.09
6/28/2019	12:00:14 AM	17226	1600.33	25.22	-0.09
6/28/2019	12:00:15 AM	13625	1265.79	19.95	-0.09
6/28/2019	12:00:16 AM	14633	1359.44	21.42	-0.09
6/28/2019	12:00:17 AM	32825	3049.52	48.06	-0.05
6/28/2019	12:00:18 AM	48850	4538.28	71.52	-0.02
6/28/2019	12:00:19 AM	20544	1908.58	30.08	0.02

Figure 8 Data on excel

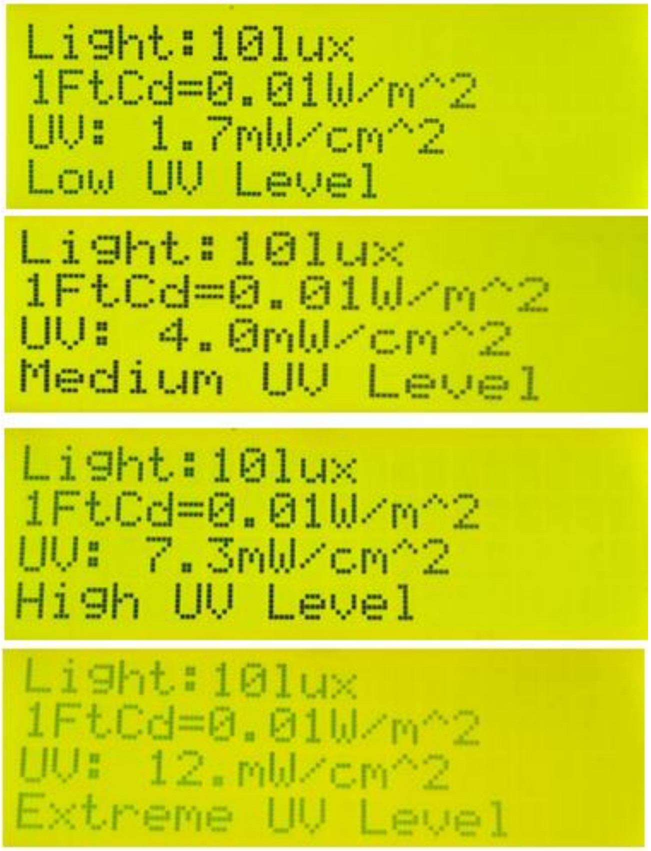

```
Light:10lux
1FtCd=0.01W/m^2
UV: 1.7mW/cm^2
Low UV Level
```

```
Light:10lux
1FtCd=0.01W/m^2
UV: 4.0mW/cm^2
Medium UV Level
```

```
Light:10lux
1FtCd=0.01W/m^2
UV: 7.3mW/cm^2
High UV Level
```

```
Light:10lux
1FtCd=0.01W/m^2
UV: 12.mW/cm^2
Extreme UV Level
```

Figure 9 Testing UV index and light intensity

Conclusion

In UV data measured in the room light, it takes negative. The output voltage of 0.99 V is referred to 0 mW/cm^2. When voltage is less than 0.99V in room light,UV intensity takes the negative value. There are some advantages and disadvantages of effects of UV radiation. The purpose of the UV Index is to help people effectively protect themselves from UV radiation, which has health benefits in moderation but in excess causes sunburn, skin aging,DNA damage, skin cancer, immunosuppression,[1] and eye damage such as cataracts.

Acknowledgements

The authors would like to acknowledge Professor Dr Khin Khin Win, Head of Department of Physics, University of Yangon, for her valuable suggestion and comments for this work. I would like to thank Professor Dr Nge Nge Khaing, Head of Department of Physics, Taungoo University, for her kind permission to carry out this work.

References

Banzi M, 2009"Getting Started with Arduino" U.S.A.

Boxall J, 2013 " Arduino Workshop", No Starch Press, San Fransisco.

Göransson A ,2013 "Android™ Open Accessory Programming with Arduino" ,John Wiley & son inc.

Monk S, 2010"Arduino™ + Android™ Projects for the Evil Genius" Tab .

Monk S, 2010 "30 arduino projects for the evil geneius" Mc Graw-Hill
Companies, Inc.

Purdun J,2012 "Beginning C

J. Myanmar Acad. Arts Sci. 2020 **Vol. XVIII.No.2B**

INVESTIGATION OF ENERGY BAND GAP OF Sb DOPED SnO_2 THIN FILMS

Zin Mar Win[1], Ohn Mar Swe[2], Amy Than[3] and Moht Moht Than[4]

Abstract

Undoped SnO_2 and different Sb concentration (2 mol%, 4 mol%, 6 mol% & 8 mol%) were doped with SnO_2 thin films by sol-gel process. *Undoped SnO_2* and *Sb doped SnO_2 thin films* were grown in glass substrate by using spin coating technique and annealed at 500˚C for 1hour. The structural, and optical properties of deposited and doped samples were studied. XRD analysis was carried out to determine the lattice parameters, unit cell volume and *crystallite size* of the samples. According to the X-ray diffraction spectra the samples were formed with tetragonal structure and preferred orientation alone (110) plane. The dislocation density of the samples are also calculated. From the UV-Visible spectrum, absorption coefficient and the *band gap energy* of the samples are evaluated.

Keywords: Undoped SnO_2 and Sb doped SnO_2 thin films, crystallite size, and band gap energy

Introduction

Semiconductors are one of the most interesting and most useful solids. They have been investigated many times because of their flexibility, electricity and optical features.SnO_2 is one of these semiconductors. The SnO_2 with a wide-band-gap (E_g = 3.6 ~ 4.0 eV) is one of the excellent semiconductors which can be applied to solid state gas sensors, sensing arrays, solar cells, photovoltaic cells, organic light emitting diodes, touch sensitive screens and thin film transistors. [Bagheri Mohaghegi M M et al (2008), Khan AF et al (2010), Moharrami F et al (2012)]. The SnO_2 thin films can be fabricated by a number of techniques such as chemical vapour deposition (CVD), metalorganic deposition, rf sputtering, sol-gel dip coating, spin coating and spray pyrolysis. [Maekava T et al (2001), Yin LT et al (2000), Yin LT et al (2000), Ouerfelli J et al (2008).] It was clearly established spin coating that structural, electronic transport and optical properties of SnO_2 films are very sensitive to preparation method, deposition conditions, dopant atoms and amount of dopant atoms. Tin dioxide (SnO_2) has been intensively investigated because of its rich physical properties and large applications in commercial devices.

Experimental

The glass substrates were ultrasonically cleaned by keeping in ethanol and in the distilled water, for ten minutes, respectively. Then the glass substrates were dried. The films deposited on the glass substrates by spin coating technique. In order to prepare the coating solution, firstly, undoped SnO_2 and different Sb concentration (2 mol%, 4 mol%, 6 mol% & 8 mol%) were doped with thin films by sol-gel process. The mixture powder is ground by agate mortor to obtain the homogeneous and uniform grain size of powder. This powder is heat treated at 500ºC for 1 hr. The crystalline powder, were mixed with 2-methoxyethanol solution by using sol-gel method.

---

[1] Dr, Lecturer, Department of Physics, University of Yangon.

[2] Lecturer, Department of Physics, University of Yangon.

[3] Lecturer, Department of Physics, University of Yangon.

[4] Associate Professor Department of Physics, Mohnyin Degree College.

And then these pastes were coated on glass substrates and annealed at 500ºC for 1 hr, respectively.

Results and Discussion

The structure of prepared films were characterized by X-ray diffraction (Rigaku Multiflex, Japan) with Cu K_α source (λ =1.54056 Å).

The XRD analysis of the as-synthesized undoped SnO_2 and with different concentration of Sb thin films on glass is shown in figure 1 (a ~ e). The diffraction patterns of the samples match the tetragonal structure. Furthermore, increasing the antimony content did not yield any other crystalline phase. The films show a preferred orientation along the (110), (101), (200) and (211) planes. The lattice constants a and c for the tetragonal phase structure are determined by the relation,

$$\frac{1}{d^2}=\left(\frac{h^2}{a^2}+\frac{k^2}{a^2}\right)+\left(\frac{l^2}{c^2}\right)$$

where d and (hkl) are interplanar distance and Miller indices, respectively. The lattice constant a and c, the unit cell volumes are calculated as given in Table 1. They match well with the standard JCPDS data card. In order to determine the variation of crystallite size with increasing Sb doping, the size of the crystallites oriented along the (110) plane is calculated using Scherrer's formula,

$$L=\frac{0.9\lambda}{\beta\cos\theta}$$

where β,θ and λ are the broadening of the diffraction line measured at half its maximum intensity in radians, the diffraction angle, and the X-ray wavelength, respectively. The calculated values of unit cell volume are given in Table 1. Dislocation density and crystallite size are given in Table 2.

Table 1 The structural properties of undoped SnO_2 and Sb doped SnO_2 thin films on glass substrate

Samples	***Maximum peak***	***Lattice constant "a"(Å)***	***Lattice constant "c"(Å)***	***Unit cell volume "V" (nm)^3***
Undoped SnO_2	(110)	4.8365	3.2068	0.0750
Sb (2mol%) doped SnO_2	(110)	4.8138	3.1941	0.0740
Sb (4mol%) doped SnO_2	(110)	4.8609	3.1973	0.0755
Sb (6mol%) doped SnO_2	(110)	4.8024	3.1931	0.0736
Sb (8mol%) doped SnO_2	(110)	4.8519	3.1950	0.0752

Table 2 The values of dislocation density and crystallite size of undoped SnO_2 and Sb doped SnO_2 thin films on glass substrate

Samples	*Maximum peak*	*Crystallite size "L" (nm)*	*Dislocation density "δ" $(m)^{-2}$*
Undoped SnO_2	(110)	61.3222	2.6593×10^{14}
Sb (2 mol%) doped SnO_2	(110)	58.2183	2.9504×10^{14}
Sb (4 mol%) doped SnO_2	(110)	57.8355	2.9896×10^{14}
Sb (6 mol%) doped SnO_2	(110)	55.1036	3.2934×10^{14}
Sb (8 mol%) doped SnO_2	(110)	52.5894	3.6158×10^{14}

The optical transmittance (T%) spectrum of undoped SnO_2 and Sb doped SnO_2 thin films was taken in the wavelength range 300 ~ 1100 nm. Figure 2 (a ~ e) shows the variation of optical transmittance with the wavelength of thin films. The fundamental absorption corresponding to the optical transition of the electrons from the valence band to the conduction band can be used to determine the nature and value of the optical band gap E_g of the films.

The optical absorption coefficient (α) was calculated from transmittance using the following relation,

$$\alpha = \frac{1}{d}\log(\frac{1}{T})$$

where T is the transmittance and d is the thickness of the films. The films under study have an absorption coefficient (α) obeying following relation for high photon energies (hν)

$$\alpha = \frac{A(h\nu - E_g)^{\frac{1}{2}}}{h\nu}$$

where E_g is the optical band gap of the films and A is a constant. A plot of variation of $(\alpha h\nu)^2$ versus hν is shown in Figure 3 (a ~ e). E_g is evaluated using the extrapolation of the linear part. The intercept on energy axis gives the value of band gap energy. Upon increasing the Sb concentration, the band gap of the films was found to increase from 3.43 eV to 4 eV. Optical band gap energy with different Sb doped SnO_2 thin films is shown in Table (3).

Table 3 Optical band gap energy with different Sb doped SnO_2 thin films.

Sb doped SnO_2	**Band gap energy (eV)**
Undoped SnO_2	3.43eV
Sb (2mol%) doped SnO_2	3.85eV
Sb (4mol%) doped SnO_2	3.91eV
Sb (6 mol%) doped SnO_2	3.98eV
Sb (8mol%) doped SnO_2	4 eV

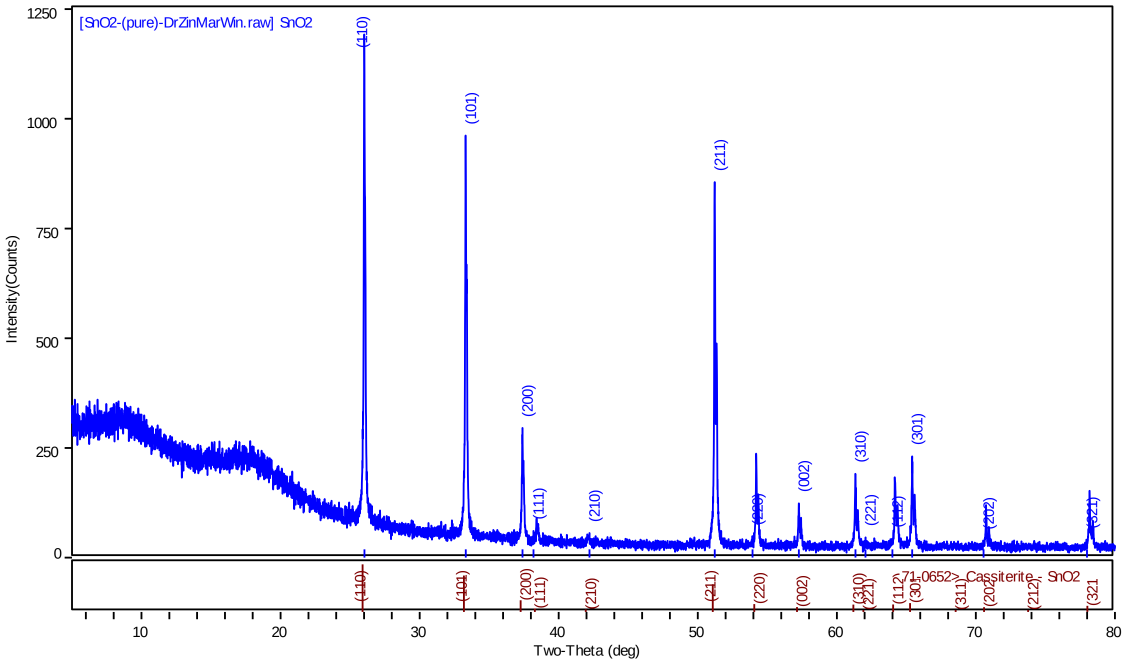

Figure 1 (a) XRD pattern of undoped SnO_2 thin film on glass

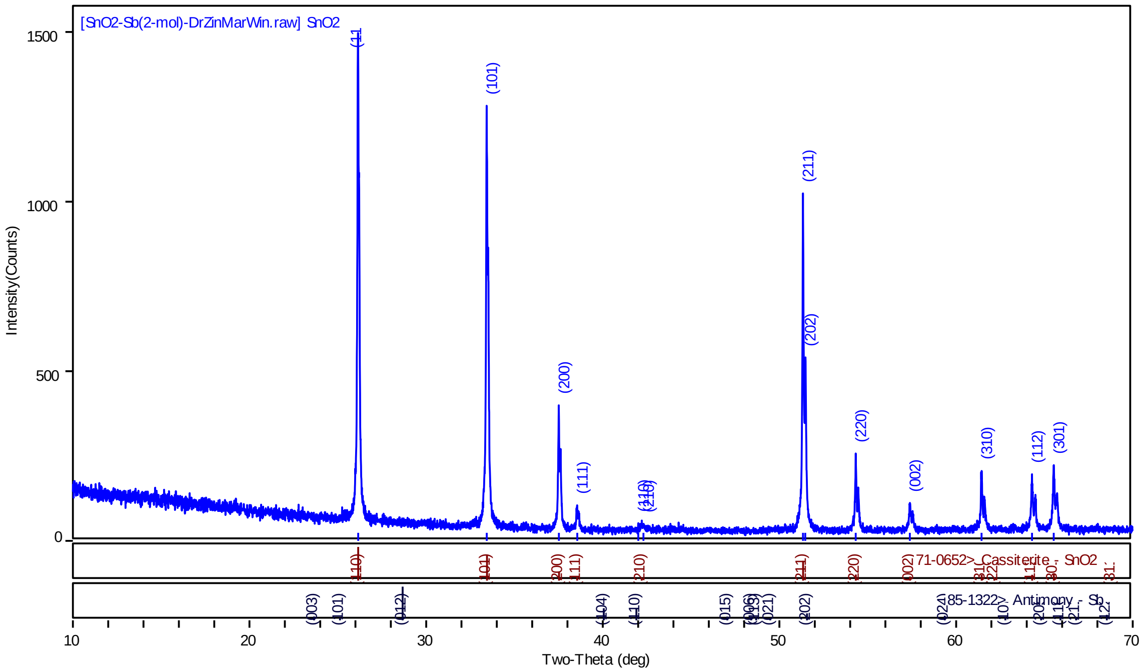

Figure 1 (b) XRD pattern of Sb (2 mol%) doped SnO_2 thin film on glass

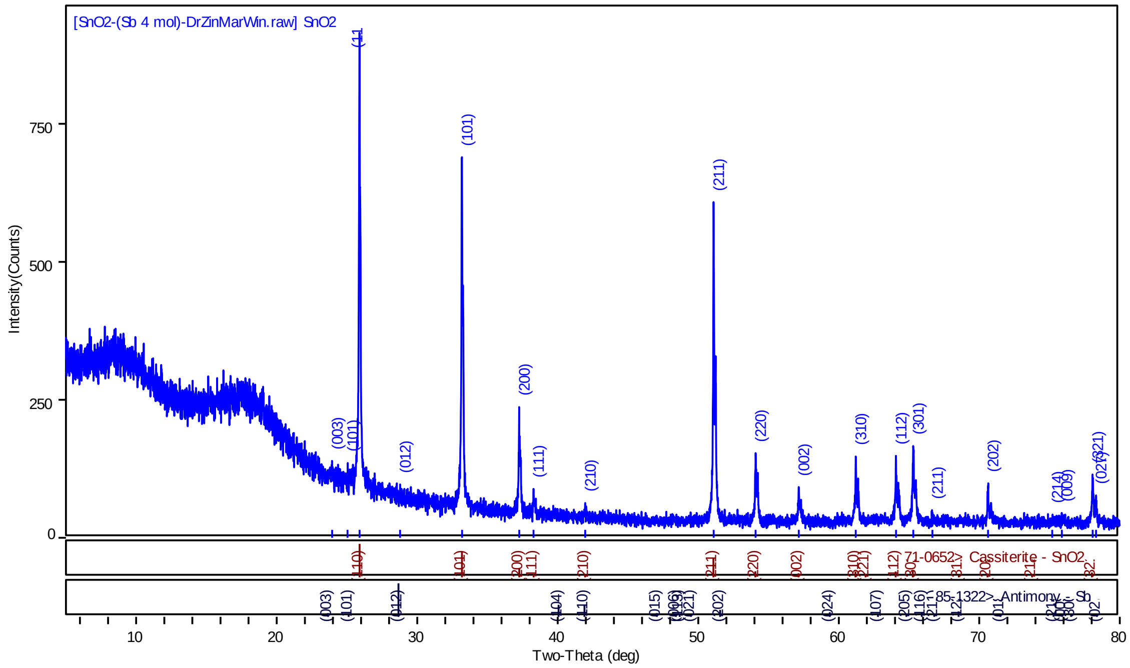

Figure 1 (c) XRD pattern of Sb (4 mol%) doped SnO_2 thin film on glass

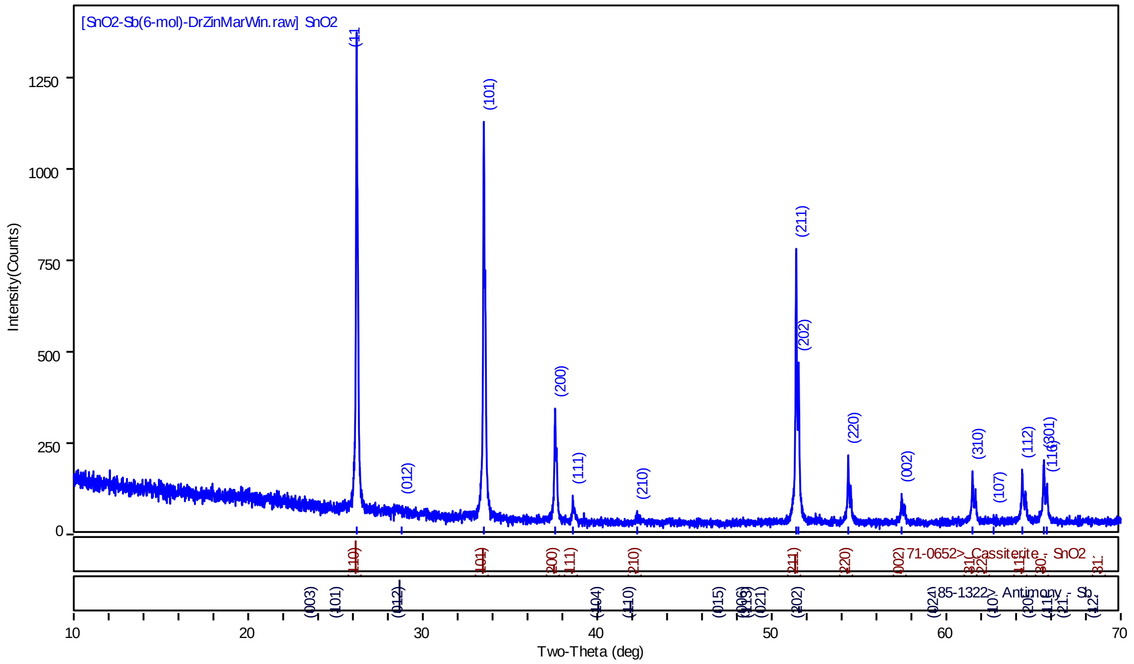

Figure 1 (d) XRD pattern of Sb (6 mol%) doped SnO_2 thin film on glass

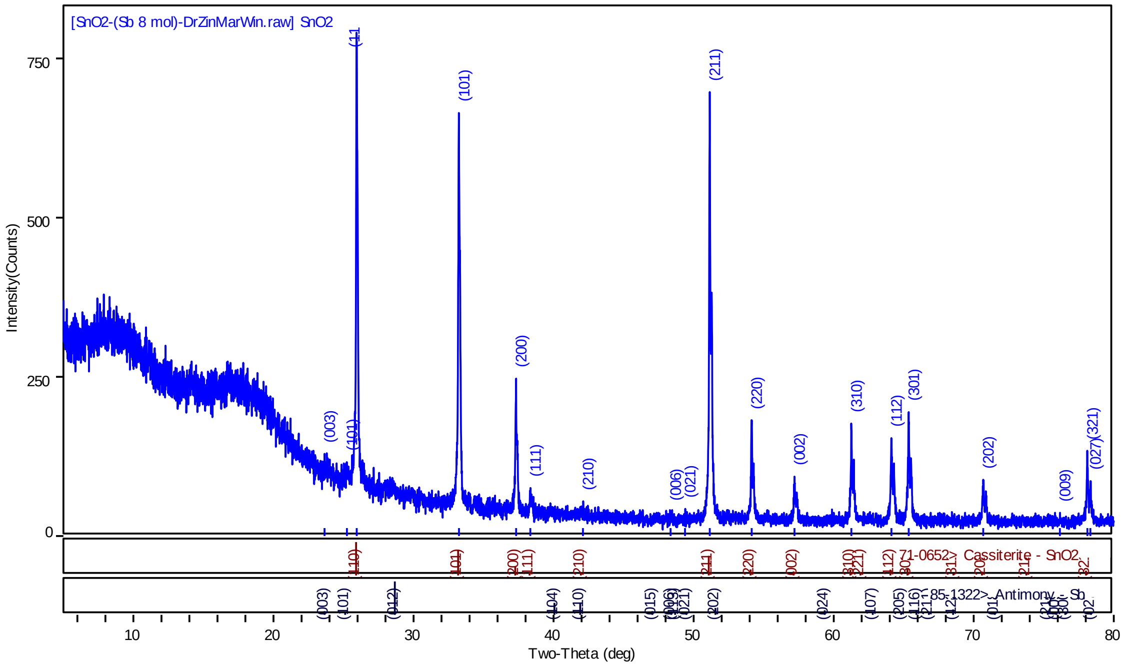

Figure 1 (e) XRD pattern of Sb (8 mol%) doped SnO_2 thin film on glass

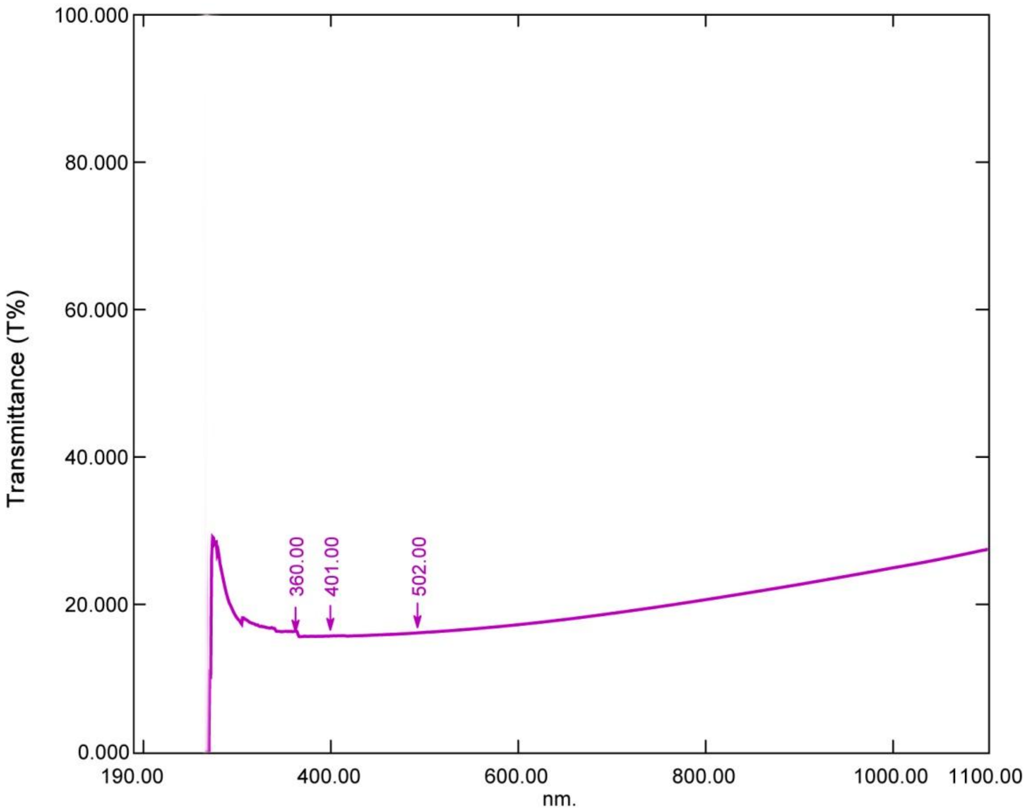

Figure 2 (a) Transmittance (T%) spectra for undoped SnO_2 thin film on glass

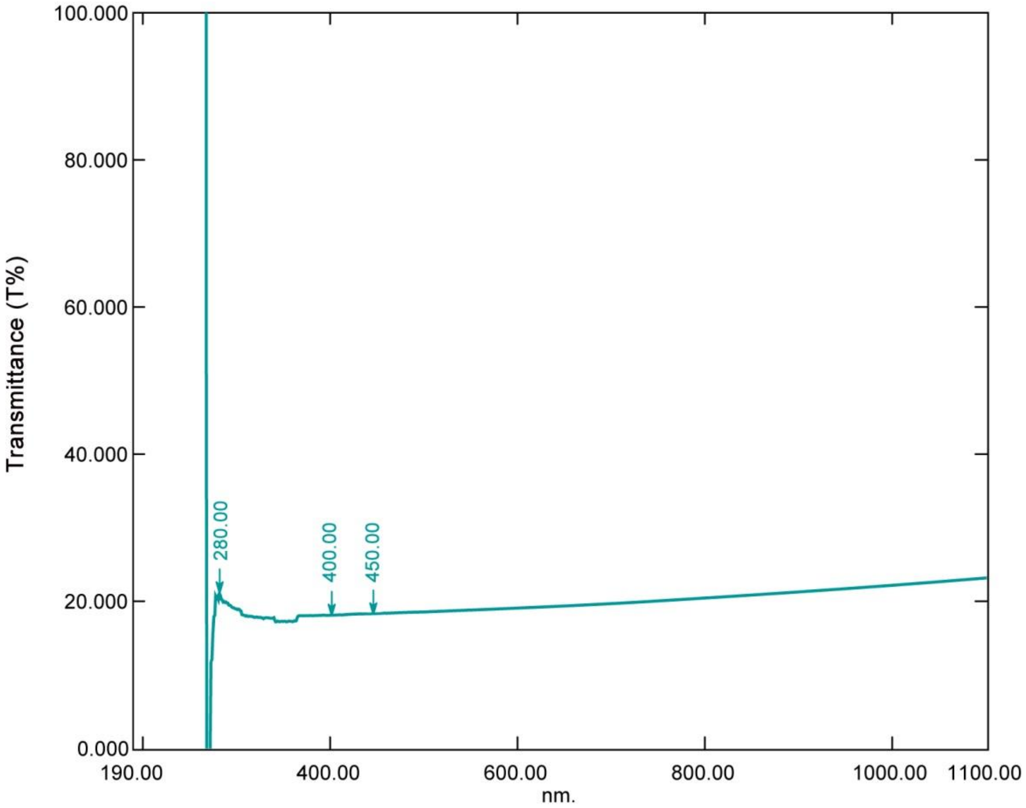

Figure 2 (b) Transmittance (T%) spectra for Sb (2 mol%) doped SnO_2 thin film on glass

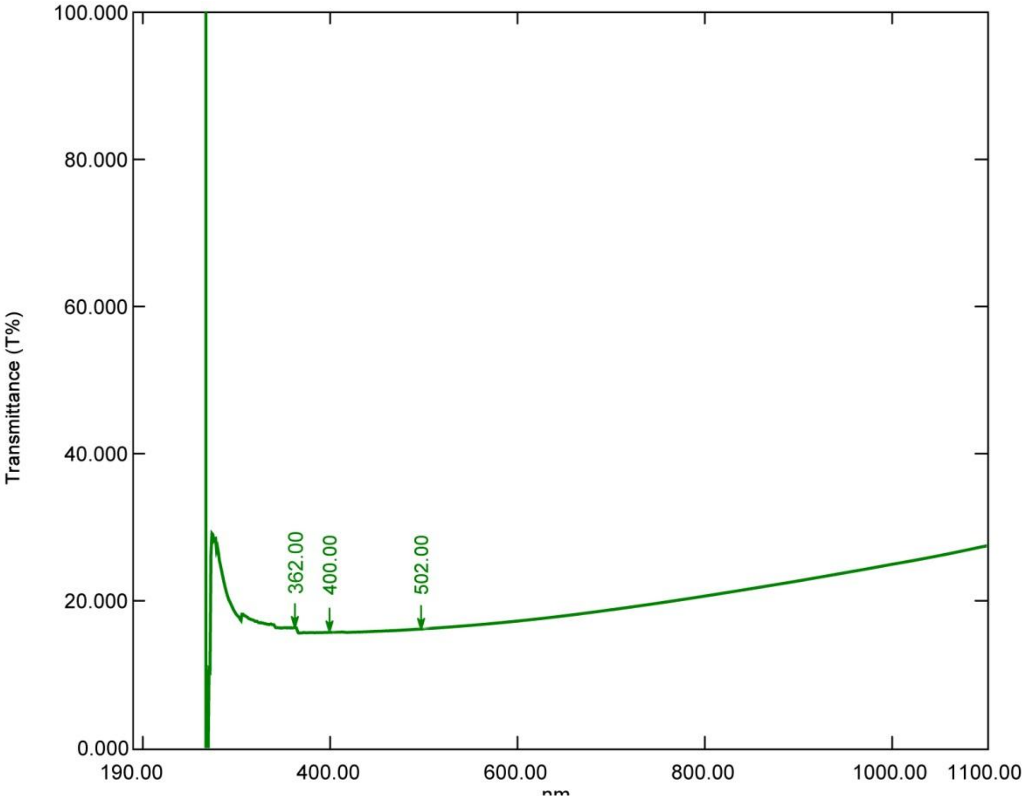

Figure 2 (c) Transmittance (T%) spectra for Sb (4 mol%) doped SnO_2 thin film on glass

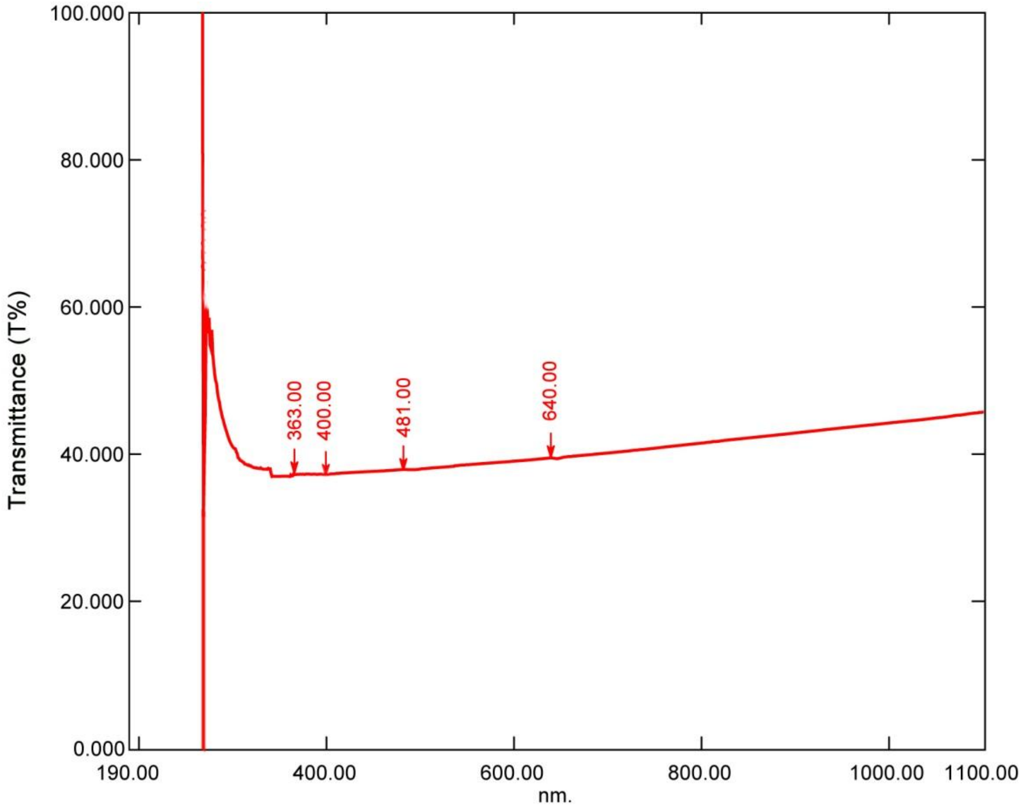

Figure 2 (d) Transmittance (T%) spectra for Sb (6 mol%) doped SnO_2 thin film on glass

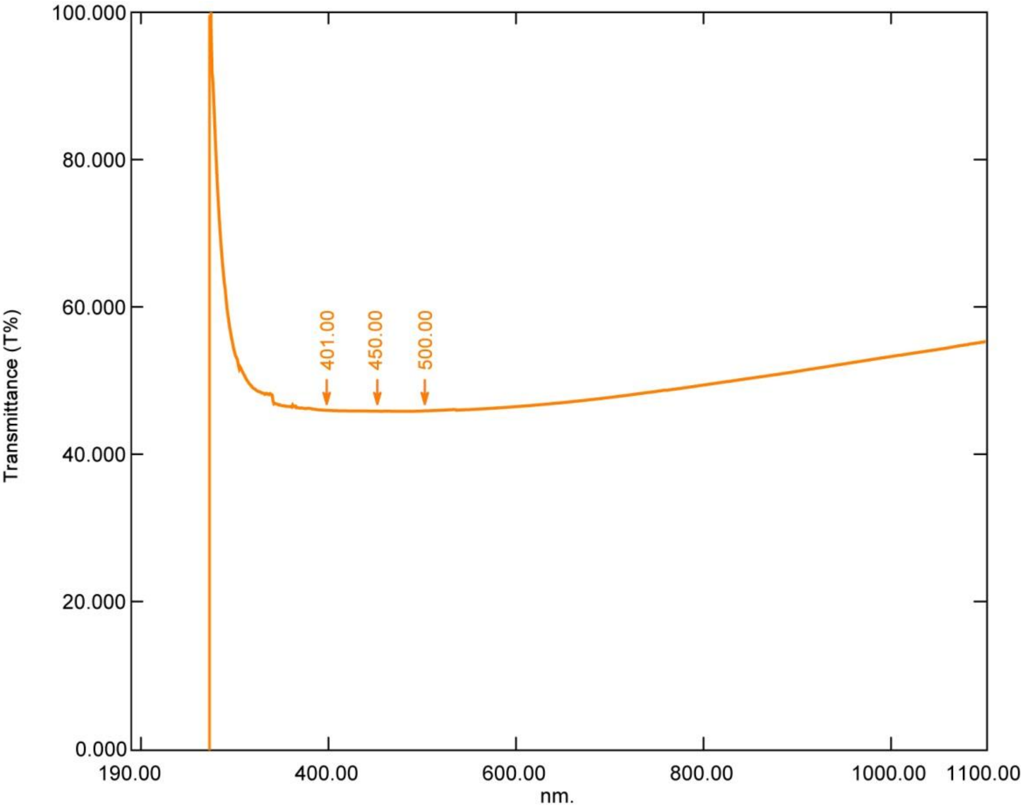

Figure 2 (e) Transmittance (T%) spectra for Sb (8 mol%) doped SnO_2 thin film on glass

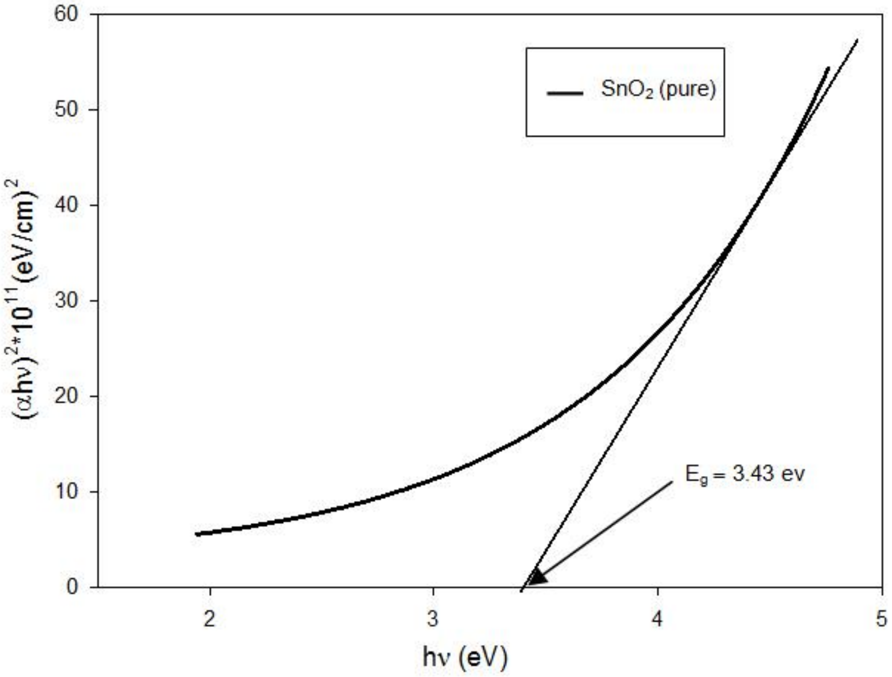

Figure 3 (a) Plot of $(\alpha h\nu)^2$ versus hν (undoped SnO_2)

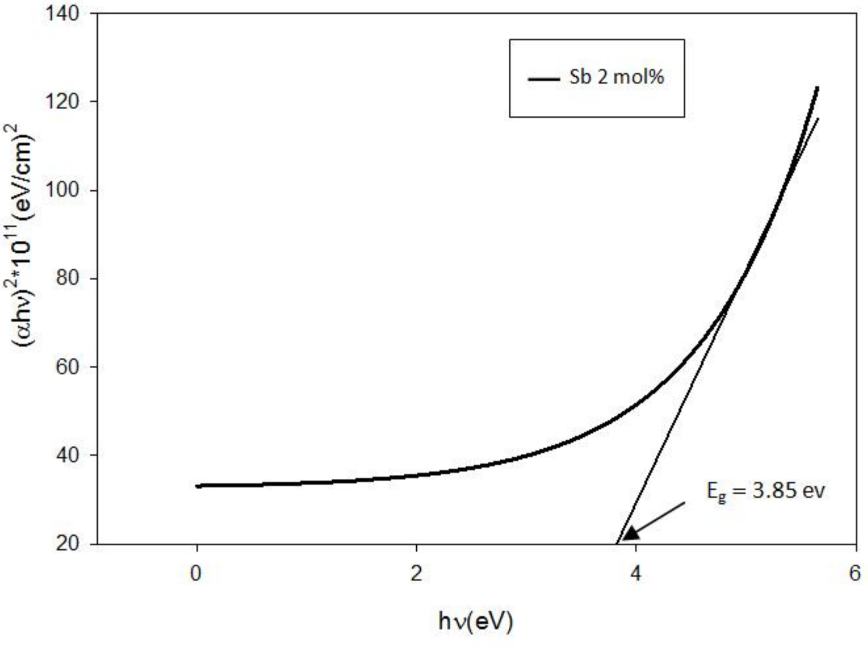

Figure 3 (b) Plot of $(\alpha h\nu)^2$ versus hν (Sb 2 mol% doped)

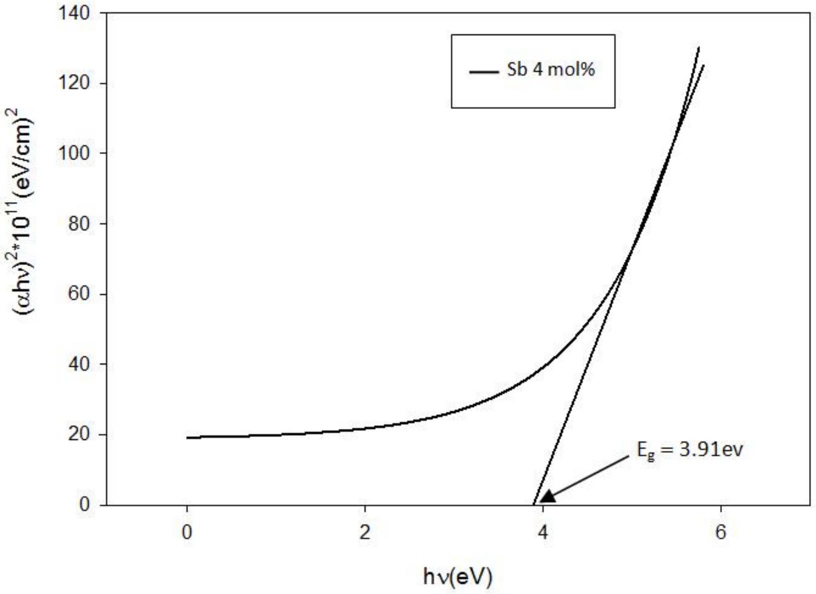

Figure 3 (c) Plot of $(\alpha h\nu)^2$ versus hν (Sb 4 mol% doped)

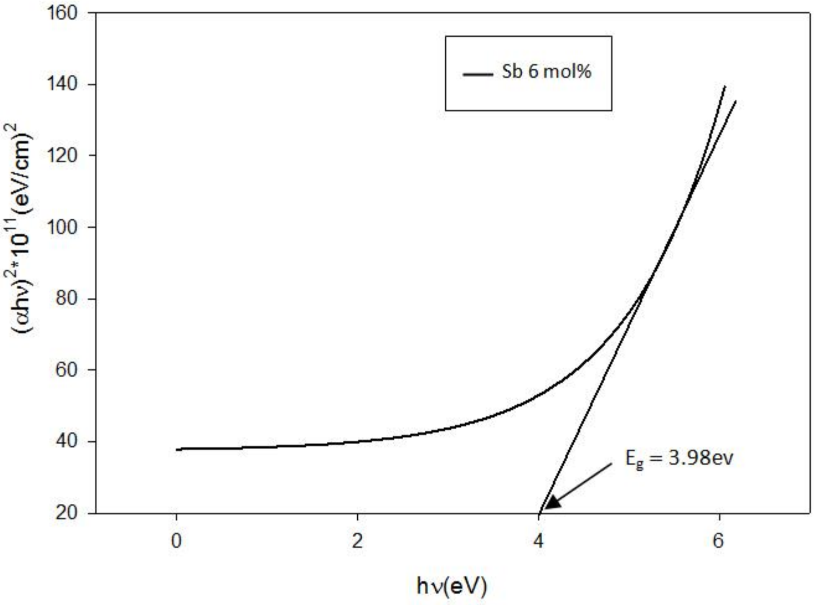

Figure 3 (d) Plot of $(\alpha h\nu)^2$ versus hν (Sb 6 mol% doped)

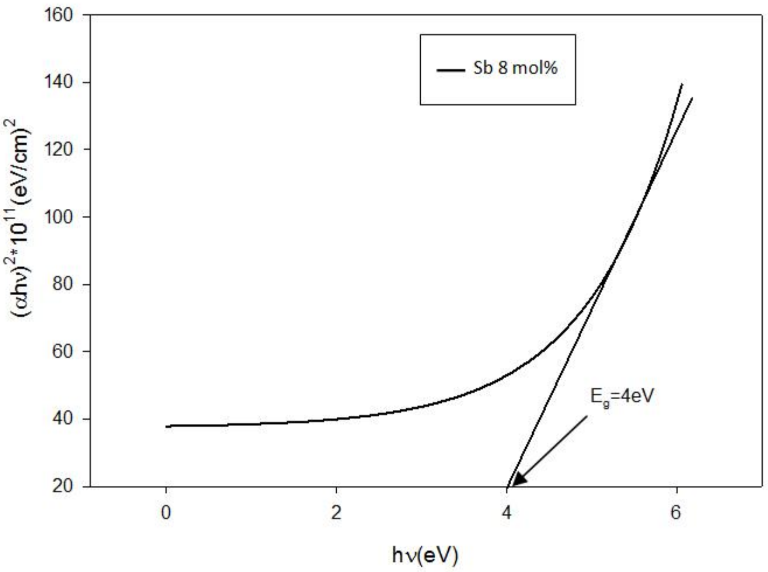

Figure 3 (e) Plot of $(\alpha h\nu)^2$ versus hν (Sb 8 mol% doped)

Conclusion

The undoped SnO_2 and Sb doped SnO_2 thin films on glass were prepared by using sol-gel and spin coating method. The Sb doped concentration changed from 2 mol% to 8 mol%. The X-ray measurements, the lattice constants were a = b= 4.83Å and c = 3.20Å. It was also observed that the different Sb concentration did not change the lattice parameters. The average crystallite size of the samples was in the range 52 ~ 61 nm. The band gap energy of the samples is varied from 3.43 eV to 4 eV. The study of these results shows that the Sb doped SnO_2 thin films can be suitable for optoelectronic applications.

Acknowledgements

I wish to express my sincere thanks to Professor Dr Khin Khin Win, Head of Department of Physics, Yangon University, for her kind permission to carry out this research.

I would like to express my sincere thanks to Dr Myo Lwin, Professor, Dr Ye Chan, Professor and Head, Universities' Research Center, Dr Aye Aye Thant, Professor, Department of Physics, Dr Yin Maung Maung, Professor, Department of Physics and Dr Than Zaw Oo, Professor, Universities' Research Center, University of Yangon, for their suggestion and comments for this work.

References

Agashe C et al (2009); Solar Energy Materials and Solar Cells 93, P 1256-1253

Bagheri Mohaghegi MM et al (2008); Physica B 403, P 2431-2437

Khan AF et al (2010); Applied Surface Science 256, P 2252-2258,

Kikuchi N et al (2002); Vacuum, 66 P 365-371

Moharrami F et al (2012); Solid films, 520, P 6503-6509

Maekava T et al (2001); Sensors and Actuators, B 80, P 51-58

Ouerfelli J et al (2008); Materials Chemistry and Physics, 112, P 198-201

Rani S et al (2007); Sensos and Actuators, B 122, P 204-210

Yin LT et al (2000); Sensors and Actuators, B 71, P 106-111

J. Myanmar Acad. Arts Sci. 2020 **Vol. XVIII.No.2B**

STURCTURE IDENTIFICATIOIN AND OPTICAL PROPERTIES OF SPIN COATED Cu DOPED CdO THIN FILMS

Amy Than[1], Zin Mar Win[2], Ohn Mar Swe[3] and Moht Moht Than[4]

Abstract

Pure CdO and Cu (1 mol%, 2 mol%, 3 mol% & 4 mol%) doped CdO thin films on glass substrate were successfully fabricated by using the spin coating technique. The samples were annealed at 500˚C for 1 hour. The films structures were studied by X-ray diffraction (XRD). From the XRD analysis, lattice parameters, unit cell volume and crystallite size of the samples are calculated. Also XRD studies reveal that pure CdO and Cu doped CdO thin films are showed cubic structure with maximum peak (111) planes. Furthermore, the XRD data, dislocation density and microstrain are also evaluated. From the optical properties, absorption coefficient and the band gap energy of the samples are calculated.

Keywords: Cu doped CdO thin films, crystallite size, optical band gap $E_{g,}$ Spin coating method

Introduction

Cadmium oxide (CdO) is n-type semiconductor used as a transparent conductive material prepared as a transparent conducting film back. Cadmium oxide has been used in applications such as photodiodes, phototransistors, photovoltaic cells, transparent electrodes, liquid crystal displays, IR detectors and anti reflection coat [Cai Z et al 2004, Jang J et al 2007, John X et al 2005 and Paul A et al 2008]. The wide band gap properties of semiconductors, like CdO, are of interest particularly for applications such as solar cells and transparent electrodes. Cadmium oxide (CdO) one of these important semiconductors oxide which has high optical properties. According to these properties it has vast applications. Where it show high transparency in the visible region of solar spectrum and has high electrical properties which were represented low ohmic resistance. Although it is difficult to obtain simultaneously a high transmission coefficient, thin films have been carried out. In this work pure CdO and Cu doped CdO films were deposited on glass substrate by using the spin coating technique. The electrical, structure and optical properties were studied.

Experimental

Pure CdO and Cu (1 mol%, 2 mol%, 3 mol% & 4 mol%) doped CdO thin films are synthesized by solid state reaction method, using high purity (99.9 % reagent grade) CdO and Cu powders. There powders were weighed on the basis of stoichiometric composition. The resultant, stoichiometric composition of the pure CdO and Cu (1 mol%, 2 mol%, 3 mol% & 4 mol%) doped CdO powders were ground by agate mortar to obtain the homogeneity. The mixed powders were annealed at 500˚C for 1 hour. The glass slides were cleaned by acetone, HCl and deionized water. Pure CdO and Cu (1 mol%, 2 mol%, 3 mol% & 4 mol %) doped CdO were mixed with 2-methoxyethanol solution by using sol-gel method. And then these pastes were coated on glass substrates by using spin coating technique and annealed at 500˚C for 1hour. The structure of prepared films were characterized by X-ray diffraction (Rigaku Multiflex, Japan)

---

[1] Dr, Lecturer, Department of Physics, University of Yangon

[2] Lecturer, Department of Physics, University of Yangon

[3] Lecturer, Department of Physics, University of Yangon

[4] Associate Professor, Department of Physics, Mohnyin Degree College

with CuK_α source (λ =1.54056 Å). The optical transmittance of the samples was recorded using UV-Vis spectrophotometer.

Results and Discussion

XRD patterns of the CdO and Cu doped CdO thin films on glass substrates were shown in Figure 1(a~ e). Well defined peaks at (111), (200), (220), (311) and (222) planes at respected 2θ values. This indicates that all samples are polycrystalline and matched the characteristics peaks due to the cubic structure.

The lattice constants "a" and unit cell volume "V" for the cubic phase structure are determined by the relation,

$$\frac{1}{d^2} = \frac{h^2 + k^2 + l^2}{a^2} \text{ and } V = a^3$$

where d and (hkl) are interplanar distance and Miller indices, respectively. The lattice constant a and the unit cell volumes are calculated as given in Table 1. They match well with the standard JCPDS data card. In order to determine the variation of crystallite size with increasing Cu doping, the size of the crystallites oriented along the (111) plane is calculated by using Scherrer's formula,

$$D = \frac{0.9\lambda}{\beta \cos\theta}$$

where, β, θ and λ are the broadening of the diffraction line measured at half its maximum intensity in radians, the diffraction angle, and the X-ray wavelength, respectively. The calculated values of crystallite size are given in Table 1. Dislocation density and microstrain are also calculated are given in Table 1.

The optical transmittance (T%) spectrum of CdO and Cu doped CdO thin films on glass substrates was taken in the wavelength range 400-1100nm. Figure 2 (a ~ e) shows the variation of optical transmittance with the wavelength of thin films. The fundamental absorption corresponding to the optical transition of the electrons from the valence band to the conduction band can be used to determine the nature and value of the optical band gap E_g of the films.

The optical absorption coefficient (α) was calculated from transmittance using the following relation,

$$\alpha = \frac{1}{d}\log\left(\frac{1}{T}\right)$$

where, T is the transmittance and d is the thickness of the films. The films under study have an absorption coefficient (α) obeying following relation for high photon energies (hν)

$$\alpha = \frac{A(h\nu - E_g)^{1/2}}{h\nu}$$

where E_g is the optical band gap of the films and A is a constant. A plot of variation of $(\alpha h\nu)^2$ versus hν is shown in Figure 3 (a ~ e). Eg is evaluated using the extrapolation of the linear part. The intercept on energy axis gives the value of band gap energy.

Table 1 The structural properties of pure CdO and Cu doped CdO thin films on glass substrate

Samples	***Maximum peak***	***Lattice constant “a”(Å)***	***Unit cell volume “V” (nm)^3***	***Crystallite size “D” (nm)***	***Dislocation density “δ” ×10^{14} (m)$^{-2}$***	***Strain “ε”×10^{-4}***
Pure CdO	(111)	4.6958	0.1035	93.0846	1.1541	3. 7238
Cu (1mol%) doped CdO	(111)	4.6939	0.1034	65.2360	2.3498	5.3134
Cu (2mol%) doped CdO	(111)	4.6956	0.1035	93.0848	1.1541	3.7238
Cu (3mol%) doped CdO	(111)	4.6943	0.1035	66.2791	2.2764	5.2298
Cu (4mol%) doped CdO	(111)	4.6961	0.1036	111.951	0.7979	3.0962

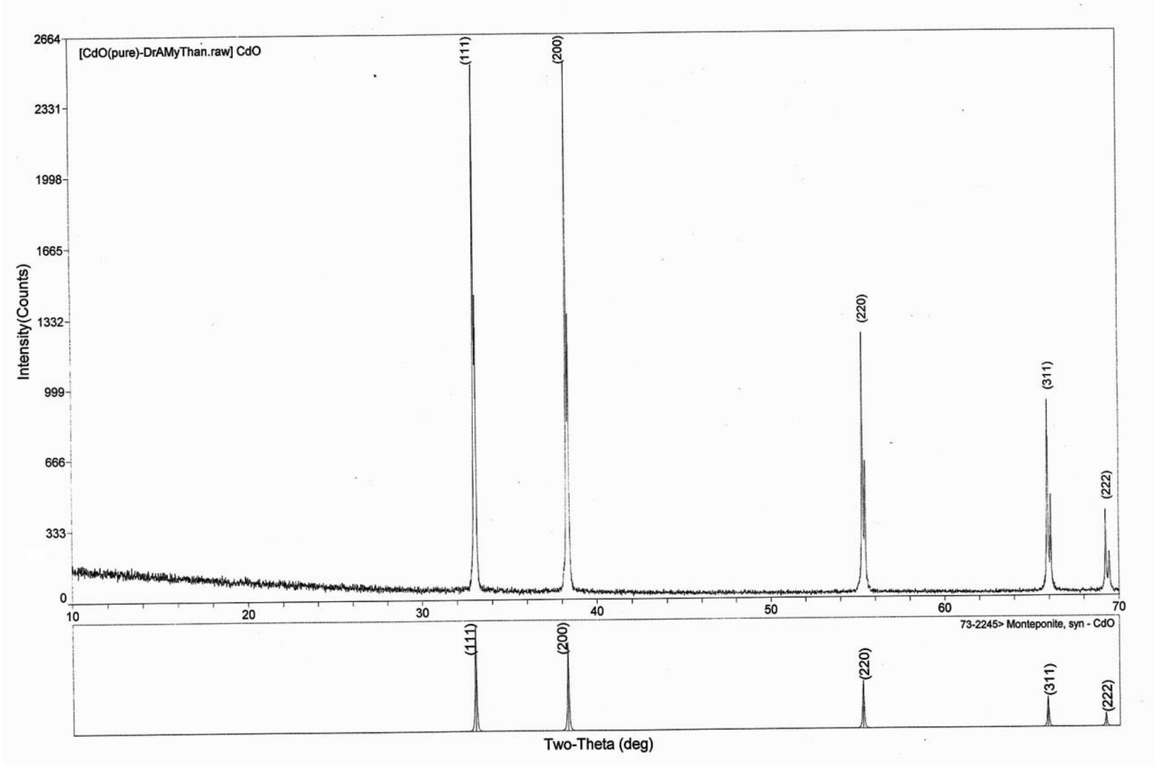

Figure 1(a) XRD pattern of pure CdO thin film on glass substrate

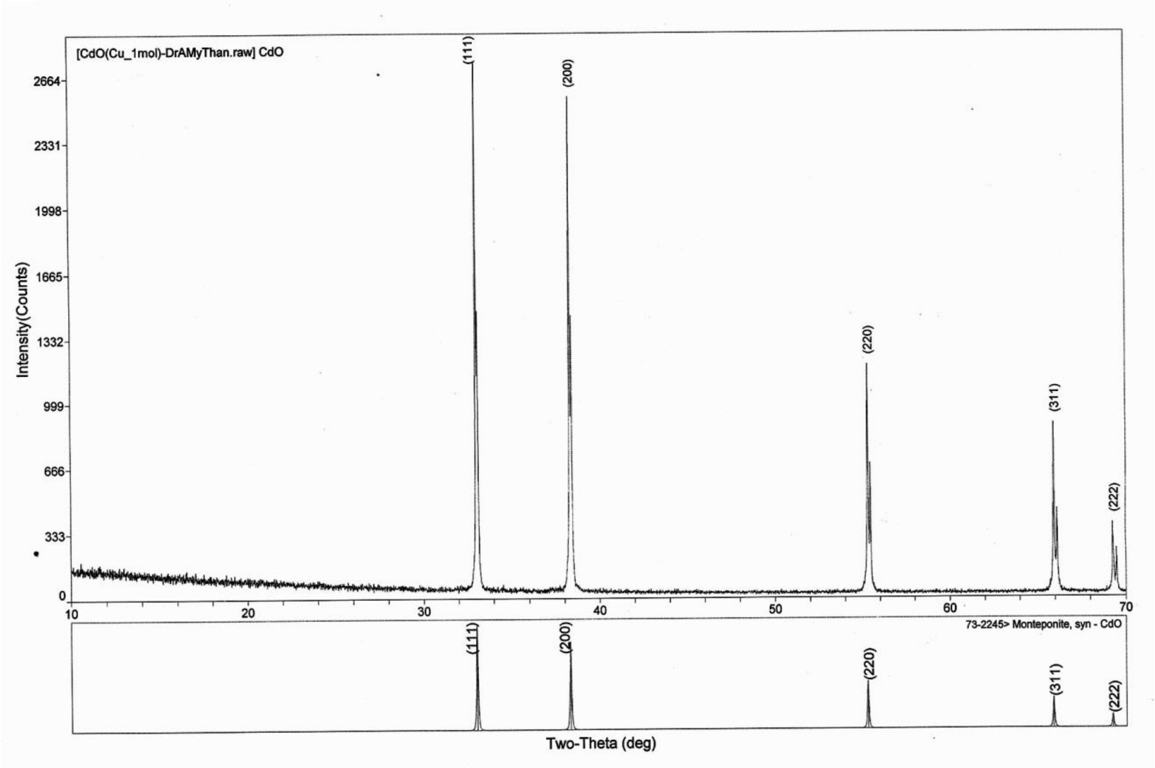

Figure 1(b) XRD pattern of Cu (1 mol%) doped CdO thin film on glass substrate

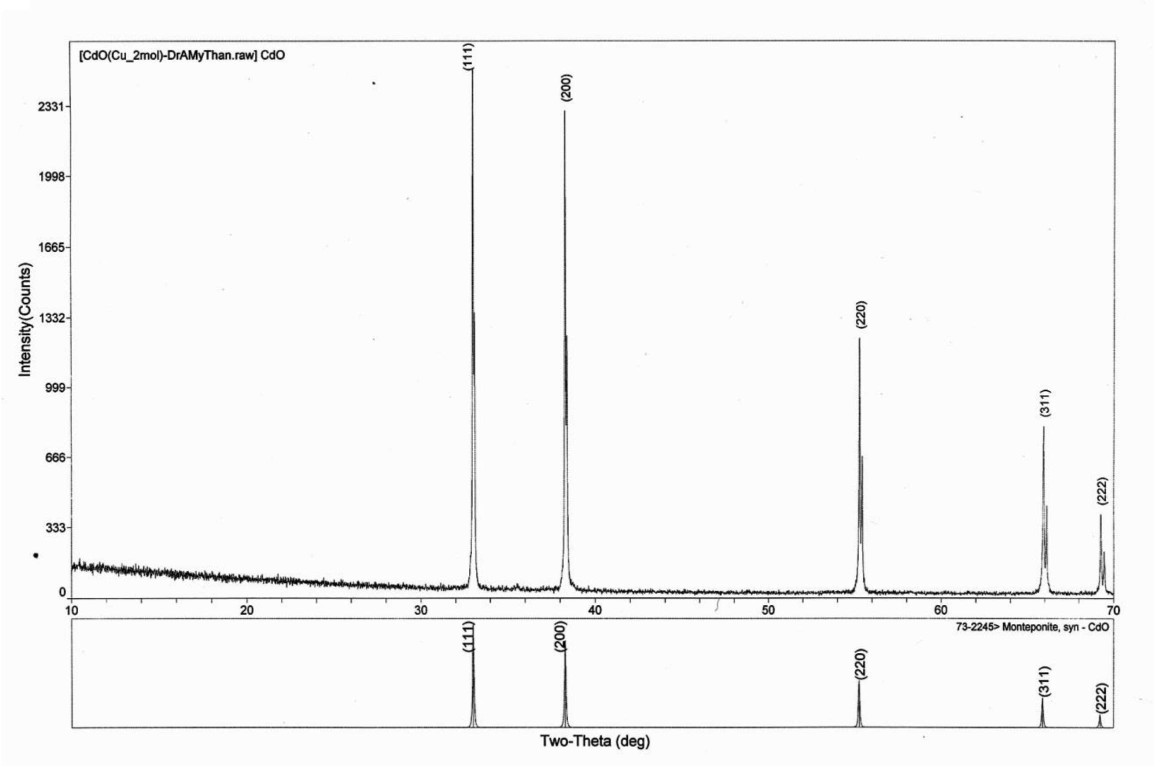

Figure 1(c) XRD pattern of Cu (2 mol%) doped CdO thin film on glass substrate

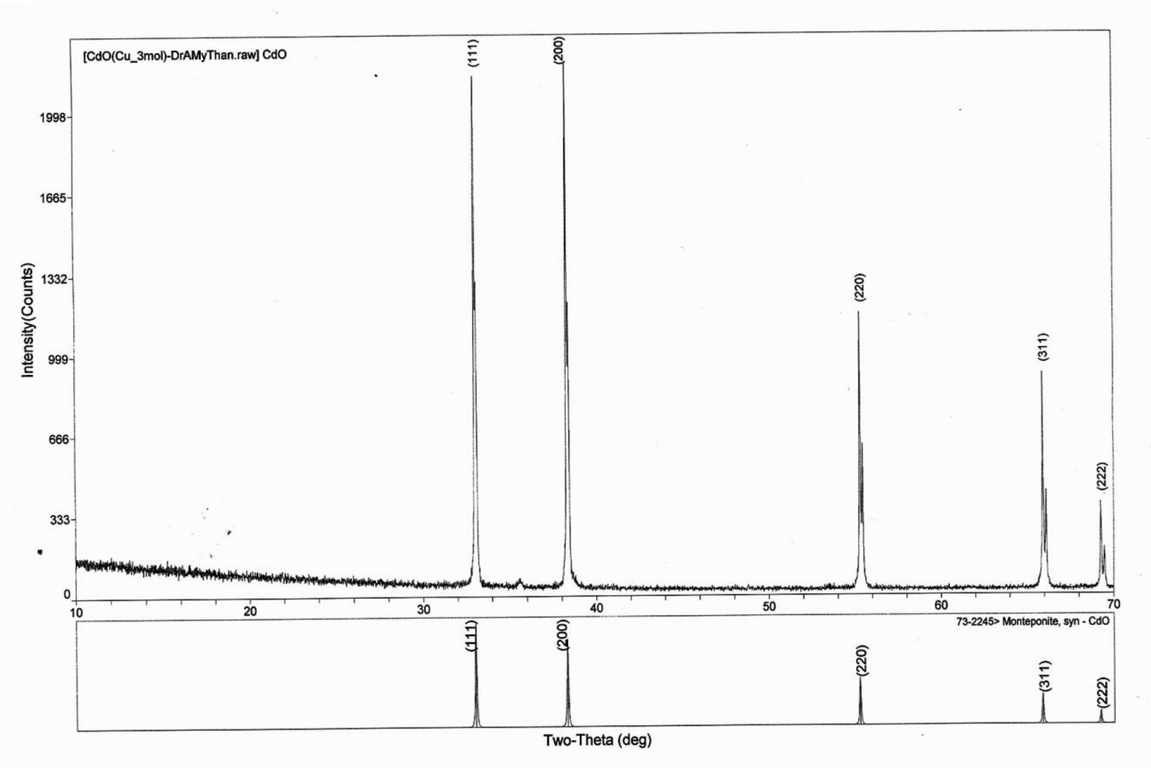

Figure 1(d) XRD pattern of Cu (3 mol%) doped CdO thin film on glass substrate

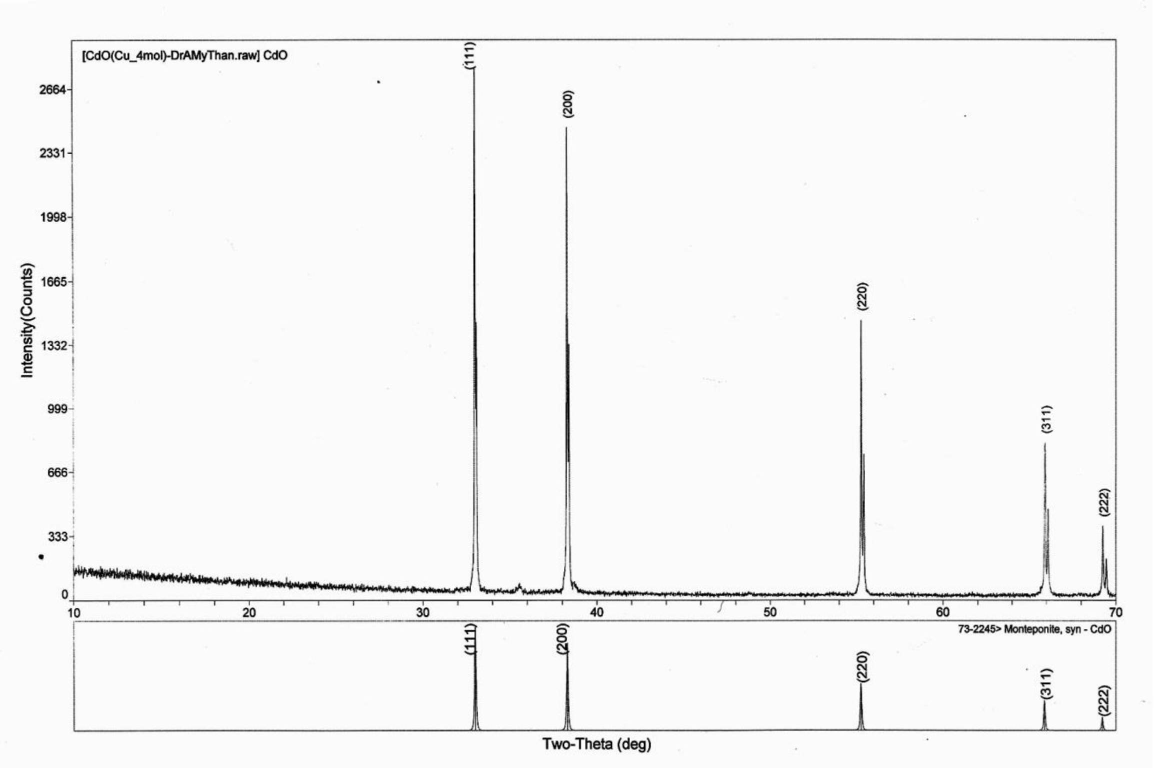

Figure 1(e) XRD pattern of Cu (4 mol%) doped CdO thin film on glass substrate

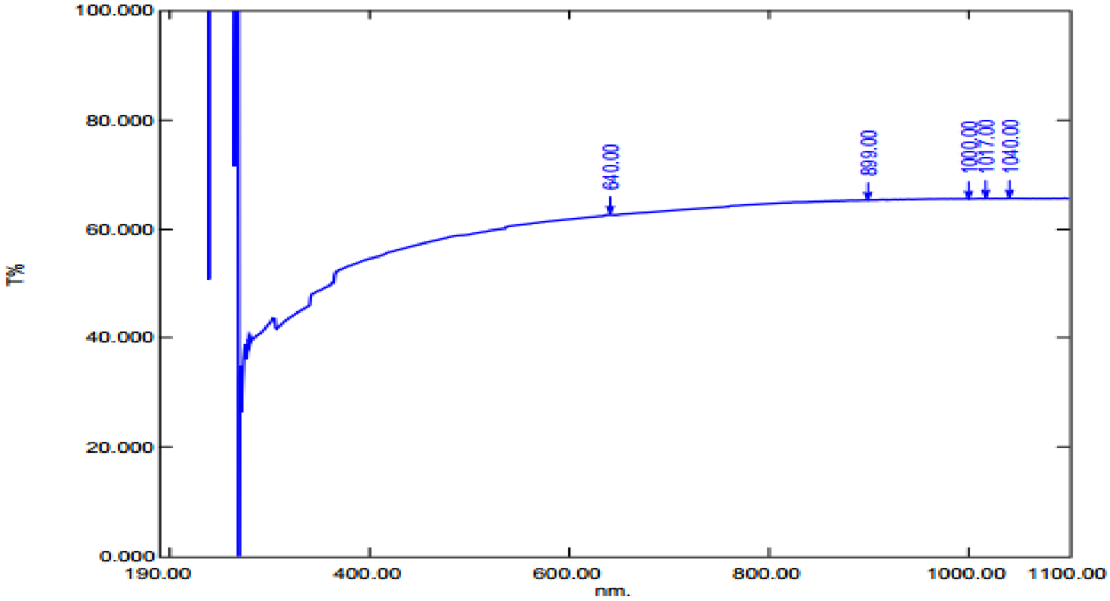

Figure 2(a) Optical transmittance (T) spectra of pure CdO thin film on glass substrate

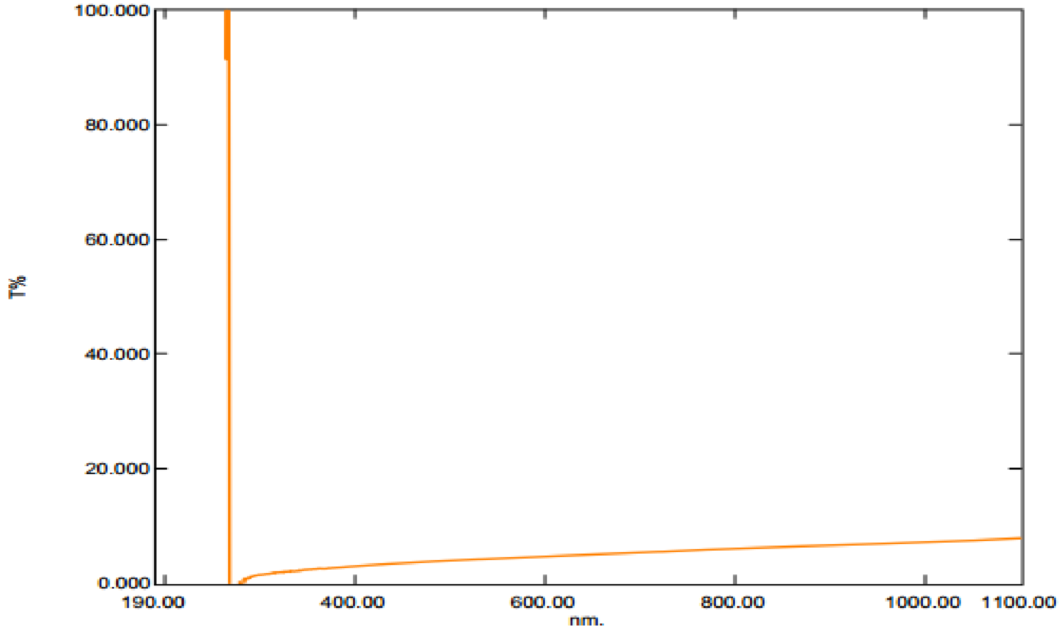

Figure 2(b) Optical transmittance (T) spectra of Cu (1 mol%) doped CdO thin film on glass substrate

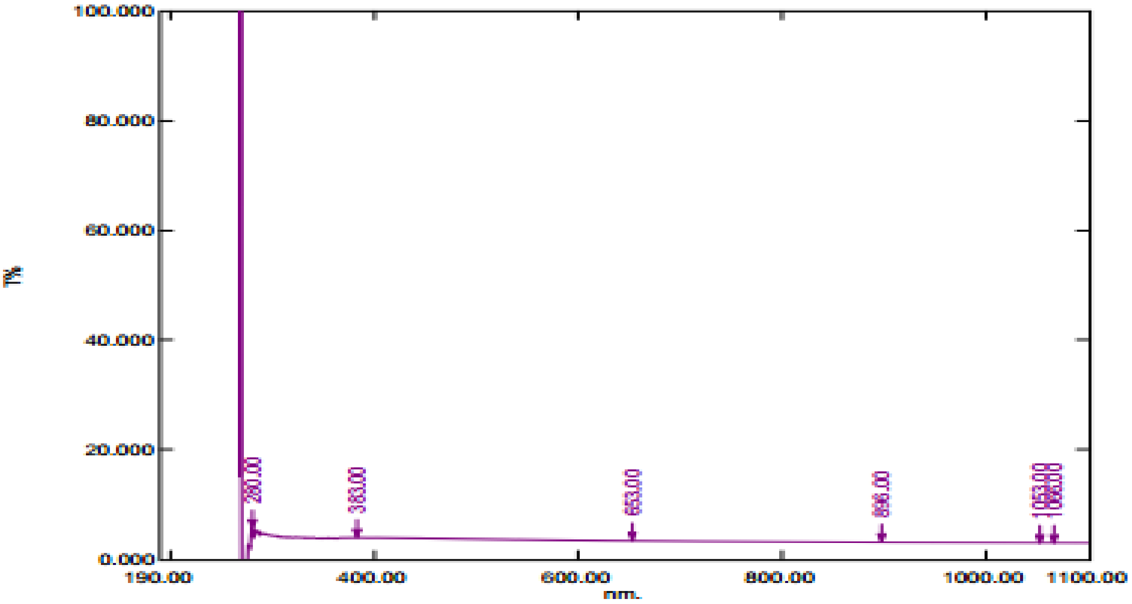

Figure 2(c) Optical transmittance (T) spectra of Cu (2 mol%) doped CdO thin film on glass substrate

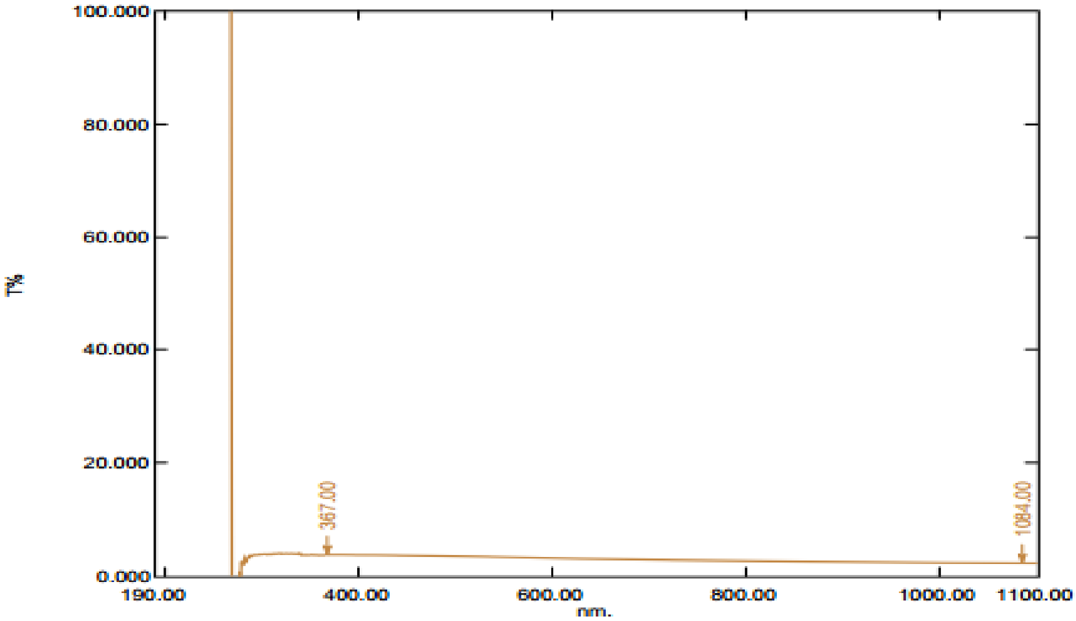

Figure 2(d) Optical transmittance (T) spectra of Cu (3 mol%) doped CdO thin film on glass substrate

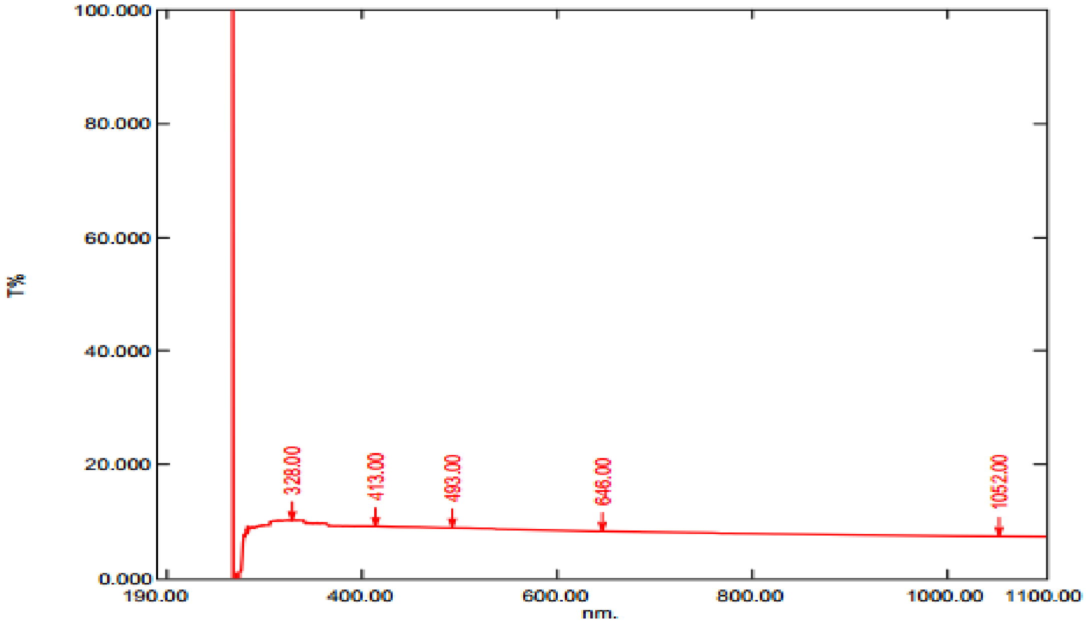

Figure 2(e) Optical transmittance (T) spectra of Cu (4 mol%) doped CdO thin film on glass substrate

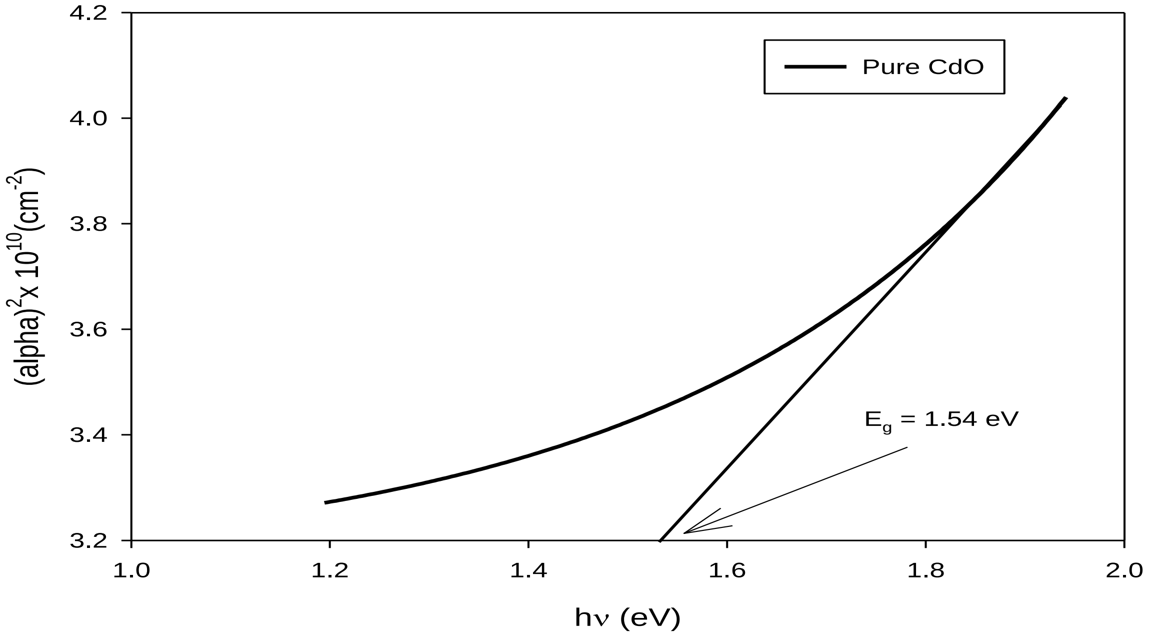

Figure 3(a) Plot of α^2 versus hν curve of pure CdO thin film on glass substrate

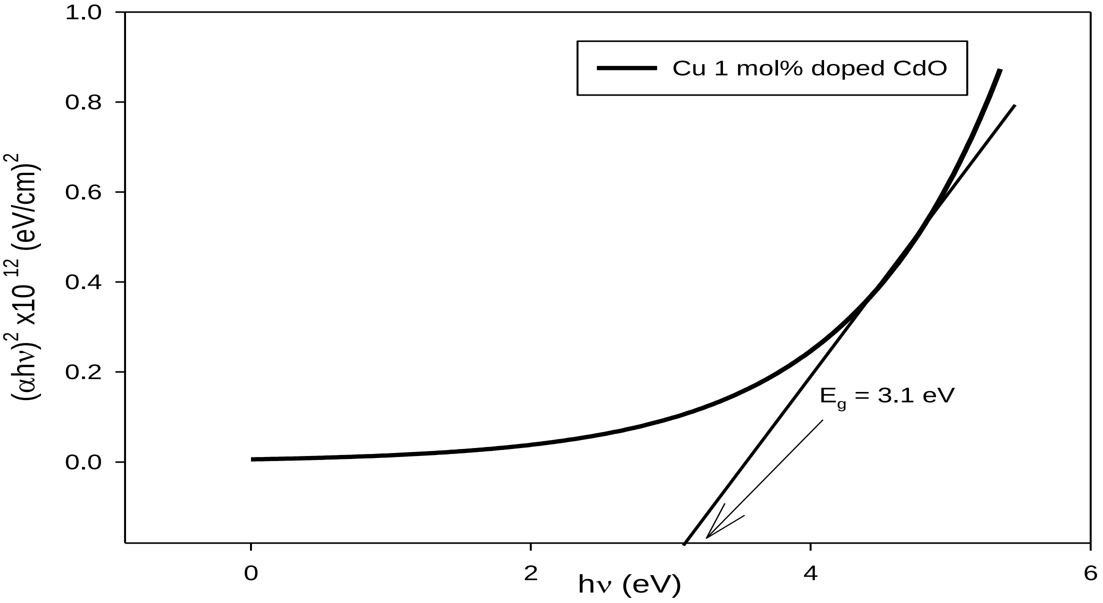

Figure 3(b) Plot of $(\alpha h\nu)^2$ versus hν curve of Cu (1 mol%) doped CdO thin film on glass substrate

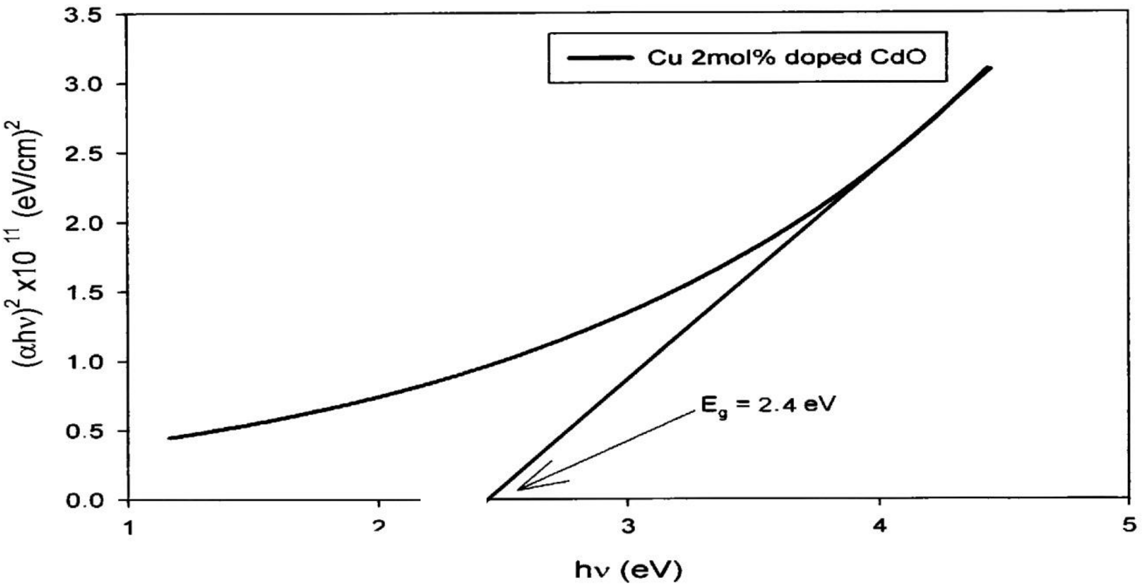

Figure 3(c) Plot of $(\alpha h\nu)^2$ versus hν curve of Cu (2 mol%) doped CdO thin film on glass substrate

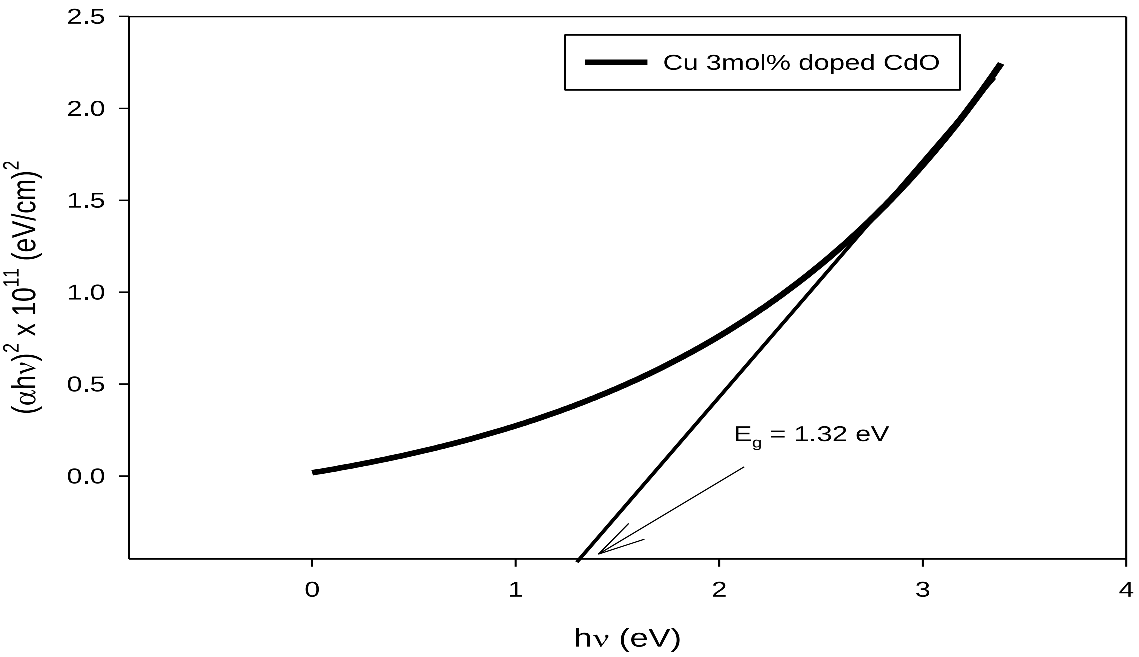

Figure 3(d) Plot of $(\alpha h\nu)^2$ versus hν curve of Cu (3 mol%) doped CdO thin film on glass substrate

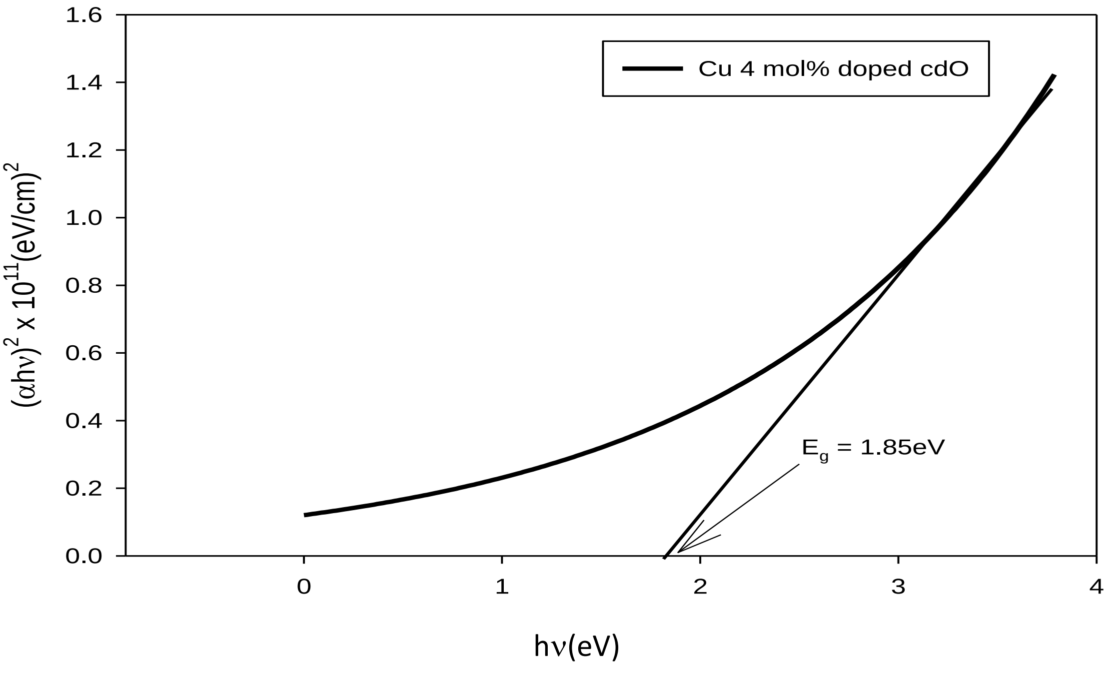

Figure 3(e) Plot of $(\alpha h\nu)^2$ versus hν curve of Cu (4 mol%) doped CdO thin film on glass substrate

Conclusion

The pure CdO and Cu doped CdO thin films on glass were prepared by using sol-gel and spin coating method. The Cu doped concentration changed from 1mol% to 4 mol%. XRD patterns of all samples is found to have a better polycrystalline nature oriented along the (111), (200), (220), (311) and (222) planes at 33.012˚, 38.305˚, 55.290˚, 65.927˚ and 69.260˚ respectively. The average crystallite size of all samples is found to be 85.927 nm. The optical band gap of the samples, measured by employing a UV-Vis spectrophotometer, observed that at 1.32 eV to 3.1 eV. The doped CdO with Cu improved the photoconductive gain.

Acknowledgements

I wish to express my sincere thanks to Professor Dr Khin Khin Win, Head of Department of Physics, Yangon University, for her kind permission to carry out this research.

I would like to express my sincere thanks to Dr Myo Lwin, Professor, Department of Physics, Dr Ye Chan, Professor and Head, Universities' Research Center, Dr Aye Aye Thant, Professor, Department of Physics, Dr Yin Maung Maung, Professor, Department of Physics and Dr Than Zaw Oo, Professor, Universities' Research Center, Yangon University, for their suggestion and comments for this work.

References

Cai Z et al (2004) ; Journal of Material Sciences 39, 4001-4003

Jang J et al (2007); Macromolecular Research 15,154-159

John X et al (2005); Journal of Applied Polymer Science 98, 2149-2156

Paul A et al (2008); Journal of Polymer Science Part B 46,1952-1965

Sexena V et al (2003); Current Applied Physics 3, 293-305

Zheng B J et al (2011); Vacuum 85, 861-865

J. Myanmar Acad. Arts Sci. 2020 **Vol. XVIII.No.2B**

MICROBIAL ELECTRIC ENERGY HARVESTING FROM THE LIVING PLANT MICROBIAL FUEL CELL (P-MFC)

Lwin Maung[1], Cherry Moh Moh Than [2], Hlaing Darli Soe [3], Nyi Nyi Yin [4], Pho Kaung[5]

Abstract

Living Plant Microbial Fuel Cell (P-MFC) is the kind of bio volt-photo galvanic cell which converts solar energy into green electricity. The plant synthesized Rhizo-deposit, mostly in the form of carbohydrate, at the sphere of the root through the photo-synthesis process. The microbes of the Rhizo sphere decompose the Rhizo-deposit and converts into electric energy via the Microbial Fuel Cell. The carbon blocks were used as the electrode of the microbial fuel cell. Hsin ngou Grass (*Eleusine indica*) was used to examine the performance of the plant microbial fuel cell and achieved the maximum electric power is 13.86mWm^{-2}, open circuit voltage is 0.35V and short circuit current density is 162.5mAm^{-2} as prepared cell. The open circuit voltage is fluctuated with the life time of the microbial fuel cell and the maximum open circuit voltage, 0.8V was observed at the 10th day of the fabrication of the microbial fuel cell.

Keywords: Plant Microbial Fuel Cell (P-MFC), Rhizo-deposit, microbes, Hsin ngou Grass (*Eleusine indica*), Electric energy

Introduction

The standard of society status depends on the degree of the availability of energy. The level of energy consumption by the humans on the earth in 2006 was approximately 15.8 terawatts (TW). The 84% of consumption energy is derived from fossil-fuel sources, 6.5% is from nuclear power plants, 7% is from hydroelectric and 2.5% is from wind energy [Cunningham William.P, et al]. The nuclear energy is roughly equal to hydroelectricity but we can not rely on it due to its risky situation and then the fossil fuels become primary energy source. Since fossil fuel sources become rapidly depleted and enhance the depletion of ozone layer and global warming, more and more alternative energy sources are required to be searched and our society faces the challenges of the energy crisis. One of the clean renewable energy sources is the solar energy.

Living Plant Microbial Fuel Cell (P-MFC) is the kind of Microbial Solar Cell which is a type of solar cells used for the light/electricity conversion with living phototrophic microbes serving as catalysts for the conversion of solar energy to electric energy [Logan.BE, et al]. In the (P-MFC) , photosynthetic microbes, such as microalgae and cyanobacteria, use the light energy to liberate high energy-level electrons from the water molecules and these electrons are transferred through photosynthetic electron-transport chains and finally used to fix carbon dioxides and synthesize organic molecules.

The aim of the P-MFC is to transform solar energy into electrical energy through oxidation of rhizo deposits by electrochemically active bacteria. Photosynthesis in plants occurs in its leaves whereby the solar energy is used to fix carbon dioxide in the form of carbohydrates. Depending on plant species, age, and environmental conditions up to 60% of the net fixed carbon can be transferred from its leaves to the roots. The plant root system produces and releases

---

[1] Dr, Assistant Lecturer, Department of Physics, Pathein University

[2] Demonstrator, Department of Physics, Pathein University

[3] Demonstrator, Department of Physics, Pathein University

[4] Professor &Head, Department of Physics, Pathein University

[5] Dr' Rector, University of Yangon

different types of organic compounds into the soil, which includes exudates of sugars, organic acids, polymeric carbohydrates, enzymes, lysates of dead cell materials, and gases like ethylene and CO_2. Summation of these released products by plants is termed as plant rhizo deposits and these process is called as rhizo deposition [Gust.D, et al].

The biochemical reactions taking place in P-MFC are as mentioned below in equation 1 and 2 and the schematic representation of plant microbial fuel cell comprising of plants is as depicted in (Figure 1).

Anode Reaction: $C_6H_{12}O_6 + 6H_2O \rightarrow 6CO_2 + 24H^+ + 24e^-$ --------1

Cathode Reaction: $6O_2 + 24H^+ + 24e^- \rightarrow 12H_2O$ ------- 2

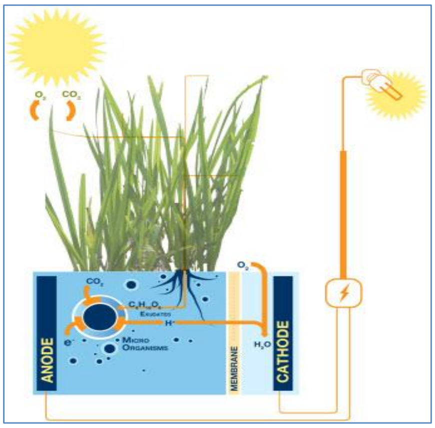

Figure 1 Schematic representation of P-MFC in power generation [Gowtham.R, et al].

Materials and Method

Materials

Agar, NaCl, Salt Bridge Substrate, Plastic Box, Carbon electrodes, Water, conducting wires, Digital multi meter and Hsin ngou Grass (*Eleusine indica*) with the soil as the biological specimen (Figure 2) are the constituents of the living plant Microbial Fuel Cell (P-MFC).

Figure 2 Hsin ngou Grass (*Eleusine indica*) with the soil as the biological specimen.

Double Chambered P-MFC

The Plastic box of size, 15cm × 10cm× 5cm, was portioned to be two chambers, (10cm×10cm) and (5cm×10cm) by the Agar salt bridge. The large chamber is the Anode Chamber .The carbon electrodes ($2.5\times10^{-3}m^2$) were fixed to the each side of the salt bridge of the two chambers. Conducting wire was fixed on the carbon electrodes. In the anode compartment, the plants having fibrous roots, Hsin ngou Grass (*Eleusine indica*), with the cultured soil of plant and some drainage water was added.

Cathode compartment was containing only water and carbon electrode. Both the compartments were connected to the external circuit having external variable resistance (10KΩ) with the help of conducting wire. The current-voltage readings were taken with the help of digital multi meter (Figure 3).

Figure 3 Experimental Setup of the double chambered P-MFC.

Salt Bridge

The simple low-cost salt bridge, (Figure 4), was prepared to be served as the proton exchange membrane by the 300ml gelatin agar powder, 75g table salt, 200ml water to make agar solution. Then, it was boiled and solidified in salt bridge substrate [Gude.V].

Figure 4 Agar gelatin Salt Bridge for the proton exchange membrane.

Results and Discussion

The double chambered living plant microbial fuel cell (P-MFC) was set up as in the Figure-3 and the investigation of the current-voltage characterization was conducted using a digital multi-meter for a period of 10days.

The results are as depicted in the (Figure - 5 and 6) of the electrical characterization of double chambered living plant microbial fuel cells. Living Plant microbial fuel cell(P-MFC) was achieved the maximum electric power is 13.86mWm^{-2}, open circuit voltage is 0.35V and short circuit current density is 162.5mAm^{-2} for the as prepared cell. The open circuit voltage is fluctuated with the life time of the microbial fuel cell and the maximum open circuit voltage, 0.8V was observed at the 10th day of the fabrication of the microbial fuel cell.

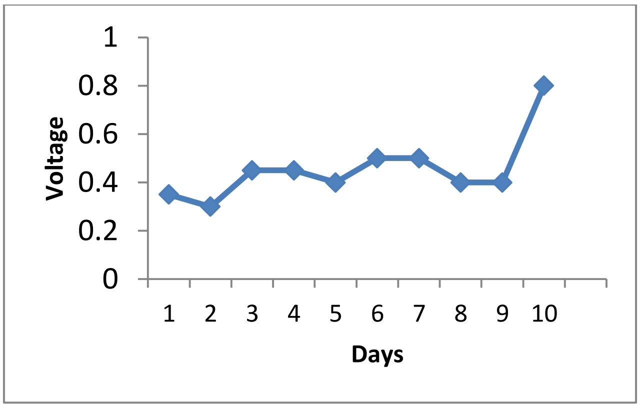

Figure 5 Voltage Fluctuation of double chambered P-MFC for the 10 days.

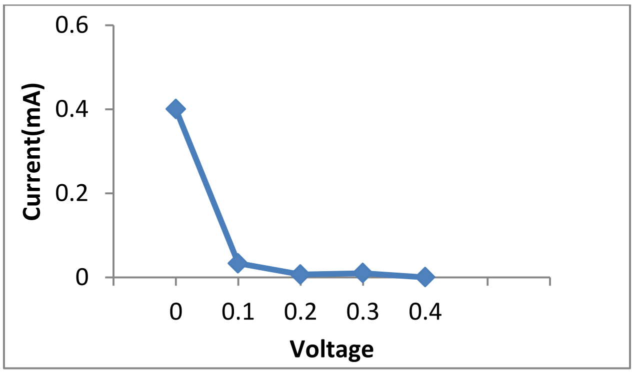

Figure 6 Current-Voltage characteristic of the as prepared double chambered P-MFC.

Conclusion

Soil microbes in the rhizo-deposits of the Hsin ngou Grass (Eleusine indica) are able to convert the solar energy into electricity through the Photosynthesis process. Although the voltage output of the living plant microbial fuel cell (P-MFC) was fluctuated with the days of life time, the maximum open circuit voltage of 0.8V was attained on the 10th day by using Hsin ngou Grass (Eleusine indica) P-MFC. Further optimizations in terms of area of the electrode, salt bridge composition, etc are needed to increase the efficiency of P-MFC.

Acknowledgements

The authors would like to acknowledge Professor Dr Pho Kaung, Rector, University of Yangon, Professor Dr Khin Khin Win, Head of Department of Physics, University of Yangon and Professor Dr Nyi Nyi Yin, Head of Department of Physics, Pathein University, for their valuable suggestion and comments for this research.

References

Cunningham William. P, Mary A, (2006), Principles of Environmental Science (New York: McGraw-Hill)

Gust.D, Moore, T, (1993), Molecular mimicry of photosynthetic energy and electron transfer. Chem. Res. 26, 198–205.

Gowtham. R, Sundar.K, (2015), Generating Current From Plants Plant-e Technology, International Journal of Recent Advances in Engineering & Technology, 3, , 2347 – 2812

Gude.V. (2016), Microbial fuel cells for waste water treatment and energy generation, 247-285.

Logan.BE, Regan.J, (2006), Electricity-producing bacterial communities in microbial fuel cells. *Trends Microbiol.* 14, 512-518.

J. Myanmar Acad. Arts Sci. 2020 **Vol. XVIII.No.2B**

EFFECT OF SAMARIUM SUBSTITUTION ON THE TRUCTURAL AND DIELECTRIC PROPERTIES OF ZINC FERRITE

Ni Ni Tin[1], Thet Mar Win[2] and Aye Aye Thant[3]

Abstract

Samarium substituted Zinc ferrites, $ZnFe_{2-2x}Sm_{2x}O_4$ (x= 0.0000, 0.0125, 0.0250, 0.0375, 0.0500) have been synthesized by Conventional Ceramic Method. The structural properties have been investigated by the X-ray Diffraction (XRD), Scanning Electron Microscopy (SEM), Fourier Transform Infrared Spectroscopy (FTIR) and dielectric measurements. The XRD analysis has confirmed the single cubic spinel phase of $ZnFe_{2-2x}Sm_{2x}O_4$with various compositions. The surface morphology has been observed from SEM micrographs. The average grain size has become smaller due to the substitution of Sm ion with larger ionic radius compared to that of Fe ion. FTIR analysis indicates the specific molecular vibrations at the spinel lattice in the wavelength range of 400 - 4000cm^{-1}. The dielectric constant was measured in the frequency range of 1kHz to 1MHz.

Keywords: Samarium, Conventional ceramic method, XRD, SEM, FTIR, Dielectric constant

Introduction

Ferrites are magnetic ceramics containing iron oxide as a major constituent in it. It is now some 70 years since ferrites debuted as an important new category of magnetic materials. Today ferrites are employed in a truly wide range of applications, and have contributed to the advances in electronics. In the area of new materials, ferrites with permeabilities up to 30,000 and power ferrites for frequencies upto 10 MHz have been made available commercially (Gopchandran KG et al., 1997). Even though, improvements and innovations continue to take place; many new applications, theories and preparation technologies are currently under development in field of ferrites.

Zinc ferrite is a good example of the direct relation between the nanoparticle structure, composition, and properties. When prepared as a bulk material, the zinc-iron oxide has a spinel structure AB_2O_4 with a tetrahedral A site occupied by Zn^{2+} ions and an octahedral B site by Fe^{3+}ions. Several methods including ceramic synthesis, co-precipitation method, tartrate precursor method, hydrothermal, combustion, auto-combustion, polymeric precursor route, solvothermal and sol-gel technique etc. have been used to fabricate the precursor (Safwat A M et al., 2011).

In this work, samarium substituted zinc ferrites ($ZnFe_{2-2x}Sm_{2x}O_4$) have been synthesized by Conventional Ceramic Method followed by the investigation of their structural, morphological vibrational analysis and dielectric measurement.

Experimental Procedure

Samarium substituted Zinc ferrites having the chemical formula $ZnFe_{2-2x}Sm_{2x}O_4$ (where x = 0.0000, 0.0125, 0.0250, 0.0375, 0.0500) have been synthesized by Conventional Ceramic Method. The starting materials are Zinc Oxide (ZnO), Ferric Oxide (Fe_2O_3), and Samarium Oxide (Sm_2O_3). Pure oxides have been mixed and ground into a very fine powder. The mixture

---

[1] Lecturer, Department of Physics, West Yangon University

[2] Associate Professor, Department of Engineering Physics, Technological University (Thanlyin)

[3] Professor, Department of Physics, University of Yangon

has been pre-sintered at 900˚C for 5h in furnace with heating rate of 20°C/min and cooled down to room temperature. The powder has been again grounded and re-powdered about 15 min. The structural properties of the pre-sintered samples have been analyzed by X-ray diffraction (XRD) technique.

The pre-sintered samples have been prepared into pellets by using hydraulic press and final sintered for 5h at a temperature which is 100ºC higher than the pre-sintering temperature. After final sintering process, the phase formation and surface morphology of the synthesized samples have been carried out by X-ray diffraction (XRD)using Rigaku Multiflex X-ray Diffractometer with CuK_α radiation λ=1.54056 Ǻ) and Scanning Electron Microscope (SEM), respectively.

Fourier Transform Infrared (FTIR) spectra of $ZnFe_{2-2x}Sm_{2x}O_4$ samples have been recorded using (Perkin Elmer Spectrum IR version 10.6) in the range 4000-400 cm^{-1}. Dielectric measurements have been done by (GW INSTEK LCR-8110G) meter over a wide range of frequency from 20 Hz up to 20 MHz with drive voltage 1V at room temperature.

Results and Discussion

Structural Analyses

The XRD spectra for the comparison on phase formation of the synthesized samples are shown in Figure 2. The XRD spectra show that all samples of $ZnFe_{2-2x}Sm_{2x}O_4$ where x = 0.0000, 0.0125, 0.0250, 0.0375, 0.0500) are successfully formed spinel phase cubic structures. The X-ray patterns of the ferrite display sharp and well-resolved diffraction peaks with good crystallinity. No additional peak of the second phase has been observed in the XRD patterns, showing that the ferrites have consisted of only spinel $ZnFe_2O_4$ phase. Therefore, it has been confirmed that Sm has totally entered into the lattice site of spinel ferrite. The diffraction peaks are indexed to be (220), (311), (222), (400), (331), (422), (511) and (440) of the crystal planes of spinel Zn ferrite respectively. The crystallite size has been estimated from the X-ray peak broadening of the (311) peak using Scherrer's equation. It is estimated to be about 34 nm without Sm substitution and the size has been decreased with increase in Sm substitution. It might be due to the decrease in crystallinity resulted from Sm substitution which slows down the crystallization process in ferrite. However, the lattice parameter is mostly constant and it is not affected by the Sm dopants. Table 1 shows variation of crystallite size for $ZnFe_{2-2x}Sm_{2x}O_4$ with composition of x.

The average crystallite size (D) of $ZnFe_{2-2x}Sm_{2x}O_4$ ferrite is calculated using Debye Scherrer's formula,

$$D = \frac{K\lambda}{\beta\cos\theta}$$

where, the constant K is taken to be 0·94, λ the wavelength of X-ray used which is CuK_α radiation (λ = 1.54 Å), β the full width at half maximum of the diffraction peak and θ is the diffraction angle.

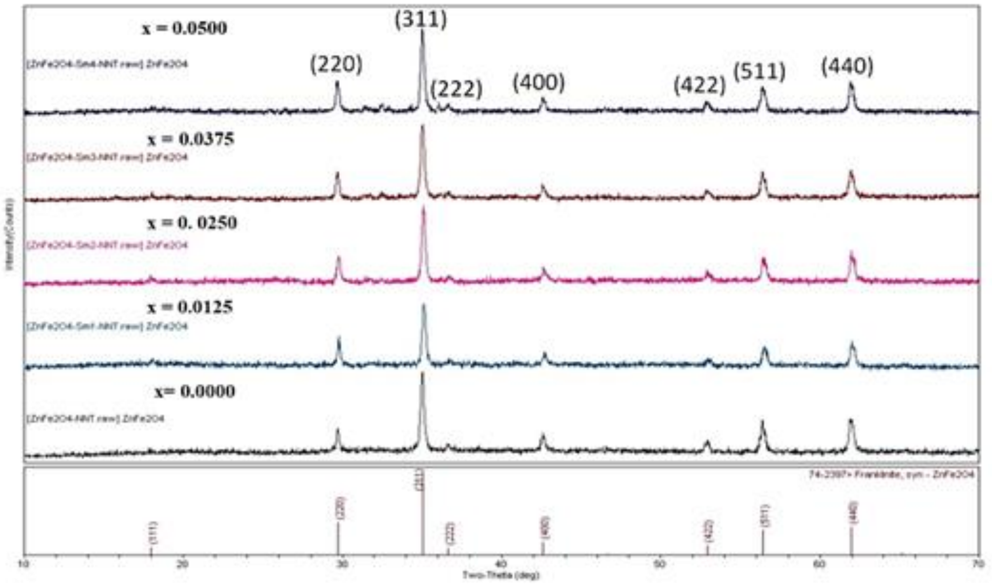

Figure 1 Comparison on phase formation of $ZnFe_{2-2x}Sm_{2x}O_4$ samples for (x=0.0000, 0.0125, 0.0250, 0.0375, 0.0500)

Table 1 Comparison on structural properties of $ZnFe_{2-2x}Sm_{2x}O_4$ sample

Composition (x)	Lattice parameter a (Å)	Crystallite size D(nm)
0.0000	8.4794	33.50
0.0125	8.4661	30.05
0.0250	8.4851	29.90
0.0375	8.4953	28.70
0.0500	8.4951	26.47

Surface Morphology

Surface morphology of Samarium substituted Zinc ferrite ($ZnFe_{2-2x}Sm_{2x}O_4$) has been examined by Scanning Electron Microscope (SEM). SEM images of $ZnFe_{2-2x}Sm_{2x}O_4$ final sintered at 1000°C are shown in Figure 2. The grains of Zinc ferrites are found to be uniform and it exhibits a homogenous grain distribution. However, with the substitution of Sm, smaller grains of Sm are formed on the surface of larger grains of $ZnFe_2O_4$. The number of smaller grains increased with increase in Sm concentration. Furthermore, it is found that pores are quite rare to visualize in the structure. The observation of homogeneous surfaces in SEM images well agrees with the single phase formation of spinel structures for all compositions of Sm dopants. The values of the grain size in $ZnFe_{2-2x}Sm_{2x}O_4$are shown in Table 2. The ionic radii of ions in the spinel ferrite are 0.964 Å for Sm, 0.74 Å for Zn and 0.645 Å for Fe. Therefore, it is worth to note that the grain formation has also been slow downed due to the substitution of Sm ion with larger ionic radius for Fe ion with smaller ionic radius resulting in smaller grains.

Table 2 Comparison on grain sizes of $ZnFe_{2-2x}Sm_{2x}O_4$

Composition (x)	Grain size (µm)
0.0000	1.28
0.0125	0.90
0.0250	0.80
0.0375	0.69
0.0500	0.53

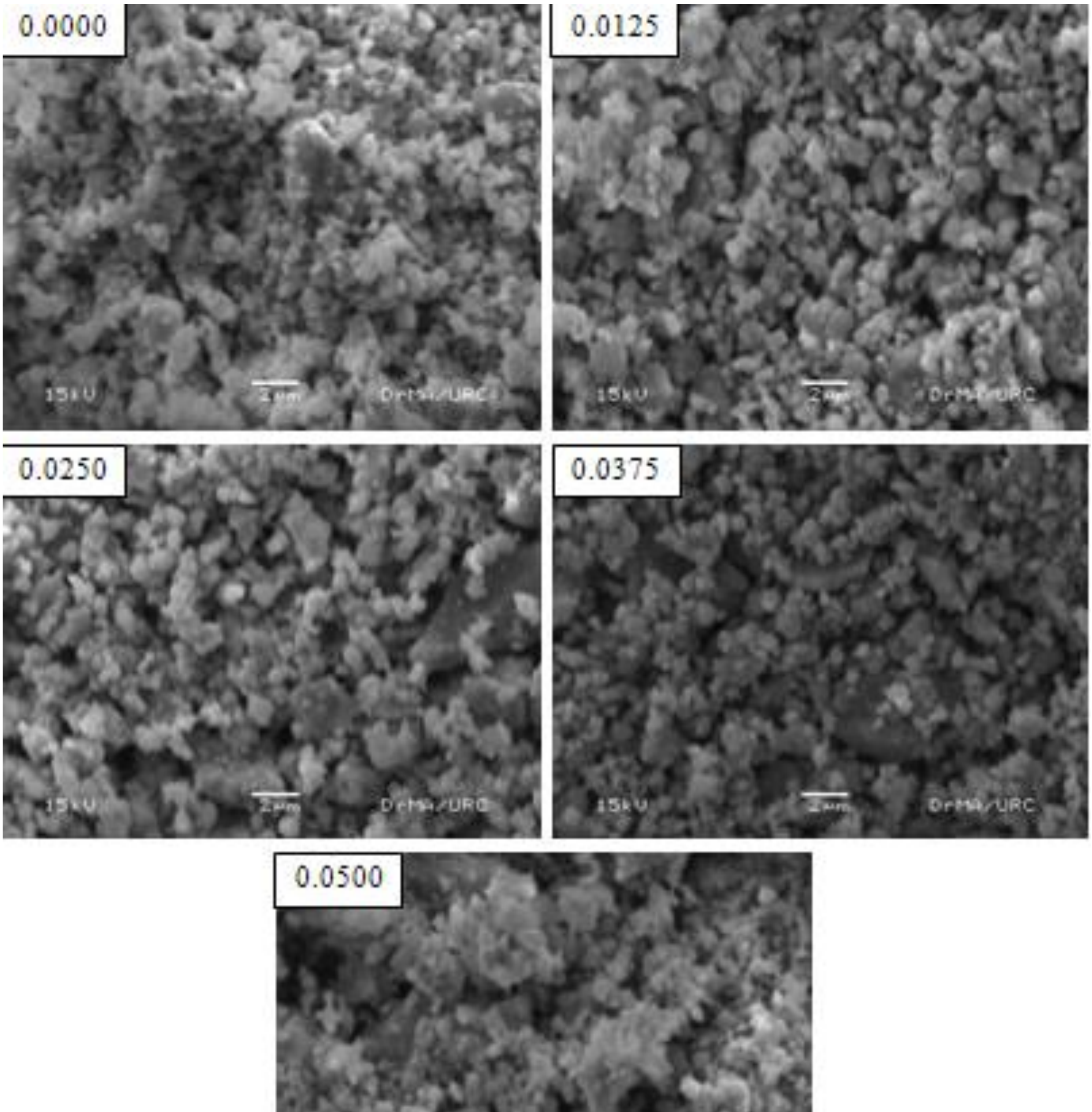

Figure 2 Variation of grains size in $ZnFe_{2-2x}Sm_{2x}O_4$ samples with Sm composition (x = 0.0000, 0.0125, 0.0250, 0.0375, 0.0500)

Fourier Transform Infrared Spectroscopic Analyses

In the wave number range of 4000–400 cm^{-1}, the infrared bands of solids are usually assigned to vibration of ions in the crystal lattice. Two main broad metal oxygen bands are seen in the IR spectra of all spinels, and ferrites in particular.

The highest band $\nu_1$is generally observed in the range 600–450 cm^{-1} corresponds to intrinsic stretching vibrations of the metal ions at the tetrahedral site. The lowest band $\nu_2$usually observed in the range 450–385cm^{-1}, is assigned to octahedral-metal stretching. FTIR spectra of the investigated $ZnFe_{2-2x}Sm_{2x}O_4$samples in the wave number range 900–450 cm^{-1} are shown in Figure 3. The prominent bands ν_1 present in all the samples. In order to see the ν_2 mode, the characterization has to be done in the range until 350 cm^{-1}. The vibrational frequencies of the IR bands are in agreement with the reported values in literature. Importantly, the value of $\nu_1$has shifted to lower frequency side with increasing samarium content. A slight broadening of the absorption band ν_1 is also noticed with increase in samarium concentration. This may be attributed to the substitution of Fe^{3+} ions by Sm^{3+} ions. It is known that increasing site radius reduces the fundamental frequency and therefore the central frequency should shift towards the lower frequency side.

Dielectric Measurements

The frequency dependence of the dielectric constant for all the samples has been studied at room temperature. The variation in dielectric constant (έ) with frequency range (1 kHz-1 MHz) at room temperature for the various $ZnFe_{2-2x}Sm_{2x}O_4$ samples with different Sm concentrations is shown in Figure 4. Comparison of dielectric constant for ferrite samples with different Sm concentration is shown in Table 3.

There is a fluctuation in έ values in the lower frequency range. However, the dielectric constant tends to be stable in the higher frequency range and importantly the dielectric constant has increased with increasing Sm content in Zinc ferrite. Theoretically the ferrite materials are applicable in the higher frequency region as the effect of microstructure especially grain boundaries can be eliminated in that region. It is worth to note that the large amount of rare earth Sm could make the ferrite to have larger value of dielectric constant. The observed variation in the dielectric constant with Sm concentration could be explained that the hoping of electrons in the spinel lattice may be enhanced by the octahedral site occupancy of Sm ions on the basis of local displacement of charge carriers in the presence of external electric field (Benny J et al., 1999 & **Chena H L et al., 2005).**

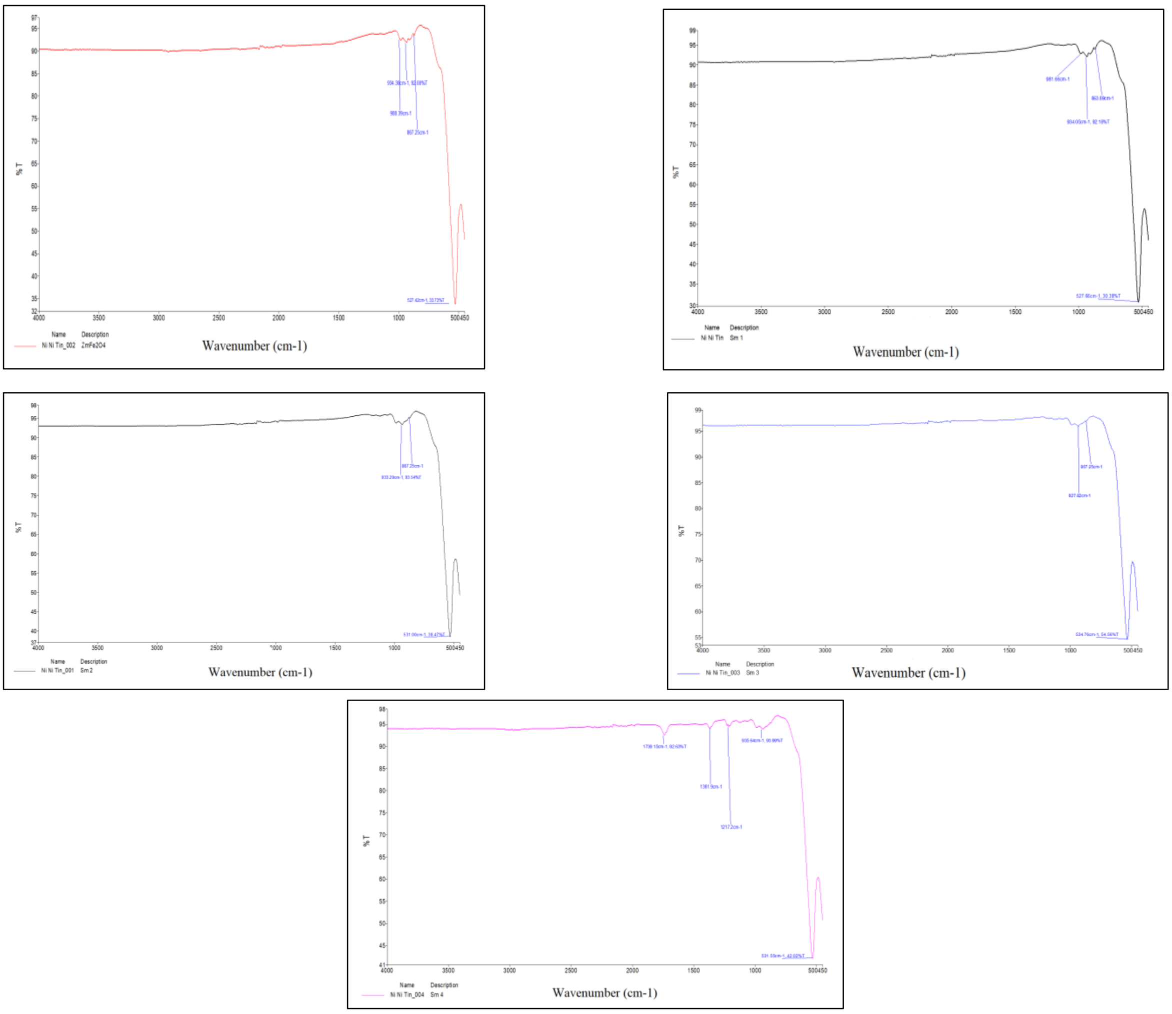

Figure 3 FTIR spectrum of $ZnFe_{2-2x}Sm_{2x}O_4$, (x = 0.0000, 0.0125, 0.0250, 0.0375, 0.0500)

Table 3 Comparison of dielectric constant for $ZnFe_{2-2x}Sm_{2x}O_4$ ferrite samples in the frequency range (1kHz - 1 MHz)

Frequency 10^3 (Hz)	**Dielectric Constant**				
	$ZnFe_{2-2x}Sm_{2x}O_4$				
	x = 0.0000	**x = 0.0125**	**x = 0.0250**	**x = 0.0375**	**x = 0.0500**
1.00E+00	7.7830	6.4417	7.3182	2.1324	3.5100
1.12E+02	0.4830	0.4973	0.4819	0.4459	0.4474
2.23E+02	0.4409	0.4735	0.4961	0.4991	0.5108
3.34E+02	0.4213	0.4538	0.4762	0.4749	0.4855
4.45E+02	0.3800	0.4155	0.4388	0.4357	0.4458
5.56E+02	0.3670	0.4020	0.4252	0.4204	0.4307
6.67E+02	0.3943	0.4310	0.4534	0.4485	0.4580
7.78E+02	0.4141	0.4514	0.4740	0.4689	0.4784
8.89E+02	0.4297	0.4673	0.4905	0.4851	0.4946
1.00E+03	0.4412	0.4800	0.5029	0.4976	0.5069

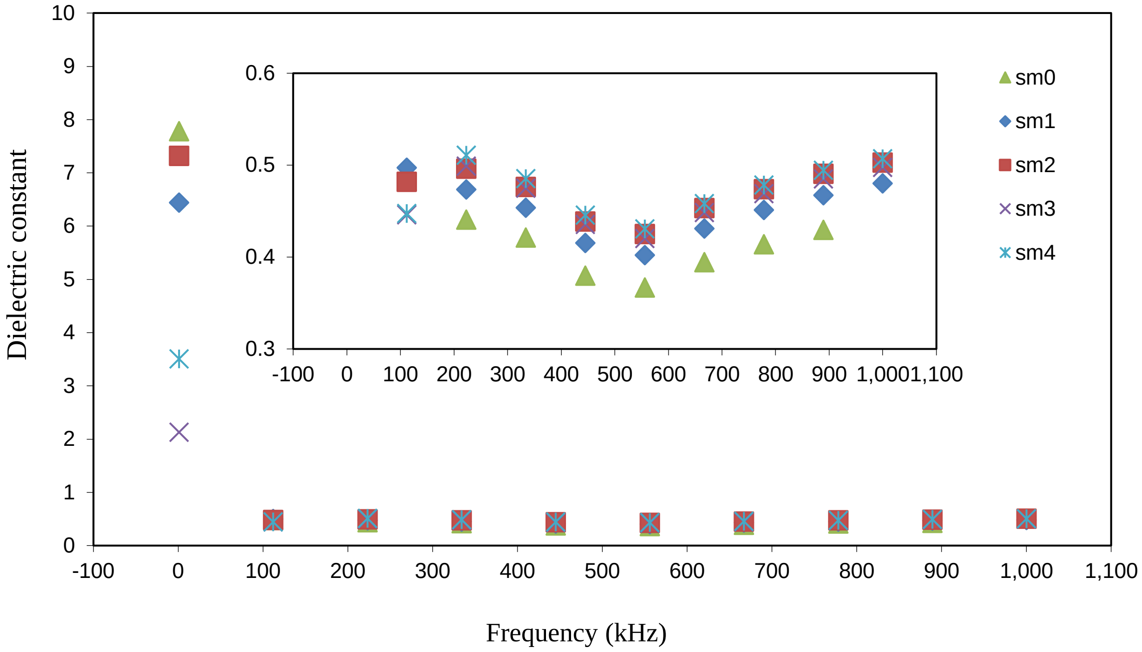

Figure 4 Frequency dependence of dielectric constant for $ZnFe_{2-2x}Sm_{2x}O_4$ ferrite nanoparticles (x = 0.0000, 0.0125, 0.0250, 0.0375, 0.0500) in the frequency range (1kHz-1MHz) (Inset : Frequency dependence of dielectric constant in small scale)

Conclusions

Samarium substituted Zinc ferrites ($ZnFe_{2-2x}Sm_{2x}O_4$) have been synthesized by Conventional Ceramic Method involving pre-sintering temperature at 900°C and final-sintering temperature of 1000°C. The structural, surface morphological and vibrational analyses of $ZnFe_{2-2x}Sm_{2x}O_4$ have been confirmed by XRD, SEM, FTIR. Dielectric measurements were performed in the range of 1 kHz-1 MHz. XRD analysis reveals that the samples are single phase inverse spinal cubic structure with crystallize sizes in the range of 26.47 nm to 33.5 nm which indicates the formation of nano-crystallize size. It is note to worth that the crystallize size has decreased with an increase in Sm doping. Sm dopants do not affect the lattice parameter in this process. Morphological analysis shows that the grain sizes are in the range of 0.53 µm to 1.28 µm. The grains are found to be homogeneously distributed on the surface and the grains become smaller with the substitution of Sm ions in $ZnFe_{2-2x}Sm_{2x}O_4$. The absorption bands are observed between the wave number 600-450 cm^{-1} due to the stretching vibrations in the tetrahedral metal oxygen bond. It is found that the dielectric constant of Sm substituted $ZnFe_{2-2x}Sm_{2x}O_4$ ferrite is higher than that of $ZnFe_2O_4$. It is concluded that small amount of Samarium substitution could affect on the Structural and dielectric properties of zinc ferrite.

Acknowledgements

We are grateful to Professor Dr Khin Khin Win, Head of Department of Physics, University of Yangon for her kind permission to carry out this research work.

References

Gul I. H., et al., (2008). "Electrical and magnetic characterization of nanocrystalline Ni–Zn ferrite synthesis by co-precipitation route". Journal of Magnetism and Magnetic Materials, 320:270-275.

Hashim M, et al., (2012). "Structural, magnetic and electrical properties of Al^{3+} substituted Ni-Zn ferrite nanoparticles". Journal of Alloys and Compounds, 511(1):107-114.

Jayanna, H.S., et al., (2009). "Structural and magnetic susceptibility studies of samarium substituted magnesium–zinc ferrites". Journal of Alloys and Compounds, 482, 147–150.

Ladole, A., (2012)."Preparation and Characterization of Spinel Zinc Ferrite $ZnFe_2O_4$ Internal Journal of chemistry" Volume 10(3), 1230-1234.

Moneesha F., et al., (2016). "Synthesis and Structural, Morphological& FTIR Studies on Ferrite Powders $Bafe_{(12-X)}Ti_XO_{19}$, Using Sol-Gel Method"Journal of Applied Physics (IOSR-JAP), Volume 8.

Mohammed, E.M., et al (2013). "Effect of Samarium Substitution on the Structural and Magnetic Properties of nanocrystalline Cobalt Ferrite". Journal of Nanoscience, Volume. Article ID 524380.

J. Myanmar Acad. Arts Sci. 2020 **Vol. XVIII.No.2B**

INVESTIGATION ON PROTON AND LEPTON CONCENTRATION IN SUPERNOVA EXPLOSIONS SIMULATIONS

Chan Myae Hlaing[1], Shwe Sin Phyo[2] and KhinNyan Linn[3]

Abstract

This research describes the effective chiral mean field model to construct the relativistic equation of state (EOS) of nuclear matter at finite temperature and density with various proton fractions and lepton fractions for the use in the supernova simulations. This model is based on chiral symmetry and we have adopted the RMF theory with the non-linear $\sigma - \omega$ terms, which was a success in describing the properties of both stable and unstable nuclei. In supernovae, the EOS determines the non-linear the dynamics of the collapse and the outgoing shock, and determines whether the remnant ends up as a neutron star or black hole. The various properties of supernova matter are investigated within the effective chiral mean field model. The outcome is demonstrated at zero entropy (neglecting thermal effect), the various proton fractions ranging from (Y_p=0.1~0.5) and various lepton fractions ranging from (Y_e=0.13~0.5) to be used for the simulations.

Keywords: supernova explosions, equation of state, effective chiral mean field model

Introduction

The equation of state (EOS) of nuclear matter is important in various astrophysical phenomena such as supernova explosions and the formation of neutron stars and black holes. The EOS in nuclear astrophysics purposes depends on a series of thermodynamic properties which are obtained for certain temperatures, densities and matter composition. The relativistic equation of state (EOS) of nuclear matter is designed for the use of supernova simulations in the wide density and temperature range with various proton fractions. We have adopted the RMF theory with the non-linear $\sigma - \omega$ terms, which was a success in describing the properties of both stable and unstable nuclei. The various properties of supernova matter are investigated within the effective chiral mean field model. The outcome is demonstrated at zero entropy (neglecting thermal effect), the various proton fractions ranging from (Y_p=0.1~0.5) and various lepton fractions ranging from (Y_e=0.13~0.5) to be used for the simulations in this article.

Chirality and Chiral Symmetry

Chiral comes from the Greek for "Hand". An object that cannot be superimposed on its mirror image is called chiral. Most generally chirality means: the structural characteristic of a finite system (molecule, atom and particle) that makes it impossible to superimpose it on its mirror image. The most straightforward example of chiral symmetry is the mirror symmetry shown by your left and right hand. In quantum field theory, chiral symmetry is a possible symmetry of the Lagrangian under which the left-handed and right-handed parts of Dirac fields transform independently. The chiral symmetry transformation can be divided into a component that treats the left-handed and the right-handed parts equally, known as vector symmetry, and a component that actually treats them differently, known as axial symmetry.

---

[1] Dr, Assistant Lecturer, Department of Physics, Yadanabon University, Mandalay, Myanmar

[2] Department of Physics, Yadanabon University, Mandalay, Myanmar

[3] Department of Physics, University of Mandalay, Mandalay, Myanmar

Equation of State in the Chiral Su (3) Model

The model has been found to describe the hadronic masses of the various SU(3) multiplets, finite nuclei, hypernuclei and excited nuclear matter reasonably well. It consists of a chiral $SU(3)_L$ x $SU(3)_R$ σ – ω type model. This means that its most important feature is allowing a chirally symmetric phase. The relevant degrees of freedom are baryons that interact through mesons. The scalar mesons (as the σ) represent the attractive part of the strong force while the vector mesons (as the ω) generate the repulsive part. The basic assumptions in the present chiral model are (1) the Lagrangian is constructed with respect to the nonlinear realization of chiral $SU(3)_L \times SU(3)_R$ symmetry; (2) the masses of the heavy baryons and mesons are generated by spontaneous symmetry breaking; (3) the masses of the pseudoscalar mesons are generated by explicit symmetry breaking; (4) a QCD-motivated field χ enters, which describe gluon condensate and baryons and mesons are grouped according to their quark structures.

The total Lagiangian of the chiral $SU(3)_L \times SU(3)_R$ model can be written as

$$\mathcal{L} = \mathcal{L}_{Kin} + \mathcal{L}_{int} + \mathcal{L}_{scal} + \mathcal{L}_{vec} + \mathcal{L}_{SB}$$

where , $\mathcal{L}_{Kin}$ = the kinetic energy term

$\mathcal{L}_{int}$ = the interaction term between baryons and mesons

$\mathcal{L}_{scal}$= the self-interaction term for the spin-0 mesons

$\mathcal{L}_{vec}$ = the self-interaction term for the spin-1 mesons

$\mathcal{L}_{SB}$ = the explicit symmetry breaking term

Each of these Lagrangian parts will be explained in the following.

$$\mathcal{L}_{Kin} = iTr\left(\overline{B}\gamma_\mu D^\mu B\right) + \tfrac{1}{2}Tr\left(D_\mu X D^\mu X\right) + Tr\left(\mu_\mu X \mu^\mu X + X\mu_\mu \mu^\mu X\right)$$

$$+\tfrac{1}{2}Tr\left(D_\mu Y D^\mu Y\right) + \tfrac{1}{2}Tr\left(D_\mu \chi D^\mu \chi\right) - \tfrac{1}{4}Tr\left(\tilde{V}_{\mu\nu}\tilde{V}^{\mu\nu}\right) - \tfrac{1}{4}Tr(\tilde{A}_{\mu\nu}\tilde{A}^{\mu\nu})$$

$$\mathcal{L}_{int} = -\sqrt{2}g_8^w\left\{\alpha_w\left[\overline{B}\mathcal{O}BW\right]_{AS} + (1-\alpha_w)\left[\overline{B}\mathcal{O}BW\right]_S\right\} - g_1^w\frac{1}{\sqrt{3}}Tr\left(\overline{B}\mathcal{O}B\right)Tr(W)$$

$$\mathcal{L}_{scal} = \mathcal{L}_{scal} - k_4\chi^4 - \tfrac{1}{4}\chi^4 ln\frac{\chi^4}{\chi_0^4} + \tfrac{\delta}{3}\chi^4 ln\frac{I_3}{det\langle \mathrm{X}\rangle_0}$$

$$\mathcal{L}_{vec} = \tfrac{1}{2}m_v^2\frac{\chi^2}{\chi_0^2}Tr\left(V_\mu V^\mu\right) + 2g_4^4 Tr(V_\mu V^\mu)^2$$

$$\mathcal{L}_{SB} = -\frac{\chi^2}{\chi_0^2}Tr(f\Sigma)$$

$$= -\frac{\chi^2}{\chi_0^2}\left[m_\pi^2 f_\pi \sigma + \left(\sqrt{2}m_{\mathrm{K}}^2 f_{\mathrm{K}} - \tfrac{1}{\sqrt{2}}m_\pi^2 f_\pi\right)\zeta\ \right]$$

To apply the effective chiral model to the description of equation of state for supernova matter, we perform the mean-field approximation. The mesons are treated as classical fields, i.e., they are replaced by their expectations values, which are classical fields. Furthermore, if rotational invariance holds, the expectation value of the three vector part of the vector mesons vanishes.

$$\sigma(x) = \langle\sigma\rangle + \delta\sigma \rightarrow \langle\sigma\rangle \equiv \sigma;$$

$$\zeta(x) = \langle\zeta\rangle + \delta\zeta \rightarrow \langle\zeta\rangle \equiv \zeta,$$

$$\omega_\mu(x) = \langle\omega\rangle\delta_{0\mu} + \delta\omega_\mu \rightarrow \langle\omega_0\rangle \equiv \omega;$$

$$\phi_\mu(x) = \langle\phi\rangle\delta_{0\mu} + \delta\phi_\mu \rightarrow \langle\phi_0\rangle \equiv \phi.$$

The total Lagrangian density in the mean field approximation can be written as

$$\mathcal{L}_{MFT} = \mathcal{L}_{Kin} + \mathcal{L}_{int} + \mathcal{L}_{scal} + \mathcal{L}_{vec} + \mathcal{L}_{SB}$$

where, $\mathcal{L}_{Kin} = -\bar{\psi}\gamma_i\partial^\mu\psi - \frac{1}{2}\sum_{\varphi=\sigma,\zeta,\chi,\omega,\rho}\partial_\mu\varphi\partial^\mu\phi,$

$$\mathcal{L}_{int} = -\sum_i \bar{\psi}_i\,(m_i^* + g_{i\omega}\gamma_0\omega^0 + g_{i\phi}\gamma_0\phi^0 + g_{Np}\gamma_0\tau_3\rho_0)\psi_i$$

$$\mathcal{L}_{scal} = -\frac{1}{2}k_0\chi^2(\sigma^2+\zeta^2) + k_1(\sigma^2+\zeta^2)^2 + k_2\left(\frac{\sigma^4}{2}+\zeta^4\right) + k_3\chi\sigma^2\zeta$$

$$+ k_{3m}\chi\left(\frac{\sigma^3}{\sqrt{2}}+\zeta^3\right) - k_4\chi^4 - \frac{1}{4}\chi^4 ln\frac{\chi^4}{\chi_0^4} + \frac{\delta}{3}\chi^4 ln\frac{\sigma^2\zeta}{\sigma_0^2\zeta_0}$$

$$\mathcal{L}_{vec} = \frac{1}{2}\frac{\chi^2}{\chi_0^2}\left(m_\omega^2\omega^2 + m_\rho^2\rho^2\right) + g_4^4(\omega^4 + 6\omega^2\rho^2 + \rho^4)$$

$$\mathcal{L}_{SB} = -\frac{\chi^2}{\chi_0^2}\left[m_\pi^2 f_\pi\sigma + \left(\sqrt{2}m_{\mathrm{K}}^2 f_{\mathrm{K}} - \frac{1}{\sqrt{2}}m_\pi^2 f_\pi\right)\zeta\,\right]$$

In order to determine the supernova matter properties, the thermodynamical potential of the grand canonical ensemble has to be solved. It is defined as

$$\frac{\Omega}{V} = -\mathcal{L}_{vec} - \mathcal{L}_{SB} - \mathcal{L}_{scal} - \mathcal{V}_{vac} - \sum_i \frac{\gamma_i}{(2\pi)^3} \times \int d^3k[\,E_i^*(k) - \mu_i^*]$$

The energy density and the pressure follow from the Gibbs-Duhem relation,

$$\epsilon = \Omega/V + \mu_i\rho^i$$

and $P = -\Omega/V$

Results and Discussion

After the calculation of equation of state, we investigate the properties of supernova matter. Some conditions are used to investigate the properties of supernova matter.

In a supernova core, neutrinos are trapped and form an ideal Fermi-Dirac gas. Thus, the weak process is

$$p + e^- \leftrightarrow n + \nu_e$$

The chemical equilibrium requires

$$\mu_p + \mu_e = \mu_n + \mu_\nu$$

The second condition is charge neutrality,

$$\rho_e + \rho_\mu = \rho_p,$$

where ρ_e and ρ_μ are the electron and muon number densities respectively.

The third condition is to fix proton concentration,

$$Y_p = \frac{1}{2}\left(\frac{\rho_p - \rho_n}{\rho_p + \rho_n}\right)$$

where ρ_p and ρ_n are the proton and neutron number densities respectively.

The fourth condition is to add lepton concentration in stellar matter.

$$Y_l = \frac{\rho_e + \rho_\nu}{\rho} \equiv Y_e + Y_\nu$$

The pressure P versus the energy density ε is displayed in Figure.1 for nuclear matter varying proton fraction (Y_p = 0.1 to 0.5). The EOS is found to be considerably softer for the bigger Y_p in the effective chiral model compared with the EOS for the smaller Y_p. The pressure is the same until the energy density of ~ 170 MeV/fm^3 for all Y_p. Above this energy density the pressure is higher as the bigger value of Y_p. For Y_p = 0.5, the EOS is considerably softer than the EOS with smaller value of Y_p.

Figure.2 shows the energy per baryon as a function of baryon density for varying proton fraction calculated in the effective chiral model. With increasing proton fraction the energy per baryon decreases around saturation density. If the baryon density is larger than the saturation density, it is found that the energy per baryon rapidly increases for the larger proton fractions.

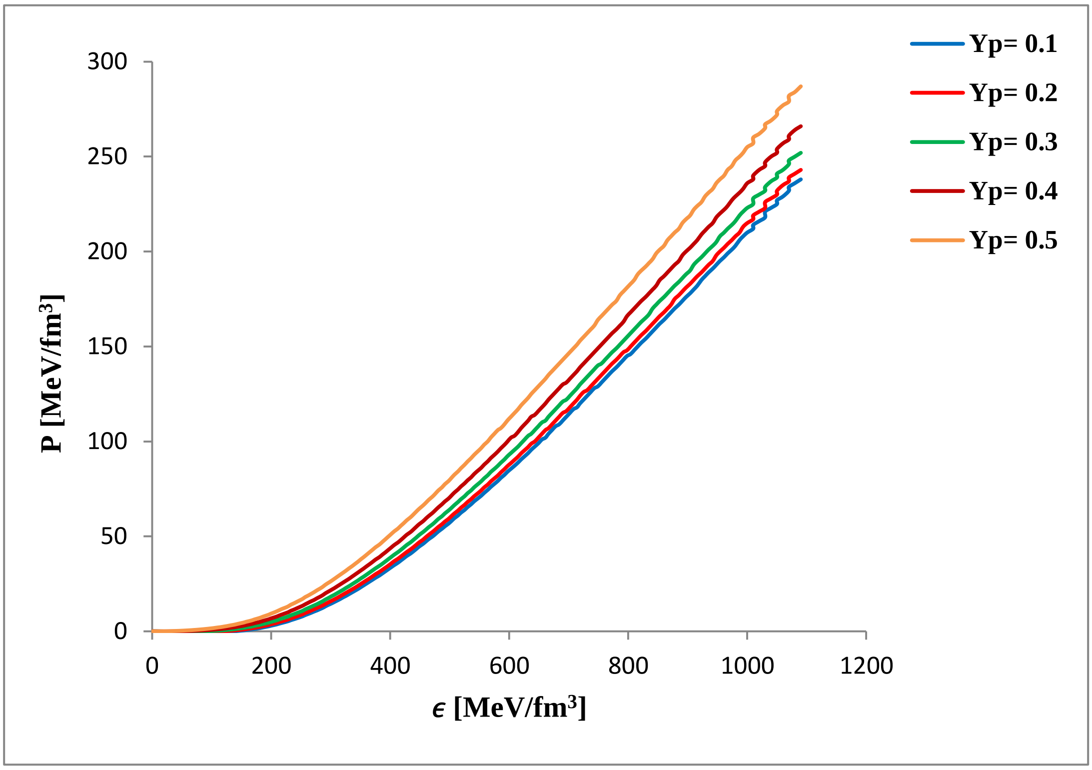

Figure 1 The equation of state (i.e. the pressure vs. energy density) with various proton fractions (Y_p).

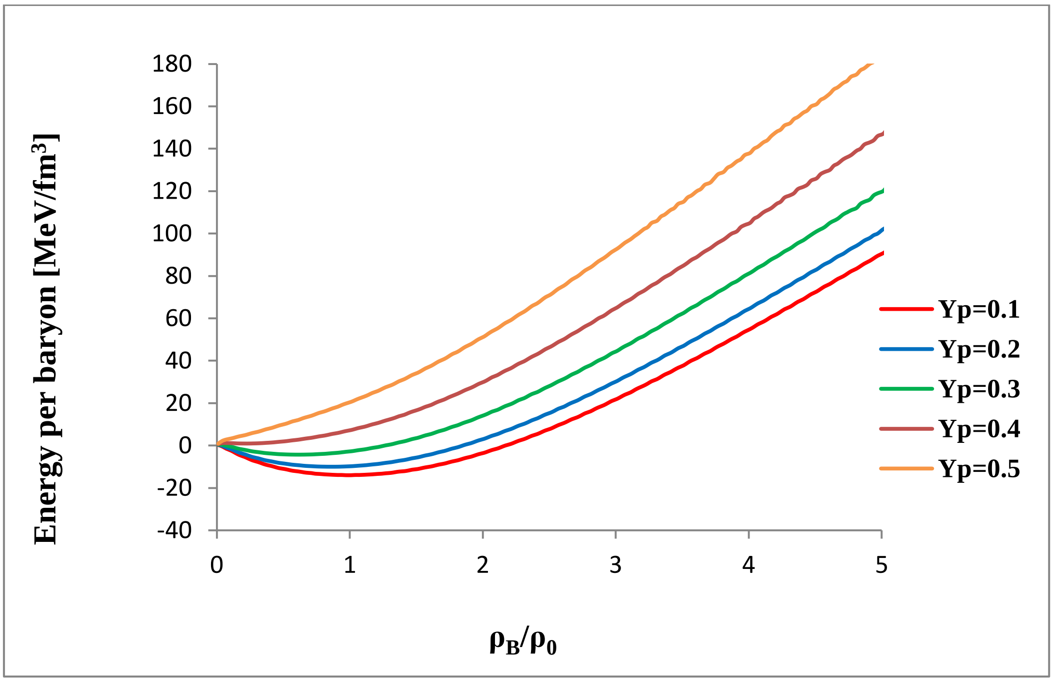

Figure 2 Binding energy per baryon vs. baryon density with Y_p=0.1 to 0.5.

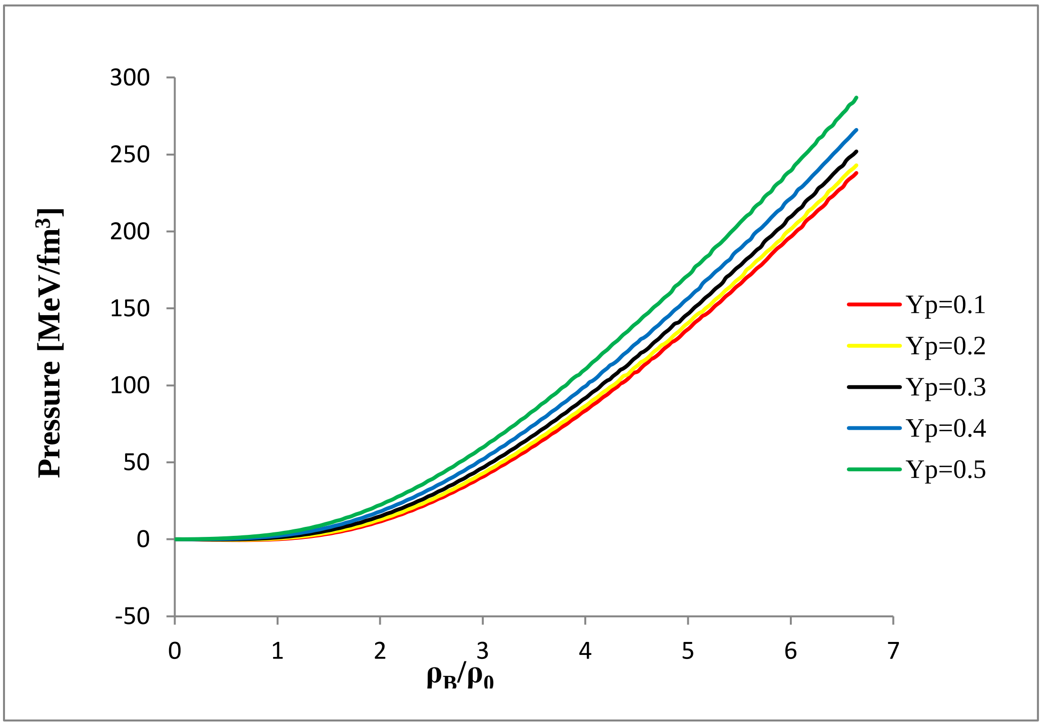

Figure 3 The pressure P as a function of baryon density ρ_B/ρ_0.

The pressure p as a function of the baryon density varying proton fraction is plotted in Figure 4.3. The pressure is the same around the saturation density. The pressure is nearly the same for the case of $Y_p = 0.1$ and $Y_p = 0.2$ although the pressure is higher when $Y_p > 0.2$.

In order to calculate the equation of state with lepton fractions, the extra chemical potential has added. The external chemical potential is used to fix the electron (plus muon) number. The pressure P versus the energy density ε is displayed in Figure.4 for supernova matter varying electron fraction (Y_e = 0.13 to 0.5). In Figure.1, Stellar matter is charge neutral, so if a fraction Y_e=0.2, Y_p=0.2 in order to have as many electrons and protons to achieve charge neutrality. In Figure.4, we have calculated star matter, which includes also leptons, i.e. electrons. The contributions of electrons are added to the total energy, thus energy per baryon are increased. The more neutrinos are emitted through the electron capture on protons. As a result, the bigger electron fraction (Y_e), the softer equation of state is formed.

The pressure p as a function of the baryon density varying electron fraction is plotted in Figure 5. When there are bigger Y_e, the pressure increases rapidly as the baryon density increases.

Figure 6 shows the energy per baryon as a function of baryon density for varying electron fraction calculated in the effective chiral model. According to added the lepton fraction, the binding energy per baryon are increased significantly. Due to the neutrino emission through the electron capture on protons, the star becomes neutron rich, leading to a cold neutron star.

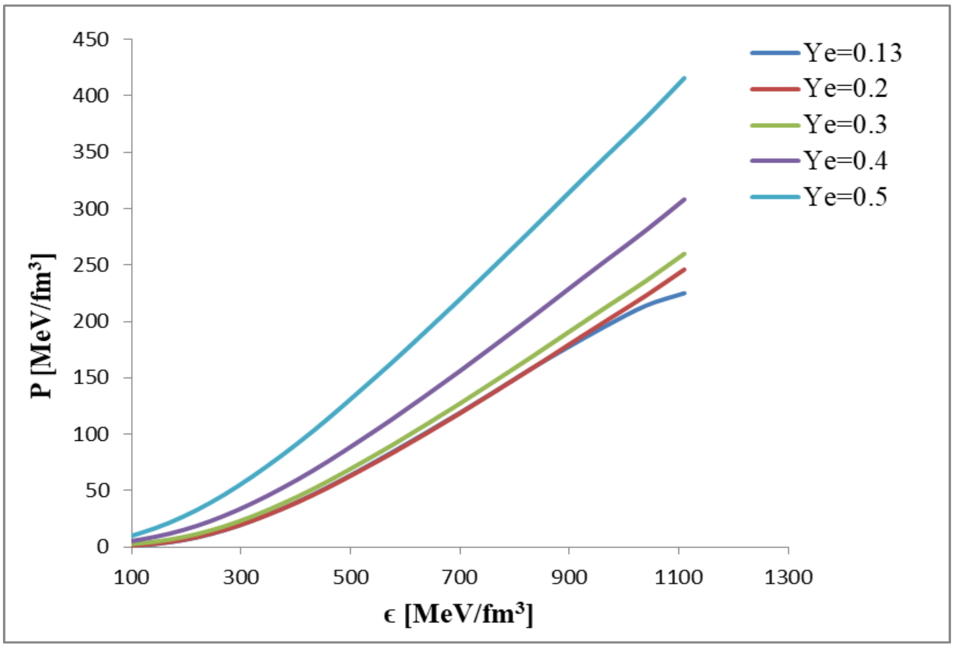

Figure 4 The equation of state (i.e. the pressure vs. energy density) with various electron fractions (Y_e=0.13 to 0.5).

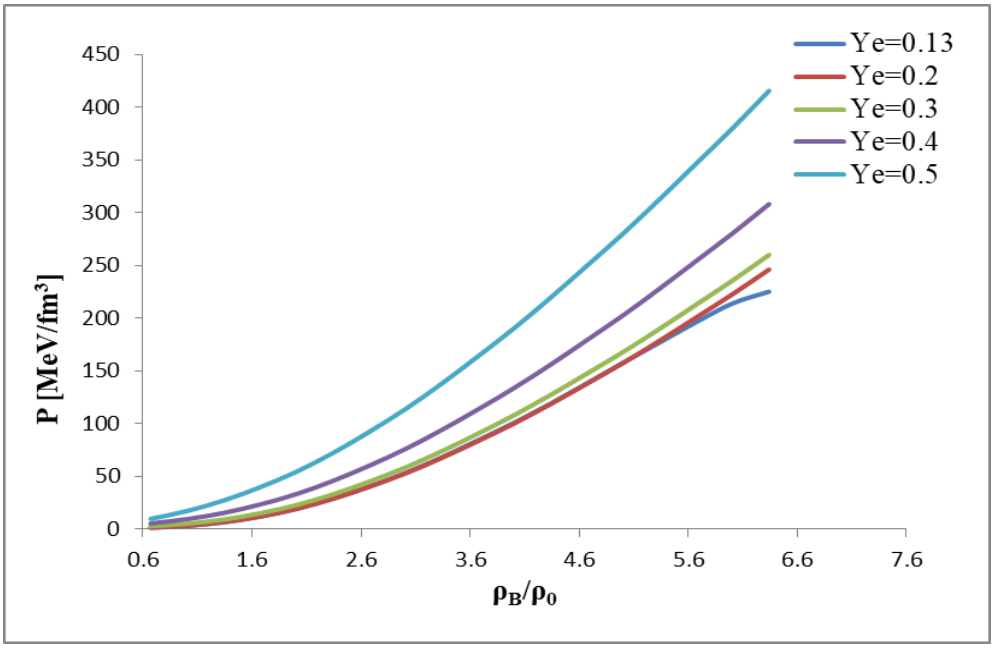

Figure 5 The pressure P as a function of baryon density ρ_B/ρ_0 (Ye=0.13 to 0.5).

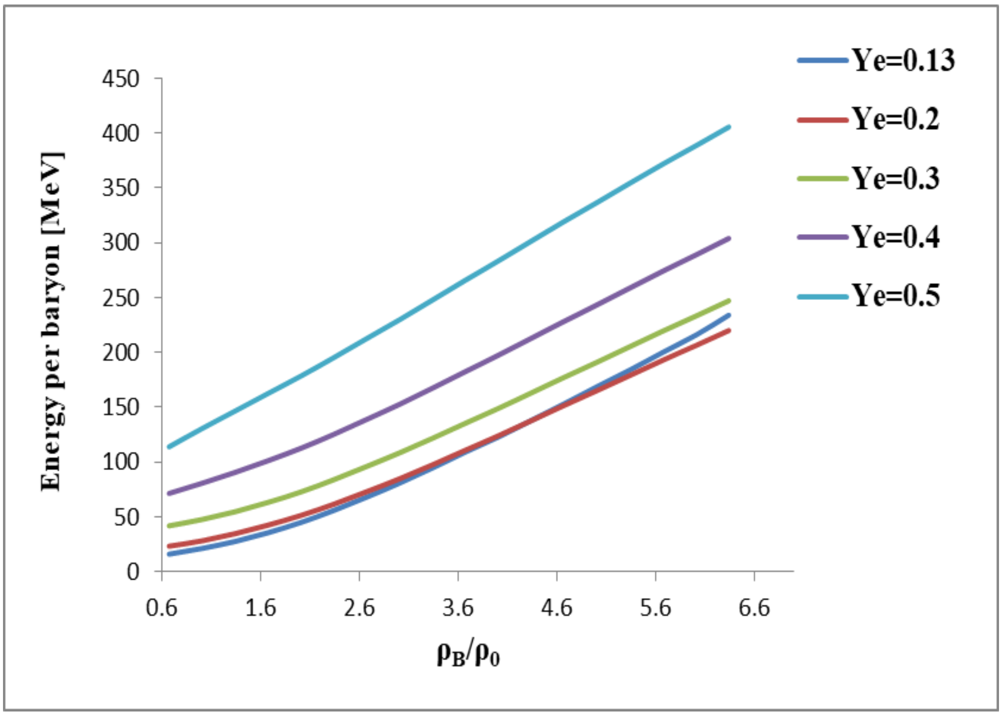

Figure 6 Binding energy per baryon vs. baryon density with Ye=0.13 to 0.5.

Conclusion

In this article, we have presented set of EOS table covering the wide range of baryon density, various proton fraction Y_p, electron fraction Y_e and temperature T = 1MeV for the use of core collapse supernova simulations. In our EOS, we have compared the equations of state with and without electron concentrations. The equation of state without electron fractions, Y_e, stellar matter is charge neutral, so if a fraction Y_e=0.2, Y_p=0.2 in order to have as many electrons and protons to achieve charge neutrality. The nuclear matter likes to be isospin symmetric if one neglects Coulomb interaction. The EOS is found to be considerably softer for the bigger Y_p in the effective chiral model compared with the EOS for the smaller Y_p. The EOS with electron fractions, Y_e, the extra chemical potential is added, the energy per baryon is increased significantly. This is due to the neutrino emission through the electron capture on protons. In addition to the properties of dense matter, it is mandatory to provide the rates of neutrino reactions with the dense matter in the supernova core. The reaction rates depend on the energy and the structure of nuclei. Therefore, implementing the neutrino reaction rates is also a challenging task for the numerical simulation of supernova explosion.

Acknowledgements

The authors are grateful to Prof. Stefan Schramm, Fellow of Frankfurt Institute for Advanced Studies (FIAS) Johann Wolfgang Goethe-Universität, Executive Director, and Center for Scientific Computing (CSC) Frankfurt am Main, Germany, for his instruction, guidance, advice and stimulating discussion as well as for broadening our knowledge horizon significantly as to nuclear astrophysics in all areas of nuclear physics. We are deeply indebted to his kindness, his confidence in us, and his inexhaustible efforts as a mentor.

References

B.D. Serot and J.D. Walecka, Int. J. Mod.Phys. **C6**, (1997) 515.

P. Papazoglou et al., Phys. Rev. **C 57**, (1998) 2576.

P. Papazoglou et al., Phys. Rev. **C 59**, (1999) 411.

S. Schramm, Phys. Rev. **C 66** (2002) 064310.

Shen et al., preprint arXiv:1005.1666v**2**, (2011).

J. Myanmar Acad. Arts Sci. 2020 **Vol. XVIII.No.2B**

INVESTIGATION OF RADON CONCENTRATION AND ANNUAL EFFECTIVE DOSE OF FIVE DIFFERENT TILE SAMPLES

Aye Aye Soe[1], Tin Tin Phyo Lwin[2], Myint Myint Maw[3],
Shwe Nan Htet[4], Cho Cho Aung[5]

Abstract

Radon is a colourless and odourless inert gas and its isotopes can be found in the uranium and thorium decay sequences occurring in the nature. An alpha particle is emitted during its decay. Its progeny elements are formed as a result of series of decays which are also radioactive. A study of radon concentration has been carried out in the five different tile samples, using LR-II5 type II Solid State Nuclear Track Detectors (SSNTDs). According to the present measurement, it was found that, the value of radon ranges from 219.05 ± 11.90 Bqm^{-3} to 441.90 ± 32.86 Bqm^{-3} with an average value 337.86 ± 23.24Bqm^{-3}. The annual effective dose ranges from 3.76 ± 0.20 mSvyr^{-1} to 7.6 ± 0.57 mSvyr^{-1} with an average value of 5.81 ± 0.40 mSvyr^{-1}.

Keywords: Radon concentration, annual effective dose.

Introduction

Radon is a natural occurring radioactive gas and requires special instruments to detect its present. Radon is everywhere, but generally at very low concentration. Uranium is found in varying quantities in all rocks and soil, so consequently there are variations in the amount of radon depending where you are. Radon is slowly released from the ground, water and some building materials that contain very small amounts of uranium, such as concrete, bricks, tiles and gypros. Building materials (such as soil, brick, concrete, color cement and tile etc) are one of the major sources of indoor radon concentration in dwellings. The detection and radon concentration measurements are one of the most important procedures in environmental protection. In the present study, the radon concentration from the tile samples have been measured. Tiles samples have been collected from building shop in Yangon and are manufactured in Myanmar, Thailand, Malaysia and China. To estimate the radon concentration in these samples, solid state nuclear track detection technique (Can technique) was used. Figure (1) shows radioactive decay scheme of ^{22}Rn.In this radon concentration measurements, one type of solid state nuclear track detectors (SSNTDs), LR-115 type II was used. The principle of this technique was based on the production of track in the detector due to alpha particles emitted from radon and its progeny. After exposure, the tracks are made visible by etching and counted manually under the microscope. From the alpha track detection, we carried out alpha track densities, the radon concentrations and annual effective doses. The plastic track detector LR-115 Type II used in this work is a cellulose nitrate red dyed film, manufactured by Kodak Pathe France, LR-115 is a solid state nuclear track detector (SSNTD) based on cellulose nitrate and has been commonly used for measurement of concentration of radon gas and / or radon progeny. The sensitive surface for alpha particle, red dyed, is of 10μm thickness of cellulose nitrate (CN) layer on a colorless inert backing material and the base is 100μm polyester. The composition of LR-115 Type II ($C_6H_8O_9N_2$) is shown in fig

---

[1] Dr, Assistant Lecturer, Department of Physics, Yangon University

[2] Assistant Lecturer, Department of Physics, Yangon University

[3] Assistant Lecturer, Department of Physics, Yangon University

[4] Lecturer, Department of Physics, Yangon University

[5] Associate Professor, Department of Physics, Yangon University

(2). Its advantage is that after suitable etching, the tracks appear as colorless holes against a red background. Obviously, only one side of this film is sensitive, and this must be determined before used. Etched tracks show up as bright holes in a dark red background, and are very clearly visible under a low power microscope of magnification.

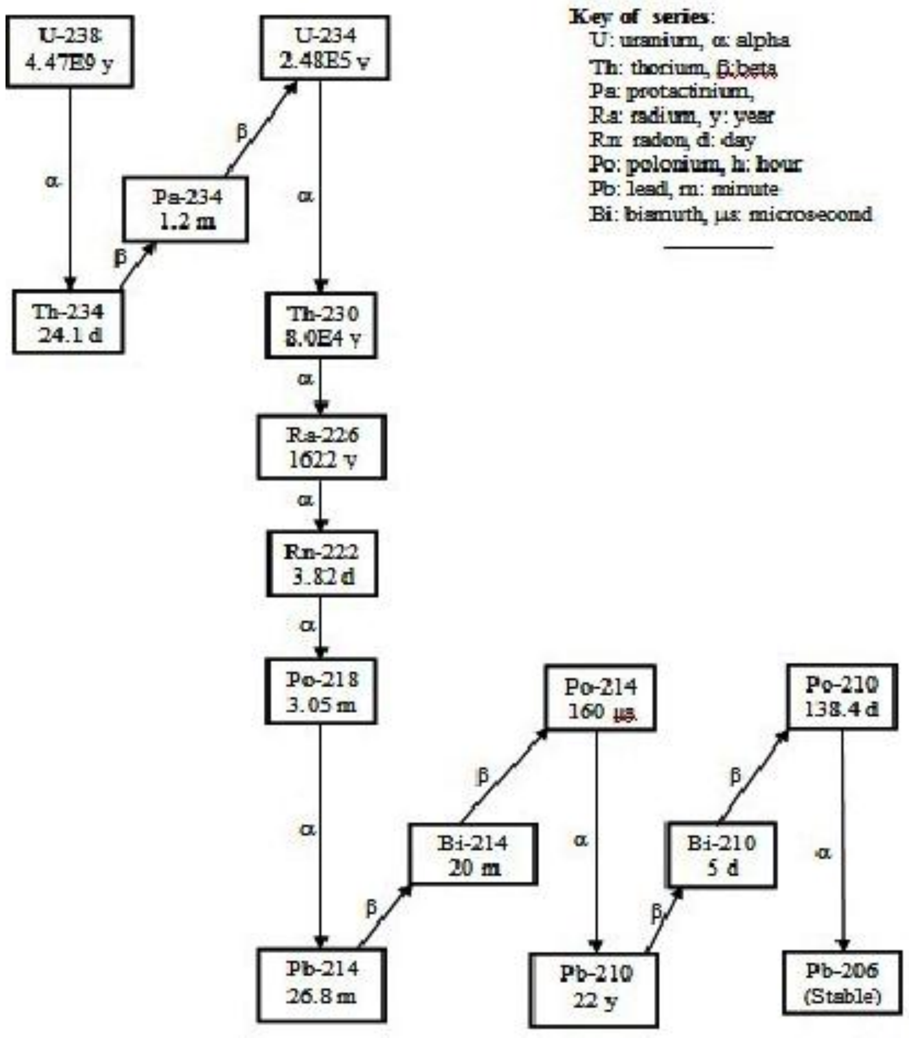

Figure 1 Radioactive decay scheme of uranium ^{238}U

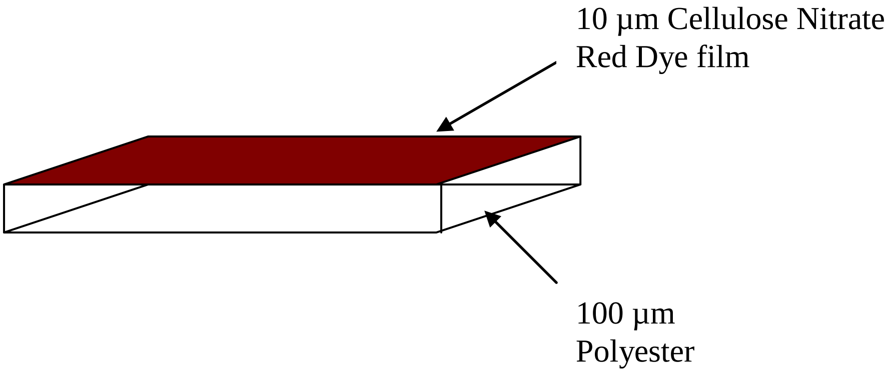

Figure 2 The Structure of the Solid State Nuclear Track Detector LR -115 Type II Cellulose Nitrate film

Sample Collection

To measure the radon concentration and annual effective doses, five kinds of tile were collected in the building materials shop in Yangon. Table (1) shows source of tile sample manufacture by Myanmar, Thailand, Malaysia and China. Figure (3) shows five kind of tile.

Table 1 Tile Sample are manufactured by Myanmar, Thailand, Malaysia and China

Sample Code	Source of Tile Sample Manufactured
T1	Benhur (Thailand)
T2	ATC (Sagging)
T3	Roma (Malaysia)
T4	Five Star (China)
T5	Tharyarwadi (Myanmar)

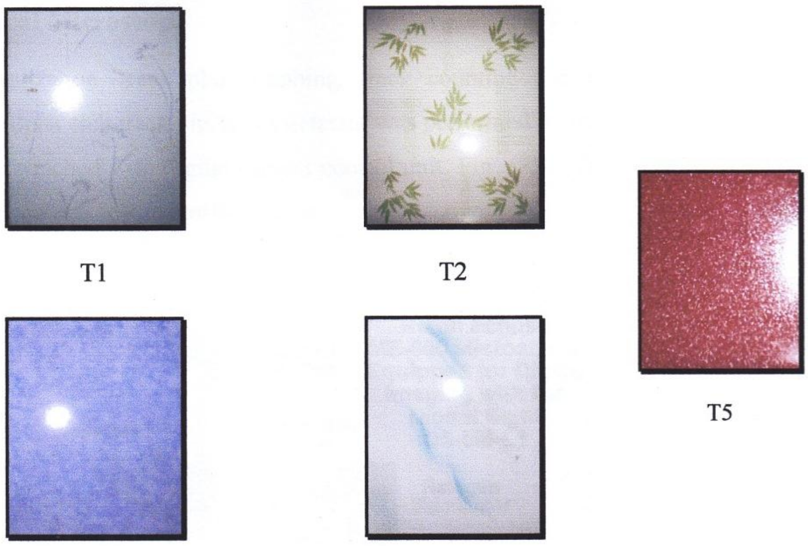

T1 T2 T5 T3 T4

Figure 3 Five kinds of tile

Experimental Details

In this work, a known amount 100g of five different tiles samples were placed in a plastic cans. Figure (4) shows the balance that was used to measure the NaOH pellets. LR-115 Type II CN detector about (1cm× $1cm$) were fixed on the bottom of the lid of each can with tape such that, sensitive side of detector faced the specimen. The can was tightly closed from the top and sealed. The geometrical parameters of plastic can were diameter 6.8 cm, height 9.9 cm, volume $360cm^3$ as illustrated in Figure (5). In order to eliminate any background counts due to assembly set up, LR-115 Type II was fixed on the bottom of the lid of can without tile samples. At the end of the exposure time, the detectors were removed from the lid of plastic can and subjected to a chemical etching process. The LR-115 detectors were etched in 2.5 N NaOH solution at 60 ˚C for 80 mins. During etching, the temperature was kept constant with an n accuracy for 1˚C and without stirring. The etching process detector is show in figure (6).

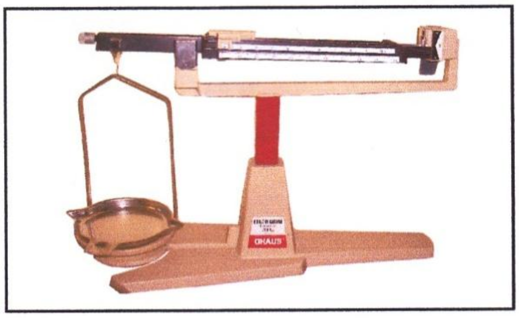

Figure 4 The balance that was used to measure the NaOH pellets

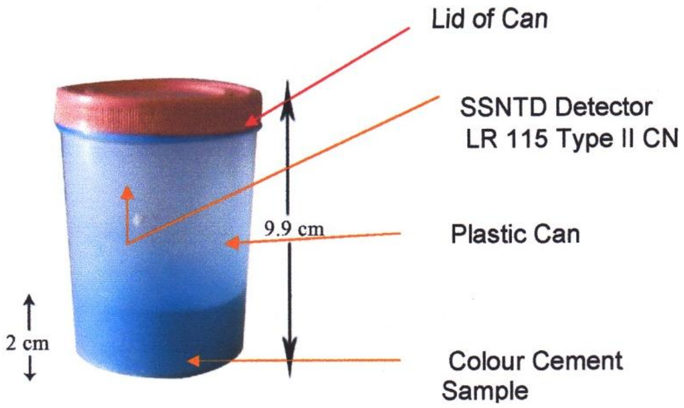

Figure (5) The photograph of the can technique

Track Counting

After etching, the solution in the beaker is poured into another beaker through small plastic sieve with handle. Thus, the detectors can be easily and fastly collected. Then the detectors were washed with water until the surface of the detectors became cleaned. Finally, the detectors were taken out and dried on the filter paper and the tracks produced by particles were observed and counted using Nikon Eclipse ME-600 Microscope Equipped for Digital imaging with the Digital Sight DS-5M-L1, Department in Yangon University. The mostly used method of track counting employs an optical microscope is as shown in figure (7). According to the observation views of the screen of microscope, alpha tracks were counted to reduce the statistical errors. The photographs of alpha tracks in LR-115 detectors are shown in figure (8) to figure (12).

In this work, alpha tracks were counted for different fifty views and the track densities were calculated by using equations:

$$\text{Track Density (track cm}^{-2}\text{) day}^{-1}\text{)} = \frac{\text{Number of Net Tracks}}{\text{Area of counted view} \times \text{Exposure time}} \quad (1)$$

$$\text{Radon } (\text{Bqm}^{-3}) = \frac{\text{Track Density}}{\text{Calibration Factor}} \quad (2)$$

$$\text{Annual Effective Dose} = \text{Radon Concentration} \times 0.0172\ \text{mSvyr}^{-1} \quad (3)$$

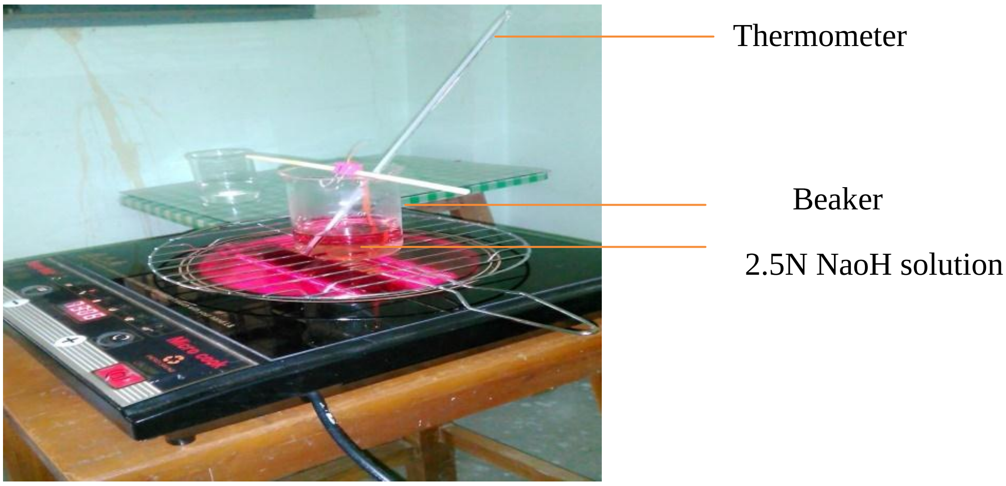

Figure 6 Etching Process of Detectors

Figure 7 Optical Microscope and Camera Control Unit

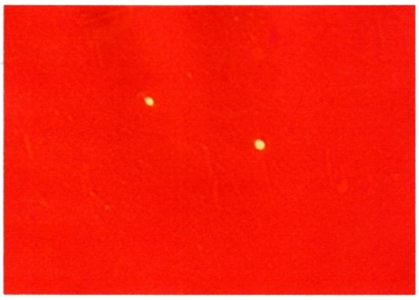

Figure 8 Photomicrograph of alpha tracks in LR-115 Type II CN for Tile T1 (Benhur)

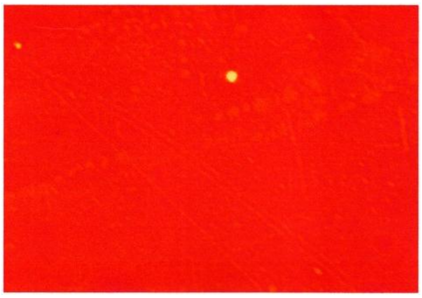

Figure 9 Photomicrograph of alpha tracks in LR-115 Type II CN for Tile T2 (ATC)

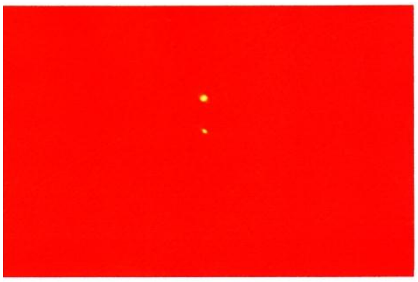

Figure 10 Photomicrograph of alpha tracks in LR-115 Type II CN for Tile T3 (Roma)

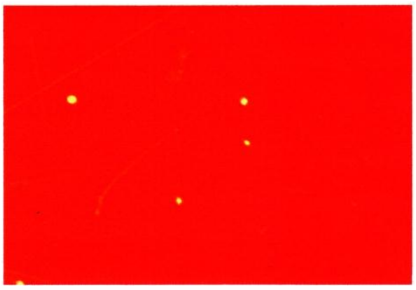

Figure 11 Photomicrograph of alpha tracks in LR-115 Type II CN for Tile T4 (Five Star)

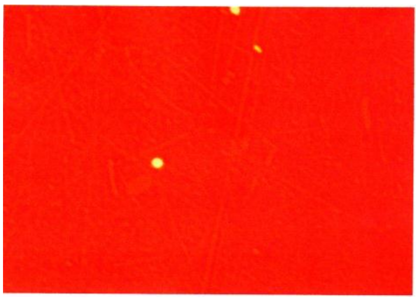

Figure 12 Photomicrograph of alpha tracks in LR-115 Type II CN for Tile T5 (Tharyarwadi)

Results and Discussion

From the experimental work, the estimate of radon concentrations and the annual effective doses were carried out. Average number of alpha tracks and track densities of each sample were calculated by using equation (1). By using calibration factor 0.05016 track cm^{-2} day^{-1} = 1 Bqm^{-3}, radon concentrations can be calculated from equation (2). And then the annual effective doses were calculated by using equation(3).The average number of tracks and track densities were mentioned in Table (2). The radon concentrations and annual effective doses were mentioned in Table (3) and Table (4).The graphs of alpha track densities, radon concentrations and annual effective doses from three different places are shown in Fig (13) to Fig (15).The comparison graph of ICRP Level and Samples in annual effective doses are shown in Fig (16).

Table 2 The Alpha Track Densities (track cm^{-2} day^{-1}) for three different floors

Sr. No.	Name of Samples	Average number of Alpha Tracks	Alpha Track Densities (track cm^{-2} day^{-1})
1	T1	9.48 ± 0.67	9.28 ± 2.10
2	T2	8.60 ± 0.54	8.42 ± 0.56
3	T3	7.34 ± 0.49	7.15 ± 0.52
4	T4	6.20 ± 0.39	6.03 ± 0.42
5	T5	4.76 ± 0.23	4.60 ± 0.25

Table 3 The radon concentrations (Bq m^{-3}) for three different floors

Sr. No.	Name of Samples	Radon concentrations (Bq m^{-3})
1	T1	441.90 ± 32.86
2	T2	400.90 ± 26.67
3	T3	340.48 ± 24.76
4	T4	287.14 ± 20.00
5	T5	219.05 ± 11.90

Table 4 The Annual Effective Doses (m Sv yr^{-1}) for three different floors

Sr. No.	Name of Samples	Annual Effective Doses (m Sv yr^{-1})
1	T1	7.60 ± 0.57
2	T2	6.89 ± 0.46
3	T3	5.86 ± 0.43
4	T4	4.94 ± 0.34
5	T5	3.76 ± 0.20

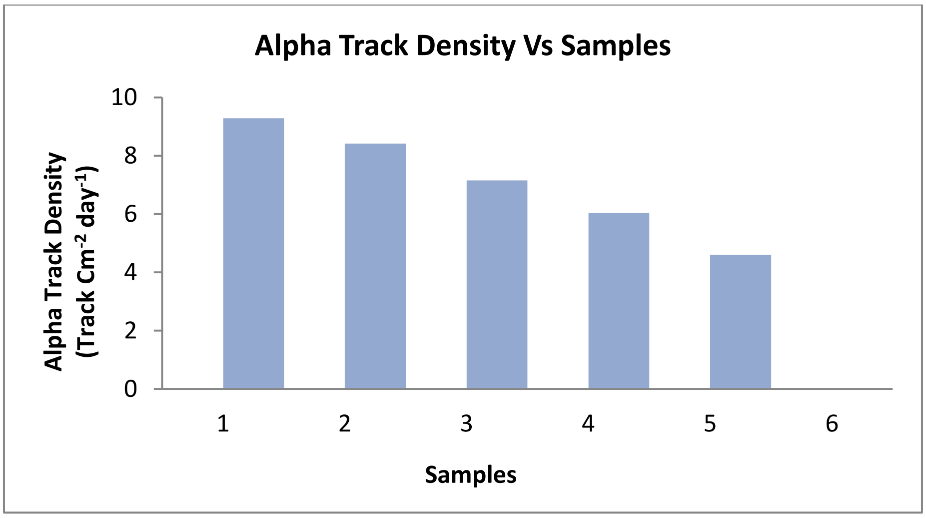

Figure 13 Comparison graph of alpha track densities for five different tiles

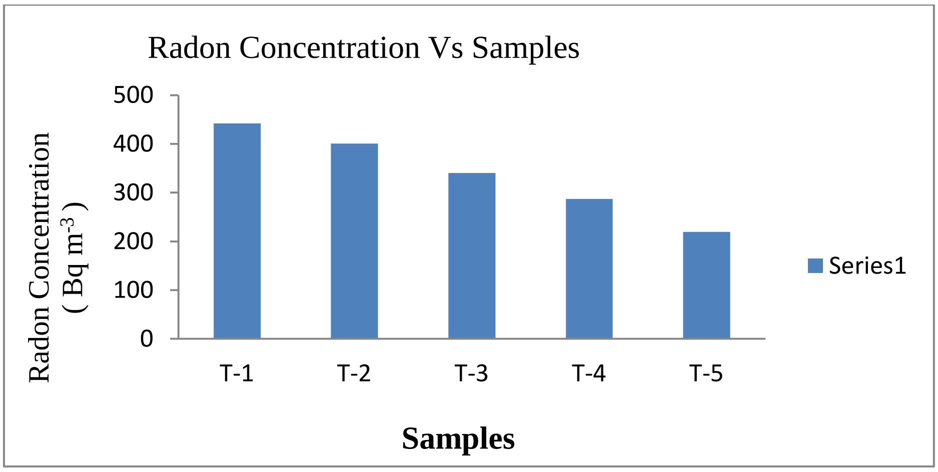

Figure 14 Comparison graph of radon concentrations for five different tiles

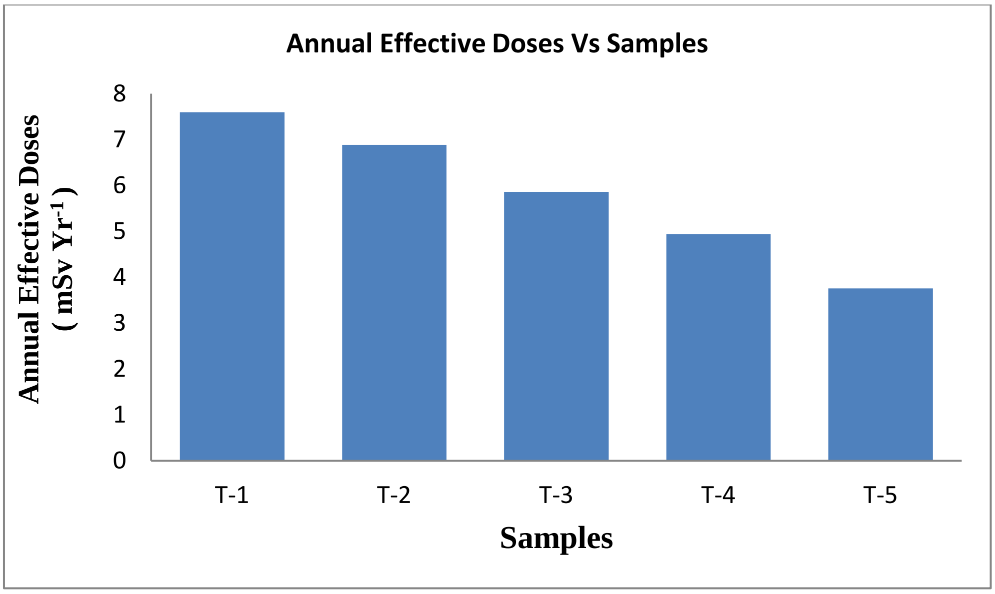

Figure 15 Comparison graph of annual effective doses for five different tiles

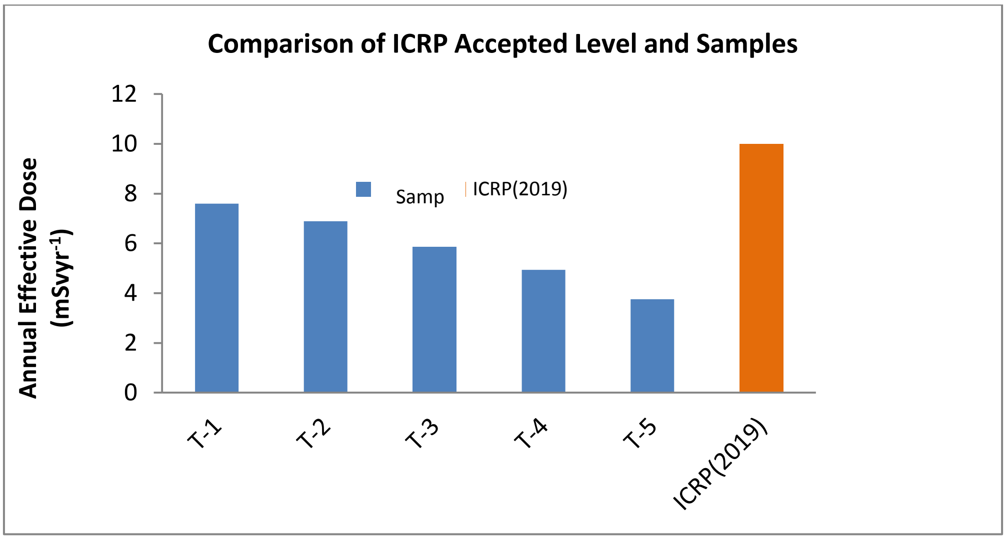

Figure 16 Comparison of ICRP Accepted Level and Samples

Conclusion

Radon is the biggest contributor to natural radiation in the environment and causes long term health concern. Therefore, the measurement of radon concentration is needed for environmental purpose. The results of indoor radon concentration measured with LR-115 type II were presented in this work. The results have been found lower than that of ICRP limited level. In general, the studied tiles samples are safe to use as construction material, and there is a good covenant between all measurements of radon concentration and annual effective dose.

Acknowledgements

I would like to thank Dr Khin Khin Win, Professor and Head, Department of Physics, University of Yangon for her kind permission to carry out this research,

I would like to express my sincere thanks to all of Professors, University of Yangon, for their suggestion and comments for this work.

We would like to thank all the people who encourage and support me during the understanding of this work.

References

http://www.radon-chart.html

http://www.thetiledoctor.com

http://www.epa.gov/radon-methods.html

http://www.barc.gov.in:

http://www.Khan.pdf

http://www.sciencedirect.com

Tsoulfanidis Nicholas, (1995) "Measurement and Detection of Radiation", (London: Taylor & Francis)

J. Myanmar Acad. Arts Sci. 2020 **Vol. XVIII.No.2B**

DETERMINATION OF RADIOLOGICAL HAZARDS WITH THE RADIOACTIVITY LEVELS OF SOIL IN THE INDUSTRIAL AREA, MANDALAY

Lay Thi Tar Oo[*]

Abstract

The activities of naturally occurring radionuclides in five soil samples from the industrial area of Mandalay were calculated from experimental results which were obtained by using a NaI(Tl) detector. From these results, the percentage contribution of the radioactivity in the soil samples was shown with the greater percentage K-40 (81.08%), Ra-226 (10.29%) and Th-232 (8.63%). The calculated amounts of radionuclides were compared with their maximum admissible limits of UNSCEAR (2000). In order to assess the radiological hazards of the radioactivity in soil, radium equivalent activity, absorbed dose rate, external and internal hazard indices were calculated and the computed hazards were shown with average values of 228.33 Bq/kg, 106.26 nGy/h, 0.62 and 0.84 respectively. The present result was shown that the mean external and internal hazard indices value was less than 1.0, as recommended for safety globally (EC, 1999).

Keywords: Natural radioactivity, radiation hazards, soil, NaI(Tl) detector

Introduction

The spontaneous decomposition or disintegration of a nucleus forming a different nucleus and producing one or more additional particles is called Radioactivity. Natural radionuclide in soil contributes a significant amount of background radiation exposure to the population through inhalation and ingestion. The main contributors of radionuclides are ^{226}Ra, ^{232}Th and ^{40}K. Since these radionuclides in soil are not uniformly distributed and vary from region to region. The radioactivity concentration of these nuclides above permissible level is very harmful to the human body. Therefore, measurements of natural radioactivity in soil and the radiation doses are of great interest to the researchers which have led the nationwide surveys throughout the world. Naturally occurring radionuclides are known as to be present in varying proportions in rocks and soil of different geological formations around the world. Their concentrations and associated external doses in different environments depend on the geology and geographical conditions in such environments. Exposure to natural terrestrial radiation in the outdoor environment is predominantly from radionuclides that are present in the upper 30 cm layer of the soil. Human exposure pathways include: root uptake from contaminated soil, direct ingestion of radionuclides deposited on plant leaves, consumption of water animals, ingestion of contaminated water, inhalation of soil dust, and the direct exposure to gamma ray emitted from primordial radionuclides in the indoor and outdoor environments, etc.

Soil pollution, also known as soil contamination, is caused by man-made, harmful chemicals penetrating the earth and causing deterioration. There are many health risks associated with soil pollution, through direct contact with the soil or from air contaminants. Whether it’s in industrialized countries where soil pollution has regulations, or in developing countries with no such capabilities, the matter of soil pollution is a major problem.

The present study area lies within the sub-humid tropical zone and soil samples were randomly collected from five different locations in Industrial Zone, Mandalay. The aim of the

---

[*] Dr, Lecturer, Department of Physics, Kalay University

present work is to search the possibility of uranium deposition as ore and health risk assessment associated with thorium and potassium in the study area. This work was undertaken to measure the activity concentrations and γ-ray absorbed doses of the naturally occurring radionuclides in soil samples of industrial zone. Moreover, another aim of the present work is to create the public awareness about the radiation hazards and the workers those who are working in this area. This study will also be helpful to establish a research base line in this area.

Theoretical Background

Efficiency of a Detector

The efficiency of a detector is the proportionality constant which relates the activity of the source being counted and the number of counts observed. This efficiency is calculated by using the following relation

$$\varepsilon = \frac{N_A}{A_t\, t P_\gamma} \qquad (1)$$

where, ε = detector efficiency, N_A= the net area of the full energy peak, A_t = the present activity of the standard sources, t = counting time, P_γ=gamma emission rate

Activity Concentrations of Soil Samples

The activity concentrations of radionuclides in the samples were determined by well-known standard gamma ray spectrometry using a NaI(Tl) detector. The activity concentration of each radionuclide in the soil samples was calculated using the following equation.

$$A = \frac{N_A}{\varepsilon P_\gamma\ mt} \qquad (2)$$

where, A = activity concentrations of the sample in $Bqkg^{-1}$, N_A = the net area of the full energy peak, ε = detector efficiency, P_γ = gamma emission rate,

m = mass of the measured sample (in kg), t = counting time (in second)

Some Radiological Indices

(i) Radium Equivalent Activity

To represent the activity levels of ^{226}Ra, ^{232}Th and ^{40}K by a single quantity, which takes into account the radiation hazards associated with each component, a common radiological index has been introduced (Diab et al., 2008). This index is called the Radium Equivalent Activity (Ra_{eq}) and is mathematically defined by (UNSCEAR, 2000):

$$Ra_{eq}=A_{Ra}+ 1.43A_{Th}+ 0.077A_K \qquad (3)$$

(ii) External Radiation Hazard Index

The model of the external hazard index (H_{ex}) places an upper limit to the external gamma radiation dose from building materials to unity, which corresponds to a radium equivalent activity of 370 Bq/kg. It is defined as:

$$H_{ex} = (A_{Ra}/370\ (Bq/kg) + A_{Th}/259(Bq/kg) + A_K/4810(Bq/kg)) \leq 1 \qquad (4)$$

(iii) Internal Radiation Hazard Index

Radon and its short-lived products are also hazardous to the respiratory organs. So, internal exposure to radon and its short-lived products is quantified by internal hazard index and is expressed mathematically as

$$H_{in} = (A_{Ra}/185 + A_{Th}/259 + A_K/4810) \leq 1 \qquad (5)$$

(iv) Calculation of Absorbed Dose Rate (D)

Absorbed dose measures the energy deposited in a medium by ionizing radiation per unit mass, which may be measured as joules per kilogram when it is represented by the equivalent SI unit, gray (Gy). The external terrestrial gamma radiation absorbed dose in air at 1 m above the ground level is calculated by using the following equation (UNSCEAR 2000; Kurnaz et al. 2007):

$$D = 0.462\ A_{Ra} + 0.621\ A_{Th} + 0.0417\ A_K \qquad (6)$$

where, A_{Ra}, A_{Th} and A_K are the mean activity concentrations of ^{226}Ra, ^{232}Th and ^{40}K in Bq/kg, respectively.

Materials and Methods

Description of the Study Area

This study was carried out with the industrial zones in Mandalay, Myanmar. Mandalay is located 21.97 latitude and 96.08 longitudes and it is situated at 83 meters above sea level. According to reports, over 1100 factories were situated in the Mandalay Industrial Zones. The study area is surrounded by factories.

Sample Collection and Preparation

Untreated soil samples (S-1) to (S-5) were collected randomly from five different locations of the industrial zone. The geographic location of the study area and the photograph of samples were shown in figure (1).

The top surfaces of the soils at all the soil sampling sites were scraped off to remove stones, vegetation and organic debris. Thereafter, the soil samples at each of the sites were collected at a depth of 15cm, thoroughly mixed and loaded in the polyethylene bags. The soil samples were sun dried and then carefully placed for drying at a room temperature to achieve a constant weight, then pulverized and sieved. 200 g of each sample which packed into a tightly closed plastic container and sealed with a tape, was stored for at least one month to ensure secular equilibrium.

Experimental Set Up and Procedure

The samples' radionuclide contents were measured and analyzed by Gamma-ray spectrometric measurements using NaI(Tl) scintillation detector (3"×3") connected to MCA and Gamma Vision 32 software. In this present work, coarse gain is 20, fine gain is 13 and conversion gain is 2048 with counting time 10800s. Firstly, the gamma ray spectrometer was be calibrated by using the four standard sources (Ba-133 (0.276 and 0.384MeV, 10.3 years), Co-60 (1.173 and 1.332MeV, 5.27 years), Cs-137 (0.622MeV, 30.07 years) and Na-22 (0.511MeV, 2.6 years)) with their activities 1μCi. The energy calibration curve as a function of channel number was shown in figure (2). This experiment work was performed at the Experimental

Nuclear Lab, University of Mandalay. The energy calibration was made using different point sources in the energy range 276 keV–1332 keV while the efficiency calibration of the detector was made using a 200 g mixed IAEA-448 soil standard containing ^{226}Ra, ^{214}Pb, ^{214}Bi and ^{228}Ac. The detector efficiency calibration curves as a function of energy was shown in figure (3).

Prior to measurement of samples, the environmental background radiation at the laboratory site was determined with an identical empty container used in the sample measurement with counting time 10800s. Next, each sample was placed in face to face geometry with the detector within the same period. The resultant spectra of each sample were recorded. Measurement condition was shown in figure (4). And then, this experiment was performed with keeping the samples one by one on the top of the detector.

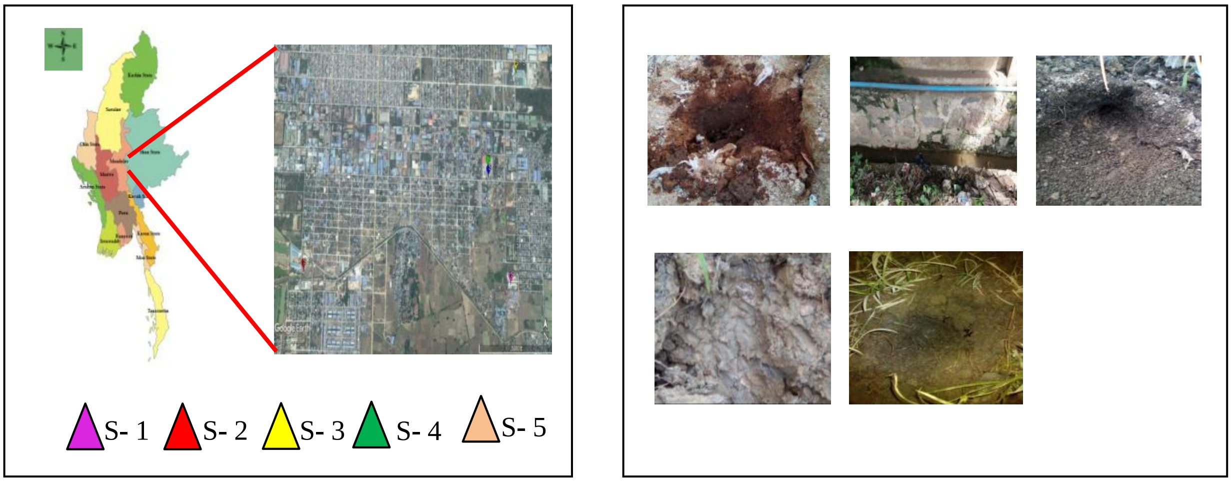

Figure 1 The geographic location of study area and the photographs of selected soil samples (S-1 to S-5)

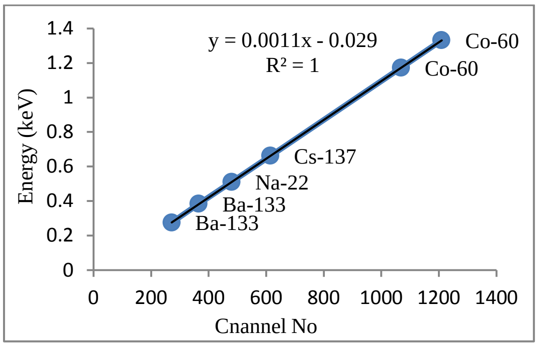

Figure 2 The energy calibration curve of NaI(Tl) detector

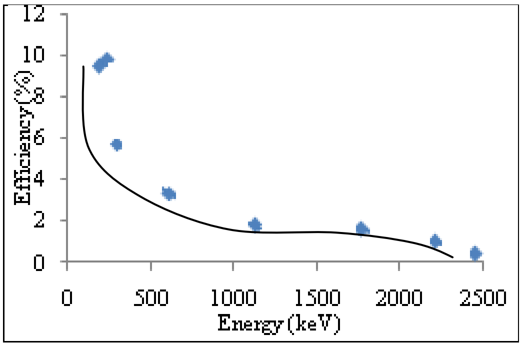

Figure 3 The efficiency curve of NaI(Tl) detector using IAEA-448 reference material

Figure 4 The measurement arrangement with the NaI(Tl) detector

Results and Discussion

The aim of the present work was to search the possibility of naturally occurring radionuclides deposition and health risk assessment associated with Th-232, Ra-226 and K-40 in the study area. From the gamma spectrometric analysis using Gamma Vision 32 software, activity concentrations of each observed naturally occurring radionuclides in the soil samples were calculated and then activity of Ra-226, Th-232 and K-40 were also determined from the results. In order to assess the health effects of each sample, the radiation hazards such as radium equivalent activity (Ra_{eq}), external (H_{ex}) and internal (H_{in}) hazard index, and absorbed dose rate (D) were calculated from the activities of Ra-226, Th-232 and K-40.

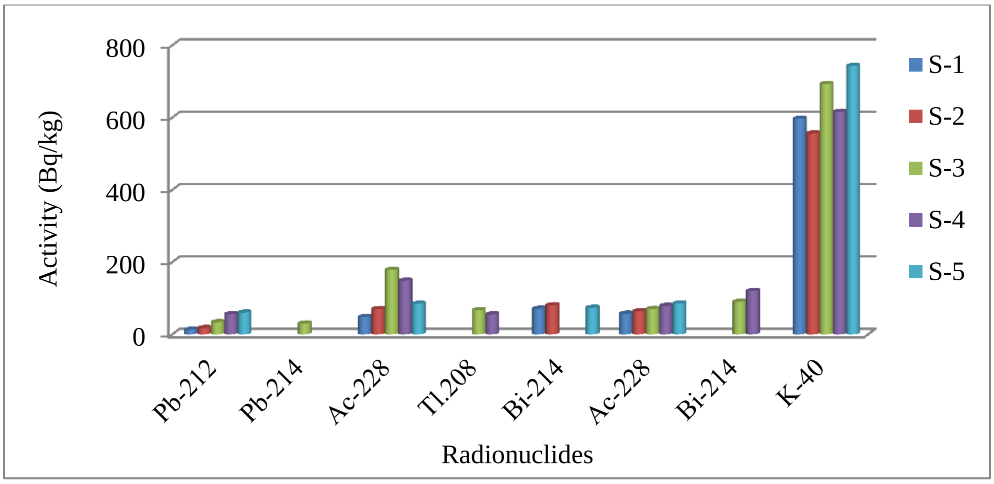

Figure 5 Comparison for natural radioactivities in soil samples at different locations for present study

Table 1 Calculated mean activity concentrations in soil samples

Sr.No	**Sample Name**	**A_{Ra}(Bq/kg)**	**A_{th}(Bq/kg)**	**A_k(Bq/kg)**
1	S-1	71.17±13.25	39.71±18.83	596.78±49.18
2	S-2	80.91±12.17	50.73±18.68	556.32±47.09
3	S-3	60.41±24.43	87.55±17.14	693.05±50.34
4	S-4	120.47±53.54	84.89±17.05	615.97±46.85
5	S-5	73.87±12.32	78.39±20.34	742.93±50.81
Minimum		60.41±24.43	39.71±18.83	556.32±47.09
Maximum		120.47±53.54	87.55±17.14	742.93±50.81
Average		81.366±23.14	68.254±18.41	641.01±48.85
Standard		35	35	420

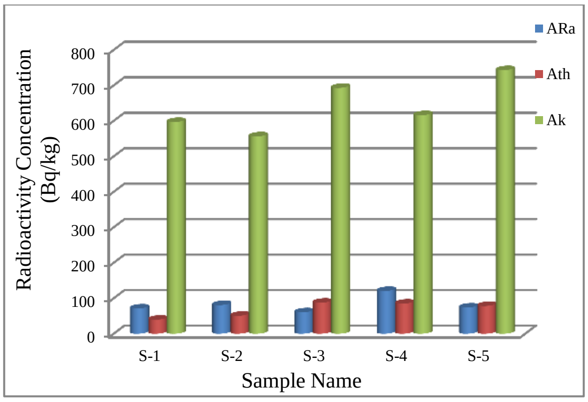

Figure 6 The variation of mean activity concentrations in soil samples

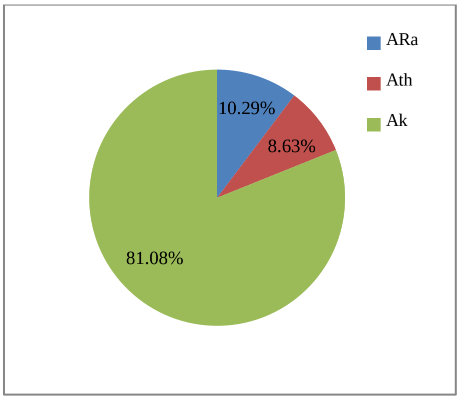

Figure 7 Percentage in mean activity concentrations in soil samples

The overall result was indicated that ^{40}K was contributed the most to the radionuclides content of soil while ^{232}Th contributes the least in the case. The results have shown that, for soil samples, the activity of Th-232 was ranged between (39.71 Bq/kg) to (87.55 Bq/kg), with the average value (68.25 Bq/kg), the activity of Ra-226 was ranged between (60.41 Bq/kg) to (120.47 Bq/kg), with the average value of (81.37 Bq/kg), while the activity of K-40 was ranged between (556.32 Bq/kg) to (742.93 Bq/kg), with the average value of (641.01Bq/kg). The Figure was shown the percentage contribution of the radionuclides in the soil samples with the greater percentage K-40 (81.08%), Ra-226 (10.29%) and Th-232 (8.63%).

Table 2 Calculated radiological hazards of the radioactivity in soil samples

Sr.No	**Sample Name**	**Ra_{eq} (Bq/kg)**	**H_{ex}**	**H_{in}**	**D(nGy h^{-1})**
1	S-1	173.91	0.47	0.66	82.01
2	S-2	196.29	0.53	0.75	91.69
3	S-3	238.97	0.65	0.81	110.69
4	S-4	289.29	0.78	1.11	133.63
5	S-5	243.17	0.66	0.86	113.27
Minimum		173.91	0.47	0.66	82.01
Maximum		289.29	0.78	1.11	133.63
Average		228.33	0.62	0.84	106.26
Standard		370	1.0	1.0	60

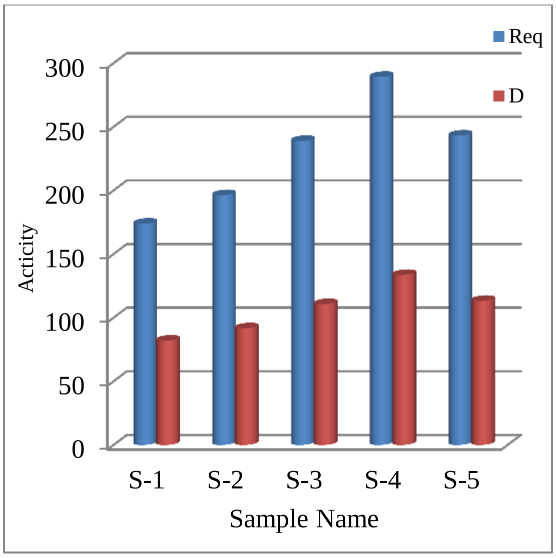

Figure 8 Comparison plot for concentration of Radium equivalent activity and absorbed dose rate of soil samples

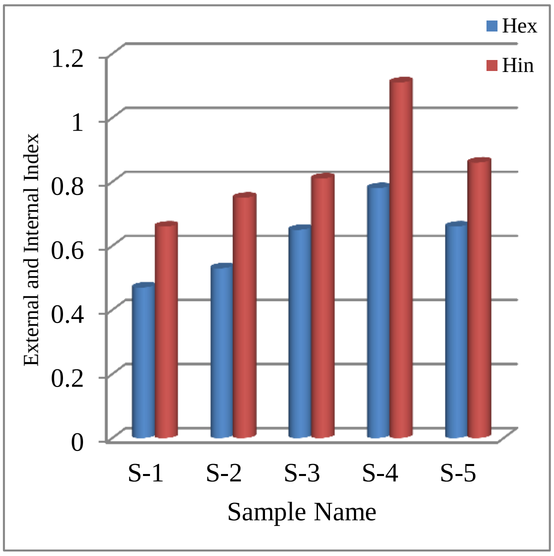

Figure 9 Variation of External and internal hazard index of soil samples

The highest radium equivalent activity and absorbed dose rate were obtained to be 289.29 and 133.63 while the lowest were 173.91 and 82.01. The mean values were calculated to be 228.33 and 106.26. Furthermore, the highest external and internal hazard index were obtained to be 0.78 and 1.11 while the lowest were 0.47 and 0.66. The mean value was calculated to be 0.62 and 0.84.

Conclusion

This present study was evaluated the activity concentrations of radionuclides and hazard indices for soil in the industrial area of Mandalay with the use of gamma spectrometer. These data was shown that the activity concentration of naturally occurring radionuclides in soil samples was within the world average range which are 420(100-700) Bq/kg for K-40 but that of Ra-226 and Th-232 were slightly higher than the range [35(10-50) and 35(7-50)] respectively (UNSCEAR, 2000). The slight variation of the radioactivity content in soil with different locations was mainly observed due to soil type, formation and transport process involved in the study area. The average radium equivalent activity in all samples was below the standard recommended values except for absorbed dose rate. But, the external and internal hazard indices were also found less than unity [European Commission on Radiation Protection (EC,1999)] which indicates that there is no probability of immediate health effect on workers and public due to natural radioactivity present in the samples of the study area and the radiation exposure of the people in this area from the surface soils does not pose any negative radiological effect on them and their environs. So, it is concluded that this present work was only established the information on the natural radioactivity status of only five locations in industrial area and other soil properties should also be considered in further research studies for all soil samples.

Acknowledgements

First of all, I would like to express my sincere thank to Prof. Dr Khin Khin Win, Head of Department of Physics, Yangon University, Prof. Dr Thar Tun Maung, Rector of Kalay University and Professor Dr Ah Mar Kyawe, Head of Department of Physics, Kalay University, for their kind permission to carry out this work.

References

G.F.Knoll, (2000) Radiation Detection and Measurement, Third.ed, Wiley, New York.

N. Tsaulfanidis, (1995) "Measurement and Detection of Radiation", Second ed, University of Missouri-Rolla, Taylor & Francis.

United Nations Scientific Committee of the effect of Atomic Radiation (UNSCEAR), (2000) “Sources and Effects of Ionizing Radiation”, Report on General assembly, United Nations, New York.

J. Myanmar Acad. Arts Sci. 2020 **Vol. XVIII.No.2B**

ASSESSMENT OF HEAVY METALS CONTAMINATION IN SOILS AND HEALTH RISK IN RICE

Khin Maung Htwe[1], Hla Win Aung[2, T]in Htun Naing[3]

Abstract

Environmental pollution with excess content of heavy metals can lead to the possible contamination of the rice and associated soil. Rice is mainly food and nutrient for people in Myanmar. Eating rice is the most important route for accumulation most chemical elements. The purposes of this study were to assess heavy metal contamination and the potential risk in some soil and rice samples by using EDXRF techniques. Eight rice samples and associated eight soils are collected from Kyaukse, Sinkaing, Amarapura, Patheingyi and Madaya. The mean levels of selected metals concentrations in soil samples and rice samples were found to be less than safe limit but Hg's concentration values for soil and rice are 2.85 mg/kg and 1.25 mg/kg respectively. The values of Hg are above the safe limit values 1.3 mg/kg for soil and 0.03 mg/kg for rice by USEPA (1997), FAO/WHO (1992). The mean transfer values of selected metals are less than one but Hg's transfer factor value is the highest value of all the elements. EDIM value 0.007 (mg/kg day) of Pb was found higher than the permissible value 0.001 (mg/kg day) but the rest metals of EDIM values were lower. The potential health risk has been evaluated for the local adults. The risk assessment results of 2017 showed that health risk associated with these elements through consumption of rice were not present. However, regular monitoring of accumulation of heavy metals in rice and soil has been conducted by using more precise and modern techniques.

Keywords: EDXRF, heavy metals, risk assessment, transfer factor, DIM

Introduction

Rice is the main crops and it is the staple food of local residents. Rice is mainly food and nutrient for people in Myanmar. Eating rice is the most important route for accumulation most chemical elements. Chemical elements consist of essential elements and toxic elements. The present study was conducted to assess the heavy metals (Cr, Hg, Ni, Pb, As, Cu, Zn, Fe and Mn) concentration in soils of rice field and rice grown in Madaya Township, Amarapura Township, Sintgine (Sinkaing) Township and Kyaukse Township. Cu, Zn, Mn and Fe are essential heavy metals in plants nutrition but many heavy metals do not play any significant role in the plants physiology. Some of the elements in heavy metal are naturally present at very low concentrations in environment and human bodies are able to detoxify them in limited mounts. Numerous reports indicate that water, soil, vegetables and dust have been heavily polluted by lead (Pb), Arsenic (As), copper (Cu), Zinc (Zn) and cadmium (Cd) from many sources. Pb, As, Cu, and Zn are important toxic heavy metals and have been identified as health risks by World Health Organization (WHO). Due to their potential toxicity, as well as their persistent and irreversible accumulation characteristics, heavy metals, such as Pb, Hg, and Cr are listed as key monitoring pollutants by the Myanmar. Most of the heavy metals are the natural constituents of earth's crust and from there they are taken by plants and thus transferred to food chain. These metal concentrations transfer from soil to plants are accumulated in the human body through the food chain, thus posing a serious threat to human health. Heavy metals contamination is a major

---

[1] Dr, Lecturer, Department of Physics, Kalay University

[2] Dr, Lecturer, Department of Physics, Yadanabon University

[3] Dr, Lecturer, Department of Physics, Shwebo University

problem of our environment and they are also one of the major contamination agents of our food supply. This problem is receiving more and more attention all over the world.

The main aims of this study are to assess some heavy metals contaminations in soils, to evaluate the transfer factor from soil to rice and to calculate the health risk with respect to daily consumption of rice for general adult.

Study Area

The study area, near Mandalay region is located in the central zone of Burma by the Irrawaddy River at 21.98 North, 96.08 East, 80 meters (260 feet) above sea level. Mandalay features a tropical wet and dry climate and noticeably warmer and cooler periods of the year. The study region consists of Kyaukse Township, Sinkaing Township, Amarapura Township, Patheingyi Township and Mataya Township. The investigated area comprises functional areas as shown in Figure (1).

Method and Material

Sample Collection

There are two types of sample which are rice samples and soil samples in our research. All rice samples and soil samples were collected from agricultural lands of paddy fields. Sample positions were obtained via the global position system and all samples have been collected from Kyaukse Township, Sinkaing Township, Amarapura Township, Patheingyi Township and Mataya Township during the harvest time of 2017. GPS data of study sites were expressed in Table (1). At each sampling site, samples were collected from the paddy field by means of a random sampling method. Edible parts of crops and their rooted soil samples (at 0 - 15 cm in depth) were collected in their paddy fields. All samples were sealed in polyethylene bags.

Samples Preparation for XRF Measurement

Sample preparation is an important role in XRF measurement. Prepared pellets must be homogenized. If the sample is inhomogeneous, the surface layer is not representative for the whole sample. All measurement samples were made cleaned and dried under the room temperature for one week. Besides, these samples were weighed by using analytical balance (PW 254). And then, it is needed to grind the powdered samples and to get very fine powders. The powder samples were passed through the mesh. After getting very fine powder, the sample was weighed 5g. These powder samples were performed pellet type by using pellet machine. Finally, each pellet sample was placed in a small plastic bag.

Experimental Set up for Soil pH Measurement

The following procedures are performed for the soil pH measurement. The mixture of 40 g of soil with 40 mL of distilled water (1:1 soil to water ratio) was filled into the beaker and stirred with a spoon until the soil and water are thoroughly mixed. The soil-water mixture was stirred for 30 seconds. The mixture was allowed to settle (clearer liquid above the settled soil) forms for about 5 minutes. The pH of the supernatant was measured using the pH meter. According to the above procedure, each soil sample was measured in five times and then records these results on the soil pH data worksheet.

Analyzing Data and Risk Assessment

Transfer Factor (TF)

Soil to rice metal transfer was computed as transfer factor (TF), which was calculated by using following equation.

$$\text{TF} = \frac{C_{plant}}{C_{soil}} \quad (1)$$

Where C_{plant} and C_{soil} represents the toxic metal concentration in extracts of rice and soils on dry weight basis respectively.

Estimated Daily Intake of Metal (EDIM)

Estimated Daily intake of metal was calculated by the following equation (Eq.(2))

$$\text{EDIM} = \frac{\text{C}_{\text{metal}} \times \text{D}_{\text{foodintake}} \times \text{C}_{\text{f}}}{\text{B}_{\text{averageweight}}} \quad (2)$$

Where, C_{metal}= heavy metal concentrations in rice (mg/ kg).

EDIM = Estimated Daily intake of metal concentration in foodstuff

(0.425 kg of rice per day)

$C_f =$ Concentration Factor (C_f= 1 was used for rice sample)

$\text{B}_{\text{averageweight}}$ =Average body weight (for Adult 55 kg)

Health Risk Index (HRI)

The value of Health Risk Index (HRI) depends on the estimated daily intake of metals (EDIM) through foodstuff and oral reference dose (R_fD). R_fD is an estimated per day exposure of metal to human body that has no hazardous effect during life time (US-EPA IRIS, 2006). The health risk index for Cr, Mn, Co, Ni, Cu, Zn, As, Cd, and Pb by consumption of rice was calculated by the following equation Eq. (3) obtained from literature (Cui et al., 2004).

$$\text{HRI} = \frac{DIM}{RfD} \quad (3)$$

Oral reference doses (mg/kg/day) for Cr, Mn, Ni, Cu, Zn, Pb were 1.500, 0.033, 0.020, 0.040, 0.300, 0.020, 0.00 (US-EPA IRIS, 2006), for Fe 60.00(Feriberg et al.1984) and for As 0.500 (Esri Corporation, USA) respectively. Estimated exposure is obtained by dividing estimated daily intake of heavy metals by their safe limit. An index more than 1 is considered as not safe for human health (USEPA, 2002).

Hazard Index (HI)

To evaluate the potential risk to human health through more than one heavy metal, the hazard index (HI) has been developed (USEPA, 1989). The hazard index is the sum of the hazard quotients as described in the following equation Eq. (4).

$$HI = \sum HQ = HQ_{Cr} + HQ_{Hg} + HQ_{As} + HQ_{Pb} \quad (4)$$

Statistical Analysis

A standard statistical analysis (mean, standard deviation, etc.) was performed to describe one of soil properties (pH) in eight study areas. Statistical analysis had been done using Statistical Package for the Social Sciences (SPSS Inc., Chicago, IL, USA. Version 23).

Results and Discussions

In this research work, eight soils and eight rice samples were measured by using Energy Dispersive X- ray fluorescence Spectrometer, at Experimental Nuclear Lab, Physics department, Mandalay University. The X-rays machines of SPECTRO XEPOS EDXRF spectrometer and XLab Pro 4.5 Software have been supported by International Atomic Energy Agency (IAEA). The mean concentrations of selected heavy metal content in eight soil samples are represented in Table (1). The means concentration of Cr in eight soil samples is (96.81±20.65) mg/kg. This value is below EU standard (2006) and USEPA (1997) values of (100 and 400) mg/kg but above the world average value (47 mg/kg). The mean concentration of Mn is (647.99±238.14) mg/kg. The mean concentration of Fe in all samples is (43280±7087.04) mg/kg. This value is higher than USEPA (1997) of 2100mg/kg. Ni was detected in all samples analyzed with mean concentration is (9.58±5.28) mg/kg. This value is within USEPA (1997), EU standard (2006) and world average value of (50, 50 and 13) mg/kg respectively. The observed means concentration value of Cu is (25.32±13.64) mg/kg. This value is above the world average value of 13 mg/kg but lower than safe value and EU standard value of (50 and 100) mg/kg. The mean concentration of Zn is (87.41±15.31) mg/kg. The mean value is above world average value of 45mg/kg and lower than of safe value and EU standard is (200 and 300) mg/kg. Similarly, the mean concentration of As in measured samples is (4.74±1.82) mg/kg. This value is within the USEPA (1997) of value 40mg/kg and EU standard of 10.9 mg/kg but over the world average value of 4.4 mg/kg. The Hg mean concentration value is (2.85 ±0.48) mg/kg. This value is higher than safe limit value of 1.3 mg/kg in FAO/WHO (1992).The analyzed mean concentration value of Pb is (37.09± 8.46) mg/kg. This value is lower than of safe limit and EU standard of (300 and 100 mg/kg) but higher than of WAV of 22 mg/kg. The pH range of all measured samples is from (6.56-7.33) with average temperature at 30.23°C. This value is within the optimum pH range (5.5 and 7.5) for most plants.

The concentration of heavy metals in rice samples that Cr, Mn, Fe, Ni, Cu, Zn, As, Hg, and Pb are represented in Table (2).The mean concentration level of Cr (9.60±0.87) mg/kg of all sample is lower than the world health organization (WHO,1996) permissible limits 50mg/kg. The mean concentration value of Fe (173.50±63.67) mg/kg is less than in FAO/WHO food standard program (1999, 2001) value of 425.00mg/kg. The mean concentration value of Ni in all sample value (0.50±0.16) is lower than food and nutrition Board Institute of medicine, 2010 acceptable value is 4 mg/kg. The mean level of Cu in all sample (3.00±0.87)mg/kg is lower than the standards value of 73.00mg/kg in FAO/WHO food standard program (2001,1999) and FAO/WHO (2004) value of 20mg/kg. The observed mean concentration value of Zn (16.10±2.62)mg/kg is below the maximum permissible limit (100mg/kg) of FAO/WHO food standard program (2001, 1999). The mean concentration value of Zn is less than the value (100 mg/kg) of FAO/WHO food standard program (1999, 2001)and higher than value of (5.00mg/kg) FAO/WHO (2004). The mean concentration value of As (0.56±0.05)mg/kg is less than the world health organization (WHO 1996) with permissible value is 7 mg/kg. Similarly, the mean concentration value of Hg (1.20±0.05) is higher than world Health organization (WHO 1996) with value is 0.03 mg/kg. The observed mean concentration value (1.01) mg/kg of Pb is lower than safe limit (Codex & Alimentarius, 2001) with value (10) mg/kg.

Transfer Factor of metals from soil to rice values are expressed in Table (3). The TF value for all selected heavy metals of rice samples varied greatly between different areas. The difference in TFs between locations may be related to soil nutrients management and soil properties. The increasing order of mean TF value order is Hg>Zn> As>Cu>Cr>Ni>Pb>Fe. The TF value of mercury is the highest in all other samples. This metal is a widespread pollutant and a threat to human health and a strong toxicant. The estimated daily intake of metal in rice data are represented in Table (4). The estimated daily intakes of metal (EDIM) values for some heavy elements have been calculated based on the 55 kg per day for adult, the food intake value of adult is 0.425 and their conversion factor is one. These data revealed that the values of daily intake of Cr, Fe, Ni, Cu, Zn of As, and Hg are within the recommended value suggested by different organization. EDIM of Pb was found higher than permissible (WHO, 1993) value because the oral reference dose is higher than in other values. The HRI values for heavy metals in all rice samples have been calculated and as shown in Table (4) for adult. The result exposed that health risk index (HRI) for adult of Cr (0.042-0.056) is lower than 1, that indicating no risk. HRI of Fe (0.014-0.035) Ni (0.155-0.348), Cu (0.309-0.773), Zn (0.353-0.564), As(0.008-0.009) and Hg(0.001-0.002) values of adult which are acceptable value. The integrated health risk values of all rice samples are less than one. Most of the HRI values were less than one.

Conclusion

Analyzing of heavy metals concentration in soil and rice is important for health risk assessment during food consumption. This kind of study can be used as a tool for the farmers so that they may adopt such strategies which lead them to reduce the health problems related to metal toxicities. The mean concentration of selected heavy metal (Cr, Fe, Ni, Cu, Zn, As, and Pb) in all the soil samples are lower than recommended value by USEPA, WHO/FAO not including Hg. The mean concentration value (2.85mg/kg) of Hg is greater than 2 times by FAO/WHO (1992) value of 1.3 mg/kg. The most of selected mean concentrations in rice sample are less than acceptable value by WHO/FAO concentration value except of mercury. Moreover, the mean concentration of mercury (1.2 mg/kg) is significantly greater than the acceptable value (0.03mg/kg) by WHO (1996). All of the transfer values of selected heavy metals are less than one. EDIM mean values of nine selected metal in rice samples are within permissible value by WHO/FAO except of lead. The daily intake of lead value is higher than of safe limit value. Health risk assessment value is the ratio of daily intake of metal by oral reference dose. If the oral reference dose is greater, health risk index is lower value. In conclusion, it has been found that eating rice cannot be risk for human health. Therefore, we can recommend that regular monitoring of toxic and heavy metal in soil samples, rice samples and other foodstuff are essential to prevent their excessive build up in food chain. The factors leading to the different levels of heavy metals will be investigated in our future studies.

Acknowledgements

The authors would like to acknowledge Dr Khin Khin Win Head of Department of Physics, University of Yangon, Dr Tha Htun Maung, Rector of Kalay University and Prof. Dr. Ah Mar Kywe, Head of Department of Physics, Kalay University, for their encouragement.

Reference

C. Magamage, W.H.M.C.U. Waidyaratna, W.P.A.P. Dhanapala and D.M.Panampitiya, “Determination of Heavy Metals in Rice Available in Kandy District, Sri lanka”, Annals of Sri Lanka Department of Agriculture. 19: 351 – 368, 2017.

Daping Song, Jiangying Fu and QiaoWang, “Integrated Health Risk Assessment of Heavy Metals in Suxian Country, South China”Int.J. Environ. Res. Public Health 2015, 12, 7100-7117(14 May 2015).

Farooq Ahmad “ Karnal/Kallar grass cultivation in stoic alkaline soils in Pakistan” (January 22, 2013)

IvanGržetić and Rabia H. Ahmed Ghariani, “Potential health risk assessment for soil heavy metal contamination in the central zone of Belgrade (Serbia)”, *J. Serb. Chem. Soc. 73* (8–9) 923–934 (2008)

Jennifer Clever and Ma Jie“China Maximum Levels for Contaminants in Foods’’ USDA Forgein Agricultural Service, Global Agricultural Information Network, (12 November 2014)

John Peterson, Margargaret MacDonell, Lynne Haroun, and Fred Monett “Radiological and Chemical Fact Sheets to Support Health Risk Analyses for Contaminated Areas’’ Argon National Laboratory, Environmental Science Division, U.S Department of Energy Richland Operations Office. (March 2007)

Khin Phyu Phyu, Mya Mar Lar, Tin New Htwe, Tin Tin Han, Khin Moe Latt, Ohnmar Win, KyawSoe&Myat Phone Kyaw, “Accumulation and Distribution of Heavy Metals in Rice Grains, Soil and Water in Kyonpyaw Township”, *Myanmar Health Sciences Research Journal*, Vol. 29, No. 2, 2017.

Tasrina et al., J Environ Anal “ChemResearch article Open Access Heavy Metals Contamination in Vegetables and its Growing Soil’’ Atomic Energy Center, Dhaka-1000, Bangladesh and Shizuoka University, Japan (2 March 2015)

WHO, World Health Organization, “Provisional Tolerable Weekly Intake of Toxic Heavy Metals”, (2003).

Figure 1 Samples Location Map

Table 1 Coordination of study site

Study site	N	E
Position - 1,Madaya	22□ 3□ 39□	96□ 6□ 21□
Position - 2,Madaya	22□ 4□ 40□	96□ 6□ 13□
Position - 3, Patheingyi	21□ 54□ 52□	96□ 10□ 33□
Position - 4, Patheingyi	21□ 58□ 36□	96□ 10□ 1□
Position - 5, Amarapura	21□ 53□ 37□	96□ 4□ 24□
Position - 6, Amarapura	21□ 53□ 38□	96□ 3□ 47□
Position - 7, Sintkaing	21□ 43□ 27□	96□ 7□ 36□
Position - 8, Kyaukse	21□ 36□ 1□	96□ 11□ 3□

Table 2 Elemental concentrations in soil sample (mg/kg)

	Cr	Fe	Ni	Cu	Zn	As	Hg	Pb
Mean	**96.81**	**43280**	**9.58**	**25.32**	**87.41**	**4.74**	**2.85**	**37.09**
Min	57.00	28750	3.70	7.90	56.80	2.00	2.3	26.20
Max	120.60	51500	14.80	39.60	100.90	7.90	3.6	52.90
SD	20.65	7087.04	5.28	13.64	15.31	1.82	0.48	8.46
Safe value	400^{a}	21000^{a}	50^{a}	50^{a}	200^{a}	40^{a}	1.3^{b}	300^{a}
Standard	100^{x}	-	50^{x}	100^{x}	300^{x}	10.9^{x}	-	100^{x}
WAV	47^{y}	-	13^{y}	13^{y}	45^{y}	4.4^{y}	-	22^{y}
Number of sample	8	8	8	8	8	8	8	8

a= USEPA (1997); b= FAO/WHO (1992); x=European Union Standard (2006)
y=World Average Value (Pendias and Pendias, 2000)

Table 3 Elemental concentrations in rice sample (mg/kg)

	Cr	Fe	Ni	Cu	Zn	As	Hg	Pb
Mean	9.60	173.50	0.50	3.00	16.10	0.50	1.20	<1.01
Min	8.1	111.4	0.4	1.6	13.7	0.5	1.1	0
Max	10.9	271.3	0.9	4	21.9	0.6	1.3	0
SD	0.87	63.67	0.16	0.87	2.62	0.05	0.05	0.00
Safe limit	50.00*	425.00#	4.00$	73.00#	100.00#	7.00*	0.03*	10.00@
FAO/WHO	-	-	-	20.00	5.00	-	-	0.20
Number of sample	8	8	8	8	8	8	8	8

*= WHO, 1996; #=FAO/WHO food standard program (2001), FAO/WHO,1999
$=Food and Nutrition Board, Institute of Medicine, 2010; @= Codex & Alimentarius, 2001

Table 3 Transfer factor (TF) values of analyzed samples (n = 8)

	Cr	Fe	Ni	Cu	Zn	As	Hg	Pb
Mean	**0.104**	**0.004**	**0.069**	**0.154**	**0.197**	**0.133**	**0.432**	**0.028**
Min	0.075	0.003	0.028	0.051	0.142	0.063	0.306	0.019
Max	0.168	0.007	0.108	0.291	0.287	0.300	0.522	0.038
SD	0.032	0.002	0.034	0.097	0.059	0.076	0.078	0.006

Table 4)Estimated Daily intake of metal and Health Risk Index of rice; N = 8

Element	**Estimated Daily intake of metal (mg/kg. bw/day),**					**Health Risk Index of rice**			
	Mean	SD	Min	Max	R- value	Mean	SD	Min	Max
Cr	0.074	0.007	0.063	0.084	0.05-0.20*	0.049	0.004	0.042	0.056
Fe	1.341	0.492	0.861	2.096	-	0.022	0.008	0.014	0.035
Ni	0.004	0.001	0.003	0.007	0.005‡	0.193	0.063	0.155	0.348
Cu	0.023	0.007	0.012	0.031	2.00-3.00	0.580	0.169	0.309	0.773
Zn	0.124	0.020	0.106	0.169	1.00*	0.415	0.067	0.353	0.564
As	0.004	0.000	0.004	0.005	0.001	0.008	0.001	0.008	0.009
Hg	3E-5	3E-6	3E-5	4E-5	-	0.001	0	0.001	0.002
Pb	0.008	0.00	0.008	0.008	0.0036§	-	-	-	-

R-value =recommended value, * JECFA, †FAO/WHO, ‡ WHO1997; § WHO 1993
SD= standard deviation N, = number of sample

J. Myanmar Acad. Arts Sci. 2020 **Vol. XVIII.No.2B**

ELEMENTAL ANALYSIS OF PARTS OF CHILI

Myint Myint Maw[1] and Win Sin[2]

Abstract

Different parts of raw green and ripe red chilies have been analysed using EDX-7000 to study the elements contained in each parts and the change in concentrations of elements due to varying parts, such as seed, skin or stalk. The major elements found in each part are potassium, sulphur, copper and iron.

Keywords: Chili, EDXRF, Elemental Analysis

Introduction

Chili peppers are one of the very popular spices known for their medicinal and health benefiting properties. The chili is a fruit pod of the plant belonging to the nightshade family (Solanaceae), of the genus, **Capsicum**.

Chili peppers contain a substance called capsaicin, which gives peppers their characteristic pungency, producing mild to intense spice when eaten. Capsaicin is being studied as an effective treatment for sensory nerve fibre disorders, including pain associated with arthritis, psoriasis, and diabetic neuropathy.

Red chili peppers have been shown to reduce blood cholesterol, triglyceride levels, and platelet aggregation, while increasing the body's ability to dissolve fibrin, a substance integral to the formation of blood clots. Cultures where hot pepper is used liberally have a much lower rate of heart attack, stroke and pulmonary embolism.

Chili peppers contains Vitamin A, Vitamin C, Vitamin B6, Vitamin K1, Potassium and Copper. Chilli peppers are rich in various vitamins and minerals but usually eaten in small amounts - so they don't contribute significantly to our daily micronutrient intake.

We are interested in minerals contained in chili, the concentration of minerals in each part of fruit, and comparison to green and red ones. So we have chosen EDXRF method to embody the minerals contained in chili.

Theoretical Background

When a sample is irradiated with x-rays from an x-ray tube, the atoms in the sample generate unique x-rays that are emitted from the sample. Such x-rays are known as "fluorescent x-rays" and they have a unique wavelength and energy that is characteristic of each element that generates them. Consequently, qualitative analysis can be performed by investigating the wavelengths of the x-rays. As the fluorescent x-ray intensity is a function of the concentration, quantitative analysis is also possible by measuring the amount of x-rays at the wavelength specific to each element.

---

[1] Dr, Assistant Lecturer, Department of Physics, University of Yangon

[2] Dr, Associate Professor, Department of Physics, West University of Yangon

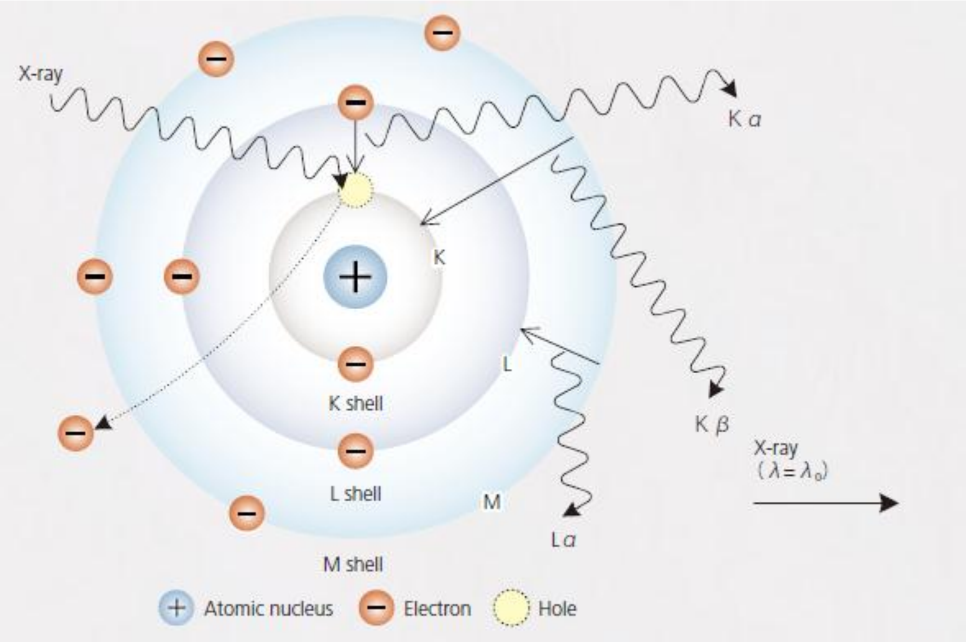

Figure 2.1 Electron Paths and Principle of X-ray Generation Expressed as a Bohr Model

Main Specifications of Shimadzu EDX-7000 Spectrometer

Measurement principle	X-ray fluorescence spectrometer
Measurement method	Energy dispersive
Target samples	Solids, liquids, powders
Measuring range	11 Na to 92 U

X-ray Generator (EDX-7000)

X-ray tube	Rhodium (Rh) target
Voltage	4 kV to 50 kV
Current	1µA to 1000 µA
Cooling method	air cooling (with a fan)
Irradiated area	10 mm diameter (standard)
Primary filters	Automatic selection from among 5 types of filter

Detector

Type	Silicon drift detector (SDD)

Sample Chamber

Measurement Atmosphere	Air, vacuum, helium
Sample replacement	12- sample turret
Sample observations	Semiconductor camera

Sample Collection and Preparation

Green and red chilies grown at home were collected. Stalk, seeds and skin were separated and placed in the cells covering with film. The cells were put into chamber and analysed.

Results and Discussions

The elemental concentrations of various parts of chili are shown in Table 1 and the respective graph is shown in Figure 1. Major elements found are potassium, sulfur and calcium. The minor elements found are copper, iron and zinc.

The elemental concentrations of various parts of green chili are shown in Table 2 and the respective graph is shown in Figure 2. Major elements found are potassium, sulfur and calcium. The minor elements found are copper, iron and zinc. Potassium is mostly found in stalk. Sulfur is mostly found in stalk and seed. Calcium is only found in stalk. Seeds contain more copper than stalk and skin. Iron is found in all parts.

The elemental concentrations of various parts of red chili are shown in Table 3 and the respective graph is shown in Figure 3. Major elements found are potassium, sulfur and calcium. The minor elements found are copper, iron and zinc. Potassium is mostly found in stalk. Sulfur is mostly found in stalk and seed. Calcium is found in all parts. Copper and Iron are found in all parts.

The comparisons of minerals contained in stalks of green and red chilies are shown in Figure 4. The stalk of Red chili contains more minerals than stalk of green chili.

The comparisons of minerals contained in seeds of green and red chilies are shown in Figure 5. Both contain nearly the same minerals. Calcium is only found in red chili seeds.

The comparisons of minerals contained in fruit-wall of green and red chilies are shown in Figure 6. The fruit-wall of red chili contains more minerals than that of green chili.

```
Sample  : Chilli_R_Bone
Operator: DRWLO
Comment : with mylar film
Group   : FP balance 10mm
Date    : 2019-03-15 12:48:30

Measurement Condition
------------------------------------------------------------------------------------
Instrument: EDX-7000   Atmosphere: Air   Collimator: 10(mm)      Sample Cup:Mylar
------------------------------------------------------------------------------------
Analyte               TG kV   uA      FI   Acq.(keV) Anal.(keV)  Time(sec)    DT(%)
------------------------------------------------------------------------------------
Al-U                  Rh 50   69-Auto ----   0 - 40   0.00-40.00  Live- 100    30
```

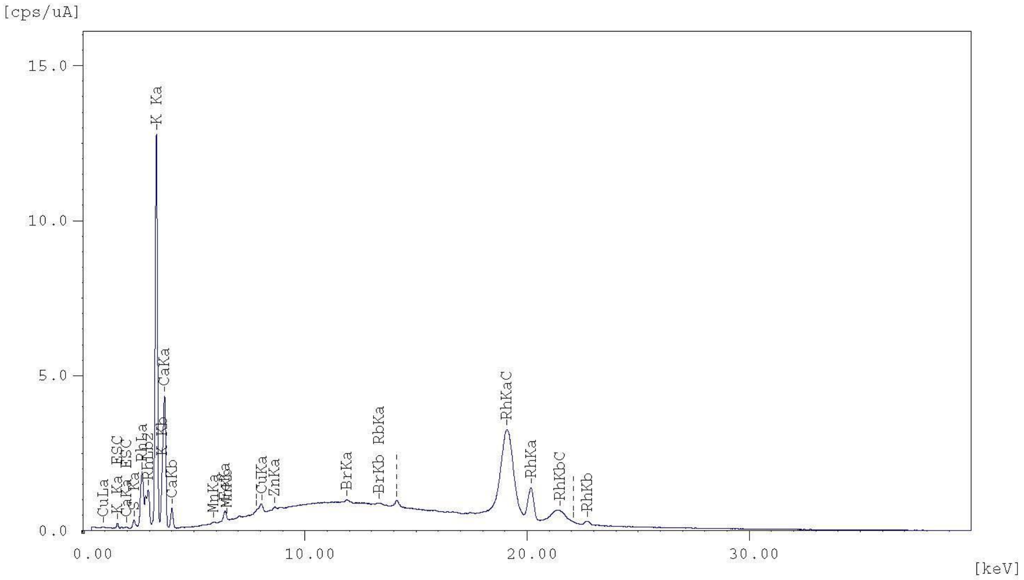

```
Qualitative Result
------------------------------------------------------------------------------------
Element: Cu, K , Ca, S , Rh, Mn, Fe, Zn, Br, Rb

Quantitative Result
------------------------------------------------------------------------------------
Analyte                 Result           [3-sigma] Proc.-Calc. Line   Int.(cps/uA)
------------------------------------------------------------------------------------
K                        1.013 %          [ 0.004] Quan-FP     K Ka      75.1816
Ca                       0.198 %          [ 0.001] Quan-FP     CaKa      24.0894
S                        0.086 %          [ 0.003] Quan-FP     S Ka       1.4851
Fe                       0.002 %          [ 0.000] Quan-FP     FeKa       2.4435
Cu                       0.001 %          [ 0.000] Quan-FP     CuKa       2.9934
Zn                       0.000 %          [ 0.000] Quan-FP     ZnKa       1.0496
Mn                       0.000 %          [ 0.000] Quan-FP     MnKa       0.3159
Br                       0.000 %          [ 0.000] Quan-FP     BrKa       1.1855
Rb                       0.000 %          [ 0.000] Quan-FP     RbKa       0.9106
CH                      98.699 %          [------] Balance     -------- --------
```

```
Sample   : Chilli_G_Bone
Operator: DRWLO
Comment  : with mylar film
Group    : FP balance 10mm
Date     : 2019-03-15 12:43:17

Measurement Condition
-------------------------------------------------------------------------------------
Instrument: EDX-7000   Atmosphere: Air   Collimator: 10(mm)      Sample Cup:Mylar
-------------------------------------------------------------------------------------
Analyte                TG kV   uA      FI    Acq.(keV) Anal.(keV)  Time(sec)    DT(%)
-------------------------------------------------------------------------------------
Al-U                   Rh 50   61-Auto ----   0 - 40   0.00-40.00  Live- 100    30
```

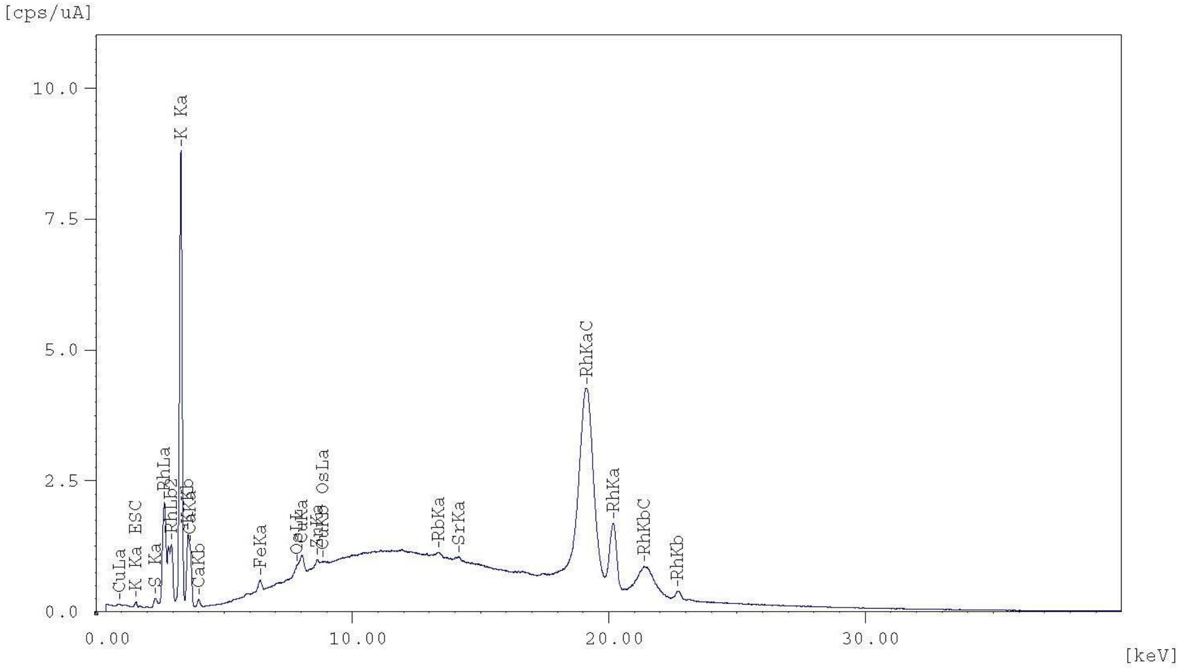

```
Qualitative Result
-------------------------------------------------------------------------------------
Element: Cu, K , S , Rh, Ca, Fe, Os, Zn, Rb, Sr

Quantitative Result
-------------------------------------------------------------------------------------
Analyte                    Result          [3-sigma] Proc.-Calc. Line   Int.(cps/uA)
-------------------------------------------------------------------------------------
K                           0.676 %         [ 0.004] Quan-FP     K Ka      51.3476
S                           0.063 %         [ 0.003] Quan-FP     S Ka       1.1038
Ca                          0.039 %         [ 0.000] Quan-FP     CaKa       5.1626
Cu                          0.001 %         [ 0.000] Quan-FP     CuKa       3.3525
Fe                          0.001 %         [ 0.000] Quan-FP     FeKa       1.5709
Zn                          0.000 %         [ 0.000] Quan-FP     ZnKa       1.6310
Os                          0.000 %         [ 0.000] Quan-FP     OsLa       0.5811
Rb                          0.000 %         [ 0.000] Quan-FP     RbKa       1.2438
Sr                          0.000 %         [ 0.000] Quan-FP     SrKa       1.0075
CH                         99.218 %         [------] Balance     -------- --------
```

```
Sample  : Chilli_R_Seed
Operator: DRWLO
Comment : with mylar film
Group   : FP balance 10mm
Date    : 2019-03-15 12:45:53

Measurement Condition
----------------------------------------------------------------------------------
Instrument: EDX-7000   Atmosphere: Air   Collimator: 10(mm)      Sample Cup:Mylar
----------------------------------------------------------------------------------
Analyte              TG kV   uA      FI   Acq.(keV) Anal.(keV)  Time(sec)    DT(%)
----------------------------------------------------------------------------------
Al-U                 Rh 50   53-Auto ----   0 - 40   0.00-40.00  Live- 100    30
```

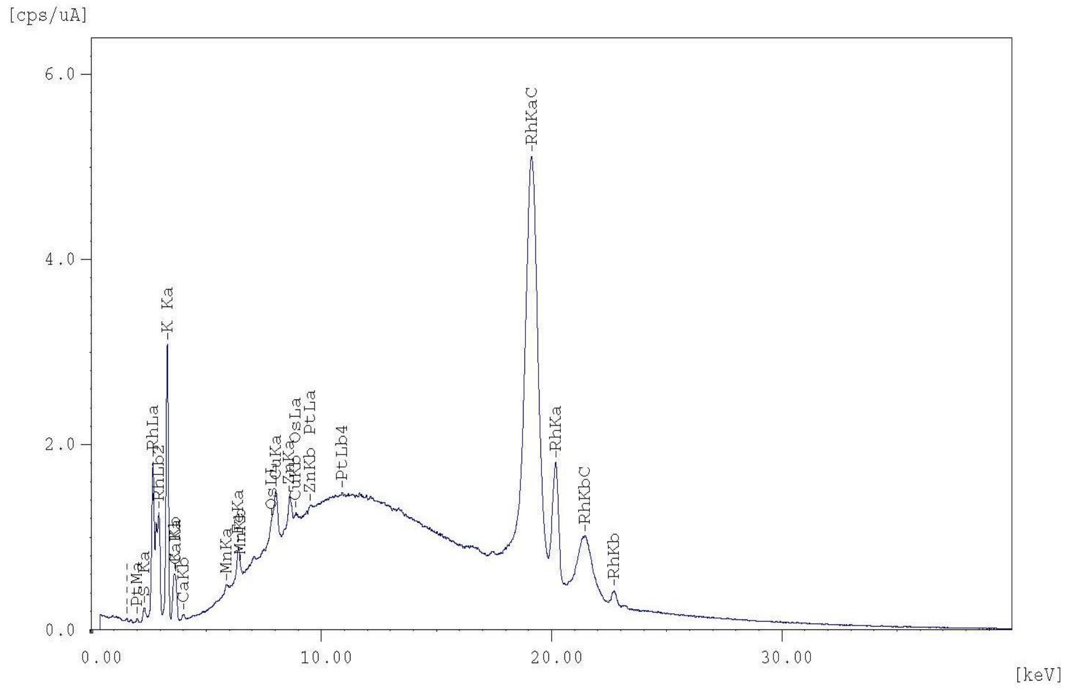

```
Qualitative Result
----------------------------------------------------------------------------------
Element: Pt, S , Rh, K , Ca, Mn, Fe, Os, Cu, Zn

Quantitative Result
----------------------------------------------------------------------------------
Analyte                 Result           [3-sigma] Proc.-Calc. Line   Int.(cps/uA)
----------------------------------------------------------------------------------
K                        0.224 %          [ 0.002] Quan-FP    K Ka      17.4608
S                        0.052 %          [ 0.003] Quan-FP    S Ka       0.9052
Ca                       0.014 %          [ 0.001] Quan-FP    CaKa       2.1021
Fe                       0.002 %          [ 0.000] Quan-FP    FeKa       2.6759
Cu                       0.001 %          [ 0.000] Quan-FP    CuKa       5.0654
Zn                       0.001 %          [ 0.000] Quan-FP    ZnKa       3.5531
Mn                       0.001 %          [ 0.000] Quan-FP    MnKa       0.6309
Os                       0.000 %          [ 0.000] Quan-FP    OsLa       0.6922
Pt                       0.000 %          [ 0.000] Quan-FP    PtLa       0.5159
CH                      99.704 %          [------] Balance    -------- --------
```

```
Sample   : Chilli_G_Seed
Operator: DRWLO
Comment : with mylar film
Group    : FP balance 10mm
Date     : 2019-03-15 12:40:41

Measurement Condition
----------------------------------------------------------------------------------
Instrument: EDX-7000   Atmosphere: Air   Collimator: 10(mm)     Sample Cup:Mylar
----------------------------------------------------------------------------------
Analyte                TG kV   uA      FI    Acq.(keV) Anal.(keV)  Time(sec)    DT(%)
----------------------------------------------------------------------------------
Al-U                   Rh 50   44-Auto ----   0 - 40   0.00-40.00  Live- 100    30
```

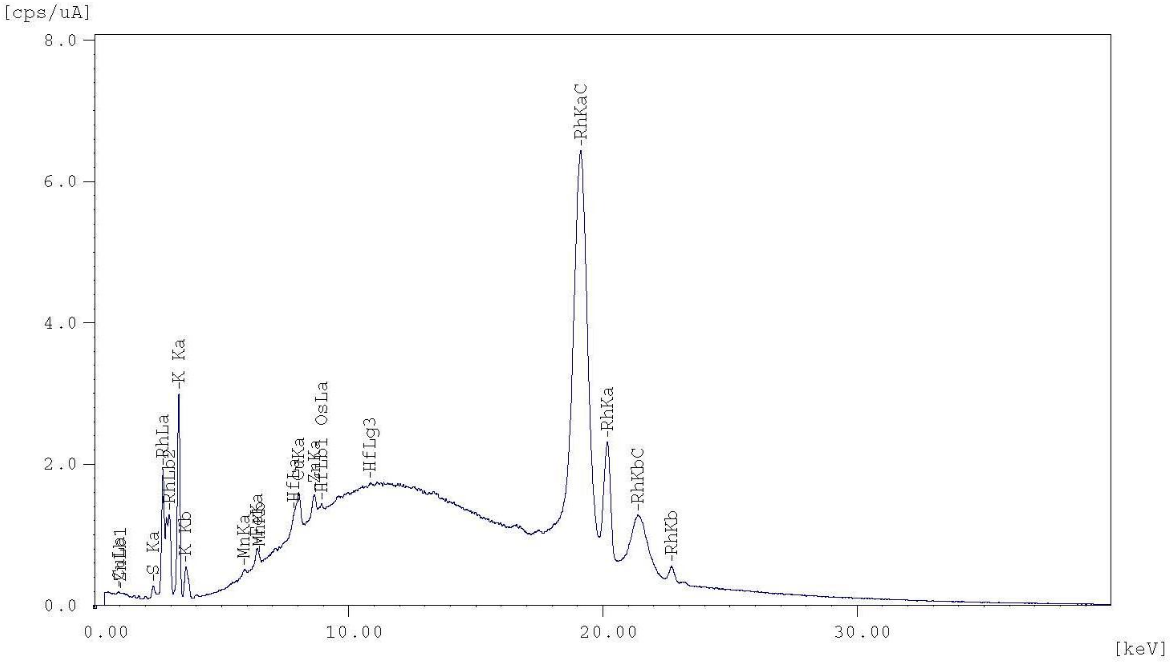

```
Qualitative Result
----------------------------------------------------------------------------------
Element: Cu, Zn, S , Rh, K , Mn, Fe, Hf, Os

Quantitative Result
----------------------------------------------------------------------------------
Analyte                   Result           [3-sigma] Proc.-Calc. Line    Int.(cps/uA)
----------------------------------------------------------------------------------
K                          0.219 %          [ 0.002] Quan-FP     K Ka      16.9864
S                          0.063 %          [ 0.004] Quan-FP     S Ka       1.0936
Hf                         0.003 %          [ 0.000] Quan-FP     HfLa       2.8399
Cu                         0.002 %          [ 0.000] Quan-FP     CuKa       5.2118
Fe                         0.001 %          [ 0.000] Quan-FP     FeKa       1.9560
Zn                         0.001 %          [ 0.000] Quan-FP     ZnKa       3.5360
Mn                         0.001 %          [ 0.000] Quan-FP     MnKa       0.6297
Os                         0.000 %          [ 0.000] Quan-FP     OsLa       0.3127
CH                        99.712 %          [------] Balance     -------- --------
```

```
Sample  : Chilli_R_Shell
Operator: DRWLO
Comment : with mylar film
Group   : FP balance 10mm
Date    : 2019-03-15 13:00:56

Measurement Condition
--------------------------------------------------------------------------------
Instrument: EDX-7000   Atmosphere: Air   Collimator: 10(mm)      Sample Cup:Mylar
--------------------------------------------------------------------------------
Analyte                TG kV   uA      FI   Acq.(keV) Anal.(keV)  Time(sec)    DT(%)
--------------------------------------------------------------------------------
Al-U                   Rh 50   71-Auto ----   0 - 40   0.00-40.00  Live- 100    30
```

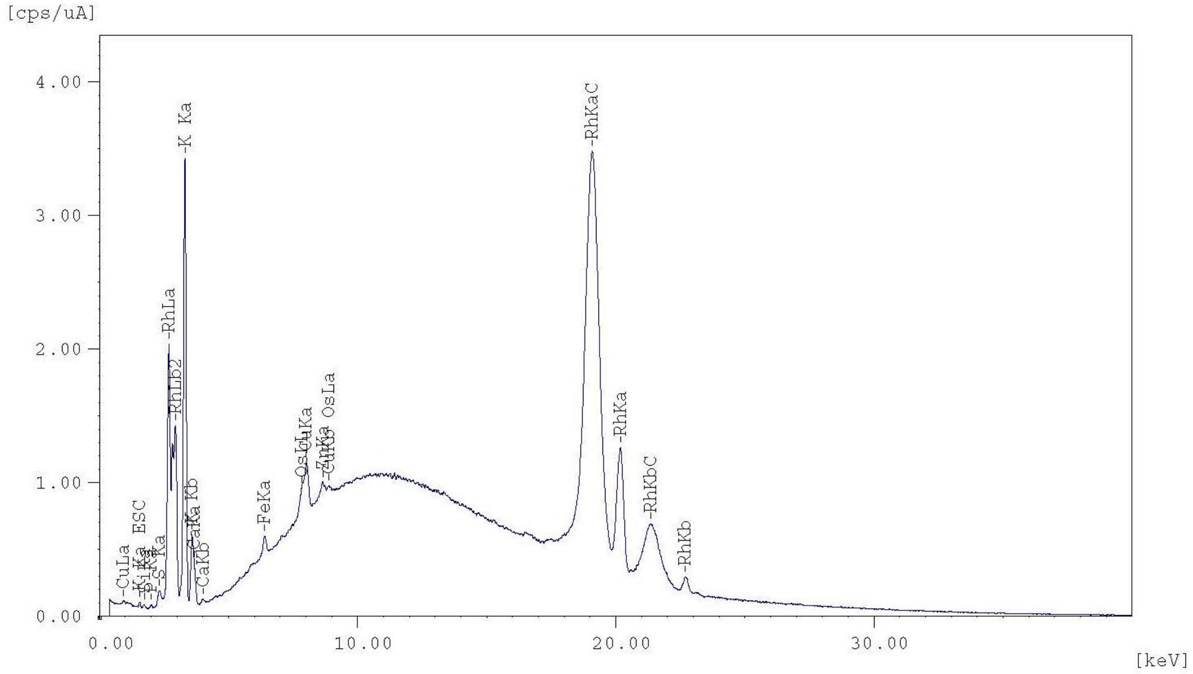

```
Qualitative Result
--------------------------------------------------------------------------------
Element: Cu, K , Si, P , S , Rh, Ca, Fe, Os, Zn

Quantitative Result
--------------------------------------------------------------------------------
Analyte                  Result          [3-sigma] Proc.-Calc. Line   Int.(cps/uA)
--------------------------------------------------------------------------------
K                         0.256 %         [ 0.002] Quan-FP     K Ka      19.6584
Si                        0.095 %         [ 0.026] Quan-FP     SiKa       0.1088
S                         0.042 %         [ 0.003] Quan-FP     S Ka       0.7297
P                         0.025 %         [ 0.006] Quan-FP     P Ka       0.1207
Ca                        0.008 %         [ 0.001] Quan-FP     CaKa       1.1951
Cu                        0.001 %         [ 0.000] Quan-FP     CuKa       3.4240
Fe                        0.001 %         [ 0.000] Quan-FP     FeKa       1.2965
Zn                        0.000 %         [ 0.000] Quan-FP     ZnKa       1.7208
Os                        0.000 %         [ 0.000] Quan-FP     OsLa       0.6493
CH                       99.571 %         [------] Balance     -------- --------
```

```
Sample   : Chilli_G_Shell
Operator: DRWLO
Comment : with mylar film
Group    : FP balance 10mm
Date     : 2019-03-15 12:38:04

Measurement Condition
------------------------------------------------------------------------------------
Instrument: EDX-7000   Atmosphere: Air   Collimator: 10(mm)      Sample Cup:Mylar
------------------------------------------------------------------------------------
Analyte                TG kV   uA      FI    Acq.(keV) Anal.(keV)  Time(sec)    DT(%)
------------------------------------------------------------------------------------
Al-U                   Rh 50   58-Auto ----   0 - 40   0.00-40.00  Live- 100    31
```

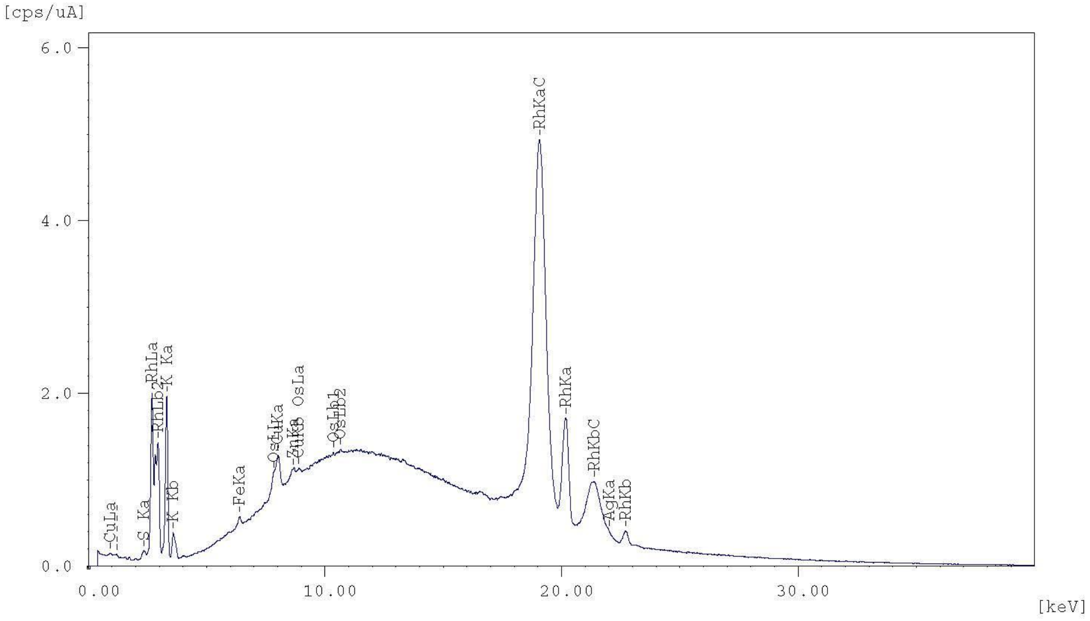

```
Qualitative Result
------------------------------------------------------------------------------------
Element: Cu, S , Rh, K , Fe, Os, Zn, Ag

Quantitative Result
------------------------------------------------------------------------------------
Analyte                 Result          [3-sigma] Proc.-Calc. Line   Int.(cps/uA)
------------------------------------------------------------------------------------
K                        0.140 %         [ 0.002] Quan-FP    K Ka      10.9472
S                        0.039 %         [ 0.003] Quan-FP    S Ka       0.6794
Cu                       0.001 %         [ 0.000] Quan-FP    CuKa       3.9761
Ag                       0.001 %         [ 0.000] Quan-FP    AgKa       1.3351
Fe                       0.001 %         [ 0.000] Quan-FP    FeKa       0.8829
Zn                       0.000 %         [ 0.000] Quan-FP    ZnKa       1.7980
Os                       0.000 %         [ 0.000] Quan-FP    OsLa       0.7262
CH                      99.818 %         [------] Balance    -------- --------
```

Table 1 Elemental Concentration (W%) of parts of green and red chilies

Element	**Green Chili**			**Red Chili**		
	Stalk	**Seeds**	**fruit-wall**	**Stalk**	**Seeds**	**fruit-wall**
K	0.676	0.219	0.140	1.013	0.224	0.256
S	0.063	0.063	0.039	0.086	0.052	0.042
Ca	0.039	0.000	0.000	0.198	0.014	0.008
Cu	0.001	0.002	0.001	0.001	0.001	0.001
Fe	0.001	0.001	0.001	0.002	0.002	0.001
Zn	0.000	0.001	0.000	0.000	0.001	0.000
Hf	0.000	0.003	0.000	0.000	0.000	0.000
Mn	0.000	0.001	0.000	0.000	0.001	0.000
Ag	0.000	0.000	0.001	0.000	0.000	0.000
Si	0.000	0.000	0.000	0.000	0.000	0.095
P	0.000	0.000	0.000	0.000	0.000	0.025

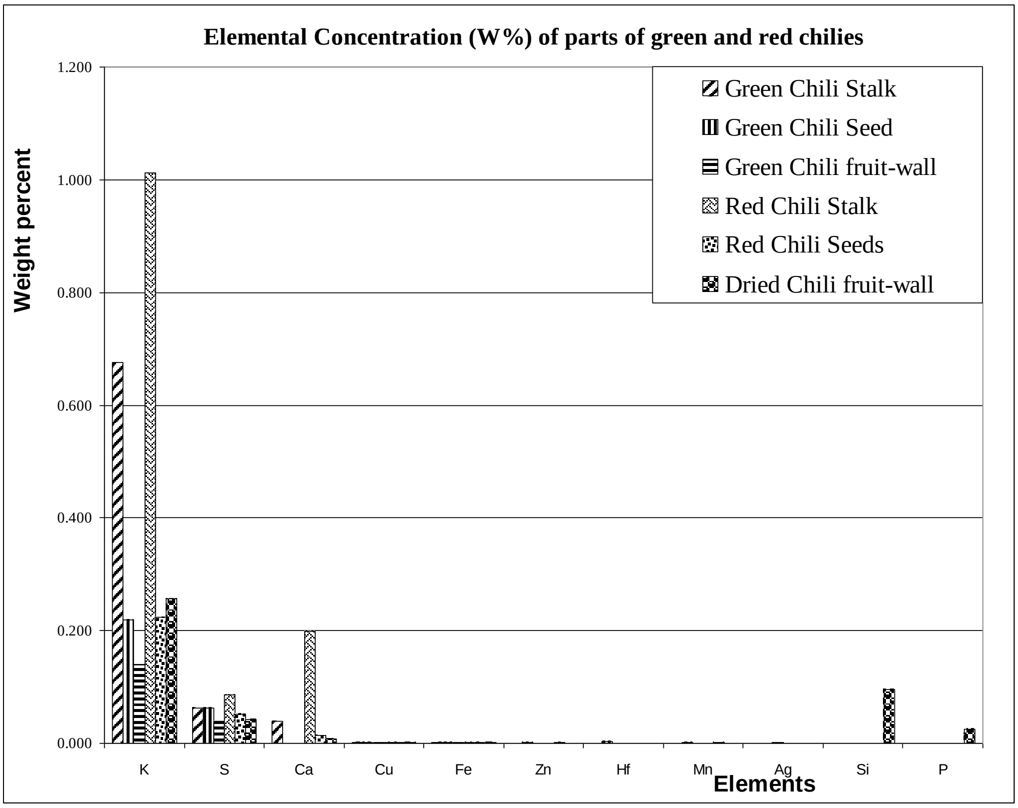

Figure 1 Elemental Concentration (W%) of parts of green and red chilies

Table 2 Elemental Concentration (W%) of parts of green chili

Element	Stalk	Seeds	fruit-wall
K	0.676	0.219	0.140
S	0.063	0.063	0.039
Ca	0.039	0.000	0.000
Cu	0.001	0.002	0.001
Fe	0.001	0.001	0.001
Zn	0.000	0.001	0.000
Hf	0.000	0.003	0.000
Mn	0.000	0.001	0.000
Ag	0.000	0.000	0.001

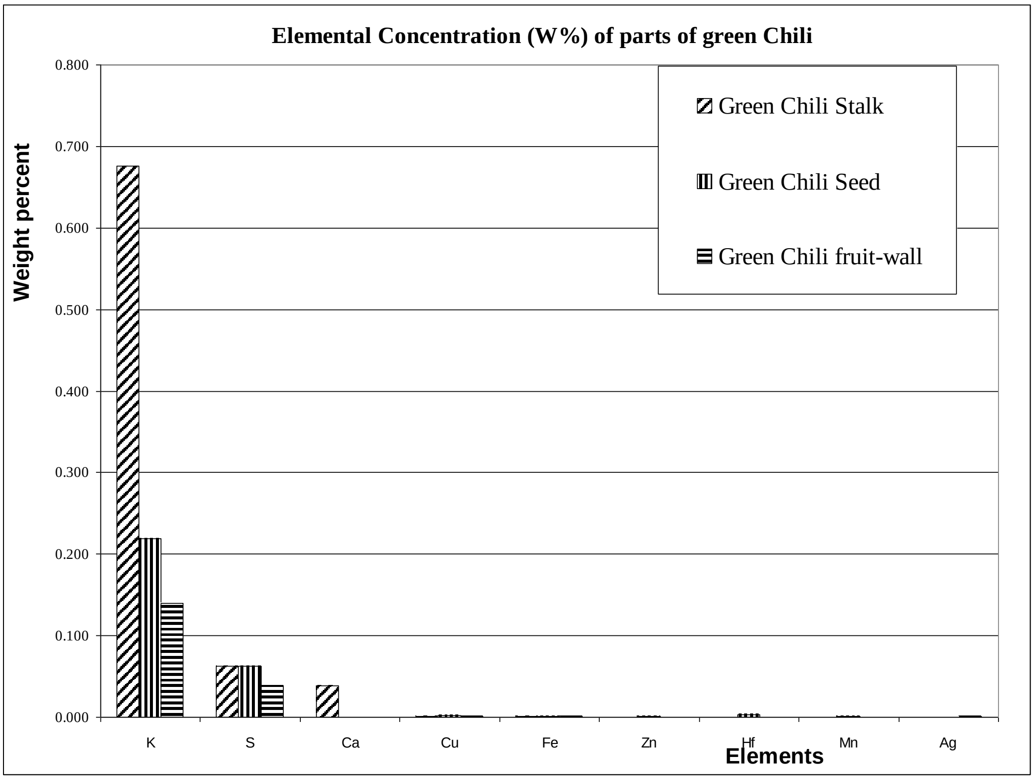

Figure 2 Elemental Concentration (W%) of parts of green chili

Table 3 Elemental Concentration (W%) of parts of red chili

Element	Stalk	Seeds	fruit-wall
K	1.013	0.224	0.256
S	0.086	0.052	0.042
Ca	0.198	0.014	0.008
Cu	0.001	0.001	0.001
Fe	0.002	0.002	0.001
Zn	0.000	0.001	0.000
Mn	0.000	0.001	0.000
Si	0.000	0.000	0.095
P	0.000	0.000	0.025

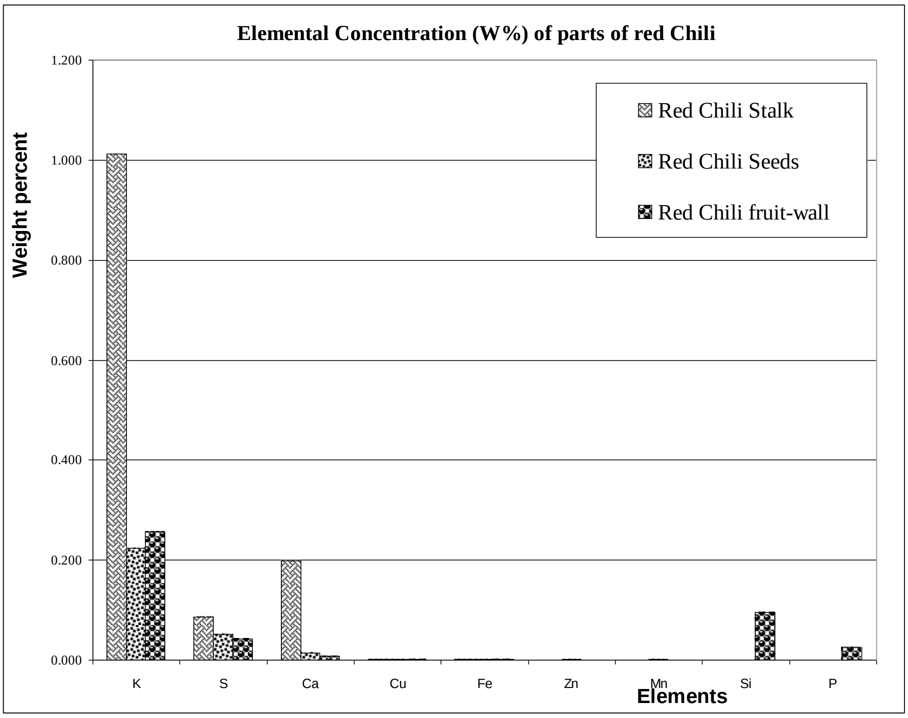

Figure 3 Elemental Concentration (W%) of parts of red chili

Table 4 Comparison of Elemental Concentration (W%) of stalks of green and red chilies

Element	Green Chili Stalk	Red Chili Stalk
K	0.676	1.013
S	0.063	0.086
Ca	0.039	0.198
Cu	0.001	0.001
Fe	0.001	0.002

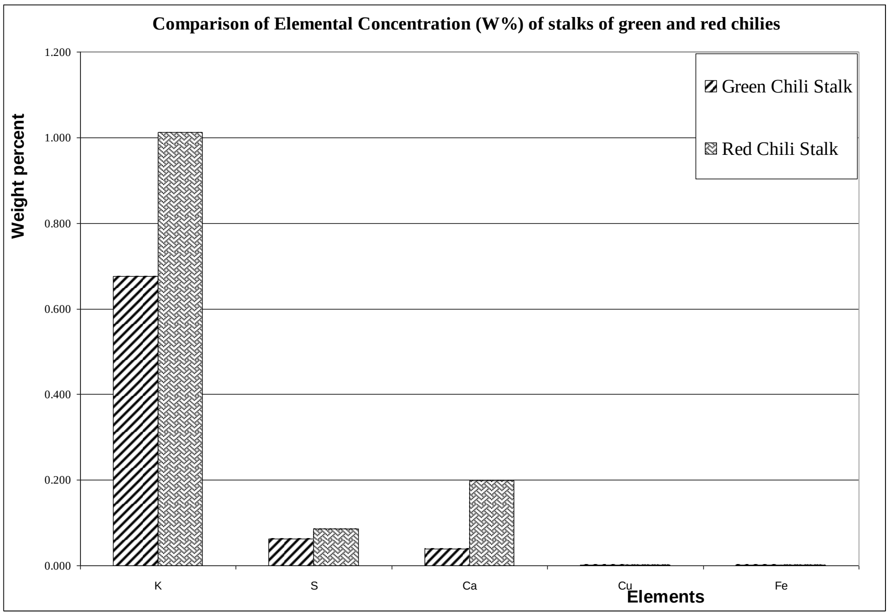

Figure 4 Comparison of Elemental Concentration (W%) of stalks of green and red chilies

Table 5 Comparison of Elemental Concentration (W%) of seeds of green and red chilies

Element	Green Chili Seeds	Red Chili Seeds
K	0.219	0.224
S	0.063	0.052
Ca	0.000	0.014
Cu	0.002	0.001
Fe	0.001	0.002
Zn	0.001	0.001
Hf	0.003	0.000
Mn	0.001	0.001

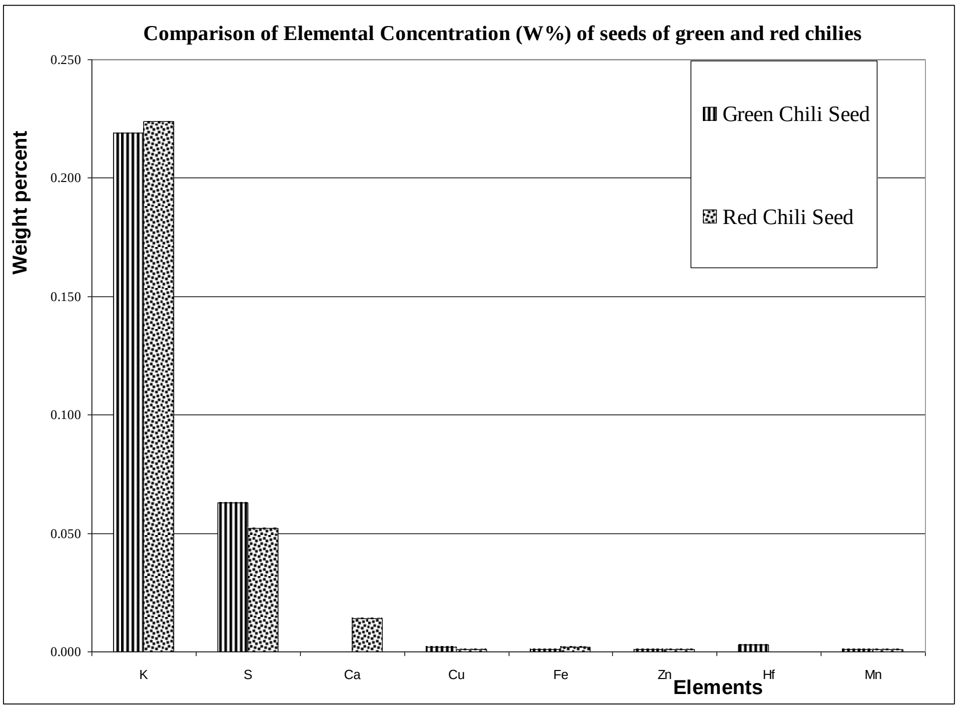

Figure 5 Comparison of Elemental Concentration (W%) of seeds of green and red chilies

Table 6 Comparison of Elemental Concentration (W%) of fruit-walls of green and red chilies

Element	Green Chili fruit-wall	Red Chili fruit-wall
K	0.140	0.256
S	0.039	0.042
Ca	0.000	0.008
Cu	0.001	0.001
Fe	0.001	0.001
Ag	0.001	0.000
Si	0.000	0.095
P	0.000	0.025

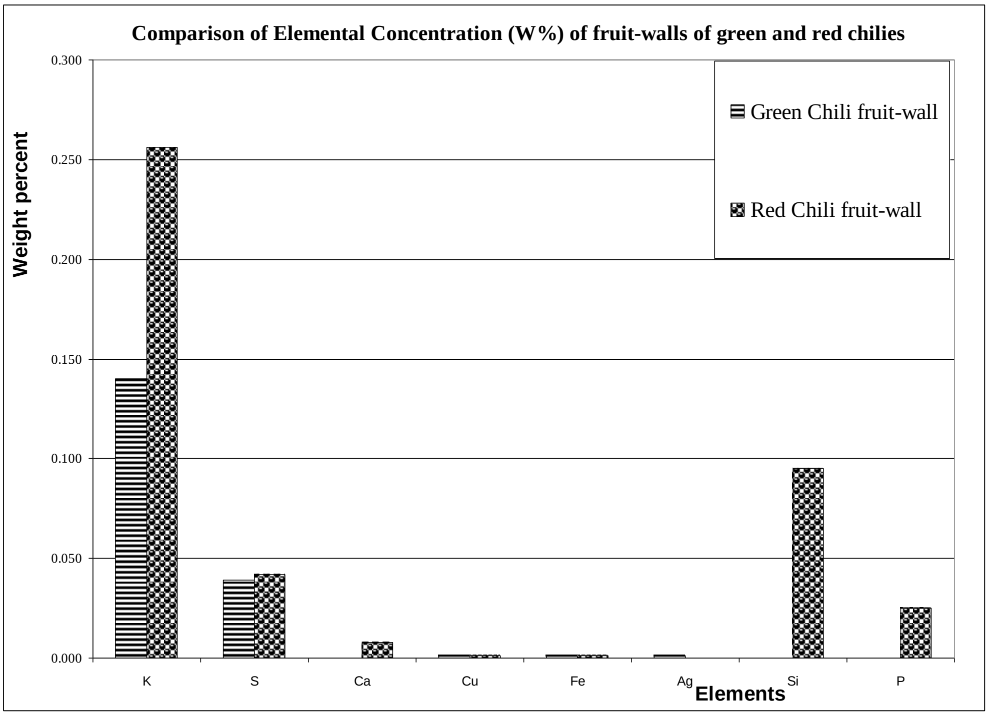

Figure 6 Comparison of Elemental Concentration (W%) of fruit-walls of green and red chilies

Conclusion

Potassium lowers blood pressure, protects against loss of muscle mass, preserves bone mineral density, and reduces the formation of kidney stones.

Sulfur makes up vital amino acids used to create protein for cells, tissues, hormones, enzymes, and antibodies. Sulfur is needed for insulin production.

Calcium can build and maintain strong bones. Our heart, muscles and nerves also need calcium to function properly.

Copper is essential for infant growth, bone strength, red and white blood cell maturation, iron transport, cholesterol and glucose metabolism, heart muscle contraction and brain development.

From our study, chili is found to contain essential macrominerals. It is surprisingly found that the chili stalks which we throw away contain more valuable minerals. Red chili, not dried chili, is better than green chili.

Acknowledgements

I would like to thank Professor Dr Khin Khin Win, Head of Department of Physics, University of Yangon for her kind permission to carry out this research.

I would like to express my sincere thanks to Dr Myo Lwin, Professor, Department of Physics, Dr Ye Chan, Professor and Head, Universities' Resarch Centre, Dr Aye Aye Thant, Professsor, Department of Physics, Dr Yin Maung Maung, Professor, Department of Physics and Dr Than Zaw Oo, Professor, Universities' Resarch Centre, University of Yangon for their suggestion to carry out this work.

References

Cesareo R (2000) “X-Ray Physics: Interaction with Matter, Production, Detection” (Bologna: La Rivista del Nuovo Cimento)

Chevallier, A. (1996). The encyclopedia of medicinal plants. London: Dorling Kindersely Limited.

Donal E Leydon (1999) “Fundamentals of X-Ray Spectrometry as Applied to Energy Dispersive Techniques”, Spectrace Instruments Technical Paper

Jekins RE (1999) “X-Ray Fluorescence Spectrometry” (New York: Wiley- Interscience)

Peter N. Brouwer, (2003) Theory of XRF 1st ed PANalytical B.V The Netherlands.

Rene E, Van Grieken, Andrzej (1993) “ Handbook of X ray Spectrometry Methods and Techniques” (New York : Marcle Dekker)

Tertain R & Classie F (1982) “Principles of Quantitative X ray Fluorescence Analysis” (London: Heyden)

J. Myanmar Acad. Arts Sci. 2020 **Vol. XVIII.No.2B**

CONSTRUCTION AND DATA ACQUISITION OF UV RADIATION METER

Wint Shwe War Hlaing[*]

Abstract

The ML8511 UV sensor detects 280 nm – 390 nm light, this wavelength is categorized as part of the UVB-burning rays spectrum and most of the UVA-tanning rays spectrum. The sensor ML8511 has a UV photodiode and internal amplifier which will converts photo current to voltage output depending on the UV light intensity. UV intensity is directly proportional to output voltage so that the program is written according to their relation. The UV intensity in mW/cm^2 is displayed on LCD which is processed by Arduino microcontroller. At the same time, data are sent to the Microsoft (MS) excel spreadsheet via parallex data acquisition (PLX-DAQ) software. Data accompanying with current date and time are uploaded directly from Arduino to MS excel spreadsheet.

Keywords: UV sensor, data acquisition, Excel

Introduction

Ultra violet (UV) index is the one of the important factor for health and environment. Ultraviolet or UV light is filtered to a large degree by the Earth’s Ozone layer, a protective layer of gas in the upper atmosphere that absorbs UV radiation. But the ozone layer is not a perfect filter and as a consequence some of the UV makes it through. Too much exposure to UV light can cause serious health problems ranging from burns to skin cancer. Cost effective UV meter can be constructed by using microcontroller and UV sensor. And then, these data are directly transferring to the Microsoft (MS) Excel spreadsheet by using parallax-data acquisition (PLX-DAQ) software.

Background Theory

Ultraviolet (UV) designates a band of the electromagnetic spectrum with wavelength from 10 nm to 400 nm, shorter than that of visible light but longer than X-rays. UV radiation is present in sunlight, and contributes about 10% of the total output of the Sun. It is also produced by electric arcs and specialized lights, such as mercury-vapor lamps, tanning lamps, and black lights. Although long-wavelength ultraviolet is not considered an ionizing radiation because its photons lack the energy to ionize atoms, it can cause chemical reactions and causes many substances to glow or fluoresce. Consequently, the chemical and biological effects of UV are greater than simple heating effects, and many practical applications of UV radiation derive from its interactions with organic molecules.

Sunburn is familiar effects of over-exposure of the skin to UV, along with higher risk of skin cancer. Living things on dry land would be severely damaged by ultraviolet radiation from the Sun if most of it were not filtered out by the Earth's atmosphere. More energetic, shorter-wavelength "extreme" UV below 121 nm ionizes air so strongly that it is absorbed before it reaches the ground. Ultraviolet is also responsible for the formation of bone-strengthening vitamin D in most land vertebrates, including humans (specifically, UVB). The

---

[*] Dr, Lecturer, Department of Physics, University of Yangon

UV spectrum thus has effects both beneficial and harmful to human health.

The ultraviolet section of the electromagnetic spectrum extends from 400 nm to 100 nm, just below the X-ray section of the spectrum. It is actually divided into three sections:

UVA – This is the range from 400 nm to 315 nm. The so-called "black lights" that are used for eerie lighting effects fall into this range. UVA is not absorbed by the ozone layer.

UVB – This is the range from 315 nm to 280 nm. The lights used in tanning booths usually are in this range. Most of the Sun's UVB energy is absorbed by the ozone layer but some gets through.

UVC – This is the range from 280 nm to 100 nm. UV light in this range is used in sterilization procedures as its high energy kills bacteria. It is completely absorbed by the ozone layer and upper atmosphere.

Table 1 Electromagnetic spectrum of ultraviolet

Name	Abbreviation	Wavelength (nm)	Photon energy (eV, aJ)
Ultraviolet A	UVA	315−400	3.10−3.94(0.497−0.631)
Ultraviolet B	UVB	280−315	3.94−4.43(0.631−0.710)
Ultraviolet C	UVC	100−280	4.43−12.4(0.710−1.987)
Near ultraviolet	NUV	300−400	3.10−4.13(0.497−0.662)
Middle ultraviolet	MUV	200−300	4.13−6.20(0.662−0.993)
Far ultraviolet	FUV	122−200	6.20−10.16(0.993−1.628)
Hydrogen Lyman-alpha	H Lyman-α	121−122	10.16−10.25(1.628−1.642)
Vacuum ultraviolet	VUV	10−200	6.20−124(0.993−19.867)
Extreme ultraviolet	EUV	10−121	10.25−124(1.642−19.867)

Materials and Method

Arduino microcontroller and Ultraviolet sensor are required to construct the UV meter which displays output voltage of sensor, UV light intensity in mW/cm^2, UV index and UV level in the serial monitor and UV index and UV level on LCD. The ML8511 sensor breakout uses to measure ultraviolet light intensity. The MP8511 UV Sensor outputs an analog signal in relation to the amount of UV light it detects. This can be handy in creating devices that warn the user of sunburn or detect the UV index as it relates to weather conditions. This sensor detects 280 nm - 390 nm light most effectively. This is categorized as part of the UVB (burning rays) spectrum and most of the UVA (tanning rays) spectrum.

ML 8511 UV Sensor

The ML8511 is a UV sensor, which is suitable for acquiring UV intensity indoors or outdoors. The ML8511 is equipped with an internal amplifier, which converts photo-current to voltage depending on the UV intensity. This unique feature offers an easy interface to external circuits such as ADC. In the power down mode, typical stand by current is 0.1 μA, thus enabling a longer battery life.

Its features are-

- Photodiode sensitive to UV-A and UV-B
- Embedded operational amplifier
- Analog voltage output
- Low supply current (300 μA) and low standby current (0.1 μA)
- Small and thin surface mount package

The output voltage is directly proportional to the incident UV intensity. The Figure 2(a) shows the relation of output voltage with respect to UV intensity at wavelength of 365 nm with different temperature. It has straight line characteristics. Within the temperature 75˚C and -25 ˚C, the output voltage is slightly changed. From Figure 2(b), it observes that the relative responsibility of sensor is good enough within the wavelength of 280 nm and 400 nm.

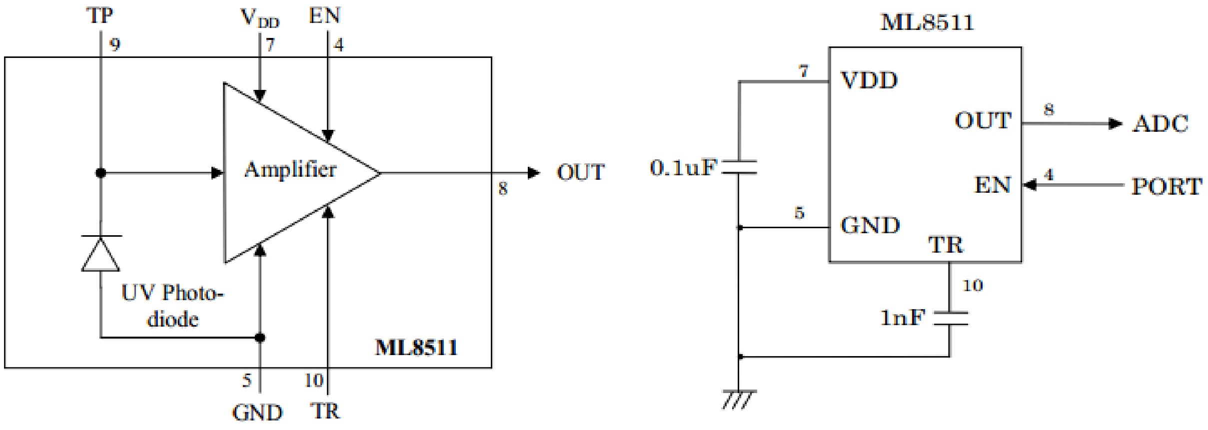

Figure 1 ML8511UV sensor and circuit connection

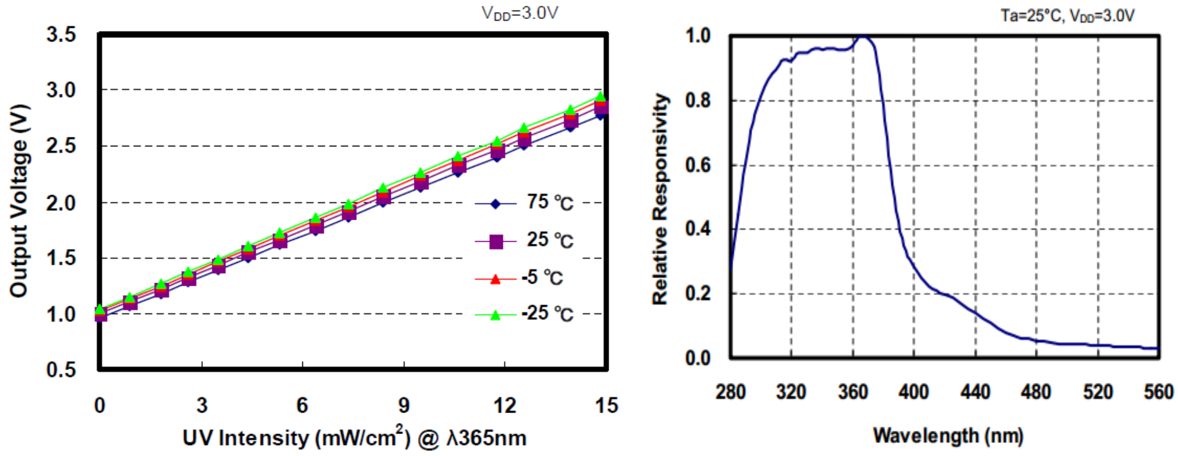

(a) (b)

Figure 2(a) Characteristics of ML8511UV sensor **(b)** Spectral responsibility characteristics

Parallax Data Acquisition (PLX-DAQ)

Parallax Data Acquisition tool (PLX-DAQ) software add-in for Microsoft Excel acquires up to 26 channels of data from any Parallax microcontrollers and drops the numbers into columns as they arrive. PLX-DAQ provides easy spreadsheet analysis of data collected in the field, laboratory analysis of sensors and real-time equipment monitoring.

PLX-DAQ is a Parallax microcontroller data acquisition add-on tool for Microsoft Excel. Any of microcontrollers connected to any sensor and the serial port of a PC can now send data directly into Excel. PLX-DAQ has the following features:

- Plot or graph data as it arrives in real-time using Microsoft Excel
- Record up to 26 columns of data
- Mark data with real-time (hh: mm: ss) or seconds since reset
- Read/Write any cell on a worksheet
- Read/Set any of 4 checkboxes on control the interface
- Baud rates up to 128 K

Experimental Setup

Arduino microcontroller, ML8511 UV sensor, LCD are used in construction of UV meter. For data acquisition, parallax data acquisition (PLX-DAQ) software is used. Figure 3 shows the block diagram of the construction of UV meter and data acquisition. Table 2 shows the circuit connections of Arduino with LCD and Figure 4 shows the connection between Arduino and ML8511 UV sensor. The schematic circuit diagram drawn by Proteus software is shown in Figure 5.

Table 2 The circuit connections of Arduino with LCD

Arduino	LCD
D7	RS
D6	E
D5	DB4
D4	DB5
D3	DB6
D2	DB7

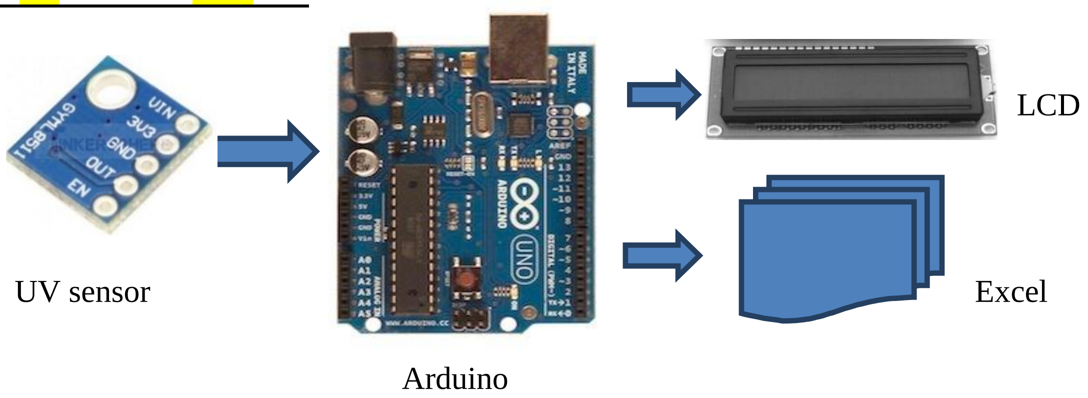

Figure 3 Block diagram of UV meter

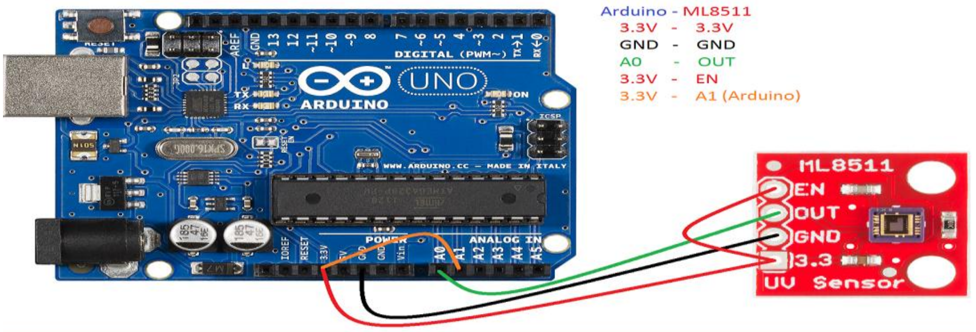

Figure 4 Circuit connections between Arduino and ML8511 UV sensor

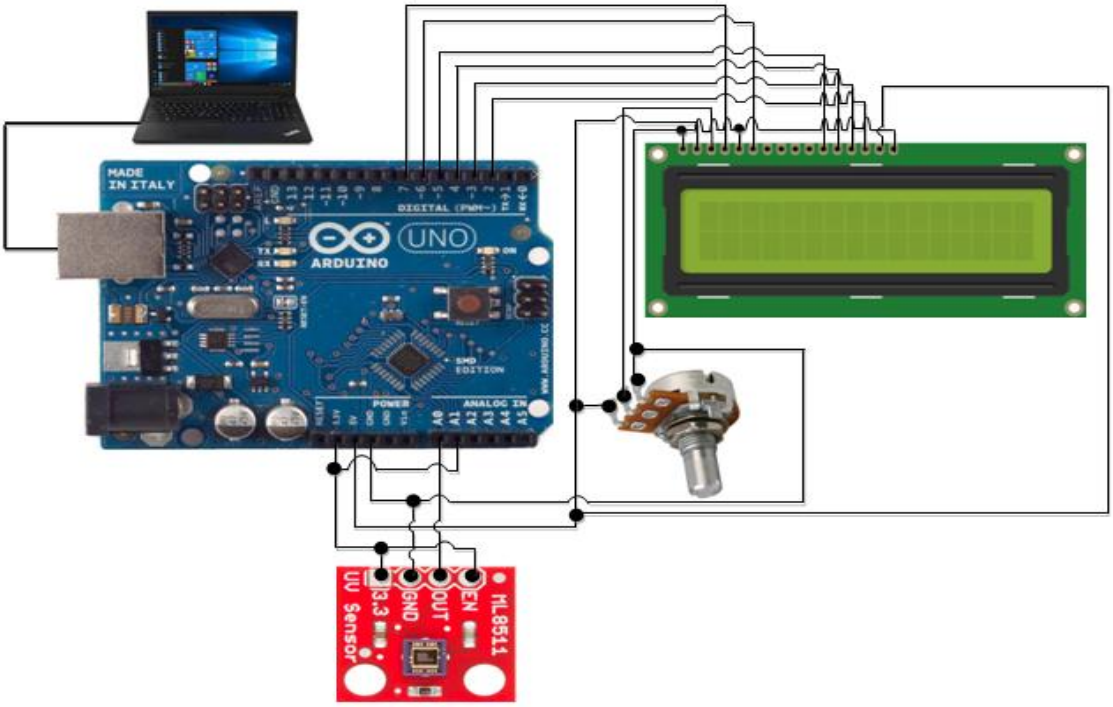

Figure 5 Schematic circuit diagram of UV meter

Operation

In the Setup routine the serial monitor is initialized at 9600 bauds. Make sure that the serial monitor on Arduino IDE is also set to the same speed, if not then change either the code or the serial monitor speed setting to make them match. The reference voltage level is selected as;

```
unsigned int UVOUT = A0; //Output from the sensor
intREF_3V3 = A1; //A1 is connected to 3.3V on-board power supply
```

The output voltage is determined as;

```
Unsigned int uvLevel = average Analog Read (UVOUT);
unsigned int refLevel = average Analog Read (REF_3V3);
float uvIntensity = mapfloat (output Voltage, 0.99, 2.9, 0.0, 15.0);
```

Dependency of UV intensity on output voltage is linearity. In the UV region voltage is varied between 0.99 V and 2.9 V. Using the map instruction, the UV intensity can be determined.

The data are processed to display on LCD as follows. The UV intensity is measured in mW/cm^2. UV level is also displayed on LCD.

The UV Index scale was developed by Canadian scientists in 1992, then adopted and standardized by the WHO in 1994. According to WHO standard, four UV levels are classified as the following program.

```
lcd.setCursor(1, 1);
lcd.print(uvIntensity);
lcd.setCursor(7, 1);
lcd.print("mW/cm^2");
lcd.setCursor(0,0);
if (uvIntensity< 3.0)
{
lcd.print("Low UV Level");
}
else if (uvIntensity>= 3 &&uvIntensity< 6)
{
lcd.print("Medium UV Level");
}
else if (uvIntensity>= 6 &&uvIntensity< 8)
{
lcd.print("High UV Level");
}
else
{
lcd.print("Extreme UV Level");
}
Serial.println();
```

Results and Discussion

In the cloudy day, the UV intensity and UV level are displayed on LCD as shown in Figure 7. This shows UV level is low. The data measured are directly transferred to excel spreadsheet and can be logged in hard drive of PC. The graph can be drawn by excel format as shown in Figure 8 and Figure 9. As the output voltage of UV sensor is directly proportional to the UV intensity the curve of output voltage and UV intensity are same but different values. It is observed clearly in the Figure 10.

Using UV touch light and sunlight, the test measurement of UV meter is observed. The data are expressed in Figure 11 (a) and Figure 11 (b). These data show that the UV meter (Figure11 (a) and Figure 11 (b)) constructed properly works.

The Figure 11 (b) shows that there are high levels of sunlight in the winter and in the summer when there are UV rays in the sun.

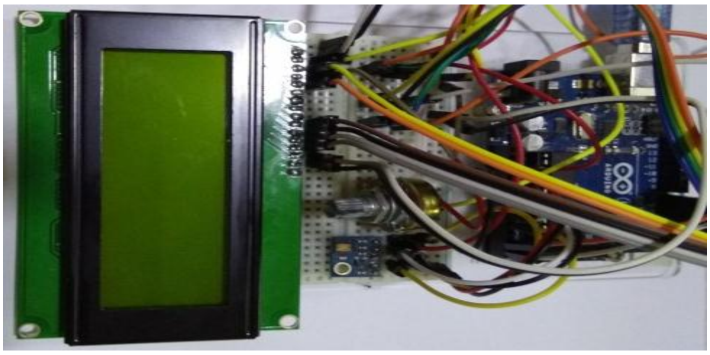

Figure 6 Experimental setup

Figure 7 UV intensity and UV level on LCD

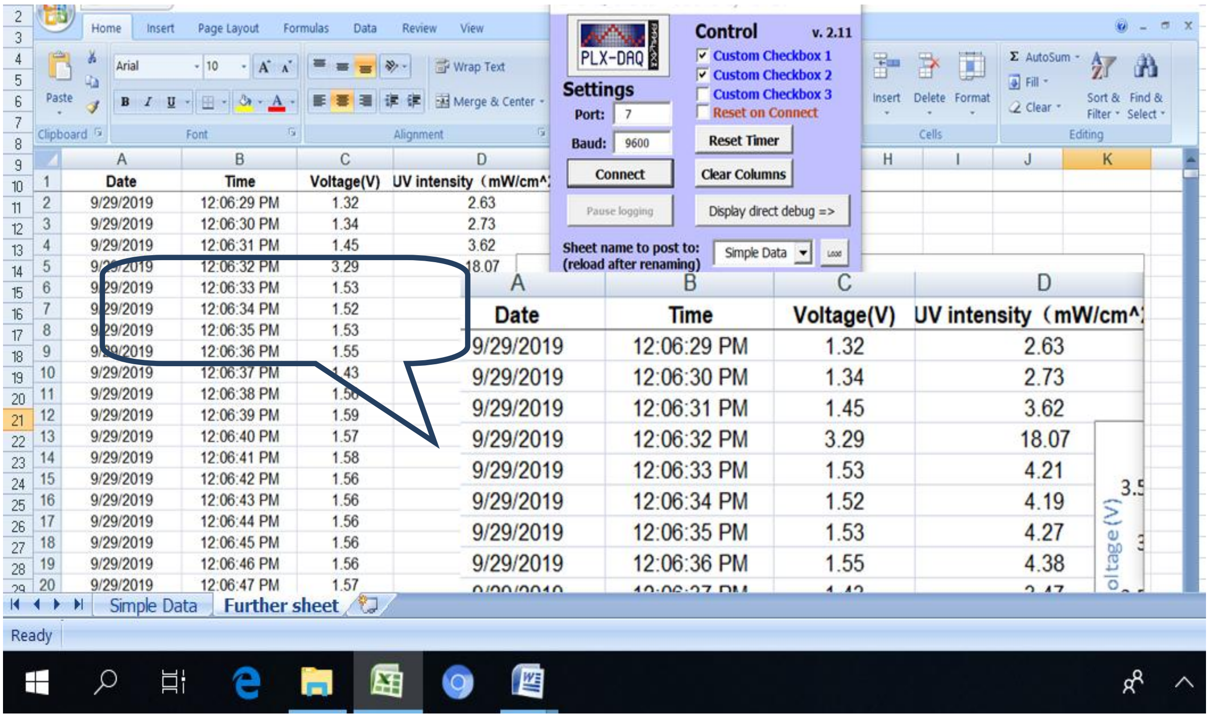

Settings
Port: 7
Baud: 9600

☑ Custom Checkbox 1
☑ Custom Checkbox 2
☐ Custom Checkbox 3
☐ Reset on Connect

Sheet name to post to: (reload after renaming) Simple Data

	A	B	C	D
1	Date	Time	Voltage(V)	UV intensity（mW/cm^2
2	9/29/2019	12:06:29 PM	1.32	2.63
3	9/29/2019	12:06:30 PM	1.34	2.73
4	9/29/2019	12:06:31 PM	1.45	3.62
5	9/29/2019	12:06:32 PM	3.29	18.07
6	9/29/2019	12:06:33 PM	1.53	
7	9/29/2019	12:06:34 PM	1.52	
8	9/29/2019	12:06:35 PM	1.53	
9	9/29/2019	12:06:36 PM	1.55	
10	9/29/2019	12:06:37 PM	1.43	
11	9/29/2019	12:06:38 PM	1.56	
12	9/29/2019	12:06:39 PM	1.59	
13	9/29/2019	12:06:40 PM	1.57	
14	9/29/2019	12:06:41 PM	1.58	
15	9/29/2019	12:06:42 PM	1.56	
16	9/29/2019	12:06:43 PM	1.56	
17	9/29/2019	12:06:44 PM	1.56	
18	9/29/2019	12:06:45 PM	1.56	
19	9/29/2019	12:06:46 PM	1.56	
20	9/29/2019	12:06:47 PM	1.57	

A	B	C	D
Date	Time	Voltage(V)	UV intensity（mW/cm^2
9/29/2019	12:06:29 PM	1.32	2.63
9/29/2019	12:06:30 PM	1.34	2.73
9/29/2019	12:06:31 PM	1.45	3.62
9/29/2019	12:06:32 PM	3.29	18.07
9/29/2019	12:06:33 PM	1.53	4.21
9/29/2019	12:06:34 PM	1.52	4.19
9/29/2019	12:06:35 PM	1.53	4.27
9/29/2019	12:06:36 PM	1.55	4.38

Figure 8 Data logging in excel directly

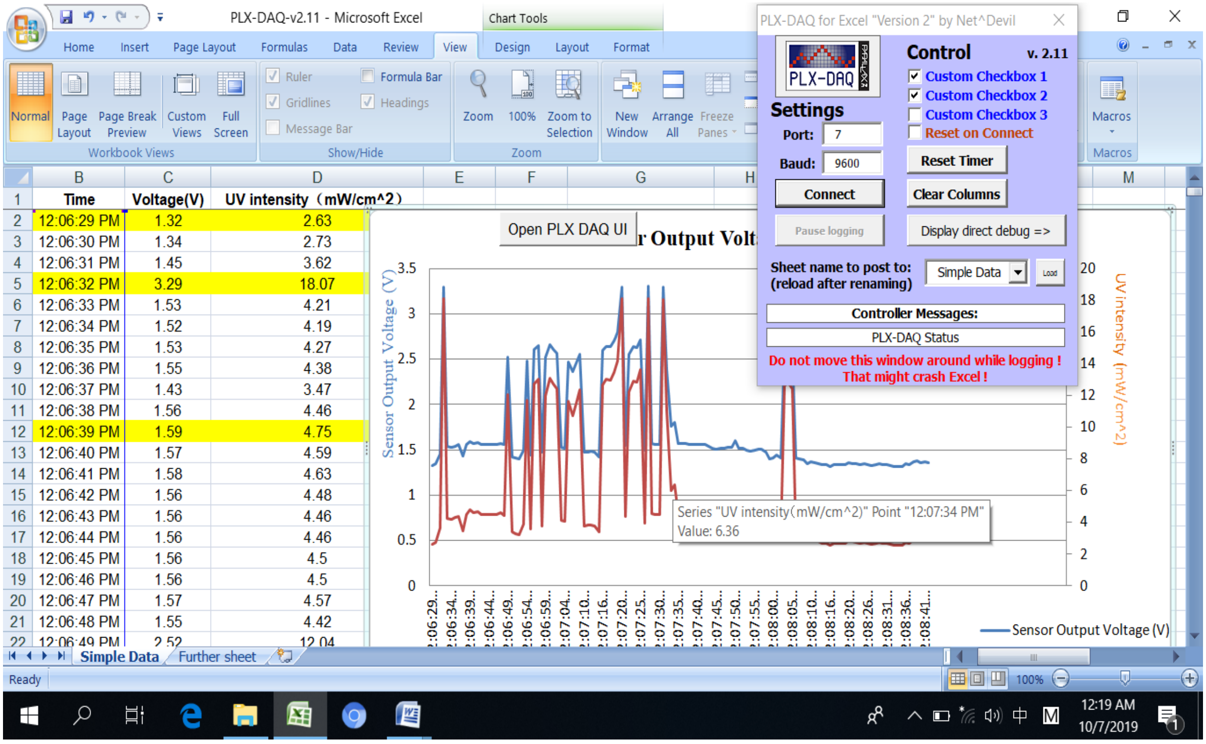

	B	C	D
1	Time	Voltage(V)	UV intensity（mW/cm^2）
2	12:06:29 PM	1.32	2.63
3	12:06:30 PM	1.34	2.73
4	12:06:31 PM	1.45	3.62
5	12:06:32 PM	3.29	18.07
6	12:06:33 PM	1.53	4.21
7	12:06:34 PM	1.52	4.19
8	12:06:35 PM	1.53	4.27
9	12:06:36 PM	1.55	4.38
10	12:06:37 PM	1.43	3.47
11	12:06:38 PM	1.56	4.46
12	12:06:39 PM	1.59	4.75
13	12:06:40 PM	1.57	4.59
14	12:06:41 PM	1.58	4.63
15	12:06:42 PM	1.56	4.48
16	12:06:43 PM	1.56	4.46
17	12:06:44 PM	1.56	4.46
18	12:06:45 PM	1.56	4.5
19	12:06:46 PM	1.56	4.5
20	12:06:47 PM	1.57	4.57
21	12:06:48 PM	1.55	4.42
22	12:06:49 PM	2.52	12.04

Series "UV intensity(mW/cm^2)" Point "12:07:34 PM"
Value: 6.36

PLX-DAQ for Excel "Version 2" by Net^Devil

Control v. 2.11

☑ Custom Checkbox 1
☑ Custom Checkbox 2
☐ Custom Checkbox 3
☐ Reset on Connect

Settings

Port: 7
Baud: 9600

Connect | Reset Timer | Clear Columns | Pause logging | Display direct debug =>

Sheet name to post to: (reload after renaming) Simple Data

Controller Messages:
PLX-DAQ Status

Do not move this window around while logging !
That might crash Excel !

Figure 9 Graph drawn in excel

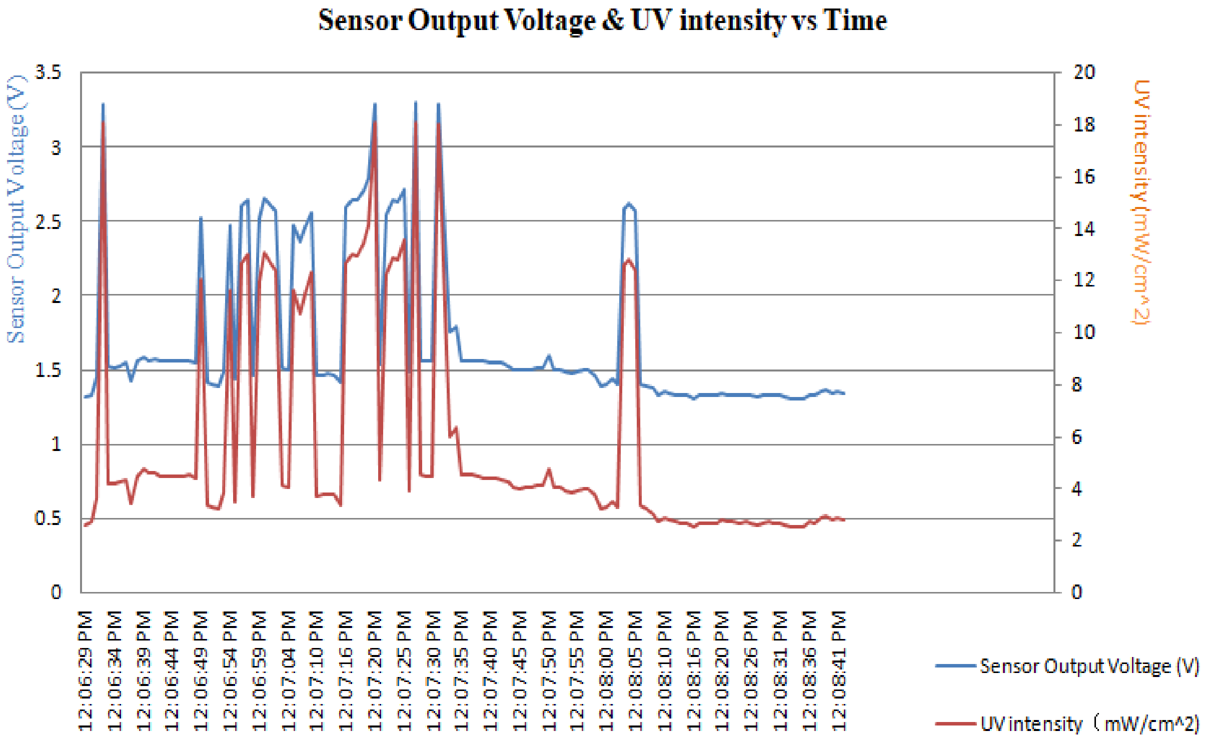

Figure 10 Graph of sensor output voltage and UV intensity

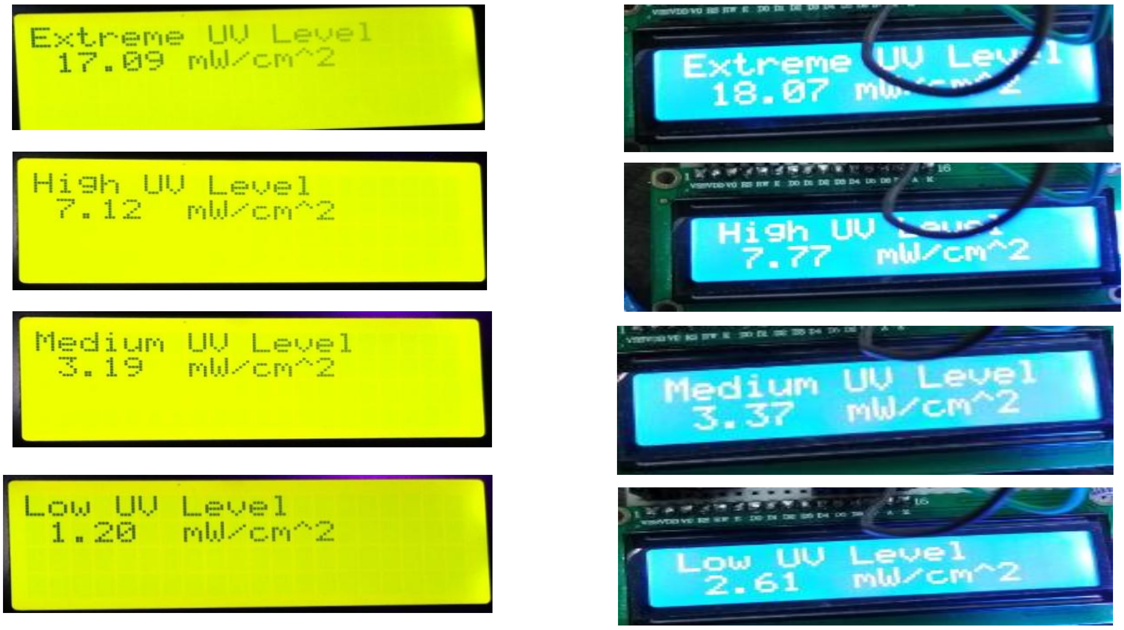

(a) (b)

Figure 11(a) UV level testing with touch light **(b)** UV level testing from sunlight

Conclusion

UV sensor which is the surface mount type package is very susceptible to heat in reflow mounting and humidity absorbed in storage. Do not press or rub the surface of the resin covering the top of the package where, which is on the UV-ray is light received. In addition, do not apply pressure at high temperature. This UV Index meter can be a valuable tool in protecting from the harmful effects of the Sun's rays.

Acknowledgements

I am highly grateful thanks Professor Dr Khin Khin Win, Head of Department of Physics, and Professor Dr Myo Lwin, Professor Dr Aye Aye Thant, Professor Dr Yin Maung Maung, Department of Physics, University of Yangon and Professor Dr Ye Chan, Head of Universities' Research Center, Professor Dr Than Zaw Oo, Universities' Research Center, University of Yangon, for their permission to do and their encouragement throughout this paper. I would like to express appreciation to Rector Dr Phoe Kaung, Pro-rector Dr Ohnmar Kyaw, Dr Thaung Htaik, University of Yangon for their encouragement and kind permission to undertake the present research. I also would like to thank Professor Dr Ohn Than (Rtd.), Department of Physics, Kyauk Se University for help during this work.

References

Banzi M, (2009) *Getting Started with Arduino*. U.S.A.

Boxall J, (2013) *Arduino Workshop*. San Francisco, No Starch Press.

Haigh, Joanna D, (2007) *The Sun and the Earth's Climate: Absorption of solar spectral radiation by the atmosphere*. U.S.A.

NASA Science, (2009) *Reference Solar Spectral Irradiance: Air Mass*. U.S.A.

Purdun J, (2012) *Beginning C for Arduino Apress*. New York.

Wackern M, Holick M F (2013) *Sunlight and Vitamin D*. U.S.A.

J. Myanmar Acad. Arts Sci. 2020 **Vol. XVIII.No.2B**

PREPARATION AND CAPACITANCE PROPERTIES OF BARIUM, CALCIUM AND TIN DOPED STRONTIUM TITANATE THIN FILMS

May Kalayar Kyaing[1], Amy Aung[2], Moht Moht Than[3], San San Oo[4] and Hnin Yu Wai[5]

Abstract

Sol-gel method was used in this study to prepare barium, calcium and tin doped strontium titanate thin films deposited onto silicon substrates by spin-coating technique. The effects of the dopant materials on the structural and capacitance properties of the films were examined by various characterization procedures. Morphological analysis of the samples was performed using scanning electron microscopy and all the films were found to be well grown and homogeneous structure. The structural modification was investigated by X-ray diffraction and the crystalline phases of the films were observed to be cubic perovskite structure. Measurements of capacitance-voltage characteristics were carried out by using LCR meter in the frequency range of 1 kHz to 100 kHz with the various applied voltages. From Mott-Schottky analysis, built in potential "V_{bi}", effective dopant concentration "N_D" and depletion layer width "W" of the films were also evaluated.

Keywords: Sol-gel, Doped strontium titanate, Capacitance-voltage measurements

Introduction

In the coming years, capacitors will be increasingly fabricated into microelectronic substrates in some manner since there are clear benefits in functional density, performance, and reliability relative to surface mount discretes [Woong Choi. et al., (2010)]. The main questions to be resolved involve the choice of materials, configurations, and fabrication processes to implement integrated capacitors in a cost effective manner. The purpose of this article is to compare and contrast, for integrated capacitor applications, the two major classes of dielectric materials: paraelectrics and ferroelectrics, respectively [Victor Williams, R., (2015)]. First, the mechanisms of charge storage are briefly reviewed for the two classes in order to elucidate the differences in fabrication options, electrical performance, and the effects of operational conditions such as temperature, bias, frequency, and film thickness [Malic, B. et al., (2007)]. Then, the two types of dielectrics are compared, based on these physical and electrical properties, for use in the integrated capacitor applications of decoupling, analog functions, and termination. It will be shown that the fundamental difference in the way the two materials store charge is very important to their respective suitability for these applications [S. Maletica and D. Maleticb, (2014)]. It will also be shown that selecting the dielectric with the largest k is not always the optimal choice. The ability of a dielectric material to store energy under the influence of an electric field results from the separation and alignment of electric charges brought about by that field. The larger the dipole moment arm the separation of charges in the direction of the field, and the larger the number of these dipoles, the higher the material's dielectric constant [Jae-Yeol Hwang et al., (2006)]. There are several possible contributions to this polarizability which, depending on the mechanisms operative in a given dielectric, determine not only the value of k, but also how it varies with frequency, temperature, bias, impurity concentration, and crystal

---

[1] Dr, Assistant Lecturer, Department of Physics, University of Yangon

[2] Assistant Lecturer, Department of Physics, University of Yangon

[3] Associate Professor, Department of Physics, Mohnyin Degree College

[4] Assistant Lecturer, Department of Physics, University of Yangon

[5] Assistant Lecturer, Department of Physics, University of Yangon

structure. The three general mechanisms important to candidate materials for integrated capacitors are electronic, atomic, and ionic polarization [F. M. Pontes et al., (2000)].

Strontium titanate in the perovskite structure exhibits high charge storage capacity, good insulating properties and excellent optical transparency in the visible region. Thus it is a potential material for a wide range of electronic and optical applications, such as dielectric thin film memory capacitors in microwave integrated circuits, dynamic random access and insulating layers for limiting current in thin film electroluminescent displays [Xiaoyong Wei and Xi Yao, (2007)]. In the present research, the influence of doping by the barium, calcium and tin ions on the capacitance properties of the strontium titanate thin films were examined. In order to understand the study of changes in the structural and electrical properties of the films that arise as a result of the incorporation of different cations is essential.

Experimental Procedure

The perovskite samples of barium, calcium and tin doped strontium titanate were prepared by conventional solid state reaction method and the starting materials were SrO, TiO_2, BaO, CaO and SnO_2. All the powders were having more than 99% purity and the stoichiometric composition of the $SrBaTiO_3$, $SrCaTiO_3$ and $SrSnTiO_3$ powders were thoroughly mixed in an agate mortar to obtain the homogeneity. The mixed powders were calcinated at 700 °C for 1 hr. Each mixture of the powders was mixed with 2-methoxyethanol ($CH_3OCH_2CH_2OH$) solution and then heated up to 100°C with indirect heat treatment for 1 hr. Finally, homogeneous precursor solutions or coating solutions were obtained. The silicon substrates were cleaned by standard cleaning method and the resulting precursor solutions were deposited on silicon substrates by spin coating technique. After spin coating, deposited thin films were heat treated at 700°C for 1hr. The surface morphologies of the films were studied using scanning electron microscope (SEM) and the crystallographic properties of the films were investigated by X-ray diffractiometer. Measurement of capacitance was carried out using LCR Meter in a frequency range of (1 kHz- 100 kHz) for the three $SrTiO_3$ thin films with different doping materials.

Results and Discussion

Surface Morphology and Microstructure

The surface morphologies of the thin films deposited on silicon substrates were examined by using SEM with accelerating voltage 15 kV and photo magnification 5,500. SEM images of the Ba, Ca and Sn doped $SrTiO_3$ thin films are shown in Figure 1 (a-c). All the films showed the formation of uniformly distributed microcrystalline grains over the entire surface of the substrates. According to the result, it was observed that calcium doped strontium titanate thin film has the smallest grain size. In this Ca^{2+} has smaller ionic radius than Sr^{2+} and the grain sizes of the film depend on the dopant materials incorporated into the structure. The average grain sizes of the films were estimated using the line intercept method and the determined values were collected in Table 1.

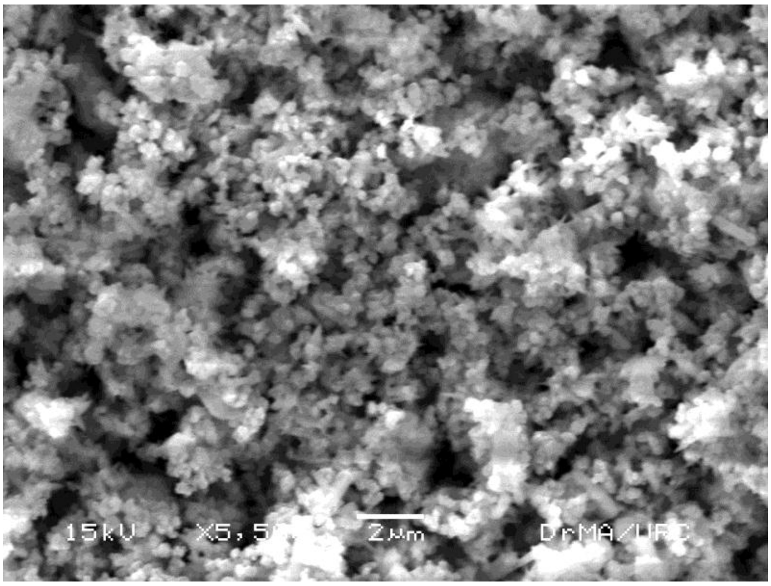

Figure 1 (a) SEM image of barium doped strontium titanate thin film

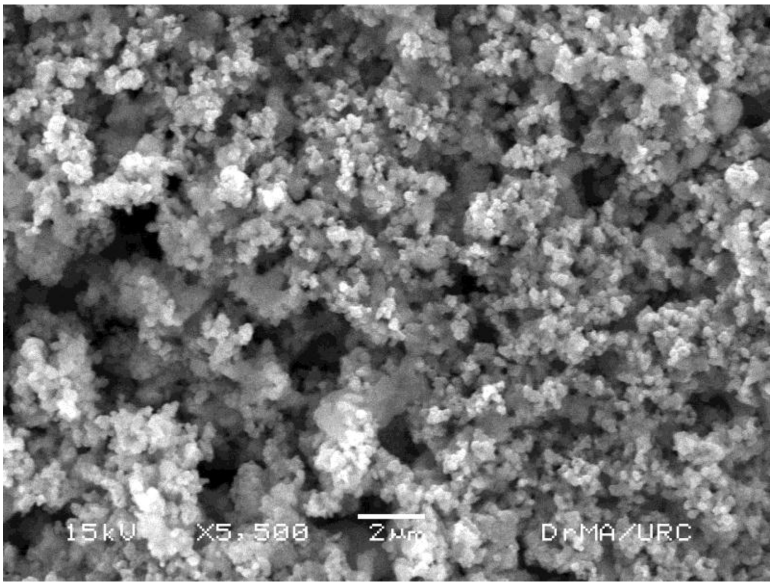

Figure 1 (b) SEM image of calcium doped strontium titanate thin film

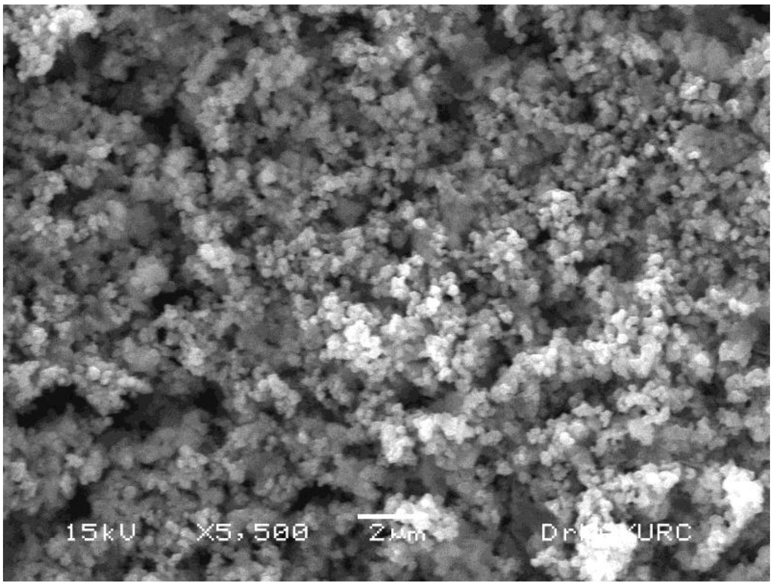

Figure 1 (c) SEM image of tin doped strontium titanate thin film

Table 1 Grain sizes of the Ba, Ca and Sn doped $SrTiO_3$ thin films

Thin Film	Average Grain Size (μm)
Ba doped $SrTiO_3$	0.475
Ca doped $SrTiO_3$	0.350
Sn doped $SrTiO_3$	0.413

Crystallographic Structure

The crystallographic structures of the thin films were determined by X-ray diffraction and Figure 2 show the XRD patterns of barium, calcium and tin doped strontium titanate thin films. XRD was usually used for identification of the crystalline nature and estimation of the crystallite size. The variation in the lattice parameters of doped strontium titanate thin films with the change in dopant materials may be attributed to the change in ionic radius. From the investigation of dopant materials, XRD analysis indicated that all deposited films are cubic perovskite structure. Average crystallite sizes were calculated based on widening the diffraction using Scherrer's formula,

$$D = \frac{0.9\lambda}{\beta cos\theta} \qquad (1)$$

where D is the crystallite size(nm), λ is the wavelength of the X-ray source (1.59 nm), B is the full-width at half maximum (FWHM) in radians, and θ is half of the diffraction angle. The results showed that the widening the diffraction pattern was influenced by the crystallite size, where the wider diffraction pattern indicated the smaller crystallite size. The average crystallite sizes were determined using the diffraction peaks with preferred orientation at (110) planes. The determined crystallite sizes are shown in Table 2.

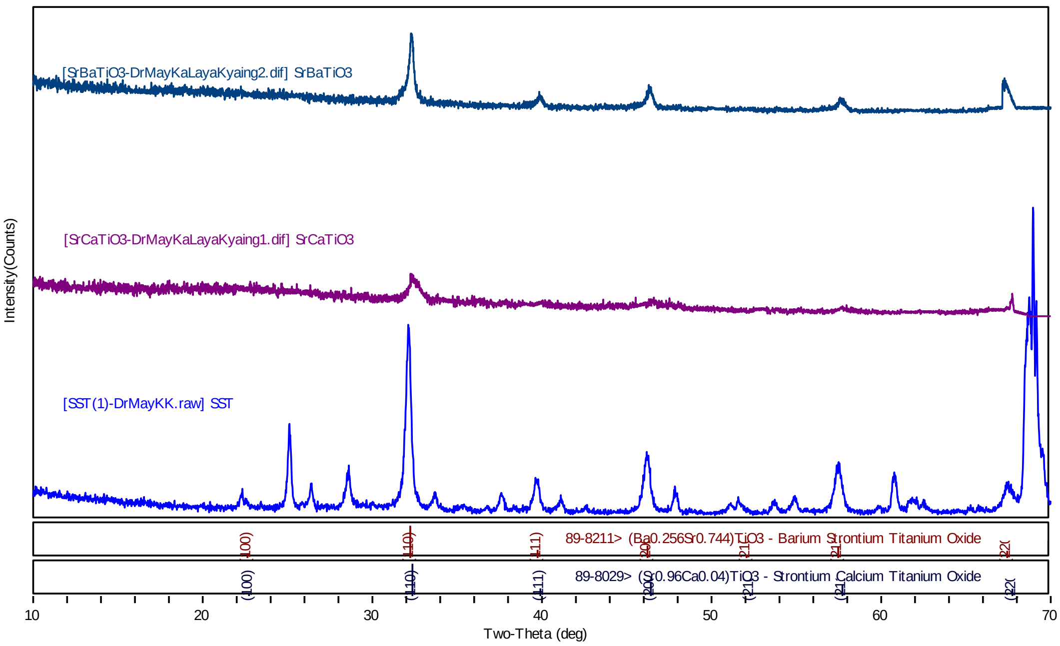

Figure 2 X-ray diffraction patterns of barium, calcium and tin doped strontium titanate thin films

Table 2 The peak positions (2θ), intensity, full width half maximum (FWHM), lattice parameters (a) and average crystallite sizes (D) of the thin films at (110) plane

Thin Film	Peak position (2θ)	Intensity (cps)	FWHM	a (nm)	D(nm)
Ba doped $SrTiO_3$	32.311	277	0.390	3.915	21.2081
Ca doped $SrTiO_3$	32.320	108	0.560	3.914	14.782
Sn doped $SrTiO_3$	32.135	724	0.368	3.935	22.467

Capacitance Properties

The capacitance-voltage (C-V) measurements as a tool of analyzing the electrical properties of the films were examined by a LCR Meter at the frequency range of 1 kHz to 100 kHz. The maximum capacitance value was occurred at the tin doped strontium titanate thin film at a frequency of 1 kHz. Figure (3) shows the frequency dependence of the capacitance of the thin films and the measured values are presented in Table 3. The capacitance-voltage characteristics are useful in obtained information about the potential barrier at the junction, the semiconductor doping density and the presence of traps in materials. Figure 4 (a-c) shows the 1/C^2 versus V graphs for Ba, Ca and Sn doped $SrTiO_3$ thin films. Measurement of “C” as a function of applied voltage can be used to determine the built - in voltage and the dopant concentration near the junction. According to equation (2),

$$C = A\left[\frac{q\varepsilon_s}{2(V_{bi}-V)}N_D\right]^{1/2} \qquad (2)$$

a plot of $1/C^2$ as a function of V is a straight line whose intercept on the voltage axis gives V_{bi}, and the slope can be used to determine the effective dopant concentration N_D. The depletion layer capacitance associated with a Schottky device is given by equation (3),

$$\frac{1}{C^2} = \frac{2(V_{bi} - V)}{A^2 q \varepsilon_s N_D} \qquad (3)$$

where "N_D" is the effective dopant concentration, "A" is the diode area, "V_{bi}" is the built in voltage and "ε_S" is the permittivity of the diffusion layer. The value of depletion layer width "W" was given by equation (4),

$$W = \frac{\varepsilon_s A}{C} \qquad (4)$$

The values of V_{bi}, N_D, and W of the thin films are summarized in Table 4.

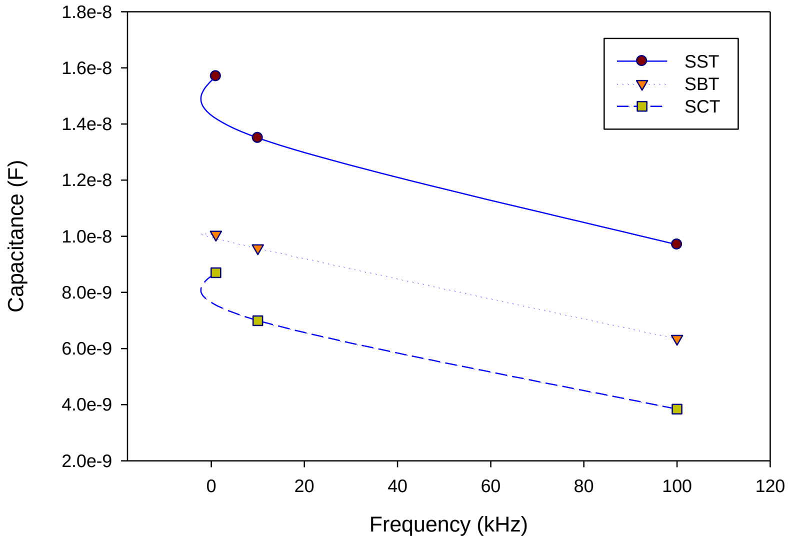

Figure 3 Frequency dependence of the capacitance of Ba, Ca and Sn doped $SrTiO_3$ thin films

Table 3 The capacitance values of the thin films as a function of frequency

Thin film	f(1 kHz)	Capacitance (nF) f(10 kHz)	f(10 kHz)
Ba doped $SrTiO_3$	10.06	9.58	6.35
Ca doped $SrTiO_3$	8.70	6.99	3.84
Sn doped $SrTiO_3$	15.70	13.54	9.70

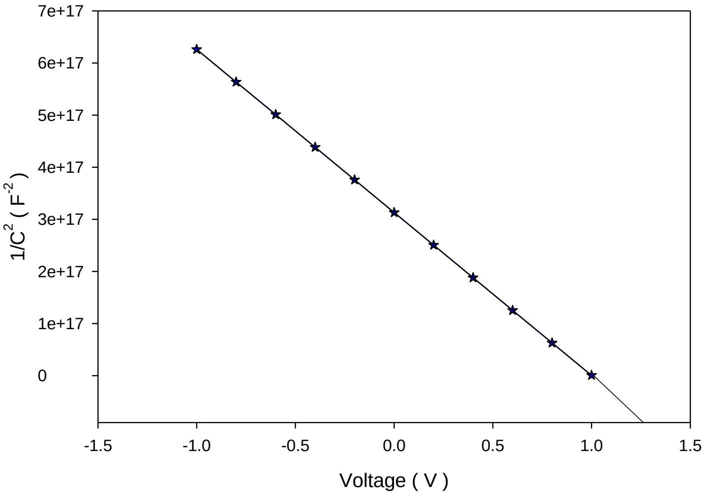

Figure 4 (a) $1/C^2$ versus V characteristics of Ba doped $SrTiO_3$ thin film

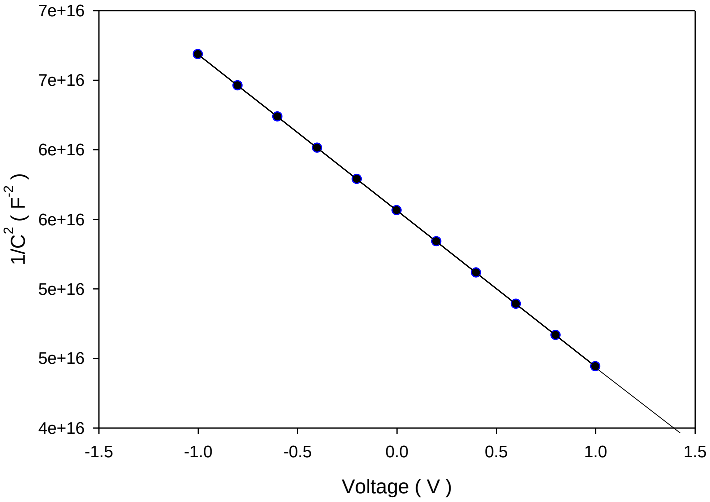

Figure 4 (b) $1/C^2$ versus V characteristics of Ca doped $SrTiO_3$ thin film

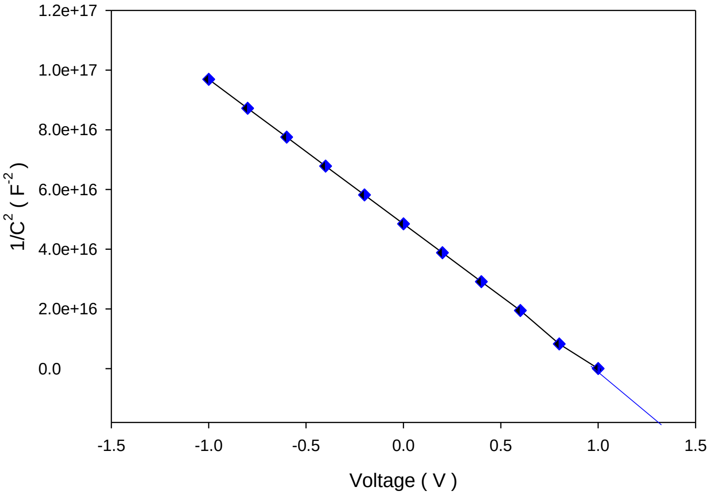

Figure 4 (c) $1/C^2$ versus V characteristics of Sn doped $SrTiO_3$ thin film

Table 4 The values of V_{bi}, N_D, and W of Ba, Ca and Sn doped $SrTiO_3$ thin films

Thin Film	V_{bi} (V)	$N_D(cm^{-3})$	W (cm)
Ba doped $SrTiO_3$	1.2574	8.81×10^{14}	10.11×10^{-4}
Ca doped $SrTiO_3$	1.3872	1.96×10^{14}	10.08×10^{-4}
Sn doped $SrTiO_3$	1.2598	2.43×10^{15}	10.09×10^{-4}

Conclusions

Barium, calcium and tin doped strontium titanate thin films deposited onto silicon substrates were prepared by sol-gel method. Morphological analysis of the samples was performed using scanning electron microscopy and all the films showed the compact structures which composed of small and densely packed microcrystals. The structural modification was investigated by X-ray diffraction and all the crystallographic planes and orientations were expressed with reference to the cubic perovskite unit cells. Measurements of capacitance-voltage characteristics were carried out by using LCR meter in the frequency range of 1 kHz to 100 kHz with the various applied voltages. From Mott-Schottky analysis, built in potential "V_{bi}", effective dopant concentration "N_D" and depletion layer width "W" of the films were also evaluated. According to the results of good characteristics and electrical properties, Ba, Ca and Sn doping effects on $SrTiO_3$ are useful for selecting materials in the manufacturing of technological applications.

Acknowledgements

The authors sincerely thank Professor Dr Khin Khin Win, Head of Department of Physics, University of Yangon, for her kind permission to carry out this research. I would like to express my sincere thanks to Dr Myo Lwin, Professor, Department of Physics, Dr Ye Chan, Professor and Head, Universities' Research Center, Dr Aye Aye Thant, Professor, Department of Physics, Dr Yin Maung Maung, Professor, Department of Physics and Dr Than Zaw Oo, Professor, Universities' Research Center, University of Yangon, for their permission to this paper.

References

F. M. Pontes et al., (2000), "High dielectric constant of $SrTiO_3$ thin films prepared by chemical process," *Journal of Material Science*, 35, 4783 - 4787

Jae-Yeol Hwang et al., (2006) " Dielectric Properties of Artificially Textured $(Ba_{0.5}Sr_{0.5})TiO_3$ Thin Film Prepared by Pulsed Laser Deposition," *Journal of the Korean Physical Society*," 49, 447- 696

Malic, B. et al., (2007) "Processing and dielectric characterization of $Ba_{0.3}Sr_{0.7}TiO_3$ Thin Films" *Journal of the European Ceramic Society*, 27, 2945-2948

S. Maletica) and D. Maleticb, (2014) "Dielectric and infrared properties of SrTiO3 single crystal doped by 3d (V, Mn, Fe, Ni) and 4f (Nd, Sm, Er) ions" *Chinese Physical Society and IOP*, 23, 026102

Victor Williams, R., (2015) "Structural and Electrical behavior of Tin Doped $Ba_{0.6}Sr_{0.4}TiO_3$ Thin Films," *International Journal of Development Research*, 5, 5725-5732

Woong Choi et al.,(2010),"Capacitance-voltage characteristics of SrTiO3 /LaVO3 epitaxial heterostructures ," *Applied Physics Letters*, 96, 212903

Xiaoyong Wei and Xi Yao, (2007) "Preparation, structure and dielectric property of barium stannate titanate ceramics," *Materials Science and Engineering B*, 137, 184-188

J. Myanmar Acad. Arts Sci. 2020 **Vol. XVIII.No.2B**

STRUCTURAL AND ELECTRICAL PROPERTIES OF Ba DOPED $CaTiO_3$ THIN FILMS

San San Oo[1], May Kalayar Kyaing[2], Hnin Yu Wai[3], Saw Moh Moh Oo[4]
and Myat Wut Yee Han[5]

Abstract

Calcium titanate and barium doped calcium titanate, $Ca_{1-x}Ba_xTiO_3$ (x = 0.1, 0.2, 0.3) thin films deposited onto silicon substrates were prepared by spin coating technique. The prepared undoped and Ba doped $CaTiO_3$ thin films were studied by various characterization techniques aimed at understanding the structural and electrical properties of the samples. These films were characterized by a smooth surface with uniform, crack-free microstructure and densely packed, which is in agreement with the scanning electron microscopy (SEM) analysis. The effect of composition on the phase formation of these samples was investigated by recording X-ray diffraction patterns (XRD) and it was observed that the lattice parameter varied with increasing the dopant concentration of barium. The dielectric constants of all the films were determined by a capacitance-voltage measurement using a LCR meter in the frequencies range of (0.1 kHz to 100 kHz).

Keywords : Calcium titanate thin films, SEM, XRD, Capacitance-voltage

Introduction

Calcium titanate ($CaTiO_3$) is one of a group of metal titanate compounds with a perovskite structure $CaTiO_3$ has long been known as a ceramic dielectric with a high dielectric constant and large positive temperature coefficient. Electroceramics based on $CaTiO_3$ has been studied various physical properties by a number of researchers [T. Bongkran and W. Khiawwangthong,(2008)]. Physical properties of $CaTiO_3$ that have been studied including electrical properties, especially electrical conductivity, while the optical properties were widely studied including the nature of the absorption of UV-Vis and photoluminescence performance.

Perovskite materials have been extensively studied due to a wide range of low-temperature structural distortions. These structures have become fundamental interests in physics in technological applications such as microwave devices and phase transitions [W. Sun, Y. et al., (2010)].

The $CaTiO_3$ based solid solution can also be applied as high performance capacitors. $CaTiO_3$ has an important application in microwave communication systems. $CaTiO_3$ also be used as an electronic ceramic material in particular as ferroelectric materials and dielectric materials in general. $CaTiO_3$ has an orthorhombic structure and it has a dielectric permittivity of approximately 180 at room temperature that changes with experimental conditions[E. Cockayne, B.P. Burton, (2000)].

They usually undergo several phase transitions with increase in temperature and pressure. It is utilized in the construction of field devices and sensors for the study of rheology of earth mantle and in the electroceramic industry [Xiaoyong Wei and Xi Yao,(2007)]. The dopants

---

[1] Dr, Assistant Lecturer, Department of Physics, University of Yangon

[2] Assistant Lecturer, Department of Physics, University of Yangon

[3] Assistant Lecturer, Department of Physics, University of Yangon

[4] Assistant Lecturer, Department of Physics, University of Yangon

[5] Assistant Lecturer, Department of Physics, Pinlon University

induce polarization giving rise to lattice distortion in this compound. So far only a handful amount of crystallographic data for $CaTiO_3$ with different dopants is available in the literature. Generally it is revealed that crystal structure of $CaTiO_3$ is orthorhombic which confirmed by X-ray diffraction experiments [P. Boutinaud, E. Tomasella, A. Ennajdaoui, R. Mahiou, (2006)].

In the present study, synthesis of pure $CaTiO_3$ as well as doped with Ba on B-Site has been carried out through conventional solid-state reaction method. The effect of Ba content on the structural, morphological and electrical properties of the $CaTiO_3$ thin films were studied.

Experimental Details

Calcium titanate, $CaTiO_3$ and barium doped calcium titanate, $Ca_{1-x}Ba_xTiO_3$ (x = 0.1, 0.2, 0.3) thin films were synthesized by solid state reaction method, using high purity CaO, BaO and TiO_2 powders. These powders were weight on the basis of stoichiometric composition. The resultant, stoichiometric composition of the mixed powders were ground by agate mortar to obtain the homogeneity and the mixed powders were annealed at 700°C for 1 hour. Each powder was mixed with 2-methoxyethanol ($CH_3OCH_2CH_2OH$) solution and then heated up to 100˚C with indirect heat treatment for 1hr. Finally, homogeneous precursor solutions or coating solutions were obtained. The silicon substrates were cleaned by standard cleaning method. The resulting precursor solutions were deposited on silicon substrates by spin coating technique. After spin coating, deposited thin films were heat treated at 700˚C for 1hr. The surface morphology and the thickness of the films were analyzed by scanning electron microscope (SEM). The phase and crystallinity of the films were characterized by X-ray diffraction (XRD) analysis with Cu-$K_{\propto 1}$ radiation. The capacitance- voltage measurements and the dielectric properties of the films were carried by using LCR meter.

Results and Discussion

SEM Analysis

The surface morphology and the cross sectional view of the undoped and barium doped calcium titanate thin films were evaluated using SEM as shown in Fig 1 (a-h). These results showed a well-developed grain size and dense microstructure in all samples. The values of the average grain sizes and thickness of the thin films were presented in Table 1. The average grain size increases with the increasing of barium content. The effect of doping on grain size is usually interpreted in terms of dopant solubility and distribution of doping ions between the surface and interior parts of the grain.

Table 1 The values of the average grain sizes and thickness of the undoped and barium doped calcium titanate thin films

Thin films	Average Grain Size (μm)	Thickness (μm)
Undoped $CaTiO_3$	0.35	7.5
10% Ba doped $CaTiO_3$	0.41	9.4
20% Ba doped $CaTiO_3$	0.42	9.1
30% Ba doped $CaTiO_3$	0.48	5.9

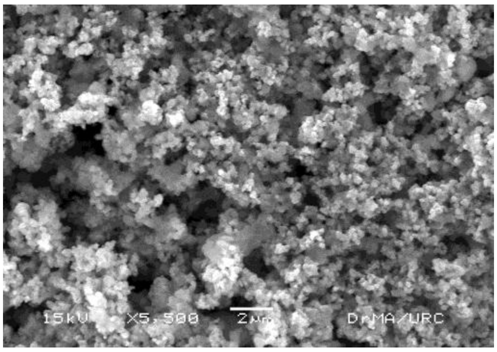

Figure 1 (a) SEM image of CT thin film

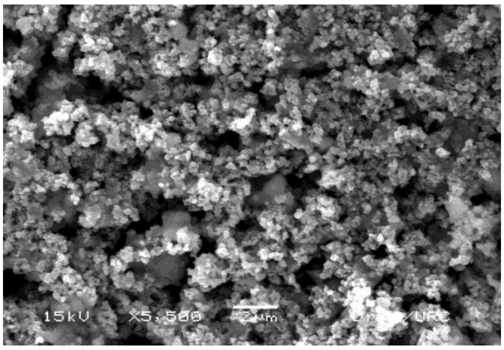

Figure 1 (b) SEM image of 10% Ba doped CT thin film

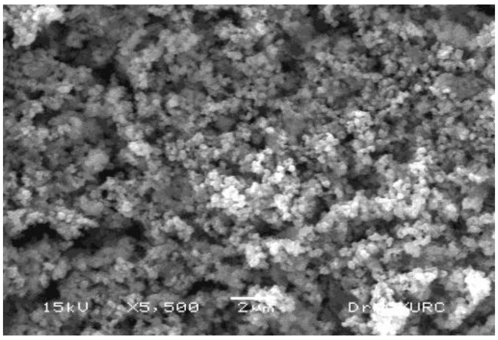

Figure 1(c) SEM image of 20% Ba doped CT thin film

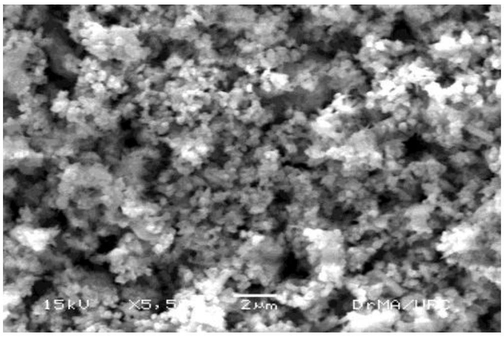

Figure 1 (d) SEM image of 30% Ba doped CT thin film

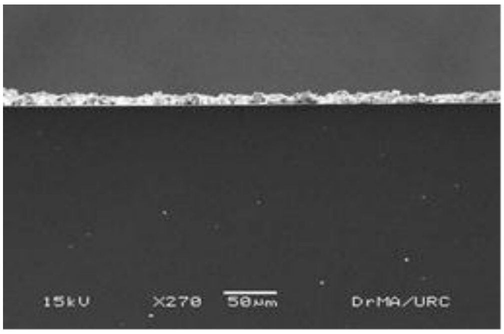

Figure 1 (e) Cross sectional image CT thin film

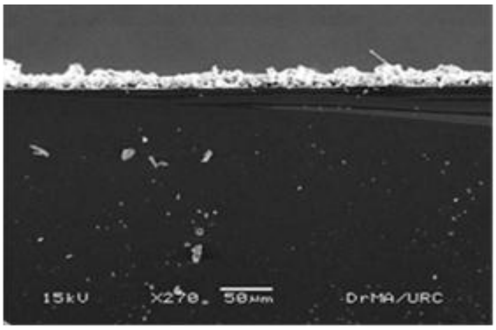

Figure 1 (f) Cross sectional image 10% Ba doped CT thin film

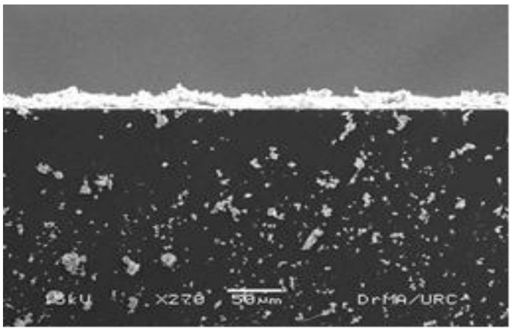

Figure 1 (g) Cross sectional image 20% Ba Ba doped CT thin film

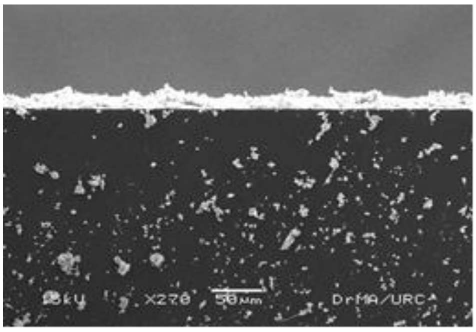

Figure 1 (h) Cross sectional image 30% doped CT thin film

X-ray Diffraction (XRD) Analysis

Structural properties of Ba doped $CaTiO_3$ samples were studied by X-ray diffraction from which can be determined the crystal phase and crystallite size of $CaTiO_3$ samples. Fig. 2(a-d) show the X-ray diffraction pattern for the $CaTiO_3$ samples with different dopant concentration of barium. There were significant differences in the diffraction patterns of each sample indicating that the dopant material affects the structural properties of the samples. XRD characterization was conducted to obtain the information both quantitatively and qualitatively on the crystal structure of $CaTiO_3$. Based on the diffraction pattern can be determined the crystal phases and crystallite sizes of $CaTiO_3$ samples. The samples were scanned from ($2\theta = 27.624 - 48.010$) using XRD machine with Cu source which has a wavelength of 0.154 nm. Widening the diffraction pattern is influenced by the crystallite size, where the wider diffraction pattern indicates the smaller crystallite size. Average crystal size (ACS) can be calculated based on widening the diffraction peaks using Scherrer formula by the equation below

$$D = \frac{0.9\lambda}{\beta \cos\theta}$$

The peak position, full width half maximum (FWHM) and crystallite sizes (D) of $CaTiO_3$ and barium doped calcium titanate, $Ca_{1-x}Ba_xTiO_3$ (x = 0.1, 0.2, 0.3) thin films are listed in Table 2.

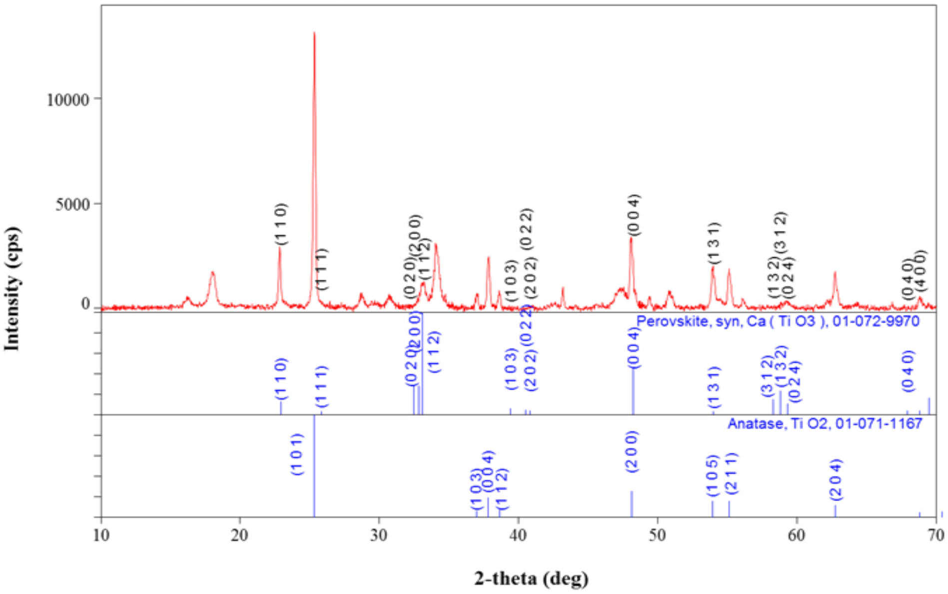

Figure 2 (a) X-ray diffraction of $CaTiO_3$ thin film

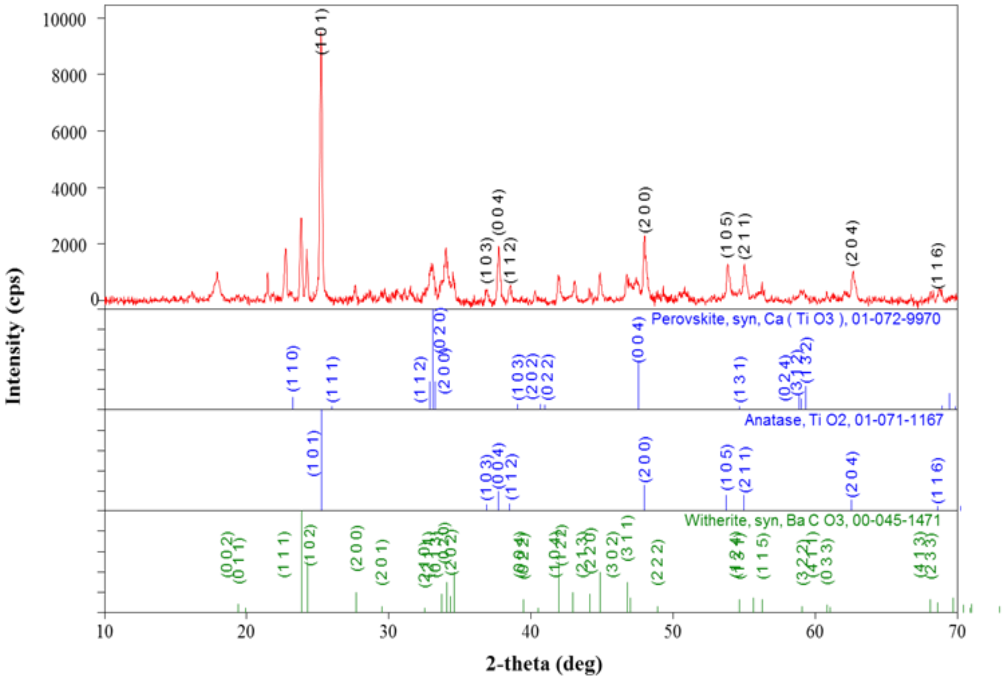

Figure 2 (b) X-ray diffraction of 10% Ba doped $CaTiO_3$ thin film

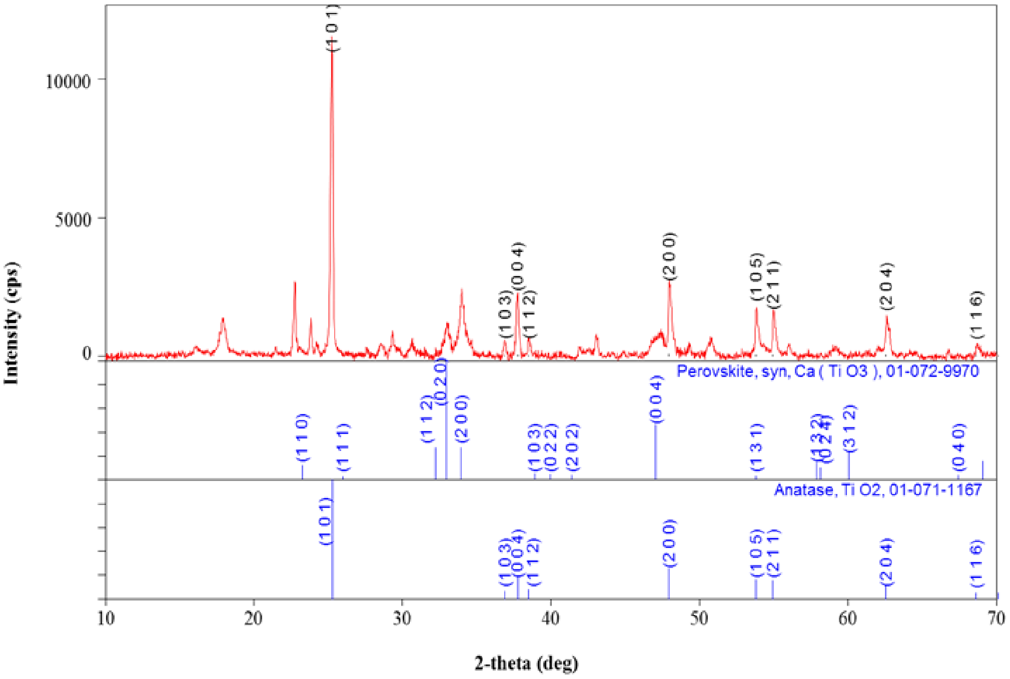

Figure 2 (c) X-ray diffraction of 20% Ba doped $CaTiO_3$ thin film

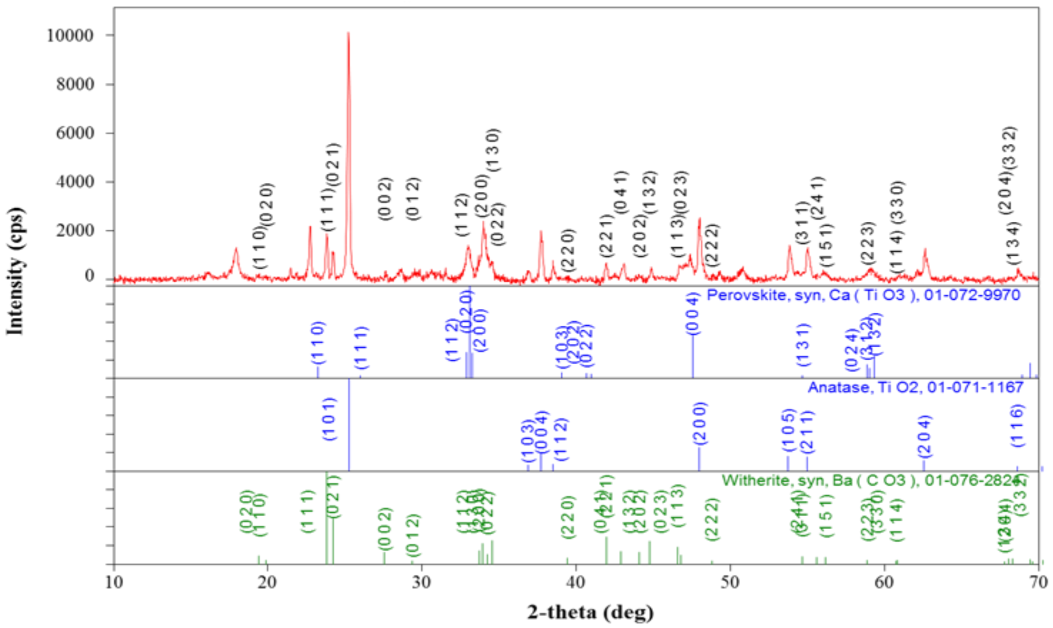

Figure 2 (d) X-ray diffraction of 30% Ba doped $CaTiO_3$ thin film

Table 2 The peak positions (2θ), full width half maximum (FWHM), lattice parameters and crystallite sizes (D) of undoped and Ba doped $CaTiO_3$ thin films at (200) plane

Thin Films	**(hkl) plane**	**Peak positions (2 θ)**	**FWHM**	**Lattice parameter**	**D (nm)**
Undoped $CaTiO_3$	(200)	33.111	0.48	a = 5.4501 b = 5.5129 c = 7.5388	17.267
10% Ba doped $CaTiO_3$	(200)	34.010	0.416	a = 5.2790 b = 5.5523 c = 7.7190	19.971
20% Ba doped $CaTiO_3$	(200)	48.010	0.145	a = 5.3850 b = 5.4965 c = 7.6692	59.999
30% Ba doped $CaTiO_3$	(200)	27.624	0.120	a = 5.3805 b = 5.4819 c = 7.6918	68.184

Dielectric Properties

The dielectric constants of undoped and barium doped calcium titanate, $Ca_{1-x}Ba_xTiO_3$ ($x = 0.1, 0.2, 0.3$) thin films were evaluated from capacitance-voltage measurements at the frequency range of 0.1 kHz to 100 kHz. Dielectric constant (ε) can be calculated by the equations below,

$$C_0 = \varepsilon_0 A/t,$$
$$\varepsilon = C/C_0$$

where

C = capacitance using the material as the dielectric in the capacitor,
C_0 = capacitance using vacuum as the dielectric
ε_0= Permittivity of free space (8.85×10^{-12} F/m)
A = Area of the plate/ sample cross section area
t = Thickness of the sample

The maximum value of dielectric constant was occurred at the 10% barium doped calcium titanate thin film measured in a frequency range of 0.1 kHz. The frequency dependence of the dielectric constants for undoped and barium doped calcium titanate thin films are shown in Fig 3 (a & b) and the results are listed in Table 3.

Table 3 The values dielectric constant of undoped and Ba doped $CaTiO_3$ thin film as a function of frequency

Thin Films	Dielectric Constant			
	f = 0.1 kHz	f =1kHz	f = 10kHz	f = 100kHz
Undoped $CaTiO_3$ thin film	433.8983	271.7186	258.3050	111.7694
10% Ba doped $CaTiO_3$ thin film	735.8434	573.3333	310.1333	273.3333
20% Ba doped $CaTiO_3$ thin film	451.3189	407.3928	373.8757	105.36497
30% Ba doped $CaTiO_3$ thin film	430.3290	392.3163	347.3092	101.1065

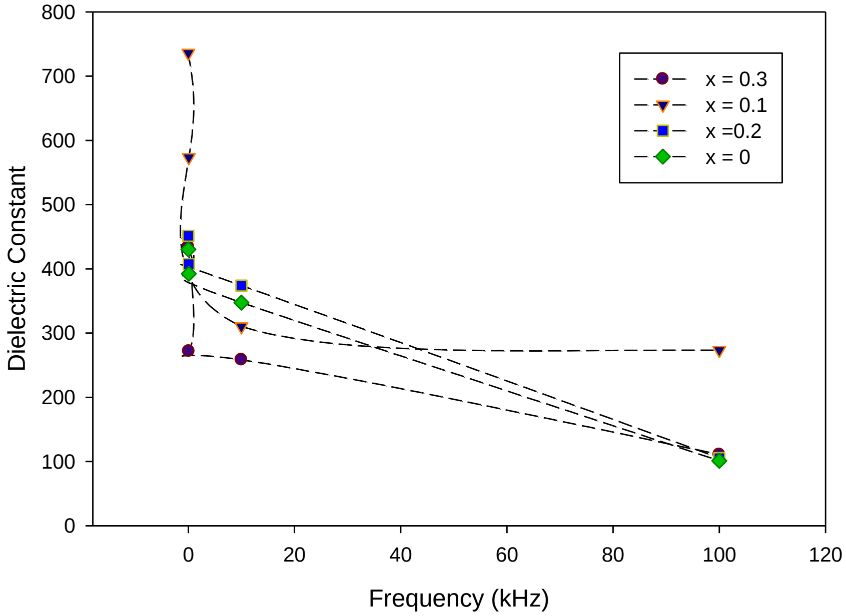

Figure 3 (a) The dependence of dielectric constant of the $CaTiO_3$ thin films as a function of frequency

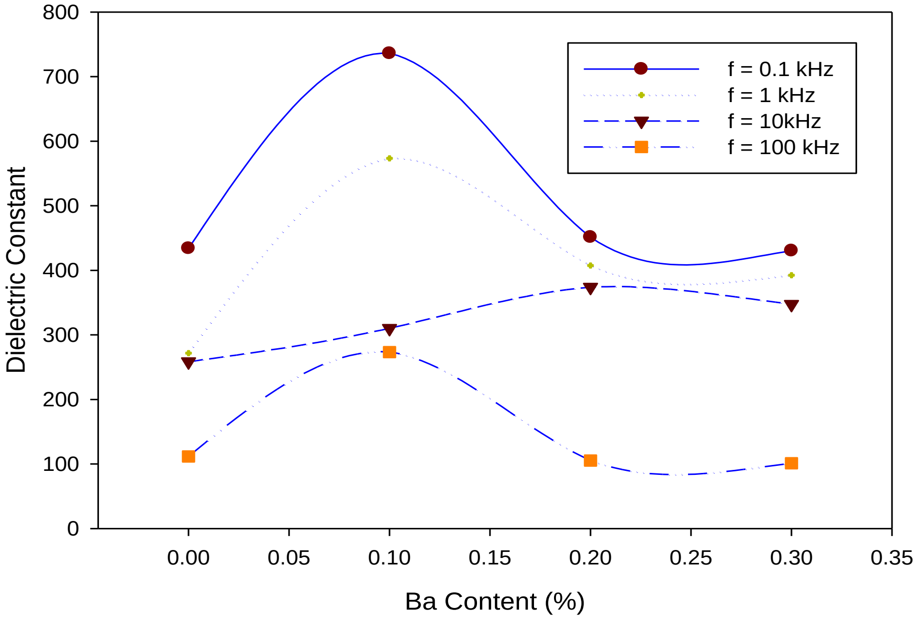

Figure 3 (b) The dependence of dielectric constant of the $CaTiO_3$ thin films on the Ba content

Conclusions

Calcium titanate, $CaTiO_3$ and barium doped calcium titanate, $Ca_{1-x}Ba_xTiO_3$ (x=0.1, 0.2, 0.3) thin films were successfully synthesized by the sol-gel method. SEM results showed the existence of well-developed grain sizes and dense microstructures in all samples. The average grain size increases with the increasing of barium content. XRD patterns indicated that all the films were well crystallized and orthorhombic perovskite structure. The lattice parameters were slightly increased with the increasing of barium content. The dielectric constants of all the films were determined by a capacitance-voltage measurement and the maximum value of dielectric constant was occurred at the 10% barium doped calcium titanate thin film measured in a frequency range of 0.1 kHz. These results showed that the morphological, structural and electrical properties of the films were dependent on the barium concentrations.

Acknowledgements

The authors sincerely thank Professor Dr Khin Khin Win, Head of Department of Physics, University of Yangon, for her kind permission to carry out this research.

I would like to express my sincere thanks to Dr Myo Lwin, Professor, Department of Physics, Dr Ye Chan, Professor and Head, Universities' Research Center, Dr Aye Aye Thant, Professor, Department of Physics, Dr Yin Maung Maung, Professor, Department of Physics and Dr Than Zaw Oo, Professor, Universities' Research Center, University of Yangon, for their permission to this paper.

References

E. Cockayne, B.P. Burton, (2000) "Phonons and static dielectric constant in $CaTiO_3$ from first principles," *Phys. Rev. B* , 62 , 3735-3743

P. Boutinaud, E. Tomasella, A. Ennajdaoui, R. Mahiou, (2006) "Structural characterization and luminescent properties of $CaTiO_3$:Pr3þ thin films deposited by radio frequency sputtering," *Thin Solid Films,* 515 2316-2321

T. Bongkran and W. Khiawwangthong, (2008) "The Preparation of Barium Stannate Titanate Ceramics via Solid State Reaction Method," *Advanced Materials Research*, 57, 181-184

W. Sun, Y. et al., (2010), "$CaTiO_3$:Eu3þ layers coated SiO2 particles: core-shell structured red phosphors for near-UV white LEDs," *J. Alloys Compd*, 493, 561-564

Xiaoyong Wei and Xi Yao, (2007) "Preparation, structure and dielectric property of barium stannate titanate ceramics," *Materials Science and Engineering B*, 137, 184-188

.

J. Myanmar Acad. Arts Sci. 2020 **Vol. XVIII.No.2B**

DERIVATIONS AND VISUALIZATIONS OF COSMOLOGICAL FLUID EQUATIONS

Zar Zar Myint Aung[1], Nyein Thida[2]

Abstract

The fundamental notion of fluid cosmology has been briefly studied. In order to derive various physical and geometrical aspects of mass, momentum, density and equation of state, it is essentially needed to make use of the governing equation frequently used in astrophysics and cosmology. Then, it has been known clearly in this research. Some interesting and informative visualization of the results are done with the help of Mathematica Software.

Keywords*: geometrical aspects of mass, momentum, density and equation of state*

Introduction

Fluid dynamics is one of the most important of all areas of physics life as we know it would not exist without fluids. The air we breathe and the water we drink (and which makes up most of our body mass) are fluids. Motion of air keeps us comfortable in a warm room, and air provides the oxygen we need to sustain life. Similarly, most of our (liquid) body fluids are water based. It is clear that fluids are completely necessary for the support of carbon based life forms. [Brown, J. D., etal (1994)]

The three main approaches to the study of fluid dynamics:

(i) Theoretical,

(ii) Experimental and

(iii) Computational.

Fluid Properties

There are two main classes of fluid properties: transport properties and physical properties. Three basic transport properties are viscosity, thermal conductivity and mass diffusivity. The physical properties are density and pressure, both of which might be viewed as thermodynamic properties, especially in the context of fluids. [Batchelor George, K., (1967)]

The viscosity is a measure of the resistance of a fluid which is being deformed by either shear stress or tensile stress. In everyday terms viscosity is "thickness" or "internal friction". Viscosity describes a fluid's internal resistance to flow and may be thought of as a measure of fluid friction with the exception of super fluids, all real fluids have some resistance to stress and therefore are viscous.

Thermal conductivity is the transport property that mediates diffusion of heat through a substance in a manner analogous to that already discussed in considerable detail with respect to viscosity and momentum. Thermal energy, so thermal conductivity provides an indication of how quickly thermal energy diffuses through a medium. Fourier’s law of heat conduction,

---

[1] Dr, Demonstrator, Department of Physics, Lashio University

[2] Dr, Associate Professor, Department of Physics, University of Yangon

$$q = -k\frac{dT}{dy} \tag{1}$$

where, q = heat flux.

k = thermal conductivity.

$\frac{dT}{dy}$ = component of the temperature gradient in the y direction

The Fundamental Fluid Dynamics Equations

The equations of fluid dynamics are best expressed via conservation laws for the conservation of mass, momentum and energy.

Conservation of Mass

We consider the rate of change of mass within a fixed volume. This the changes as a result of the mass flow through the bounding surface.

$$\frac{\partial}{\partial t}\int_v \rho dV = -\int_s \rho V_i n_i ds \tag{2}$$

Using the divergence theorem,

$$\frac{\partial}{\partial t}\int_V \rho dV + \int_V \frac{\partial}{\partial x_i} \rho V_i n_i ds = 0 \tag{3}$$

$$\int_{\boldsymbol{V}} [\frac{\boldsymbol{\partial\rho}}{\boldsymbol{\partial t}} + \frac{\partial}{\partial x_i}(\rho V_i)]dV = 0 \tag{4}$$

The continuity equation, since the volume is arbitrary,

$$\frac{\boldsymbol{\partial\rho}}{\boldsymbol{\partial t}} + \frac{\partial}{\partial x_i}(\rho V_i) = 0 \tag{5}$$

Conservation of Momentum

We consider the rate of change of momentum within a volume. This decreases as a result of the flux of momentum through the bounding surface and increases as the result of body forces (in our case, gravity) acting on the volume.

Let Π_{ij} = Flux of component of momentum in the direction

f_i = Body force per unit mass

then,

$$\frac{\partial}{\partial t}\int_V \rho V_i dV = -\int_S \Pi_{ij}\, n_i\, dS + \int_V \rho f_i \,\mathrm{dV} \tag{6}$$

There is an equivalent way of thinking of Π_{ij} , which is often useful, and that is $\Pi_{ij}\, n_i\, dS$, is the ith component of the force exerted on the fluid exterior to S by the fluid interior to S.

Again using the divergence theorem,

$$\int_V [\frac{\partial}{\partial t}(\rho V_i) + \frac{\partial \Pi_{ij}}{\partial x_j}]dV = \int_V \rho f_i \,\mathrm{dV} \tag{7}$$

$$\frac{\partial}{\partial t}(\rho V_i) + \frac{\partial \Pi_{ij}}{\partial x_j} = \rho f_i \tag{8}$$

For gravity we use the gravitational potential

$$f_i = -\frac{\partial \emptyset_G}{\partial x_i} \tag{9}$$

For a single gravitating object of mass M,

$$\emptyset_G = -\frac{GM}{r} \tag{10}$$

And for a self-gravitating distribution,

$$\nabla^2 \emptyset_G = 4\pi G\rho \tag{11}$$

$$\emptyset_G = -G\int_{V'} \frac{\rho(x_i)}{|x_i - x_i'|} d^3x' \tag{12}$$

Where G is Newton’s constant of gravitation.

The momentum flux is composed of a bulk part plus a part resulting from the motion of particles moving with respect to the center of mass velocity of fluid (v_i). For a perfect fluid, we take ρ to be the isotopic pressure, then,

$$\Pi_{ij} = \rho V_i V_j + p\delta_{ij} \tag{13}$$

The equations of motion are then,

$$\frac{\partial}{\partial t}(\rho V_i) + \frac{\partial \Pi_{ij}}{\partial x_j} = \rho f_i \tag{14}$$

$$\frac{\partial}{\partial t}(\rho V_i) + \frac{\partial}{\partial x_j}\left(\rho V_i V_j + \rho\delta_{ij}\right) = -\rho\frac{\partial \emptyset_{ij}}{\partial x_i} \tag{15}$$

$$\frac{\partial}{\partial t}(\rho V_i) + \frac{\partial}{\partial x_j}\left(\rho V_i V_j\right) = -\rho\delta_{ij} - \rho\frac{\partial \emptyset_{ij}}{\partial x_i} \tag{16}$$

There is also another useful form for the momentum equation derived using the continuity equation

$$\frac{\partial}{\partial t}(\rho V_i) + \frac{\partial}{\partial x_i}\left(\rho V_i V_j\right) = V_i\frac{\partial \rho}{\partial t} + \rho\frac{\partial V_i}{\partial t} + V_j\frac{\partial}{\partial x_j}\left(\rho V_j\right) + \rho V_j\frac{\partial V_i}{\partial V_j} \tag{17}$$

$$= -V_i\left[\frac{\partial \rho}{\partial t} + \frac{\partial}{\partial x_j}\left(\rho V_j\right) + \left[\rho\frac{\partial V_i}{\partial t} + \rho V_j\frac{\partial V_i}{\partial V_j}\right]\right. \tag{18}$$

$$\frac{\partial}{\partial t}(\rho V_i) + \frac{\partial}{\partial x_i}\left(\rho V_i V_j\right) = \rho\frac{\partial V_i}{\partial t} + \rho V_j\frac{\partial V_i}{\partial V_j} \tag{19}$$

Hence, another form of the momentum equation is

$$\rho\frac{\partial V_i}{\partial t} + \rho V_j\frac{\partial V_i}{\partial x_j} = -\frac{\partial \rho}{\partial x_i} - \rho\frac{\partial \emptyset_G}{\partial x_i} \tag{20}$$

On dividing by the density,

$$\frac{\partial V_i}{\partial t} + V_j\frac{\partial V_i}{\partial x_i} = -\frac{1}{\rho}\frac{\partial \rho}{\partial x_i} - \frac{\partial \emptyset_G}{\partial x_i} \tag{21}$$

Conservation of Energy

We take the momentum equation in the form,

$$\rho \frac{\partial V_i}{\partial t} + \rho\, V_j \frac{\partial V_i}{\partial x_j} = -\frac{\partial p}{\partial x_i} - \rho \frac{\partial \emptyset_G}{\partial x_i} \tag{22}$$

Take the scalar products with the velocity,

$$\rho V_i \frac{\partial V_i}{\partial t} + \rho\, V_j V_i \frac{\partial V_i}{\partial x_j} = -V_i \frac{\partial p}{\partial x_i} - \rho V_i \frac{\partial \emptyset_G}{\partial x_i} \tag{23}$$

$$\rho \frac{\partial}{\partial t}[\tfrac{1}{2} V_i V_i] + \rho\, V_j \frac{\partial}{\partial x_j}[\tfrac{1}{2} V_i V_i] = -V_i \frac{\partial p}{\partial x_i} - \rho V_i \frac{\partial \emptyset_G}{\partial x_i} \tag{24}$$

$$\rho \frac{\partial}{\partial t}[\tfrac{1}{2} V^2] + \rho\, V_j \frac{\partial}{\partial x_j}[\tfrac{1}{2} V^2] = -V_i \frac{\partial p}{\partial x_i} - \rho V_i \frac{\partial \emptyset_G}{\partial x_i} \tag{25}$$

Before we use the continuity equation to move the ρ and ρV_ioutsides the differentiations. Now we can use the same technique to move them inside and we recover the equation.

$$\frac{\partial}{\partial t}[\tfrac{1}{2}\, \rho\, V^2] + \frac{\partial}{\partial x_j}[\tfrac{1}{2} \rho\, V_j V^2] = -V_i \frac{\partial p}{\partial x_i} - \rho V_i \frac{\partial \emptyset_G}{\partial x_i} \tag{26}$$

The aim of the following is to put the right hand side into some sort of divergence form. We consider the first term.

$$-V_i \frac{\partial p}{\partial x_i} = \rho k T V_i \frac{\partial s}{\partial x_i} - \rho V_i \frac{\partial h}{\partial x_i} \tag{27}$$

$$-V_i \frac{\partial p}{\partial x_i} = \rho k T V_i \frac{ds}{dt} - \rho k T \frac{\partial s}{\partial t} - \rho V_i \frac{\partial}{\partial x_i} \tag{28}$$

$$= \rho k T \frac{ds}{dt} - \frac{\partial \varepsilon}{\partial t} + h \frac{\partial \rho}{\partial t} - \rho V_i \frac{\partial h}{\partial x_i} \tag{29}$$

We now eliminate the $\frac{\partial \rho}{\partial t}$ term suing continuity.

$$\frac{\partial \rho}{\partial t} = -\frac{\partial}{\partial x_i}(\rho V_i) \tag{30}$$

And we obtain

$$-V_i \frac{\partial p}{\partial x_i} = \rho k T \frac{ds}{dt} - \frac{\partial \varepsilon}{\partial t} + h \frac{\partial}{\partial x_i} - \rho V_i \frac{\partial h}{\partial x_i} \tag{31}$$

$$-V_i \frac{\partial p}{\partial x_i} = \rho k T \frac{ds}{dt} - \frac{\partial \varepsilon}{\partial t} - \frac{\partial}{\partial x_i}(\rho h V_i) \tag{32}$$

The term

$$-\rho V_i \frac{\partial \emptyset_G}{\partial x_i} = -\frac{\partial}{\partial x_i}(\rho \emptyset_G V_i) + \emptyset_G \frac{\partial}{\partial x_i}(\rho V_i) \tag{33}$$

$$= -\frac{\partial}{\partial x_i}(\rho \emptyset_G V_i) + \emptyset_G \frac{\partial \rho}{\partial x_i} \tag{34}$$

$$= -\frac{\partial}{\partial x_i}(\rho \emptyset_G V_i) - \frac{\partial}{\partial t}(\rho \emptyset_G) + \rho \frac{\partial \emptyset}{\partial x_t} \tag{35}$$

When the gravitational potential is constant in time, $\frac{\partial \emptyset_G}{\partial t} = 0$

$$-\rho V_i \frac{\partial \emptyset}{\partial x_i} = -\frac{\partial}{\partial x_i}(\rho \emptyset_G V_i) - \emptyset_G \frac{\partial}{\partial x_i}(\rho \emptyset_G) \tag{36}$$

Hence the energy equation,

$$\frac{\partial}{\partial t}\left[\frac{1}{2}\rho V^2\right]+\frac{\partial}{\partial x_i}\left[\frac{1}{2}\rho V^2 V_j\right]=-V_i\frac{\partial p}{\partial x_i}-\frac{\partial \emptyset_G}{\partial x_i}(\rho V_i) \tag{37}$$

$$\frac{\partial}{\partial t}\left[\frac{1}{2}\rho V^2\right]+\frac{\partial}{\partial x_i}\left[\frac{1}{2}\rho V^2 V_j\right]=\rho kT\frac{ds}{dt}-\frac{\partial \varepsilon}{\partial t}-\frac{\partial}{\partial x_i}(\rho h V_i)-\frac{\partial h}{\partial x_i}(\rho\emptyset_G V_i)-\frac{\partial}{\partial t}(\rho\emptyset_G) \tag{38}$$

Bringing terms over to the left hand side;

$$\frac{\partial}{\partial t}\left[\frac{1}{2}\rho V^2+\varepsilon+\rho\emptyset_G\right]+\frac{\partial}{\partial x_j}\left[\frac{1}{2}\rho V^2 V_j+\rho h V_j+\rho\emptyset_G V_j\right]=\rho kT\frac{ds}{dt} \tag{39}$$

When the fluid is adiabatic

$$\rho kT\frac{ds}{dt}=0 \tag{40}$$

And we have the energy equation for a perfect fluid

$$\frac{\partial}{\partial t}\left[\frac{1}{2}\rho V^2+\varepsilon+\rho\emptyset_G\right]+\frac{\partial}{\partial x_j}\left[\frac{1}{2}\rho V^2 V_j+\rho h V_j+\rho\emptyset_G V_j\right]=0 \tag{41}$$

The total energy per unit volume is

$$E=\frac{1}{2}\rho V^2+\varepsilon+\rho\emptyset_G \tag{42}$$

$$\varepsilon := 1;\emptyset_G := 4$$

Show [Plot 3D [(1/2 ρ v^2+ε +$\rho\emptyset_G$), { ρ,-8 Pi,8Pi},{v,-6 Pi,6 Pi},Plot Points → 35, Axes →True, Axes Label → {"ρ", "v", "ε"}, Display Function → $ Display Function]]

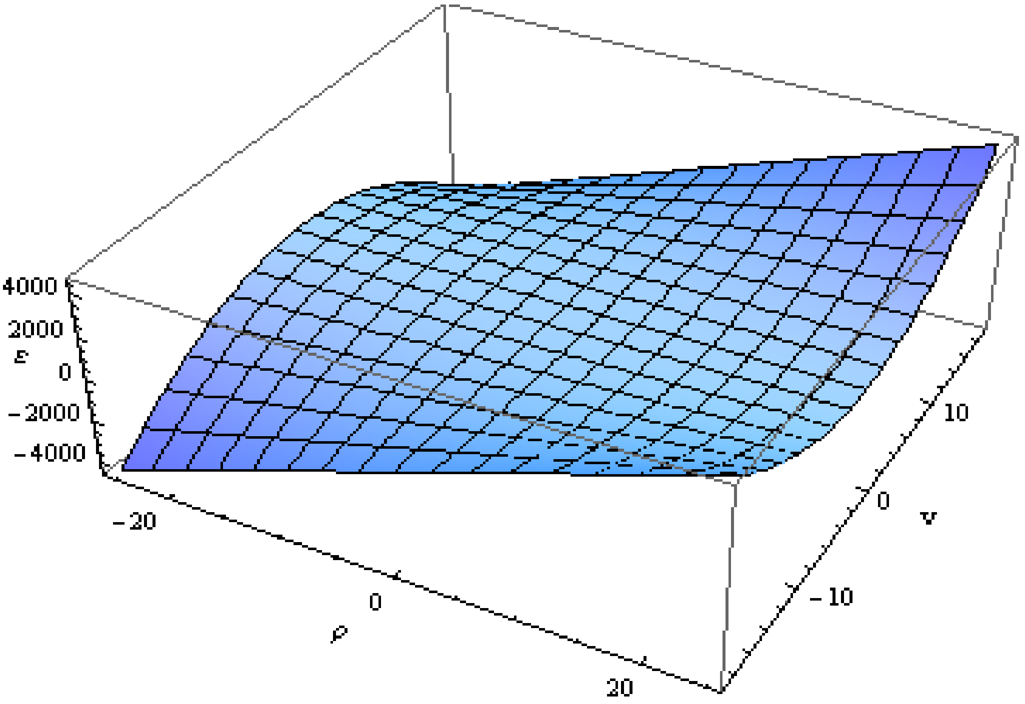

Figure 1 3D variation of energy with density and velocity.

Thermodynamic and its physical Properties

Thermodynamic

The thermodynamics of a volume element of fluid and the variables used to describe its state as

m=mass of element

ε = internal energy density per unit volume

p =pressure

S = entropy per unit mass

T =temperature (in degree Kelvin)

The second law of thermodynamic tells us that the change in entropy of mass of a gas is related to change in other thermodynamic variables as follows;

$$kTdS = dU + pdU \tag{43}$$

$$kTd(ms) = d\frac{m\varepsilon}{\rho} + pd\frac{m}{\rho} \tag{44}$$

$$kTds = d\left(\frac{\varepsilon}{\rho}\right) + pd(\frac{1}{\rho})$$

$$= \frac{1}{\rho}d\varepsilon - \left(\frac{\varepsilon+p}{\rho^2}\right)d\rho \tag{45}$$

Expanding the differentials and multiply by ρ ,

$$\rho kTds = d\varepsilon - \left(\frac{\varepsilon+p}{\rho^2}\right)d\rho \tag{46}$$

In terms of derivatives along the trajectory of the element

$$\rho kT\frac{ds}{dt} = \frac{d\varepsilon}{dt} - \left(\frac{\varepsilon+p}{\rho^2}\right)\frac{d\rho}{dt} \tag{47}$$

The equation of continuity

$$\frac{\partial\rho}{\partial t} + \frac{\partial}{\partial x_i}(\rho V_i) = 0 \tag{48}$$

$$\frac{\partial\rho}{\partial t} + V_i\frac{\partial\rho}{\partial x_i} + \rho\frac{\partial v_i}{\partial x_i} = 0 \tag{49}$$

can be expressed in the form

$$\frac{\partial V_i}{\partial x_i} = -\frac{1}{\rho}\frac{d\rho}{dt} \tag{50}$$

So that

$$\rho kT\frac{ds}{dt} = \frac{d\varepsilon}{dt} - (\varepsilon + p)\frac{\partial V_i}{\partial x_i} \tag{51}$$

Enthalpy

The care of an isotropic distribution function (perfect fluid) introduces the enthalpy density defined by

$$H = \varepsilon + p \tag{52}$$

And the specific enthalpy (enthalpy per unit mass),

$$h = \frac{\varepsilon+p}{\rho} \tag{53}$$

for a monatomic gas,

$$\varepsilon = \frac{3}{2}nkT \tag{54}$$

$$p = nkT \tag{55}$$

And $\rho = \mu n m_p$

Where μ the mean is molecular weight and m_p is the mass of a proton. Hence,

$$h = \frac{(\frac{3}{2}kT+nkT)}{\mu n m_p} \tag{56}$$

$$h = \frac{5}{2}\frac{kT}{\mu m_p} \tag{57}$$

using the specific enthalpy, the energy flux,

$$F_E = (\rho\frac{1}{2}V^2 + h + \emptyset)V_i \tag{58}$$

Specific Enthalpy

A commonly used thermodynamic variable is the specific enthalpy,

$$h = \frac{\varepsilon+p}{\rho} \tag{59}$$

In terms of the specific enthalpy, the equation,

$$kTds = d\left(\frac{\varepsilon}{\rho}\right) + pd(\frac{1}{\rho}) \tag{60}$$

becomes,

$$kTds = d\left(\frac{\varepsilon+p}{\rho}\right) - d(\frac{p}{\rho}) + pd(\frac{1}{\rho}) \tag{61}$$

$$kTds = dh - \frac{dp}{\rho} \tag{62}$$

After dividing by the time increment of a volume element,

$$\rho kT\frac{ds}{dt} = \frac{d\varepsilon}{dt} - \frac{(\varepsilon+p)}{\rho}\frac{d\rho}{dt} \tag{63}$$

$$kT\frac{ds}{dt} = \frac{dh}{dt} - \frac{1}{\rho}\frac{d\rho}{dt} \tag{64}$$

The fluid is adiabatic when there is no transfer of heat in or out of the volume element,

If $$kT\frac{ds}{dt} = 0 \tag{65}$$

$$\frac{d\varepsilon}{dt} - \frac{(\varepsilon+p)}{\rho}\frac{d\rho}{dt} = 0 \tag{66}$$

$$\frac{dh}{dt} - \frac{1}{\rho}\frac{d\rho}{dt} = 0 \tag{67}$$

The equation ds,dε, dp are prefect differentials and these relationships are valid relations from point to point within the fluid two particular relationships we shall use in the following are

$$\rho kT\frac{ds}{dt} = \frac{d\varepsilon}{dt} - h\frac{\partial\rho}{\partial t} \tag{68}$$

$$\rho kT\frac{\partial s}{\partial x_i} = \rho\frac{\partial h}{\partial x_i} - \frac{\partial\rho}{\partial x_i} \tag{69}$$

Equation of State

Consider the following form of the entropy, internal energy, pressure relation;

$$\rho kTds = d\varepsilon - \frac{(\varepsilon+p)}{\rho^2}d\rho \tag{70}$$

$$p = \frac{\rho kT}{\mu m_p} \tag{71}$$

Where,μ is the mean molecular weight.

$$p = (\gamma-1)\varepsilon \tag{72}$$

$$\varepsilon + p = \gamma\varepsilon$$

hence, $$\mu m_p(\gamma-1)\varepsilon ds = d\varepsilon - \frac{\gamma\varepsilon}{\rho}d\rho \tag{73}$$

$$\mu m_p(\gamma-1)\varepsilon ds = \frac{d\varepsilon}{\varepsilon} - \frac{\gamma}{\rho}d\rho \tag{74}$$

$$\mu m_p(\gamma-1)(s-s_0) = ln\varepsilon - \gamma ln\rho \tag{75}$$

$$\frac{\varepsilon}{\rho r} = \exp[\mu m_p(\gamma-1)(s-s_0)] \tag{76}$$

$$= \exp[\mu m_p(\gamma-1)s] \tag{77}$$

We can discard s_0 since the origin of entropy arbitrary. Therefore,

$$\varepsilon = \exp[\mu m_p(\gamma-1)s] \times \rho\gamma \tag{78}$$

$$p = (\gamma-1)\exp[\mu m_p(\gamma-1)s] \times \rho\gamma \tag{79}$$

$$p = k(s)\rho\gamma \tag{80}$$

The function k(s) is often referred to as the pseudo-entropy. For a completely ionized monatomic gas $\gamma = \frac{5}{3}$.

Table[Plot3D[Bessel1J[0,((ε+p)/ρ)],{ ρ,-2,2},{p,1,5}, Plot Range→{-0.5,1}, Plot Label →Row[{ “ε=”, padded Form[1* ε,1]}],Axes →True, Axes Label→ {“ ρ”, “p”, “ ε “ },Displayed Function Identity],{ ε,1,6}]//Short

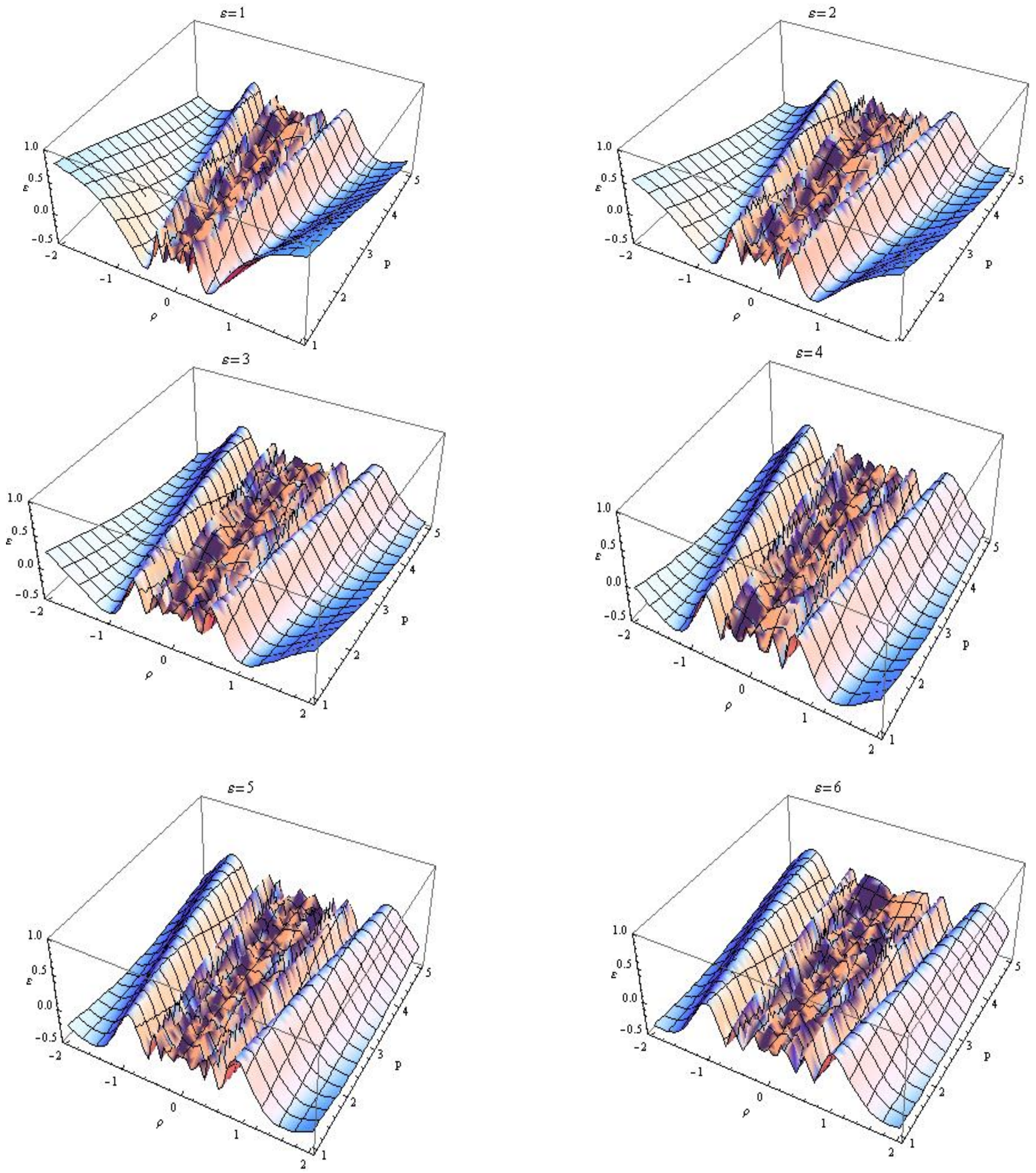

Figure 2 3D animated plot of specific enthalpy against density and pressure with ε from 1 to 6

Conclusion

We have attempted to provide an introduction to basic physics of fluid. The other various fluid properties, most of which are familiar with elemental physics and thermodynamics are carried out. Detailed computations of conservations of mass, momentum and energy are also presented. It is continued to probe the derivation of equation of state in very simple way. Next, the specific enthalpy which is commonly used in thermodynamics for the pressure or some other thermodynamic variable and the most natural is the entropy.

Acknowledgements

The author acknowledges the support of Professor Dr Khin Khin Win, Head of Department of Physics, University of Yangon. I wish to express I would like to express my deepest gratitude to my respectful Rector, Dr Kyaw Tun, Pro-rector Dr Yaw Han Htun and Pro-rector Dr Hla Hla Tin, Lashio University, for giving me a chance to write this research paper. Also, I would like to acknowledge Professor Dr Ko Ko Naing, Professor and head of Physics Department, Lashio University, for his valuable suggestion and comments for this paper.

References

Batchelor George, K., (1967) "Introduction to Fluid Dynamics" Cambridge: Cambridge University Press.

Brown, J. D., etal (1994) "In Physics Origins of Time Asymmetry" Cambridge : Cambridge University Press.

Kerr, R.P., (1963) "Gravitational Fied of a Spinning Mass as an Example of Algebraically Special Metrics" *Phys. Rev. Lett.11, 237-238.*

Peebles, P. J. E., etal (2003) "The Cosmological Constant and Dark Energy" *Rev. Mod Phys.* 75 559.

Tritton, D. J., (1990) "Physical Fluid Dynamics, 2nd Ed" Oxford: Oxford University Press.

Wheeler, J. A., (1990) "A Journey into Gravity and Spacetime" New York: Freeman.

----------------(1994) " In Physics Origins of Time Asymmetry" Cambridge : Cambridge University Press.

J. Myanmar Acad. Arts Sci. 2020 **Vol. XVIII.No.2B**

THE MICROSCOPIC CALCULATION OF THREE-NUCLEON SYSTEM

Htun Htun Oo[1], Aung Zaw Moe[2], Eaint Thae Khine[3]

Abstract

In this research, the Faddeev technique is applied to compute the ground state binding energy of three-**nucleon** system. Yukawa type malflit-Tjon potential is used for nucleon-nucleon interaction. The three-nucleon binding energy for s wave ($\ell = 0$) interaction is 7.538 MeV and for $\ell = 0,2$ the binding energy becomes 7.550 MeV.

Keywords: Fadeev, three-boson, T-matrix.

Introduction

Historically, the study of the three-body problems is decisive importance for nuclear physics. The bound state of three nucleons is still not understood since the nuclear interactions cannot be calculated rigorously from an underlying theory. Therefore test of similar basic nature still lie in the future. At present one uses purely phenomenological forces based on meson theory [Machleidt R,1989] and adjusts them to describe two-nucleon observables. The question is then whether these forces are also sufficient to describe three interacting nucleons or whether in addition three-nucleon forces are needed [Friar J.L, Gibson B.F, and Payne G.L, 1984]. Since the three-body Schrödinger equation can be solved numerically in a precise manner, the three-nucleon system plays a very significant role in answering that question. In the three-body problem one has to face the geometrical difficulty of a three-body, spin- and iso-spin degrees of freedom and the violent variation of the nuclear force at short distances which induces high momentum components into the wave function.

Some other approaches used to treat three-body systems are variational calculations [Delves L.M, 1972], the use of hyperspherical harmonics [Fabre de la Ripelle M,1987], and the Green's function Monte Carlo technique [Schmidt K.E, 1987]. The Faddeev equations have been discussed extensively [Glockle W, 1983]. We shall present only the momentum space treatment of Faddeev equation. The momentum space is the natural one if one uses field theoretical potentials like the OBEP(one-boson-exchange potential)[Holinde K, Machleidt R,1975].

The three- and four-body problems present an interesting challenge to do research. Therefore, we are interested in the three-nucleon system (triton). Before going to solve real ${}^{3}_{1}\mathrm{H}$ system, we will start with a simple system called three-boson system. In this case all three nucleons are considered as spinless particles. The real problem of three nucleons (triton) will be described in the following articles.

The Basic Definition for Three-Body System

In a three-body system there are three different two-body subsystems. We can choose one of them and if we choose the particle “1” as a spectator, only particle “2” and “3” will interact. There are relative motions of particle “1” to the center of mass position of the pair (2,3) and we call this state channel “1” and for example it is shown in Fig.(1).

---

[1] Dr, Associate professor, Department of Physics, Lashio University
[2] Dr, Lecturer, Department of Physics, Lashio University
[3] Demonstrator, Department of Physics, Lashio University

For channel “1”

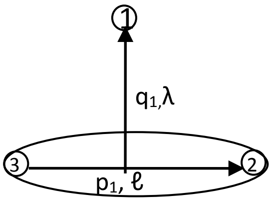

$\mathbf{k_1}$ = momentum of particle 1
$\mathbf{k}_2$= momentum of particle 2
$\mathbf{k}_3$= momentum of particle 3

Figure 1 Particle configuration for channel “1”.

For identical particles, m1=m2=m3 and therefore

$$\mathbf{p}_1 = \frac{1}{2}(\mathbf{k}_2 - \mathbf{k}_3) \,, \quad \mathbf{q}_1 = \frac{2}{3}\left\{\mathbf{k} - \frac{1}{2}(\mathbf{k}_2 + \mathbf{k}_3)\right\}$$

Generally, we can express for other channels as

$$\mathbf{p}_\mathrm{i} = \frac{1}{2}(\mathbf{k}_\mathrm{j} - \mathbf{k}_\mathrm{k}) \,, \quad \mathbf{q}_i = \frac{2}{3}\left\{\mathbf{k}_\mathrm{i} - \frac{1}{2}(\mathbf{k}_\mathrm{j} + \mathbf{k}_\mathrm{k})\right\} .$$

For the simplest case of three identical particles called bosons, we can write the state for channel “1” is $|\mathrm{pq}(\ell\lambda)\mathrm{LM}\rangle_1 \equiv |\mathrm{pq}\alpha\rangle_1$, where “p” is the relative momentum and “ℓ” is the relative orbital angular momentum of particle “2” and “3”, “q” is the relative momentum and “λ”is the orbital angular momentum of particle “1” with respect to the subsystem(2,3). The relative motion of three particles is conveniently described by Jacobi momenta.

$$\mathbf{p}_1 = \frac{\mathrm{m}_3\mathbf{k}_2 - \mathrm{m}_2\mathbf{k}_3}{\mathrm{m}_2 + \mathrm{m}_3} \,, \quad \mathbf{q}_1 = \frac{(\mathrm{m}_2 + \mathrm{m}_3)\mathbf{k}_1 - \mathrm{m}_1(\mathbf{k}_2 + \mathbf{k}_3)}{\mathrm{m}_1 + \mathrm{m}_2 + \mathrm{m}_3}$$

For identical particles,

$$\mathbf{p}_1 = -\frac{1}{2}\mathbf{p}_2 + \frac{3}{4}\mathbf{q}_2 \,, \quad \mathbf{q}_1 = -\mathbf{p}_2 - \frac{1}{2}\mathbf{q}_2 \,, \quad \mathbf{p}_1 = -\frac{1}{2}\mathbf{p}_3 - \frac{3}{4}\mathbf{q}_3 \,, \quad \mathbf{q}_1 = \mathbf{p}_3 - \frac{1}{2}\mathbf{q}_3$$

and their states are $|\mathrm{p}_1\mathrm{q}_1\rangle_1$, $|\mathrm{p}_2\mathrm{q}_2\rangle_2$ and $|\mathrm{p}_3\mathrm{q}_3\rangle_3$.

The two-body subsystem can be transformed by the permutation operators P12P23 and P13P23 as

$$P_{12}P_{23}|\mathrm{pq}\rangle_1 = P_{12}P_{23}(1{,}23) = (2{,}31) = |\mathrm{pq}\rangle_2 \,, \quad P_{13}P_{23}|\mathrm{pq}\rangle_1 = P_{13}P_{23}(1{,}23) = (3{,}12) = |\mathrm{pq}\rangle_3$$

The operators have to be evaluated in the same type of basis vectors such as

$${}_1\langle \mathbf{p_1q_1} | \mathbf{p_2q_2}\rangle_2 = {}_1\left\langle \mathbf{p_1q_1} \middle| -\frac{1}{2}\mathbf{p_2} + \frac{3}{4}\mathbf{q_2}, -\mathbf{p_2} - \frac{1}{2}\mathbf{q_2} \right\rangle_1$$

$${}_1\langle \mathbf{p_1q_1} | \mathbf{p_3q_3}\rangle_3 = {}_1\left\langle \mathbf{p_1q_1} \middle| -\frac{1}{2}\mathbf{p_3} - \frac{3}{4}\mathbf{q_3}, \mathbf{p_3} - \frac{1}{2}\mathbf{q_3} \right\rangle_1$$

Three-Body Faddeev Equations

The Faddeev equations [Faddeev L.D, 1961] have been proven to be very useful and we shall concentrate on them in this paper. The Faddeev equations transcribe the content of the Schrödinger equation in a unique manner into a set of three coupled equations.

The Schrödinger equation for a three-body system is

$$(H_0+\sum_{i=1}^{3}\mathrm{V}_i)\Psi=\mathrm{E}\Psi \tag{1}$$

where $V_i \equiv V_{jk}$, $\mathrm{i}\neq\mathrm{j}\neq\mathrm{k}$ (Interaction in two-body subsystem), H_0 is the kinetic energy of the relative motion for three particles.

The solution of Schrödinger equation is

$$\Psi=\frac{1}{\mathrm{E}-\mathrm{H}_0}\sum_{\mathrm{i}=1}^{3}\mathrm{V}_\mathrm{i}\Psi \tag{2}$$

$$\Psi=\mathrm{G}_0\sum_{\mathrm{i}=1}^{3}\mathrm{V}_\mathrm{i}\Psi \tag{3}$$

where $G_0 \equiv \dfrac{1}{E-H_0}$ and G0 is free three-body propagator. Ψ is decomposed into 3-components and these are called Faddeev components.

$$\Psi=\sum_{\mathrm{i}=1}^{3}\psi_\mathrm{i} \tag{4}$$

We define

$$\psi_\mathrm{i}\equiv\mathrm{G}_0\mathrm{V}_\mathrm{i}\Psi \tag{5}$$

Eq.(4) is inserted for Ψ on the right hand side in the Eq.(5),

$$\psi_\mathrm{i}=\mathrm{G}_0\mathrm{V}_\mathrm{i}\sum_{\mathrm{j}=1}^{3}\psi_\mathrm{j} \tag{6}$$

simply rearrange Eq.(6) and becomes

$$(1-\mathrm{G}_0\mathrm{V}_\mathrm{i})\psi_\mathrm{i}=\mathrm{G}_0\mathrm{V}_\mathrm{i}\sum_{\mathrm{j}\neq\mathrm{i}}\psi_\mathrm{j} \tag{7}$$

We can expand $(1-\mathrm{G}_0\mathrm{V}_\mathrm{i})^{-1}$ by using binomial theorem

$$(1-G_0V_i)^{-1}\,G_0V_i = (1+\mathrm{G}_0\mathrm{V}_\mathrm{i}+\mathrm{G}_0\mathrm{V}_\mathrm{i}\mathrm{G}_0\mathrm{V}_\mathrm{i}+---)\ \mathrm{G}_0\mathrm{V}_\mathrm{i}$$

$$=\mathrm{G}_0(\mathrm{V}_\mathrm{i}+\mathrm{V}_\mathrm{i}\mathrm{G}_0\mathrm{V}_\mathrm{i}+\mathrm{V}_\mathrm{i}\mathrm{G}_0\mathrm{V}_\mathrm{i}\mathrm{G}_0\mathrm{V}_\mathrm{i}+---)= G_0T_i$$

We define T_i as follow

$$\mathrm{T}_\mathrm{i}=\mathrm{V}_\mathrm{i}+\mathrm{V}_\mathrm{i}\mathrm{G}_0\mathrm{T}_\mathrm{i} \tag{8}$$

where T_i is the two-body T operator for the pair i.

The Eq.(7) becomes

$$\psi_i = G_0 T_i \sum_{j \neq i} \psi_j \tag{9}$$

If we expand

$$\psi_1 = G_0 T_1 (\psi_2 + \psi_3) \tag{10}$$

$$\psi_2 = G_0 T_2 (\psi_3 + \psi_1) \tag{11}$$

$$\psi_3 = G_0 T_3 (\psi_1 + \psi_2) \tag{12}$$

This is a set of 3-coupled equation called Faddeev equation. For identical particles, the three equations can be reduced to a single one by using permutation operators. Therefore, the Faddeev equation for three identical particles is

$$\psi = G_0 T P \psi \tag{13}$$

where, P is the permutation operator and it is defined as

$$P \equiv P_{12}P_{23} + P_{13}P_{23} \tag{14}$$

The Faddeev Equation in Momentum Space for Three-Boson System

We consider the Faddeev equation (ψ=G0TP ψ) in the momentum space representation. We project ψ on the three particle basis state $\langle pq(\ell\lambda)LM| \equiv \langle pq\alpha|$

$${}_1\langle pq\alpha|\psi\rangle_1 = {}_1\langle pq\alpha|G_0 TP\psi\rangle_1 \tag{15}$$

$${}_1\langle pq\alpha|\psi\rangle_1 = \frac{1}{E - \frac{p^2}{m} - \frac{3q^2}{4m}} \, {}_1\langle pq\alpha|TP\psi\rangle_1 \tag{16}$$

Then, we insert the completeness relation

$${}_1\langle pq\alpha|\psi\rangle_1 = \frac{1}{E - \frac{p^2}{m} - \frac{3q^2}{4m}} \sum_{\alpha'} \int p'^2 dp' \int q'^2 dq' \sum_{\alpha''} \int p''^2 dp'' \int q''^2 dq'' \; {}_1\langle pq\alpha|T|p'q'\alpha'\rangle_1$$

$${}_1\langle p'q'\alpha'|P|p''q''\alpha''\rangle_1 \, {}_1\langle p''q''\alpha''|\psi\rangle_1 \tag{17}$$

The two-body T-matrix term from the Eq.(17) must have the following condition

$${}_1\langle pq\alpha|T|p'q'\alpha'\rangle_1 = \frac{\delta(q-q')}{qq'} \delta_{\alpha\alpha'} t_\ell (p, p', E - \frac{3q^2}{4m}) \tag{18}$$

For ground state, one has L=0 and consequently $\ell = \lambda$ and first we consider the simplest case of pure s-wave interaction (ℓ =0). The Faddeev component from the Eq.(17) is defined as

$$\langle pq(\ell = 0, \lambda = 0, L = 0)\, M = 0 | \psi \rangle \equiv \psi(pq) \tag{19}$$

Evaluation of permutation operator P from the Eq.(17) is the purely geometrical problem.

$$_1\langle p'q'\alpha' | P | p''q''\alpha'' \rangle_1 = {}_1\langle p'q'\alpha' | (P_{12}P_{23} + P_{13}P_{23}) | p''q''\alpha'' \rangle_1 \tag{20}$$

$$_1\langle p'q'\alpha' | P | p''q''\alpha'' \rangle_1 = {}_1\langle p'q'\alpha' | p''q''\alpha'' \rangle_2 + {}_1\langle p'q'\alpha' | p''q''\alpha'' \rangle_3 \tag{21}$$

Again P13P23 = P23P12P23P23 and

$$_1\langle p'q'\alpha' | p''q''\alpha'' \rangle_3 = {}_1\langle p'q'\alpha' | P_{23}P_{12}P_{23}P_{23} | p''q''\alpha'' \rangle_1 \tag{22}$$

$$_1\langle p'q'\alpha' | p''q''\alpha'' \rangle_3 = (-1)^{\ell}\, {}_1\langle p'q'\alpha' | p''q''\alpha'' \rangle_2 (-1)^{\ell'} \tag{23}$$

For bosons both ℓ and ℓ' have to be even and therefore,

$$_1\langle p'q'\alpha' | p''q''\alpha'' \rangle_3 = {}_1\langle p'q'\alpha' | p''q''\alpha'' \rangle_2 \tag{24}$$

Therefore Eq.(21) can be written as

$$_1\langle p'q'\alpha' | P | p''q''\alpha'' \rangle_1 = 2\, {}_1\langle p'q'\alpha' | p''q''\alpha'' \rangle_2 \tag{25}$$

For $(\ell = 0)$

$$_1\langle p'q'\alpha' | p''q''\alpha'' \rangle_2 = \frac{1}{2} \int_{-1}^{1} dx \, \frac{\delta(p' - \pi_1)}{p^2} \, \frac{\delta(p'' - \pi_2)}{p''^2} \tag{26}$$

Then, Eq.(17) becomes

$$\psi(pq) = \frac{1}{E - \frac{p^2}{m} - \frac{3q^2}{4m}} \int q'^2 dq' \int_{-1}^{1} dx \, t_0\!\left(p, \pi_1, E - \frac{3q^2}{4m}\right) \psi(\pi_2 q') \tag{27}$$

This integral equation in two variables is the three-boson Faddeev equation for pure s-wave interaction.

Again we consider the ℓ up to two. Generally for any ℓ

$$\begin{aligned} {}_1\langle pq\alpha | p'q'\alpha' \rangle_2 = \delta_{LL'} & \sum_{\ell_1+\ell_2=\ell} \sum_{\ell'_1+\ell'_2=\ell'} (-)^{\ell'} (\tfrac{1}{2})^{\ell'_1+\ell_2+1} \sqrt{\hat{\ell}\hat{\ell}'\hat{\lambda}\hat{\lambda}'} \, \frac{(q)^{\ell_2+\ell'_2} (q')^{\ell_1+\ell'_1}}{(\pi_1)^{\ell} (\pi_2)^{\ell'}} \\ & \sqrt{\frac{\hat{\ell}!\hat{\ell}'!}{(2\ell_1)!(2\ell_2)!(2\ell'_1)!(2\ell'_2)!}} \sum_f \sum_{f'} \begin{Bmatrix} \ell_1 & \ell_2 & \ell \\ \lambda & L & f \end{Bmatrix} \begin{Bmatrix} \ell'_2 & \ell'_1 & \ell' \\ \lambda & L & f' \end{Bmatrix} C(\ell_2 \lambda f;00)\, C(\ell'_1 \lambda' f';00) \\ & \sum_k P_k(x) \begin{Bmatrix} f & \ell_1 & L \\ f' & \ell_2 & k \end{Bmatrix} C(k\ell_1 f';00)\, C(k\ell'_2 f;00)\, \hat{k} \end{aligned} \tag{28}$$

where $\hat{\ell} = 2\ell + 1$

$$\pi_1 = \sqrt{\tfrac{1}{4}q^2 + q'^2 + qq'x} \qquad \pi_2 = \sqrt{q^2 + \tfrac{1}{4}q'^2 + qq'x}$$

The Fadeev equation in momentum space representation for three-boson system becomes as the following equation

$$\psi_\alpha(pq)=\frac{1}{E-\frac{p^2}{m}-\frac{3q^2}{4m}}\sum_{\ell'}\int q'^2dq'\int_{-1}^{1}dx\, t_\ell(p,\pi_1,E-\frac{3q^2}{4m})\,G_{\alpha\alpha'}(q,q',x)\,\psi_{\alpha'}(\pi_2 q') \qquad (29)$$

where

$$G_{\alpha\alpha'}(q,q',x)=(-1)^{\ell'}\sum_{\ell_1+\ell_2=\ell}\;\sum_{\ell'_1+\ell'_2=\ell'}\frac{(q)^{\ell_2+\ell'_2}(q')^{\ell_1+\ell'_1}\left(\frac{1}{2}\right)^{\ell_2+\ell'_1}}{(\pi_1)^{\ell}(\pi_2)^{\ell'}}\sqrt{\frac{\hat{\ell}!\hat{\ell}'!}{(2\ell_1)!(2\ell_2)!(2\ell'_1)!(2\ell'_2)!}}$$

$$\sum_f\sum_{f'}\begin{Bmatrix}\ell_1 & \ell_2 & \ell\\ \lambda & L & f\end{Bmatrix}\begin{Bmatrix}\ell'_2 & \ell'_1 & \ell'\\ \lambda & L & f'\end{Bmatrix}C(\ell_2\lambda f;00)\,C(\ell'_1\lambda' f';00)$$

$$\sum_k P_k(x)\begin{Bmatrix}f & \ell_1 & L\\ f' & \ell_2 & k\end{Bmatrix}C(k\ell_1 f';00)\,C(k\ell'_2 f;00)\,\hat{k}$$

Calculation of Two-Body T-Matrix Embedded In three-body space

For studying the three-body system, we require to know the two-body off shell T-matrix. We have known T = V+VG0T and the two-body T-operator in the three particle basis state is

$$\langle pq\alpha|T|p'q'\alpha'\rangle=\langle pq\alpha|V|p'q'\alpha'\rangle+\langle pq\alpha|VG_0T|p'q'\alpha'\rangle \qquad (30)$$

We insert the completeness relation $\sum_\alpha\int p^2dp\int q^2dq|\,pq\alpha\rangle\langle pq\alpha|=1$ in the second term on the right hand side.

$$\langle pq\alpha|VG_0T|p'q'\alpha'\rangle=\sum_{\alpha''}\sum_{\alpha'''}\int p''^2dp''\int q''^2\,dq''\int p'''^2dp'''\int q'''^2\,dq'''\langle pq\alpha|V|p''q''\alpha''\rangle$$

$$\langle p''q''\alpha''|G_0|p'''q'''\alpha'''\rangle\;\langle p'''q'''\alpha'''|T|p'q'\alpha'\rangle$$

Then

$$\langle pq\alpha|VG_0T|p'q'\alpha'\rangle=\int p''^2dp''\,V_\ell(p,p'')\frac{1}{E-\frac{p''^2}{m}-\frac{3q^2}{4m}}\;\langle p''q\alpha|T|p'q'\alpha'\rangle \qquad (31)$$

The two-body T-operator in the three particles basis is clearly diagonal in the spectator quantum numbers “q” and “λ” but depends on “q” through the kinetic energy in G0. The energy available to the interacting two-body subsystem is $E-3q^2/4m$: consequently the T-operator is

$$\langle pq\alpha|T|p'q'\alpha'\rangle=\frac{\delta(q-q')}{qq'}\delta_{\alpha\alpha'}t_\ell\left(p,p',E-\frac{3q^2}{4m}\right) \qquad (32)$$

The two-body interaction in the three-particle basis is

$$\langle pq\alpha|V|p'q'\alpha'\rangle=\frac{\delta(q-q')}{qq'}\delta_{\alpha\alpha'}V_\ell(p,p') \qquad (33)$$

Then the two-body T-matrix for three-boson system is

$$t_\ell\left(p, p', E-\frac{3q^2}{4m}\right) = V_\ell(p,p') + \int p''^2 dp'' V_\ell(p,p'') \frac{1}{E-\frac{p''^2}{m}-\frac{3q^2}{4m}} t_\ell\left(p'', p', E-\frac{3q^2}{4m}\right) \quad (34)$$

This equation can be solved by using the Gauss Elimination Method.

Numerical Technique

The integral equation Eq.(35) is discretized in the variable “q”. We have to choose the appropriate quadrature points “q” and “x”. We introduce a cut-off value qmax and distribute properly Gauss-Legendre quadrature points over the intervals $0 \le q \le q_{\max}$. But the skew arguments (π_2) in ψ under integral require an interpolation. The maximal value of π_2 is $3q_{\max}/2$. This fact is important in keeping the number of discretization points as low as possible. The two- body subsystem is controlled by the variable “p”. The value $3q_{\max}/2$ is much lower than the typical cut-off value in p-variable beyond which $\psi(pq)$ can be neglected. Faddeev equation Eq.(35) is solved in that smaller interval.

We now consider an interpolation in the form

$$f(x) = \sum_k S_k(x) f(x_k) \quad (35)$$

where Sk(x) are known function and {xk} is a set of discrete grid point distributed over an interval in which function “f” has to be determined. We apply this form to the p-variable in the Faddeev equation Eq.(35).

$$\psi(p,q) = \frac{1}{E-\frac{p^2}{m}-\frac{3}{4m}q^2} \int_0^\infty q'^2 dq'$$

$$\times \sum_m \sum_k \int_{-1}^{1} dx\, t_\ell\left(p, p_m, E-\tfrac{3}{4m}q^2\right) S_k(\pi_2) S_m(\pi_1) \psi(p_k, q') \quad (36)$$

Then we introduce Gaussian quadrature in the variable “q” and then

$$\psi(p_j, q_i) = \sum_\ell \sum_{ix} W_\ell q_\ell^2 W_{ix} \frac{1}{E-\frac{p^2}{m}-\frac{3}{4m}q^2}$$

$$\sum_m \sum_{k'} t_\ell\left(p, p_m, E-\tfrac{3}{4m}q^2\right) S_k(\pi_2) S_m(\pi_1) \psi(p_k, q') \quad (37)$$

This is the Faddeev equation for three-boson system and it can easily be solved numerically.

Numerical Accuracy

Our three-boson Faddeev equation is an integral equation and we will solve it numerically. And hence, we will present the convergence of the three-boson binding energy by varying the number of integration grid points. In order to solve the Faddeev components we have defined Nq is a number of discrete "q" points which represent the spectator momentum, Np is the number of grid points of relative momentum of two-body subsystem which is divided into two parts Np1 and Np2 and Nx is the corresponding number of x integration. We have taken two parts of integration limit in the momentum "p" range, the first interval is taken by 0.0fm^{-1} to $\text{p}_{\text{max}} = \frac{3\text{q}_{\text{max}}}{2} + 0.3\text{fm}^{-1}$ and the range of the second interval from p_{max} to p_{cut}. First we take Np1=10, Np2=10, Np=10, $\text{q}_{\text{max}} = 5.0\text{fm}^{-1}$ and $\text{p}_{\text{cut}} = 40.00\text{fm}^{-1}$ arbitrarily and then we studied the precision of binding energy by varying the number of grid points Np1 in the first interval. We have found that the binding energy is converged to three decimal places at the number of grid point Np1=30. These results are displayed in Table 1.

Table 1 The convergence of binding energy by varying the number of grid point points Np1 in the first interval for $\text{p}_{\text{cut}} = 40\text{fm}^{-1}$.

Np$_1$	**Np$_2$**	**Nq**	**Nx**	q_{max}	p_{cut}	**BE(MeV)**
10	10	10	10	5.00	40.00	7.7732
20	10	10	10	5.00	40.00	7.5698
30	10	10	10	5.00	40.00	7.5675
40	10	10	10	5.00	40.00	7.5670

Then, we fixed the parameters of first interval and we studied the precision of binding energy by varying the number of grid point Np2 of the second interval. We observed that the binding energy is converged to four decimal places at the number of grid point Np2=16. The results are shown in Table 2.

Table 2 The convergence of binding energy by varying the number of grid point points Np$_2$ in the second interval for $p_{cut} = 40fm^{-1}$.

Np$_1$	**Np$_2$**	**Nq**	**Nx**	q_{max}	p_{cut}	**BE(MeV)**
30	**12**	10	10	5.00	40.00	7.5673
30	**14**	10	10	5.00	40.00	7.5673
30	**16**	**10**	**10**	**5.00**	**40.00**	**7.5672**
30	**18**	10	10	5.00	40.00	7.5672
30	**20**	10	10	5.00	40.00	7.5672

We fixed these data set such as Np1=30, Np2=16 and $\text{p}_{\text{cut}} = 40\text{fm}^{-1}$, then vary Nq, the binding energy is converged to four decimal places at Nq=20. The results are shown in Table 3.

Table 3 The convergence of binding energy by varying the number of grid point points Nq for $p_{cut} = 40fm^{-1}$.

Np1	Np2	Nq	Nx	q_{max}	p_{cut}	BE(MeV)
30	16	**16**	10	5.00	40.00	7.5369
30	16	**18**	10	5.00	40.00	7.5366
30	**16**	**20**	**10**	**5.00**	**40.00**	**7.5367**
30	16	**22**	10	5.00	40.00	7.5367
30	16	**24**	10	5.00	40.00	7.5367

Then we increase the p_{cut} value to $50.0fm^{-1}$. By varying the number of grid points Np2, the binding energy is converged to 7.5376 MeV at Np2=16 which is shown in Table 4.

Table 4 The convergence of binding energy by varying the number of grid point points Np2 in the second interval with $p_{cut} = 50fm^{-1}$.

Np1	Np2	Nq	Nx	q_{max}	p_{cut}	BE(MeV)
30	**16**	**10**	**10**	**5.00**	**50.00**	**7.5376**
30	**18**	10	10	5.00	50.00	7.5376
30	**20**	10	10	5.00	50.00	7.5376
30	**22**	10	10	5.00	50.00	7.5376
30	**24**	10	10	5.00	50.00	7.5376

Again we increase the q_{max} value to $7.00fm^{-1}$. We studied the precision of binding energy by varying the number of grid point Np1 and Np2 and Nq as the same procedure given above (Here we will not show the tables to save the page). The binding energy is converged to 7.5376 MeV and we have found that a small change in binding energy in the comparing the result of $q_{max} = 5.00fm^{-1}$. So we decide $q_{max} = 5.00fm^{-1}$ is enough for that system. Therefore we choose the parameter set of Np1=30, Np2=16, Nq=20, $p_{cut} = 50.00fm^{-1}$ and $q_{max} = 5.00fm^{-1}$ for that system and the binding energy of three-boson system is 7.5376MeV.

Result and discussion

We have found that the binding energy of the ground state of three-boson system is 7.538 MeV for pure s-wave interaction (ℓ=0) and when we increase ℓ up to two, the binding energy becomes 7.550 MeV. Our result does not agree with the experimental value of triton binding energy 8.48 MeV. The disagreement of our result and experimental value can be the following reasons: the two-body potential which we have used is not realistic potential and our system is not the realistic description of three-nucleon problem, it has been reduced to be a simple problem say three-boson system. We expect that our result will nearly agree with the experimental value if we include the spin and iso-spin. The realistic three-nucleon (triton) system will be presented in the upcoming paper.

Acknowledgements

We would like to express our sincere gratitude to Rector, Dr. Kyaw Tun, Pro-Rector, Dr. Yaw Han Htun and Pro-rector Dr. Hla Hla Tin, Lashio University for giving us a chance to write this research paper. We also thank Dr. Ko Ko Naing, Professor and Head of Physics Department, Dr. Nwe Nwe Yi, Professor of Physics Department, Lashio University for their moral support.

References

Delves L.M (1972), Adv. Nucl. Phys. 5

Fabre de la Ripelle M, (1987), Lecture Notes in Physics 273 283

Faddeev L.D(1961), Sov. Phys. JETP 12 1014

Friar, B.F. Gibson J.L, and Payne G.L(1984), (1986), Ann. Rev. Nucl. Part. Sci. 34 403, P.U. Sauer, Prog. Part. Nucl. Phys. 16 35

Gloeckle W,(1983), The Quantum Mechanical Few-Body Problem (Springer, Berlin, Heidelberg

Holinde K, Machleidt R, Nucl. Phys. A247,495(1975)

Machleidt R, (1989), Adv. Nucl. Phys. 19 189

J. Myanmar Acad. Arts Sci. 2020 **Vol. XVIII.No.2B**

EVOLUTION OF DYNAMICAL FIFTH DIMENSION IN BRANEWORLD COSMOLOGY

Han Win Than [1], Nyein Thida [2], Myo Maung Maung[3], Thant Zin Naing[4]

Abstract

Evolutions of the dynamical system in braneworld cosmology are of main issues on astrophysics and cosmology alike. One can think of extra dimension as important contributor of spacetimes evolution and gives the some interesting cosmological solutions. The solutions are in the form of travelling wave-like nature and visualizations of the solutions are given.

Keywords: Braneworld cosmology, extra dimension.

Introduction

There has been recently a lot of activity on the possibility in a three-dimensional world embedded in a higher dimensional space. Modifying the old Kaluza-Klein picture (Bailin, D., A. Love, 1987), where the extra-dimensions must be sufficiently compact, these recent developments are based on the idea that ordinary matter fields could be confined to a three-dimensional world, corresponding to the apparent Universe, while gravity could live in a higher dimensional space (Arkani-Hamed, N., S. Dimopoulos, G. Dvali, 1998). The usual constraints on Kaluza-Klein models could therefore be relaxed (Arkani-Hamed, N., S. Dimopoulos, G. Dvali, 1999), and "large" extra-dimensions would be conceivable, thus leading to a fundamental Planck mass much lower than its apparent three-dimensional value, even as low as the *TeV* scale.

The purpose of the present work is to solve the five-dimensional Einstein's equations for *any type of matter in the brane* with a cosmological constant in the bulk. It can be seen that Einstein's equations admit a first integral, which in particular provides directly the cosmological evolution of the brane. In the following , it will be shown that an additional assumption, namely that the metric along the fifth dimension does not evolve in time, enables us to solve for the whole space-time metric, i.e. to find explicitly the dependence of the metric on the transverse coordinate as well as time. Finally, in the last section, it will solve analytically, for different cases, the new Friedmann equation obtained in the present work and discuss the consequences.

Solving Einstein's equations

Let's present here the general framework. It should be considered five-dimensional space-time metrics of the form

$$ds^2 = \tilde{g}_{AB} dx^A dx^B = g_{\mu\nu} dx^\mu dx^\nu + b^2 dy^2 \tag{1}$$

where y is the coordinate of the fifth dimension. Throughout this article, one will focus our attention on the hypersurface defined by $y = 0$, which one can identify with the world volume of

---

[1] Dr, Assistant Lecturer, Department of Physics, University of Yangon.

[2] Associate Professor, Department of Physics, University of Yangon.

[3] PhD candidate, Department of Physics, University of Yangon.

[4] Retired Pro-Rector (Admin), International Theravāda Buddhist Missionary University, Yangon.

the brane that forms our universe. Since one can be interested in cosmological solutions, it can be taken a metric of the form

$$ds^2 = -n^2(\tau, y)d\tau^2 + a^2(\tau, y)\gamma_{ij}dx^i dx^j + b^2(\tau, y)dy^2 \tag{2}$$

Where γ_{ij} is a maximally symmetric 3-dimensional metric ($k = -1, 0, 1$ will parametrize the spatial curvature).

The five-dimensional Einstein equations take the usual form

$$\tilde{G}_{AB} = \tilde{R}_{AB} - \frac{1}{2}\tilde{R}_{\tilde{g}_{AB}} = \kappa^2 \tilde{T}_{AB} \tag{3}$$

where $\tilde{R}_{AB}$ is the five-dimensional Ricci tensor and $\tilde{R} = \tilde{g}^{AB}\tilde{R}_{AB}$ the scalar curvature and the constant κ is related to the five-dimensional Newton's constant $G_{(5)}$ and the five-dimensional reduced Planck mass $M_{(5)}$, by the relations

$$\kappa^2 = 8\pi G_{(5)} = M_{(5)}^{-3} \tag{4}$$

Inserting the ansatz (2) for the metric, the non-vanishing components of the Einstein tensor $\tilde{G}_{AB}$ are found to be

$$\tilde{G}_{00} = 3\left\{\frac{\dot{a}}{a}\left(\frac{\dot{a}}{a} + \frac{\dot{b}}{b}\right) - \frac{n^2}{b^2}\left(\frac{a''}{a} + \frac{a'}{a}\left(\frac{a'}{a} - \frac{b'}{b}\right)\right) + k\frac{n^2}{a^2}\right\}, \tag{5}$$

$$\tilde{G}_{ij} = \frac{a^2}{b^2}\gamma_{ij}\left\{\frac{a'}{a}\left(\frac{a'}{a} + 2\frac{n'}{n}\right) - \frac{b'}{b}\left(\frac{n'}{n} + 2\frac{a'}{a}\right) + 2\frac{a''}{a} + \frac{n''}{n}\right\}$$

$$+\frac{a^2}{n^2}\gamma_{ij}\left\{\frac{\dot{a}}{a}\left(-\frac{\dot{a}}{a} + 2\frac{\dot{n}}{n}\right) - 2\frac{\ddot{a}}{a} + \frac{\dot{b}}{b}\left(-2\frac{\dot{a}}{a} + \frac{\dot{n}}{n}\right) - \frac{\ddot{b}}{b}\right\} - k\gamma_{ij} \tag{6}$$

$$\tilde{G}_{05} = 3\left(\frac{n'}{n}\frac{\dot{a}}{a} + \frac{a'}{a}\frac{\dot{b}}{b} - \frac{\dot{a}'}{a}\right) \tag{7}$$

$$\tilde{G}_{55} = 3\left\{\frac{a'}{a}\left(\frac{a'}{a} + \frac{n'}{n}\right) - \frac{b^2}{a^2}\left(\frac{\dot{a}}{a}\left(\frac{\dot{a}}{a} - \frac{\dot{n}}{n}\right) + \frac{\ddot{a}}{a}\right) - k\frac{b^2}{a^2}\right\}. \tag{8}$$

In the above expressions, a prime stand for a derivative with respect to y, and a dot for a derivative with respect to τ.

The stress-energy-momentum tensor can be decomposed into two parts,

$$\tilde{T}^A_B = \breve{T}^A_B\Big|_{bulk} + T^A_B\Big|_{brane} \tag{9}$$

where $\breve{T}^A_B\Big|_{bulk}$ is the energy momentum tensor of the bulk matter, which will be assumed in the present work to be of the form

$$\breve{T}^A_B\Big|_{bulk} = diag(-\rho_B, P_B, P_B, P_B, P_T), \tag{10}$$

where the energy density ρ_B and pressures P_B and P_T are independent of the coordinate *y*. Later, one will be specially interested in the case of a cosmological constant for which $-\rho_B = P_B = P_T$.

The second term $T^A_B\big|_{brane}$ corresponds to the matter content in the brane ($y = 0$). Since it can be considered here only strictly homogeneous and isotropic geometries inside the brane, the latter can be expressed quite generally in the form

$$T^A_B\Big|_{brane} = \frac{\delta(y)}{b}\, diag(-\rho_b, P_b, P_b, P_b, 0), \tag{11}$$

where the energy density ρ_b and pressure p_b are independent of the position inside the brane, i.e. are functions only of time adding some other brane sources with similar energy momentum tensor.

The assumption that $\tilde{T}_{05} = 0,$ which physically means that there is no flow of matter along the fifth dimension, implies that $\tilde{G}_{05}$ vanishes. It then turns out, remarkably, that the components (0, 0) and (5, 5) of Einstein's equations, in the bulk, can be rewritten in the simple form

$$F' = \frac{2a'a^3}{3} k^2 \breve{T}_0^{\ 0}, \tag{12}$$

$$\dot{F} = \frac{2\dot{a}a^3}{3} k^2 \breve{T}_5^{\ 5}, \tag{13}$$

where *F* is a function of τ and *y* defined by

$$F(\tau, y) = \frac{(a'a)^2}{b^2} - \frac{(\dot{a}a)^2}{n^2} - ka^2. \tag{14}$$

Since $\breve{T}_0^0 = -\rho_B$ is here independent of *y*, one can integrate Equation (12), which gives

$$F + \frac{k^2}{6} a^4 \rho_B + C = 0, \tag{15}$$

where *C* is a constant of integration which a priori depends on time. Assuming in addition that, $\breve{T}_0^0 = \breve{T}_5^5$ one finds using the time derivative of Equation (12) and the *y*-derivative of Equation (13) that is constant in time. This also implies that *C* is constant in time. In order to deal with the last component of Einstein's equations, it is convenient to use the Bianchi identity

$$\nabla_A \tilde{G}^{A0} = 0, \tag{16}$$

which can be rewritten

$$\partial_\tau \left(\frac{F'}{a'} \right) = \frac{2}{3} \dot{a} a^2 \gamma^i_j \tilde{G}^j_i \,. \tag{17}$$

One finds that this equation is identically satisfied if $-\rho_B = P_B$. Hence, when the bulk source is a cosmological constant, any set of functions *a*, *n*, and *b* satisfying Equation (15) or, more explicitly,

$$\left(\frac{\dot{a}}{na}\right)^2 = \frac{1}{6}k^2\rho_B + \left(\frac{a'}{ba}\right)^2 - \frac{k}{a^2} + \frac{C}{a^4} \tag{18}$$

together with $\tilde{G}_{05} = 0$, will be solution of all Einstein's equations Equation (3), locally in the bulk.

The brane can then be taken into account by using the junction conditions, which simply relate the jumps of the derivative of the metric across the brane to the stress-energy tensor inside the brane. The relevant expressions are

$$\frac{[a']}{a_0 b_0} = -\frac{k^2}{3}\rho_b, \tag{19}$$

$$\frac{[n']}{n_0 b_0} = \frac{k^2}{3}(3\rho_b + 2\rho_b), \tag{20}$$

where the subscript 0 for *a; b; n* means that these functions are taken in $y = 0$, and $[Q] = Q(0^+) - Q(0^-)$ denotes the jump of the function Q across $y = 0$.

Assuming the symmetry $y \leftrightarrow -y$ for simplicity, the junction condition in Equation (19) can be used to compute a' on the two sides of the brane, and by continuity when $y \to 0$, (18) will yield the generalized (first) Friedmann equation

$$\frac{\dot{a}_0^2}{a_0^2} = \frac{k^2}{6}\rho_B + \frac{k^4}{36}\rho_b^2 + \frac{C}{a_0^4} - \frac{k}{a_0^2}. \tag{21}$$

The salient features of this equation are that, first, the bulk energy density enters linearly, second, the brane energy density enters quadratically, and finally the cosmological evolution depends on a free parameter *C* (related to the choice of initial conditions in the whole space-time), whose influence corresponds to an effective radiation term.

Explicit dependence on the fifth dimension for a stabilized bulk

In this section, it will be shown that, with the help of an additional assumption, namely that the fifth dimension is static, in the sense that

$$\dot{b} = 0 \tag{22}$$

it is then possible to solve the full space-time metric, i.e. to determine the explicit dependence of the metric on the coordinate *y*. The restriction Equation (22) allows to go to the gauge

$$b = 1 \tag{23}$$

It then follows immediately from equation $\tilde{G}_{05} = 0$, that ***n*** can be expressed in terms of ***a*** according to the relation

$$\frac{\dot{a}}{n} = \alpha(t), \tag{24}$$

where α is a function that depends only on time (and not on *y*). Inserting this into Equation (12) yields the following differential equation

$$\alpha^2 + k - (aa')' = \frac{k^2}{3}\rho_B a^2 \tag{25}$$

which is valid everywhere in the bulk (but not in the brane) on the two sides of the brane separately. It can be integrated in y, yielding

$$a^2 = A\cosh(\mu y) + B\sinh(\mu y) + C \tag{26}$$

with

$$\mu = \sqrt{-\frac{2k^2}{3}\rho_B}, \tag{27}$$

in the case of $\rho_B < 0,$ or

$$a^2 = A\cos(\mu y) + B\sin(\mu y) + C \tag{28}$$

with

$$\mu = \sqrt{\frac{2k^2}{3}\rho_B}, \tag{29}$$

in the case of $\rho_B > 0,$ or finally

$$a^2 = (\alpha^2 + k)y^2 + Dy + E, \tag{30}$$

for $\rho_B = 0$. In the following, it should focus on the first case $\rho_B < 0,$ but all the equations will apply as well to the case $\rho_B > 0,$ up to the transformation $\mu \to i\mu, B \to iB.$

The coefficients A, B, C, D, E are functions of time, and C is expressible in terms of α as

$$C = 3\frac{\alpha^2 + k}{k^2\rho_B}, \tag{31}$$

and the others can be determined by the junction conditions. The symmetry $y \leftrightarrow -y$ imposes the relations $A_+ = A_- \equiv \overline{A},\ \ B_+ = -B_- \equiv \overline{B}$ between the coefficients on the two sides of the brane. Using Equation (19) and Equation (20), one then finds

$$\frac{\mu\overline{B}}{\overline{A} + C} = -\frac{k^2}{3}\rho_b,\ \ \frac{2\mu\dot{\overline{B}}}{\dot{\overline{A}} + \dot{C}} = k^2\left(p_b + \frac{1}{3}\rho_b\right). \tag{32}$$

Note that one can check explicitly energy conservation in the brane from these relations, i.e.

$$\dot{\rho}_b + 3\frac{\dot{a}_0}{a_0}(\rho_b + p_b) = 0. \tag{33}$$

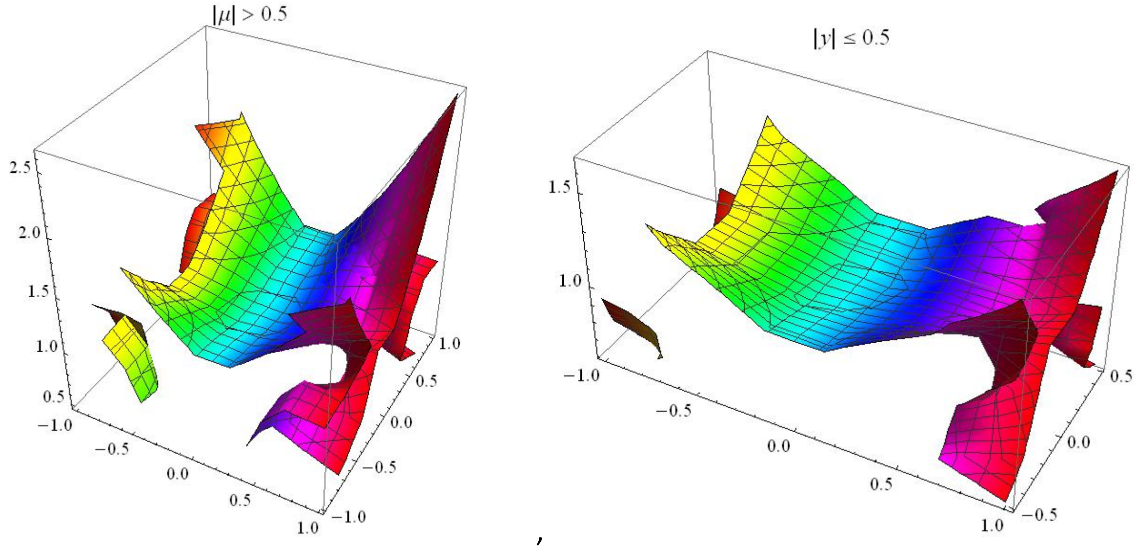

Figure 1 List surface 3D plot of ***a*** in terms of $\boldsymbol{\mu}$ and ***y***

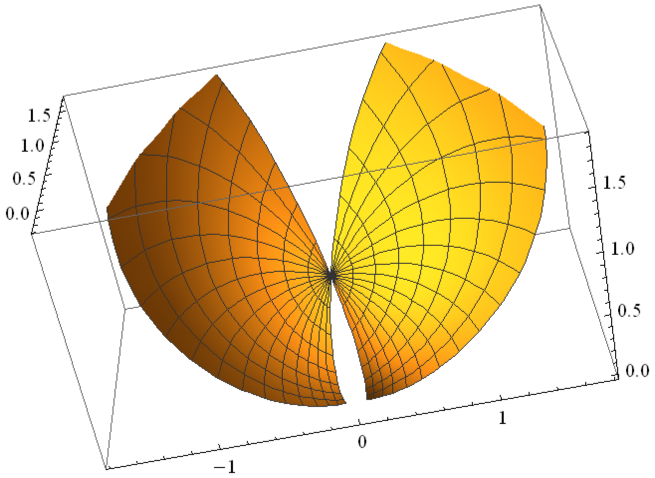

Figure 2 Spherical 3D plot of **a** in terms of $\boldsymbol{\mu}$ and **y**

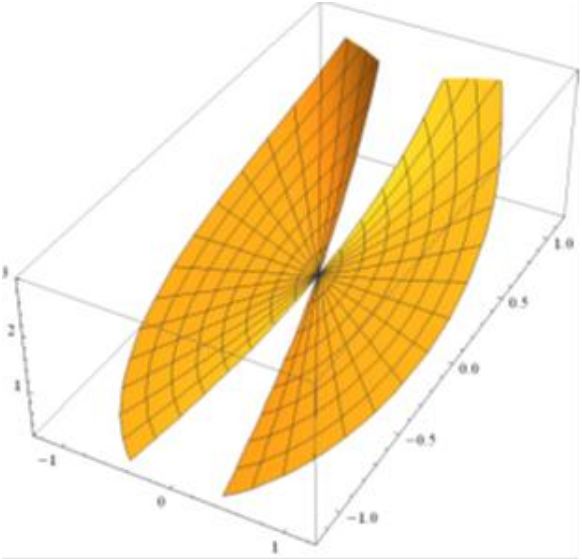

Figure 3 Revolution 3D plot of **a** in terms of $\boldsymbol{\mu}$ and **y**

Conclusions

It is concluded that the brane structure is of main importance in higher dimension spacetimes. First, it has been shown that one can obtain a first integral of Einstein's equations, which provides, on the brane, a relation analogous to the (first) Friedmann equation and which depends only on the geometry and matter content of the brane, except for a constant parameter. Second, when $\dot{b} = 0$, one can extend explicitly the solution found on the brane to the whole space-time. The travelling waves solution has been visualized and formal wave-like patterns are retained.

Acknowledgement

I would like to thank Dr Khin Khin Win, Professor and Head, Department of Physics, University of Yangon, for her kind permission and encouragements to carry out this work.I would like to thank Dr Myo Lwin, Dr Aye Aye Thant and Dr Yin Maung Maung, Professors, Department of Physics, University of Yangon, for their encouragements to carry out this work. Special thanks are due to Professor, Dr Thant Zin Naing, Retired Pro-rector (Admin), International Theravāda Buddhist Missionary University, for his valuable guidance and helpful advice to carry out this work.

References

Arkani-Hamed, N., S. Dimopoulos, G. Dvali, (1998) Phys.Lett. B429, (1998) 263, and hep-ph/9807344.

Arkani-Hamed, N., S. Dimopoulos and G. Dvali, (1999) Phys. Rev. ***D59*** 086004.

Bailin, D., A. Love, (1987) Rep. Prog. Phys. 50 1087.

Binetruy, P., C.De_ayet, D.Langlois, hep-th/9905012.

Csaki, C., M.Graesser,C.Kolda,J.Terning, hep-ph/9906513.

Cline, J.M., C.Grosjean, G.Servant, hep-ph/9906523.

Kaloper, N., hep-th/9905210.

Kanti, P., I.I. Kogan, K.A. Olive, M.Pospelov. UMN-TH-1820-99, hep-ph/9909481

Randall, L., R.Sundrum, hep-ph/9905221.

Randall, L., R.Sundrum, hep-th/9906064.

Rubakov, V.A., M.E.Shaposhnikov, (1983) Phys.Lett.B125,139.

Squires, E.J., (1986) Phys.Lett. B167, 286.

Visser, M., (1985) Phys.Lett.B159,22.

J. Myanmar Acad. Arts Sci. 2020 **Vol. XVIII.No.2B**

FABRICATION AND CHARACTERIZATION OF STRONTIUM DOPED CALCIUM TITANATE THIN FILMS

Hnin Yu Wai[1], May Kalayar Kyaing[2], San San Oo[3], Myat Wut Yee Han[4] and
Amy Aung[5]

Abstract

Strontium doped calcium titanate, $Ca_{1-x}Sr_xTiO_3$ (x = 0.1, 0.2, 0.3, 0.4) thin films deposited onto silicon substrates were prepared by sol-gel method and heated at 700°C for 1 hr. The sol-gel method offers numerous advantages such as good homogeneity of the powders and low processing temperature. Microstructural observation of the $Ca_{1-x}Sr_xTiO_3$ thin films was investigated from scanning electron microscopy (SEM) images and it was found that the grain sizes varied with increase in concentration of strontium. The structural identification with different dopant concentrations of the films examined using X-ray diffraction (XRD) analysis showed the complete crystallization in the perovskite structure. Capacitance-voltage (C-V) measurements were carried out by using a LCR meter for various frequencies (0.1 kHz to 100 kHz) and the values of dielectric constant for all the films were also determined.

Keywords: $Ca_{1-x}Sr_xTiO_3$ thin films, SEM, XRD, C-V

Introduction

$CaTiO_3$ belong to the perovskite class materials (ABO_3) and it is also a chemistry and thermally stable ceramic oxide, which is widely studied due to its dielectric and photoluminescent properties. $CaTiO_3$(CTO) has an orthorhombic structure and it has a dielectric permittivity of approximately 180 at room temperature that changes with experimental conditions [Malic, B. et al., (2007)]. Perovskite materials have been extensively studied due to a wide range of low-temperature structural distortions. These structures have become fundamental interests in physics in technological applications such as microwave devices and phase transitions. The $CaTiO_3$ based solid solution can also be applied as high performance capacitors. They usually undergo several phase transitions with increase in temperature and pressure [Mascot, M., Fasquelle, D. and Carru, J. C. (2011)].

$CaTiO_3$ is one of the most important ferroelectric perovskite which has been considerably used for radioactive waste and as a dopant in electric materials due to its dielectric behaviors and flexibility in structural transformations. Four phases of CTO were suggested by using neutron diffraction method at ambient pressure. As temperature decreases, CTO undergoes a sequence of phase transitions [Jae-Yeol Hwang et al., (2006)]. Body centered tetragonal (T > 1580 K) cubic (T = 1580 K), centered orthorhombic (T = 1500 K) and primitive orthorhombic (T = 1380 K). Unfortunately phase transition temperature has not yet pinpointed experimentally the possible number of phases of CTO. However, the high-pressure behavior of CTO at room temperature is not clear. CTO has the ideal cubic perovskite structure for temperature at 1580 K. In which the structure have been demonstrated the stability under high temperature and pressure. An investigation on cubic CTO is carried out because of its suggested analogy with geologically

---

[1] Dr, Assistant Lecturer, Department of Physics, University of Yangon

[2] Assistant Lecturer, Department of Physics, University of Yangon

[3] Assistant Lecturer, Department of Physics, University of Yangon

[4] Assistant Lecturer, Department of Physics, Pinlon University

[5] Assistant Lecturer, Department of Physics, University of Yangon

relevant ABO_3 perovskites under high pressure and temperature. Therefore pressure analogy can be developed with temperature due to direct correspondence [B.D. Lee, H.R. .et.al., (2005)]. First principles calculations of $CaTiO_3$ were also performed by Cockayne et al. and Wang et al., but they were mainly focused on the dielectric constant, optical properties, and the surface structures. Like higher temperatures, when the pressure is relatively large enough by bond compression, than up to what extent material show stable phase. Theoretically, phase transitions between different structure phases under temperature and pressure are difficult to characterize [T. Bongkran and W. Khiawwangthong, (2008)].

Various methods can be performed to synthesize $CaTiO_3$, including sol-gel, precipitation, mechano-chemical milling, electro-chemical deoxidation, mechanical alloying and hydrothermal. Each of these methods has advantages and disadvantages. Sol-gel is a promising method for the preparation process is simple, in addition to the product produced has crystallinity better than the other method [F. M. Pontes et al., (2000)]. In this study, strontium doped calcium titanate thin films were synthesized by sol-gel method to improve the good crystallinity of the product.

Experimental Details

Strontium doped calcium titanate, $Ca_{1-x}Sr_xTiO_3$ (x = 0.1, 0.2, 0.3, 0.4) powders were synthesized by solid state reaction method, using high purity (99.9 % reagent grade) CaO, SrO and TiO_2 powders. These powders were weighed on the basis of stoichiometric composition. The resultant, stoichiometric compositions of powders were ground by agate mortar to obtain the homogeneity. Each mixed powder was annealed at 700°C for 1 hour and mixed with 2-methoxyethanol ($CH_3OCH_2CH_2OH$) solution and then heated up to 100˚C with indirect heat treatment for 1 hr. Finally, homogeneous precursor solutions were obtained. The silicon substrates are cleaned by standard cleaning method. The resulting precursor solutions are deposited on silicon substrates by spin coating technique. After spin coating, deposited thin films are heat treated at 700˚C for 1hr. The surface morphology and the thickness of the films were analyzed by scanning electron microscope (SEM). X-ray Diffraction analysis was used as the major tool for identification of phase of prepared thin films. The capacitance- voltage measurements and the dielectric properties of the films were carried by using LCR meter.

Results and Discussion

Morphological Analysis

The surface morphology and the cross sectional view of the strontium doped calcium titanate thin films were evaluated using scanning electron microscopy as shown in Fig 1 (a-h). SEM images indicated that all the films were composed of densely packed microcrystals. The values of the average grain sizes and thickness of the thin films were presented in Table 1. The average grain size increases with the increasing of strontium content.

Table 1 The values of the average grain sizes and thickness of the strontium doped calcium titanate thin films

Thin film	Average Grain Size (μm)	Thickness (μm)
10% Sr doped $CaTiO_3$	0.45	7.8
20% Sr doped $CaTiO_3$	0.48	8.8
30% Sr doped $CaTiO_3$	0.58	10.7
40% Sr doped $CaTiO_3$	0.59	11.4

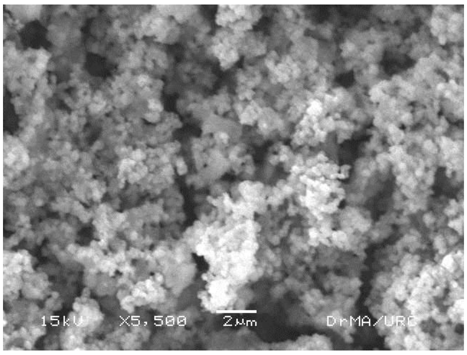

Figure 1 (a) SEM image of 10% Sr doped CTO thin film

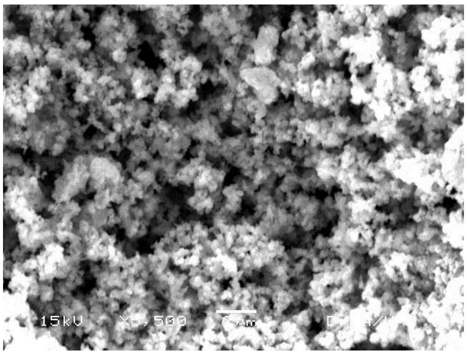

Figure 1 ((b) SEM image of 20% Sr doped CTO thin film

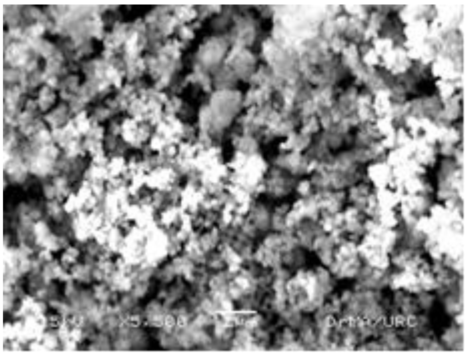

Figure 1 (c) SEM image of 30% Sr doped CTO thin film

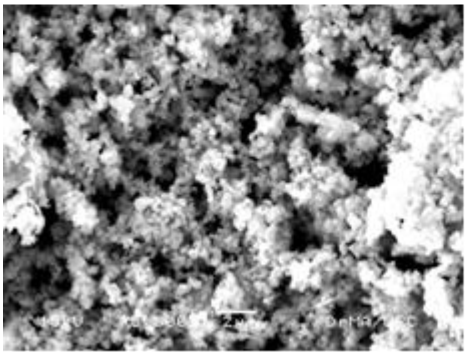

Figure 1 (d) SEM image of 10% Sr doped CTO thin film

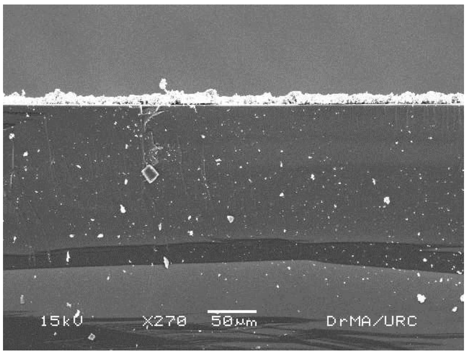

Figure 1 (e) Cross sectional image 10% Sr doped CTO thin film

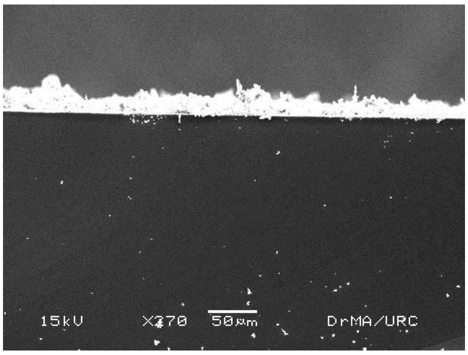

Figure 1 (f) Cross sectional image 20% Sr doped CTO thin film

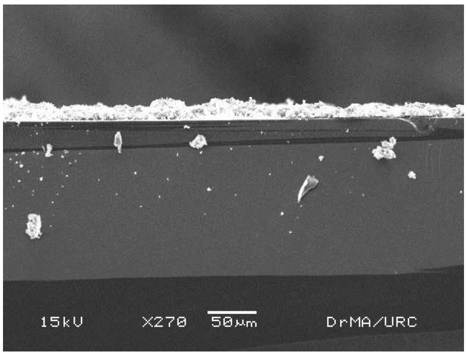

Figure 1 (g) Cross sectional image 30% Sr doped CTO thin film

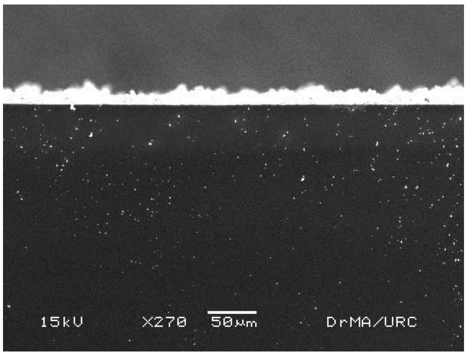

Figure 1 (h) Cross sectional image 40% Sr doped CTO thin film

Structural Analysis

XRD characterization was conducted to obtain the information both quantitatively and qualitatively on the crystal structure of $CaTiO_3$. Based on the diffraction pattern can be determined the crystal phases and crystallite sizes of $CaTiO_3$ samples. The samples were scanned from (2θ = 22.755 – 23.36) using XRD machine with Cu source which has a wavelength of 0.154 nm. X-ray diffraction pattern of strontium doped calcium titanate thin films onto silicon substrates with various dopant concentrations are shown in Fig 2 (a-d). The characteristics peaks in the XRD patterns confirmed the presence of CST material and also indicated that all the films are well crystallized and orthorhombic perovskite structure. The lattice parameters were slightly increased with the increasing of strontium content. The variation in the lattice parameters of strontium doped CTO thin films with change in dopant concentration may be attributed to the change in ionic radius. The XRD patterns showed that the increased dopant concentration leads to decrease in intensity of diffraction peaks with preferred orientation at (110) planes. The crystallite size was calculated using Scherrer's formula,

$$D = \frac{0.9\lambda}{\beta \cos\theta}$$

The (hkl) plane, full width half maximum (FWHM) and crystallite sizes (D) of all the films are listed in Table 2 (a-d).

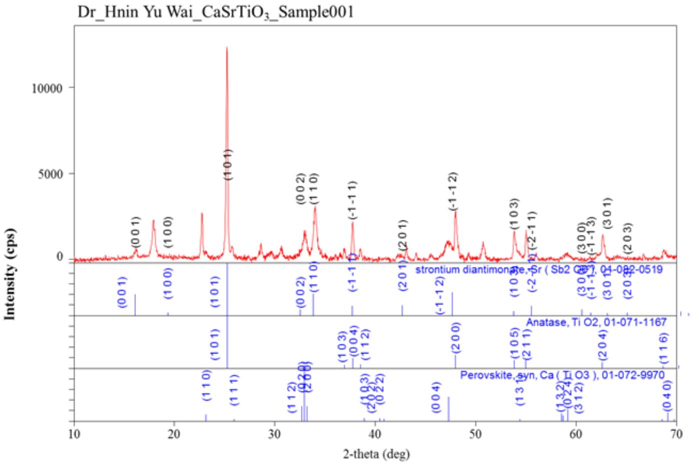

Figure 2 (a) X-ray diffraction of 10% Sr doped $CaTiO_3$ thin film

Table 2 (a) (hkl) plane, full width half maximum (FWHM) and crystallite sizes (D) of $Ca_{1-x}Sr_xTiO_3$ (x = 0.1) thin film

N0	(hkl) plane	FWHM (deg)	Crystallite size (nm)
1	(101)	0.19	40.747
2	(110)	0.48	16.207
3	(103)	0.12	62.778
Average crystallite size			39.911

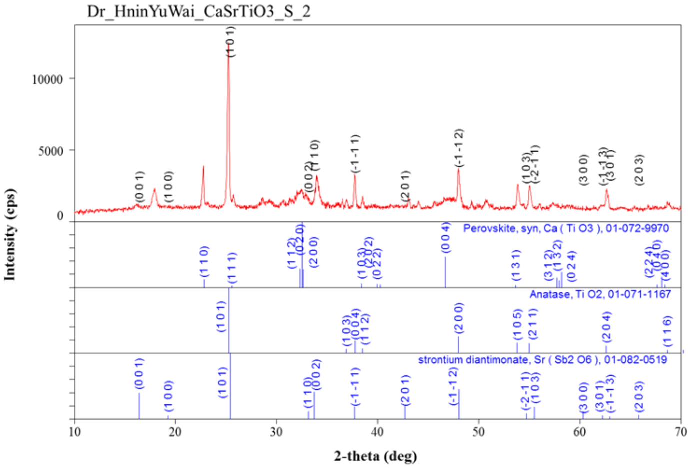

Figure 2 (b) X-ray diffraction of 20% Sr doped $CaTiO_3$ thin film

Table 2 (b) (hkl) plane, full width half maximum(FWHM) and crystallite sizes (D) of $Ca_{1-x}Sr_xTiO_3$ (x = 0.2) thin film

No	(hkl) plane	FWHM (deg)	Crystallite size (nm)
1	(101)	0.168	48.494
2	(110)	0.420	18.530
3	(103)	0.164	43.324
Average crystallite size			36.783

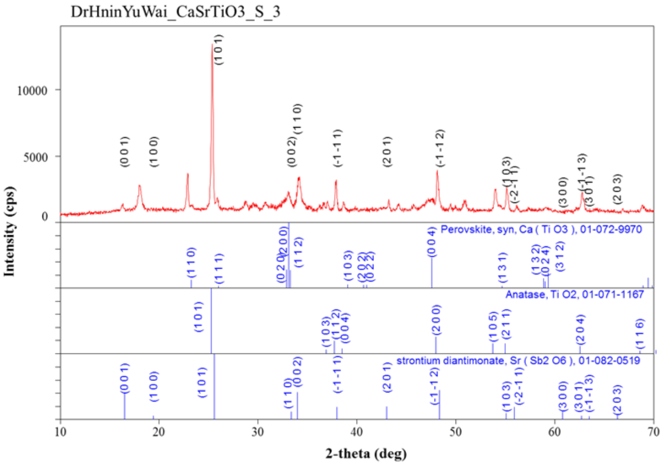

Figure 2 (c) X-ray diffraction of 30% Sr doped $CaTiO_3$ thin film

Table 2 (c)) (hkl) plane, full width half maximum(FWHM) and crystallite sizes (D) of $Ca_{1-x}Sr_xTiO_3$ (x = 0.3) thin film

N0	(hkl) plane	FWHM (deg)	Crystallite size (nm)
1	(101)	0.197	39.340
2	(110)	0.179	43.499
3	(103)	0.090	83.307
Average crystallite size			55.382

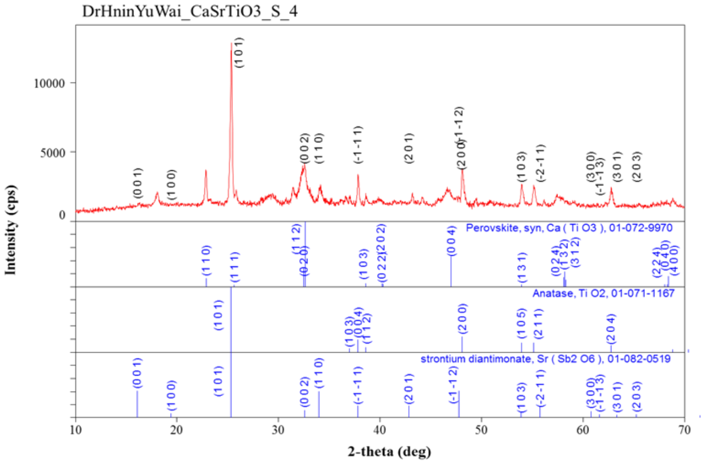

Figure 2 (d) X-ray diffraction of 40% Sr doped $CaTiO_3$ thin film

Table 2 (d) (hkl) plane, full width half maximum(FWHM) and crystallite sizes (D) of $Ca_{1-x}Sr_xTiO_3$ (x = 0.4) thin film

N0	(hkl) plane	FWHM (deg)	Crystallite size (nm)
1	101	0.184	43.312
2	110	0.174	44.759
3	103	0.130	57.956
Average crystallite size			48.675

Table 3 The peak positions(2θ), full width half maximum(FWHM), lattice parameters and crystallite sizes (D) of strontium doped calcium titanate thin films at (110) plane

Thin Films	(hkl) plane	Peak Positions (2θ)	FWHM	Lattice parameter	D (nm)
10% Sr doped $CaTiO_3$	(110)	23.36	0.48	a = 5.2783 b = 5.5408 c = 7.5520	16.207
20% Sr doped $CaTiO_3$	(110)	23.17	0.42	a = 5.3882 b = 5.4711 c = 7.6789	18.530
30% Sr doped $CaTiO_3$	(110)	22.861	0.179	a = 5.4871 b = 5.5053 c = 7.7251	43.499
40% Sr doped $CaTiO_3$	(110)	22.755	0.174	a = 5.4792 b = 5.5383 c = 7.7719	44.759

Dielectric Properties

The dielectric constants of strontium doped calcium titanate thin films were calculated from capacitance-voltage measurements at the frequency range of 0.1 kHz to 100 kHz. The dielectric constant varies with the applied voltage. The dielectric constant (ε) can be calculated by the equations below,

$$C_0 = \varepsilon_0 A/t,$$

$$\varepsilon = C/C_0$$

where

C = capacitance using the material as the dielectric in the capacitor,
C_0 = capacitance using vacuum as the dielectric
ε_0= Permittivity of free space (8.85×10^{-12} F/m)
A = Area of the plate/ sample cross section area
t = Thickness of the sample

The maximum value of dielectric constant was occurred at the 20% strontium doped calcium titanate thin film measured in a frequency range of 0.1 kHz. The dielectric constant of the films as function of frequency and strontium content are shown in Fig 3 (a & b) and the results are listed in Table 4.

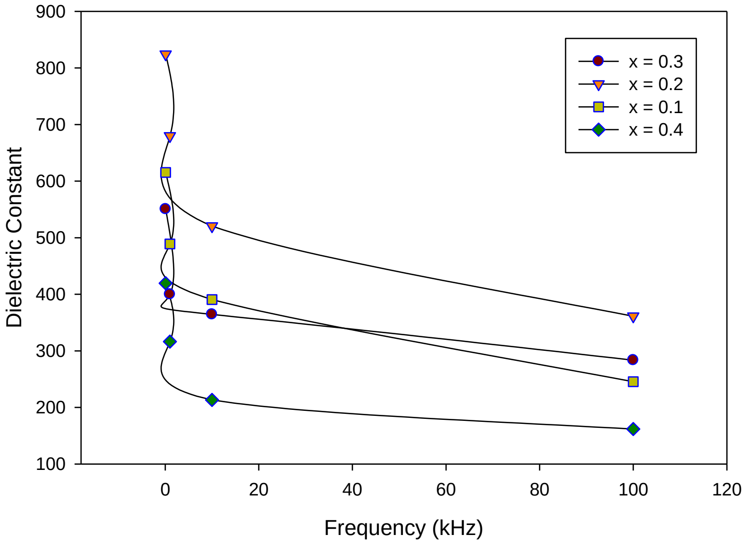

Figure 3 (a) The dependence of dielectric constant of the Sr doped $CaTiO_3$ thin films as a function of frequency

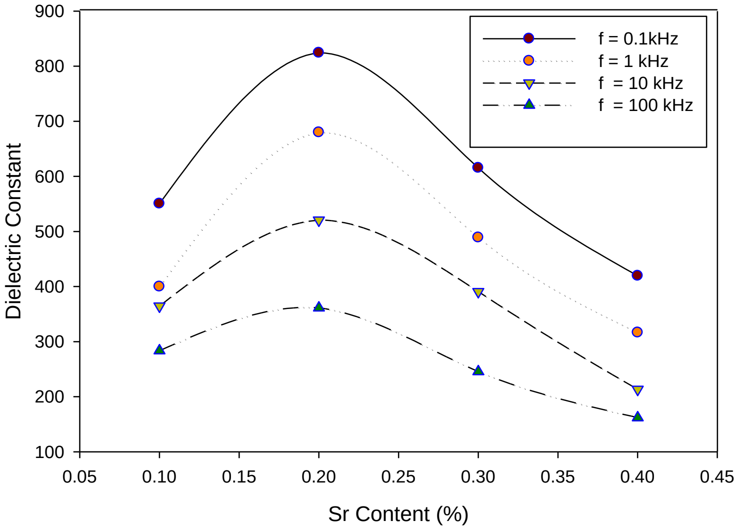

Figure 3 (b) The dependence of dielectric constant of the $CaTiO_3$ thin films on the Sr content

Table 4 The values dielectric constant of Sr doped $CaTiO_3$ thin films as a function of frequency

Thin Films	Dielectric Constant			
	f = 0.1 kHz	**f =1kHz**	**f = 10kHz**	**f = 100kHz**
10 % Sr doped $CaTiO_3$	550.3499616	399.6955028	364.3960678	283.535652
20 % Sr doped $CaTiO_3$	824.3014282	679.7182784	520.4414423	361.1646061
30 % Sr doped $CaTiO_3$	615.2501695	488.9084746	390.6911186	245.4707797
40 % Sr doped $CaTiO_3$	419.4169492	316.3661017	213.3152542	161.7898305

Conclusions

Strontium doped calcium titanate, $Ca_{1-x}Sr_xTiO_3$ (x = 0.1, 0.2, 0.3, 0.4) thin films deposited onto silicon substrates were prepared by sol-gel method. SEM images showed that all the films were composed of densely packed microcrystals. XRD patterns indicated that all the films were well crystallized and orthorhombic perovskite structure. The lattice parameters were slightly increased with the increasing of strontium content. Widening the diffraction pattern is influenced by the crystallite size, where the wider diffraction pattern indicates the smaller crystallite size. XRD patterns of strontium doped calcium titanate thin films were observed a better polycrystalline nature oriented along with (110) planes. The maximum value of dielectric constant was occurred at the 20% strontium doped calcium titanate thin film measured in a frequency range of 0.1 kHz. The dielectric constants of the films decrease with the increasing frequencies. These results suggested that strontium concentration offers a good control of structural and dielectric properties.

Acknowledgements

The authors sincerely thank Professor Dr Khin Khin Win, Head of Department of Physics, University of Yangon, for her kind permission to carry out this research. I would like to express my sincere thanks to Dr Myo Lwin, Professor, Department of Physics Dr Ye Chan, Professor and Head, Universities' Research Center, Dr Aye Aye Thant, Professor, Department of Physics, Dr Yin Maung Maung, Professor, Department of Physics and Dr Than Zaw Oo, Professor, Universities' Research Center, University of Yangon, for their permission to this paper.

References

B.D. Lee, H.R. .et.al., (2005), " Effect of Stacking layers on the microwave dielectric properties of MgTiO3/CaTiO3 multilayered thin films," *J. Am. Ceram. Soc,* 88 , 493-499

F. M. Pontes et al., (2000), "High dielectric constant of $SrTiO_3$ thin films prepared by chemical process," *Journal of Material Science*, 35, 4783 - 4787

Jae-Yeol Hwang et al., (2006) " Dielectric Properties of Artificially Textured $(Ba_{0.5}Sr_{0.5})TiO_3$ Thin Film Prepared by Pulsed Laser Deposition," *Journal of the Korean Physical Society*," 49, 447- 696

Malic, B. et al., (2007) "Processing and dielectric characterization of $Ba_{0.3}Sr_{0.7}TiO_3$ Thin Films" *Journal of the European Ceramic Society*, 27, 2945-2948

Mascot, M., Fasquelle, D. and Carru, J. C. (2011), "Very high tunability of $BaSn_xTi_{1-x}O_3$ ferroelectric thin films deposited by sol-gel," *Functional Materials Letters*, 4, 49-52

T. Bongkran and W. Khiawwangthong, (2008) " The Preparation of Barium Stannate Titanate Ceramics via Solid State Reaction Method," *Advanced Materials Research,* 57, 181-184

J. Myanmar Acad. Arts Sci. 2020 **Vol. XVIII.No.2B**

SYNTHESIS AND CHARACTERIZATION OF CALCIUM TITANATE ($CaTiO_3$) POWDER FOR PHOTOVOLTAIC APPLICATION

Shwe Sin Aung[1], ToeToeWai[2], Nway Han Myat Thin[3], Zin Min Myat[4]

Abstract

Calcium titanate ($CaTiO_3$) powders with perovskite structure were synthesized by a co-precipitation method by using $CaCO_3$, TiO_2 and NaOH as the starting materials. The effect of calcinations temperature in phase formation, morphology and particle size distribution of proposed powders were examined. The dried gels were calcined at 500°C, 600°C and 700 °C respectively. The Structural analysis was calculated by using X-ray Diffraction Method (XRD). The functional groups were examined by using Fourier Transformed Infrared Spectrophotometer (FTIR). The surface morphology was examined by Scanning Electron Microscopy (SEM). The crystallite phase and the morphology of $CaTiO_3$ were highly influence by the calcinations temperature.

Keywords: nanopowder, $CaTiO_3$, co-precipitation

Introduction

Among the metal oxide, titanium dioxide (TiO_2) is well known n-type semiconductor and non-toxic, cheap, highly efficient photovoltaic material. It has three crystalline forms anatase, rutile and brookite. Different phases have different energy band gap. So it is extensively use in various applications like photoconductors, dielectric materials and solar cell etc . It is also use as an ingredient in sunscreen lotions and food products as a pigment.Calcium titanium oxide or Calcium titanate ($CaTiO_3$) is the member of perovskite structure (ABO_3) family and it was discovered by Gustav Rose in 1839 and named in honour of the Russian mineralogist Count Lev Alekseevich Perovski (1792-1856) . $CaTiO_3$ is ferroelectric with an orthorhombic phase at room temperature and at higher temperature 870K it exhibits tetragonal structure and at around 1273K it is transformed to cubic structure . Nowadays due to world high population global demand for energy is increasing rapidly. So the researchers are interested the photovoltaic perovskite solar cell to solve energy problem. $CaTiO_3$ is widely used in various electronics devices as a result of dielectrics, photo luminescent, photovoltaic and electronic conduction properties. Moreover there is no need for extremely high temperature and long reaction time producing $CaTiO_3$ powders possible for large scale synthesis. Due to these distinctive properties and numerous uses, $CaTiO_3$ has lots of attraction among the researchers. $CaTiO_3$ powders can be synthesized by several methods such as solid state reaction method, chemical co-precipitation method, wet chemical method (so-gel), hydrothermal technique, milling, physical and chemical vapour processing, precipitation from a precursor solution in a strong alkaline water, chemical bath deposition and many others. Although all these methods have their own advantage and most of them need high temperature and pressure. Among of them the co- precipitation method is very practical, low cost, simple and precise control of the composition so we have been used this method for the synthesis of calcium titanate ($CaTiO_3$) powders.

---

[1] Dr, Assistant Lecturer, Department of Physics, University of Yangon
[2] Dr, Assistant Lecturer, Department of Physics, University of Yangon
[3] Dr, Assistant Lecturer, Department of Physics, University of Yangon
[4] Dr, Assistant Lecturer, Department of Physics, University of Yangon

In this work the synthesis of $CaTiO_3$ powder is carried out through the mixtures containing titanium dioxide, calcium carbonate, sodium hydroxide as precursor and the effect of calcinations temperatures on the structural properties are operating.

Experimental Procedure

$CaTIO_3$ powders were synthesized by co-precipitation method. Calcium carbonate ($CaCO_3$), titanium dioxide (TiO_2) and sodium hydroxide (NaOH) were used as starting materials. 0.2 mol of NaOH was dissolved in 100ml distilled water and 0.1 mol of $CaCO_3$ was added to the NaOH solution. Then the mixture was magnetically stirred for one and half hours and added to 100ml distilled water and 0.1 mol of titanium dioxide solution. The mixture was magnetically stirred for 3 hours. The mixture has been filtered with filter paper for removing water. The resulting precipitations were kept at room temperature for 24 hours. Final products were dried in hot air oven at 80 °C for 15 hours. The dried precipitations were collected and grounded in an agate motor for 2 hours. The resulting synthesized powder were calcined at 500 °C, 600 °C and 700 °C for 2 hours in a muffle furnace and as synthesized $CaTiO_3$ powders were obtained.

Result and Discussion

XRD Analysis

The structural properties of $CaTiO_3$ powder were studied by X-ray diffraction from which significant differences in the diffraction patterns of each calcined temperature at 500°C, 600°C and 700°C, as shown in Figure 1 (a-c). At calcined temperature 500°C of $CaTiO_3$ powder was still dominated by the phase of the starting materials especially TiO_2. Phase of $CaCO_3$ is also appeared with weak intensity. At calcined temperature 600°C the sample was also needed to cause a complete reaction to produce crystalline phase of $CaTiO_3$. But furthering calcined temperature at 700°C the perovskite $CaTiO_3$ phase were formed. At that temperature the dominated phase of $CaTiO_3$ pattern indicated by the characteristic with very high intensity and pure perovskite $CaTiO_3$ were formed, as shown in Figure 1(c). All of $CaTiO_3$ peaks appeared in diffraction pattern as can be identified at an angle (2θ) of 33.02°, 47.46° and 59.16° corresponding to the phase of diffraction (h,k,l) respectively to (020), (024), (132) and (204). All the peaks in XRD pattern match well with reported characteristic reflection peaks of $CaTiO_3$JCPDS file No, (01-089-8033). The crystallite size have been estimated from the X-ray peak of (h,k,l) diffraction using Scherrer formula. The average crystallite size of $CaTiO_3$calcined powder at 500°C, 600°C and 700°C were 39 nm, 36 nm and 26 nm respectively. As the calcinations temperature increased the crystallite size also decreased.

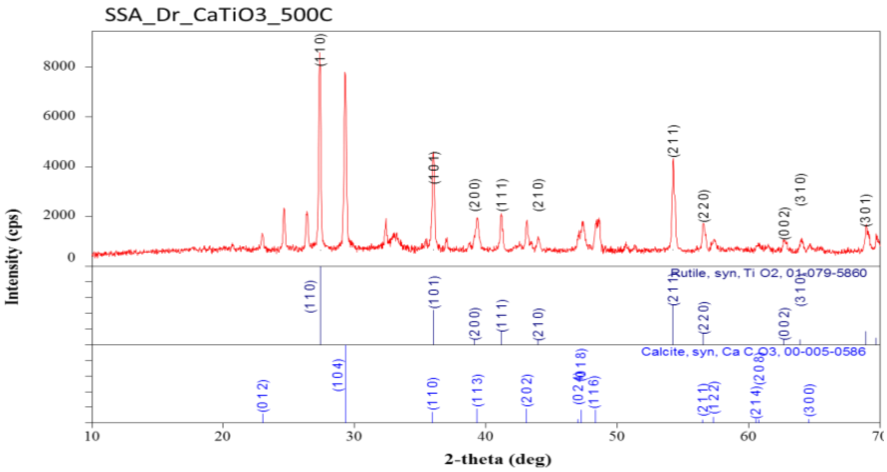

Figure 1 (a) XRD Pattern of CaTiO$_3$powders prepared at 500˚C

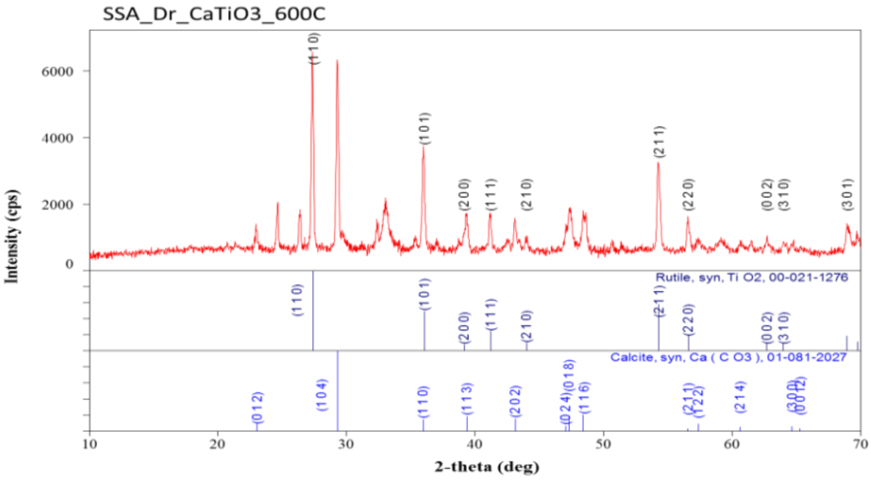

Figure 1 (b) XRD Pattern of CaTiO$_3$powders prepared at 600˚C

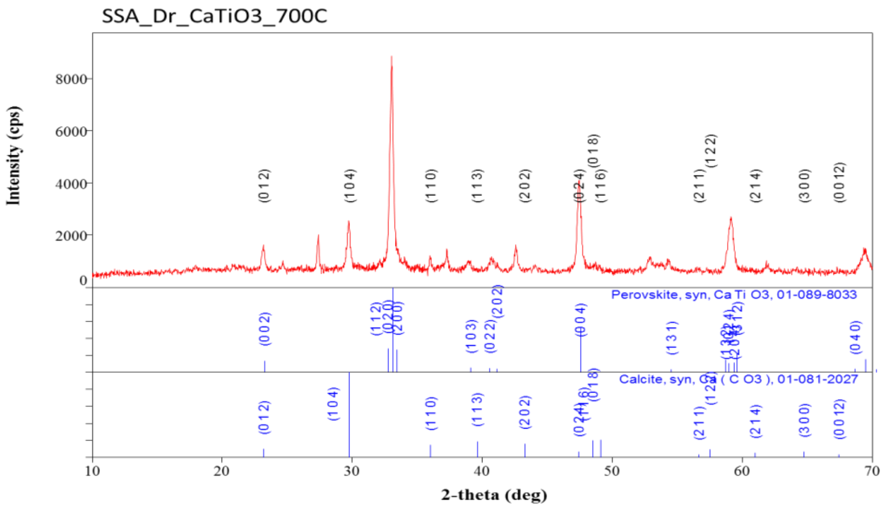

Figure 1 (c) XRD Pattern of CaTiO$_3$powders prepared at 700˚C

SEM Analysis

Calcium titanate nanoparticles were obtained by calcinations of the gels of the composite carbonate. Figure 2(a-c) shows the SEM analysis of $CaTiO_3$ particles sintered at 500 °C – 700 °C exhibit grained microstructure and nanostructure with small crystallite size. The grain sizes were calculated by using well known bar code system. The average grain size of $CaTiO_3$ particle was found to be about 0.21 µm-0.28 µm. This figure indicated that most of the grain size was regular structure and a few number of large grain size were found. It looks fairly dense and rough.

This fact indicated that structural properties were influenced by different temperatures. From the images, it was clearly found that the little amount of pores and grain growth were examined with the increase in process temperatures. The orientation of grain was towards left for all images. The grain size of $CaTiO_3$ particles seen to be uniform but some of the grain size were slightly large. From detail analysis of figure 2(a) showed the dense particle with fine grains and without any cracks calcined at 500 °C.

In figure 2 (b), the SEM photograph was examined to be non-uniform and crack free, this photo also indicated that the particles were dense, smooth and fine grain at 600 °C. SEM studied on the particle at 700 °C was represented at figure 2(c), this figure indicated the dense particle with fine grains, uniform and smooth but some pores were observed. All figures exhibited the smooth in morphology.

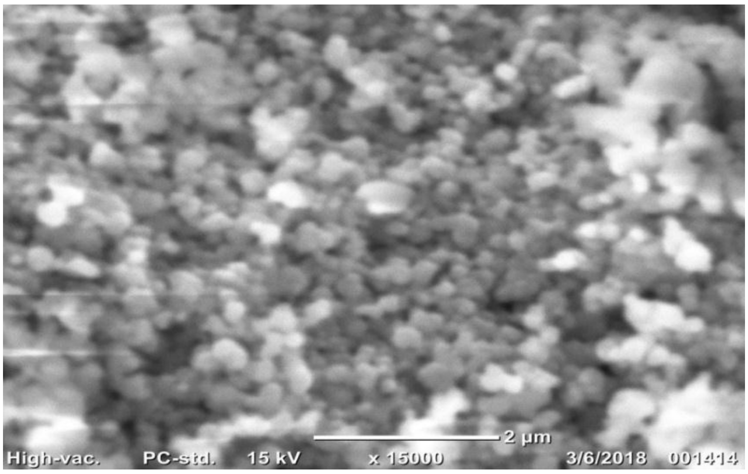

Figure 2 (a) SEM photograph of $CaTiO_3$powders prepared at 500˚C

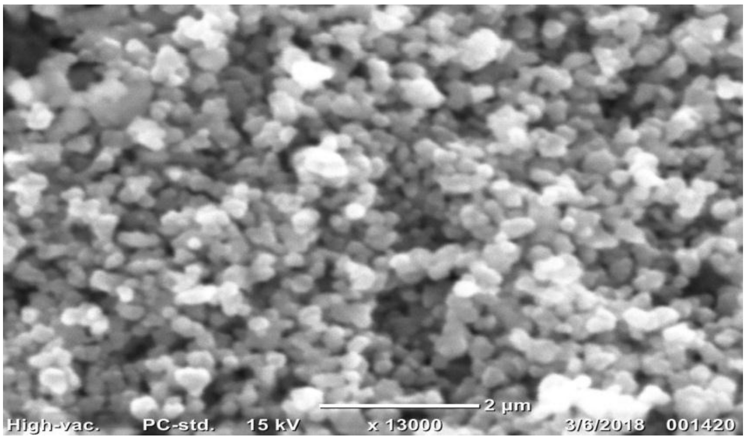

Figure 2 (b) SEM photograph of CaTiO$_3$powders prepared at 600˚C

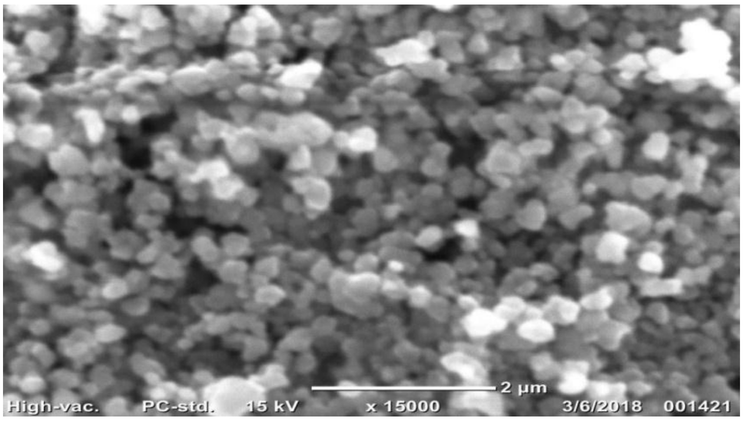

Figure 2 (c) SEM photograph of CaTiO$_3$powders prepared at 700˚C

FTIR Analysis

FTIR analysis were performed for the powder sample calcinations temperature at 500 °C , 600 °C and 700 °C in Fig (3) (a-c). The band around 655.82 cm^{-1}, 653.89 cm^{-1}, 601.81 cm^{-1},590.24 cm^{-1} , 580.59 cm^{-1}, 569.02 cm^{-1}, 418.57 cm^{-1}, 428.21 cm^{-1} and 443.64 cm^{-1} in Figure 3(a-c) were possibly caused by the stretching vibration due to the interactions produced between the oxygen and metal bonds. The broad band's at 873.78 cm^{-1} in Figure 3(a) and (b) were both assigned to the symmetric stretching of C-H bands in aromatic functional group. The bands at 1161.19 cm^{-1}, 1168.90 cm^{-1}, 1118.75 cm^{-1} and 1068.60 cm^{-1} in Figure 3(a-c) were C-O stretching vibration of carboxylic acid group. The C-H stretching band was occurred at 1442.80 cm^{-1}, 1452.45 cm^{-1}, 1427.37 cm^{-1} and 1413.87 cm^{-1} and 1440.87 cm^{-1} in alkanes functional groups. Another C-H stretching band was also found at 2982.05 cm^{-1} and 2980.12 cm^{-1} of Figure 3(a) and (b) in alkanes group. The O-H stretching band was occurred in alcohol group at 3661.01 cm^{-1} , 3659.09 cm^{-1} and 3641.73 cm^{-1} in Figure 3 (a-c).

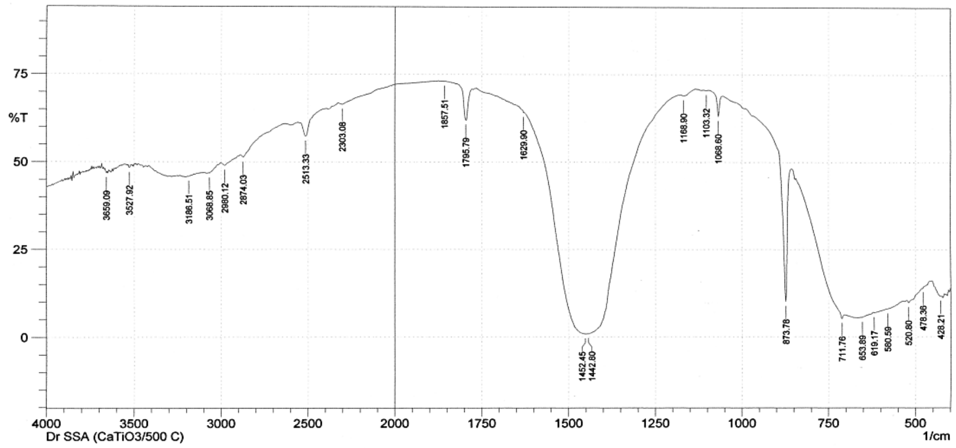

Figure 3 (a) FTIR spectra of $CaTiO_3$powders prepared at 500°C

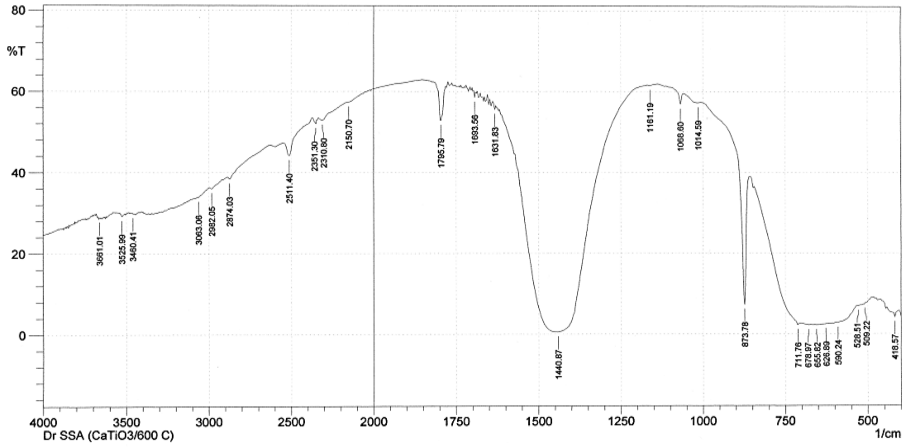

Figure 3(b) FTIR spectra of $CaTiO_3$powders prepared at 600°C

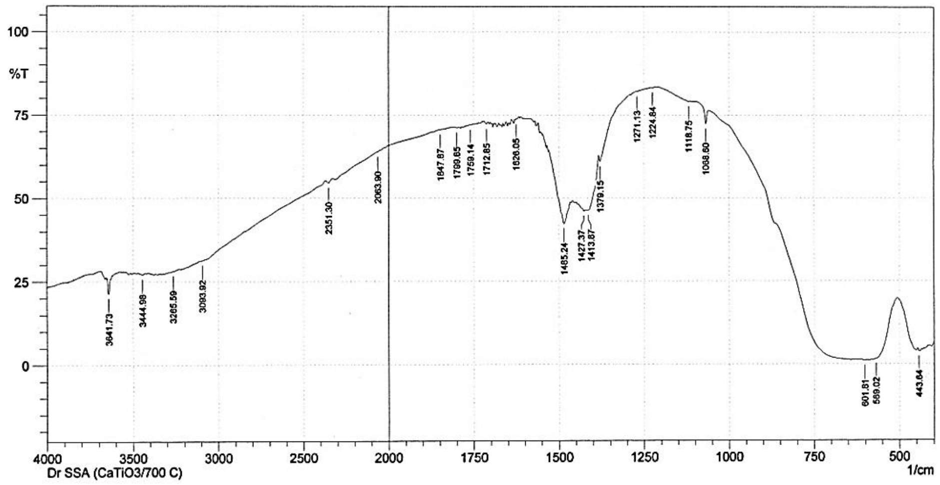

Figure 3 (c) FTIR spectra of $CaTiO_3$powders prepared at 700°C

Conclusion

Calcium titanate ($CaTiO_3$) powders have been successfully synthesized by co-precipitation method, its surface morphology and structural properties have been studied. From this studied, the desire phase and crystalline size was obtained at 700 °C calcinations temperature. The XRD analysis showed that, as the temperature increase, the intensity of the peaks were clear and sharp. As a result, XRD analysis confirmed that the formation of pure $CaTiO_3$ powders with perovskite structure. The SEM result showed that the higher the calcinations temperature, the greater the grain size due to solid-grain diffusion. According to FTIR analysis, all temperatures of $CaTiO_3$ is suitable for their absorption band due to C-H bands in aromatic functional group, O-H stretching band in alcohol functional group and C-O stretching vibration of carboxylic acid group. According to the experimental results, $CaTiO_3$ powder can be used in photovoltaic and thin films applications.

Acknowledgement

I would like to express my sincere thanks to Professor Dr Khin Khin Win, Head of the Department of Physics, University of Yangon for her kind encouragement and permission to perform this research work.

I would like to thank Professor Dr Aye Aye Thant, Professor Dr Myo Lwin, Professor Dr Yin Maung Maung, Professor Dr Than Zaw Oo, Department of Physics, University of Yangon, for their kind advice and suggestions for this research.

References

Chenguo Hu, Yi Xi, Hong Liu, Zhong Lin Wang, J. Mater. Chem.,(2009), 19, 358

Gmelines Handbook of Inorganic Chemistry, Leipzig, (1951), Vol. 41-42

G. Pfaff, Synthesis of calcium titanate powders by sol-gel process, Chem. Maters. 6 (1994) 58-62

G.Z Wang, R. Saeterli, P. M. Rorvik, A. T. J. van Helvoort, R. Holmestad, T. Grande and M. A. Einarsrud, Chem. Mater., (2007),19 (9), 2213-2221

H. Liu, C. G. Hu and Z. L. Wang, WanoLett.,(2006), 6, 1535.

H. F. Kay, P.C. Bailey, Structure and properties of $CaTiO_3$, ActaCryst. 10 (1957) 219-226

Jing Miao, Chenguo Hu, Hong Liu, Yu fengXiong, Materials Letters, (2008), 62, 235

M. Dawber K.M.Rabe and J.F. Scott, *Rev. Mod*. Phys.,(2005),77 (4), 1083-1130

Petrovic, Vera " Synthesis of calcium titanate ($CaTiO_3$)"

S. Redfern, " J. Phys. Condens. Matter", (1996), Vol.8, pp. 8267-8275

Szafraniak I, Polomska M, Hilczer B. XRD, TEM, and Raman scattering studies of $PbTiO_3$nanopowders Crystal Research and Technology. (2006); 41: 576-9

X. Zhang, J. Zhang, X. Ren, X. –J. Wang, The dependence of persistent phosphorescence on annealing temperatures in $CaTiO_3$: Pr3+ nanoparticles prepared by a co-precipitation technique, J. Solid State Chem. 181 (2008) 353-398

YahongXie, Shu Tin, Takatoshi Hashimoto, Yuichi Tokano, Journal of the European Creamic Society (2010), 30, 699

J. Myanmar Acad. Arts Sci. 2020 **Vol. XVIII.No.2B**

COMPARISON OF NEUTRON ELASTIC DIFFERENTIAL CROSS-SECTIONS FOR ^{60}Ni WITH INCIDENT ENERGIES 4.34 MeV, 4.92 MeV, 6.44 MeV AND 7.54 MeV

Khin Nyein Chan[1], Aung Kyi Myint[2]

Abstract

The neutron elastic differential cross-sections for ^{60}Ni with incident energies 4.34 MeV, 4.92 MeV, 6.44 MeV and 7.54 MeV are calculated by using SCAT2 computer code. Five optical model potential parameter sets for neutron reactions, Wilmore Hodgson, Bechetti Grenless, Ferer Rapaport, Bersillon Cindro and Madland are used to calculate the require elastic differential cross-sections. Experimental elastic differential cross-section data are obtained from EXFOR experimental nuclear reaction data Library. Comparisons of calculated and experimental elastic differential cross-sections for different optical model potential parameter sets are made in each incident neutron energy. The best fit optical model potential parameter sets for the reactions in accordance with experimental results are also discussed.

Keywords: Optical Model, Potential Parameter Set, Elastic Differential Cross-sections, Computer Code, Potential Depth Parameters, Form Factors

Introduction

There are many different models, which explain nuclear reactions. But the most well known models used in research works are optical, statistical and pre-equilibrium models. The present work concerns with optical model. In optical model, the nuclear potential is taken to be complex to describe absorption of particles by the nucleus. This is similar to physical optics where the refractive index is taken to be complex to describe absorption of light by translucent materials. Some part of wave can be reflected from the surface, some part can be absorbed inside the nucleus, and some part can be transmitted through the nucleus. Due to the similarity between nucleus and translucent material, the term "Optical Model" has been applied. There are two types of optical potential namely deformed and spherical potential. Deformed potential should be used for the nuclei in the region $40 \leq N \leq 112$ and $Z \leq 88$ due to their large spin values. For medium nuclei, $N \leq 34$ and $Z \leq 30$, it requires only to consider spherical optical potential. A spherical optical potential may consist of many adjustable parameters and one suitable set of these parameters can be called a set of parameterization [Enge H A, (1975)].

Spherical Optical Model

The spherical optical potential is generally written as

$$U(r) = V_c(r) - V_r f(r) - i[-4W_D g(r) + W_V f(r) + W_D' g'(r)] + \vec{\ell}.\vec{s} C_{so} V_{so} h(r)$$

where the six terms represent a Coulomb potential, a real volume potential, an imaginary surface potential, an imaginary volume potential, a second form of imaginary surface potential and a spin-orbit potential respectively. f(r), g(r), g'(r) and h(r) are the form factors. Five potential terms except Coulomb potential are adjustable in accordance with experiments.

---

[1] Dr, Assistant Lecturer, Department of Physics, University of Yangon

[2] Dr, Associate Professor, Department of Physics, Yangon University of Distance Education

Optical Model Parameterizations

The adjustable values of optical model potential are called optical model parameters. V_r, W_D, W_V, W'_D and V_{so} are called depth parameters and their values may depend on charge and mass of target nucleus and incident energy.

The reduced radius, r_i and diffuseness or surface thickness, a_i, ($i = 1 \rightarrow 4$) are called geometric parameters which specify from factors of each potential. They may also have charge, mass and energy dependent values. a_i cause an effect on the slope of form factor. It is evident that a_i is less than r_i for the respective pair.

One of the long-standing tasks in the field of nuclear data evaluation is the search for a unique set of optical potential parameters, which can accurately describe as much experimental data as possible in wide regions of neutron energies and nuclear masses [Blatt J M, and V F Weiskoff, (1952)].

Angular Distributions for Neutrons

The shape elastic angular distribution is

$$\frac{d\sigma_{\mathrm{E}}}{\mathrm{d}\omega} = |A(\theta)|^2 + |B(\theta)|^2$$

$$A(\theta) = \frac{i}{2k}\sum_{\ell=0}^{\infty}[(\ell+1)(1-\eta_\ell^+) + \ell(1-\eta_\ell^-)]P_\ell(\cos\theta)$$

$$B(\theta) = \frac{-i}{2k}\sum_{\ell=0}^{\infty}(\eta_\ell^+ - \eta_\ell^-)]P_\ell^1(\cos\theta)$$

where the incident energy is expressed in MeV, the total cross section in barns and the differential cross section in barns/steradian [Kaplan I, (1962)].

The SCAT2 Computer Code

The first version of spherical optical model code SCAT 2 is created in 1977 in order to produce evaluated nuclear data files. New 1991 version of SCAT 2 program includes 19 subroutines.

Input part of the program includes physical system: charge and mass of incident particle and target nucleus and optical model potential parameters [Bersillon O, (1992)].

Application of the Code

The SCAT2 computer code uses two input files and four output files. The first input file is a collection of the five file names of second input file and the four output files that we have named particularly. The name of this first file is SCAT2.DAT in PC version. We need to describe the names of five following files in SCAT2.DAT.

1. The input data file
2. The output (listing) file
3. The transmission coefficient file
4. The temporary file
5. The summary file

The usual extension names of these files are *.dat, *.lst, *.gna, *.scr and *.sum.

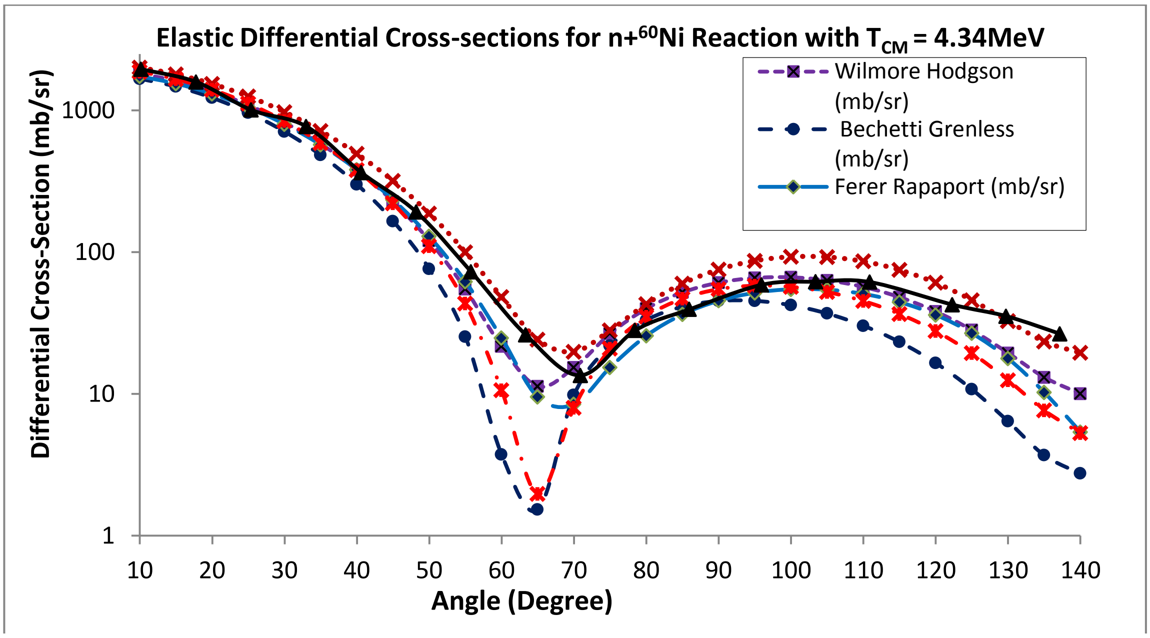

Figure 1 Elastic Differential Cross-sections for n+^{60}Ni Reaction with T(CM) = 4.34MeV

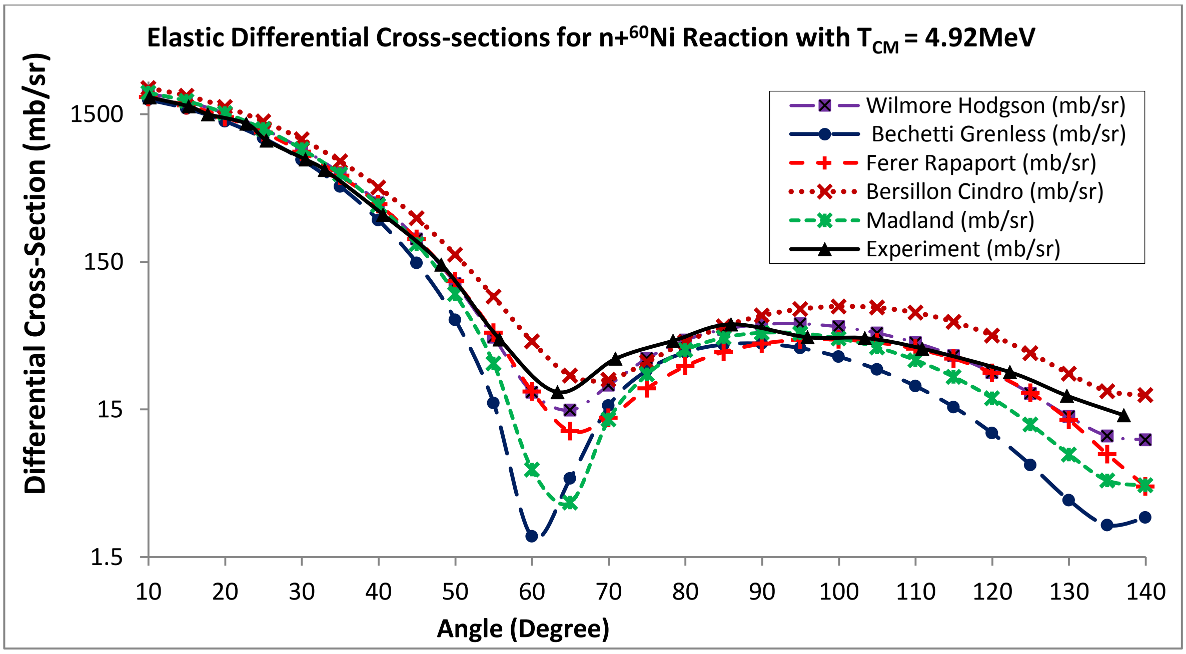

Figure 2 Elastic Differential Cross-sections for n+^{60}Ni Reaction with T(CM) = 4.92MeV

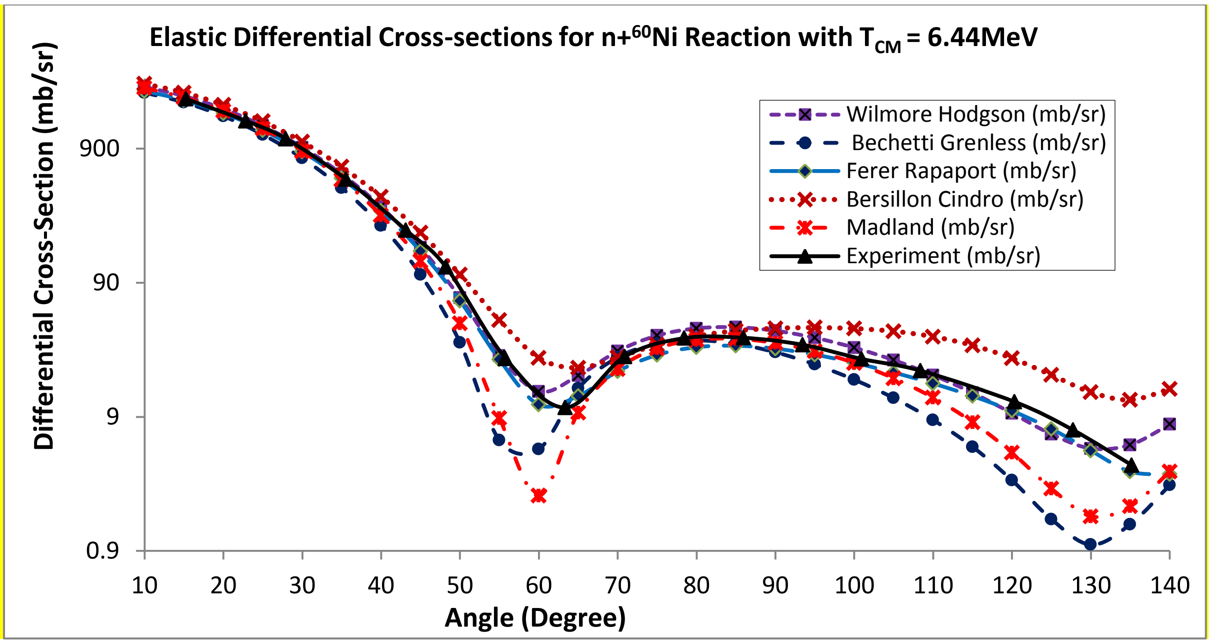

Figure 3 Elastic Differential Cross-sections for n+^{60}Ni Reaction with T(CM) = 6.44 MeV

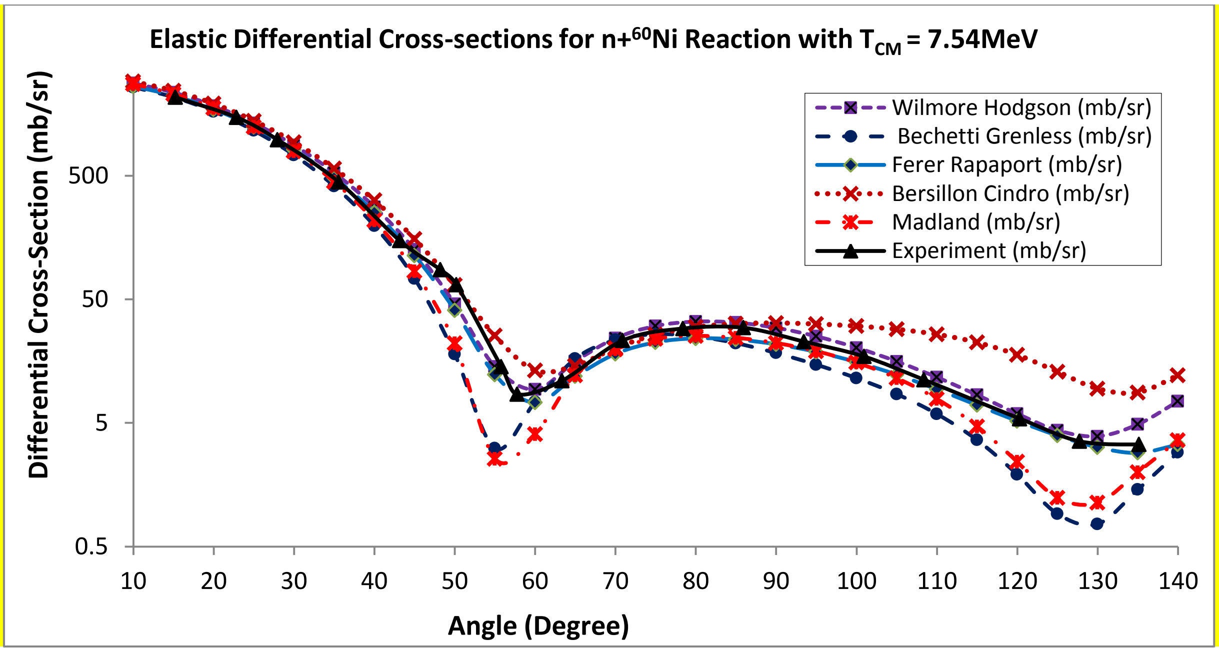

Figure 4 Elastic Differential Cross-sections for n+^{60}Ni Reaction with T(CM) = 7.54 MeV

Results and Discussion

For the reaction with incident neutron energy 4.34 MeV calculated elastic differential cross-sections obtained from Ferer Rapaport optical model potential parameters set are the most consistent with experimental elastic differential cross-sections. Calculated elastic differential cross-sections that are the second most consistent with experimental elastic differential cross-sections are those obtained from Wilmore Hodgson optical model potential parameters set. Third most consistent with experimental results are the results obtained from Bersillon Cindro optical model potential parameters set.

For the reaction with incident neutron energy 4.92 MeV calculated elastic differential cross-sections obtained from Wilmore Hodgson optical model potential parameters set are the most consistent with experimental elastic differential cross-sections. Calculated elastic differential cross-sections that are the second most consistent with experimental elastic differential cross-sections are those obtained from Ferer Rapaport optical model potential parameters set. The results obtained from Bersillon Cindro optical model potential parameters set are the third most consistent with experimental results.

Similar to the first case, calculated elastic differential cross-sections obtained from Ferer Rapaport optical model potential parameters set are the most consistent with experimental elastic differential cross-sections for the reaction with incident neutron energy 6.44 MeV. Calculated elastic differential cross-sections that are the second most consistent with experimental elastic differential cross-sections are those obtained from Wilmore Hodgson optical model potential parameters set. The results obtained from Bersillon Cindro optical model potential parameters set are the third most consistent with experimental results.

Similar to incident neutron energy 4.92 MeV, it was also found that the calculated elastic differential cross-sections obtained from Wilmore Hodgson optical model potential parameters set are the most consistent with experimental elastic differential cross-sections for the reaction with incident neutron energy 7.54 MeV. Calculated elastic differential cross-sections that are the second most consistent with experimental elastic differential cross-sections are those obtained from Ferer Rapaport optical model potential parameters set. The results obtained from Bersillon Cindro optical model potential parameters set are the third most consistent with experimental results.

Conclusion

For all four cases of incident neutron energies, it was found that the results obtained from Ferer Rapaport optical model potential parameters set are the most consistent with experimental results and the results obtained from Wilmore Hodgson optical model potential parameters set are the second most consistent with experimental results. Most of the calculated and experimental elastic differential cross-sections are nearly equal for scattering angles below 45 degree. Differences in calculated and experimental elastic differential cross-sections can be seen in scattering angles above 45 degree. For further research, calculations of reaction cross-sections, scattering cross-sections and total cross-sections for this reaction in different range of incident neutron energies should be made by using Ferer Rapaport optical model potential parameters set.

Acknowledgements

I would like to thank Dr Khin Khin Win, Professor and Head, Department of Physics, University of Yangon for her kind permission to carry out this research.

I would like to express my sincere thanks to all of Professors, University of Yangon, for their suggestion and comments for this work. We would like to thank all the people who encourage and support me during the undertaking of this work.

References

Aung Kyi Myint, (2004), *Optical Model Parameter Generator*, PhD Thesis, Yangon University, Myanmar

Bersillon O, (1988), "The Computer Code SCAT2", (Vienna : IAEA)

Bersillon O, (1992), "Optical Model Calculations and Use of the Computer Code SCAT2", (Vienna : IAEA)

Blatt J M, and V F Weiskoff, (1952), *Theoretical Nuclear Physics*, (New York : Wiley)

Enge H A, (1975), *Introduction to Nuclear Physics*, (Sydney : Addison-Wesley)

Grimes S M, (1992), "Nuclear Reaction Theory", (Vienna : IAEA)

Kaplan I, (1962), *Nuclear Physics*, (Sydney : Addison-Wesley)

Preston M A, (1965), *Physics of Nucleus*, (Sydney : Addison-Wesley)

http://www.nea.fr/html/dbdata

http://www.nea.fr/dbdata/x4/